Transactions of the ASME®

Technical Editor, **T. H. OKIISHI (1998)**
Associate Technical Editors
Aeromechanical Interaction
R. E. KIELB (1996)
Gas Turbine
C. J. RUSSO (1995)
Heat Transfer
M. G. DUNN (1996)
Nuclear Engineering
H. H. CHUNG (1996)
Power
P. H. GILSON (1996)
Turbomachinery
N. A. CUMPSTY (1995)

BOARD ON COMMUNICATIONS
Chairman and Vice-President
R. MATES

Members-at-Large
T. BARLOW, N. H. CHAO, A. ERDMAN, G. JOHNSON, L. KEER, E. M. PATTON, S. PATULSKI, S. ROHDE, R. SHAH, F. WHITE, J. WHITEHEAD, K. T. YANG

OFFICERS OF THE ASME
President, **D. T. KOENIG**
Executive Director
D. L. BELDEN
Treasurer
R. A. BENNETT

PUBLISHING STAFF
Managing Director, Engineering
CHARLES W. BEARDSLEY
Director, Technical Publishing
JANET M. WEINRIB
Managing Editor, Technical Publishing
CYNTHIA B. CLARK
Managing Editor, Transactions
CORNELIA MONAHAN
Senior Production Editor,
VALERIE WINTERS
Production Assistant,
MARISOL ANDINO

Transactions of the ASME, Journal of Turbomachinery (ISSN 0889-504X) is published quarterly (Jan., Apr., July, Oct.) for $150.00 per year by The American Society of Mechanical Engineers, 345 East 47th Street, New York, NY 10017. Second class postage paid at New York, NY and additional mailing offices. POSTMASTER: Send address changes to Transactions of the ASME, Journal of Turbomachinery, c/o THE AMERICAN SOCIETY OF MECHANICAL ENGINEERS, 22 Law Drive, Box 2300, Fairfield, NJ 07007-2300.
CHANGES OF ADDRESS must be received at Society headquarters seven weeks before they are to be effective. Please send old label and new address.
PRICES: To members, $40.00, annually; to nonmembers, $150.00.
Add $24.00 for postage to countries outside the United States and Canada.
STATEMENT from By-Laws. The Society shall not be responsible for statements or opinions advanced in papers or ... printed in its publications (B7.1, Par. 3).

INDEXED by Applied Mechanics Reviews and Engineering Information, Inc.
Canadian Goods & Services Tax Registration #126148048

Journal of Turbomachinery

Published Quarterly by The American Society of Mechanical Engineers

VOLUME 117 • NUMBER 4 • OCTOBER 1995

TECHNICAL PAPERS

(Contents continued on page 513)

(Contents continued)

TECHNICAL BRIEF

ANNOUNCEMENTS

The Effect of Adding Roughness and Thickness to a Transonic Axial Compressor Rotor

K. L. Suder

R. V. Chima

A. J. Strazisar

NASA-Lewis Research Center,
Cleveland, OH 44135

W. B. Roberts

Flow Application Research and Sermatech International Inc.,
Fremont, CA 94539

The performance deterioration of a high-speed axial compressor rotor due to surface roughness and airfoil thickness variations is reported. A 0.025 mm (0.001 in.) thick rough coating with a surface finish of 2.54–3.18 rms μm (100–125 rms μin.) is applied to the pressure and suction surface of the rotor blades. Coating both surfaces increases the leading edge thickness by 10 percent at the hub and 20 percent at the tip. Application of this coating results in a loss in efficiency of 6 points and a 9 percent reduction in the pressure ratio across the rotor at an operating condition near the design point. To separate the effects of thickness and roughness, a smooth coating of equal thickness is also applied to the blade. The smooth coating surface finish is 0.254–0.508 rms μm (10–20 rms μin.), compared to the bare metal blade surface finish of 0.508 rms μm (20 rms μin.). The smooth coating results in approximately half of the performance deterioration found from the rough coating. Both coatings are then applied to different portions of the blade surface to determine which portions of the airfoil are most sensitive to thickness/roughness variations. Aerodynamic performance measurements are presented for a number of coating configurations at 60, 80, and 100 percent of design speed. The results indicate that thickness/roughness over the first 2 percent of blade chord accounts for virtually all of the observed performance degradation for the smooth coating, compared to about 70 percent of the observed performance degradation for the rough coating. The performance deterioration is investigated in more detail at design speed using laser anemometer measurements as well as predictions generated by a quasi-three-dimensional Navier–Stokes flow solver, which includes a surface roughness model. Measurements and analysis are performed on the baseline blade and the full-coverage smooth and rough coatings. The results indicate that adding roughness at the blade leading edge causes a thickening of the blade boundary layers. The interaction between the rotor passage shock and the thickened suction surface boundary layer then results in an increase in blockage, which reduces the diffusion level in the rear half of the blade passage, thus reducing the aerodynamic performance of the rotor.

Introduction

Industries that use gas turbine engines have a continuing need for data on in-service performance loss due to component deterioration. This need is especially great in the airline industry, for which fuel burn and performance retention in high bypass ratio turbofan engines is a major concern. The single component of a high-bypass engine that absorbs the greatest amount of energy and accounts for the greatest fuel burn is the transonic fan. Furthermore, fan blades suffer the most rapid erosion and surface roughening due to lower-atmosphere particulates and runway debris. If the performance effects of fan blade in-service deterioration can be quantified, cost-effective repair strategies and replacement intervals can be deduced (see the technical note by Roberts in this issue). In addition, understanding of the mechanisms by which blade deterioration degrades performance may allow manufacturers to develop design and manufacturing strategies aimed at minimizing long-term performance deterioration.

Engine component deterioration and overall loss in performance have been documented by a number of investigators, including Sallee et al. (1978), Kramer et al. (1980), Covey et al. (1978), and the DOE/FAA Symposium (1981). Since turbomachinery blading performance loss is generally attributed to increased surface roughness as well as particulate impact damage to blade leading edges, a number of investigators have studied the effect of surface roughness on blading performance. The effects of roughness on turbine aerodynamic performance have been investigated experimentally by Roelke and Haas (1983) and Boynton et al. (1993). Boyle (1994) recently predicted the efficiency loss due to roughness measured by Boynton by using a quasi-three-dimensional Navier–Stokes analysis in which he augmented a mixing length model to account for the effects of surface roughness. The effect of roughness on compressor blade aerodynamic performance was reported by Moses and Serovy (1951), who documented the performance changes that resulted from polishing an initially rough blade. Reid and Urasek (1973) investigated the effect of leading edge thickness by documenting the change in performance of a transonic axial-flow fan as a result of cutting back the rotor leading edge. While documenting that roughness and leading edge thickness have an impact on the aerodynamic performance of turbomachinery blading, these previous investigations have not provided a definitive explanation of the mechanism through which roughness impacts performance.

The present investigation was triggered by the application of a special antireflective paint to a transonic compressor rotor. The paint derived its antireflective properties from the presence of small silica particles embedded in the paint, which create a rough surface that diffuses rather than reflects incident light. The paint was applied during the laser anemometer investigation

Contributed by the International Gas Turbine Institute and presented at the 39th International Gas Turbine and Aeroengine Congress and Exposition, The Hague, The Netherlands, June 13–16, 1994. Manuscript received by the International Gas Turbine Institute March 2, 1994. Paper No. 94-GT-339. Associate Technical Editor: E. M. Greitzer.

of the rotor flow field reported by Suder and Celestina (1994) in an attempt to suppress laser light reflections from the blading. However, the painted rotor suffered a significant deterioration in performance, with pressure ratio dropping by 9 percent and efficiency dropping by 6 points at an operating condition near the design point. When the paint was removed, the aerodynamic performance returned to its previous level. As a result, the anemometer optics and electronics were modified to reject light reflected from the blading, and the paint was not used by Suder and Celestina while acquiring laser anemometer measurements.

Comparison of surface finish measurements from the painted test rotor and a typical aircraft gas turbine engine fan blade prior to blade refurbishment showed that the antireflective paint provided roughness levels that were a reasonable model of in-service roughness levels. Therefore, at the conclusion of the previous test program, the paint was once again applied to the rotor to study the effects of roughness on performance deterioration.

Figure 1 shows a comparison of the fan blade leading edge and the test rotor leading edge with the rough paint applied. There are two important differences between the in-service damage observed on the engine fan blade and the roughness applied to the research rotor in this experiment. First, the fan blade leading edge is visibly pitted due to particle impact, as can be seen in Fig. 1(*b*), while the research rotor leading edge is not pitted. The coatings applied to the research rotor were much softer than the blade itself and did suffer impact damage at the leading edge during testing. However, we did not measure nor did we attempt to control the level of this impact damage. Second, in-service damage generates surface roughness by removing material from the blade, but in this investigation we are creating surface roughness by adding material to the blade. In drawing conclusions on in-service performance deterioration based on the results presented herein, one must therefore assume that performance deterioration is dependent on the roughness level but is independent of how the roughness was created.

Both smooth and rough paint coatings were applied to the entire blade surface in an attempt to separate the effects due to adding thickness to the blade from those due to adding surface roughness to the blade. Both coatings were then applied to different portions of the blade surface to determine which portions of the airfoil were most sensitive to thickness/roughness variations. Aerodynamic performance measurements are presented for a number of smooth and rough coating configurations at 60, 80, and 100 percent of design speed to quantify the performance sensitivity to thickness and roughness variations over a wide range of operating conditions.

The largest degradation in performance occurred at the design speed operating condition when the entire blade surface was coated. As a result, the baseline (bare metal) rotor, full-coverage smooth coating, and full-coverage rough coating cases were selected for further investigation. Detailed laser fringe anemometer (LFA) measurements were acquired at design speed for these three cases. LFA measurements were acquired upstream, within, and downstream of the blade.

Flow field predictions generated with a quasi-three-dimensional Navier–Stokes flow solver were used to complement the LFA measurements by providing insight into the flow development in regions near the blade leading edge and near the blade surface where LFA data could not be acquired. The viscous analysis code featured a **C**-grid for accurate resolution of the

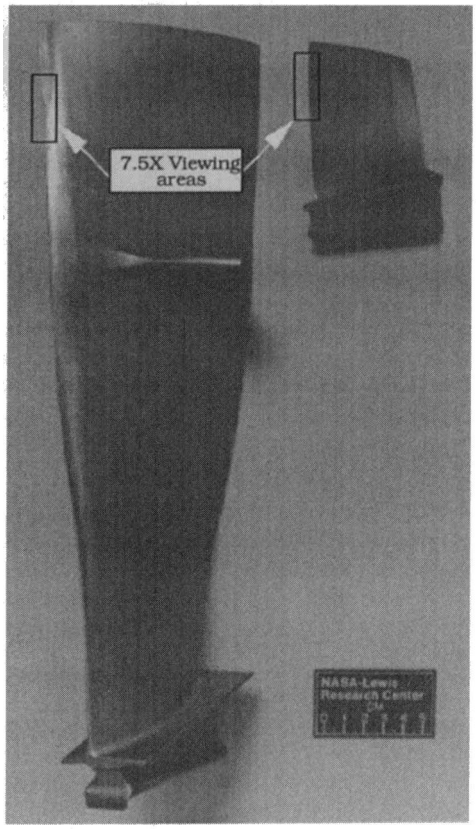

Fig. 1(*a*) Comparison between engine fan blade and the research rotor blade

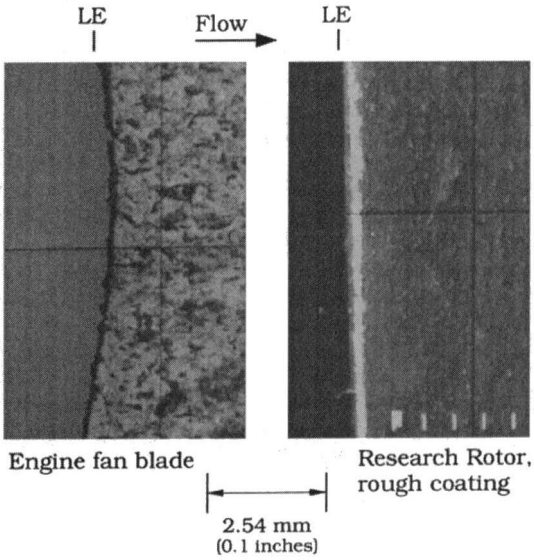

Fig. 1(*b*) 7.5× view of fan blade and coated research rotor leading edges

Nomenclature

H = total enthalpy
$\dot{m}$ = massflow rate, kg/s
M_{rel} = relative Mach number
P_4 = total pressure at Station 4; see Fig. 2
PR = total pressure ratio
P_{ref} = standard-day total pressure = 101,325 n/m^2
ps = denotes pressure surface
r = radius, m
ss = denotes suction surface
T_4 = total temperature at Station 4; see Fig. 2
T_{ref} = standard day total temperature, 288.2 K

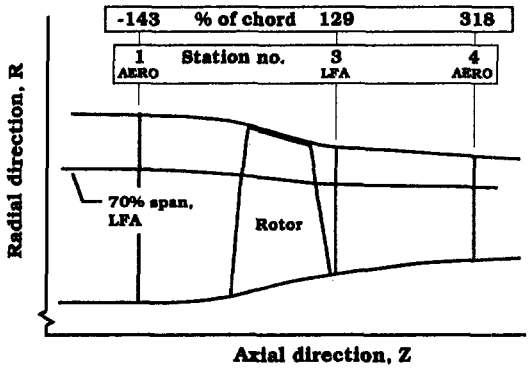

Fig. 2 Laser anemometer and aerodynamic survey stations

leading edge region and included a surface roughness model. Analysis was performed on the baseline blade, on a blade profile with added thickness with and without added roughness, and on a blade profile with a noncircular leading edge.

Test Compressor

The test compressor for the present study is a low-aspect-ratio transonic core compressor inlet stage, designated NASA Stage 37. The results reported here were obtained from a rotor-only configuration with the stator removed. This configuration eliminates blade row interactions and thus allows comparison of the measurements with numerical predictions based on circumferentially uniform upstream and downstream conditions.

The rotor design pressure ratio is 2.106 at a mass flow of 20.19 kg/s. The inlet relative Mach number is 1.13 at the hub and 1.48 at the tip at the design tip speed of 454 m/s. The rotor aspect ratio is 1.19 and the hub/tip radius ratio is 0.70. The rotor tip clearance at design speed is 0.40 mm (0.016 in.), which corresponds to 0.7 percent of chord. Details of the rotor aerodynamic design were reported by Reid and Moore (1978). Overall aerodynamic performance of the stage was reported by Moore and Reid (1980).

Instrumentation and Measurement Techniques

Massflow is measured using a calibrated orifice located far upstream of the compressor. The orifice measurements are corrected to standard-day conditions at the rotor inlet. Radial distributions of total and static pressure, total temperature, and flow angle are measured at stations 1 and 4 shown in Fig. 2. Stage 37 is a close-coupled stage, and there is not sufficient space for a survey station between the rotor and stator. Since additional survey stations were not added in the present work, Station 4, which is normally used to survey the stator outlet flow, is the first available aerodynamic survey station downstream of the rotor. The measurement uncertainties are: massflow, ±0.3 kg/s; flow angle, ±0.5 deg; total pressure, ±0.01 N/cm^2; total temperature, ±0.6 K. The probe measurements are corrected for Mach number and streamline slope based on a calibration of each probe used and on the design streamline slope. All measurements are corrected to sea-level standard-day conditions at the rotor inlet. Radial distributions of total temperature are mass averaged across the annulus. Radial distributions of total pressure are energy averaged by converting them to their enthalpy equivalents and then mass averaging them across the annulus.

A laser fringe anemometer system (LFA) is used to obtain detailed flow field velocity measurements. This instrument is a two-channel system configured to provide simultaneous measurements of the axial and tangential velocity components. Optical access to the compressor is provided by a 2.5-mm-thick glass window, which conforms to the shroud contour, thus preserving the proper tip clearance over the rotor. Polystyrene latex seed particles are injected into the flow field far upstream of the test compressor to enable LFA measurements. These particles are manufactured using the process developed by Nichols (1987) and their size is determined using scanning electron microscope (SEM) photographs. The range of particle sizes used in the present investigation is 0.7–0.9 μm. The SEM photographs indicate that although the particle size varies within this range between batches, the size within a given batch is uniform to within 0.1 μm. Particle batches were not mixed during research runs. Therefore, all LFA data were acquired with uniformly sized particles, although the mean particle size varied between 0.7–0.9 μm. The error in the LFA measurements is approximately 1 m/s for absolute velocity and 0.5 deg for absolute flow angle and is independent of the particle size over the size range used. Further details concerning the LFA system and measurement technique are reported by Suder and Celestina (1994).

LFA data were acquired from hub to tip downstream of the rotor at Station 3, shown in Fig. 2, to provide an assessment of roughness/thickness effects at a location close to the rotor trailing edge. LFA data was also acquired on the blade-to-blade streamsurface at 70 percent span shown in Fig. 2. The choice of the 70 percent span location was driven by several factors. First, aerodynamic performance measurements acquired for the coated blade indicated that at design speed the degradation in pressure and temperature rise was largest near the tip of the blade. Second, previous LFA data acquired in this rotor indicated the tip clearance flow penetrates to at least 90 percent span, causing a steep gradient in flow properties across the outer 10 percent of blade span. Finally, LFA data had already been acquired for the baseline blade at 70 percent span during previous testing of this rotor. The 70 percent span streamsurface was therefore chosen as a compromise between our desire to survey the flow field near the tip of the blade and our desire to survey the flow field at a spanwise location at which radial gradients in flow properties were not too strong.

Measurements within the blade passage were acquired at axial intervals of 5 percent chord. At each axial/radial measurement location, data were acquired across all 36 blade passages at a circumferential resolution of 184 points across one blade pitch. All LFA results presented in this paper represent the flow field within an averaged blade passage, which was calculated by ensemble-averaging the measurements acquired in each individual blade passage.

The relative Mach number is calculated from the relative velocity and the local speed of sound at each point in the flow field using the procedure discussed by Strazisar et al. (1989). All Mach numbers presented in this report are "two-dimensional" Mach numbers in that they are calculated ignoring the radial velocity component, which cannot be measured by the LFA system. Suder and Celestina (1994) have calculated the Mach numbers in rotor 37 with and without the radial velocity component using a three-dimensional Navier–Stokes flow field solution and found that ignoring the radial velocity component led to a maximum error of 2 percent in relative Mach number.

Experimental Procedure

Coating Application and Inspection. All coatings used in this investigation were applied to the blade surface with a brush using spanwise brush strokes, which provided a uniform coating thickness around the blade leading edge. Chordwise brush strokes were not used since they tended to scrape paint from the brush onto the leading edge, resulting in poor control of the coating thickness at the leading edge. When only part of the blade was coated, a template was used to insure that all blades were painted over a given chordwise area from hub to tip. A flat aluminum plate was coated with the same paint using the same brush that was used on the blades and the paint film

Table 1 Comparison of coating thickness as measured by various techniques

Meas. Method	Accuracy mm (in.)	Gauge block paint thickness, mm (inches)		
		Minimum	Maximum	Average
Micrometer	0.005 (0.0002)	0.028 (0.0011)	0.064 (0.0025)	0.046 (0.0018)
Comparator	0.012 (0.0005)	0.041 (0.0016)	0.043 (0.0017)	0.042 (0.0016)
Eyelash machine	0.025 (0.001)	0.025 (0.001)	0.051 (0.002)	0.038 (0.0015)

Table 2 The rms surface finished for engine fan blade and rotor 37 blade

Configuration	RMS surface finish		Equivalent sand roughness Reynolds No.
	microns	μin.	
Rotor 37, baseline blade	0.508	20	93
Rotor 37, smooth coating	0.254–0.508	10-20	47-93
Rotor 37, rough coating	2.54–3.18	100-125	470-580
fan blade, pressure surface	4.31-6.10	170-240	960-1350
fan blade, suction surface	1.14-1.65	45-65	250-370

thickness was measured using a micrometer. The paint thickness on the test plate varied from 0.017 mm (0.0007 in.) to 0.030 mm (0.0012 in.) for both rough and smooth coatings.

At the conclusion of the test program, several blades painted with the rough coating were inspected in an eyelash machine to determine the uniformity of the coating on the actual blades. After inspecting a painted blade, the paint was removed while the blade was mounted in the eyelash machine and the blade was re-inspected, thus providing back-to-back inspections to determine the in-situ coating thickness. The eyelash inspections indicated that the paint film on the blade surface ranged in thickness from 0.013–0.025 mm (0.0005–0.0010 in.). The ability of the eyelash machine to measure the painted blade accurately was assessed by painting a gage block and determining the paint thickness using a micrometer, an optical comparator, and the eyelash machine. The accuracy of each measurement technique and the coating thickness measured with each technique are shown in Table 1.

Note that the average micrometer reading was high compared to that of the comparator and that the eyelash machine was performing at the limits of its resolution. Based on this calibration exercise, the test plate inspections, and the blade eyelash inspections, we conclude that the coating thickness on each surface of the blade was nominally 0.025 mm (0.001 in.) and was certainly no greater than 0.050 mm (0.002 in). A coating thickness of 0.025 mm on the blade pressure and suction surface corresponds to 10 percent of the leading edge thickness at the hub, to 20 percent of the leading edge thickness at the tip, and to only 0.3 percent of the throat width at the blade tip. Furthermore, the amount of thickness added to the blade surfaces by the coatings was well within the overall blade thickness manufacturing tolerance of ±0.125 mm (0.005 in.), and is comparable to the leading edge blade thickness manufacturing tolerance of ±0.050 mm (0.002 in.).

The results of the eyelash inspection for a single blade at 90 percent span coated with rough paint are shown in Fig. 3. A circle of arbitrary diameter has been fit to the blade leading edge simply to help gage the degree to which the leading edge is not circular. For this blade at this radius the coating actually tends to make the leading edge more circular than it is for the bare metal blade. The figure also shows that a relatively sharp shoulder exists for both the smooth and coated blade where the leading edge blends into the suction surface. The impact of such a shoulder on the flow development along the blade was investigated computationally, and the results will be discussed later.

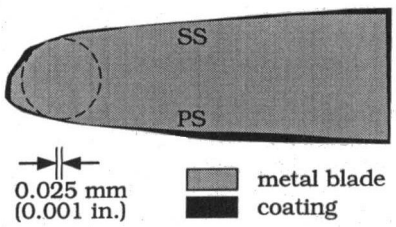

Fig. 3 Eyelash inspection results for a rough-coated blade at 90 percent span; ss = suction surface; ps = pressure surface

The nominal rms surface finishes determined with a profilometer are shown in Table 2. Also listed in the table are surface finish readings from the engine fan blade shown in Fig. 1 and the equivalent roughness Reynolds numbers, calculated following the method of Koch and Smith (1975). According to Koch and Smith, the blade surface is considered hydraulically smooth for roughness Reynolds numbers less than 90.

Aerodynamic Performance Measurements. Aerodynamic performance measurements were acquired for the baseline and fully coated configurations at 60, 80, and 100 percent of design speed. The relative inlet Mach numbers for each speed are given in Table 3. These three speeds were chosen to investigate the correlation between Mach number and performance deterioration due to roughness/thickness. At design speed the relative flow is supersonic from hub to tip. At 80 percent of design speed the relative flow is transonic, which is typical of low hub/tip ratio fans. At 60 percent of design speed, the relative flow is subsonic everywhere, which is more characteristic of middle- and exit-stage core compressor blading.

The coating configurations and the measurements acquired for each configuration are summarized in Table 4. The column labeled "coating configuration" summarizes the area of the suction and pressure surface (denoted as ss and ps respectively), which was coated. For example, case D featured a coating that was applied from 2–10 percent chord on both the pressure and suction surface. Case A corresponds to a single coat of smooth paint, with a nominal thickness of 0.0125 mm (0.0005 in.). The nominal coating thickness for all other cases is 0.025 mm (0.001 in.).

Aerodynamic performance measurements were first acquired for the bare metal rotor at 60, 80, and 100 percent of design speed to establish baseline aerodynamic performance. The blades were then coated over their entire surface with the rough paint (case I) and the aerodynamic measurements were repeated to document performance degradation. The coating was then removed using a solvent and wire brush, and the aerodynamic performance measurements on the bare metal blade were re-

Table 3 Rotor 37 inlet relative Mach numbers

% speed	M_{rel} at hub	M_{rel} at tip
60	0.68	0.89
80	0.90	1.18
100	1.13	1.48

Table 4 Summary of coating configurations and aerodynamic survey conditions

I.D.	Coating configuration		Coating type	Speed surveyed (% design)
	ps (%chord)	ss (%chord)		
A	0-100	0-100	smooth (1/2 thick)	60,80,100
B	0-100	0-100	smooth	60,80,100
C	0-10	0-10	smooth	100
D	2-10	2-10	rough	100
E	- - -	20-30	rough	100
F	2-100	55-100	rough	100
G	0-10	0-10	rough	100
H	0-10	0-50	rough	100
I	0-100	0-100	rough	60,80,100

peated. These measurements agreed with the baseline performance measurements to within measurement accuracy, thus verifying that the process of applying and removing the rough coating had not altered the rotor performance.

By applying a rough coating to the blade we added both thickness and surface roughness to the baseline blade. To separate the effects due to thickness from those due to surface roughness, a smooth coating of polyurethane was applied over the entire blade, thereby adding thickness without adding roughness. It was found that two coats of polyurethane were required to develop a coating thickness equal to that of the rough paint. Aerodynamic performance measurements were obtained at 60, 80, and 100 percent of design speed for both a single coating of polyurethane (case A) and a double coating (case B). At the completion of these measurements the blade was once again cleaned and the baseline aerodynamic performance was once again verified.

To determine which regions of the blade surface contributed most to the observed performance degradation, additional measurements were acquired for a number of partially coated configurations (cases C through H). All partially coated configurations were investigated only at design speed, since the performance degradation at design speed for the fully coated blade was much larger than the degradation observed at part-speed conditions. After measurements were completed on each configuration, the blade was cleaned and the baseline aerodynamic performance was spot-checked for repeatability at several points along the design speed operating line.

Aerodynamic Performance Results

Fully Coated Configurations. The smooth- and rough-coated performance is compared to the baseline performance in Figs. 4 and 5. The data points surrounded by circles in Fig. 4 indicate those points for which detailed radial distributions of flow properties will be discussed later. The results in Fig. 4 raise a question as to whether the degradation scales with tip speed. To address this issue, we normalized the pressure rise with tip speed and plotted this quantity against massflow. The results, which are not shown here, also indicated a significantly larger degradation at design speed than at part-speed conditions. Therefore, neither pressure ratio nor pressure rise scale with tip speed. This indicates that the rotor shock system, which generates much of the pressure rise at design speed, plays an important role in the degradation in pressure rise capability at design speed.

The stall line is not affected by coating the blades, but the maximum massflow achieved by the coated rotor is lower than that of the baseline rotor at all speeds. However, at design speed the highest massflows presented in Fig. 4 correspond to choking

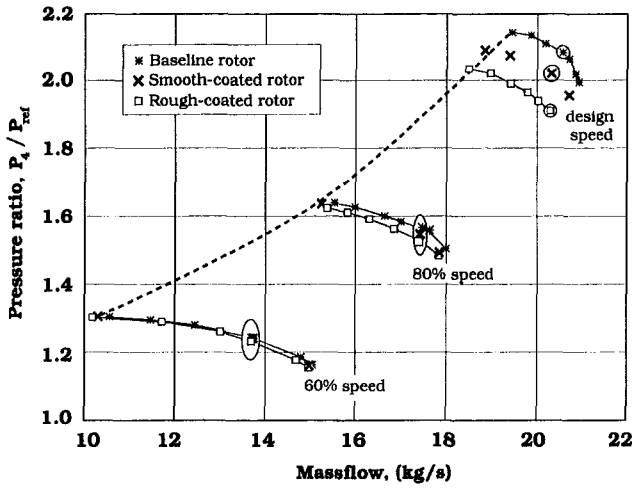

Fig. 4 Pressure rise characteristics for full-coverage coatings; circled points indicate operating conditions for which radial distributions of flow properties are presented

of the facility diffuser located between the rotor and the throttle valve, rather than choking of the rotor itself. Diffuser choke occurred prior to rotor choke because the diffuser was designed to accept the axial outflow of stage 37 rather than the swirling outflow of rotor 37. Subsequent testing with the stator in place, which removes the rotor outlet flow swirl before the flow enters the diffuser, has verified that the isolated rotor configuration was choked at 60 and 80 percent speed but was not choked at design speed.

The results shown in Fig. 5 indicate that for a given massflow the efficiency penalty for the coated rotor configurations is on the order of 1–3 points at 60 percent speed, 0.5–2 points at 80 percent speed, and 2.5 points at design speed. Note that the efficiency penalty at design speed is not much larger than that at 60 percent speed. In addition, the efficiency levels measured for the smooth and rough coatings are nearly identical. This fact suggests that the efficiency is adversely impacted by the addition of thickness alone, and that the surface roughness level used in the present investigation does not have an appreciable impact on efficiency. However, this conclusion is misleading since both the pressure ratio and efficiency are changing.

A clearer view of the efficiency changes at design speed is shown by plotting efficiency against pressure ratio, as shown in Fig. 6. With both efficiency and pressure ratio changing appreciably, it seems appropriate to assess the efficiency penalty

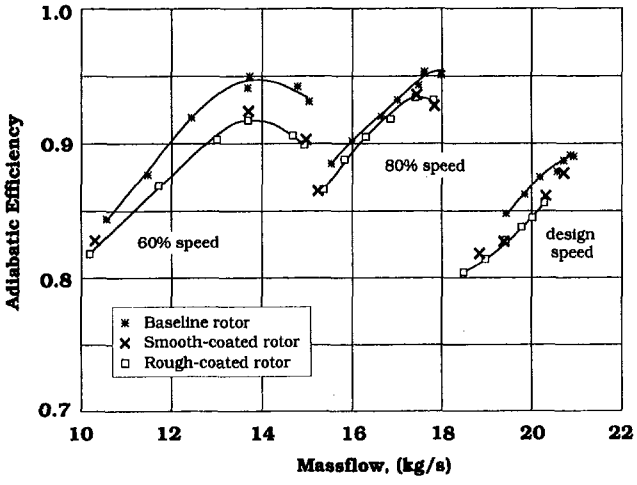

Fig. 5 Efficiency characteristics for full-coverage coatings

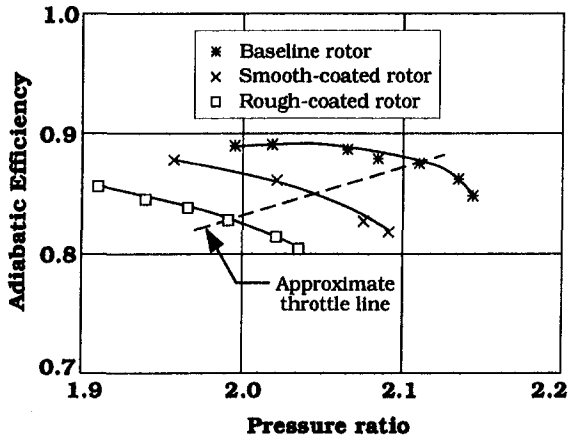

Fig. 6 Efficiency pressure ratio characteristics at design speed

for both a constant pressure rise and a constant throttle resistance. For a constant pressure rise, the efficiency loss is on the order of 2.5–6.5 points for the smooth coating and 6–8.5 points for the rough coating. These loss levels would be experienced in compressor applications that require a constant pressure rise, such as pipeline pumping and stationary power generation. In contrast, aircraft engine fans and compressors operate against a fixed throttle resistance, and the operating point will move along a constant-throttle line as the compressor deteriorates in service. An approximate throttle line is shown in Fig. 6. The efficiency loss along this line is 2.5 points for the smooth coating and 5 points for the rough coating.

Figure 7 illustrates the spanwise variation of pressure ratio, temperature ratio, and adiabatic efficiency for the circled operating points shown in Fig. 4. The massflow chosen for comparison of the baseline and coated configurations at 60 and 80 percent speed corresponds to the peak efficiency massflow for the baseline rotor. At design speed, the massflow chosen corresponds to the maximum massflow achieved by the rough-coated rotor. Note that by comparing the baseline and coated blade performance at a constant massflow for each speed, we are maintaining a constant incidence angle for the performance comparison at a given speed.

The spanwise variation of flow properties measured at 100 percent of design speed is shown in Fig. 7(*a*). Note that for the smooth coating the degradation in pressure ratio is relatively constant below 50 percent span, but then nearly doubles in level between midspan and the tip. Also note that the efficiency penalty for the coated blades only becomes appreciable outboard of 40–60 percent span. Alber et al. (1973) have shown that for $M_{rel} \geq 1.4$, the pressure rise through a normal shock is strong enough to cause boundary layer separation. At design speed, the inlet relative Mach number for Rotor 37 varies from 1.13 at the hub to 1.48 at the tip. However, due to expansion along the suction surface, the Mach number at the face of the passage shock is greater than 1.4 outboard of midspan, and a strong shock/boundary layer interaction is therefore possible over the outer half of the blade span. These facts, coupled with the results shown in Fig. 7(*a*), indicate that the shock boundary layer interaction is an important contributor to the design speed performance degradation. This point is investigated in more detail later in this paper.

The spanwise variation of flow properties at 80 and 60 percent speed is shown in Figs. 7(*b*) and 7(*c*). The rotor shock system is quite weak at 80 percent speed and is only present in the outer half of the span. The performance decrement at part-speed conditions is much smaller than at design speed and more uniform in magnitude across the span. These results suggest that at lower Mach numbers, the coating effect on the blade surface boundary layers is the important flow phenomenon and

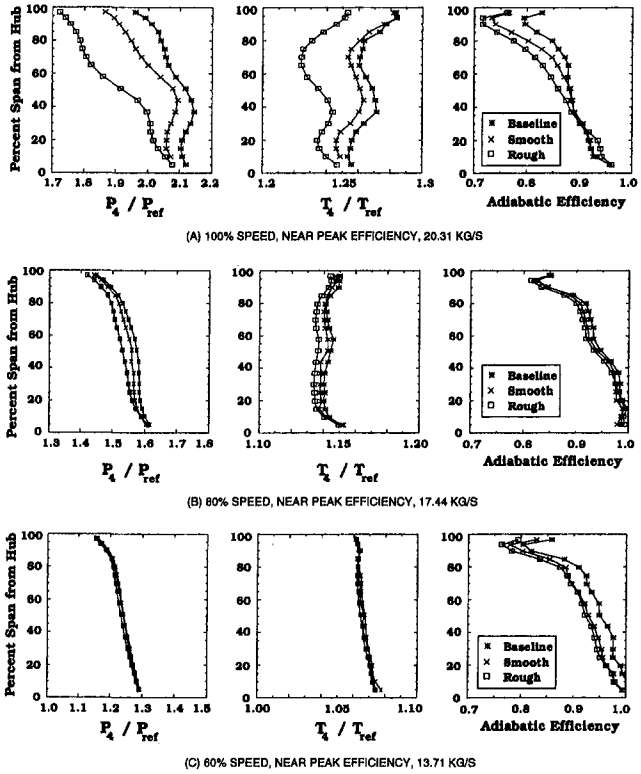

Fig. 7 Radial distributions of pressure ratio, temperature ratio, and efficiency

that this effect is much weaker than the shock/boundary layer interaction effects that occur at design speed.

Partially Coated Configurations. Modern aircraft fans and compressors often operate under supersonic relative flow conditions over part of the blade span. The high Mach number results of the current study are therefore of particular interest. Since the preceding results have shown that the largest deterioration in rotor pressure rise occurs at design speed, we decided to coat various regions of the blade surface with smooth and rough coatings and acquire additional performance measurements at design speed to determine those areas of the blade surface that display the greatest sensitivity to the addition of thickness and roughness.

The results of the partial-coating study are shown in Figs. 8 and 9 for the nine coating configurations listed in Table 4. For

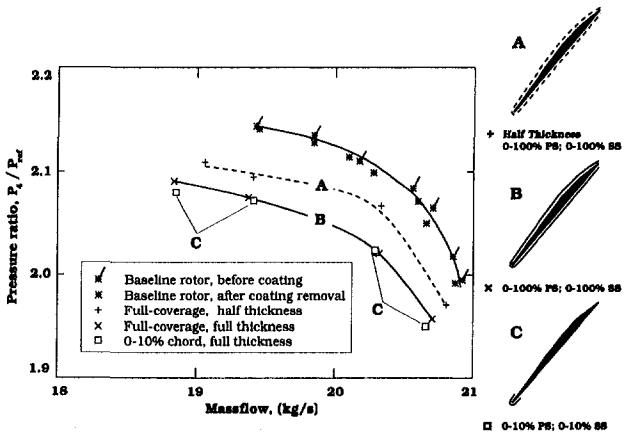

Fig. 8 Pressure rise characteristics for the smooth coatings at design speed

the baseline performance in both figures, the flagged data points were measured before any coatings were applied, while the unflagged points were measured on several different occasions after removal of coatings. The agreement between the flagged and unflagged points indicates that the baseline blade performance was not affected by the continued application and removal of coatings.

The pressure rise characteristics for the smooth-coated configurations A–C are compared to those of the baseline rotor in Fig. 8. Coatings A and B are full-coverage coatings with coating A being only half as thick as all other coatings. Coating C covers only the first 10 percent of blade chord. It can be seen that performance for the half thickness coating falls approximately halfway between that of the baseline and full thickness coating. However, the most dramatic result in Fig. 8 is that the performance deterioration for case C, in which only the leading edge region is coated, is virtually identical to that of case B in which the entire blade is coated. This result indicates that the added blade profile thickness from 10–90 percent chord does not contribute to the performance deterioration observed for Case B.

Figure 9 shows the decrease in design speed pressure ratio for rough coating configurations D–I listed in Table 4. The lowest massflows shown for cases G and H do not reflect the stall massflow—the stall point was simply not determined for these cases. As expected, the full coverage of rough paint, case I, gives the greatest deterioration in performance. This coating was applied on two separate occasions and yielded identical performance characteristics, thereby verifying the repeatability of the hand-application coating process. Case G, in which only the first 10 percent of chord is coated, exhibits approximately 70 percent of the performance degradation of the full roughness coverage. In case H the suction surface is coated up to the point at which the rotor passage shock impinges on the suction surface. Cases G, H, and I together indicate that the addition of roughness to the blade leading edge and the suction surface up to the point of shock impingement accounts for most of the performance degradation seen for the fully coated blade.

Cases D, E, and F all feature partial coatings, which did not cover the leading edge of the blade. Case D is similar to Case G except that the first 2 percent of the blade chord is not coated. Case E represents an attempt to trip the suction surface boundary layer by adding a strip of roughness in the high Mach number region between 20–30 percent chord. This case shows virtually no performance deterioration relative to the baseline blade.

Further discussion of the partial coating results will be easier if we can summarize the information in Figs. 8 and 9 in a single, quantitative format. Figure 10 summarizes the degradation in design speed pressure ratio as a function of the blade surface area covered by the full-thickness smooth and rough coatings. The plot abscissa represents an "unwrapped" blade surface with the blade leading edge at the center. The plot ordinate is the percent reduction in pressure ratio, defined as

$$100 * \frac{(PR)_{\text{baseline}} - PR}{(PR)_{\text{baseline}}}$$

The shaded bars represent the coated areas of the blade surface for each case. The results are shown for a massflow of 20.3 kg/s. This is the highest massflow reached for case I in Fig. 9. It is also the massflow used for the comparisons in Fig. 7, and is near the baseline rotor design point massflow of 20.19 kg/s.

After studying the results shown in Fig. 10 for cases B–I, it became clear to us that coating just the leading edge was an important case that we had not run. We therefore applied the smooth and rough coatings to the leading edge by running a brush along the leading edge. These coatings were applied after a stator had been installed behind the rotor. The stage with the coated rotor leading edge was run at a massflow of 20.3 kg/s, and the results are labeled "stage, le smooth" and "stage, le rough" in Fig. 10.

Figure 10 illustrates the magnitude of the performance degradation at a fixed flow rate while Figs. 8 and 9 illustrate that the level of degradation is not strongly dependent on the flow rate. The following conclusions for the design speed condition can be drawn from these results:

1 There is little performance degradation when the leading edge is left uncoated (Cases D, E, F).
2 Performance degradation is triggered by additional thickness and/or roughness at the leading edge.

- Cases D and G are geometrically similar except that Case D has no coating at the leading edge (0–2 percent chord). Case G exhibits performance degradation while Case D does not, which suggests that the coating on the first 2 percent of chord is the cause of the degradation observed for case G.
- Cases B and C exhibit identical degradation levels even though Case C is uncoated over much of the blade surface.
- The coated leading edge cases run in the stage configuration ("stage, le rough" and "stage, le smooth") display degradation levels that are similar to those of cases C and G (first 10 percent of chord coated) run on the isolated rotor
- Case G (first 10 percent of surface coated) exhibits 70 percent of the degradation level of Case I (entire surface coated).

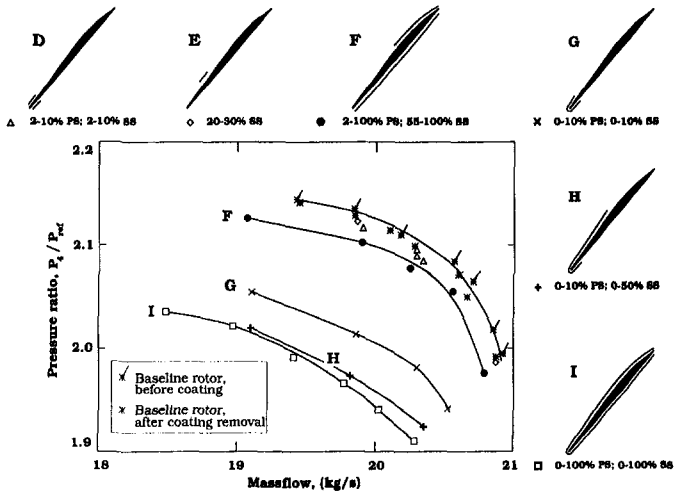

Fig. 9 Pressure rise characteristics for the rough coatings at design speed

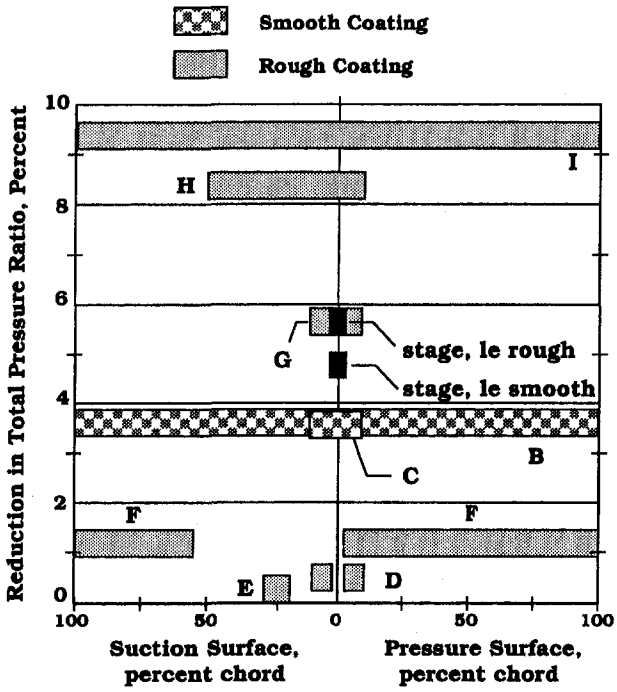

Fig. 10 Pressure ratio degradation as a function of blade surface area covered by smooth and rough coatings at design speed; massflow = 20.3 kg/s

3 Pressure surface roughness has little impact on performance degradation.

- Case F, in which the entire pressure surface was coated, demonstrates little degradation.
- There is little difference in degradation between cases H and I. The pressure surface is completely coated for case I and is uncoated from 10–100 percent chord in Case H.

4 Roughness on the uncovered portion of the suction surface has an impact on performance degradation.

- Cases G and H differ only in the extent of the roughness on the suction surface.

The results shown in Fig. 10 clearly indicate that the leading edge region plays a critical role in the performance degradation and that coating the leading edge results in performance loss. In coating the leading edge we increased its thickness by 10 percent at the hub and by 20 percent at the tip. Both the smooth and rough coatings had a lower surface hardness than the bare metal blade. As a result, coating the blade also increased the roughness at the leading edge because the coated blades suffered particle impact damage at the leading edge during testing that was not suffered by the baseline metal blade. We cannot separate the effects due to increased leading edge thickness from those due to increased leading edge roughness based on the measurements alone. However, the numerical analysis presented later in this paper indicates that the observed performance degradation is *not* a thickness effect.

Laser Anemometer Results

All LFA data reported herein were acquired at design speed for the baseline blade as well as the full-coverage smooth and rough coating configurations (cases B and I) at 70 percent span. The pressure ratio versus massflow characteristics for the 70 percent span streamsurface for these three cases are shown in Fig. 11. The massflow at which LFA data were acquired for each case is shown by the circled symbols. The characteristics are shown for the 70 percent span streamsurface to facilitate comparison to the CFD predictions made on the same streamsurface. The massflow and pressure ratio have been normalized by their respective maximum values for the baseline blade for the same reason.

Spanwise Velocity Distributions. The aerodynamic performance measurements presented above were based on measurements acquired with aerodynamic survey probes at Station 4 (see Fig. 2). Since Station 4 was two rotor chords downstream of the trailing edge, there was some concern that mixing that occurs between the rotor trailing edge and Station 4 might cause the aerodynamic measurements to provide an inaccurate view of the effects of roughness/thickness variations on rotor performance. LFA data were therefore acquired at Station 3, close to the rotor exit, for comparison with the aerodynamic survey measurements obtained far downstream at Station 4. The measured total temperature rise was chosen for this comparison since it is a measure of the work input across the rotor.

The Euler equation for turbomachinery was used to calculate the radial distribution of total temperature at Station 3 from the LFA velocity measurements. Figure 12 is a comparison between the aerodynamic probe measurements at Station 4 and the pitch-averaged total temperature ratios determined from the LFA measurements at Station 3. Comparison of the temperature distributions in Fig. 12 indicates that the temperature changes measured by the aerodynamic survey probes at Station 4 are qualitatively similar to those calculated from the LFA measurements near the trailing edge. In both cases the coatings cause a decrease in temperature rise across the entire blade span. The aerodynamic performance measured by the probes at Station 4 is therefore taken to be an accurate representation of the rotor performance.

Blade-to-Blade Flow Details. Figure 13 illustrates the distribution of local relative Mach number determined from the LFA measurements on the 70 percent span streamsurface for the baseline, smooth-coated, and rough-coated blades. The Mach number contour increment is 0.10. The shaded area in the lower blade passage in each contour plot indicates the area downstream of the shock for which the Mach number is greater than 0.90. The inset shows the shock location, as defined by the M_{rel} = 1.3 contour line, for each case. The 20, 40, 65, 90, and 115 percent chord locations are also noted because blade-to-blade distributions of Mach numbers at these locations will be presented below.

The Mach number distributions upstream of the shock are quite similar. The passage shock angle is slightly more oblique

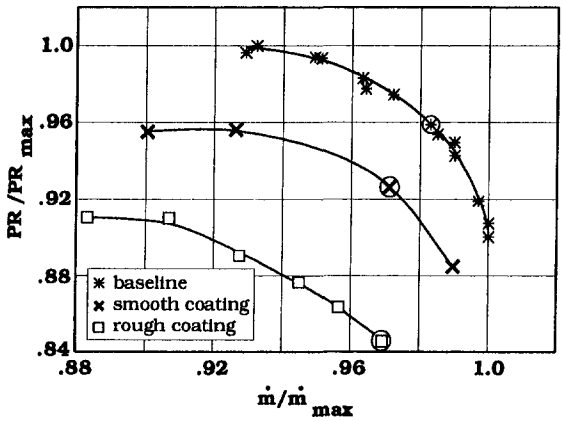

Fig. 11 Pressure ratio versus massflow characteristics at 70 percent span; circled points indicate operating conditions during laser anemometer surveys

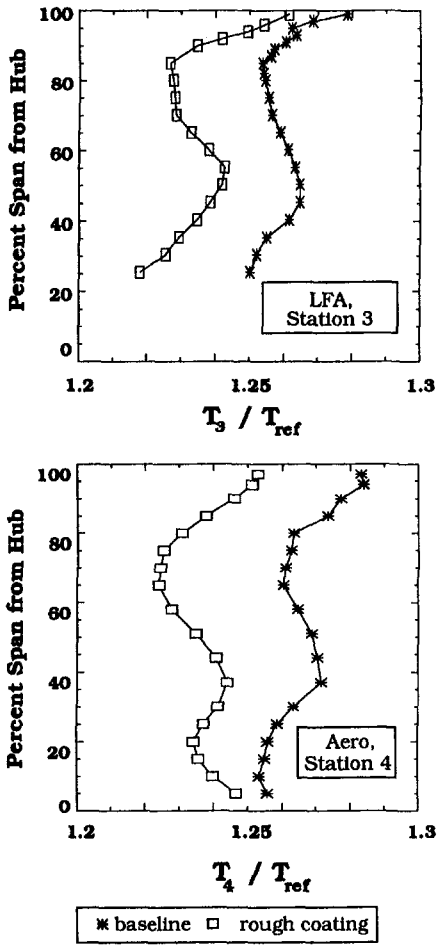

Fig. 12 Comparison between temperature ratios measured near the rotor trailing edge with the LFA and far downstream with aerodynamic survey probes

for the baseline case compared to the coated cases, but this is attributed more to the baseline data being acquired at a slightly higher massflow (see Fig. 11) than to flow field changes caused by coating the blade. The shock stand-off distance from the blade leading edge changes very little between the baseline and coated blade cases. This agrees with data presented by Liepmann and Roshko (1967) on the stand-off distance for circular cylinders as a function of cylinder diameter and Mach number. Although the coatings increased the leading edge thickness by 15 percent at 70 percent span, the cylinder data indicate that the expected change in stand-off distance for this thickness change at a Mach number of 1.4 is only one-half of the leading edge diameter.

The similarities in the flow fields ahead of the shock are consistent with the fact that the massflow, and therefore the incidence angle, is nearly the same for all three cases. Since the shock geometry is similar, the question remains as to why the pressure rise across the rotor varies considerably for these three cases. The pressure rise across the shock accounts for much of the overall pressure rise across the rotor, and the loss in pressure rise for the coated cases must therefore be due to changes in the flow field downstream of the shock. Both coated cases display a more prominent lambda shock foot than the baseline case, followed by a region of low Mach number along the suction surface downstream of the shock impingement point. This behavior is not observed in the baseline blade Mach number distribution. These results indicate that the shock/boundary layer interaction generates a larger region of low-momentum fluid near the suction surface in the coated cases. This additional blockage downstream of the shock results in less diffusion and higher Mach numbers in the rear of the blade passage, as illustrated by the increased size of the shaded area in which the Mach number is above 0.90.

A more quantitative view of the Mach number differences between the coated and baseline blades is provided by the streamwise Mach number distributions shown in Fig. 14, which displays the distribution of Mach number along the midpitch line, denoted by A–A. The baseline data are denoted by the * symbols, while the smooth-coated and rough-coated data are denoted by the solid and broken lines, respectively. The location and strength of both the bow shock and passage shock are nearly identical for all three cases, providing quantitative evidence that the flow field ahead of the shock and the pressure rise across the shock are not sensitive to the presence of the coatings. The baseline passage shock lies slightly downstream of that for the coated blades, which is consistent with the baseline data being acquired at a slightly higher massflow. The main difference between the three cases shown in Fig. 14 is in the levels of reacceleration and subsequent diffusion downstream of the shock. The net result is a higher Mach number at the trailing edge and a decrease in the overall diffusion between the leading edge and trailing edge. This is consistent with the reduced pressure rise observed for the coated cases.

A final comparison of the flow fields in the baseline and coated blades is provided by the blade-to-blade Mach number distributions shown for selected chordwise locations in Fig. 15. Note that although the minimum and maximum value of the ordinate scale is different for each chordwise location, the sensitivity of the ordinate scale is uniform throughout the figure (1 division = 0.1). The abscissa in each plot in Fig. 15 covers one blade pitch. The blade suction surface is on the left and the local blade section thickness is denoted by the cross-hatched region on the right. The LFA measurements are plotted at each of the 184 measurement points across the blade pitch. Regions in which there are no measurements are the result of optical blockage of the laser beam paths due to radial twist in the blade. In particular, the LFA data did not provide any information concerning separation of the suction surface boundary layer in the rear of the rotor because the LFA beams are blocked by the blade for the first 5–8 percent of pitch.

The 20 and 40 percent chord locations are upstream of the point at which the passage shock impinges on the blade suction surface. At 20 percent chord the flow near the blade surfaces shows little change in character for the coated blades relative to the baseline blade, while at 40 percent chord there is evidence of a thicker suction surface boundary layer on the coated blades. Although the shock strength (as judged by the Mach number change across the shock) is identical for all three cases, the shock is located slightly farther from the suction surface for the baseline blade than for the coated blades. As previously discussed, this is consistent with the fact that the baseline data were acquired at a slightly higher massflow than the coated blade data.

The Mach number distributions at the 65 and 90 percent chord locations provide insight into blockage changes downstream of the shock. The 65 percent chord location is just downstream of the shock impingement point on the blade suction surface. At this location the extent of the low Mach number region near the suction surface is larger for the coated cases than for the baseline case. The Mach number levels across the pitch are nearly identical, with the smooth- and rough-coated cases displaying levels just slightly above those of the baseline case. At 90 percent chord it is clear that the coated blade Mach number distributions display a significantly larger region of low Mach number fluid near the suction surface. Consistent with the increased blockage near the suction surface, the coated blade Mach number levels are higher than those of the baseline case across most of the blade pitch.

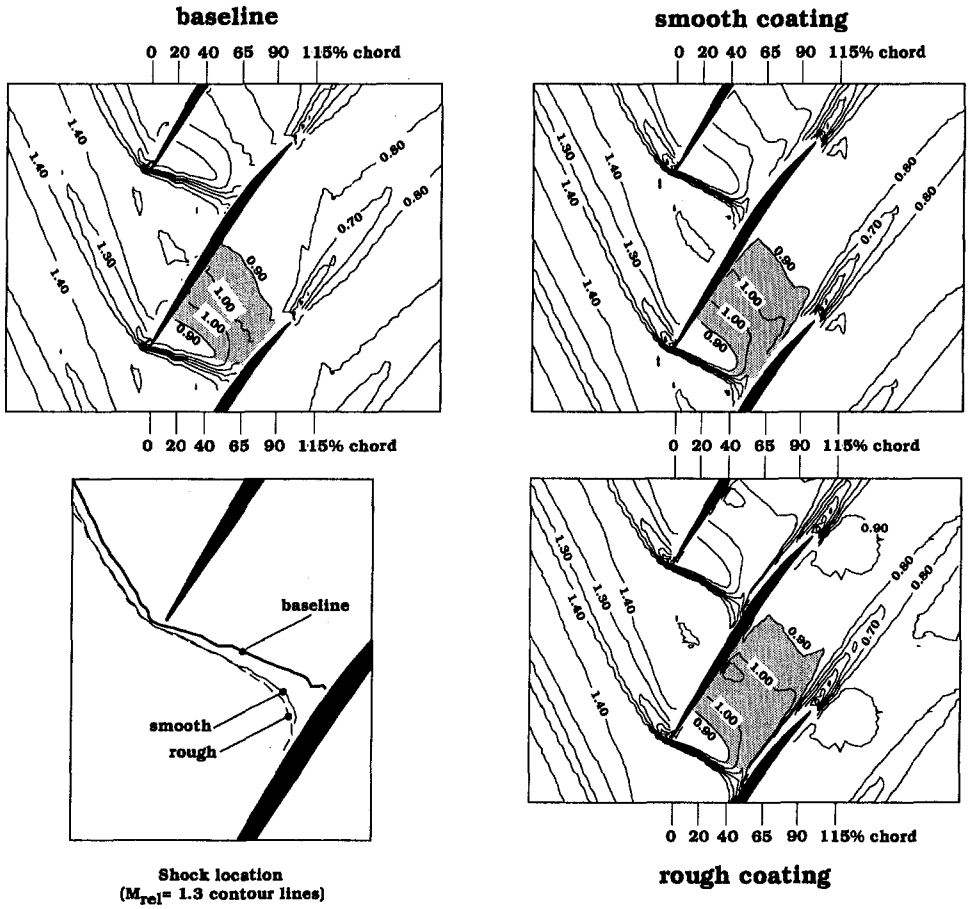

Fig. 13 Laser anemometer measurements of relative Mach number on the 70 percent span streamsurface

The final set of Mach number distributions presented in Fig. 15 was acquired at 15 percent of blade chord downstream of the trailing edge. This is the first location at which the LFA beam path is completely free from optical blockage by the blade and therefore affords us the first opportunity to obtain LFA data across the entire blade wake. The results indicate a well-behaved increase in free-stream Mach number and in wake momentum deficit (and therefore blade profile loss) as we move from the baseline case to the smooth-coated and the rough-coated cases.

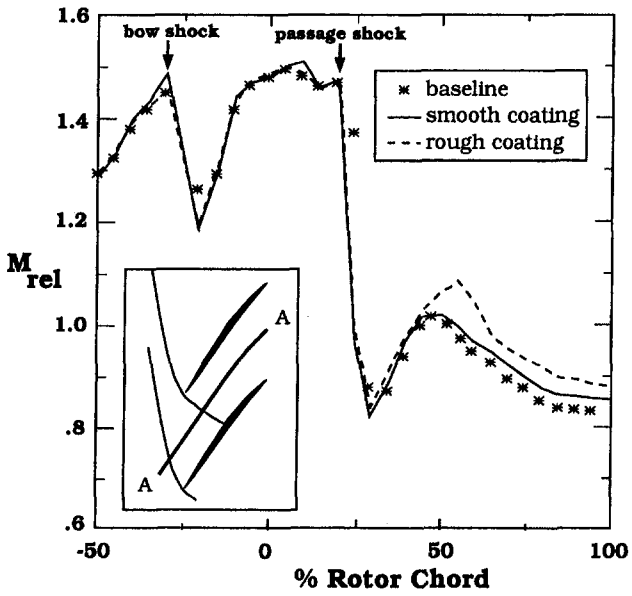

Fig. 14 Laser anemometer measurements of relative Mach number along the midpitch line, A–A, at 70 percent span

In summary, the LFA measurements indicate that the flow field upstream of the rotor passage shock and the shock itself are not altered by adding the smooth or rough coating to the blade. However, the interaction between the rotor passage shock and the suction surface boundary layer results in an increase in blockage along the suction surface downstream of the shock impingement point, which in turn results in higher Mach numbers in the rear of the blade passage.

The blockage increase is the principle flow field change that contributes to the observed performance deterioration. The pitch-averaged Mach numbers measured at 90 percent chord for the baseline and rough-coated blades are 0.840 and 0.900, respectively. The area ratio function, A/A^*, is equal to 1.024 and 1.009 for these Mach numbers. Therefore, at the relatively high exit Mach numbers that exist in Rotor 37, a blockage increase of only 1.024 − 1.009 = 0.015, or 1.5 percent, is required to account for the observed changes in Mach number in the rear of the blade passage. The shock/boundary layer interaction is a key factor in this process. This explains why the performance deterioration at part-speed conditions is much less than that at design speed, since the shock is much weaker at 80 percent speed and is not present at all at 60 percent speed.

Numerical Analysis

The purpose of the numerical analysis performed in this investigation is to complement the LFA measurements in those regions in which the measurements could not be easily acquired (near the leading edge and near the blade surface) and to provide a qualitative assessment of the flow mechanisms that cause

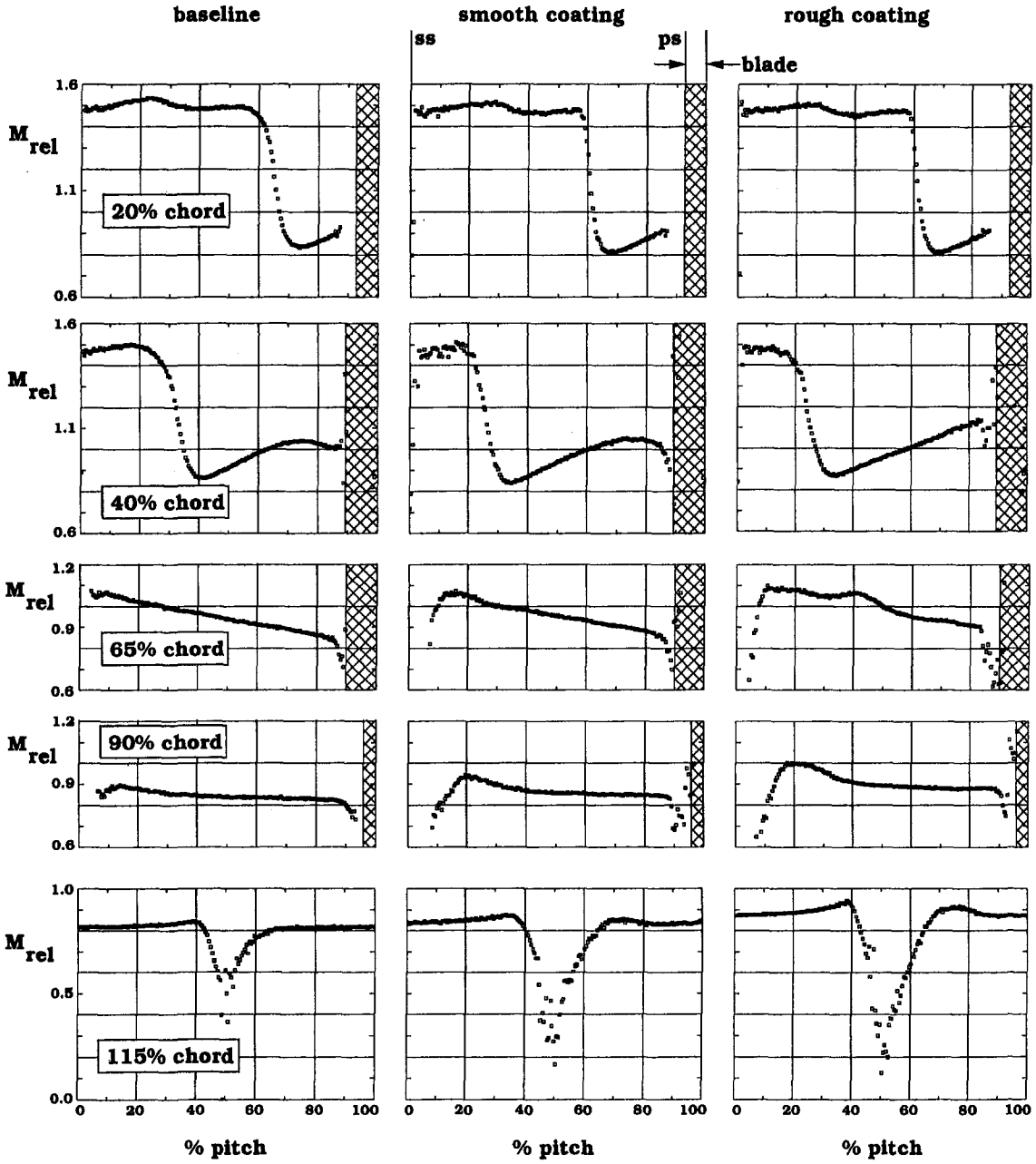

Fig. 15 Laser anemometer measurements of relative Mach number across the blade pitch on the 70 percent span streamsurface

the observed performance degradation. To meet these goals with a minimum of computational resources we chose to use a quasi-three-dimensional rather than a full-three-dimensional analysis technique. Use of a quasi-three-dimensional technique allowed us to run many different cases while varying blade thickness, grid topology, transition location, and roughness model parameters. These variations would have required an inordinate amount of computer time had they been made while using a three-dimensional analysis code. A limited number of flow field solutions were also generated using the full-three-dimensional Navier–Stokes code developed by Dawes (1988). The quasi- and full-three-dimensional solutions were compared to insure that there were no qualitative differences in the roughness/thickness effects predicted by the two approaches.

The quasi-three-dimensional results are generated using a thin-layer Navier–Stokes analysis code developed by Chima (1987). The code includes radius change and variable streamtube thickness, which were estimated from the flowpath convergence. An explicit four-stage Runge–Kutta time-marching algorithm is used with residual smoothing to improve convergence. The code employs the Baldwin–Lomax algebraic turbulence model (1978). The model is fairly accurate for attached flows, but not as good for shock-induced separation. Transition is modeled by calculating a turbulent viscosity profile along each blade-to-blade grid line, but setting the entire profile to zero if the maximum is less than a constant (usually 14) times the laminar viscosity. The model does not account for free-stream turbulence effects. The transition model was proposed in the original Baldwin–Lomax paper but it is not considered to be especially accurate. Surface roughness is modeled by increasing the turbulent mixing length using the approach of Cebeci and Chang (1978). The additional mixing length is a function of the equivalent sand grain roughness height, which is fairly small for the roughness considered here. The addition of this model to the code has been discussed in detail by Boyle and Civinskas (1991) and Boyle (1994).

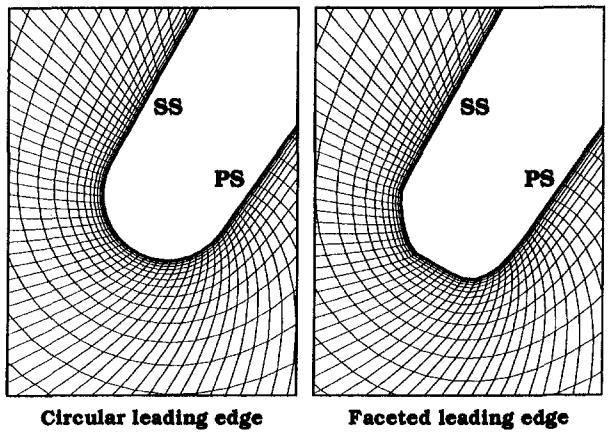

Fig. 16 CFD grid detail at the leading edge

The blade geometry at 70 percent span is used for the baseline blade profile. A C-type grid is used to provide good resolution around the blade leading edge and in the wake. The grid has 319 points around the blade with roughly 100 points on each surface and 60 points downstream. There are 45 points from the blade to midpitch, or 90 points blade-to-blade. The first grid point from the blade surface is located 0.0025 mm (0.0001 in.) from the blade surface, which corresponds to about one-tenth of the thickness of the coatings applied to the blade, or to about $y^+ = 2.5$ in turbulent wall units.

Solutions were all run for 2500 iterations, which reduced the maximum residual between four and five orders of magnitude. Solution times were about 4.5 minutes on a Cray Y-MP.

Numerical Results

Three different blade geometries were analyzed with the quasi-three-dimensional analysis code: (*i*) the baseline blade; (*ii*) the baseline blade with a constant thickness added normal to the blade surface; (*iii*) the thickened blade with a noncircular leading edge. The noncircular leading edge case was analyzed to assess the effect of leading edge manufacturing imperfections on the predicted performance. The noncircular shape used was a generic shape developed on the basis of eyelash inspections of several blades. Detailed views of the grids around the leading edges are shown in Fig. 16.

The thickness added to each blade surface was 0.025 mm (0.001 in.), which was the coating thickness measured during the experiment. The baseline and smooth-coated blade configurations were modeled by using the baseline geometry and the thickened geometry with the roughness model deactivated. The rough-coated blade was modeled by using the thickened geometry and activating the roughness model. For both the smooth and rough coatings, leading edge roughness due to particle impact damage was modeled by forcing transition at the leading edge.

The analysis code was first run assuming that the leading edge is smooth, i.e., that transition does not occur at the leading edge. For this case the analysis code predicts that transition will occur for both the baseline and thickened blades at about 36 percent chord on the suction surface, where it is probably triggered by the pressure rise through the foot of the shock which extends slightly upstream from the main shock in a classic lambda pattern. Transition is predicted at about 29 percent chord on the pressure surface. Although the transition locations predicted using the Baldwin–Lomax model are not considered to be particularly reliable, the results do indicate a sizable laminar flow region, especially on the suction surface.

The overall pressure rise characteristics predicted by the analysis for the baseline and smooth-coated blade are compared to the characteristic measured for the smooth-coated blade in Fig. 17. The purpose of Fig. 17 is to display *trends* in the predicted performance deterioration as thickness is added to the blade leading edge. The shape of the pressure rise characteristic predicted by the quasi-three-dimensional analysis will not, in general, agree with that of the actual characteristic due to limitations in the quasi-three-dimensional approach, which models three-dimensional flow effects through simple changes in radius and streamtube thickness. The measured baseline performance is therefore not presented in Fig. 17, and the measured smooth-coated performance is shown only to indicate the general *level* of the measured performance deterioration.

The three predicted characteristics shown in Fig. 17 are for the baseline blade with natural transition (*), the smooth-coated blade with natural transition (Δ), and the smooth-coated blade with transition forced at the leading edge (X). There is also a single point shown for the baseline blade with transition forced at the leading edge (flagged *). The roughness model was deactivated for all of these solutions, i.e., the blade surface was treated as being hydraulically smooth.

For a smooth leading edge the predicted performance deterioration between the baseline blade (*) and the smooth-coated blade (Δ) is far less than that observed in the experiment. On the other hand, the deterioration predicted simply by forcing either the baseline (flagged *) or the smooth-coated (X) blade boundary layer to be turbulent from the leading edge while treating the blade surface as hydraulically smooth is in closer agreement with that measured in the experiment for the smooth-coated blade. This result indicates that the performance deterioration observed for the smooth-coated blade is not due to an increase in blade thickness but rather from the boundary layer being tripped at the leading edge due to increased leading edge roughness as a result of particle impact damage. This is certainly a possibility since the smooth coating was relatively soft and therefore resulted in a smooth-coated blade that was more susceptible to damage at the leading edge than was the baseline blade.

A limited number of predictions were also generated using the full-three-dimensional Dawes code. The three-dimensional analysis was performed to investigate the impact of manufacturing tolerances on aerodynamic performance. Therefore, a thickness of 0.062 mm (0.0025 in.) was added to each surface, which represents the maximum manufacturing tolerance specified for Rotor 37 when it was fabricated. Note that this thickness was 2.5 times that added to the blade for the quasi-three-dimensional analysis. The three-dimensional analysis was performed on the baseline blade and on the thickened blade and transition was

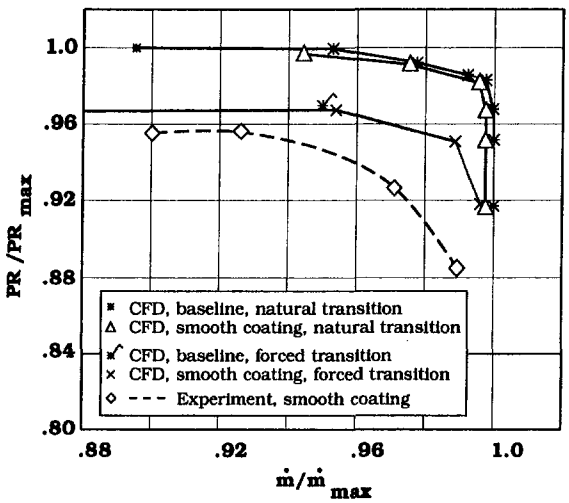

Fig. 17 Comparison between predicted and measured pressure rise versus massflow characteristics at 70 percent span for the smooth-coated blade

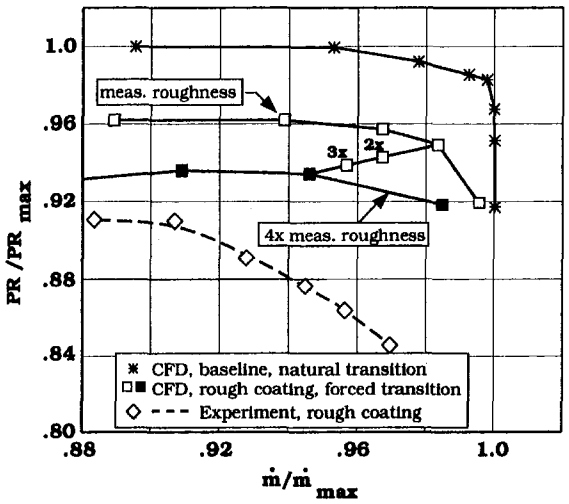

Fig. 18 Comparison between predicted and measured pressure rise versus massflow characteristics at 70 percent span for the rough-coated blade

forced at the leading edge in both cases. The results, which are not shown here, agree qualitatively with the quasi-three-dimensional results. The full-three-dimensional results indicate a stronger dependence of the choke flow rate on the addition of thickness, but this is probably due in part to the larger thickness added for the three-dimensional analysis. However, for values of $\dot{m}/\dot{m}_{max} \leq 0.98$, the full-three-dimensional results predict only a 2 percent loss in normalized pressure ratio, which agrees with the quasi-three-dimensional predictions. Based on this exercise, we conclude that the trends in performance degradation with increased thickness predicted by the quasi-three-dimensional analysis are independent of the quasi-three-dimensional solution approach, i.e., both quasi-three-dimensional and three-dimensional analyses predict a very weak dependence between pressure rise capability and added blade thickness.

The rough-coated rotor performance was simulated by running the analysis code with the roughness model activated for equivalent surface roughness heights equal to 1, 2, 3, and 4 times that measured for the rough-coated blade in the experiment. All predictions for the rough-coated blade were generated with transition forced at the leading edge, since this procedure gave reasonable results for the smooth-coated blade case when compared to the experimental data. When the code was run in the natural transition mode with the roughness model activated, transition was still predicted to occur far from the leading edge on both the suction and pressure surface. These solutions, which are not shown here, predicted very little additional performance deterioration when compared to the smooth-coated blade solution with the boundary layer tripped at the leading edge.

The predicted results for the rough-coated and baseline blade are compared to the experimental results for the rough-coated blade in Fig. 18. As in Fig. 17, the measured performance characteristic for the rough-coated blade is included in the figure only to indicate the measured level of performance deterioration. Two different predicted characteristics are shown for the rough-coated blade. The open symbol curve represents a roughness equal to that measured in the experiment, while the solid symbol curve represents a roughness height which is four times that used in the experiment. The symbols labeled "2×" and "3×" show single points calculated for a roughness height equal to 2 and 3 times the measured roughness height. The rough-coated results shown in Fig. 18 indicate that the predicted compressor performance characteristics are sensitive to the addition of surface roughness. However, the surface roughness model significantly underpredicts the performance changes measured in the experiment.

It was quite difficult to obtain high-quality LFA measurements near the blade surface due to light reflections from the surface and optical blockage caused by blade twist. The numerical results were therefore used to provide additional insight into the flow behavior near the blade surface by using lines of constant entropy to visualize the predicted boundary layer growth. Entropy levels are highest at the blade surface and decrease to their minimum values upstream of the blade passage. The entropy levels across the shock lie between the upstream and blade surface levels. The smallest entropy level that encompasses the blades but not the shock is therefore a reasonable representation of the boundary layer edge. This entropy level is shown in Fig. 19 for the baseline, smooth-coated, and rough-coated cases. The same entropy level is used for each case. The baseline blade results are for natural transition, while the smooth and rough results are for transition forced at the leading edge. The rough-coated result is for a roughness height, which is four times that measured in the experiment. The results clearly indicate a thickening of the boundary layer near midchord, where the passage shock impinges on the blade suction surface. The trend toward increased boundary layer thickness for the coated cases agrees qualitatively with the measured trend toward higher exit Mach numbers in the coated cases. The predictions also indicate that the changes in boundary layer thickness are greater for the suction surface than for the pressure surface. This result is in qualitative agreement with the partial-coating aerodynamic performance results, which indicated less performance degradation for pressure surface roughness than for suction surface roughness.

LFA measurements did not provide information on the existence of boundary layer separation near the suction surface in the rear of the blade passage due to optical blockage of the LFA laser beams. We therefore inspected the predicted blade-to-blade Mach number distributions for the baseline and coated cases in this region to determine if the analysis code predicted boundary layer separation downstream of the shock. This exercise revealed a thin separated zone near the surface for all three cases (baseline, smooth-coated, and rough-coated) with a thickness that is relatively independent of the backpressure. The separation is limited to the first eight grid points from the surface and is therefore quite small, since the surface-normal distance

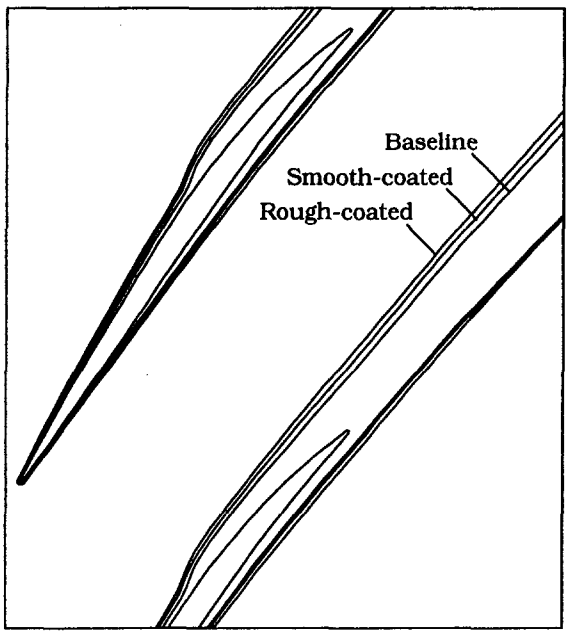

Fig. 19 Predicted boundary layer growth visualized as a locus of constant entropy

covered by these grid points corresponds to only 1 percent of the boundary layer thickness at the trailing edge.

All of the numerical results discussed above were generated using the nominal circular leading edge blade shape shown in the left half of Fig. 16. However, there are several reasons that might lead one to wonder if a circular leading edge is the proper geometry to use when trying to simulate the experimental measurements. First, the eyelash inspections of several blade leading edges showed that the leading edge is not, in general, circular (as shown in Fig. 3). Second, the coatings applied to the blade in the experimental investigation had a much lower surface hardness than the baseline metal blade, making the coated blade much more susceptible to particle impact damage at the leading edge. Finally, the smooth-coated predictions do not capture the experimental trends in performance deterioration unless transition is forced to occur at the leading edge. This raises the question: "Can a noncircular leading edge cause transition to occur earlier than it would if the leading edge were circular?"

To investigate the sensitivity of the flow field to a noncircular leading edge shape, the analysis code was run using the faceted leading edge shape shown in the right half of Fig. 16. This shape was developed on the basis of eyelash inspection of several blades. Refined grids with 449 points around the blade (about 40 points around the leading edge) were used to study leading edge effects. When run in the natural transition mode, the analysis indicates that transition still occurs on the blade surface far from the leading edge. Furthermore, the analysis indicates that the sharp corners formed by the faceted leading edge shape do not cause the formation of a separation bubble or any strong shock features. In fact the flow expands from the stagnation point all around the leading edge, and only sees a weak adverse pressure gradient when it reaches the flat part of the blade surface. Calculations were performed for operating points near choke (low incidence) and near stall (high incidence) and indicate that the noncircular leading edge shape chosen for this analysis does not have a significant impact on the predicted blade row performance at any operating condition. This issue certainly warrants further investigation using better transition models.

Conclusions

The results of this investigation indicate that adding roughness to a transonic axial-flow compressor rotor can result in a significant degradation in overall performance. The nominal coating thickness of 0.025 mm (0.001 in.) on each blade surface corresponded to an increase in leading edge thickness of 10 percent at the hub and 20 percent at the tip of the blade. The addition of a smooth coating resulted in a 4 percent loss in pressure ratio across the rotor at an operating point near design massflow. This coating did not increase roughness over the blade surface except at the leading edge, where roughness increased due to particle impact damage to the coating. The addition of a rough coating of equal thickness with a surface finish of 2.54–3.18 μm (100–125 μin.), resulted in a 9 percent loss in pressure ratio across the rotor at the same operating point. The largest degradation in pressure rise occurs over the outer half of the blade span at design speed.

When assessed at a constant pressure ratio, the adiabatic efficiency degradation at design speed is on the order of 3–6 points for the smooth coating and 6–8 points for the rough coating. Aerodynamic efficiency decreases at all speeds tested, even at fully subsonic operating conditions. At 60 percent of design speed, the effect of roughness on the blade boundary layer development is still significant, resulting in a loss in adiabatic efficiency of 1–3 points. Therefore, surface roughness should not be ignored during the manufacture or refurbishment of subsonic blading.

The conclusions of this investigation are:

1 A detailed investigation into which areas of the blade surface are most sensitive to roughness effects at design speed identified the leading edge and the front half of the suction surface as critical regions in this regard. All partially coated configurations in which the leading edge was coated suffered a significant performance degradation when compared to those for which the leading edge was uncoated. In coating the leading edge, we increased both its thickness and roughness. However, flow field predictions generated using both quasi- and full-three-dimensional Navier–Stokes codes indicate that adding thickness to the blade has little impact on performance. These facts lead to the suggestion that in the manufacture and repair of transonic axial blading, the blade leading edges should be as smooth as possible and designed to stay that way for as long as possible in service.

2 The flow field predictions generated with a quasi-three-dimensional flow solver indicate the existence of significant laminar flow regions on both the pressure and suction surface of the airfoil when the blade boundary layers are allowed to undergo natural transition. This result suggests that fan blades, which operate in a clean flow environment free of upstream blades and struts, may be more susceptible to performance deterioration due to leading edge erosion than are core compressor blades, which operate in a highly disturbed environment.

3 The simple roughness model used in the quasi-three-dimensional calculations yields the proper trends in performance deterioration but underpredicts the impact of surface roughness on performance. Reasonable agreement between flow field predictions and the experimental data for the rough-coated blade cannot be achieved by using roughness levels higher than those measured in the experiment.

4 The quasi-three-dimensional analysis of a noncircular leading edge indicates that transition at the leading edge is not triggered simply by the noncircular leading edge shape considered herein.

5 Laser anemometer measurements indicate that the sensitivity of Rotor 37 to thickness/roughness at design speed is primarily due to blockage changes in the rear of the blade passage. Coating the blade increases the suction surface boundary layer thickness upstream of the shock, which results in a significant thickening of the suction surface boundary layer downstream of the shock/boundary layer interaction. The resulting blockage reduces the overall diffusion across the blade passage, thereby reducing the pressure and temperature rise through the rotor. The rather tight throat area margin and high exit Mach numbers in Rotor 37 make it quite sensitive to small blockage changes. A rotor that features lower exit Mach numbers than Rotor 37 could therefore be expected to be less sensitive to added thickness and roughness.

Acknowledgments

The authors would like to thank the NASA Lewis Research Center for supporting the research effort reported herein, and Mr. Jerry Wood for performing the full-three-dimensional Dawes-code analysis of added thickness effects and for his helpful comments. The last author would particularly like to thank Sermatech International for their support of his participation in this research effort. Finally, the authors would like to thank Aviation Product Support Inc. for providing sample fan blades for inspection of in-service blade surface deterioration.

References

Alber, I. E., Bacon, J. W., Masson, B. S., and Collins, D. J., 1973, "An Experimental Investigation of Turbulent Transonic Viscous–Inviscid Interactions," *AIAA Journal*, Vol. 11, No. 5, pp. 620–627.

Baldwin, B. S., and Lomax, H., 1978, "Thin-Layer Approximation and Algebraic Model for Separated Turbulent Flows," AIAA Paper No. 78-257.

Boyle, R. J., and Civinskas, K. C., 1991, "Two-Dimensional Navier–Stokes Heat Transfer Analysis for Rough Turbine Blades," AIAA Paper No. 91-2129; also NASA TM 106008.

Boyle, R. J., 1994, "Prediction of Surface Roughness and Incidence Effects on Turbine Performance," ASME JOURNAL OF TURBOMACHINERY, Vol. 116, pp. 745–751.

Boynton, J. L., Tabibzadeh, R., and Hudson, S. T., 1993, "Investigation of Rotor Blade Roughness Effects on Turbine Performance," ASME JOURNAL OF TURBOMACHINERY, Vol. 115, pp. 614–620.

Cebeci, T., and Chang, K. C., 1978, "Calculation of Incompressible Rough-Wall Boundary Layer Flows," *AIAA Journal,* Vol. 16, July, pp. 730–735.

Chima, R. V., 1987, "Explicit Multigrid Algorithm for Quasi-Three-Dimensional Viscous Flows in Turbomachinery," *Journal of Propulsion and Power,* Vol. 3, No. 5, pp. 397–405.

Covey, R. R., Mascetti, G. J., and Roessler, W. U., 1978, "Examination of Commercial Aviation Operational Energy Conservation Strategies," The Aerospace Corporation, Aerospace Report No. ATR-79(7761)-1, Vol. 2.

Dawes, W. N., 1988, "Development of a 3-D Navier Stokes Solver for Application to All Types of Turbomachinery," ASME Paper No. 88-GT-70.

DOE/FAA, 1981, *Proceedings of the DOE/FAA Symposium on Commercial Aviation Energy Conservation Strategies,* Apr.

Koch, C. C., and Smith, L. H., 1976, "Loss Sources and Magnitudes in Axial-Flow Compressors," ASME *Journal of Engineering for Power,* Vol. 98, pp. 411–424.

Kramer, W. H., Paas, J. E., Smith, J. J., and Wulf, R. H., 1980, "CF6-6D Engine Short-Term Performance Deterioration," NASA CR-159830.

Liepmann, H. W., and Roshko, A., 1967, *Elements of Gasdynamics,* Wiley, New York.

Moore, R. D., and Reid, L., 1980, "Performance of a Single-Stage Axial-Flow Transonic Compressor With Rotor and Stator Aspect Ratios of 1.19 and 1.26, Respectively, and With Design Pressure Ratio of 2.05," NASA TP 1659.

Moses, J. J., and Serovy, G. K., 1951, "Effect of Blade-Surface Finish on Performance of a Single-Stage Axial-Flow Compressor," NASA RME51c09.

Nichols, C. E., Jr., 1987, "Preparation of Polystyrene Microspheres for Laser Velocimetry in Wind Tunnels," NASA TM 89163.

Reid, L., and Urasek, D. C., 1973, "Experimental Evaluation of the Effects of a Blunt Leading Edge on the Performance of a Transonic Rotor," ASME *Journal of Engineering for Power,* Vol. 95, pp. 199–204.

Reid, L., and Moore, R. D., 1978, "Design and Overall Performance of Four Highly-Loaded, High-Speed Inlet Stages for an Advanced High-Pressure-Ratio Core Compressor," NASA TP 1337.

Roelke, R. J., and Haas, J. E., 1983, "The Effect of Rotor Blade Thickness and Surface Finish on the Performance of a Small Axial Flow Turbine," ASME *Journal of Engineering for Power,* Vol. 105, pp. 377–382.

Sallee, G. P., Kruckenburg, H. D., and Toomey, E. H., 1978, "Analysis of Turbofan Engine Performance Deterioration and Proposed Follow-on Tests," NASA CR-134769.

Strazisar, A. J., Wood, J. R., Hathaway, M. D., and Suder, K. L., 1989, "Laser Anemometer Measurements in a Transonic Axial-Flow Fan Rotor," NASA TP 2879.

Suder, K. L., and Celestina, M. L., 1994, "Experimental and Computational Investigation of the Tip Clearance Flow in a Transonic Axial Compressor Rotor," ASME Paper 94-GT-365; accepted for publication in ASME JOURNAL OF TURBOMACHINERY.

Unsteady Three-Dimensional Flow in a Single-Stage Transonic Fan: Part I—Unsteady Rotor Exit Flow Field

M. A. Cherrett

J. D. Bryce

R. B. Ginder

Defence Research Agency,
Pyestock, Farnborough,
Hampshire, United Kingdom

Detailed unsteady aerodynamic measurements have been taken in a single-stage transonic fan with a very high stator-hub loading. Two-dimensional dynamic yawmeter probes, capable of measuring mean and fluctuating levels of stagnation pressure, static pressure, and yaw angle have been traversed at rotor exit, and downstream of the stator along with several types of pneumatic three-dimensional probe. Part I of this paper describes the dynamic yawmeters and their performance, and presents ensemble-averaged stagnation pressure and random stagnation pressure unsteadiness measurements taken at rotor exit. These are used to illustrate the salient features of the rotor flow field, and the effects of compressor aerodynamic loading. Part II presents measurements taken at stator exit.

Introduction

It is required that future aeroengines be lighter and have a reduced cost of ownership, while achieving improved levels of performance. When applied to compressors, these goals dictate that designs become more compact and that higher levels of aerodynamic loading and Mach numbers are allowed. For military applications in particular, the use of low aspect blading is preferable. These trends greatly increase the complexity of the compressor flow field and make it more difficult to design machines that achieve their design performance with adequate stability margin. It is anticipated that to design such machines to achieve optimum performance in the future, design tools that take account of aspects of the flow field ignored by current methods should be employed. In particular, the effects of blade row proximity and flow field unsteadiness need to be modeled. However, it is only in recent years that transient instrumentation capable of withstanding the arduous environment in high-speed compressor flows has become available. Therefore, there is an acute lack of measurements detailing unsteady flow fields in engine-relevant machines. Hence, fundamental understanding of the complex unsteady flows, and how they interact, is poor and there is little with which to assess the integrity of predictions made by the growing number of time-accurate CFD codes.

Ng and Epstein (1985) and Gertz (1986) have presented flow field unsteadiness measurements taken behind the rotors of three different transonic fans. All three fans showed the same characteristics, i.e., large-amplitude fluctuations in stagnation pressure and temperature within the inviscid core flow between the rotor wakes. The frequency of these oscillations was three to four times that of rotor passing, and was attributed to rotor shock system movement driven by periodic vortex shedding in the blade wakes; see Epstein et al. (1988). However, Cherrett and Bryce (1992) presented similar phenomena in measurements taken behind the first three rotors of a core compressor, where strong rotor shock systems were not present. This anomaly showed that there is some way to go to understand fully the mechanics of the flow field unsteadiness.

Part I of this paper describes the high-frequency yawmeter probes and their performance, and presents unsteady flow field measurements taken at rotor exit. These measurements are used to illustrate the salient features of the viscous flow field associated with the rotor.

Part II of the paper presents steady and unsteady area traverse measurements taken behind the stator row of the fan. Unlike the rotor exit measurements (which were taken during a traverse in the radial direction only) the stator measurements illustrate the time dependence of both the circumferential and radial variations of the flow field, and are able to shed light on the effects of blade row interaction on the development of the flow phenomena within the stator passage.

The C148 Transonic Fan

The C148 single-stage transonic fan was derived from an existing Rolls-Royce multistage fan designed in the early 1980s. Its design concept and major aerodynamic features are described by Bryce et al. (1995). The fan was designed to have a rotor tip inlet relative Mach number of 1.5 and a high aerodynamic stage loading at the hub, which resulted in near-sonic Mach numbers at inlet to the stator hub and high deflection through the stator (>57 deg turning to axial at stator exit).

The stage is illustrated in Fig. 1 where it can be seen that it has a small, but engine-relevant, rotor/stator gap of around 20 percent of rotor axial chord in the inner half of the annulus. Geometric and aerodynamic information relevant to this paper are given in Table 1. Bryce et al. showed (using surface oil-flow visualization and pneumatic stator exit traverse measurements) that the stator hub flow is dominated by a large endwall corner stall. A significant high loss region is associated with the corner stall, and a region of high total pressure (and Mach number) is found between adjacent high loss regions. A smaller corner stall was also found at the stator casing. Although the stator flow was dominated by three-dimensional viscous effects, the rotor flow was found to be modeled with reasonable success using essentially two-dimensional S1-S2 methods.

The overall performance of the fan is shown in Fig. 2. This paper will concentrate on detailed flow field measurements taken at two operating points on the design speed characteristic, i.e., at peak efficiency (A) percentage at near surge (C) and at peak efficiency operation (B) on the 80 percent speed characteristic. Part II will concentrate on measurements at point A only.

Contributed by the International Gas Turbine Institute and presented at the 39th International Gas Turbine and Aeroengine Congress and Exposition, The Hague, The Netherlands, June 13–16, 1994. Manuscript received by the International Gas Turbine Institute February 18, 1994. Paper No. 94-GT-223. Associate Technical Editor: E. M. Greitzer.

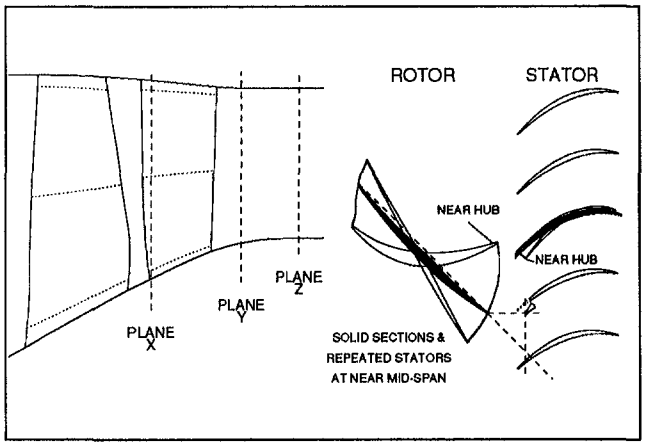

Fig. 1 The C148 transonic fan

Table 1 C148 parameters

Number of rotor blades	25
Rotor pitch/ chord ratio (mid span)	0.65
Number of stator blades	52
Stator pitch/ chord ratio (mid span)	0.55
Corrected mass flow (kg/s)	53.3
Stage pressure ratio	1.807
Stage temperature rise ratio ($\Delta T/T$)	0.214
Stage hub loading ($\Delta H/U^2$)	1.21
Rotor tip speed (m/s)	442
Rotor inlet tip diameter (mm)	633
Stage inlet hub/tip ratio	0.39
Stage exit hub/tip ratio	0.62

Instrumentation

Detailed flow field traversing was carried out with two-dimensional dynamic and three-dimensional pneumatic probes at rotor exit (plane X in Fig. 1), and at two planes 36 and 118 percent of stator axial chord downstream of the stator trailing edge (planes Y and Z in Fig. 1, although only measurements taken at plane Y are shown in Part II). While area traversing could be undertaken at stator exit, probe movement was restricted to the radial direction at rotor exit. In addition, because of the small axial rotor–stator gap, a stator with a cut-back leading edge had to be used to allow probe insertion and radial movement. Unfortunately, the close proximity of the probe sensing head to the cut-back leading edge led to aerodynamic interference between the probe static pressure sensors and the pressure field around the cutback stator. This corrupted the yaw angle and static pressure measurements, and meant that only the stagnation pressure data could be used at rotor exit, although the full potential of the yawmeters could be exploited at stator exit.

In addition, C148 was fitted with a range of instrumentation not normally used in high-speed turbomachinery, including several removable single-blade, and double-blade, stator cassettes. These facilitated the use of dynamic and steady-state instrumentation mounted on the stators. However, only steady-state stagnation pressure measurements taken with pneumatic Pitots attached to the leading edge of an otherwise standard single-blade cassette are presented in this paper.

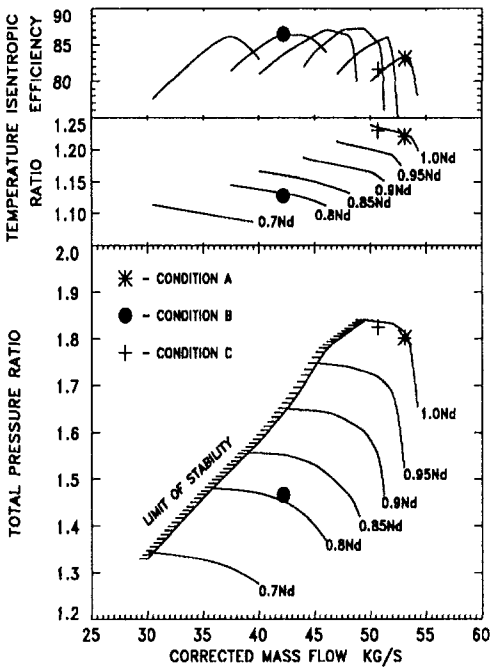

Fig. 2 C148 performance map

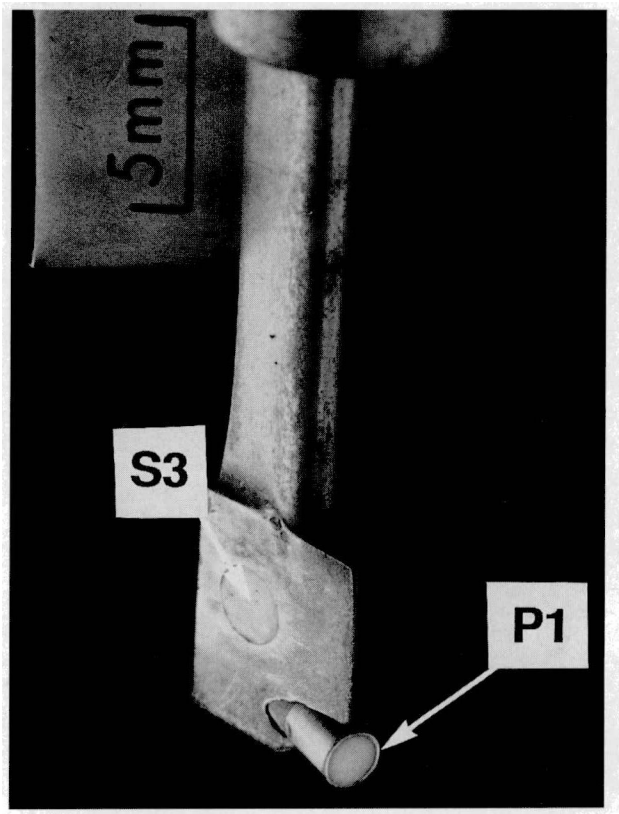

Fig. 3 A dynamic yawmeter

Dynamic Yawmeter

Construction. Figure 3 shows a dynamic yawmeter of the type developed at Rolls-Royce, with UK Government support, by Cook (1989). Two identical yawmeters were used in C148. The wedge-shaped cross section of the probe head has an included angle of 30 deg and an axial chord of 5.6 mm. Three semiconductor pressure transducers (designated P1, S2, and S3) are contained within the sensing head of the probe. The transducer for measuring stagnation pressure (P1) is a Kulite type XCQ-062, while the two static pressure transducers are

Kulite type LQ-047. All transducers used in the C148 yawmeters had a range of 344 kPa absolute and were coated with a 0.05–0.08 mm layer of silastomer rubber for protection. The two static pressure transducer diaphragms lie flush with the probe surface.

Yawmeter Aerodynamic Calibration. The aerodynamic characteristics of both dynamic yawmeters were determined during calibrations carried out at the Whittle Laboratory, Cambridge University, which are reported fully by Cherrett et al. (1992). The calibrations were carried out at Mach numbers of 0.2, 0.5, 0.7, and 0.9, and showed that the operating incidence (yaw angle) range of the probe was approximately ±35 deg. At highest incidences the flow separated completely from the leeward wedge surface. At lower incidence settings, i.e., between 10 and 25 deg, the flow on the leeward side of the probe wedge was characterized by a separation and reattachment, where the point of reattachment moved rearward on the wedge surface with increasing incidence. Although this introduced flow field unsteadiness close to the probe, the amplitude of the resultant pressure fluctuations was small compared to those that would occur in a high-speed compressor.

The calibrations also showed that Reynolds number effects were negligible in the range 36×10^3 to 90×10^3 (based on a wedge length of 5.7 mm) where the midspan Reynolds numbers at the rotor and stator exit were 55×10^3 to 65×10^3, respectively, in C148. The yawmeters were also calibrated at pitch angles of −5, 0, +5, 10, and 15 deg. This revealed that the blockage associated with the probe stem caused fluid to move "radially inward" toward the sensing head of the probe.

An identical pneumatic yawmeter was also calibrated in great detail. This mirrored the performance of the dynamic probes, and provided further confidence in the integrity of the dynamic probe calibrations. The pneumatic yawmeter was not used in C148.

Frequency Response. The frequency response of transducers coated with silastomer rubber, similar to those used in the yawmeters, have been shown to be flat to 100 kHz while displaying negligible phase-angle lag; see Ainsworth et al. (1991). However, this is not the only issue affecting the yawmeter measurement bandwidth. Transducer spacing needs to be taken into account and related to how the flow around the probe head behaves during rapid changes of direction and velocity. Such effects may be complex, especially if vortices are shed from the wedge apex. It is not known what effect such phenomena may have on the yawmeter's performance, nor how valid it is to use the steady-state aerodynamic calibration in a highly unsteady compressor flow field. More work is required to investigate these issues.

Transducer Thermal Compensation and Temporal Drift. Compensation for the temperature sensitivity of the pressure transducers was achieved using a system developed at DRA, which has been described in detail by Cherrett and Bryce (1992). Implementation of this system requires that the transducers be calibrated over a given pressure cycle, at a series of constant temperatures. Therefore, the transducer pressure sensitivity (V_{OS}) and null-pressure output (V_{OZ}) can be expressed as a function of the transducer's diaphragm temperature. By monitoring the voltage (V_S) across a thermally stable resistor placed in series with the transducer, V_S can be correlated with the diaphragm temperature. Therefore, when used in the compressor, the transducer's pressure output voltage (V_O) is converted to pressure using the following equation:

$$\text{pressure} = \frac{(V_O - V_{OZ})}{V_{OS}}$$

where V_{OS} and V_{OZ} are determined for the diaphragm temperature derived from the V_S output.

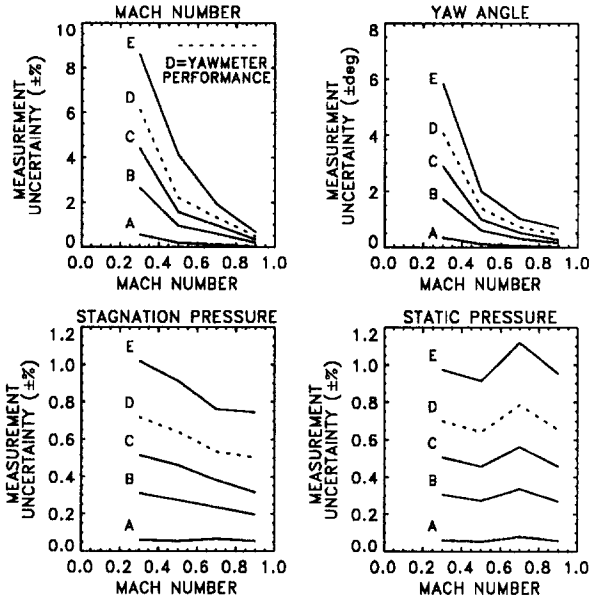

Fig. 4 The effects of transducer pressure measurement uncertainty on yawmeter accuracy: *A* = ±0.1 kPa uncertainty; *B* = ±0.5 kPa uncertainty; *C* = ±0.9 kPa uncertainty; *D* = ±1.2 kPa uncertainty; *E* = ±1.7 kPa uncertainty; *D* = yawmeter performance.

The yawmeter transducers were calibrated repeatedly during a one year period, including immediately before and after being used in C148. This showed that the transducer's V_{OS}, V_{OZ}, and V_S characteristics changed with time, and that the most pronounced changes occurred when the yawmeters were used in C148. While the largest changes were found in V_{OZ} (which were potentially correctable via periodic reference to barometric pressure), the experience did highlight the need for regular and frequent calibration to monitor changes in the other transducer characteristics.

Analysis was carried to assess the impact of these changes. This showed that, as long as corrections for V_{OZ} drift were made by daily reference to ambient barometric pressure levels, transducer measurement accuracy could generally be maintained to within ±0.3 to ±0.4 percent of full-scale deflection. This could have been reduced by calibrating more frequently within the C148 test series, although this was not undertaken in order to minimize risk of damaging the yawmeters during repeated probe installation. Similarly, the effects of drift could have been reduced further by using smaller range transducers, as the 344 kPa range transducers were somewhat oversized for C148 in order to allow their use in other compressors.

Yawmeter Accuracy. Because each of the yawmeter transducers were prone to drift, resulting in pressure measurement uncertainty, further analysis was undertaken to assess the consequences for Mach number, yaw angle, stagnation pressure, and static pressure measurement accuracy. The results are shown in Fig. 4, for different levels of transducer measurement uncertainty; where the analysis assumed that the pressure levels were compatible with those found at stator exit in C148, and that the same magnitude of pressure measurement uncertainty applied to each of the three transducers. (An average value of uncertainty was derived considering all possible permutations of the error between the three probe sensors.) The figure shows that Mach number and yaw angle accuracy are strongly dependent on the flow field Mach number, especially below Mach 0.5, while stagnation and static pressure accuracies are more acceptable. The ±1.2 kPa (±0.35 percent FSD) data are the most representative yawmeter performance, while the curves for the two smallest levels of pressure measurement uncertainty (i.e.,

±0.1 kPa and ±0.5 kPa) are equivalent to very good pneumatic system performance, and significant errors arise even here.

While this analysis is useful to assess the order of magnitude and qualitative variation of measurement accuracy, it can be pessimistic because it is unlikely that the same degree of uncertainty would affect all three transducers at the same time. In order to gain further confidence in the yawmeter performance, the measurements were compared with those taken with two types of three-dimensional pneumatic probe design at condition A at stator exit (plane Y). These data are presented in Part II and show that the yawmeter measurements compare very favorably with the pneumatic results.

Data Capture and Processing. All of the unsteady aerodynamic signals were amplified at the rig and transmitted over 20 m cables to the facility control room. Here, the data were recorded on a high-speed digital data acquisition system that has been described in detail by Cherrett and Bryce. The data were sampled in two modes. That is, either as continuous records, or as multiple "discontinuous" records captured in response to a once-per-revolution trigger signal. The latter were processed on-line to determine the following parameters:

(a) Ensemble-averaged signal:

$$\tilde{P}_{(t)} = \frac{1}{N}\sum_{n=1}^{N} P_{(n,t)}$$

(b) Average random unsteadiness:

$$\tilde{p}'_{(t)} = \sqrt{\frac{1}{N}\sum_{n=1}^{N} (P_{(n,t)} - \tilde{P}_{(t)})^2}$$

where: $P_{(n,t)}$ is an instantaneous AC coupled signal; N is the number of consecutive rotor revolutions during which phase-locked data capture was carried out in response to a once-per-revolution pulse, normally 128; t is the temporal duration of each of the segmented data records (typically 512 or 2048 samples depending on the recorder module capacity).

Processing data in this manner is a well-established technique that accentuates the periodic unsteadiness correlated with the rotor. As the data are captured in response to a once-per-revolution signal, the rotor is in the same position each time the recording cycle is initiated and differences in the flow field associated with individual rotor passages are retained.

The trigger pulse was generated by a small magnet located in one of the rotor blade tips passing underneath a shorted bar in the FM grid intended for blade vibration monitoring during the tests. Because of uncertainty concerning the circumferential position of the shorted bar, it was not possible to position the rotor blades relative to the stator blades on receipt of each trigger pulse. While this did not affect the integrity of the measurements, i.e., the pulse was very sharp and repeatable, it would have been useful to know the actual rotor position relative to the stator frame of reference.

Rotor Exit Flow Field

The rotor exit flow field is illustrated in this paper using: (*i*) steady-state stagnation pressure measurements taken with Pitots mounted proud of the leading edge of an otherwise standard stator, (*ii*) time-varying stagnation pressure measurements derived from the P1 yawmeter transducer. During the 17-point yawmeter traverses, the probes were set at the midspan design inlet flow angle. Additional measurements taken at six spanwise positions showed that the characteristics of the dynamic pressure signals did not change significantly when the yawmeters were set at ±10, ±5, and 0 deg to the midspan flow angle.

In order to gain confidence that the yawmeter results were not corrupted by the cut-back stator interference problem, the yawmeter data were compared with measurements taken by dynamic pressure transducers fitted to an otherwise standard single-blade stator cassettes. Although not shown in this paper, these data were in excellent agreement with the yawmeter P1 transducer results.

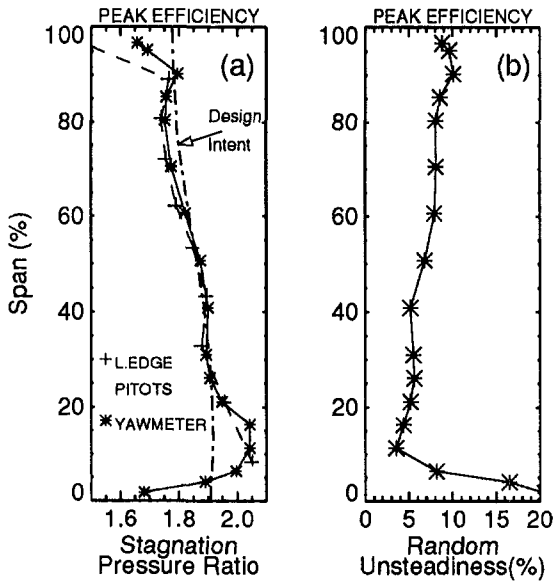

Fig. 5 Time-averaged yawmeter measurements

Time-Averaged Measurements. Figure 5(*a*) compares the pneumatic leading-edge stagnation pressure measurements taken at condition *A*, with the corresponding time-averaged yawmeter measurements. The intended design pressure distribution is also shown. Figure 5(*b*) shows the time-averaged random unsteadiness measurements derived from the yawmeter. The pressure measurements have been expressed as a ratio of fan inlet stagnation pressure, while unsteadiness has been expressed as percentage of the local stagnation pressure level.

The pneumatic measurements and yawmeter data are in good agreement (a characteristic that was also seen in the condition *B* and *C* data). This gives further assurance that the yawmeter measurements were not adversely influenced by the probe-stator interference problems. Over much of the span the measurements are in good agreement with the design intent. However, toward the hub, between 0 and 30 percent span, it is evident that the stagnation pressure levels exceed those intended in the design. As Bryce et al. (1995) explain, evidence from S1–S2 modeling of C148 indicates that this phenomenon is due primarily to two-dimensional blade row performance, and arises from shortcomings in the deviation corrections employed when the rotor was designed in the early 1980s. In the tip region, at approximately 90 percent span, there is an additional increase in measured stagnation pressure, which, although small, is clearly evident at all operating conditions. This is associated with the tip-leakage vortex flow.

Figure 5(*b*) shows that the spanwise distributions of time-averaged random unsteadiness increase toward the hub and casing, where the viscous end wall flow phenomena predominate. These are illustrated more fully in the following section.

Unsteady Flow Field Measurements. As an illustration of the unsteady measurements taken at midspan, Fig. 6 shows the random unsteadiness and ensemble-averaged stagnation pressure variations while operating at condition A. At this condition and considering the random unsteadiness data first, the rotor wakes occupy approximately 30 percent of the rotor passing period and are the singularly most notable flow feature. Unsteadiness levels within the wakes are three to four times those found elsewhere within the rotor passage. However, weaker

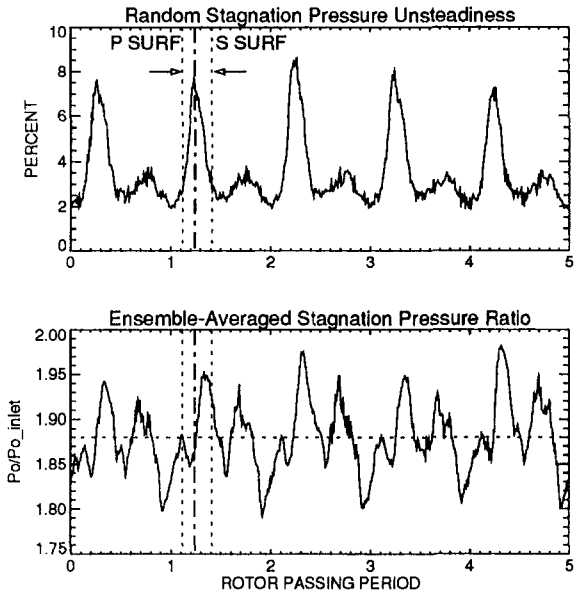

Fig. 6 Midspan pressure and unsteadiness time histories at condition *A*

peaks in random unsteadiness level are seen to be centered at approximately midpitch.

The ensemble-averaged pressure measurements are considerably more complicated than the idealized view (often reinforced by low-speed compressor measurements) of wake perturbations punctuating an otherwise monotonic pressure variation from one side of the passage to the other. In the wake region, the stagnation pressure rises rapidly from a pressure trough on the pressure surface side of the rotor wake, to reach a pressure peak on the suction surface side of the wake. The magnitude of this peak relative to the mean level is two to three times that of the pressure trough. The point in the wake region where the stagnation pressure increases above time-averaged value corresponds approximately to the position of maximum random unsteadiness.

The stagnation pressure field within the rotor passage (i.e., between the rotor wakes) is very active. A second stagnation pressure trough occurs on the suction surface side of the wake followed by a peak (to rival the strength of that attained within the suction surface side of the rotor wake) at approximately 40 percent rotor pitch. This is followed by a rapid fall in stagnation pressure to reach the minimum value at approximately 75 percent rotor pitch. The extent of the region bound by the midpitch excursion from pressure peak to trough corresponds approximately to the aforementioned region of increased intrapassage random unsteadiness. These data are discussed in more detail later, following a more complete presentation of the measurements at this, and the other, operating conditions. That is, rather than view the data as individual time histories, they have been presented below to represent the complete rotor exit flow field.

Random Unsteadiness. The random unsteadiness field at the three operating conditions is shown in Fig. 7. The time-dependent results are plotted in a form representing the two-dimensional rotor-locked pressure field, which sweeps past the "radial" traverse line. The "radial" traverse positions are shown as well as the loci of the rotor trailing edges. In order to position these loci circumferentially relative to the observed phenomena, two assumptions were made at midspan: first, that the wake could be identified with peak unsteadiness in the measured data, and second, that the wake lay along an extension of the stagger line. The positions of the trailing edge loci relative to the wake at midspan were then estimated (as shown in Fig. 1) by projecting the stagger line of the midspan rotor sections to intersect the plane where the measurements were taken. This procedure was adopted because of the uncertainty in the circumferential position of the once-per-revolution trigger pulse that triggered the data acquisition system. The data are shown such that rotor is viewed from behind looking upstream while rotating clockwise, and the nonsymmetric shape of the annulus segments arises because the measurement stations were situated along a line approximating the stator leading edge, which is not a truly radial line. The data shown document the passing of three rotors, although the total available data set documented 22 of the 25 rotor blades. There were quantitative differences in the data from passage to passage of the rotor, although these were generally small and the different rotor flow fields were in excellent agreement. The data were sampled at 500 kHz, which resulted in 90 samples across a rotor passage.

The random unsteadiness measurements give an immediate insight into the extent of the viscous flow field features where random unsteadiness levels are highest. However, caution must be exercised when interpreting the data as it must not be assumed a priori that the positions of peak levels of random unsteadiness correspond precisely to the centers of the viscous flow features they appear to indicate. That is, the highest levels of random pressure unsteadiness may occur in viscous shear layers bounding high-loss (viscous flow) regions and adjacent (inviscid) passage flow. In addition, the positioning of the sensors relative to the stator needs to be taken into account. Studies using unsteady predictions have shown that pitchwise positioning of a sensor can affect the measurements greatly; see Epstein et al. (1989), for example. All of the unsteady measurements reported here were taken by sensors close to the stator leading edge, and consequently where potential interaction effects be-

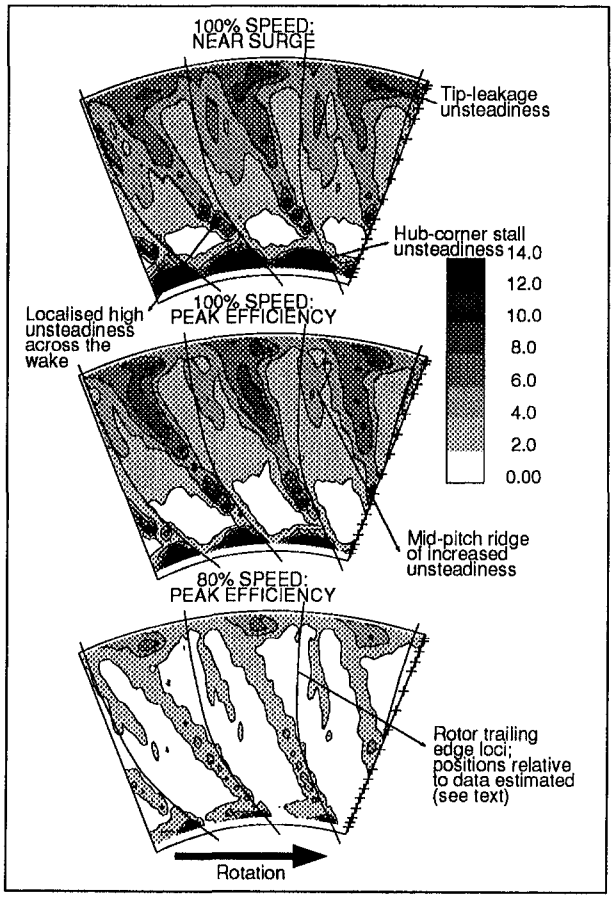

Fig. 7 Random unsteadiness measurements (contours expressed as a percentage of local time-averaged stagnation pressure)

tween the rotor and stator rows are likely to be strong (see later).

At the hub, there appear to be endwall corner stalls causing high levels of unsteadiness, the amplitude and size of which grow with increasing stage loading. The extent to which these structures lie close to the endwall and spread across the passage in the pitchwise direction is quite different to corresponding measurements taken by the authors in a multi-stage core compressor (see Cherrett and Bryce, 1992). In the core compressor, the corner stalls tended to extend up the blades in a spanwise direction.

The rotor wakes show the expected broadening with increasing span. This is in part due to increased axial spacing between the probe and rotor trailing edge with increasing span. However, the greater shock strength toward the rotor tip, and the accompanying interaction with the blade surface boundary layer, would also be expected to result in broader wakes. It is interesting to note that between 20 and 35 percent span the wake unsteadiness levels increase above those found at spanwise positions immediately below and above. This is outboard of the region of excess rotor pressure rise, but it corresponds to the region where rotor relative inlet Mach numbers approach unity. The locally near sonic flow conditions, and the necessity for reasonably high degrees of turning, cause very high values of diffusion factor in this region. Consequently, the blade sections are more difficult to design, and the measurements illustrate how the design tools employed in the early 1980s were unable to resolve these problems satisfactorily.

At the casing, the random unsteadiness distribution is characteristic of the tip-leakage vortices. Underturning of the tip leakage, and the measurements being taken some way downstream of the trailing edge, results in the vortices being positioned close to the pressure surfaces of the subsequent blade wakes. The unsteadiness regions associated with tip leakage flow become larger with increasing stage loading, although the amplitude of the unsteadiness does not increase accordingly. These observations are consistent with expected tip-leakage flow development, although the work that has studied leakage flows most thoroughly has been confined to low-speed flows, e.g., Inoue and Kuroumaru (1989).

At all operating conditions the inviscid rotor passage flow regions are characterized by low unsteadiness levels, except near midpitch in the upper part of the annulus, where there is a ridge of increased unsteadiness that lies almost radially. The unsteadiness levels within this feature increase with increased stage loading. This important feature is discussed more fully later.

Ensemble-Averaged Pressures. Attention is now turned to the AC-coupled ensemble-averaged pressure measurements in Fig. 8. The use of AC-coupling means that the significant radial profile seen in the time-averaged measurements is suppressed in Fig. 8. During interpretation of these data it is particularly important to remember that they were taken in the stationary frame of reference. In the stationary frame it is possible for stagnation pressures to be higher on the suction, rather than the pressure, surface side of the passage, and for a wake (pressure deficit) in the relative frame to appear as a jet (pressure excess) in the stationary frame. As such the data are not easy to interpret because it is intuitive to think of the flow field in rotor relative frame. Because of the cut-back stator interference problem, it was not possible to transpose into the relative frame using the unsteady yaw angle information (accepting that unsteady three-dimensional angle measurements may be necessary to avoid the risk of introducing significant errors).

In order to relate these data to the salient features identified in the random unsteadiness measurements, the rotor trailing loci have been superimposed. This shows that pressure levels are greater on the suction surface side of the rotor wakes than on the pressure surface side, and that very large pressure changes

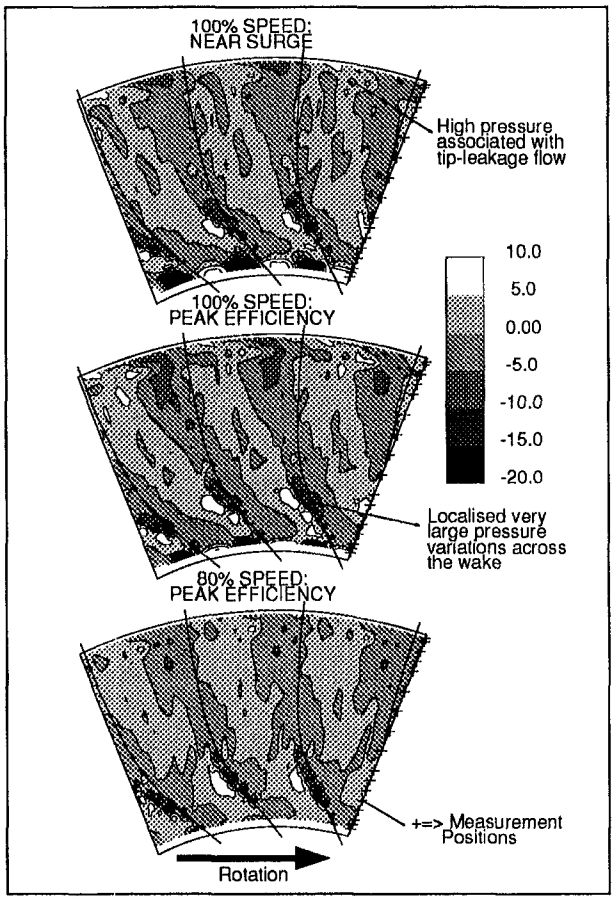

Fig. 8 Ensemble-averaged stagnation pressure (contours as a percentage of local time-averaged values)

occur on either side of the wake between 20 and 30 percent span, where the rotor inlet Mach numbers approach unity. Otherwise, the data show little change in amplitude with increased compressor loading at the same speed. In this respect, and in their qualitative form, the data are very similar to the measurements reported in other high-speed compressors. The stagnation pressure oscillations mentioned earlier are evident as the "radial" regions of high pressure extending up the inviscid core flow. However, it is difficult to appreciate the full complexity of the intrapassage oscillations using the coarse contour plots in Fig. 8.

Discussion

An explanation is needed for two of the phenomena seen in these data. First, the cause of the midpitch ridge of random unsteadiness needs to be identified. Second, the mechanism causing the high-frequency stagnation pressure oscillations needs to be discussed.

Midpitch Unsteadiness. Figure 7 shows that this feature increases in strength with increasing span and compressor aerodynamic loading. As such, it is thought to be related to the rotor shock system. The spatial position of the feature, relative to the blade wakes and the estimated trailing edge loci, indicates that it occurs during the part of the rotor passing period when the rotor trailing edge passes the stator leading edge region. With the small rotor/stator gap in C148 and the relatively severe gradients likely to occur in the stator flow field near the leading edge, this is when strong potential flow interaction between the rows might be expected. The potential interaction between the blades will induce changes in rotor circulation and lift and

perturb the rotor shock. The shock perturbation may in fact accentuate the potential interaction between the blade rows. Because of turbulence and effects such as vortex shedding, such events will not be precisely repeatable from one revolution to the next, giving rise to unsteadiness as observed.

If this hypothesis were true, it would be expected that the strength/occurrence of the ridge would depend upon the circumferential position of the sensor relative to the stator leading edge. The C148 rotor exit measurements were taken very close to this position, and it was not possible to take measurements at midpitch to see if the feature subsided. However, it is noteworthy that similar features were not seen in the random unsteadiness data reported by Cherrett and Bryce (1992), where the measurements were taken at midstator pitch. Similarly, Alday et al. (1993) showed no evidence of midpassage unsteadiness in their measurements taken behind a transonic civil fan rotor. However, in the former case strong shocks were not present and in the latter case the measurements were taken someway downstream of the rotor in the bypass duct. It would be interesting to re-evaluate the Ng and Epstein (1985) and Gertz (1986) data to look for similar behavior, as random unsteadiness data were not presented in these cited publications. Clearly it is difficult to confirm this hypothesis without corroborative data.

Stagnation Pressure Oscillations. Figure 6 shows that there is a spatial correlation between the midpitch pressure peaks and troughs in the ensemble-averaged data, and the random unsteadiness ridge. In this instance it is likely that the phenomenon discussed above is responsible for both features. However, at other spanwise positions and operating points, it is not easy to relate the stagnation pressure oscillations to the random unsteadiness data, and it is not so easy to explain the behavior.

Epstein et al. (1988) presented a hypothesis that suggested that the frequency of the oscillations was determined by vortex shedding in the rotor wakes. It was envisaged that the periodic changes in circulation that accompanied the shedding caused the rotor shock system to jitter, thus amplifying the perturbations and causing the substantial pressure oscillations in the flow field. While this is a plausible argument, the measurements taken at DRA suggest inconsistencies in the hypothesis. First, the core compressor measurements reported by Cherrett and Bryce (1992) were qualitatively and quantitatively very similar to those measured in C148, and those reported by Ng and Epstein (1985) and Gertz (1986). However, the core compressor rotors were not transonic, and therefore devoid of strong shocks. Second, frequency domain analysis of continuously sampled data (i.e., not ensemble averaged) captured in the core compressor and C148 does not show any peaks at frequencies that cannot be attributed to the blade passing frequencies or their harmonics. If vortex shedding were responsible, the characteristic frequencies are likely to be determined by the displacement thickness of the rotor wake, and therefore not correlated directly to blade passing, unless there is a mechanism for locking them in. No such mechanism yet appears to have been clearly identified.

Clearly, the analysis of the rotor exit data presented in this paper is restricted by fact that the measurements were taken in only one meridional plane. In Part II of the paper, stator exit measurements taken on a two-dimensional traverse grid are presented. Analysis of these data showed that it was difficult to understand individual pressure time histories without making reference to the perturbations occurring elsewhere on the two-dimensional traverse grid. It is recommended that a similar approach be adopted for dynamic rotor exit traverse measurements in future, and that much of the current difficulties in interpreting the rotor exit data could be alleviated if a more complete view of the complex flow field were available.

Finally, the salient features of the viscous flow field associated with the rotor are clearly evident in the random unsteadiness data, and this semi-quantitative information is of potential benefit to the development and validation of steady-state three-dimensional viscous flow solvers. However, the fact that the measurements were taken in only one meridional plane may also be significant for these data. That is, as the measurements were taken close to the stator leading edge, the data were gathered when the potential interaction between the blade rows was likely to be strongest, and this may augment the rotor viscous flow field development locally. It is not clear whether this could explain the tendency for the rotor hub corner stall to spread circumferentially, rather than radially.

Conclusions

A dynamic yawmeter probe, capable of measuring fluctuating stagnation pressure, static pressure, and yaw angle, has been used extensively in a transonic single stage fan. Using a method to compensate for semiconductor pressure transducer temperature sensitivity, it was possible to obtain absolute pressure measurements from the sensors. However, the measurement accuracy was compromised by drift in the transducer characteristics with time and more work is required to ascertain the cause of these changes and to alleviate their magnitude. Even so, with careful and frequent transducer calibration, it was possible to obtain time-averaged yawmeter measurements that compared very favorably with three-dimensional pneumatic probe measurements.

Interference between the yawmeter and the adjacent stator meant that only accurate stagnation pressure measurements could be obtained at rotor exit. These were processed to reveal the random unsteadiness and ensemble-averaged unsteady pressure fields associated with the quasi-steady flow field locked to the rotor. This revealed the following:

1 Viscous blade-wake, over-tip leakage, and rotor-hub corner stalls were clearly identified in the random unsteadiness measurements. The changes in size and intensity of these features were commensurate with expected behavior. However, the hub-corner stalls extended in a pitchwise direction and lay close to the hub endwall, which is quite different to the behavior seen elsewhere in low-speed and high-speed compressor rotors.

2 An almost radial ridge of increased random unsteadiness was seen at midpitch in the upper portion of the annulus. This feature became more pronounced with increased stage loading and it is suspected that it is a consequence of interaction of the rotor and stator flow fields influencing the rotor shock system. More work is required to investigate more fully the nature of this interaction.

3 The ensemble-averaged pressure measurements showed that, away from the viscous endwall and wake flows, the rotor passage flow was characterized by stagnation pressure fluctuations at several times blade passing frequency. Similar measurements in other transonic fans have been attributed to rotor shock system unsteadiness. However, in part II of this paper it is shown that similar measurements at stator exit can be related to global changes in stator exit stagnation pressure during the rotor passing period.

4 It is suggested that radial traverses behind high-speed compressor rotors are unable to provide sufficient information to explain the rotor flow field fully. Two-dimensional area traverses are recommended in future.

A vast amount of unsteady aerodynamic measurements have been accumulated in some 350 hours of testing the C148 transonic fan. Some of the measurements taken at stator exit are reported in part II of this paper, while other measurements, including on-blade stator-surface pressure and thin-film gage measurements will be reported in the future.

Acknowledgments

The C148 research program reported in this paper was supported by the UK MoD Strategic Research Programme and by

the Aerospace Division of the UK DTI. Thanks are due to Iain Shipman for his help in putting the paper together.

References

Ainsworth, R. W., Dietz, A. J., and Nunn, T. A., 1991, "The Use of Semiconductor Sensors for Blade Surface Pressure Measurement in a Model Turbine Stage," ASME *Journal of Engineering for Gas Turbines and Power,* Vol. 113, pp. 261–268.

Alday, J., Osborne, D. J., Morris, M. B., and Ng, W., 1993, "Flow Randomness and Tip Losses in Transonic Rotors," ASME Paper No. 93-GT-189.

Bryce, J. D., Cherrett, M. A., and Lyes, P. A., 1995, "Three-Dimensional Flow in a Highly Loaded Single-Stage Transonic Fan." ASME JOURNAL OF TURBOMACHINERY, Vol. 117, pp. 22–28.

Cherrett, M. A., and Bryce, J. D., 1992, "Unsteady Viscous Flow in a High Speed Core Compressor," ASME JOURNAL OF TURBOMACHINERY, Vol. 114, pp. 287–294.

Cherrett, M. A., Bryce, J. D., and Hodson, H. P., 1992, "3D Pneumatic and 2D Dynamic Probes: Their Development and Subsequent Use in a Transonic Fan," *Proc. 11th Symposium on Measurement Techniques for Transonic and Supersonic Flows in Cascades and Turbomachines,* Munich.

Cook, S. C., 1984, "Development and Use of a High Response Aerodynamic Wedge Probe and Its Use on a High Speed Research Compressor," *Proc. of the Ninth International Symposium on Air Breathing Engines.* Athens, Vol. 1, pp. 1113–1125.

Dring, R. P., Joslyn, H. D., and Hardin, L. W., 1982, "An Investigation of Axial Compressor Rotor Aerodynamics," ASME *Journal of Engineering for Power,* Vol. 104, pp. 84–95.

Epstein, A. H., Gertz, J. B., Owen, P. R., and Giles, M. B., 1988, "Vortex Shedding in High-Speed Compressor Blade Wakes," *Journal of Propulsion and Power,* Vol. 4, No. 3, pp. 236–244.

Epstein, A. H., Giles, M. B., Shang, T., and Sehra, A. K., 1989, "Blade Row Interaction Effects on Compressor Measurements," AGARD-CP-468.

Gertz, J. B., 1986, "Unsteady Design-Point Flow Phenomena in Transonic Compressors," MIT Report GTL No. 188.

Howard, M. A., Ivey, P. C., Barton, J. P., and Young, K. F., 1994, "Endwall Effects at Two Tip Clearances in a Multistage Axial Flow Compressor With Controlled Diffusion Blading," ASME JOURNAL OF TURBOMACHINERY, Vol. 116, pp. 635–647.

Inoue, M., and Kuroumaru, M., 1989, "Structure of Tip Clearance Flow in an Isolated Axial Compressor Rotor," ASME *Journal of Engineering for Power,* Vol. 111, pp. 250–256.

Ng, W. F., and Epstein, A. H., 1985, "Unsteady Losses in Transonic Compressors," ASME *Journal of Engineering for Gas Turbines and Power,* Vol. 107, pp. 345–353.

Poensgen, C., and Gallus, H. E., 1991, "Three-Dimensional Wake Decay Inside of a Compressor Cascade and Its Influence on the Downstream Unsteady Flow Field: Part 1—Wake Decay Characteristics in the Flow Passage," ASME JOURNAL OF TURBOMACHINERY, Vol. 113, pp. 180–189.

Poensgen, C., and Gallus, H. E., 1991, "Three-Dimensional Wake Decay Inside of a Compressor Cascade and Its Influence on the Downstream Unsteady Flow Field: Part 2—Unsteady Flow Field Downstream of the Stator," ASME JOURNAL OF TURBOMACHINERY, Vol. 113, pp. 190–200.

Unsteady Three-Dimensional Flow in a Single-Stage Transonic Fan: Part II—Unsteady Stator Exit Flow Field

M. A. Cherrett

J. D. Bryce

R. B. Ginder

Defence Research Agency,
Pyestock, Farnborough,
United Kingdom

Detailed unsteady aerodynamic measurements have been taken in a single-stage transonic fan with a very high stage-hub loading. Two-dimensional dynamic yawmeter probes, capable of measuring mean levels and fluctuations in stagnation pressure, static pressure, and yaw angle have been traversed at rotor exit and downstream of the stator, along with several types of pneumatic three-dimensional probe. Part I[1] *describes measurements taken at rotor exit. This paper, Part II, describes measurements taken at stator exit when the fan was operating at near-peak efficiency, on the design speed characteristic. The measurements indicate the effects of rotor–stator interaction on the development of the viscous endwall-corner flows at the hub and casing. In addition, they illustrate that significant changes in stagnation pressure level occur within much of the stator exit flow field during the rotor passing cycle.*

Introduction

The endwall regions of turbomachinery blade rows are dominated by complex three-dimensional viscous flows, which are not modeled well by most current design and analysis methods. However, a large proportion of the loss generated in the compressor is associated with these structures. Bryce et al. (1993) have shown that the stator endwall regions of the C148 fan, particularly at the hub, are dominated by three-dimensional corner stalls. The aim of the work reported in this paper (Part II) was to study the severity and extent of these flow features and how they vary during the rotor passing period, to elucidate the effects of blade row interaction on their development. Poensgen and Gallus (1991) have shown that flow field unsteadiness has a significant effect on the development of endwall corner stall. However, the cited work was carried out in a low-speed annular cascade with the rotor wakes simulated by cylindrical bars. There have been no measurements reported for a high-speed engine relevant compressor such as C148.

This paper presents data gathered downstream of the C148 stator, where it was possible to take more complete measurements than at rotor exit; see part I. That is, the stator exit measurements were taken on a two-dimensional area traverse grid, whereas the rotor exit measurements had been limited to a traverse in the radial direction only. In addition, interference between the dynamic yawmeter probe and the adjacent stator had restricted the rotor exit measurements to stagnation pressure only. These problems were not present at stator exit, and therefore the full measurement potential of the dynamic yawmeters could be utilized to yield transient stagnation pressure, static pressure, and tangential flow angle data.

Time-Averaged Measurements

The stator exit measurements were taken at 36 percent of axial chord downstream of the trailing edge, on a grid of 10 radial by 19 equispaced circumferential positions covering 1.3 stator pitches. These positions are shown in Fig. 1 along with an indication of yawmeter size at midspan. C148 employed 25 rotor blades and 52 stator blades; the stator exit measurements were taken immediately behind stator #12, while the rotor exit/stator inlet measurements reported in part I were taken in front of stator #18. Stator numbering started arbitrarily at the starboard casing splitline, with stator #12 being near top-dead-center. Figure 1 also shows the circumferential distribution of time-averaged random stagnation pressure unsteadiness at midspan (i.e., excluding the periodic unsteadiness due to rotor-passing) expressed as a percentage of local stagnation pressure. This shows that the wake width is approximately 30 percent of stator pitch at this position.

The yawmeters were used in conjunction with a system developed at DRA to compensate for semiconductor pressure transducer temperature sensitivity. This allowed the transducers to be used as absolute pressure sensors. However, the effectiveness of this system was compromised by long-term temporal drift in the transducer characteristics, i.e., over time periods much longer than the time needed to take the yawmeter traverse measurements (see part I). Even so, with regular calibration it was possible to obtain time-averaged yawmeter measurements that were in good quantitative agreement with pneumatic probe measurements (see below).

Pitchwise-Averaged Results. Figure 2 shows the pitchwise-averaged time-mean pressure and angle measurements taken with the yawmeter, as well as those taken with two three-dimensional pneumatic probes, i.e., a four-hole wedge probe and a sting-mounted four-hole pyramid. Both three-dimensional probes have been illustrated by Bryce et al. (1993) and discussed more fully by Cherrett et al. (1992). The stagnation pressure measurements taken with the three probes agree typically to within ±1.0 percent of the design pressure rise. Static pressure measurements agree to within ±3.0 percent of dynamic head around midspan, while yaw angle measurements agree to within 1.0–1.5 degree over much of the span. Such agreement gives confidence in the yawmeter measurements and implies that, with careful calibration and compensation, the yawmeters are capable of producing time-averaged measurements that compare favorably with pneumatic measurements. However, pneumatic measurement are themselves subject to uncertainty,

[1] A description of the C148 transonic fan is found in part I, along with the instrumentation used to take the measurements. The list of the references given in part I is common to both parts of the paper.

Contributed by the International Gas Turbine Institute and presented at the 39th International Gas Turbine and Aeroengine Congress and Exposition, The Hague, The Netherlands, June 13–16, 1994. Manuscript received by the International Gas Turbine Institute February 18, 1994. Paper No. 94-GT-224. Associate Technical Editor: E. M. Greitzer.

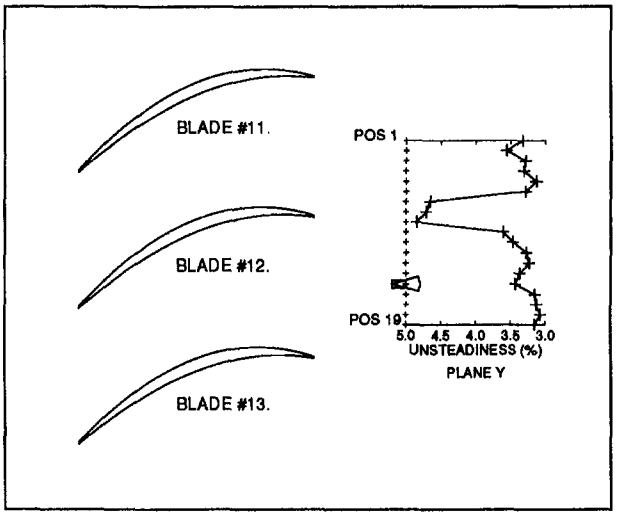

Fig. 1 The stator exit traverse positions and the midspan random unsteadiness distribution

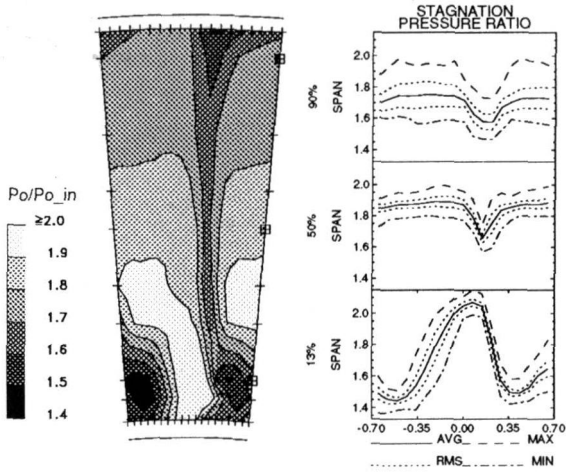

Fig. 3 Time-averaged stagnation pressure ratio measurements

not least because of the inability of such systems to resolve the fluctuating flows in turbomachinery adequately. Indeed, although the dynamic yawmeters provide an enormous amount of information not obtainable with pneumatic probes, one of the aims cited for their development was to produce probes capable of measuring turbomachinery flows more accurately than pneumatic instruments. Clearly the current levels of transducer temporal instability, discussed in part I, preclude such performance.

Full Traverse Results. Figures 3, 4, and 5 give more insight into the stator exit flow field by showing the complete time-averaged stagnation pressure, random unsteadiness, and yaw angle (i.e., tangential flow angle) data, respectively. Each figure also illustrates the pitchwise variation of the data at 13, 50, and 90 percent span (these positions and the other traverse stations are marked along the edges of the contour plots). In addition, to indicate the time variance of the results, the maximum and minimum levels occurring in the ensemble-averaged data over the sampled period (equivalent to 22 rotor passages) are shown, together with the rms variation for total pressure and angle. Note that, for the latter quantities, even larger max-min envelopes would be seen if the instantaneous raw data were considered.

The stagnation pressure measurements (Fig. 3) clearly illustrate the blade #12 wake, as well as the associated casing and hub corner stalls. The hub-corner stall to the left of the measurements originates from blade #13, and it is more vigorous than that of blade #12. Between the hub-corner stalls there is a region of high stagnation pressure passing through the reduced passage area. This arises from a hub pressure excess at rotor exit; see part I. Surprisingly, the rms and max-min pressure variations are similar at the hub and midspan, but larger toward the casing.

The random unsteadiness data (Fig. 4) show considerable activity toward the hub, particularly in the regions between the corner stalls and the high pressure region. This is because of the high unsteadiness in the vigorous shear layer between the viscous and inviscid flow regions, as well as the variation of stall cell size with time (which is discussed below). The yaw angle measurements (Fig. 5) generally show steepest gradients and greatest variations in the viscous end wall and wake flows, and they also display high rms and max-min variations in the casing region. Note that positive yaw is in the direction of rotor rotation, which is from left to right in Figs. 4, 5, and 6.

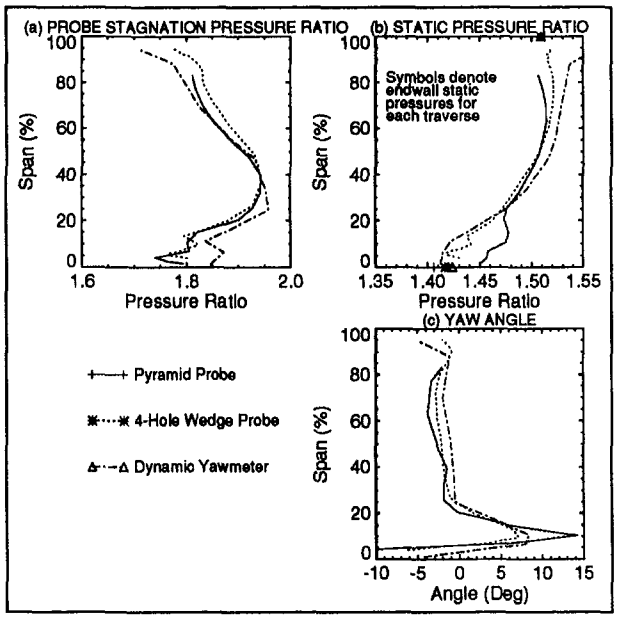

Fig. 2 A comparison of the yawmeter measurements with the three-dimensional pneumatic probe data

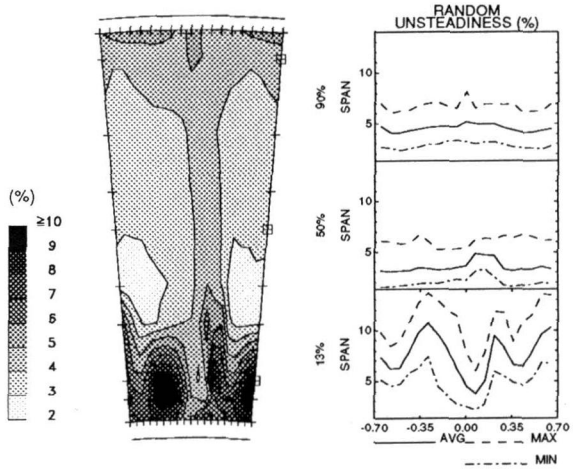

Fig. 4 Time-averaged random unsteadiness measurements

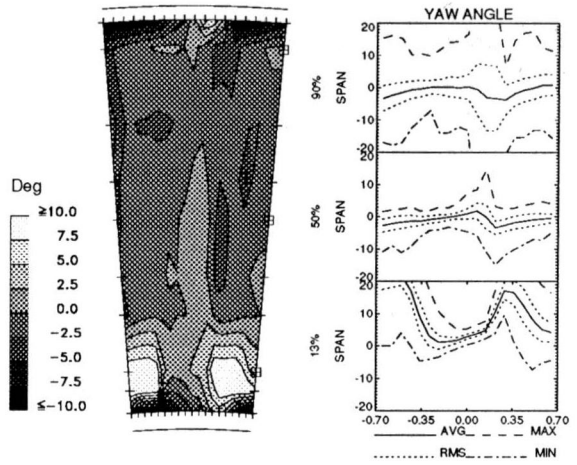

Fig. 5 Time-averaged yaw angle measurements

Unsteady Measurements

As the yawmeter measurements were taken on a two-dimensional grid downstream of the stator, they may be viewed from several perspectives. First, attention can be focused on a single location and the temporal variation examined. Secondly, the variation of the data across the passage can be viewed at each instant in time and finally, this perspective may be extended to a view of the whole measurement area at each instant in time. It is useful to look at the data from all of these perspectives.

Single Point Results. In Fig. 6, the data are viewed from the first perspective, focusing on measurements in the stator midpassage at midspan (i.e., traverse position 15 in Fig. 1). The temporal variation of random unsteadiness, ensemble-averaged stagnation pressure, and yaw angle are shown at stator inlet and exit (i.e., planes X and Y in Fig. 1 of part I). The inlet measurements were taken close to the stator leading edge and no yaw angle data are available here for reasons explained in part I. At stator inlet, the rotor wakes are clearly identifiable by high levels of unsteadiness and occupy approximately 30 percent of the rotor passing period. By plane Y, the unsteadiness level has been approximately halved and the rotor wakes broadened to occupy approximately 75 percent of the passing period.

The ensemble-averaged pressure measurements at inlet are dominated by perturbations at two and three times blade passing frequency, as discussed at length in part I. The stator exit measurements are of similar complexity, but the amplitude of the oscillations at midpassage (position 15) in plane Y are less than those at inlet, although this is not true of all the pitchwise positions in plane Y at midspan. It will be shown in the forthcoming discussion that the amplitude and frequency of the pressure oscillations at stator exit are connected with the expansion and contraction of the high-pressure region toward the hub.

The yaw angle variations at stator exit in Fig. 6 show that these are as complex as the stagnation pressure results. Relating the yaw angle data to the random unsteadiness variations, it is apparent that the flow momentarily undergoes a negative perturbation (i.e., against the direction of rotor rotation) on the pressure side of the rotor wake; followed by a positive angle perturbation on the suction surface side of the rotor wake. It would be expected that "negative jet" effects within the chopped wakes convect fluid from the suction to pressure surface sides of the passage, i.e., giving rise to a positive angle perturbation near the wake center. However, the strongest angle perturbations in Fig. 6 are in the opposite direction on the windward (pressure surface) side of the wake. The measured behavior may indicate the presence of counterrotating vortices set up on either side of the chopped wakes as they pass through the stator passage. However, without measurements on the blade-to-blade plane it is difficult to explain fully the yaw angle behavior in Fig. 6.

Area Traverse Results. A more comprehensive view of the stator exit flow field measurements is shown in Fig. 7. (In the interests of brevity, the following discussion is restricted to the consideration of ensemble-averaged stagnation pressure ratio and random unsteadiness.) Figure 7 contains several perspectives of the stator exit measurements "frozen" at the same instant in time within the rotor revolution, but derived by averaging over 128 consecutive rotor revolutions. These perspectives are described below:

(a) This is a view of the instantaneous random stagnation pressure unsteadiness field expressed as percentage of local time-averaged stagnation pressure using the same grey scale as Fig. 4.

(b) This is a view of the instantaneous ensemble-averaged stagnation pressure ratio. In this, as in (a), the stator passage is viewed from the rear looking upstream and the upstream rotor rotates clockwise. The grey scale is the same as that used in Fig. 3.

(c, d) These images show the temporal variation of ensemble-averaged stagnation pressure ratio at two positions in the midspan traverse. One point is situated on the suction surface side of the stator passage (position 18 in Fig. 1), and the other on the pressure surface side (position 11). The time ordinate in these images is expressed as a fraction of blade passing period and the instant at which time is frozen in Fig. 7 is illustrated by the * symbols superimposed on the time histories in (c) and (d).

(e) This shows the instantaneous distribution of random stagnation pressure unsteadiness across the stator passage at midspan. The instantaneous distribution is plotted as a solid line, while the time-averaged data are plotted as + symbols.

(f) This is similar to (e), but illustrates the variation of ensemble-averaged stagnation pressure ratio across the stator passage at midspan.

(g) A "clock" is shown indicating the fraction of rotor passing period at which the images in Fig. 7 have been frozen in time.

In Fig. 7(a), a rotor wake (labeled i) lies diagonally across the passage to the left of the stator wake. At midspan, see Fig. 7(e), there is a localized region where the unsteadiness levels

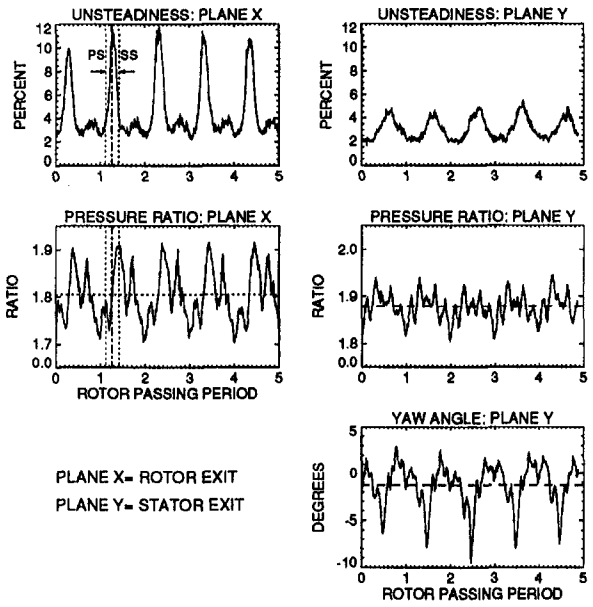

Fig. 6 Unsteady flow field measurements at stator inlet and exit

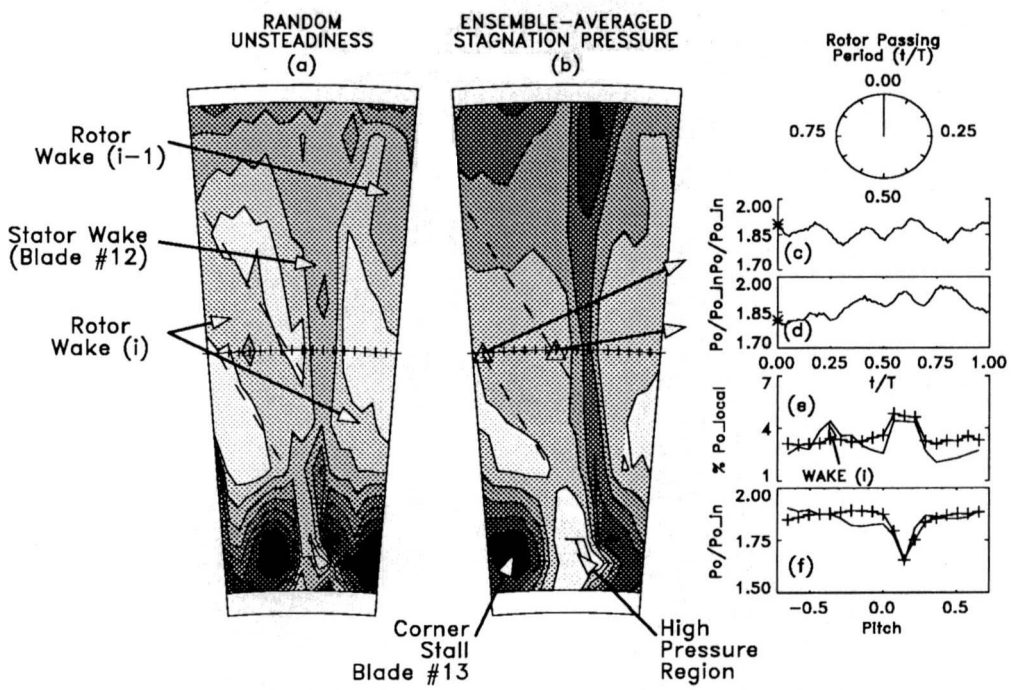

Fig. 7 Instantaneous unsteadiness and pressure ratio measurements (grey scales are the same as in Figs. 3 and 4)

in the rotor wake approach those in the stator wake, although elsewhere the rotor wake unsteadiness levels are lower than in the stator wake. Wake i, in Fig. 7(a), also appears in the passage to the right of the stator wake. It was possible to confirm that this, and the disturbance identified in the left-hand passage are parts of the same chopped wake because some rotor wakes were notably weaker than others. This allowed them to be identified easily (although this is not illustrated specifically in this paper). The previous rotor wake ($i - 1$) is also visible in the right-hand stator passage as it leaves the traversed area.

Figure 7 is part of a data set that documents a little over 22 rotor passing periods, with 92 measurements being taken within each passing period (i.e., 2048 sets of images in total). Because of the volume and complexity of the data, computer-based data animation was employed extensively to analyze the measurements and it is difficult to imagine how the data could be analyzed effectively in any other manner. However, using these techniques it was possible to animate only a small portion of the data at a time, with one or more rotor passing periods being spliced from the main data set and animated cyclically. It was found that at least 30 images per rotor passing period were necessary to construct a sequence that resolved the rotor passing period effectively. Clearly it is not practical to present such a large volume of data here, and hence eight images from a typical blade passing cycle are presented in Fig. 8 to illustrate the effects of rotor passing on the stator exit flow field. It should be noted that these images are not evenly spaced in time about the rotor blade passing period.

In Fig. 8, the data are arranged in chronological sequence starting at the top left-hand corner of the figure and preceding in a clockwise manner as indicated by the ascending Roman numerals. Rotor rotation is in the same direction, and the first image (Fig. 8_{I}) shows the same data as Fig. 7. Because of the complexity of the data in Fig. 8, the reader is advised to take a macroscopic view of the data, making reference to the observations highlighted below before attempting a more detailed interpretation. The relative coarseness of the traverse grid, particularly in the radial direction, should be borne in mind. Also, part I of this paper should be consulted to become acquainted with the structure of rotor exit flow field, particularly near the endwalls. It should also be noted that the ensemble-averaged stagnation pressure measurements presented in part I were ac-coupled, whereas those in Figs. 7 and 8 document both ac and dc-pressure components.

Behavior of the Hub-Corner Stalls. The rotor wakes are clearly visible in the random unsteadiness measurements (i.e., the equivalent images to Fig. 7a), and these data are most useful for tracking the rotor wake positions. However, insight into the effects of rotor passing is best gained through examination of the stagnation pressure ratio measurements, particularly in the left-hand passage between stators #12 and #13 as most of this is visible in the images equivalent to Fig. 7(b).

Consideration of the left-hand stator #13 hub-corner stall reveals that it is at its largest, and contains the lowest pressure levels, in Figs. 8_{I} and 8_{II}. The same stall is smallest approximately half a period later, in Figs. 8_{IV} and 8_{V}. The right-hand stall behaves in a similar manner, but is 180 deg out of phase. This is consistent with the effects of rotor passing because there are approximately two stator blades for each rotor blade (i.e., 52 versus 25). During the rotor passing period, pressure ratio variations within the center of the hub stalls are some ±5 percent of the local time-averaged values, which is comparable with the maximum-to-minimum variation found throughout most of the entire plane Y pressure field. However, because the size of the stalls waxes and wanes, pressure levels at the boundary of the stalls and the inviscid core flow vary by ±10–14 percent. These fluctuations are found within the ensemble-averaged measurements, and even higher levels would occur within the instantaneous pressure time histories from which these data are derived. However, while it is certainly responsive to rotor passing, the stator hub stall would appear to be a fundamentally steady-state phenomenon predictable (in principle) by steady-state three-dimensional viscous calculations.

Relating the hub-stall size to the rotor wake positions, it is evident that they are at their largest after the rotor wake has passed the stall, and that this swollen state persists for some time afterward. For instance, the hub end of rotor wake $i + 1$ passes the blade #13 stall between Figs. 8_{V} and 8_{VI}, yet the stall becomes and remains enlarged during sequence between Figs. 8_{VII} to 8_{II}. It is suspected that this is due to the rotor hub corner stall (see part I) that extends in a pitchwise direction across the

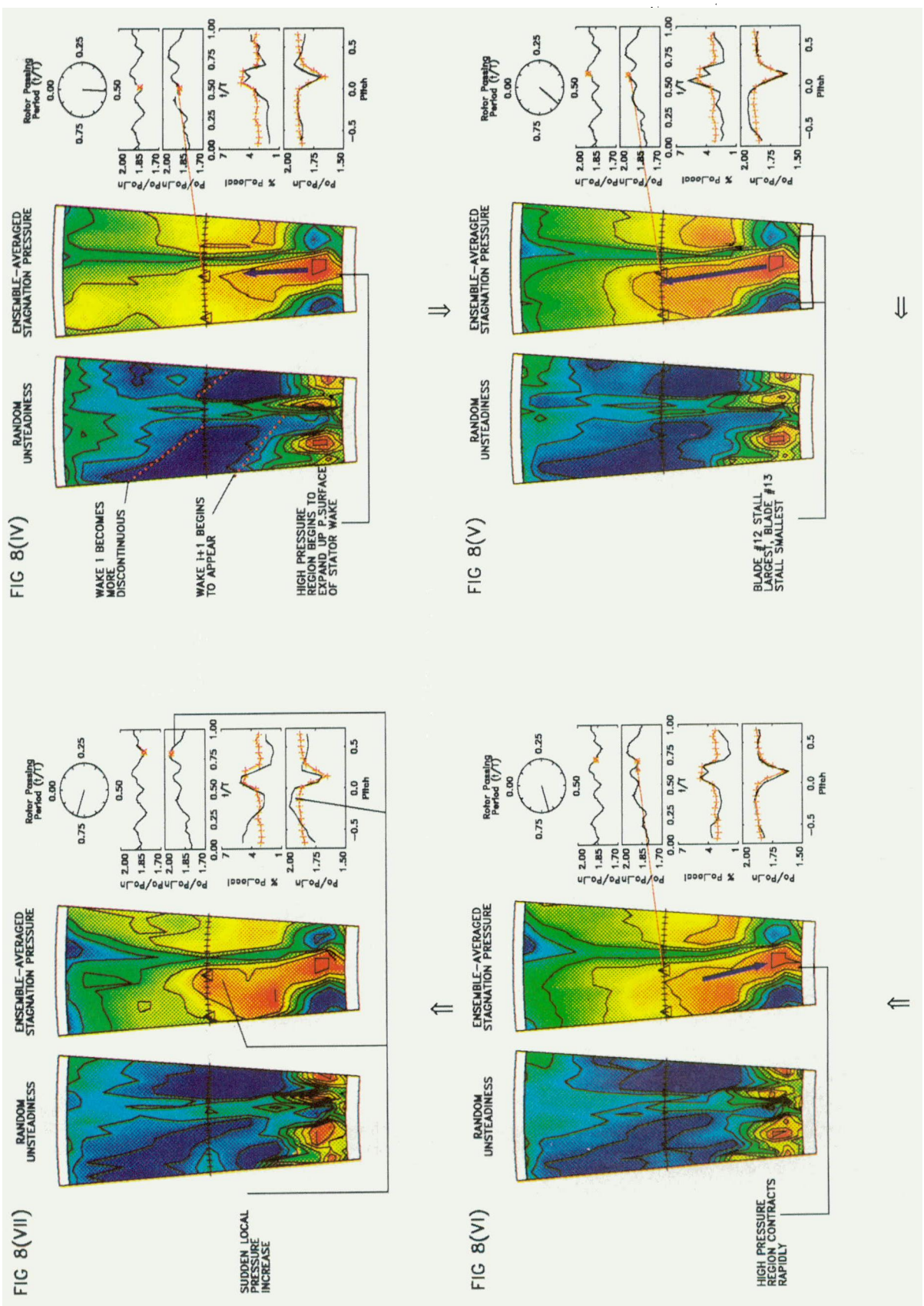

Fig. 8. The effects of rotor passing on the stator exit field

endwall for some 60 percent of the rotor pitch, or passing period. It is thought that the rapid increases in random pressure unsteadiness and large changes in pressure and incidence that accompany this region induce a growth in stator hub stall.

It should also be noted that the rotor potential field is expected to have a significant effect on the stator hub flow field. This is clear in Fig. 1 in part I, which shows the thick rotor root section juxtaposed to the slender stator hub sections. Of course, in assessing the magnitude of potential interaction, the gross distortion of the effective blade shapes by the local three-dimensional viscous flows needs to be taken into account. Therefore, although there are a number of CFD codes that provide useful insights into the magnitude of potential interaction, these are of little practical use where both blade rows are dominated by three-dimensional viscous flows.

Behavior of the Inviscid High-Pressure Region. Perhaps the most striking feature in the data in Fig. 8 is the behavior of the inviscid high-pressure region in the lower half of the annulus between blades #12 and #13. As mentioned earlier, this feature has its origin in the pressure excess noted at rotor exit in part I but it is subsequently affected strongly by blade row interaction. In Fig. 8_{I} this region is at its smallest, where it is constrained between the blade #13 stall (which is at its zenith), the pressure surface of the blade #12 wake, and leeward side of rotor wake i. As rotor wake i moves away, the stator passage becomes progressively more free of its influence, the blade #13 stall begins to subside, and the high pressure region begins to expand radially. The expansion becomes more vigorous in Fig. 8_{IV} as rotor wake $(i + 1)$ enters the passage, and the high-pressure region reaches its greatest extent during Fig. 8_{V}, after which it begins to contract.

This ordered cycle of expansion and contraction during the rotor passing appears to be contradicted in Fig. 8_{VII}, when a high-pressure region grows suddenly near the pressure surface side of the stator #12 wake near midspan. The video animation, from which these images were extracted, shows that this high-pressure region grows very suddenly from the otherwise low pressures found on the advancing side of the rotor wake and dissipates as quickly. As such it may not be linked directly to the high-pressure region between the hub corner stalls.

It should also be noted that the expansion and contraction of the high-pressure regions does not necessarily imply that the fluid is subjected to strong radial transportation. Rather, much of the observed behavior is probably be due to the fact that the rotor wake (and potential) flows are skewed circumferentially relative to the almost radially aligned stators. Therefore, the stator hub is influenced first by the rotor flow, and subsequent blade row interactions occur later at increasing blade heights.

While it is possible to make an objective assessment of the behavior of these features, it is far more difficult to explain the blade row interaction mechanisms causing the behavior. Indeed it is not clear how complete an understanding can be achieved using data taken in only one stator exit traverse plane. However, it is hoped that continued analysis, relating the stator inlet and exit flows, as well as the on-blade measurements taken throughout the passage at midspan, will shed more light on the behavior.

Rotor Wake. Closer examination of the rotor wake as it crosses the stator passage reveals that it becomes discontinuous on either side of the stator wake. This is to be expected, as the rotor wake is predicted to travel faster on the suction surface of the stator blade than on the pressure surface. This is more noticeable as the chopped rotor wakes progress up the stator wake and the difference between the arrival times of the wake segments either side of the stator wake becomes more significant, i.e., compare Figs. 8_{III} and 8_{IV}.

In Figs. 8_{VII} and 8_{VIII} the unsteadiness in wake $(i + 1)$ as it leaves the suction surface side of the stator #13 wake near midspan is higher than that attained elsewhere in the rotor wake. From the video animation this effect is also seen in wake (i) as it leaves the stator #12 wake. Similarly, it is evident that these features persist longer than the passing of the rotor wake alone can account for. It is thought that this is an artifact of localized suction surface boundary layer separation induced by the passing rotor wakes. However, it is notable that this behavior seems to be prevalent near midspan only.

Behavior of the Casing-Corner Stalls. Discussion so far has concentrated on events occurring in the bottom half of the annulus. However, in Fig. 8 it can be seen that there is significant unsteadiness toward the casing and in particular, the blade #12 casing-corner stall varies in size and strength significantly. In addition, the ranges of maximum-to-minimum ensemble-averaged pressure levels recorded within even the inviscid core flow are $\pm 8-15$ percent of the local time-averaged pressure ratios, which is somewhat larger than elsewhere in the passage. Unfortunately, random unsteadiness levels are also higher in the upper part of the annulus, which makes identification of the rotor wake positions less certain and hampers detailed interpretation of the flow field. Even so, it is clear that the casing stall is enlarged between Figs. 8_{VI} and 8_{II}, i.e., some 30 percent of the rotor passing period. The correlation between this time interval and the spatial extent of the rotor tip leakage flow (shown in part I) suggests that the casing corner stall is strongly, and adversely, influenced by the passing rotor leakage vortex. This reflects the behavior of the hub corner stalls, which were adversely affected by the rotor hub end wall flows; and is compatible with work reported by Howard et al. (1993), which showed (using time-averaged measurements) that rotor tip clearance has a significant influence on loss generation in the subsequent stator casing region.

Intrapassage Pressure Oscillations. The time-history images equivalent to Figs. 7(*c*) and 7(*d*) in Fig. 8 are of course local manifestations of the changes in the radial and circumferential extent of the stagnation pressure features measured in the two-dimensional stator exit traverse plane. For example, during the part of the cycle where the hub high-pressure region expands and contracts most vigorously (Figs. 8_{IV} to 8_{VI}) the asterisks in these time histories negotiate local peaks. While a complete explanation for all of these perturbations is not yet possible, other effects such as the passing of rotor wakes are clearly significant.

Discussion

It is clear that the flow field perturbations measured across the two-dimensional stator exit traverse plane are very complex, and that they cannot be explained fully in terms of the measured rotor exit flow field (discussed in part I) sweeping past the stator row. The reasons for this additional complexity are most likely due to the following factors: (*i*) The rotor exit flow field may change as it sweeps past the downstream stator. This was thought to be the case in part I, although this could not be confirmed because the measurements at rotor exit were taken at only one circumferential location near the stator leading edge. (*ii*) The stator flow field will be altered as the chopped rotor wakes are convected through the stator passage. (*iii*) The viscous endwall flows have been shown to alter those in the downstream stator, and this will affect the flow elsewhere in the stator passage.

The complicated co-existence of these blade row interaction effects is thought to be responsible for the pressure oscillations measured at stator exit. Similarly, because of the broadly similar nature of the oscillations at rotor exit, it seems reasonable to suppose that they too are due to blade row interaction. It is more difficult to imagine that they are connected with rotor shock oscillation due to vortex shedding as hypothesized by Epstein et al. (1988). Additionally, the most vigorous perturbations seem to be linked strongly with phenomena occurring in

the lower half of the annulus, where the rotor shock system is weakest. This is not consistent with rotor shock effects being a primary source as these would be strongest at higher radii.

These observations may also apply to the rotor exit pressure oscillations reported by Ng and Epstein (1985), Gertz (1986), and Cherrett and Bryce (1991). In formulating the oscillating shock hypothesis, Ng and Epstein (1985) did not have access to such extensive data as presented here and were constrained to seeking an explanation based on a two-dimensional blade-to-blade view of the rotor. However, it is certainly not denied that rotor shock oscillation exists, as full field optical measurements taken elsewhere clearly indicate such behavior. Rather, this may be driven by more global interactions between rotor and stator flow fields during the blade row interaction cycle. Clearly more work is required to investigate this further.

In viewing the area traverse results there are, in addition to indisputable three-dimensional effects such as interaction between rotor and stator corner stalls and tip vortices, other apparent three-dimensional effects such as the radial growth and decay of the high pressure region toward the hub. Whether the latter effects are really three-dimensional, or can be largely explained on a two-dimensional blade-to-blade basis (with apparent spanwise propagation occurring due to changes in phase along the blade span) is not yet clear. Flow calculations using unsteady viscous blade-to-blade methods may throw further light on the problem and these are being pursued.

In general it is hoped further analysis of existing data taken using on-blade pressure sensors and thin-film gages and relating them to the stator inlet and exit flow field measurements will enhance understanding. Calculations using steady, and ultimately unsteady, three-dimensional flow solvers will contribute, and the C148 measurements of course represent an excellent database for the development of these. In the longer term, more comprehensive unsteady measurements would also be helpful in reaching a better understanding. The use of three-dimensional unsteady probes that can distinguish radial components of the flow and the adoption of two-dimensional area traversing at rotor exit would be particularly beneficial.

The data clearly show the need to take such measurements in high-speed engine relevant machines. The published materials that detail the effects of rotor–stator interaction on the endwall flow development in compressor stators, tend to be of the sort reported by Gallus and Schulz and their co-workers. These excellent low-speed experiments have done much to further understanding of the effects of viscous blade wake impingement on downstream stator rows. However, as these studies utilized a rotating bar to simulate the rotor, the resulting behavior may be somewhat misleading. For instance, it has been shown in the C148 data that the stator endwall flows are strongly influenced by the viscous flow features originating in the upstream rotor endwall regions.

Conclusions

Detailed measurements have been taken with a dynamic yawmeter traverse probe downstream of a highly loaded transonic fan stator row. Using a method to counter the temperature sensitivity of the high-frequency response pressure transducers used in the probes, it was possible to obtain absolute pressure measurements from the sensors. Comparison of the yawmeter data with those taken using a variety of pneumatic probes showed the time-averaged yawmeter results to be in very good agreement with the conventional measurements. The following remarks summarize the analysis carried out to date:

1 The stator hub and casing corner stalls change in size during the rotor passing period. This behavior appears to be coupled closely to the passing of the viscous endwall features originating in the upstream rotor row.

2 Large changes in stagnation pressure occur within the inviscid stator core flow regions during the rotor passing period.

3 Because two-dimensional area traverse were carried out at stator exit, it was possible to see that the complicated individual pressure time-histories were linked to the expansion and contraction of high pressure zones in the measurement plane. As the stator exit time-histories bore close similarity to those measured at rotor exit in C148 and other high-speed compressors, it is suggested that blade row interactions are responsible for both. However, two-dimensional rotor exit traverses are needed to confirm this.

4 Computer-based animation was employed extensively to analyze the stator exit measurements, and it is difficult to imagine how else one could assimilate data of this complexity and volume.

The data presented in this paper and part I are complex, and there is much more analysis yet to be done. However, it is unlikely that a full explanation of the observed behavior can be gleaned from the stator exit results done. It is hoped that further analysis, relating the stator inlet and exit flow fields to measurements taken using on-blade pressure sensors and thin-film gages, will shed more light on the mechanisms involved. This analysis will also be supported by a range of steady-state and unsteady CFD methods.

Acknowledgments

The C148 measurements were supported by the UK MoD Strategic Research Programme and by the Aerospace Division of the UK DTI. Thanks are due to Iain Shipman for his help in putting the paper together.

References

A complete set of references applicable to parts I and II of the paper is included in part I.

Measurements of the Tip Clearance Flow for a High-Reynolds-Number Axial-Flow Rotor

W. C. Zierke

K. J. Farrell

W. A. Straka

Applied Research Laboratory,
The Pennsylvania State University,
State College, PA 16804

A high-Reynolds-number pump (HIREP) facility has been used to acquire flow measurements in the rotor blade tip clearance region, with blade chord Reynolds numbers of 3,900,000 and 5,500,000. The initial experiment involved rotor blades with varying tip clearances, while a second experiment involved a more detailed investigation of a rotor blade row with a single tip clearance. The flow visualization on the blade surface and within the flow field indicate the existence of a trailing-edge separation vortex, a vortex that migrates radially upward along the trailing edge and then turns in the circumferential direction near the casing, moving in the opposite direction of blade rotation. Flow visualization also helps in establishing the trajectory of the tip leakage vortex core and shows the unsteadiness of the vortex. Detailed measurements show the effects of tip clearance size and downstream distance on the structure of the rotor tip leakage vortex. The character of the velocity profile along the vortex core changes from a jetlike profile to a wakelike profile as the tip clearance becomes smaller. Also, for small clearances, the presence and proximity of the casing endwall affects the roll-up, shape, dissipation, and unsteadiness of the tip leakage vortex. Measurements also show how much circulation is retained by the blade tip and how much is shed into the vortex, a vortex associated with high losses.

Introduction

Beginning in the pressure surface boundary layer near the rotor blade tip of a turbomachine, a vortex sheet passes through the clearance. Under the influence of the induced velocity field of the vortex sheet, the free edge of the vortex sheet curls over and takes the form of a spiral with a continually increasing number of turns: the roll-up of the tip leakage vortex. As opposed to a wing or a rotor blade tip without an endwall, a rotor blade tip with an endwall clearance results in a higher blade loading that produces a larger pressure difference between the pressure and suction sides of the blade. This pressure difference produces a jet of fluid that carries the vortex sheet through the clearance. Storer and Cumpsty (1991) show that this distinct jet of low-loss fluid occurs downstream of the minimum pressure location on the suction surface. Besides the curling of the free edge of the vortex sheet, the formation of the tip leakage vortex also includes the strong interaction between the leakage jet and the throughflow, further complicating the roll-up of the vortex. Storer and Cumpsty (1991) feel that the interaction of the leakage jet and the throughflow produces an intense shearing that is the principal mechanism of the high loss associated with tip leakage vortices.

Questions still remain concerning the fluid dynamics of the rotor tip leakage vortex, questions that prompted two experiments performed in our high Reynolds number pump (HIREP). Axial-flow pumps and compressors are subject to many of the same design considerations in regard to tip clearance flows. However, in pumps, which are liquid handling machines, the complex flow in the tip region may lead to several types of cavitation, in addition to energy losses. In compressors, where the design is obviously not constrained by the possibility of cavitation, the intersection of the rotor pressure surface and the tip surface is purposely made sharp to promote separation and minimize the leakage mass flow rate. Pump designers, however, must assure the smooth passage of the leakage flow through the clearance to avoid flow separation and the possibility of cavitation in the gap, at the likely expense of the energy losses caused by the larger leakage mass flow rate. Designers of both types of turbomachines face the challenge of minimizing the losses associated with the vortical flows in the tip region—with the further consequence of vortex cavitation in the pump case—caused primarily by the leakage flow, or by the blade tip turning and stretching of the endwall boundary layer vorticity. While the study of cavitation in the tip region is certainly important, it is not the focus here. However, under similar water quality conditions, cavitation can be used as an important flow visualization tool for the structure, location, and relative strength of vortices, information that is paramount in the understanding of tip leakage flow phenomena. Moreover, the large physical size and robustness of pump blading allow more detailed measurements and flow visualization than can be achieved in a typical compressor rig.

Experimental Facility

These experiments were performed in the Garfield Thomas Water Tunnel at ARL Penn State. The tunnel has a 1.22-m-dia, 4.27-m-long test section, which supports water velocities up to 18.29 m/s and static pressures ranging from 20 to 414 kPa. Cavitation experiments employ a water-conditioning, or bypass, system to degas the water. Tunnel turbulence is controlled using a honeycomb placed within the plenum, 2.82 m upstream of the nine-to-one contraction nozzle, giving a measured axial component of the free-stream turbulence intensity level to be 0.107 ± 0.006 percent with 95 percent confidence. Lauchle et al. (1989) give a detailed description of the tunnel, as well as some of the basic experimental procedures.

Contributed by the International Gas Turbine Institute and based on two papers presented at the 39th International Gas Turbine and Aeroengine Congress and Exposition, The Hague, The Netherlands, June 13–16, 1994. Manuscript received at ASME Headquarters June 1995. Paper No. 94-GT-453/454. Associate Technical Editor: E. M. Greitzer.

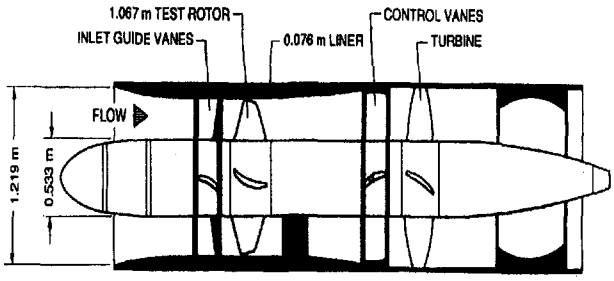

Fig. 1 High-Reynolds-number pump facility

Figure 1 shows a schematic of the HIREP facility. HIREP consists of a 1.07-m-dia pump stage driven by a 1.22-m-dia downstream turbine. The hub has a constant diameter of 0.53 m. As shown in Fig. 1, the two units rotate together on a common shaft in the test section of the water tunnel, such that the main drive impeller of the tunnel overcomes the energy losses within HIREP. The pump includes a row of 13 inlet guide vanes, a row of 7 rotating blades, and three downstream support struts. The turbine includes a row of variable pitch control vanes, a row of rotating blades, and a downstream cruciform support strut. Farrell et al. (1987) give a more detailed explanation of the HIREP facility.

The first HIREP experiment was designed explicitly to investigate the tip leakage vortices—and the subsequent vortex cavitation—that result from varying the clearance, h, between the pump rotor blades and the casing formed by the tunnel liner. The 7 rotor blades included 5 blades with different tip clearances. The rotor blades are designed with a mild blade circumferential lean or skew (skewed in the opposite direction of blade rotation). Each rotor tip section includes a rounded pressure side corner, with a radius of curvature of approximately 25 percent of the local blade thickness. Gearhart (1966) found that this rounded corner prevented local separation of the flow through the tip clearance and, thus, improved the gap cavitation performance. Table 1 presents some of the pertinent geometry and flow parameters for this HIREP design.

The second HIREP experiment focused on acquiring a larger quantity of data from the entire flow field of the pump, in order to establish a detailed database for use in testing numerical prediction methods. This experiment involved more lightly loaded blades than the first experiment and, again, Table 1 gives some of the important geometry and flow parameters for this design. These rotor blades differed from the initial blade designs in that they had substantially more blade lean.

Experimental Technique

The large-scale HIREP facility can accommodate a variety of instrumentation in both a stationary and a rotating frame of reference. A high-capacity, low-noise slip ring accommodates many measurements in the rotating frame. An incremental, optical shaft encoder provides rotor angular position and speed.

Both the first and second experiments employed many of the same experimental techniques. For surface flow visualization, we used an oil-paint method to obtain patterns of skin-friction lines. In order to apply this type of surface flow visualization technique to rotating blades, one must be assured that the centrifugal force does not affect the oil paint in a different manner than it affects the actual fluid. For our HIREP experiments, we combined gear oil with paint, which itself is a combination of linseed oil and pigment. With both the gear oil and linseed oil having a specific gravity near 0.94 (compared to 1.0 for water), the final oil paint has a specific gravity close to that of water, making the added effect of centrifugal force almost negligible. Therefore, following the work of Arakawa and Tagori (1980), this type of surface flow visualization becomes applicable to blades rotating through water, as opposed to blades rotating through air. Within the flow field, the variable pressure system within the water tunnel provides a means for viewing cavitation, a technique that provides valuable flow visualization results. Since the core of the rotor tip leakage vortex has a relatively low static pressure, cavitation visualization allows one to visualize the location and extent of this important feature of the flow field.

Calibrated five-hole pressure probes were used to obtain the HIREP inlet flow, as well as the casing endwall boundary layer upstream of the rotor blades. For studying the tip clearance flow, we acquired most of our flow field data with a two-component laser-Doppler velocimeter (LDV). The argon-ion laser and associated optics—including Bragg cells for frequency shifting—were mounted on a three-axis traversing table that helped position the location of the measurement volume at the desired flow field location. All of these measurements were made on the test section centerline through a specially designed window. Data were collected using a field point measurement method. In this procedure, the measurement volume remains stationary, and each LDV measurement sample is tagged with the angular position of the rotor, via the optical shaft encoder and a rotating

Table 1 Geometry and flow parameters for HIREP

Parameter	First HIREP Experiment		Second HIREP Experiment	
	Inlet Guide Vanes	Rotor Blades	Inlet Guide Vanes	Rotor Blades
Blade Number	13	7	13	7
Chord, c	0.16 m (hub) 0.20 m (tip)	0.34 m (hub) 0.21 m (tip)	0.18 m	0.29 m (hub) 0.27 m (tip)
Maximum Blade Thickness, t_{max}/c	12.0% (hub) 10.0% (tip)	15.0% (hub) 9.8% (tip)	11.6%	17.8% (hub) 10.0% (tip)
Solidity	1.25 (hub) 0.79 (tip)	1.41 (hub) 0.43 (tip)	1.36 (hub) 0.68 (tip)	1.19 (hub) 0.56 (tip)
Hub Radius	0.27 m	0.27 m	0.27 m	0.27 m
Tip Radius (nominal)	0.53 m	0.53 m	0.53 m	0.53 m
Rotor Tip Clearance, h/c_{tip}	-	1.07% 3.00% 3.54% 5.82% 5.89%	-	1.24%
Diffusion Factor	-	0.37 (hub) 0.12 (tip)	-	0.28 (hub) 0.12 (tip)
Reference Velocity, V_{ref}	11.0 m/sec		10.7 m/sec	
Rotor Rotational Speed	270 rpm		260 rpm	
Rotor Tip Velocity, U_{tip}	15.1 m/sec		14.5 m/sec	
Flow Coefficient, $\phi = V_{ref}/U_{tip}$	0.73		0.74	
Blade Chord Reynolds Number, $Re_{c_{tip}} = W_1 c_{tip}/\nu$	3,900,000		5,500,000	

machinery resolver. The water tunnel was seeded with 1.5 μm silicon carbide particles to increase the data collection rates. Typically, for every position of the LDV measurement volume, a total of 100,000 samples were obtained, of which approximately 50 percent were axial velocity measurements and the other 50 percent tangential.

A few experimental techniques were unique to the initial HIREP experiment. First, we implemented a dynamic gap measuring system to show that the low angular speed of the rotor did not change the rotor tip clearance from its static value. With this point proven, we did not implement the system in the second experiment. Also, one of the original rotor blades employed a two-component rotor tip force transducer to measure steady-state hydrodynamic loads over the top 10 percent of the rotor blade span. This instrumented blade was varied to measure the amount of integrated lift for rotor blades with four different tip clearances. Finally, this initial experiment employed several piezoresistive pressure transducers flush mounted on the rotor blade tip and on the inner diameter of the casing. The three transducers at 99 percent span were located at 10 and 50 percent chord on the pressure surface and at 40 percent chord on the suction surface. Also, two transducers were located at 50 percent chord, one on the tip surface and one on the casing. Farrell (1989) gives further details of the experimental technique used during this first HIREP experiment.

For the second HIREP experiment, within one rotor blade passage, both the pressure and suction surfaces included 40 static-pressure taps, each connected via tubing to a solid-state piezoresistive pressure transducer located near the centerline of the rotor hub. Relevant to this tip clearance flow study, the pressure taps provide measurements of the blade static-pressure distribution at 90 percent span, with 8 taps positioned on both the pressure and suction surface. Zierke et al. (1993) show how the measured blade static pressures were corrected for the effect of rotation. A second additional experimental technique involved the visualization of the rotor tip leakage vortex in a plane normal to the axial-flow direction using a laser light sheet technique downstream of the rotor blades. In order to view the laser light sheet in the vicinity of the rotor tip clearance region, we designed a special periscope and installed it downstream of the rotor blades through the tunnel endwall liner. Using both 10 μm microballoons (with a specific gravity of 1.1) and cavitation bubbles for illumination, this flow visualization technique proved useful for locating the rotor tip leakage vortex relative to the casing endwall.

Besides acquiring a larger quantity of data—especially LDV data—we employed fast-response total-pressure measurements in the same downstream axial plane as some of the LDV measurements, using a probe equipped with a subminiature piezoelectric pressure transducer. Zierke et al. (1993) give further details of the experimental techniques used during the second HIREP experiment.

Experimental Results

Using these techniques, we performed both experiments within HIREP in order to investigate the tip clearance flow. Since the second experiment involved a larger quantity of detailed data, we shall focus on the results from this experiment. However, results from the first experiment will also be given, especially where they give insight into the effect of a varying tip clearance. Geometrically, the rotor blades from both experiments are quite similar. In the second experiment, the tip chord length is a little larger, giving a tip chord Reynolds number of 5,500,000, compared to 3,900,000 for the first experiment.

Surface Flow Visualization. Before attempting to interpret the rotor blade surface flow visualization patterns, we first analyzed many photographs together with physical length measurements taken immediately after each test. The geometric complexities associated with blade lean and twist make such photographs difficult to interpret. Therefore, the resulting patterns have been drawn on projected surfaces. Figure 2 shows the reconstruction of the oil-paint pattern on the suction surface. As discussed further by Zierke et al. (1993), this figure shows that a rather complex, three-dimensional corner separation exists where the suction surface trailing edge meets the hub. Also, Fig. 2 shows that a line of local separation exists on the suction surface, moving from 70 percent chord near the hub to 96 percent chord near the tip.

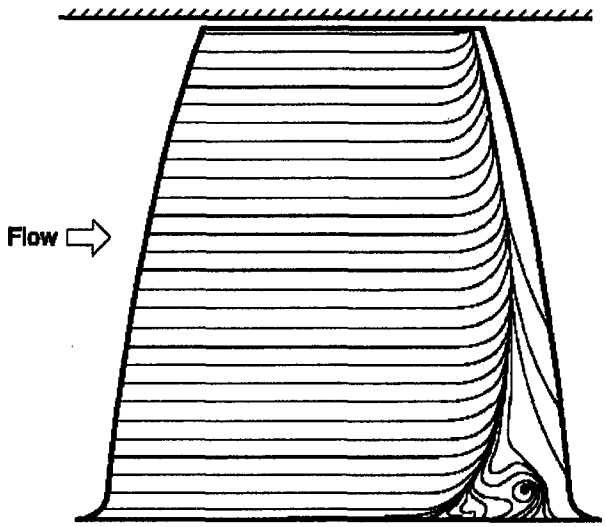

Fig. 2 Schematic of surface flow visualization on the projected rotor blade suction surface

The downstream zone of separation varies from the three-dimensional corner separation near the hub—including the spiral node of separation—to a more two-dimensional type of separation over most of the span. Just upstream of this local separation line, centrifugal effects cause the skin-friction lines to migrate radially outward. Also, skin-friction lines emanating from the pressure surface have moved around the trailing edge within the separation zone—similar to the skin-friction lines on the stator blades of Schulz and Gallus (1988)—and also migrate radially outward.

Because of the radially outward flow near the trailing edge, the surface of separation that lifts off the blade at the local separation line rolls up into a spanwise vortex. Near the casing, this vortex moves in the circumferential direction, away from the suction surface as the blade rotates in the other direction. The oil-paint surface flow visualization from the first HIREP experiment showed similar patterns on the suction surface, with a larger corner separation. In addition, we were able to visualize this vortex as it moved away from the suction surface in the circumferential direction by lowering the tunnel pressure until the vortex began to cavitate. Figure 3 shows a typical cavitation photograph of both this vortex and the tip leakage vortex. This photograph shows that this trailing-edge separation vortex lies closer to the casing than the tip leakage vortex, with both vortices rotating with the same sense. Eventually, the trailing-edge separation vortex rolls up into the tip leakage vortex as it propagates downstream. In the second HIREP experiment, we were unable to obtain a low enough tunnel pressure for this vortex to cavitate. Evidently, the higher loaded rotor blades used in the first experiment created a stronger vortex from the trailing-edge separation and the lower pressure within this vortex core led to cavitation at a higher tunnel pressure, as discussed by Farrell and Billet (1994). However, during a numerical analysis of the second HIREP experiment, Dreyer and Zierke (1994) presented particle paths calculated from their numerical compu-

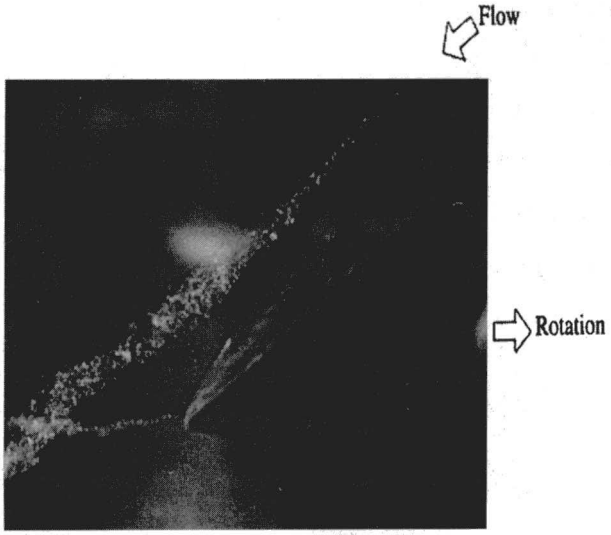

Fig. 3 Photograph of a cavitating rotor tip leakage vortex and a cavitating trailing edge separation vortex near a rotor blade tip section (Farrell, 1989)

tations that clearly showed the existence of the trailing-edge separation vortex, in addition to the rotor tip leakage vortex.

The surface flow visualization patterns over the pressure surface show a very two-dimensional flow. However, one very significant pattern does show up on the pressure surface oil-paint pattern: A radial outward flow exists over the top 8 percent of the span. This radial flow initiates the flow from the pressure surface through the tip clearance. For the second HIREP experiment, Fig. 4 shows the skin-friction lines associated with the leakage flow across the rotor blade tip section. Notice how these skin-friction lines on the rotor blade tip section are not parallel. Near the leading edge, the skin-friction line was tilted 1 deg from the circumferential direction, while near the trailing edge, the skin-friction line was tilted 16 deg from the circumferential direction. Also, recall that the pressure side corner of the rotor blade tip section was rounded to prevent local separation of the leakage flow; therefore, the oil-paint pattern shows no sign of separation. From the first HIREP experiment, the oil-paint patterns showed that the angle between the relative skin-friction lines and the chord line decreased with increasing clearance.

Visualization of the Rotor Tip Leakage Vortex. The relatively low static pressure within the core of the tip leakage vortex allowed us to visualize cavitation within the core at low tunnel pressures. Photographs and videos showed the existence of some cavitating bubbles originating in the clearance near the rotor blade leading edge. Most of the cavitation, however, appears to begin near the suction surface at 15 percent chord, a position very close to the measured minimum pressure point on the suction surface at 90 percent span. Inoue and Kuroumaru (1989) and Storer and Cumpsty (1991) contend that the onset of the vortex sheet rolling-up into the tip leakage vortex occurs near the point of minimum pressure on the suction surface. At this location, the pressure difference across the clearance reaches a maximum, creating a larger leakage jet. Therefore, this origin of the vortex marks the position where the core pressure becomes low enough to establish a cavitating flow. For the first HIREP experiment, cavitation visualization showed that the roll-up of the vortex probably originates closer to the leading edge for smaller tip clearances.

Cavitation visualization showed the circumferential position of the tip leakage vortex within the rotor blade passage. The vortex remains quite close to the suction surface until near 80 percent chord, where it begins to migrate away from the blade. From the vortex cavitation in the first HIREP experiment, we observed that the circumferential position of the vortex within the passage depended weakly on the tip clearance. For large clearances, the vortex was positioned along the suction surface; for smaller clearances, the vortex was approximately t_{max} away from the suction surface at the trailing edge. After analyzing many photographs, as well as videotapes, from the second experiment, we sketched the envelope that enclosed the cavitating vortices from all seven blades at different times. Figure 4 includes this sketch, along with the relative skin-friction lines across the rotor blade tip section as determined from the surface flow visualization. Downstream of the cavitating part of the tip leakage vortex, Fig. 4 shows the circumferential position of the vortex center as determined from the LDV data at three axial measurement planes. Also, we attempted to measure the flow within the clearance region at five chordwise and three radial locations. Within the clearance regions themselves, reflections off the blade tips gave erroneous data. This problem also occurred in the first HIREP experiment for small clearances. However, while the LDV measurement volume was located outside of the clearance regions and within the blade passages, we could measure data. Figure 4 shows our estimates of the circumferential position of the vortex from these LDV measurements. Remember that these estimates are based on data at only three closely spaced radial measurement locations. The uncertainty in the position of the vortex increases near the blade leading edge where the vortex has yet to roll up and near the trailing edge where the vortex center has moved to a radial position further inboard of the LDV measurement locations.

Before discussing further details of the position of the tip leakage vortex, let us discuss another piece of information included in Fig. 4: the position of the vortex core as computed from the similarity model of Chen et al. (1991). Over the first half of the blade, this zero blade thickness model computes a trajectory that remains within the clearance established by the actual blade thickness. Farther downstream, however, the computed trajectory matches very well with the vortex cavitation.

The similarity solution of Chen et al. (1991) holds within the blade passage to a point normal to the camber line at the blade trailing edge. Beyond this point, the trajectory of the tip leakage vortex must be computed using their complete vortex model. This model gives a slope discontinuity in the vortex core trajectory near the trailing edge. They report that even though the actual influence of the blade should drop off in a finite distance, their calculations with this slope discontinuity matched experimental results well. Figure 4 shows that our cavitation visualization also showed a change in slope of the vortex core trajectory at a location normal to the camber line at the blade trailing edge, exactly as the complete model would predict. Farther downstream, Fig. 4 shows that the trajectory of the vortex core as determined from the LDV measurements has

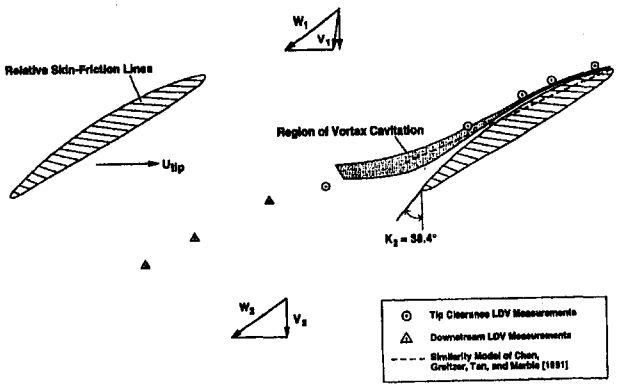

Fig. 4 Schematic of the relative skin-friction lines across the rotor blade tip section and the position of the rotor tip leakage vortex in the blade-to-blade plane

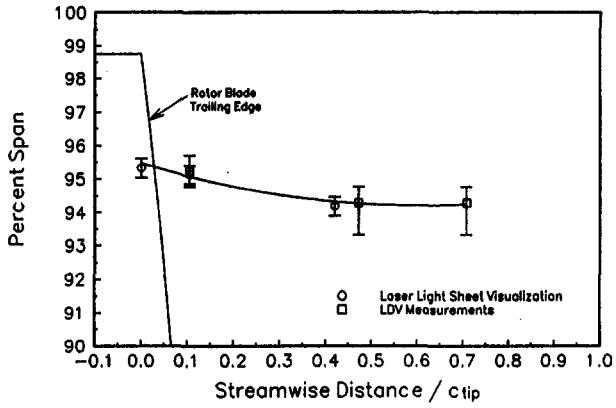

Fig. 5 Spanwise position of the core of the rotor tip leakage vortex

changed slope once again. Here, the vortex core follows the relative flow direction, as determined from a streamline curvature solution, with a 5 deg deviation. Relative to a line tangent to the camber line at the trailing edge, the deviation angle of the vortex core trajectory is 24 deg. As the vortex loses strength and convects downstream of the rotor blades, one would certainly expect that it would convect with the mean flow.

Another phenomenon occurs in the trailing-edge region that may affect the vortex core trajectory and vortex kinking. As shown in the cavitation photograph in Fig. 3 from the first experiment, the trailing-edge separation vortex moves in the circumferential direction, away from the suction surface as the blade rotates in the other direction. Figures 3 also shows that this second vortex lies closer to the casing than the tip leakage vortex. These two vortices pass one another, at different radii, near the trailing-edge plane and the interaction of these two vortices may affect the vortex core trajectory. This interaction should occur for any rotor blades where the centrifugal effects create a radial flow on the suction surface with some trailing-edge separation. In their tip leakage vortex experiment, Inoue and Kuroumaru (1989) also measured a strong radial velocity moving up the suction surface trailing edge into the endwall region. While the trailing-edge separation vortex is smaller in strength than the tip leakage vortex, it can induce an additional downstream velocity component onto the tip leakage vortex that may help the trajectory move back into the relative flow direction. Also, since the two vortices rotate with the same sense, the trailing-edge separation vortex will rotate around the stronger tip leakage vortex if the two vortices are close enough together.

As the tip leakage vortex convects downstream, the position of the vortex core moves radially. Looking through a periscope from a position downstream of the rotor blades, we observed the tip leakage vortex from a video camera during the laser light sheet visualization. The position of each frame in the video corresponded to an individual rotor blade. Visualizing the oncoming vortices at three axial positions of the laser light sheet and analyzing the LDV measurements at three different axial positions allowed us to track the radial position of the tip leakage vortices. Figure 5 presents the radial position of the tip leakage vortex within HIREP. The error bars on the position determined from the laser light sheet visualization represent 95 percent confidence bands, while the error bars on the positions determined from the LDV data represent the uncertainty that the vortex core may actually lie on an adjacent radial measurement location. Figure 5 shows that most of the radial migration of the vortex core takes place within the blade passage, with only a slight radial migration taking place downstream of the blade trailing edge. The model of Chen et al. (1991) indicates that the vortex core remains at nearly a constant radial location downstream of the trailing edge. Similar to our data, Inoue et al. (1986) report a small decrease in the radial position of the center of the vortex with streamwise direction.

Unsteadiness of the Rotor Tip Leakage Vortex. Aside from giving the location of the tip leakage vortex, both types of flow visualization also showed the unsteadiness of the tip leakage vortex. Other investigators have also observed this spatial vortex wandering. For a tip vortex trailing behind a wing or hydrofoil, Reed (1973) and Baker et al. (1974) observed oscillations and random wandering of the vortex as it convected downstream. They attributed this unsteadiness to free-stream turbulence. Using double-pulsed holography, Green (1988) performed another study of the tip vortex trailing behind a hydrofoil. He found that the primary source of core unsteadiness is associated with global core flow structure instabilities. Reconstruction of holograms allowed him to observe both vortex kinking and a second and rather chaotic unsteadiness that he labeled mini-vortex breakdown. Most of his unsteadiness was located where the initially large axial velocity excess within the vortex core would rapidly decelerate. For flows with a rotor tip clearance, Straka and Farrell (1992) extended the analysis of the tip leakage vortex data acquired in the first HIREP experiment by Farrell (1989) and found the existence of vortex wandering and kinking. Besides the effects of free-stream turbulence and vortex core instabilities, they noted that the unsteady interaction of the rotor blades with the wakes from the inlet guide vanes can contribute to the unsteadiness of the tip leakage vortex. Finally, within an axial-flow turbine, Yamamoto and his colleagues (1993) acquired hot-wire measurements of the tip leakage vortex emanating from the clearance region between stator blades and the endwall located downstream of a row of rotor blades. They found that both the strength and size of the tip leakage vortex changed with time.

Similar to the observations made by Straka and Farrell (1992), we observed unsteady wandering and kinking of the tip leakage vortices in the second HIREP experiment using videos and photographs taken during our cavitation visualization tests. The photograph in Fig. 6 shows an example of vortex kinking. While the vortex wandering and kinking appeared at all locations where the vortex core cavitated, this unsteadiness was most evident near the trailing edge where the vortex core trajectory changed slopes. Some interaction with the trailing-edge separation vortex may increase the unsteadiness of the tip leakage vortex. Farther downstream, the laser light sheet visualization showed that the tip leakage vortex experienced an

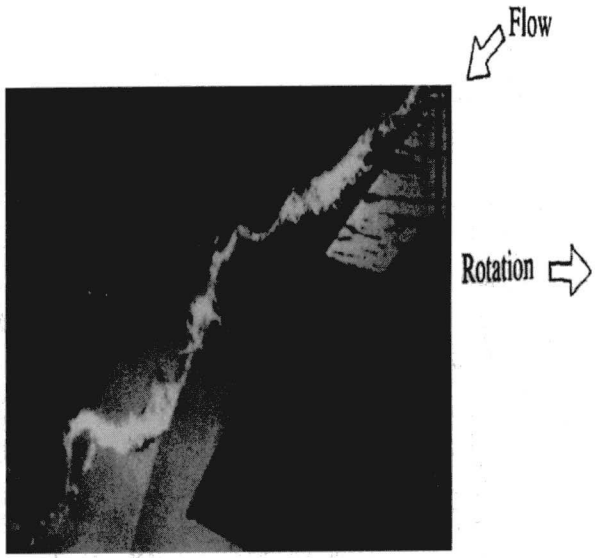

Fig. 6 Photograph of a cavitating rotor tip leakage vortex with vortex kinking

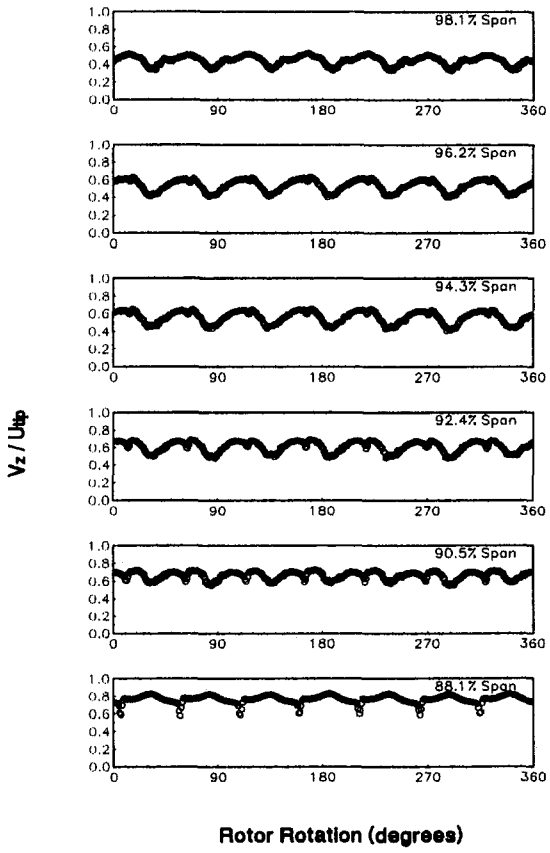

Fig. 7 Circumferential variation of the axial velocity measured 32.2 percent chord axially downstream of the rotor tip trailing edge with LDV

unsteady wandering in the circumferential and radial directions. Cavitation visualization from the first HIREP experiment showed that the vortex kinking and oscillating motion were more prevalent for vortices emanating from small tip clearances.

One detrimental effect of vortex wandering involves time-averaged flow measurements. Velocity measurements through the vortex core must be fast enough to avoid averaging errors induced by the unsteady motion of the core. For time-averaged measurements, such as LDV measurements, the effect of vortex wandering is to broaden the measured velocity profiles and reduce the magnitude of the maximum vortex tangential velocity. Straka and Farrell (1992) developed an oscillating vortex model that approximates how vortex wandering affects time-averaged velocity profiles. Using this model and their data, they applied least-squared cubic curve fits to find empirical relationships between the apparent and instantaneous values of core size and relative maximum tangential velocity. In the second HIREP experiment, we also used cavitation visualization to obtain an amplitude of oscillation in the circumferential direction normalized by an estimate of the vortex core radius, $A/r_c = 2.1$. For a broadened velocity profile measured with an LDV, the approximate model of Straka and Farrell (1992) uses this parameter to estimate an apparent core radius that is 2.04 times larger than the actual vortex core radius and an apparent maximum relative tangential velocity that is 0.64 times the actual value. In addition, our laser light sheet visualization allowed us to observe the oscillation in the radial direction. While observations allowed us to estimate an amplitude of oscillation in the radial direction of 0.5 cm, we could not estimate the instantaneous core size. Therefore, we could not apply the model of Straka and Farrell (1992) in the radial direction.

Rotor Blade Exit Flow. With all of the LDV data resolved into one degree storage windows, we analyzed the data taken in various axial planes. These measurements included one plane from the first experiment (34.0 percent chord downstream of the rotor tip trailing edge) and three planes from the second experiment (4.8, 21.4, and 32.2 percent chord downstream). An analysis showed that no inlet guide vane wake was present in the vicinity of the LDV measurement volume. The presentation here will show only a few significant results from this large quantity of data.

At the furthest downstream axial position in the second experiment, the LDV data provide information on the relative importance between the wakes and the tip leakage vortices in the casing endwall region. Near this endwall and at the farthest downstream measurement plane in the second experiment, Fig. 7 presents variations in the axial velocities around the circumference of the machine. At 88.1 percent span, Fig. 7 shows axial velocity deficits associated with the rotor blade wakes. Also at 88.1 percent span, the regions of increased axial velocity between the wakes result from the three-dimensional influence of the tip leakage vortices. Just closer to the endwall, at 90.5 percent span, the wakes have a similar deficit, but the tip leakage vortices also have a similar axial velocity deficit, with a broader profile. For the axial velocity distributions at radial locations even closer to the endwall, notice how the flow structures associated with the tip leakage vortices dominate the structures associated with the wakes, having much deeper and broader profiles. With these strong deficits in axial velocity, the tip leakage vortices would have a strong impact on any downstream blades or struts.

A more detailed investigation showed that the circumferential variations in tangential velocity and in the axial and tangential nondeterministic unsteadiness (unsteadiness that does not correlate with rotor shaft speed) also show the dominance of the tip leakage vortices. The nondeterministic unsteadiness associated with tip leakage vortices involves turbulence, as well as a random motion of the vortex structures themselves. Figure 8 presents a contour plot of the axial nondeterministic unsteadiness at the furthest downstream axial position in the second experiment. The locations of the skewed rotor blade wakes and the tip leakage vortices are very clear. In terms of turbulence intensity, the wakes within the casing endwall region reach maximum values of 14.9 percent for axial turbulence intensity and 12.1 percent for tangential turbulence intensity. Using the same free-stream velocity for normalization, the tip leakage vortices reach values of 21.2 percent for axial turbulence intensity and 22.6 percent for tangential turbulence intensity. All of the variations in velocities and unsteadiness have been examined at the two upstream measurement planes. Although similar in shape, these distributions show larger velocity deficits and increased unsteadiness levels, a trend consistent with viscous decay. Also, variations associated with potential flow effects are more evident at the upstream planes.

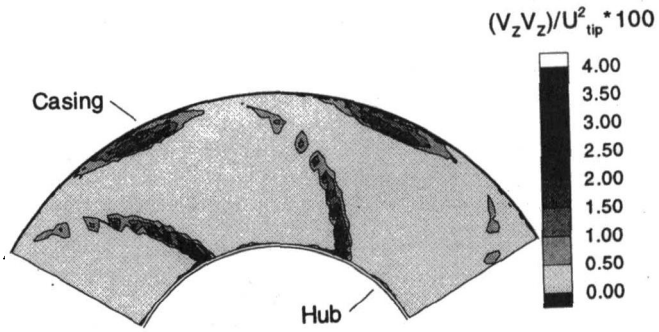

Fig. 8 Nondeterministic axial velocity correlation contours measured 32.2 percent chord axially downstream of the rotor tip trailing edge with LDV

Vortex Models. Visualization of the rotor tip leakage vortex provided very important information on the position of the vortex, as well as information on the vortex unsteadiness. However, for a complete analysis, one must also examine details about the velocity profiles and strength of the vortex. In order to examine these details associated with any vortex in a measured velocity field, one can compare the measurements with ideal formulations of a vortex velocity distribution. First, one must transform the data from a cylindrical coordinate system associated with the turbomachine to a cylindrical coordinate system aligned with the axis of the vortex. In the case where no measurements exist of radial velocity in the turbomachine coordinate system, one can attempt to find an angle between the axial direction of the turbomachine and the axial direction of the vortex and, then, transform the velocity components using this angle. Either before or after transforming the velocity components, one should also make sure that the axial and tangential velocities are velocity perturbations caused by the presence of the vortex. One can simulate these velocity perturbations by subtracting the circumferential-average velocities from the locally measured velocities. Finally, one must take the effect of vortex wandering into account.

Zierke et al. (1993) give details of the ideal formulations for the Rankine vortex and the Burgers vortex, which were used with the LDV data in the analysis of the rotor tip leakage vortex measured in HIREP. For simplicity, the formulation for axial velocity presented by Maxworthy et al. (1985) will be included as part of the Burgers vortex.

Tangential Velocities About the Tip Leakage Vortex. The roll-up of the tip leakage vortex produces a swirling flow about the centerline of the vortex. Using the procedure outlined in the previous section, we determined the tangential or azimuthal velocity about the vortex axis at the three downstream LDV measurement planes. First, we subtracted the circumferential-average values (using area averaging) from the measured axial and tangential velocities. Then, we found that the angle between the axis of the vortex and the axis of HIREP was 63 deg, an angle that allowed us to transform the data to a cylindrical coordinate system aligned with the axis of the vortex. For each of the seven tip leakage vortices, we found the point of minimum axial velocity, in order to give us the circumferential location of the centers of the seven vortices. At each of these circumferential locations, we plotted the tangential velocity distribution along a radial line. This tangential distribution could only be plotted along a radial line since the original LDV measurements contained no radial velocity data.

At all three axial planes in the second HIREP experiment, Fig. 9 shows the tangential velocity distribution within the seven different tip leakage vortices and within an average tip leakage vortex. At 4.8 percent chord downstream of the tip of the rotor blade trailing edge, Fig. 9 shows that the minimum and maximum values of tangential velocity differ, giving an asymmetric vortex. The presence of the casing endwall seems to interfere with the rolling-up of the tip leakage vortex. Also, we acquired data in this plane down to only 81.0 percent span because of the swept trailing edge. Farther downstream to positions 21.4 and 32.2 percent chord axially downstream of the tip of the blade trailing edge, the vortex appears to dissipate, with decreases in the magnitude of both the minimum and maximum values of tangential velocity. The laser light sheet visualization also showed signs of a more dissipated vortex structure in going from 4.8 percent chord to 19.1 percent chord downstream.

Axial Velocities Within the Tip Leakage Vortex. A strong coupling exists between the tangential and axial velocities of a vortex. The instabilities in the initial roll-up of a vortex can lead to either an excess or deficit of the axial velocity in the vortex core, relative to the free stream. As the vortex begins to convect downstream within the blade passage, the circulation (and maximum tangential velocity) about the core increases as

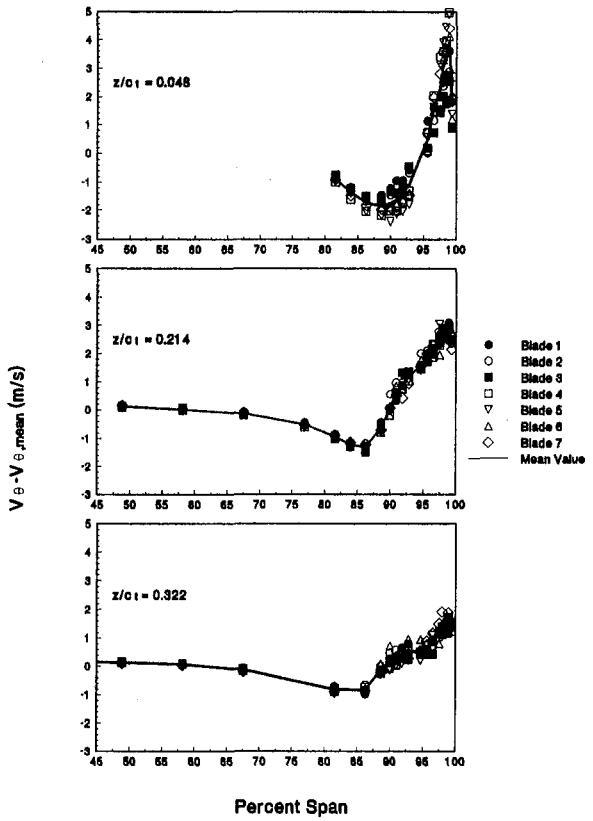

Fig. 9 Tangential velocity perturbation distributions for the rotor tip leakage vortices measured 4.8, 21.4, and 32.2 percent chord axially downstream of the rotor tip trailing edge

more vorticity is continuously wound into the core region. From the conservation of momentum across the vortex,

$$\frac{\partial p}{\partial r} = \rho \frac{V_\theta^2}{r},$$

this increase in vorticity and tangential velocity causes a drop in the centerline pressure, which, in turn, increases the axial velocity. Batchelor (1964) discusses the theory of axial velocities in tip vortices in more detail.

For tip vortices without the presence of an endwall, several investigators have found this jetlike behavior in axial velocity. For instance, Singh and Uberoi (1976) used a hot-wire probe to measure the tip vortices from a wing at an angle of attack. The tip vortex, which originated near the leading edge, contained an axial jet in the vortex core near the trailing edge. This jet decayed to zero in about 2.4 chord lengths and then further decayed into a wakelike structure, with an expansion in the core size. Two chord lengths downstream of the trailing edge, Orloff (1974) acquired LDV data through the tip vortex at three angles of attack. While he measured axial velocity defects at the two lowest angles of attack, he measured an axial velocity excess at the highest angle of attack. Measurements showed that the higher loading at the increased angle of attack gave a tip vortex with larger tangential velocities. Again, the larger tangential velocities reduce the pressure at the centerline of the vortex, which increases the axial velocity. Finally, in a similar wing experiment, Lee and Schetz (1985) used a five-hole probe to measure the tip vortex six chord lengths downstream of the trailing edge at chord Reynolds numbers ranging from 210,000 to 1,500,000. While changes with downstream distance due to viscous diffusion are slow, they found large changes in the vortex structure with Reynolds number. The tangential velocity—and, thus, the axial velocity—increased with Reynolds

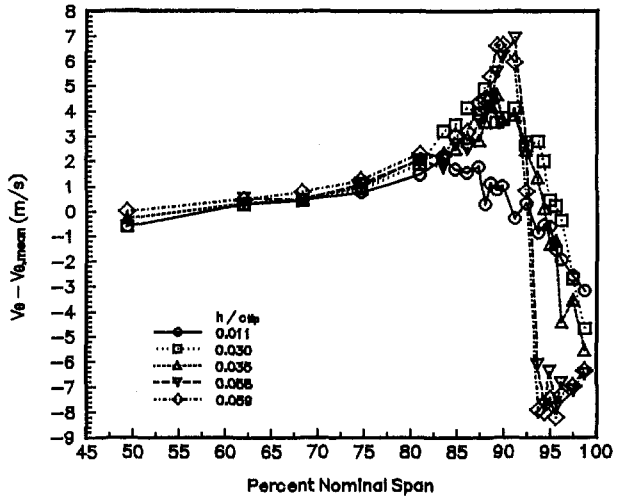

Fig. 10 Tangential velocity perturbation distributions within the tip leakage vortices from various clearances measured 34.0 percent chord axially downstream of the rotor tip trailing edge

number until the largest chord Reynolds number yielded an axial jet, even at a distance six chord lengths downstream of the trailing edge.

For tip leakage vortices, the vortex structure changes because of the presence and proximity to the endwall. From the first HIREP experiment, at a position 34.0 percent chord axially downstream of the tip of the rotor blade trailing edge, Fig. 10 shows how the tangential velocity within the tip leakage vortex changes with tip clearance, while Fig. 11 shows how the axial velocity changes. Remember that these measured vortex characteristics result from an experiment with a blade chord Reynolds number of 3,900,000. For large tip clearances (h/c_{tip} = 5.89 and 5.82 percent), large tangential velocities and jetlike profiles of axial velocity exist. As the clearance decreases (h/c_{tip} = 3.54 percent), the tangential velocity decreases and the axial velocity vanishes. Finally, for small clearances (h/c_{tip} = 3.00 and 1.07 percent), the tangential velocity is reduced further, giving wakelike profiles of axial velocity. Also, the lack of axisymmetry in the vortices for smaller clearances results from the close proximity of the endwall. Observations for smaller clearances also showed that the vortices originate closer to the leading edge and that these vortices experience more vortex kinking and oscillation.

As a possible explanation for the change in vortex structure with changing clearance, consider the pressure field in the flow external to the vortex. Within the blade passage—especially near the suction surface, closer to the vortex—the vortex is convected through a region with an adverse pressure gradient. The static pressure within the core of the vortex increases as the vortex is convected through this external adverse pressure gradient and reduces the axial velocity. Also, as Erickson (1981) points out, the pressure increase within the core will be larger than that of the external flow. This result occurs because the external adverse pressure gradient also reduces the tangential velocity of the vortex (see Fig. 10), which, in turn, increases the static pressure in the core and reduces the axial velocity. Downstream of the blade passage, the external pressure gradient diminishes and the vortex changes form only in response to viscous effects, requiring hundreds of vortex core diameters for significant structural changes. As the clearance increases, the loading of the tip section decreases and less of the circulation is retained at the blade tip. Instead, more circulation is shed into the vortex. This reduction in blade loading also decreases the streamwise adverse pressure gradient, resulting in larger axial velocities in the tip leakage vortices corresponding to larger clearances.

In a different, but related explanation, consider the leakage flow as the clearance increases and more circulation is shed into the tip leakage vortex. Recall that the oil-paint patterns from the first HIREP experiment showed that the angle between the relative skin-friction lines and the chord line decreased with increasing clearance. Erickson (1981) considered the familiar spiral sheet model of the vortex, where the inclination of the spiraling vortex lines to the vortex axis is such as to make them all induce a downstream component of velocity along the axis. If the streamlines move in a circular motion along the vortex sheet and the orthogonal vortex lines move parallel to the vortex axis, one has a circular vortex with no axial velocity. Relative to the axis, larger inclinations of the vortex lines induce larger velocities along the axis. This result corresponds to a decreasing angle between the streamlines and the vortex axis. Therefore, from the relative skin-friction lines observed in the first HIREP experiment, increases in clearance should give a larger component of velocity along the vortex axis.

The nondimensional clearance (h/c_{tip} = 1.24 percent) from the second HIREP experiment fell between the two smallest clearances from the first experiment. Therefore, as expected, the measurements from the second experiment showed a wakelike profile in axial velocity for all three axial measurement planes. Figure 12 shows these axial velocity distributions for the seven different tip leakage vortices and for an average tip leakage vortex. At 4.8 percent chord downstream of the tip of the rotor blade trailing edge, Fig. 12 shows this wakelike structure with an excess in axial velocity very close to the casing endwall. Moving further axially to 21.4 percent chord downstream of the tip of the trailing edge, the vortex becomes larger, but with a larger defect in axial velocity. One can explain this by noting that the reduced tangential velocity at this plane (see Fig. 9) will cause the centerline pressure to increase and the axial velocity to decrease.

At 32.2 percent chord downstream of the tip of the rotor blade trailing edge, viscous dissipation appears to reduce the defect in axial velocity. From Fig. 9, note that the tangential velocities also decrease; the usual coupling between that tangential and axial velocities does not hold. Also, from both the tangential and axial velocity profiles, note that the structure of the asymmetric vortex appears to be changing faster than one might expect from viscous dissipation alone. Again, the presence and proximity of the casing endwall seems to be having a strong influence on the tip leakage vortex. Phillips and Head (1980) suggest that large-scale motions within the turbulent endwall boundary layer will obscure and absorb the tip leakage

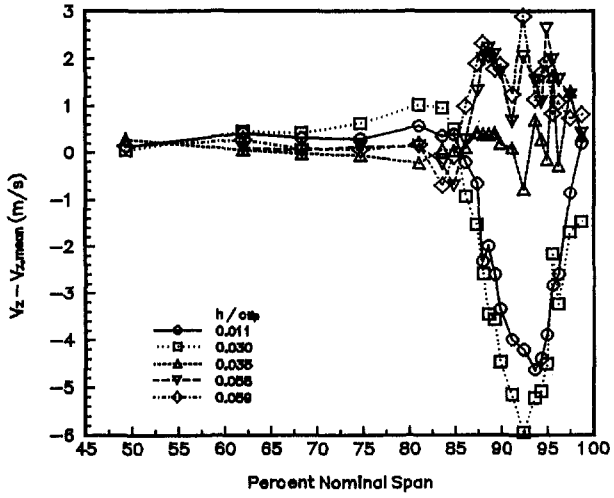

Fig. 11 Axial velocity perturbation distributions within the tip leakage vortices from various clearances measured 34.0 percent chord axially downstream of the rotor tip trailing edge

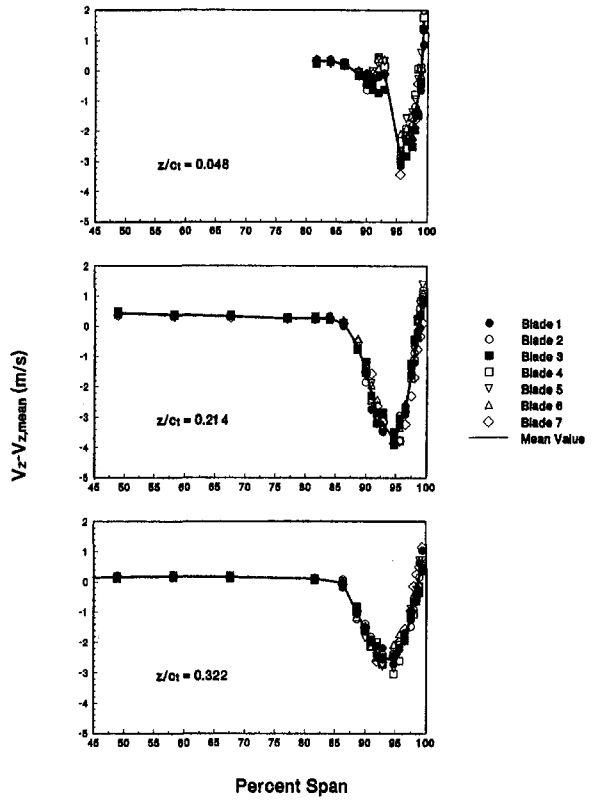

Fig. 12 Axial velocity perturbation distributions for the rotor tip leakage vortices measured 4.8, 21.4, and 32.2 percent chord axially downstream of the rotor tip trailing edge

vortex. Barker and Crow (1977) studied the interaction of a vortex pair with a wall. In the vicinity of the wall, the vortex showed a strong eccentricity, with the normally circular vortex core becoming elliptical. The deformed vortex core then became unsteady. Further complications occur in the formation of the tip leakage vortices within HIREP; namely, the casing endwall affected the vortices before they were fully rolled up. If one measured these vortices even farther downstream, they might exhibit the "rebounding" or "bouncing" effect that airplane wing tip vortices experience when interacting with the ground.

Nondimensional Velocity Distributions. The tip leakage vortices can now be presented in a dimensionless form and compared with ideal velocity distributions. First, the distance between the minimum and maximum tangential velocities defines the diameter of the vortex core, with the center of the core located half way in between these two core edges. Since the casing endwall has such a strong effect, we take $(V_\theta)_{max}$ at the edge of the core farthest from the endwall. With these values, Fig. 13 presents the nondimensional tangential velocity profiles for the tip leakage vortices at all three axial measurement planes, compared to the Rankine and Burgers vortices. The measured vortices at all three axial positions are similar, with the strong asymmetry giving a larger peak in tangential velocity at the edge of the core nearest to the endwall. The vortex farthest upstream compares better with the Burgers vortex than the downstream vortices. Next, using the minimum axial velocity with the Maxworthy et al. (1985) empirical fit for the Burgers vortex, Fig. 14 presents the nondimensional axial velocity profiles for all three tip leakage vortices. These asymmetric vortices all have minimum values of axial velocity that vary slightly from the vortex centers as found from the tangential velocity profiles. Also, the measured axial velocity gradients appear larger than those indicated by the Burgers vortex.

The measured values of r_c and $(V_\theta)_{max}$ allow us to compute the total circulation of the tip leakage vortex, $\Gamma_\infty = 2\pi r_c (V_\theta)_{max}$. Using the oscillating vortex model of Straka and Farrell (1992) and the amplitude of oscillation determined from the cavitation visualization $A/r_c = 2.1$, we approximated how the vortex parameters change from the averaging effect of vortex wandering. Table 2 presents these vortex parameters at all three measurement planes. As also seen in Fig. 13, Table 2 shows that the size of the vortex initially grows and then remains constant, while the values of $(V_\theta)_{max}$ decrease as the vortex convects downstream. Also, Table 2 shows a decrease in Γ_∞ with increasing axial distance. Actually, one might expect the vortex circulation to increase as it leaves the blade passage, since streamwise vortices within the trailing vortex sheet should be wound into the tip leakage vortex. However, viscous dissipation can reduce $(V_\theta)_{max}$ and, thus, reduce the circulation, with the casing endwall seemingly increasing this dissipation. Two other points must be considered. First, a further examination of Fig. 13 will show that the density of LDV data near the edge of the vortex core farthest from the casing endwall may not be sufficient, increasing the uncertainty of the vortex core parameters. Second, the values of $(V_\theta)_{max}$ taken at this edge of the vortex core may not be representative of the actual values of $(V_\theta)_{max}$ within this

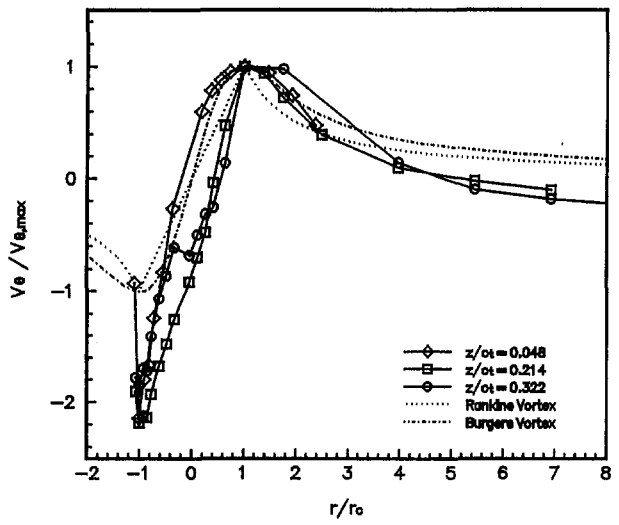

Fig. 13 Nondimensional tangential velocity distributions for the rotor tip leakage vortices: measurements and ideal formulations

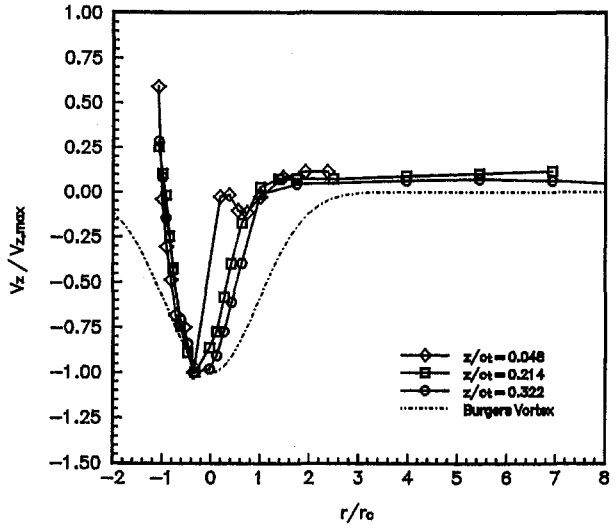

Fig. 14 Nondimensional axial velocity distributions for the rotor tip leakage vortices: measurements and ideal formulations

Table 2 Measured and corrected parameters for the rotor tip leakage vortices

z/c_{tip}	0.048	0.214	0.322
Measured Values			
r_c (mm)	13.7	16.8	16.8
$(V_\theta)_{max}$ (m/sec)	1.83	1.30	0.82
Γ_∞ (m^2/sec)	0.158	0.137	0.087
Values Corrected for Circumferential Wandering			
r_c (mm)	6.6	8.1	8.1
$(V_\theta)_{max}$ (m/sec)	2.87	2.02	1.29
Γ_∞ (m^2/sec)	0.119	0.103	0.066

asymmetric, elliptical vortex core, resulting in smaller estimates of the circulation.

Retained Lift. As mentioned previously, not all of the bound circulation in the blade is shed downstream into the rotor tip leakage vortex, unlike the case of a tip vortex without the presence of an endwall. Lakshminarayana and Horlock (1962) first suggested changing their lifting line model to account for the circulation retained at the blade tip, and this modification formed the basis for the improved model of Lakshminarayana (1970). Later, using the leakage jet model of Rains (1954), Lewis and Yeung (1977) developed another model for the retained lift. These models imply that the fluid between the tip and the endwall will effectively experience a lift force that is related to the circulation shed into the tip leakage vortex.

For the second HIREP experiment, we can determine the circulation at all spanwise locations by computing

$$\Gamma = \frac{2\pi}{N_B}\left(r_2\bar{V}_{\theta_2} - r_1\bar{V}_{\theta_1}\right)$$

along a streamsurface around the entire circumference of the machine, where N_B is the number of blades. Assuming cylindrical streamsurfaces, we used measured values of tangential velocity to compute the spanwise variation of circulation on the rotor blades. These results showed that the value of circulation at the rotor blade tip is roughly 0.325 m^2/s, and that the circulation decreases across the clearance, where the circulation should vanish at the casing. Referring back to Table 2, we can estimate the shed circulation as $\Gamma_\infty = 0.119$ m^2/s in the tip leakage vortex near the trailing edge, after correcting for the effects of wandering. Thus, 73.2 percent of the total circulation is retained at the blade tip. For the rotor clearance within HIREP, the model of Lakshminarayana (1970) predicts that 71.9 percent of the circulation will be retained at the blade tip, while the model of Lewis and Yeung (1977) predicts 84.1 percent.

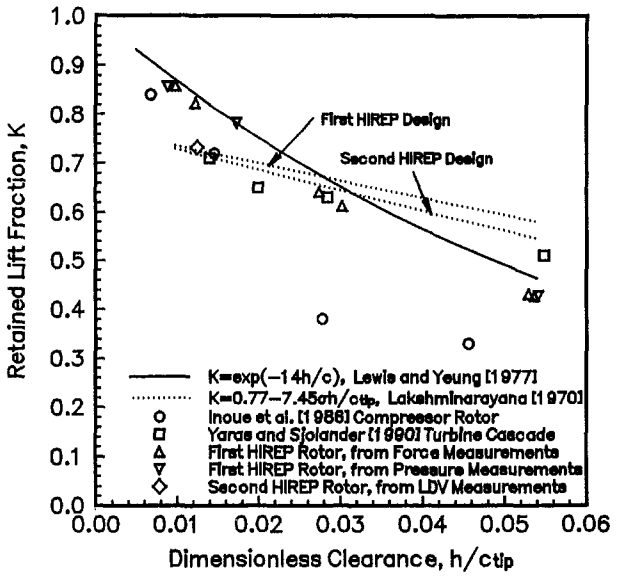

Fig. 15 Percentage of total circulation retained as lift for variations of tip clearance

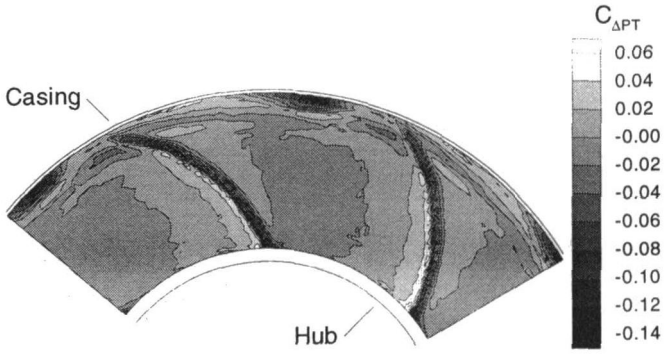

Fig. 16 Contours of the total-pressure variation coefficient measured with the fast-response, total-pressure probe 32.2 percent chord axially downstream of the rotor tip trailing edge

Using the results from the first HIREP experiment, we used two alternate methods to determine how the amount of retained lift varies with tip clearance. First, the two-component rotor tip force transducer provided direct measurements of the retained lift, albeit, an average value integrated over the top 10 percent of the blade. The normalized value of retained lift was obtained by extrapolation to zero clearance. Second, the pressure transducers flush mounted at 50 percent chord on the pressure surface and at 40 percent chord on the suction surface provide useful data. Since the position of maximum lift on the rotor tip section should occur near midchord for this design, the static-pressure data from these two transducers allowed us to estimate the variation of retained lift with clearance. Figure 15 shows these results, along with the results from the second experiment and the models of Lakshminarayana (1970) and Lewis and Yeung (1977). Both of these models resulted from experimental data, and these data—along with the data of Inoue et al. (1986) and Yaras and Sjolander (1990)—show a large scatter in retained lift (or circulation). One problem occurs in the various methods of estimating the retained lift from different types of data. And even though a broadly applicable model does not exist, these correlations do allow a designer to perform trade-off studies at normal operating clearances (h/c_{tip} = 0.01 to 0.03).

Total-Pressure Measurements. At the farthest downstream measurement plane used to acquire LDV data in the second HIREP experiment, we also performed a radial survey with a fast-response total-pressure probe. This probe continuously measured data with a response time fast enough to resolve the total pressures for instantaneous angular positions of the rotor, positions measured via the optical encoder. Even though piezoelectric transducers cannot measure the mean value of total pressure, they do provide excellent measurements of the total-pressure variation about the mean, Δp_T. For different circumferential positions of the rotor, Fig. 16 shows how the total pressure varies from the mean in terms of a pressure coefficient,

$$C_{\Delta p_T} = \frac{\Delta p_T}{\frac{1}{2}\rho V_{\text{ref}}^2}.$$

As with the LDV measurements of axial and tangential velocity, the total pressure variations of Fig. 16 clearly show the structure of the rotor tip clearance vortices and the skewed rotor blade wakes. The low total pressures in these regions—especially in the tip clearance vortices—indicate that these are regions of large total-pressure losses. In other experimental investigations, Inoue et al. (1986), Yaras and Sjolander (1990), and Storer and Cumpsty (1991) have also shown that tip clearance flows lead to high losses.

Summary

Two experiments have been performed to acquire flow measurements in the rotor blade tip clearance region of a high-Reynolds-number pump. The initial experiment involved rotor blades with varying tip clearances, while a second experiment involved a more detailed investigation of a rotor blade row with a single tip clearance.

The flow visualizations on the blade surface and within the flow field indicate that the combination of centripetal acceleration and separation near the trailing edge of the rotor blade suction surface results in the formation of a trailing-edge separation vortex, a vortex that migrates radially upward along the trailing edge and then turns in the circumferential direction near the casing, moving in the opposite direction of blade rotation. A computational analysis of this rotor corroborates the existence of this secondary vortex. Flow visualization also helps in establishing the trajectory of the tip leakage vortex core, which exhibits a kink near the trailing edge. The trailing-edge separation vortex, which lies closer to the endwall than the tip leakage vortex, seems to have an influence on this trajectory. Finally, the periodic interaction of the rotor blades with wakes from the upstream inlet guide vanes—as well as free-stream turbulence and vortex structure instabilities—will also affect the unsteadiness of the vortex. This unsteadiness will lead to averaging errors of time-averaged flow measurements.

The detailed measurements show the effects of tip clearance size and downstream distance on the structure of the rotor tip leakage vortex. The character of the velocity profile along the vortex core changes from a jetlike profile to a wakelike profile as the tip clearance becomes smaller. This change in character is related to the adverse pressure gradient in the region of the tip leakage vortex and the angle at which the vortex lines are wound into the vortex core. Also, for small clearances, the presence and proximity of the casing endwall affects the roll-up, shape, dissipation, and unsteadiness of the tip leakage vortex. The tip leakage vortices would strongly influence periodic unsteady interactions with any downstream blades, since the structure of the vortices dominates the structure of the rotor blade wakes. Several types of measurement show how much circulation is retained by the blade tip and how much is shed into the vortex. Finally, fast-response measurements show that this vortex structure includes low total pressures associated with high losses.

Acknowledgments

The first experiment was conducted under the sponsorship of the United States Navy Department, while the second experiment was supported by the Advanced Research Projects Agency.

References

Arakawa, C., and Tagori, T., 1980, "Fundamental Experiments of Oil Films on a Rotating Disk," *Flow Visualization II,* W. Merzkirch, ed., *Proceedings of the Second International Symposium on Flow Visualization,* Bochum, Federal Republic of Germany, Sept. 9–12, pp. 127–131.

Baker, G. R., Barker, S. J., Bohaf, K. K., and Saffman, P. G., 1974, "Laser Anemometer Measurements of Trailing Vortices in Water," *Journal of Fluid Mechanics,* Vol. 65, Part 2, pp. 325–336.

Barker, S. J., and Crow, S. C., 1977, "The Motion of Two-Dimensional Vortex Pairs in a Ground Effect," *Journal of Fluid Mechanics,* Vol. 82, Part 4, pp. 659–672.

Batchelor, G. K., 1964, "Axial Flow in Trailing Line Vortices," *Journal of Fluid Mechanics,* Vol. 20, Part 4, pp. 645–658.

Chen, G. T., Greitzer, E. M., Tan, C. S., and Marble, F. E., 1991, "Similarity Analysis of Compressor Tip Clearance Flow Structure," ASME JOURNAL OF TURBOMACHINERY, Vol. 113, pp. 260–271.

Dreyer, J. J., and Zierke, W. C., 1994, "Solution of the Average-Passage Equations for the Incompressible Flow Through Multiple-Blade-Row Turbomachinery," The Pennsylvania State University, Applied Research Laboratory Technical Report, No. TR 94-05.

Erickson, G. E., 1981, "Vortex Flow Correlation," Air Force Wright Aeronautical Laboratories Technical Report, AFWAL-TR-80-3143 (Northrop Corporation Report NOR-80-152).

Farrell, K. J., 1989, "An Investigation of End-Wall Vortex Cavitation in a High Reynolds Number Axial-Flow Pump," M.S. Thesis, Department of Mechanical Engineering, The Pennsylvania State University.

Farrell, K. J., McBride, M. W., and Billet, M. L., 1987, "High Reynolds Number Pump Facility for Cavitation Research," *ASME International Symposium on Cavitation Research Facilities and Techniques—1987,* FED-Vol. 57, J. W. Holl and M. L. Billet, eds., pp. 61–68.

Farrell, K. J., and Billet, M. L., 1994, "A Correlation of Leakage Vortex Cavitation in Axial Flow Pumps," ASME *Journal of Fluids Engineering,* Vol. 116, pp. 551–557.

Gearhart, W. S., 1966, "Tip Clearance Cavitation in Shrouded Underwater Propulsors," *AIAA Journal of Aircraft,* Vol. 3, No. 2.

Green, S. I., 1988, "Trailing Vortex Core Unsteadiness—An Exploratory Study of Reynolds Number Effects," presented at the AIAA First National Fluid Dynamics Congress.

Inoue, M., and Kuroumaru, M., 1989, "Structure of Tip Clearance Flow in an Isolated Axial Compressor Rotor," ASME JOURNAL OF TURBOMACHINERY, Vol. 111, pp. 250–256.

Inoue, M., Kuroumaru, M., and Fukuhara, M., 1986, "Behavior of Tip Leakage Flow Behind an Axial Compressor Rotor," ASME *Journal of Engineering for Gas Turbines and Power,* Vol. 108, pp. 7–14.

Lakshminarayana, B., and Horlock, J. H., 1962, "Tip Clearance Flow and Losses for an Isolated Compressor Blade," British A. R. C. Report and Memorandum 3316.

Lakshminarayana, B., 1970, "Methods of Predicting the Tip Clearance Effects in Axial Flow Turbomachinery," ASME *Journal of Basic Engineering,* Vol. 92, pp. 467–480.

Lauchle, G. C., Billet, M. L., and Deutsch, S., 1989, "High-Reynolds Number Liquid Flow Measurements," *Frontiers in Experimental Fluid Mechanics,* M. Gad-el-Hak, ed., Springer-Verlag, Berlin–Heidelberg, pp. 95–157.

Lee, H., and Shetz, J. A., 1985, "Experimental Results for Reynolds Number Effects on Trailing Vortices," *Journal of Aircraft,* Vol. 22, No. 2, pp. 158–160.

Lewis, R. I., and Yeung, E. H. C., 1977, "Vortex Shedding Mechanisms in Relation to Tip Clearance Flows and Losses in Axial Fans," British A. R. C. Report and Memorandum 3829.

Maxworthy, T., Hopfinger, E. J., and Redekopp, L. G., 1985, "Wave Motions on Vortex Cores," *Journal of Fluid Mechanics,* Vol. 151, pp. 141–165.

Orloff, K. L., 1974, "Trailing Vortex Wind-Tunnel Diagnostics With a Laser Velocimeter," *Journal of Aircraft,* Vol. 11, No. 8, pp. 477–482.

Phillips, W. R. C., and Head, M. R., 1980, "Flow Visualization in the Tip Region of a Rotating Blade Row," *Journal of Mechanical Sciences,* Vol. 22, pp. 495–521.

Rains, D. A., 1954, "Tip Clearance Flows in Axial Flow Compressors and Pumps," Hydromechanics and Mechanical Engineering Laboratories, California Institute of Technology, Report No. 5.

Reed, R. E., 1973, "Properties of the Lateral Random Oscillations of Trailing Vortices Observed in Wind-Tunnel Tests," Neilson Engineering and Research, Inc., NEAR TR 47.

Schulz, H. D., and Gallus, H. E., 1988, "Experimental Investigation of the Three-Dimensional Flow in an Annular Compressor Cascade," ASME JOURNAL OF TURBOMACHINERY, Vol. 110, pp. 467–478.

Singh, P. I., and Uberoi, M. S., 1976, "Experiments on Vortex Stability," *Physics of Fluids,* Vol. 19, No. 12, pp. 1858–1863.

Storer, J. A., and Cumpsty, N. A., 1991, "Tip Leakage Flow in Axial Compressors," ASME JOURNAL OF TURBOMACHINERY, Vol. 113, pp. 252–259.

Straka, W. A., and Farrell, K. J., 1992, "The Effect of Spatial Wandering on Experimental Laser Velocimeter Measurements of the End-Wall Vortices in an Axial-Flow Pump," *Experiments in Fluids,* Vol. 13, pp. 163–170.

Yamamoto, A., Mimura, F., Tominaga, J., Tomihisa, S., Outa, E., and Matsuki, M., 1993, "Unsteady Three-Dimensional Flow Behavior Due to Rotor–Stator Interaction in an Axial-Flow Turbine," ASME Paper No. 93-GT-404.

Yaras, M., and Sjolander, S. A., 1990, "Development of the Tip-Leakage Flow Downstream of a Planar Cascade of Turbine Blades: Vorticity Field," ASME JOURNAL OF TURBOMACHINERY, Vol. 112, pp. 609–617.

Zierke, W. C., Straka, W. A., and Taylor, P. D., 1993, "The High Reynolds Number Flow Through an Axial-Flow Pump," The Pennsylvania State University, Applied Research Laboratory Technical Report, No. TR 93-12.

A New Endwall Model for Axial Compressor Throughflow Calculations

J. Dunham
Propulsion Technology Department,
Defence Research Agency,
Pyestock, Farnborough, Hampshire,
United Kingdom

It is well recognized that the endwall regions of a compressor—in which the annulus wall flow interacts with the mainstream flow—have a major influence on its efficiency and surge margin. Despite many attempts over the years to predict the very complex flow patterns in the endwall regions, current compressor design methods still rely largely on empirical estimates of the aerodynamic losses and flow angle deviations in these regions. This paper describes a new phenomenological model of the key endwall flow phenomena treated in a circumferentially averaged way. It starts from Hirsch and de Ruyck's annulus wall boundary layer approach, but makes some important changes. The secondary vorticities arising from passage secondary flows and from tip clearance flows are calculated. Then the radial interchanges of momentum, energy, and entropy arising from both diffusion and convection are estimated. The model is incorporated into a streamline curvature program. The empirical blade force defect terms in the boundary layers are selected from cascade data. The effectiveness of the method is illustrated by comparing the predictions with experimental results on both low-speed and high-speed multistage compressors. It is found that the radial variation of flow parameters is quite well predicted, and so is the overall performance, except when significant endwall stall occurs.

1 Introduction

The flow through an axial compressor is three-dimensional, viscous, and unsteady. Research is in progress on algorithms for computing such flows, but meanwhile the design and analysis of turbomachines will continue to be done in two interlinked phases: computation of the "throughflow"—the time-averaged and circumferentially averaged flow through the whole machine, known as the "S2" solution—and computation of the "blade-to-blade" flow through individual blade rows in more detail, known as the "S1" solution.

Considerable advances in the blade-to-blade (S1) computations are still being made. Quasi-three-dimensional steady viscous–inviscid calculations or viscous (Reynolds-averaged Navier–Stokes) calculations are in regular use and so are fully three-dimensional steady viscous calculations. Unsteady codes are emerging. Less effort is being devoted to parallel improvements in the throughflow (S2) codes, which are needed to supply the boundary conditions for the blade-to-blade codes, and which provide the framework of all multistage designs. Codes are now available, however, which solve the viscous throughflow equations (Adkins and Smith, 1982; Gallimore and Cumpsty, 1986; de Ruyck and Hirsch, 1988; Howard and Gallimore, 1993; Ucer and Shreeve, 1992; Dunham, 1992), and it is time to improve the boundary conditions employed in doing so.

The boundary conditions required by any throughflow code are:

1 the pitchwise-averaged stagnation pressure at every calculation station, normally expressed as a loss coefficient to be applied to some upstream value;
2 the pitchwise-averaged flow angle;
3 an effective blockage, to account for boundary layers.

In principle, these boundary conditions should be supplied (except of course at inlet) from the blade-to-blade solution. In practice, quasi-three-dimensional blade-to-blade calculations (that is, calculations along a meridional stream surface produced by the throughflow calculation) are used to generate two-dimensional (2D) loss and angle values. Then, recognizing that the annulus wall boundary layers, secondary flows, and tip clearance flows have important effects in the endwall regions, three-dimensional (3D) corrections are applied and also a blockage is introduced. It should be possible—and in due course it will become possible—to predict the full 2D + 3D loss, angle, and blockage from fully 3D computations. At present, empirical 3D corrections are used.

The 3D corrections now in use have either been obtained by correlating measurements made in cascades (Roberts et al., 1988) or by indirect deductions from multistage tests—that is, by seeing what endwall assumptions seem to give the observed throughflow (Calvert et al., 1989; Dunham, 1992). These ways of arriving at 3D corrections have serious defects. It is obvious that the incoming endwall boundary layer must affect the result, as must the tip clearance, but few systematic measurements are available to correlate. Furthermore, it is believed that tailoring the aerofoil shape in the endwall region ("endbending") and tailoring the endwall shape itself can improve the performance and surge margin, presumably by changing the "3D corrections," and the correlation approach is fundamentally incapable of predicting such changes.

Leboeuf (1984) presented a complex analytical approach to predicting endwall phenomena that appears to be heading toward fully 3D computations. De Ruyck and Hirsch (1988) proposed a simpler analytical scheme, which was successful for a single stage and forms one of the starting points of the present method.

The purpose of the research reported here is to produce an analytically based endwall model, using both annulus wall boundary layer (AWBL) theory and secondary flow theory, which replaces wholly empirical 3D corrections by explicit calculations of loss, angle, and blockage in the endwall regions. By this means, the plan is to make the S1/S2 design and analysis

Contributed by the International Gas Turbine Institute and presented at the 39th International Gas Turbine and Aeroengine Congress and Exposition, The Hague, The Netherlands, June 13–16, 1994. Manuscript received by the International Gas Turbine Institute February 11, 1994. Paper No. 94-GT-75. Associate Technical Editor: E. M. Greitzer.

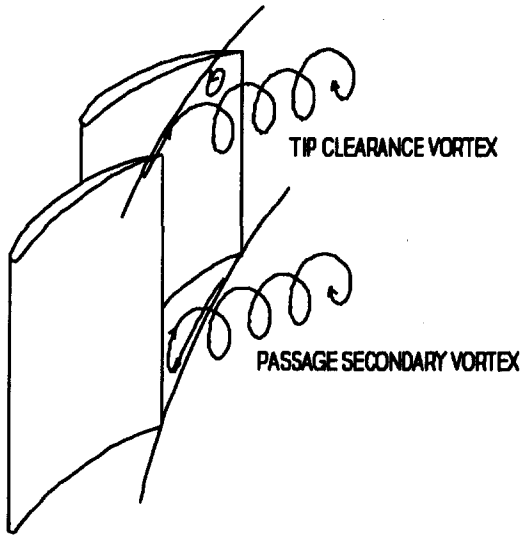

Fig. 1 Vortex patterns

system (Calvert and Ginder, 1985) predict the correct overall performance and radial distributions without using empirical losses and gas angles.

Section 2 of this paper describes the new endwall model. Sections 3 and 4 describe its application to a linear cascade and to a rotating cascade respectively, utilising extensive experimental data. Then in Section 5 some complete multistage compressors are analyzed.

2 The Endwall Model

2.1 The Physical Phenomena Modeled. A complex three-dimensional boundary layer develops along the annulus walls. For the purposes of a throughflow calculation, the circumferential average boundary layer is modeled. The displacement thickness, in particular, determines the "blockage."

Leylek and Wisler (1991) have shown that the flow within a compressor is significantly affected by the radial transfer of momentum, energy, and entropy across the meridional streamlines by two physical mechanisms: turbulent diffusion and turbulent convection. Both are modeled.

Secondary flow (Fig. 1) is a well-known phenomenon, which generates streamwise vortices that alter the pitchwise-average flow angles. At the exit from a blade passage the flow near the wall turns more than it would in midstream ("overturning") and the flow some way away from the wall (just outside the boundary layer) turns less than it would in midstream ("underturning"). Although secondary flow is an inviscid phenomenon, it only occurs to a significant extent because the incoming AWBL constitutes the normal vorticity needed to create it. The AWBL model itself, however, only predicts the crossflow within the boundary layer; a separate secondary flow model is provided to predict the underturning outside the boundary layer.

Finally, tip clearance effects are modeled. When there is a clearance between the end of the blade and the wall, air flows from the pressure side of the aerofoil to the suction side through the clearance, creating a tip clearance vortex in the opposite sense to the passage secondary vortex (Fig. 1). Measurements show that both a secondary vortex and a clearance vortex develop, but the latter is stronger. So the net vorticity generates *overturning* outside the AWBL (which the secondary flow model predicts) and *underturning* near the wall (which the AWBL model predicts).

2.2 The Annulus Wall Boundary Layer Model. The AWBL model chosen is that of Hirsch and de Ruyck (1981), with modifications. This is an integral boundary layer method, which avoids the need to use a fine grid in the AWBL regions. The key assumption in this type of method is the blade defect forces—that is, the extent to which the blade lift and drag change through the boundary layer. Hirsch and de Ruyck proposed algebraic expressions for the defect forces, in a form justified by the physical phenomena involved but with four empirical constants chosen to fit available experimental data. These expressions have been retained but with different empirical constants. The details are given in Dunham (1993), including an account of how the constants were chosen.

2.3 The Secondary Flow Model. There are two steps in the calculation of secondary flow: the calculation of the streamwise vorticity, and the calculation of the pitchwise-average tangential velocity induced by it. The equation given by Marsh (1974) is used to calculate the passage secondary vorticity, and the finite difference scheme of de Ruyck and Hirsch (1988) is used to calculate the pitchwise-average changes in flow angle. The details are given in Appendix 1.

2.4 The Tip Clearance Model. A new simple model is proposed (Fig. 2). The bound vorticity on each blade is assumed to be shed at its geometric tip. This is represented in the streamline curvature model by a vorticity at the nearest grid point adjusted to give the same induced circulation as the actual tip vortex (Dunham, 1993). This vorticity is added to the passage secondary vorticity before solving as explained in Section 2.3 for the secondary deviation. Since the tip clearance vorticity is usually larger than the passage secondary vorticity and of opposite sign, it reverses the direction of the net circulation.

2.5 The Spanwise Mixing Model. The viscous form of the streamline curvature equations, as derived by Gallimore and Cumpsty (1986), is solved, to enable spanwise mixing effects due to turbulent diffusion to be included. Following Dunham (1992), the free-stream eddy viscosity is calculated from the equation

Nomenclature

$G = r^{1.5}\Delta v_r$
GAL = turbulent diffusion constant
H = stagnation enthalpy
$\dot{m}$ = mass flow
N = number of blades in the row
r = radius
s = pitch
s' = staggered pitch, $s \cos \alpha$
S = distance along streamline
v = velocity
Δv_r = radial velocity difference across the trailing edge of a blade
W = axial velocity
x = axial distance
α = flow angle
δ = boundary layer thickness
δ^* = displacement thickness
θ_{xx} = axial momentum thickness
$\theta_{\theta x}$ = tangential momentum thickness
μ_t = eddy viscosity
ξ = vorticity
ρ = density
$r\phi$ = distance measured across staggered pitch
Ω = angular velocity

Subscripts

e = at edge of boundary layer
mid = at midpitch
r = radial
s = streamwise
sec = due to secondary flow
wall = relative to the wall
x = axial
θ = tangential
ϕ = normal to the streamline

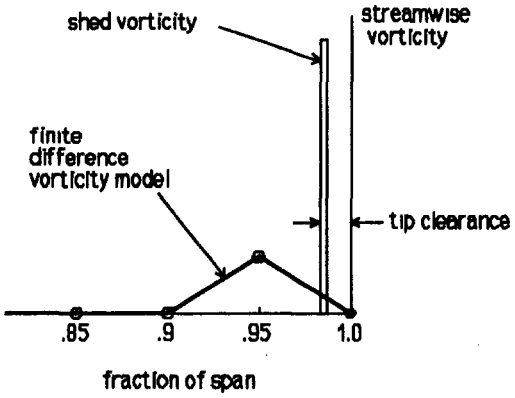

Fig. 2 Vorticity model

μ_t = density × axial velocity × span × GAL,

where GAL is an empirical constant assumed to be the same throughout the cascade or compressor.

Within turbomachinery blading, however, the strong passage vortices located near the edge of the annulus wall boundary layers, shown in Fig. 1, stir up the boundary layers, convecting mainstream fluid into them and convecting low-energy fluid into the mainstream instead. Using the radial velocities calculated in Section 2.3, an estimate is made of the mass flow exchanged between the boundary layers and the mainstream and hence the radial interchanges of momentum and entropy due to turbulent convection. The details are given in Appendix 2.

3 Application to a Linear Cascade

Salvage (1974) tested a large number of low-speed cascades over a range of conditions, and reported measurements of the spanwise variation of the pitchwise-mean local deflection and pressure loss, concentrating on the endwall region. (The local deflection is the change in gas angle from the upstream to the downstream traverse plane at that distance from the wall, and the local loss coefficient is similarly defined with respect to the upstream flow at that distance from the wall.) These measurements were used to choose values of the two empirical constants in the AWBL method that do not involve tip clearance, and also to select the value GAL = 0.0004. Several examples are given in Dunham (1993); one is shown in Fig. 3, a 45 deg camber cascade tested with δ = 13 percent span (run 35) and

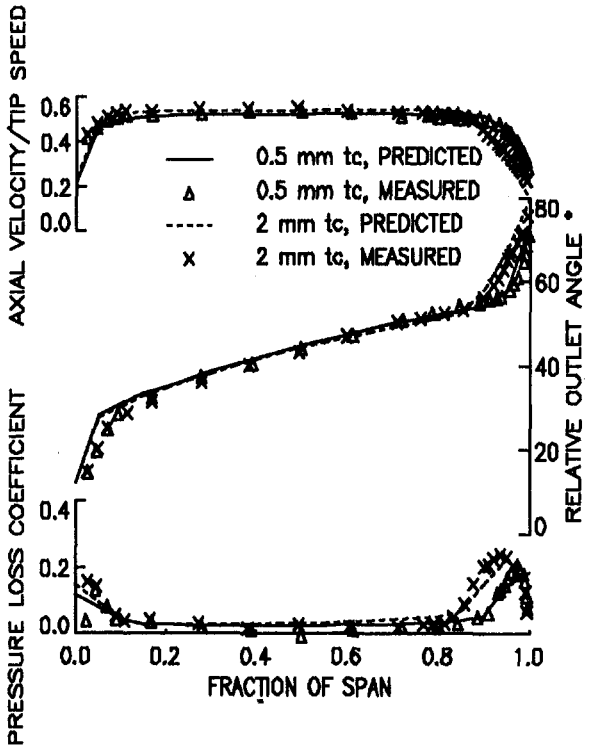

Fig. 4 Rotor: effect of tip clearance

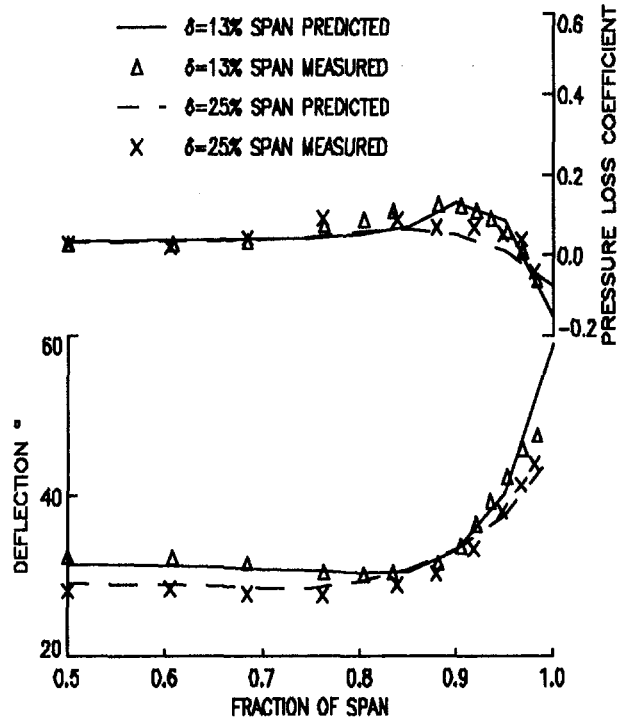

Fig. 3 Cascade: effect of inlet boundary layer

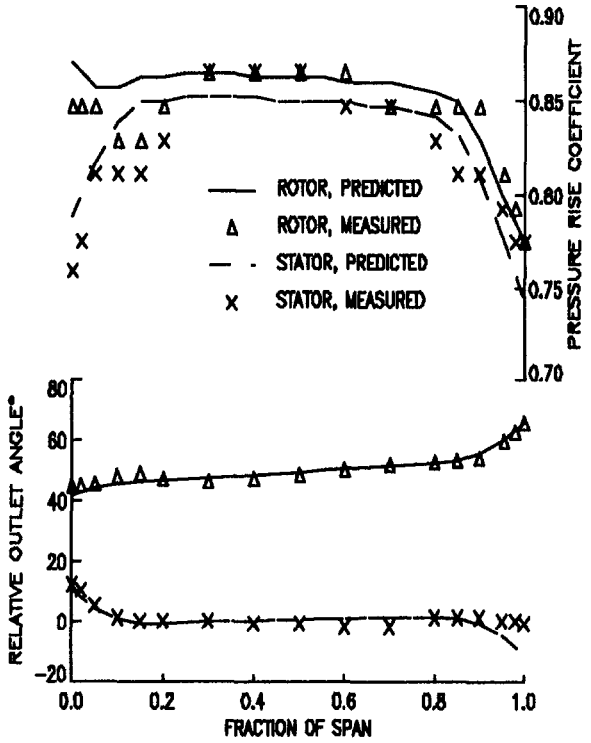

Fig. 5 Four-stage low-speed compressor

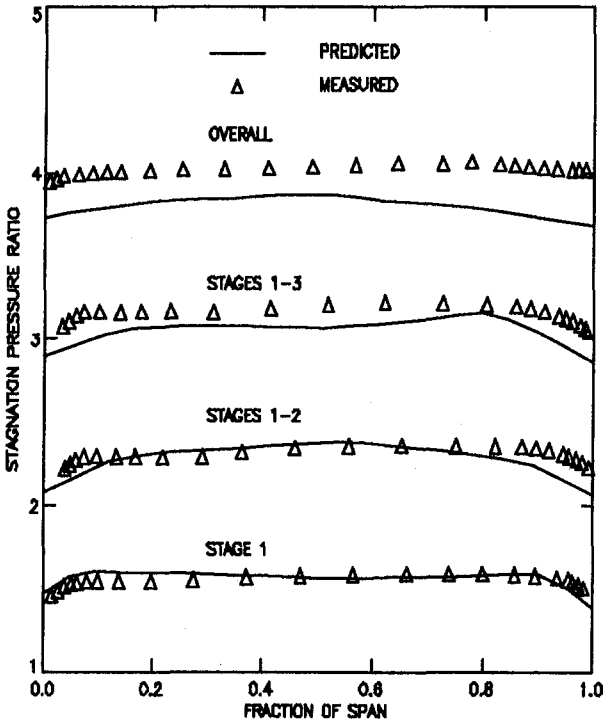

Fig. 6(*a*) C147: Pressure ratio

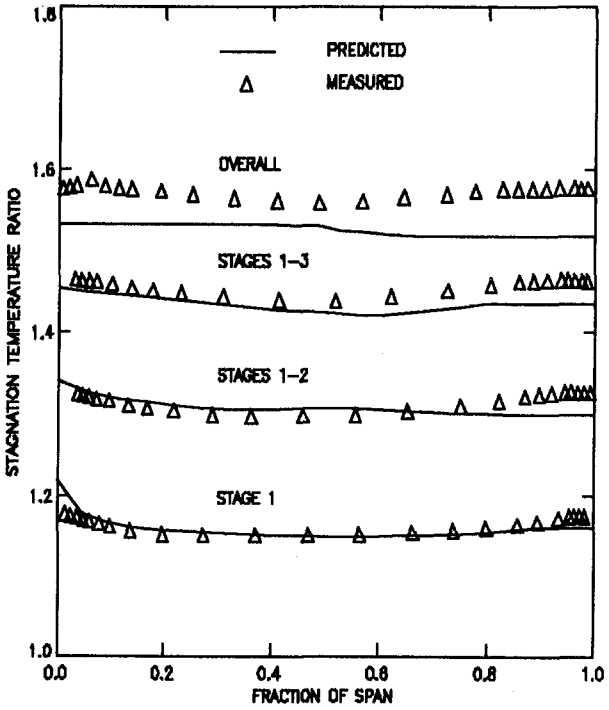

Fig. 6(*b*) C147: Temperature ratio

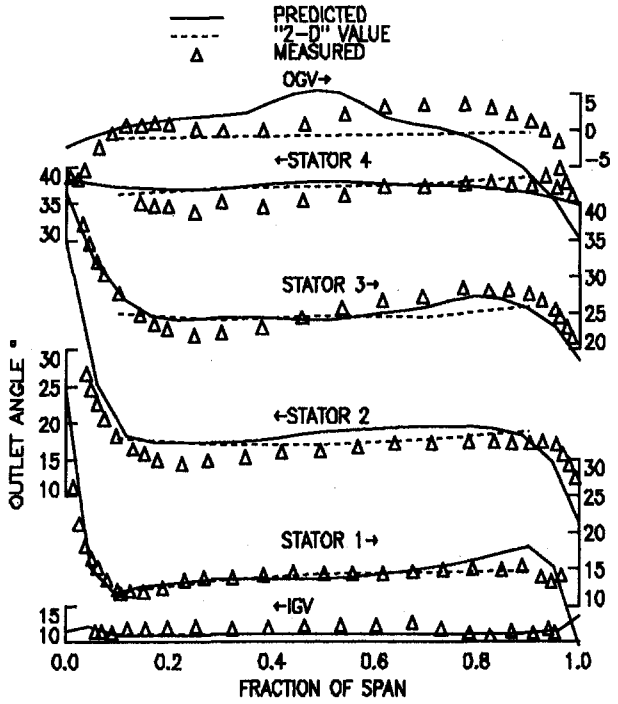

Fig. 6(*c*) C147: Stator outlet gas angles

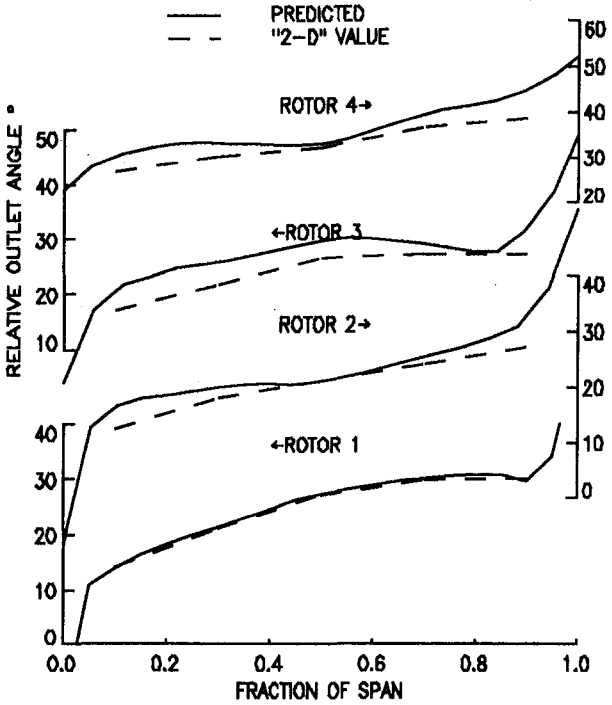

Fig. 6(*d*) C147: Rotor outlet relative gas angles

25 percent span (run V12). The predictions are remarkably good. Notice the change in midspan deflection caused by the secondary flow at the low aspect ratio of unity.

4 Application to an Isolated Rotor

Inoue et al. (1987) conducted a systematic set of tests on a low-speed isolated rotor, measuring the inlet and outlet flows, and reporting the spanwise variation of pitchwise-averaged values. They varied the tip clearance from 0.5 to 5 mm (blade height 89.5 mm). One illustration of their results has been selected. Runs 1A and 1C were with 0.5 mm and 2 mm tip clearance, respectively, at a lift coefficient of 0.5 and an inlet casing boundary layer thickness $\delta = 3.5$ percent span. (The hub inlet boundary layer was not measured in detail.) The constants chosen from the Salvage runs were retained, including GAL, and the tip clearance-related constants were chosen to match the Inoue results as far as possible.

Figure 4 compares predictions and measurements for runs 1A and 1C. The small tip clearance results are well predicted,

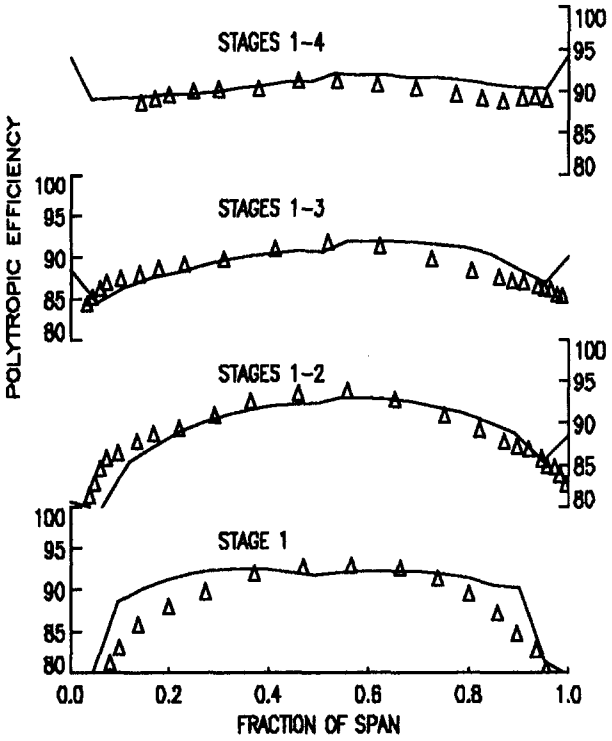

Fig. 6(e) C147: Efficiency

and the changes due to the larger tip clearance are quite well followed. Notice the extra effective blockage increases the axial velocity. The tip loss is much bigger.

5 Application to Complete Compressors

Robinson (1991) tested a low-speed four-stage compressor with stage loadings representative of an aeroengine core compressor. He reported pitchwise-averaged pressure ratios and flow angles after stage 3 rotor and stator.

Figure 5 compares the measurements on his free vortex datum build near peak efficiency with predictions using the present method. (The pressure rise coefficient is defined as the stagnation pressure rise divided by (density × mean blade speed^2).) In making the predictions, the two-dimensional loss coefficients

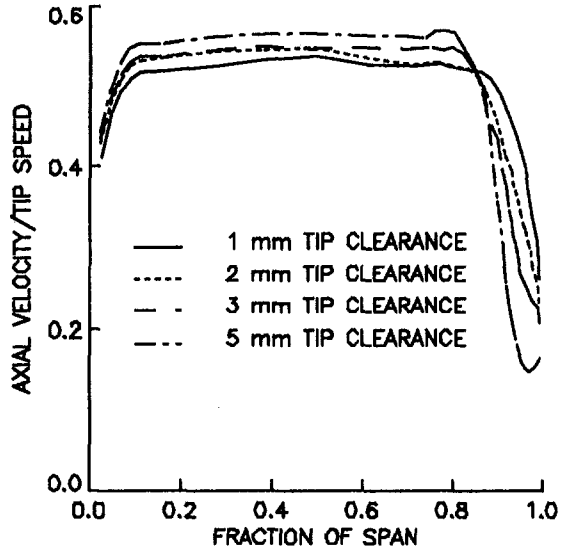

Fig. 7 Rotor: effect of tip clearance on measured velocity

were chosen to match the observed midspan results, but the four constants and GAL chosen in Sections 3 and 4 were retained. In general the endwall effects are well predicted except for the deflection at the casing end of the stators. The predicted polytropic efficiency is 86.4 percent, which compares well with the measured 86.8 percent.

Calvert et al. (1989) tested a four-stage high-speed compressor with cantilevered stators, designated C147, representative of the rear stages of an aero-engine core compressor, and undertook interstage traverses. Their results were analyzed by Dunham (1992) using fitted empirical endwall corrections. Figure 6 shows the predictions obtained using the present method employing 2D losses and gas angles calculated using the method of Calvert (1982), and again the same empirical constants. This is therefore a direct test of the S1/S2 system with the present endwall model. 39 axial planes and 21 equally spaced radial stations were used in the S2 calculation, and the S1 calculations were done at 10, 30, 50, 70, and 90 percent span.

It will be seen that the overall temperature and pressure rise at the design mass flow are underpredicted. The predicted overall polytropic efficiency is 90.1 percent as against the measured 89.1 percent. (To reach the measured pressure ratio, the flow has to be reduced by about 3 percent.) Also, the boundary layers predicted in stages 3 and 4 are much too thick, especially at the casing. These inaccuracies are directly linked. As can be seen in Figs. 6(c) and 6(d), the excessively thick predicted casing boundary layer gives rise to exaggerated secondary deviation in the mainstream and hence too low an enthalpy rise. Without the spanwise convection model this problem was much worse. Figure 6(e) shows the efficiency distribution. (The "measured" values were evaluated along the predicted streamlines.) It will be seen that the predictions are good at stage 2 outlet, but the losses in the outer half of the annulus in the later stages are underestimated.

The AWBL is not predicted to separate anywhere, but very high shape factors are predicted at both ends of stage 1 rotor: 1.82 at the hub, where a corner separation was seen in the test results (Dunham, 1992) and 1.83 at the casing. Large increases in the boundary layer thickness occur on both walls. Since the annulus height is reducing, the calculated boundary layers at the OGVs fill two-thirds of the span. They are clearly too thick.

The problem is believed to lie in an underprediction of the spanwise convection at the casing. More convection would thin the casing boundary layer, reduce the secondary flows, and increase the mainstream loss. A 50 percent increase in spanwise convection together with a change in one of the AWBL constants thins the boundary layers, aligns the pressure ratio more closely to the measurements, and reduces the predicted overall efficiency to 89.4 percent.

The radial variations of the stator outlet angles are predicted satisfactorily, though the "hump" in the gas angle at OGV exit is exaggerated and misplaced radially. (There were no traverses after the rotors.)

The low-speed results on cascades and compressors are not very sensitive to the value of the turbulent diffusion constant GAL. This is not surprising, as its main effect is to prevent high temperatures accumulating near the walls of a high-speed compressor (Dunham, 1992). The level GAL = 0.0004 chosen from the Salvage results appears satisfactory for the C147 unit. Doubling it reduces the pressure ratio by 0.025 and the efficiency by 0.5 percent. This value of GAL is far smaller than the value 0.005 needed in Dunham (1992) because in the present method the AWBL treatment prevents the high temperatures at the walls.

6 Discussion

Section 5 has shown that the turbulent mixing constant and the four "universal" constants in the AWBL blade force defect terms, chosen from cascade data, appear acceptable for the low-

speed compressor cases tried here, but predict too thick a boundary layer in the high speed compressor. A wider range of test cases at high speed is needed to resolve this question.

Salvage's measurements were made on lightly loaded cascades. There is no suggestion of endwall or corner stall in any of the measurements or calculations. But other tests on cascades and compressors in adverse aerodynamic conditions have shown clear indications of corner stall. Papailiou et al. (1976) tested a cascade similar to one of Salvage's but at higher incidence and found corner stall. Inoue's cascades were also lightly loaded, but Fig. 7 shows how the outlet velocity profile changed as the tip clearance was increased. At 5 mm tip clearance the velocity profile suggests AWBL separation at the tip. Dring (1993) pointed out that corner stall greatly increases the spanwise convection. The present method cannot predict the onset or the consequences of corner stall.

Apart from that, the comparisons (of which a selection have been shown) suggest that the method is capable of predicting the three-dimensional effects in a compressor realistically. There is a need for a more extensive assessment of its accuracy—and perhaps some refinement of the empirical assumptions—especially in the context of high-speed compressors.

7 Conclusions

The application of annulus wall boundary layer theory together with secondary flow calculations and the present spanwise diffusion and convection models appears to offer a promising foundation for a more satisfactory and more accurate way of predicting the endwall effects than any published purely empirical scheme.

The application of the method to a variety of cases draws attention once again to the significance of endwall corner separations, which the method is unable to predict. Much more research is still needed on endwall flows.

Acknowledgments

Grateful acknowledgment is made to Prof. M. Inoue who kindly supplied additional measurements from his experiments.

The research was supported by the UK Ministry of Defence and Department of Trade and Industry, but the views expressed are those of the author.

References

Adkins, G. G., and Smith, L. H., 1982, "Spanwise Mixing in Axial-Flow Turbomachines," ASME *Journal of Engineering for Power,* Vol. 104, pp. 97–110.

Calvert, W. J., 1982, "An Inviscid–Viscous Interaction Treatment to Predict the Blade-to-Blade Performance of Axial Compressors With Leading Edge Normal Shock Waves," ASME Paper No. 82-GT-135.

Calvert, W. J., and Ginder, R. B., 1985, "A Quasi-Three-Dimensional Calculation System for Transonic Axial Flow Compressors, Including Stations Within the Blade Rows," ASME Paper No. 85-GT-22.

Calvert, W. J., Ginder, R. B., McKenzie, I. R. I., and Way, D. J., 1989, "Performance of a Highly-Loaded HP Compressor," ASME Paper No. 89-GT-24.

de Ruyck, J., and Hirsch, Ch., 1988, "A Radial Mixing Computation Method," ASME Paper No. 88-GT-68.

Dring, R. P., 1993, "Radial Transport and Momentum Exchange in an Axial Compressor," ASME JOURNAL OF TURBOMACHINERY, Vol. 115, pp. 477–486.

Dunham, J., 1992, "Analysis of High Speed Multistage Compressor Throughflow Using Spanwise Mixing," ASME Paper No. 92-GT-13.

Dunham, J., 1993, "A New Approach to Predicting Annulus Wall Boundary Layers in Axial Compressors," *Proc. Instn. Mech. Engrs.,* London, Vol. 207, Pt. C (*J. Mech. Engg. Sci.*), pp. 413–425.

Gallimore, S. J., and Cumpsty, N. A., 1986, "Spanwise Mixing in Multistage Axial Flow Compressors," ASME JOURNAL OF TURBOMACHINERY, Vol. 108, pp. 2–9.

Hirsch, Ch., and de Ruyck, J., 1981, "Throughflow Calculations in Axial Turbomachines," AGARD AR 175, Chap. II. 2.3.

Howard, M. A., and Gallimore, S. J., 1993, "Viscous Throughflow Modeling for Multistage Compressor Design," ASME JOURNAL OF TURBOMACHINERY, Vol. 115, pp. 296–304.

Inoue, M., Kuroumaru, M., and Fukuhara, M., 1987, "Development of Casing Wall Boundary Layer Through an Axial Compressor Rotor," Tokyo Int. Gas Turbine Congress. Paper No. 87-TOKYO-IGTC-13.

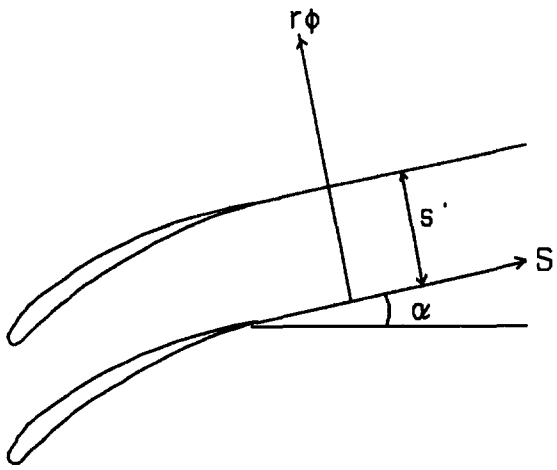

Fig. 8 Notation

Leboeuf, F., 1984, "Annulus Endwall Boundary Layer Theory," *V KI Lecture Series 1984-05.*

Leylek, J. H., and Wisler, D. C., 1991, "Mixing in Axial-Flow Compressors: Conclusions Drawn From 3-D Navier–Stokes Analyses and Experiments," ASME JOURNAL OF TURBOMACHINERY, Vol. 113, pp. 139–160.

Marsh, H., 1974, "Secondary Flow in Cascades: the Effect of Axial Velocity Ratio," *Jnl. Mech. Engg. Sci.,* Vol. 16, p. 402.

Na, T. Y., 1979, *Computational Methods in Engineering Boundary Value Problems,* Academic Press, New York.

Papailiou, K., Flot, R., and Mathieu, J., 1976, "Secondary Flows in Compressor Bladings," ASME Paper No. 76-GT-5.

Roberts, W. B., Serovy, G. K., and Sandercock, D. M., 1988, "Design Point Variation of Three-Dimensional Loss and Deviation for Axial Compressor Middle Stages," ASME JOURNAL OF TURBOMACHINERY, Vol. 110, pp. 426–433.

Robinson, C. J., 1991, "End-Wall Flows and Blading Design for Axial Flow Compressors," Ph.D. Thesis, Cranfield Institute of Technology, United Kingdom.

Salvage, W. J., 1974, "Investigation of Secondary Flow Behaviour and End Wall Boundary Layer Development Through Compressor Cascades," VKI Report TN-107.

Schlichting, H., 1968, *Boundary Layer Theory,* 6th ed., McGraw-Hill, New York.

Ucer, A. S., and Shreeve, R. P., 1992, "A Viscous Axisymmetric Throughflow Prediction Method for Multi-stage Compressors," ASME Paper No. 92-GT-293.

APPENDIX 1

Calculation of the Secondary Flow

The secondary flow is calculated in the plane normal to the mainstream flow leaving the blade row (the Trefftz plane, Fig. 8). The coordinates are S, $r\phi$, and r (radial), with velocity components, v_s, v_ϕ, and v_r respectively, and $s' = s \cos \alpha$ is the staggered pitch.

The continuity equation is

$$\frac{1}{r}\frac{\partial}{\partial r}(rv_r) + \frac{1}{r}\frac{\partial v_\phi}{\partial \phi} + \frac{\partial v_s}{\partial S} = 0 \tag{1}$$

The streamwise vorticity is defined as

$$\xi_s = \frac{1}{r}\frac{\partial}{\partial r}(rv_\phi) - \frac{1}{r}\frac{\partial v_r}{\partial \phi} \tag{2}$$

Making assumptions similar to those of de Ruyck and Hirsch,

$$\frac{\partial v_s}{\partial S} = 0 \tag{3}$$

$$v_r = \Delta v_r \frac{r}{s'}(\phi - \phi_{\text{mid}}) \tag{4}$$

where Δv_r is the difference between the radial velocities on the pressure and suction surfaces of the aerofoil at radius r and ϕ_{mid} is the value of ϕ at midpitch; and

$$v_\phi = \frac{3}{2}\,\overline{v}_{\phi\,\mathrm{sec}}\left[1 - \frac{4r^2}{s^2}(\phi - \phi_{\mathrm{mid}})^2\right] \tag{5}$$

where $\overline{v}_{\phi\,\mathrm{sec}}$ is the pitchwise mean value of v_ϕ. Since $s' = 2\pi r/N\cos\alpha$ for a row of N blades, inserting Eqs. (3), (4), and (5) into Eq. (1) gives

$$\frac{d}{dr}(r\Delta v_r) = \frac{6N}{\pi\cos\alpha}\,\overline{v}_{\phi\,\mathrm{sec}} \tag{6}$$

Inserting Eqs. (3), (4), and (5) into Eq. (2) and averaging pitchwise gives

$$\bar{\xi}_s = \frac{1}{r}\frac{d}{dr}(rv_{\phi\,\mathrm{sec}}) - \frac{N}{2\pi r\cos\alpha}\Delta v_r \tag{7}$$

Substituting for $\overline{v}_{\phi\,\mathrm{sec}}$ from Eq. (6) into Eq. (7),

$$\frac{1}{r}\frac{d}{dr}\left[\frac{\pi r\cos\alpha}{6N}\frac{d}{dr}(r\Delta v_r)\right] - \frac{N}{2\pi r\cos\alpha}\Delta v_r = \bar{\xi}_s$$

To simplify the solution by avoiding a d/dr term, put $G = r^{1.5}\Delta v_r$:

$$\frac{d^2G}{dr^2} + \left(\frac{1}{4} - \frac{3N^2}{\pi^2\cos^2\alpha}\right)\frac{G}{r^2} = \frac{6N\sqrt{r}}{\pi\cos\alpha}\,\bar{\xi}_s$$

In order to calculate the secondary flow velocity field from the known streamwise vorticity distribution $\bar{\xi}_s$, this equation is solved for G using Thomas' algorithm (Na, 1979), as recommended by de Ruyck and Hirsch (1988). Then $\overline{v}_{\phi\,\mathrm{sec}}$ is calculated from Eq. (6).

Thomas' algorithm is a numerically efficient method of integrating an ordinary differential equation between two points at which the boundary conditions are known.

APPENDIX 2

Spanwise Convection by Secondary Flow

The radial velocity due to the secondary flow is assumed to vary linearly across the passage from $\frac{1}{2}\Delta v_r$ on one side of the passage to $-\frac{1}{2}\Delta v_r$ on the other side (Eq. (4)), so the mass flow transferred across the meridional streamlines in a streamwise distance dS is

$$d\dot{m} = \rho_e\left|\frac{\Delta v_{re}}{4}\right|\frac{s'}{2}\,N dS$$

where s' = staggered pitch. But $dS = dx\sec\alpha$ and $Ns' = 2\pi r_e\cos\alpha$, so

$$d\dot{m} = \tfrac{1}{4}\pi\rho_e r_e|\Delta v_{re}|dx.$$

Δv_r is calculated only at the trailing edge of the blade row. If it is assumed that the streamwise vorticity (which gives rise to it) develops linearly through the passage, the total $\Delta\dot{m}$ across the row is

$$\Delta\dot{m} = \tfrac{1}{8}\pi\rho_e r_e|\Delta v_{re}|_{t.e.}\Delta x \tag{8}$$

As pointed out in Section 2.1, if there is an endwall clearance both a secondary vortex and a tip clearance vortex develop. The model assumes that each vortex convects mass separately; the total mass flow convected $\Delta\dot{m}$ is taken to be the sum of the amounts convected by each vortex.

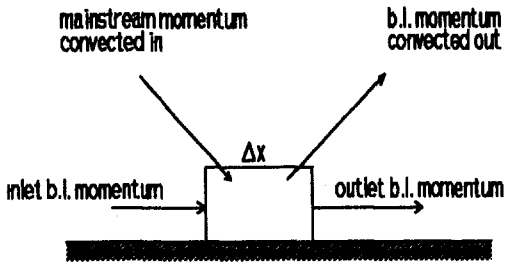

Fig. 9 Momentum exchange model

The exchange of momentum and enthalpy across the edge of the boundary layer is illustrated in Fig. 9.

The axial momentum in the incoming boundary layer is

$$\int_0^\delta 2\pi r\rho v_x^2\,dn = 2\pi\rho_e r_e x_{xe}^2(\delta - \delta_x^* - \theta_{xx})$$

So the convection of mainstream momentum into the box and boundary layer momentum out of the box increases its momentum by

$$\Delta\dot{m}\left(1 - \frac{\delta - \delta^* - \theta_{xx}}{\delta - \delta^*}\right)v_{xe}$$

Since δ and δ^* are not altered by the momentum exchange, the result is a reduction in θ_{xx} by an amount

$$\frac{1}{16}|\Delta v_{re}|_{t.e.}\Delta x\left(\frac{\theta_{xx}}{\delta - \delta^*}\right)/W_e.$$

Similarly, the angular momentum of the boundary layer is

$$\int_0^\delta 2\pi r\rho v_x v_\theta dn = 2\pi\rho_e r_e v_{xe}[v_{\theta e}(\delta - \delta^*) - v_{xe}\theta_{\theta x}]$$

and it is increased by an amount

$$\Delta\dot{m}v_{xe}\frac{\theta_{\theta x}}{\delta - \delta^*}$$

so there is a reduction in $\theta_{\theta x}$ by an amount

$$\frac{1}{16}|\Delta v_{re}|_{t.e.}\Delta x\left(\frac{\theta_{\theta x}}{\delta - \delta^x}\right)\Big/W_e. \tag{9}$$

The enthalpy in the boundary layer is

$$\int_0^\delta 2\pi r\rho v_x H dn$$

which can be integrated knowing that H_{wall}, the enthalpy relative to the wall, is constant across the boundary layer (Schlichting, 1968), to give

$$2\pi\rho_e r_e W_e[H_e(\delta - \delta^*) - \Omega_{\mathrm{wall}}r_e W_e\theta_{\theta x}].$$

Hence the change in boundary layer enthalpy ΔH_e due to the mass flow exchange is given by

$$\rho_e r_e W_e(\delta - \delta^*)\Delta H_e = \rho_e r_e^2 W_e\Omega_{\mathrm{wall}}\left[W_e\Delta\theta_{\theta x} + \frac{1}{16}|\Delta v_{re}|_{t.e.}\Delta x\frac{\theta_{\theta x}}{\delta - \delta^*}\right].$$

But from Eq. (9) the right-hand side of this equation is zero, so there is no change in boundary layer enthalpy. Turning now to the momentum and enthalpy transfers from the boundary

layer into the mainstream, the mass flow $\Delta\dot{m}$ exchanged with a streamtube at radius r is

$$\frac{1}{8}\pi\rho\frac{d}{dr}(r\Delta v_r)dr\Delta x$$

so using Eq. (6)

$$\Delta\dot{m} = 0.75\rho N \sec\alpha\, \bar{v}_{\phi\,\sec} dr\Delta x.$$

Since $\bar{v}_{\phi\,\sec}$ is known from Eq. (6), this allows the momentum exchanges with all the streamtubes outside the boundary layer to be evaluated in much the same way. Enthalpy interchanges occur only if $H \neq H_e$ so are assumed to be catered for by the turbulent diffusion terms in the streamline curvature equations.

Computation of Unsteady Viscous Flow Through Turbomachinery Blade Row Due to Upstream Rotor Wakes

Y.-H. Ho
Graduate Student.

B. Lakshminarayana
Evan Pugh Professor of Aerospace Engineering.
Fellow ASME

The Pennsylvania State University,
Department of Aerospace Engineering,
University Park, PA 16802

A time-accurate, two-dimensional, pressure-based, Navier–Stokes solver for incompressible flow is developed and used to carry out the numerical simulation of rotor–stator interaction. A low-Reynolds-number form of the two-equation turbulence model is used to account for the turbulence effects. In order to improve the accuracy of the numerical scheme, a central differencing plus an artificial dissipation scheme is implemented to provide precise control of numerical dissipation. An inner loop iteration scheme is used at each time step to account for the nonlinear effects. The computation of unsteady flow through a flat plate cascade subjected to a transverse gust reveals that the choice of grid spacing and the amount of artificial dissipation is critical for accurate prediction of unsteady phenomena. The rotor–stator interaction problem is simulated by starting the computation upstream of the stator, and the upstream rotor wake is specified from the experimental data. The results show that the stator potential effects have appreciable influence on the upstream rotor wake. The predicted unsteady wake profiles are compared with the available experimental data and the agreement is good. The numerical results are interpreted to draw conclusions on the unsteady wake transport mechanism in the blade passage.

Introduction

The unsteadiness caused by relative motion between the stator and the rotor has a major influence on the aerodynamic, mechanical, and acoustic performance of turbomachines. The mechanical reliability, life cycle, and performance are substantially altered by these interactions. Most analytical studies of this problem are based on inviscid unsteady linearized or potential flow analysis, e.g., Whitehead (1960), Fleeter (1973), Hall and Verdon (1991), Fang and Atassi (1993). These methods have successfully predicted the unsteady pressure field. The present trend toward closer blade spacing has emphasized the need for reliable analytical/computational techniques to resolve the unsteady pressure and flow field as well as the unsteady viscous effects, such as unsteady boundary layers, wakes, transition, and, most importantly, unsteady losses. Various attempts are under way to resolve the rotor–stator interaction effects through the numerical solution of the Navier–Stokes equation and the Euler equation. The work by Rai (1987), Gundy-Burlet et al. (1991), Dorney et al. (1992), Abhari et al. (1992), and Rao et al. (1992) are several examples of the numerical simulation using the Navier–Stokes equation.

The methods mentioned are mainly for compressible flow. There are very few unsteady Navier–Stokes solvers for incompressible flow. Hah (1992) used a pressure-based algorithm to compute three-dimensional, unsteady flow field inside a turbine stage. However, the results are limited primarily to unsteady pressure on the blades surfaces and global flow properties. Therefore, the major objective of this study is to utilize an accurate, efficient algorithm for the numerical simulation of unsteady, viscous, incompressible flow due to rotor–stator interaction. The main emphasis of the present paper is to compute the unsteady velocity field including the unsteady blade boundary layers, wakes, and transport mechanism of upstream wake through stator passage. A better understanding of these complicated flow phenomena will improve the advance in turbomachinery design. It is believed that this is the first attempt to utilize a pressure-based technique to compute the unsteady viscous flow inside the turbomachinery blade rows with a detailed simulation of unsteady wake transport mechanism, and unsteady velocity field inside the passage. Associated with this objective is the evaluation of the technique and the code to assess the effects of artificial dissipation (in a pressure-based technique), grid sensitivity, and high frequency.

An existing time-accurate, two-dimensional, pressure-based, Navier–Stokes solver (Ho and Lakshminarayana, 1993) for incompressible flow is modified and used to carry out the numerical simulation. A low-Reynolds-number form of the two-equation turbulence model is used for simulating the turbulence effects. In order to improve the accuracy of the numerical scheme, a central differencing plus artificial dissipation scheme is implemented to provide precise control of numerical dissipation. An inner loop iteration scheme is used at each time step to account for the nonlinear effects. The effect of frequency on the artificial dissipation scheme is analyzed and compared using the numerical results. The numerical scheme is then used to compute the flow field in a flat plate cascade subjected to a transverse gust, including grid sensitivity study.

Finally the flow field through a multistage compressor second-stage stator at midspan is computed and compared with the LDV data acquired by Stauter et al. (1991). Gundy-Burlet et al. (1991) computed the entire multistage compressor flow field at midspan location with Rai's technique. Their results are limited to the unsteady pressures on the blade surfaces and the unsteady wakes at several locations between the rotor and the stator. The decay of the rotor wake before entering the stator is compared with the experimental data, including the time-averaged and instantaneous properties. The time-mean pressure on the blade surface and stator wake is also compared with the available data. The instantaneous fluctuating velocity fields at

Contributed by the International Gas Turbine Institute and presented at the 38th International Gas Turbine and Aeroengine Congress and Exposition, Cincinnati, Ohio, May 24–27, 1993. Manuscript received at ASME Headquarters March 17, 1993. Paper No. 93-GT-321. Associate Technical Editor: H. Lukas.

various time intervals are presented to understand the rotor wake transport mechanism through the stator blade passage.

Numerical Technique

The Reynolds-averaged Navier–Stokes equations for two-dimensional, unsteady, incompressible flow in Cartesian tensor form can be written as:

$$\frac{\partial u_i}{\partial x_i} = 0 \tag{1}$$

$$\frac{\partial u_i}{\partial t} + \frac{\partial u_i u_j}{\partial x_j} = -\frac{1}{\rho}\left\{\frac{\partial p}{\partial x_j} - \frac{\partial}{\partial x_j}\left[\mu\left(\frac{\partial u_j}{\partial x_i} + \frac{\partial u_i}{\partial x_j}\right) + \rho\overline{u_i' u_j'}\right]\right\} \tag{2}$$

where u_i is the velocity, x_i the independent variables, t the time, ρ the mean density, and μ is the viscosity.

In order to simulate the turbulent flow, a two-equation, or $k-\epsilon$ turbulence model by Chien (1982) is employed. For unsteady flow computations, the momentum equations and $k-\epsilon$ equations have to be solved simultaneously ensuring that the mass is conserved during each time step. To accommodate complex geometries, the general curvilinear coordinates system is used to transform the physical coordinates. The transformed equations can be found in Ho (1995) and Hobson and Lakshminarayana (1991).

The boundary conditions include no-slip condition on the solid surfaces, and specification of time-dependent inlet velocity field. The exit velocity is computed by solving the governing equation at the exit. For the pressure equation, the normal derivative of pressure is assumed to be zero on the solid surface, which is a reasonable approach for high-Reynolds-number flows. Furthermore, the Navier–Stokes computations with low-Reynolds-number form of turbulence model usually require dense grids near the solid surfaces (typical value of y^+ is smaller than 2); therefore, the distance between the first grid point and the surface is very small. The static pressure is specified at the exit plane. Although this is not a valid approach for the unsteady flow computation, the unsteadiness is usually negligible after half a chord downstream of the blade.

For the pure transverse gust case, the streamwise pressure gradient is assumed to be zero. In the rotor–stator interaction problem, this boundary condition is not valid. In order to calculate the static pressure and its gradient at inlet, the axial momentum equation is first solved at the first grid point from the inlet by using the static pressure from the previous time step. The pressure at inlet is then updated from the axial momentum equation from the known velocity field. By using an inner iteration loop, the pressure at the inlet is calculated correctly. Since Neumann boundary conditions are used at the blade surfaces, the pressure at one grid point must be chosen. This control point is taken to be the midchannel point at the exit plane for a cascade.

The values k and ϵ are set to zero at the wall for the $k-\epsilon$ equations. The inlet turbulent kinetic energy and dissipation rate are determined by specifying an inlet turbulence intensity, T_u, and turbulent viscosity ratio factor, μ_r, associated with the inlet flow. The inlet turbulent kinetic energy is determined from:

$$k_1 = \tfrac{3}{2}(T_u \cdot V_1)^2 \tag{3}$$

where V_1 is the inlet total velocity. The inlet dissipation rate is then determined from the following relation:

$$\epsilon_1 = \rho_1 C_\mu \frac{k_1^2}{\mu_r} \tag{4}$$

where μ_r is the ratio of turbulent to laminar viscosity. The k and ϵ at the exit plane are also calculated by applying the transport equations directly.

Nomenclature

a_i = influence coefficients (Eq. (A.2))
C, C_{ref} = chord length and reference length
C_x = axial chord length
C_p = pressure coefficient = $(p - p_{tin})/Q_{Um}$
C_{Fw} = aerodynamic force coefficient = $F/\rho U_1 V_d$
E_R = relaxation factor in Eq. (A.3)
F = force on the blade surface
G_1, G_2 = contravariant velocities
J = Jacobian
k = turbulent kinetic energy
p = static pressure
p_{tin} = stagnation pressure at the multistage compressor inlet
Q_{Um} = dynamic head based on the wheel velocity U_m
r, θ, z = radial, tangential and axial coordinate system
Re = Reynolds number based on mean streamwise velocity, laminar viscosity, and the axial chord
R_ϕ, R_m = residuals for ϕ and mass
S = source terms
T = period
T_u = inlet turbulence intensity
U = free-stream total velocity for the flat plate cascade
U_m = blade velocity at midspan
u, v = axial and tangential velocity
u_i = mean velocity tensor
V = absolute velocity
V_d = gust velocity
t = physical time
W = relative velocity
x, y = axial and tangential (or boundary layer) coordinate
x_i, x_j = cartesian coordinates
y^+ = $\rho\sqrt{\tau_w/\rho}(y/\mu)$
ΔC_p = unsteady pressure coefficient (normalized by U_m)
Δt = time step
Δx = grid spacing in x direction
$\Delta\xi$, $\Delta\eta$ = grid spacing in ξ and η directions
α = angle of incidence
δ = boundary layer thickness
ϵ = turbulence dissipation
ϵ_2, ϵ_4 = coefficients of artificial dissipation
θ/C_x = momentum thickness normalized by the axial chord length (Eq. (7))
ξ, η = independent variables on transformation plane
κ = complex number in Eq. (6)
μ = molecular viscosity
μ_r = turbulent and laminar viscosity ratio (μ/μ_t)
μ_t = turbulent eddy viscosity
ν = kinematic viscosity
ρ = fluid mean density
ϕ = dependent variables, such as u, v
φ = phase angle
ω = frequency

Subscripts

1 = inlet
e = boundary layer edge
i = instantaneous value
s = steady state value
z, θ = component in z, θ direction

Superscripts

n = previous time step
$n+1$ = new time step
$*$ = intermediate value
$'$ = unsteady component

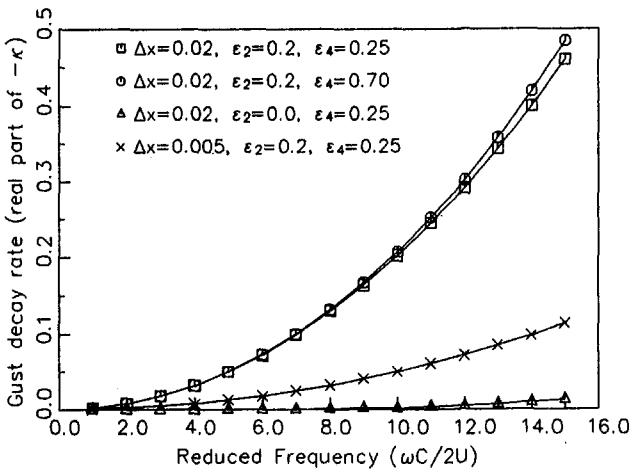

Fig. 1 The effects of the artificial dissipation on the decay rate of the gust at different reduced frequencies

A control volume approach is used in the discretization procedures for the system of governing equations and the detailed procedure can be found in Ho and Lakshminarayana (1993) and the appendix. This numerical scheme can be summarized as follows:

1 The coefficients of the momentum equations are calculated by using the previous time step solutions (u^n, v^n, p^n). This system of equations is modified according to Eq. (A.2) and solved implicitly for u and v.
2 The mass error is calculated from the new velocity field and this represents the source term in the pressure equation. The coefficients of the pressure equation are calculated from the momentum equation. This pressure equation is solved to get a new pressure field.
3 Correct (first corrector step for velocity) the velocity field from this new pressure field explicitly.
4 From the corrected velocities, recalculate the coefficients and source terms of the pressure equation and solve the implicit system of equations to obtain a new pressure field.
5 From the new pressure field, re-evaluate the velocity field (second corrector step) explicitly.
6 Solve the k and ϵ equations with a similar procedure to step (1) and update the eddy viscosity.
7 Check the convergence criteria. If the solution is not converged, go to step (1) and use the latest values of u, v, p, k, ϵ, and μ_t to calculate the influence coefficients.
8 March to the next time step.

Effects of Artificial Dissipation. It is well known that the introduction of excessive amounts of numerical dissipation into the flow field will dissipate the waves associated with unsteady flow resulting in an erroneous solution. On the other hand, convergence and stability of these solutions cannot be achieved without the introduction of artificial dissipation. It is therefore necessary to use an optimum value for the artificial dissipation to maintain good accuracy and convergence characteristics. It is well known in the traditional time-marching technique that the second-order dissipation is very dissipative. However, numerical dissipation has not been investigated thoroughly in a pressure-based method. In order to investigate the dissipative effects of artificial dissipation in incompressible, unsteady viscous flow computations, a one-dimensional analysis is performed in free space (without a cascade) with a sine wave introduced in the computational domain at the inlet plane. The free space is 2.5 C_{ref} where C_{ref} is the reference length. The flow field is assumed to be inviscid and the pressure gradient is set to zero everywhere.

As discussed in the appendix, any high-order scheme or upwind scheme is equivalent to the central difference scheme plus a certain amount of artificial dissipation. In the present approach, the artificial dissipation is added to the governing equations directly. Hence, the governing equation for one-dimensional, inviscid, unsteady flow in free space can be approximated as follows:

$$\frac{\partial v}{\partial t} + U\frac{\partial v}{\partial x} = \frac{\epsilon_2}{2}\Delta x\frac{\partial}{\partial x}\left(U\frac{\partial v}{\partial x}\right) - \frac{\epsilon_4}{8}\Delta x^3\frac{\partial}{\partial x}\left(U\frac{\partial^3 v}{\partial x^3}\right) \quad (5)$$

where Δx is the grid spacing in the mean flow direction, and the mainstream velocity U in x direction is assumed to be constant. This equation was solved to evaluate the effects of ϵ_2, ϵ_4, and Δx on the numerical accuracy at various reduced frequencies ($\lambda = \omega C/2U$, where ω is a radial frequency).

If a solution of $v(x, t) = e^{-\kappa x}e^{i\omega t}$ is assumed, the equation for κ is

$$\epsilon_4\Delta x^3\kappa^4 - 4\epsilon_2(\Delta x)\kappa^2 - 8\kappa + 8i\omega = 0 \quad (6)$$

where κ is a complex number. The real part of κ represents the decay rate of the traveling wave and the imaginary part represents its wave number.

The results for several combinations of Δx, ϵ_2, and ϵ_4 are shown in Fig. 1 and 2. Since there is no physical dissipation, the ideal case would be a traveling wave without any decay, $\kappa = 0$, and no change in wave number. As shown in Fig. 1, value of ϵ_2 has a major influence on the decay rate of the wave and its value should be set to zero as in the time marching methods for subsonic flow. The fourth-order dissipation does not have strong influence on the wave decay at all reduced frequencies. Nevertheless, the error in the solution increases with an increase in the reduced frequency. The reduced grid spacing has similar effects as the reduced numerical dissipation (see Fig. 1). Therefore, the first-order upwind scheme, which corresponds to $\epsilon_2 = 1.0$ and $\epsilon_4 = 0.0$, is inherently very dissipative and is not suitable for reduced frequencies higher than one. However, errors introduced into the wave number are insignificant, as shown in Fig. 2, for all combinations considered here.

For the one-dimensional analytical solutions (Eq. (6)), a traveling wave can be resolved accurately with 10 grid points per wave length (the wavelength for a reduced frequency of 15 is $0.2C_{\text{ref}}$ in this case). However, due to the discretization and truncation error, it is found from the numerical experiments that at least 20 grid points are required to represent a wave. In Table

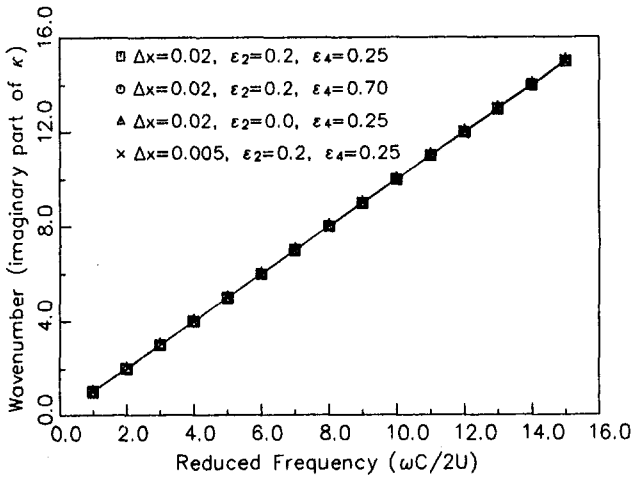

Fig. 2 The effects of the artificial dissipation on the wave number of the gust at different reduced frequencies

Table 1 The effect of the second and fourth-order dissipation on the decaying of gust (inviscid calculation and no pressure equation)

$\omega C/2U$	ε_2	ε_4	decay of input wave at 2.5 C_{ref}(%)
0.5	1.0	0.0	10.0
0.5	0.3	0.4	0.0
0.5	0.05	0.2	0.0
5.0	0.2	0.2	42.0
5.0	0.0	0.3	0.0
7.5	0.2	0.3	72.0
7.5	0.0	0.5	10.0
7.5	0.0	0.1	0.0
15.0	0.0	0.3	43.0
15.0	0.0	0.05	20.0
15.0*	0.0	0.3	6.0

* 40 grid points per wavelength.

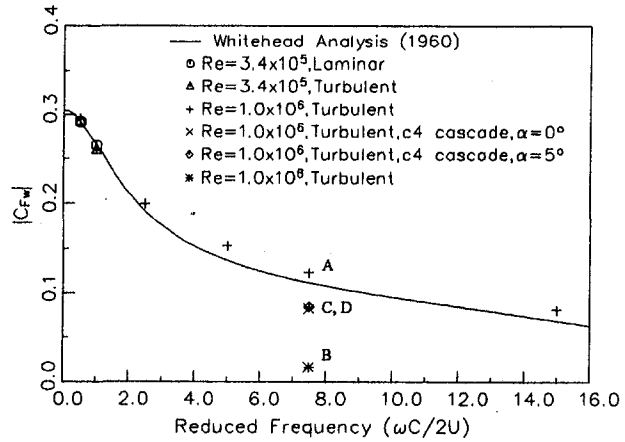

Fig. 3 The effects of grid dependency and blade thickness on the aerodynamic force function (C_{Fw}) of cascades, space chord ratio of 1, 0 deg stagger angle

1, the data from numerical experiments performed on a grid size that provide 10 grid points per wavelength at highest reduced frequency are shown, with the exception of the last case, which was computed with 40 grid points per wavelength. An obvious observation from Table 1 is that the choice of the coefficients of artificial dissipation is not very critical for low reduced frequencies, since there are 300 grid points per wavelength at a reduced frequency of 0.5. As the reduced frequency is increased, the choice of the artificial dissipation coefficients becomes more restrictive. At a reduced frequency of 15, the solution for a combination of $\epsilon_2 = 0.0$ and $\epsilon_4 = 0.05$ still has 20 percent decay of input wave after the wave travels 2.5 C_{ref}. If a grid size of 40 points per wavelength is used, the combination of $\epsilon_2 = 0.0$ and $\epsilon_4 = 0.3$ reduces the decay of the wave amplitude to only 6 percent. The other important result from this numerical experiment is that low reduced frequencies require only two to three cycles to reach the limiting solution; however, the highest reduced frequency needs 10 cycles to propagate the error out of the computational domain.

Hence, a proper choice of optimum grid size and artificial dissipation coefficients (ϵ_2, ϵ_4) for the convection terms is crucial for accurate prediction of unsteady flow. The coefficients of the artificial dissipation are limited to minimum values to maintain a stable and convergent solution.

Code Calibration: Unsteady Flow Through a Flat Plate Cascade

To validate the accuracy of the numerical technique and the code, the flow through a flat plate cascade subjected to a transverse gust was computed at various reduced frequencies and Reynolds numbers. Detailed results are presented in Ho (1995). Additional results and a brief summary are presented here. The computation is carried out at 5-deg mean incidence and the reduced frequency ($\omega C/2U$) of the transverse gust is varied from 0.5 to 15 at an inlet turbulence intensity of 5 percent. The space chord ratio is set to unity and the stagger angle is 0 deg. A systematic study is undertaken to assess the effect of grid size and the amount of artificial dissipation. At low reduced frequencies, the number of grid points required for accurate results is usually low, since the wavelength is long compared to the grid spacing and the results are very much grid independent. The grid size used for steady flow computation is usually sufficient for unsteady flow cases. However, as the reduced frequency is increased beyond 2.5, the choice of the grid size becomes very important since the required grid size for unsteady flow calculation is much smaller than that needed for the steady-state case. At reduced frequencies of 1.0 to 2.5, a grid size of 61×41 is used to predict the aerodynamic response function (C_{Fw}) for a flat plate cascade. The results agree well with the analysis by Whitehead (1960). If the same grid size and the same amount of artificial dissipation as the low reduced frequency cases are used to compute the flow field at higher reduced frequencies, considerable dissipation of the gust occurs in the inviscid region upstream of the leading edge.

The values of the aerodynamic transfer function C_{Fw} computed from the Navier–Stokes code is compared with the Whitehead's linearized analysis in Fig. 3. At reduced frequencies 1 to 2.5, no special precaution is required, while at values higher than this, grid sensitivity plays a major role. The numerical result shown at A (symbol +) for a reduced frequency of 7.5 is the value obtained from the optimum grid (172×41) and the artificial dissipation and hence represents the best prediction. The pressure field and the magnitude of C_{Fw} are mostly inviscid driven, hence, Whitehead's analysis is accurate for this case and is in good agreement with the prediction of the Navier–Stokes code. A coarse grid size of 61×41, which is the same as the one used at low reduced frequency, was also employed at this frequency and this result is shown as point B in Fig. 3. The prediction is poor due to premature decay of the gust before it reaches the leading edge. As the grid size is increased to 172×41 (the total number of grid points at upstream region is increased from 10 points to 30 points), the code captures the transport of the gust accurately and the aerodynamic response function C_{Fw} is predicted well (shown as A in Fig. 3). The local lift coefficients ($\Delta p/0.5\rho U^2$), based on the pressure difference between the instantaneous and time-mean values, are shown in Fig. 4. The flat plate cascade shows large unsteadiness near the leading edge. The unsteadiness on both surfaces becomes insignificant after 20 percent of the chord length.

To investigate the effects of blade thickness on unsteady flow, the flow field through a cascade, with circular arc, zero camber, and C4 profile (Gostelow, 1984) of 10 percent thickness, is computed. The incidence, stagger angle, and space chord ratio are kept the same as the flat plate cascade. This computation was carried out to check the accuracy of the linearized analysis in simulating practical blade geometry subjected to unsteady flow field. As shown in Fig. 3, the predicted C_{Fw} value for the C4 cascade (marked C and D in Fig. 3) is lower than the analytical solution by about 30 percent. When compared to the unsteady pressure distribution on the blade surfaces for both cases (Fig. 4), the most distinguished feature is that the unsteady pressure distribution near the leading edge of the C4 cascade is smaller and smoother than that of a flat plate cascade. This evidently shows that the leading edge thickness has a major effect on the aerodynamic transfer function. The unsteady

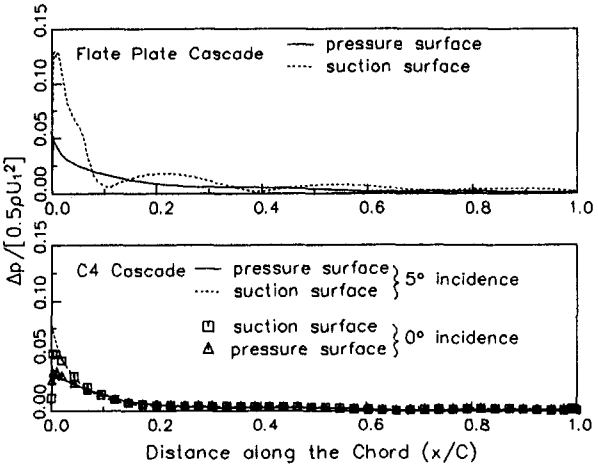

Fig. 4 Comparison of unsteady pressure on the blade surfaces for a flat plate cascade and a C4 cascade

pressures become smoother by the removal of the leading edge singularity. It is also evident that the linearized theories, which neglect the thickness effect, overpredict the unsteady response function.

An additional simulation was carried out to investigate the effect of steady loading on the unsteady blade response. All other steady and unsteady parameters were kept constants, with the exception of the incidence. The computation is carried out at 0 and 5 deg incidence. The results are represented as *C* and *D* and shown in Fig. 3. The steady loading has no effect in this particular case. This is in contradiction to results from Manwaring and Fleeter (1993), who showed that the effect of steady loading on unsteady pressure is significant, especially on the blade suction surface. A possible reason for this discrepancy is that the cases investigated here are for the blade with light blade loading, while a cambered blade with a higher steady loading is employed by Manwaring and Fleeter (1993).

Simulation of Unsteady Flow Field Inside a Compressor Stator Due to Upstream Rotor Wakes

After achieving confidence in the code, an attempt was made to compute the flow field in a complex case with a detailed simulation of rotor–stator interaction effects on the pressure and the velocity field. The case chosen here is the unsteady flow field through the second-stage stator of a multistage compressor investigated at United Technologies Research Center (UTRC). The experimental data in the second stage were acquired by Dring and Joslyn (1985) and Stauter et al. (1991). In order to reduce the computational efforts, the time-averaged wake data from the upstream rotor are decomposed into a Fourier series to derive the inlet velocity conditions for the downstream stator. The main emphasis here is to provide a detailed simulation, including wake transport, instantaneous velocity/pressure field, and the rotor wake induced unsteadiness upstream, inside, and downstream of the stator.

The UTRC multistage compressor is operated at a flow coefficient of 0.51 and at a Reynolds number of 2.5×10^5 based on the blade chord length. The flow is incompressible. The rotor blade speed at the midspan is 46.68 m/s, which represents a reduced frequency of 8.48 based on the blade passing frequency (there are 44 blades in each blade row). NACA 65 series blade profile and circular arc camber are used in both the rotor and the stator. The chord length is 0.1016 m and the hub/tip ratio is 0.8. The second stage stator space/chord ratio is 0.964 and the stagger angle is 34.2 deg. The experimental data include the time-mean static pressure distribution on the blade surface (Dring and Joslyn, 1985), unsteady rotor wakes at different locations upstream of the stator, and unsteady stator wake downstream of the stator (Stauter et al., 1991). All the unsteady flow data were acquired upstream and downstream of the second stage stator by laser-Doppler anemometer at midspan, and the flow is two-dimensional at this location.

The inlet computational domain is at 36 percent of the axial chord upstream of the second-stage stator; this corresponds to Stauter's measuring station. The measured velocity profile is used as the input and the exit plane extends to 85 percent of axial chord downstream of the stator. The computational grid consists of 200 × 96 grid points, with 60 grid points in the streamwise direction upstream (with clustering at the inlet and leading edge), 74 grid points on the blade surfaces, and 66 grid points in the downstream regions. The turbulence intensity at the inlet location is specified as 9 percent, the value suggested by Stauter (1992).

Blade Static Pressure. The computed blade surface pressure is compared with the experimental data in Fig. 5. The agreement between the computed time-mean pressure and the measurement is excellent. The computational results by Gundy-Burlet et al. (1991) are also shown in Fig. 5. The predicted pressure envelope is very similar from both computations. However, Gundy-Burlet et al. predicted higher unsteady pressure on the pressure surface as compared to the suction surface at 10 percent of the axial chord, and this is in contradiction to authors'

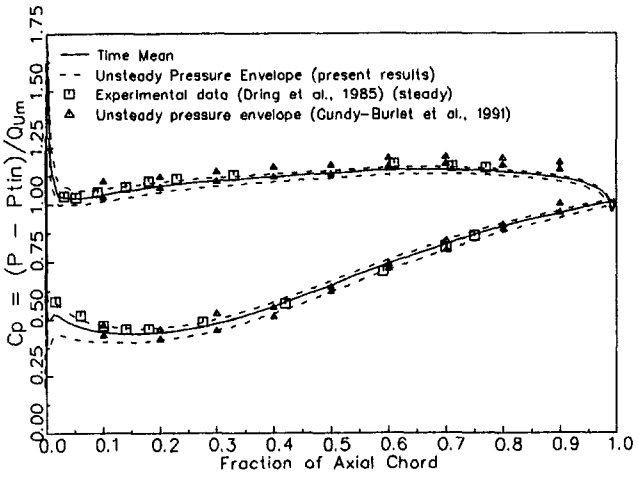

Fig. 5 Time-mean static pressure and pressure envelope of a compressor stator

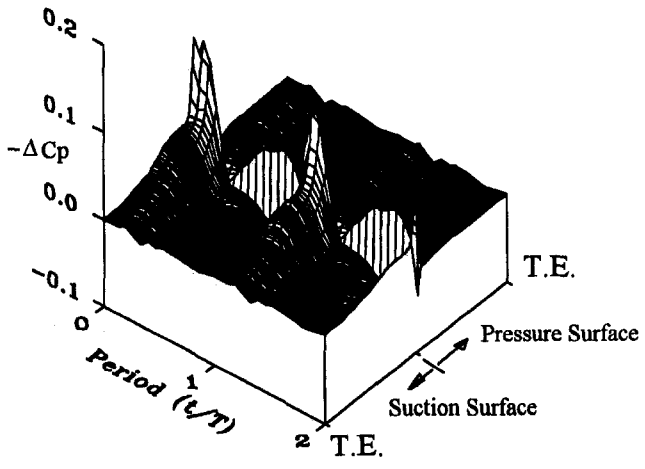

Fig. 6 Histogram of the unsteady pressure on the stator blade surface due to the upstream rotor wake

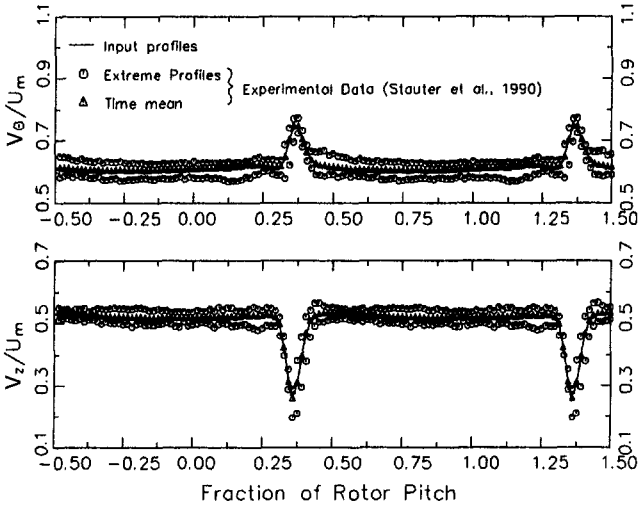

Fig. 7 The input wake profiles at the computational inlet plane (36 percent of the axial chord upstream of the stator blade)

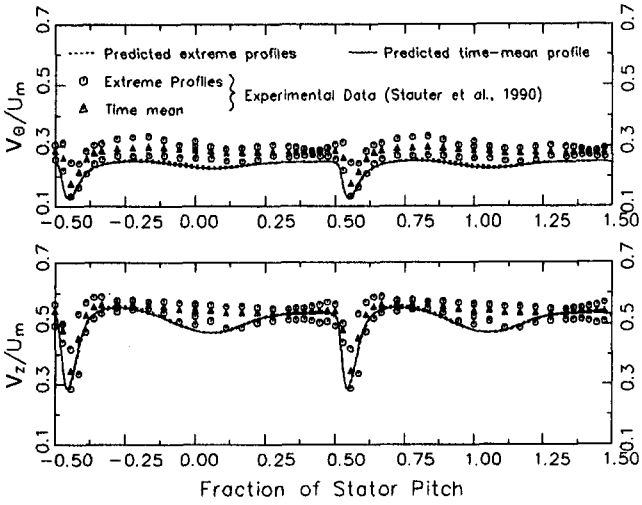

Fig. 9 Stator wake profiles at 18 percent stator axial chord downstream of the stator blade

results as well as expected trend. The histogram of the instantaneous static pressure on the pressure and the suction surfaces is shown in Fig. 6. The effect of the wake transport and its influence on the unsteady pressure is clearly seen. The major effect is on the suction side and this persists (once it is initiated) along most of the chord. The unsteady pressure decays rapidly on the pressure side. This phenomenon is different from the earlier predictions for a flat plate cascade, where the unsteadiness usually disappears after 25 percent of the chord length.

Upstream and Downstream Unsteady Flow Field. The measured inlet wake profile as well as the input profile is shown in Fig. 7. Only the time-mean motion of the wake is used as input; the unsteadiness in the upstream rotor wake is not taken into account in this computation. The relative motion of rotor is then accounted for by moving the inlet wake in the tangential direction at the same speed as the rotor. The unsteadiness in this case is therefore caused mainly by the relative wake motion and its interaction with the downstream stator blade. The predicted extreme and time-mean rotor wake profiles at 13 percent of the axial chord upstream of the stator (in the rotor frame) are shown in Fig. 8. The agreement between the predicted tangential velocity profiles and the experimental data is very good, including the extreme (unsteady maximum and minimum) wake profiles. There are differences between the measured and predicted axial velocity profiles at the wake center. The predicted wake centerline velocity (axial component) decays much faster than the measured values. As the rotor wake approaches the stator, the unsteadiness increases significantly due to potential interaction caused by the stator pressure field. The present calculation thus captures the potential or the inviscid interaction between the rotor wake and the stator blade. One severe test for the code is the validation of this effect. Considering the complexity of this flow, the instantaneous velocity profiles, including the instantaneous incidence to the rotor (except in a small region near the wake center), are captured well. It is clear that the potential effect of the stator blade rows has a dominant influence on the rotor wake in this compressor configuration, both on the wake profile and on the width of the wake.

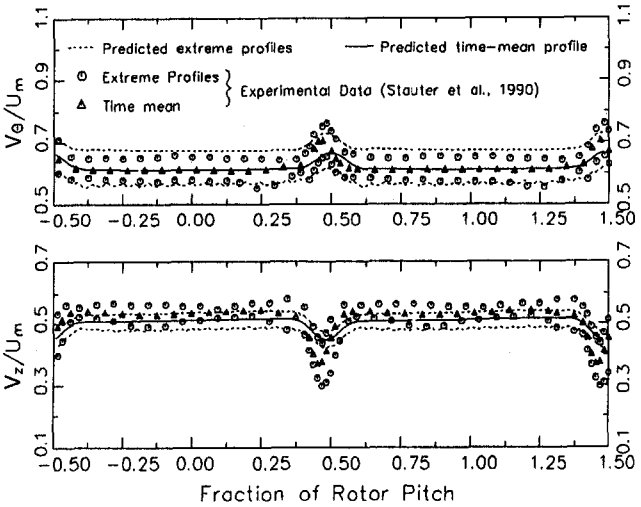

Fig. 8 Rotor wake profiles at 13 percent stator axial chord upstream of the stator blade

The unsteady stator wake profile at 18 percent axial chord downstream of the stator is shown in Fig. 9. The time-mean profiles are predicted well, but the predicted fluctuations in velocity do not agree well with the experimental data. The predicted amplitude in unsteady velocity is much smaller than the experimental data, both in the free-stream and at the wake center. However, the predictions are consistent with unsteady blade pressure data, which showed very little unsteadiness near the trailing edge (see Fig. 5). This seems to indicate that fluctuations in velocity should be small at this location.

The time histogram of velocity profiles at 20 percent upstream and at 18 percent downstream of the stator are shown in Figs. 10 and 11, respectively. The corresponding experimental data are placed side by side for comparison. In Fig. 10, the measured and predicted profiles agree very well, including distortions in the free stream. Downstream of the stator, the measured time-averaged flow field is in excellent agreement with the data, but the measured unsteadiness is higher than the predicted values.

Unsteady Flow Field Inside the Passage. The unsteady velocity field at four different instants during one period are presented in Figs. 12(b–e) to demonstrate the transport of upstream rotor wakes through the stator passage and the resulting disturbance to the stator flow field. Typical time-averaged steady and instantaneous velocity triangles are shown in Fig. 12(a). The fluctuating velocity is calculated by subtracting the time-mean absolute velocity vector from the instantaneous velocity vector. For example, the difference between V_i and V_s is V_i', pointing in a direction away from the suction surface, and this is consistent with the V_i' plot shown in Fig. 12(b),

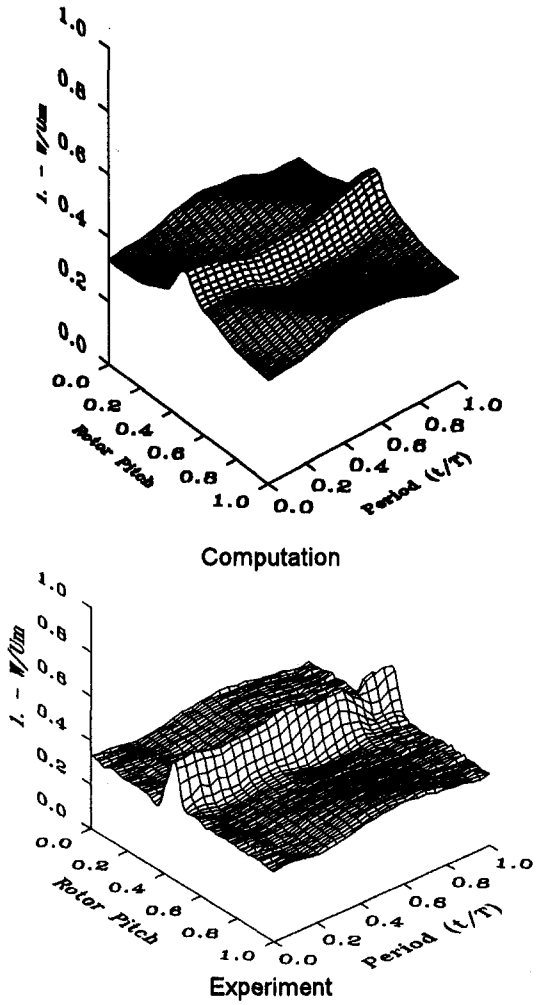

Fig. 10 Time-dependent rotor wake profile at 20 percent stator axial chord upstream of the stator blade

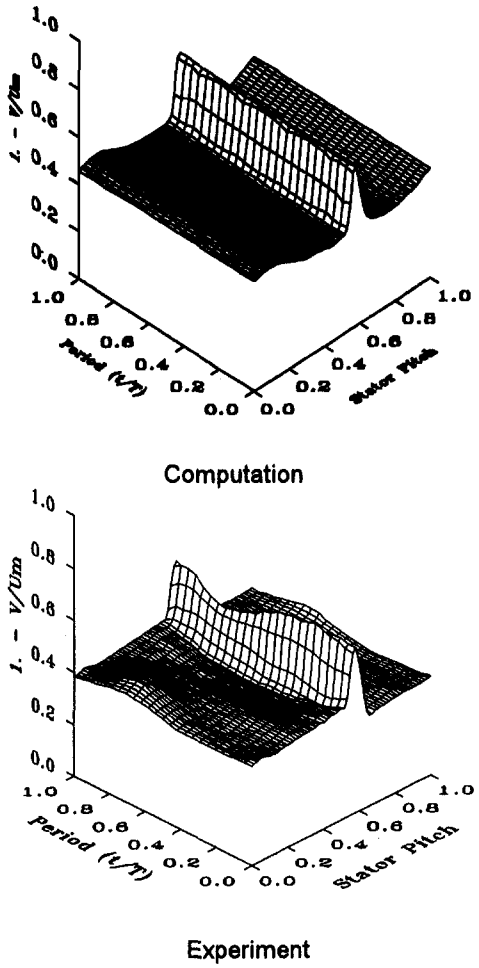

Fig. 11 Time-dependent stator wake profile at 18 percent stator axial chord downstream of the stator blade

which shows the instantaneous fluctuating velocity at $t/T = 0.0$. The rotor wake is perceived by the stator as a "negative jet."

As the rotor wake approaches the stator leading edge, the fluctuating velocity increases significantly due to rotor–stator inviscid interaction (Fig. 12*b*). The rotor wake induced incidence changes near the leading edge, causing unsteady pressure to increase substantially, which can be seen from the histogram of the unsteady pressure on the blade surface (Fig. 6). Maximum unsteady pressure on the blade surface occurs at this instant of time and the total unsteady lift on the blade also reaches its maximum value. As the rotor wake is transported through the stator passage, the wake is diffused by fluid viscosity and turbulence and the fluctuating velocity becomes smaller. The unsteady velocity and the pressure is therefore reduced correspondingly. When the rotor wake travels downstream of the leading edge (Fig. 12*d*), the rotor wake is further decayed by fluid viscosity and turbulence. As this rotor wake is transported downstream, a new rotor wake starts to approach the stator leading edge and the cycle is repeated. Similar observations were made by Adachi and Murakami (1979) based on their simulated experimental data and Hodson (1985a) based on Euler solution.

The rotor wake shed out one period earlier (Fig. 12*c*) has reached the suction side of the trailing edge and the pressure side of the leading edge. The effect of differential convective velocity between the pressure and suction surface is clearly evident from the second trace of the wake within the passage. The rotor wake on the suction side has traveled much farther than the rotor wake on the pressure side, thus distorting and elongating the wake trace. As indicated by Hodson (1985a), the jet is bowed and chopped by the blade and the amount of bowing is dependent on the convection velocity, which is higher near the suction surface, nearly zero near the leading edge. He also pointed out the reasons for distortion, confirmed by the computational results shown in Fig. 12. The high convection velocity and large streamwise gradient on suction side near the

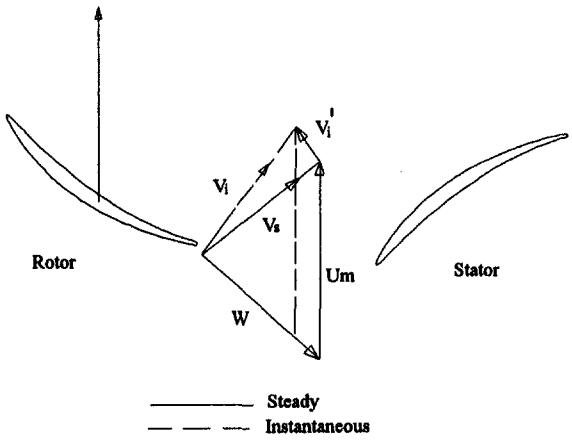

Fig. 12(*a*) The relation between the fluctuating velocity vector and the instantaneous velocity vector

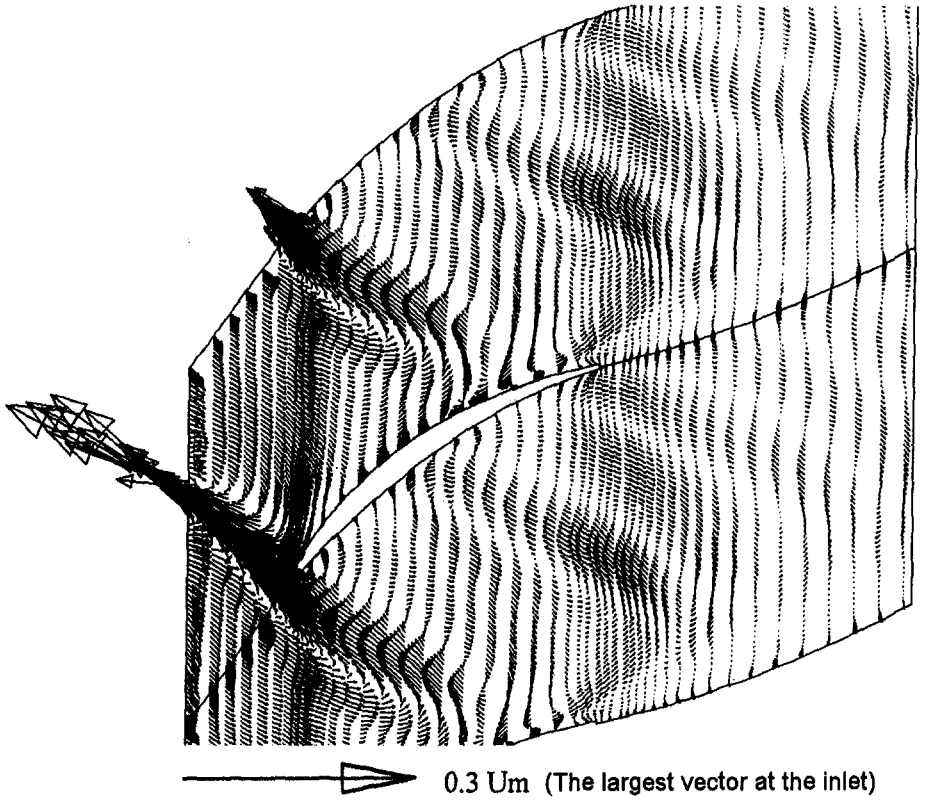

Fig. 12(*b*) The fluctuating velocity (the difference between instantaneous and time-mean velocity) vectors inside a stator (t/T = 0.00)

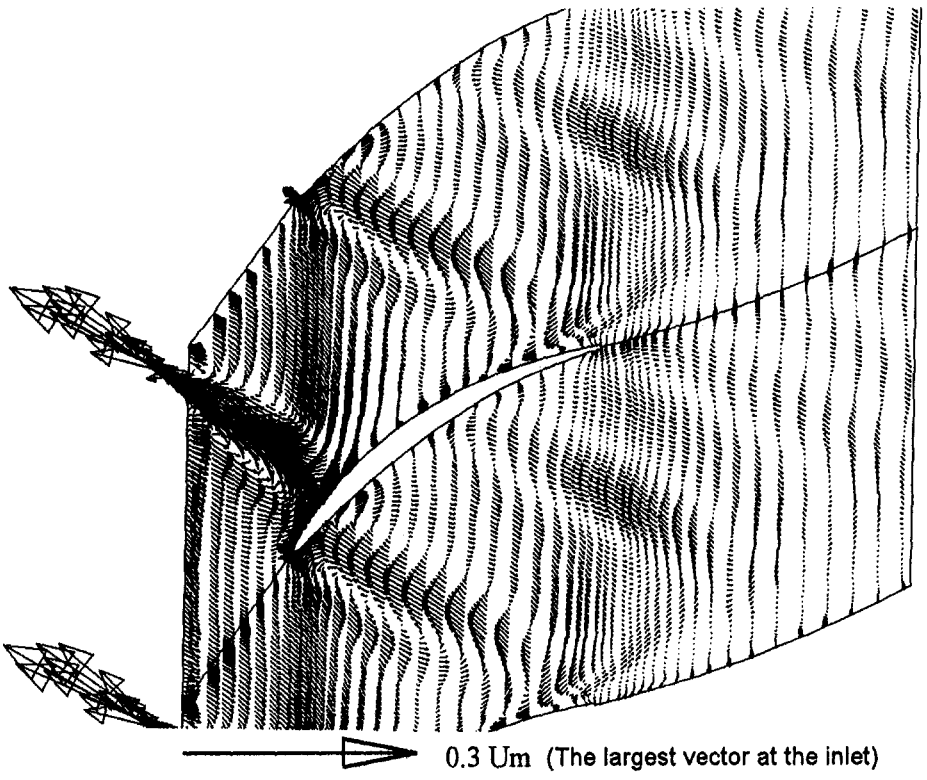

Fig. 12(c) The fluctuating velocity (the difference between instantaneous and time-mean velocity) vectors inside a stator (t/T = 0.25)

leading edge broaden the jet. The magnitude of the fluctuating velocity has also decreased considerably in the second trace, indicating that the rotor wake decay process continues through the stator blade passage.

This also indicates that the frozen wake concept proposed by Whitehead (1960) is not valid. In the linearized theories and the Euler formulations, the effect of viscosity on the wake decay is neglected. The viscosity and turbulence play a major role in

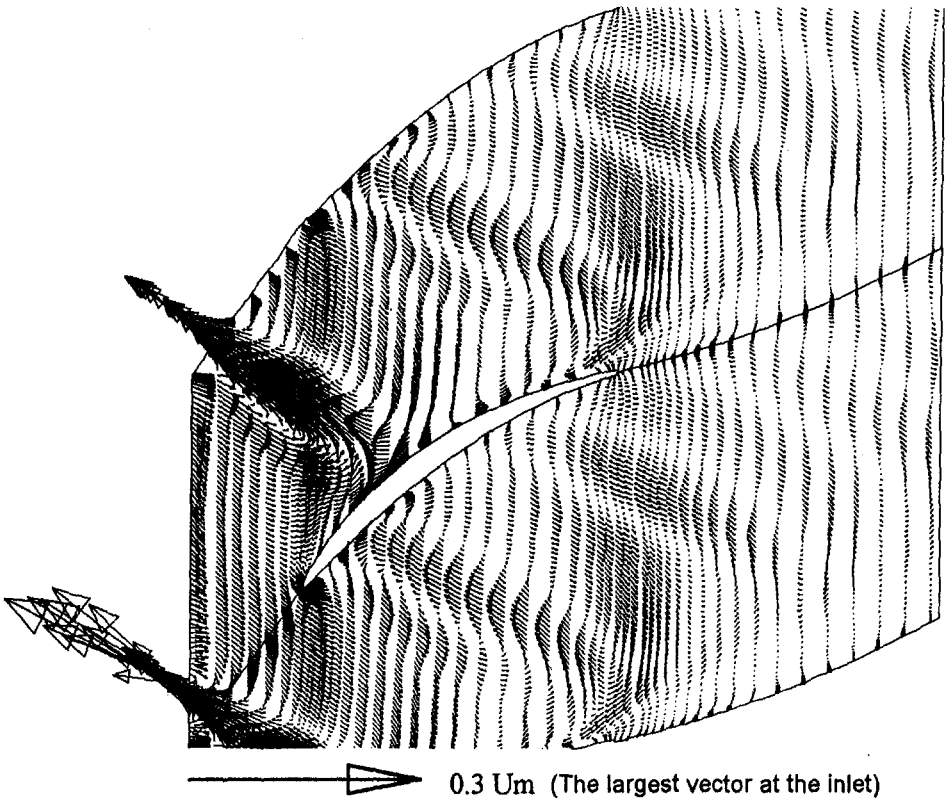

Fig. 12(*d*) The fluctuating velocity (the difference between instantaneous and time-mean velocity) vectors inside a stator (t/T = 0.50)

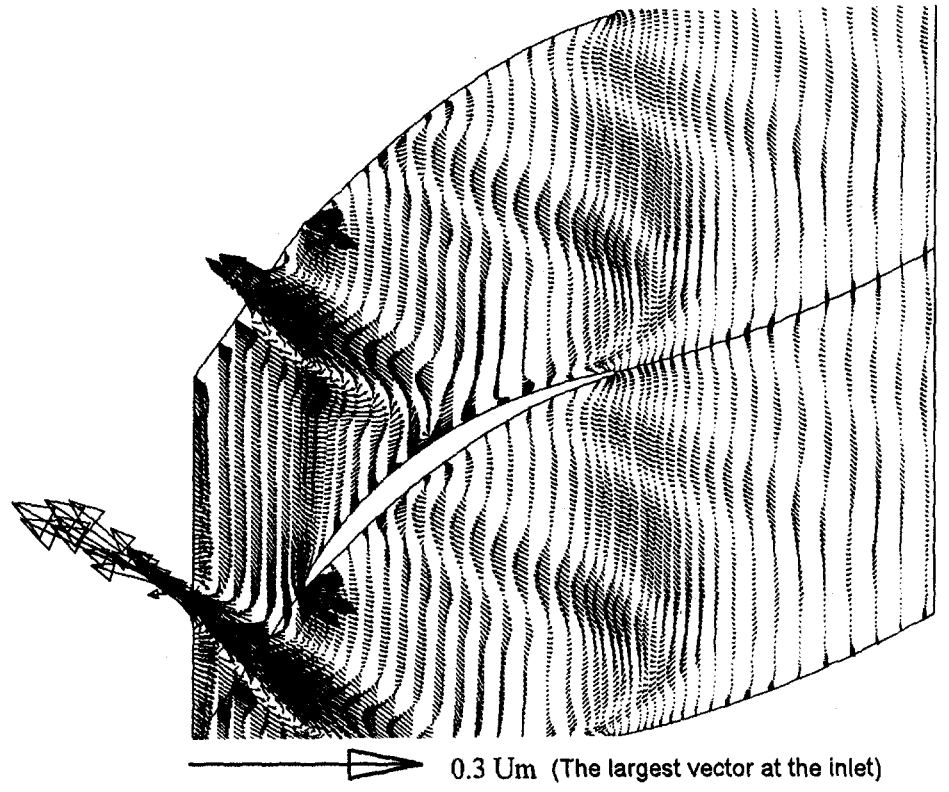

Fig. 12(*e*) The fluctuating velocity (the difference between instantaneous and time-mean velocity) vectors inside a stator (t/T = 0.75)

reducing the rotor wake velocity defect and hence the amplitude of the incoming gust. It also diffuses the wake and distorts the incoming wave. These viscous effects are not taken into account in linearized theories and Euler solutions. Hence, these theories overpredict the unsteady pressure and the amplitude of the unsteady velocity within the passage.

The "wake chopping" effect by stator leading edge can be seen clearly in Fig. 12(*c*). The wake is chopped and distorted.

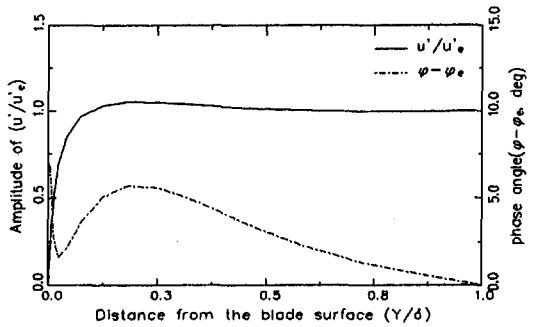

Fig. 13 Velocity fluctuation and phase shift across the boundary layer of the suction surface of a compressor stator (x/C = 0.5)

The distortion is maximum near the suction side due to large acceleration. The wake near the pressure surface is distorted less due to smaller convection velocity.

An additional feature is the disturbance caused by the interaction between the wake and the mainstream. The wake with low momentum moves toward the pressure surface. The high-momentum fluid in the free stream is forced to move in an opposite direction to replace the migrated wake. The wake acts as a "negative jet" and interacts strongly with the main stream. This interaction induces two contrarotating vortices appearing on each side of the wake and this causes changes in flow angle and velocity in these regions. This phenomenon has also been observed experimentally by Hodson (1985a, b), even though the experiment is conducted in a turbine rotor.

Since the fluctuating velocity in the main stream decreases along the blade passage (due to fluid viscosity and turbulence), the fluctuating velocity at the wake pressure side (Fig. 12*c*) becomes smaller than that of the wake suction side (Fig. 12*c*). Therefore, the vortex on the wake pressure side, which is induced by the interaction between the main stream and the wake, is larger than that on the wake suction side.

Another feature observed in the simulated results is the effect of wake impingement on the blade surface. The rotor wake is perceived by the stator as a jet as explained earlier. At the location of impingement, the jet fluid moves on either side of the impingement location, thus providing a phase angle difference of 180 deg at that location. The unsteady flow is reversed, instantaneously, at this location. This is clear from Fig. 12. It is also clear that the maximum amplitude in unsteady velocity also occurs at this location.

As the rotor wake (or jet) moves downstream of the passage, the amplitude of fluctuating velocity decreases, reaching insignificant levels at the trailing edge. This is consistent with the blade pressure distribution shown in Fig. 6. Furthermore, the fluctuating velocity is small between the traces of wake, except in the adjoining regions of the jet where counterrotating vortices are present.

Unsteady Blade Boundary Layer. A typical unsteady boundary layer on the blade surface and its behavior is shown in Fig. 13 at 50 percent of the axial chord on the suction surface. The unsteady velocity and phase angle distributions across the boundary layer are shown to demonstrate the effect of a rotor wake on the stator boundary layer. The amplitude of the velocity fluctuation has a slight overshoot near the blade surface and is nearly constant in the outer portion of the boundary layer. The phase angle shows a dip near the blade surface. This phenomenon was also reported by Fan et al. (1993) and is supported by an analysis and data of Cousteix and Houdeville (1983), which indicated the phase angle should always decrease with y in the viscous layer.

The time-dependent momentum thickness distribution on the blade surfaces is shown in Fig. 14. The expression for momentum thickness is defined by

$$\frac{\theta}{C_x} = \int^{y>\delta} \left(1 - \frac{u}{u_e}\right) \frac{u}{u_e} d\left(\frac{y}{C_x}\right) \tag{7}$$

where u_e is the boundary layer edge velocity, C_x is the axial chord, and δ is the boundary layer thickness.

It is very difficult to determine the edge velocity in cascade configurations because the edge velocity could be higher than the free-stream velocity. The edge velocity is defined here as the velocity 1.005 times larger than the next grid point closer to the surface. The effect of the rotor wake on the magnitude of blade boundary layer momentum thickness can be seen very clearly in Fig. 14. The rotor wake tends to increase inlet incidence, which has the effect of increasing the momentum thickness. There are two rotor wakes inside the passage at each instant of time. The upstream rotor wake is chopped when entering the stator passage. Since the local velocity is higher on the suction surface than on the pressure surface, the chopped wakes travel faster on the suction surface. The amplitude of time-dependent momentum thickness is not high and this is consistent with the data by Addison and Hodson (1990) on an axial flow turbine blade. They concluded that a upstream wake seems to play only a minor role in the downstream blade boundary layers development. Due to the high turbulence intensity at the inlet, the flow is fully turbulent in these passages.

Conclusion

A two-dimensional, time-accurate, Navier–Stokes code has been developed, validated, and used to compute the effect of upstream rotor wake on the stator flow and the pressure fields. The agreement between the computation and the experimental data is generally good with the exception of the unsteady flow field downstream of the stator. The effect of artificial dissipation and the grid dependency on the accuracy of unsteady flow solu-

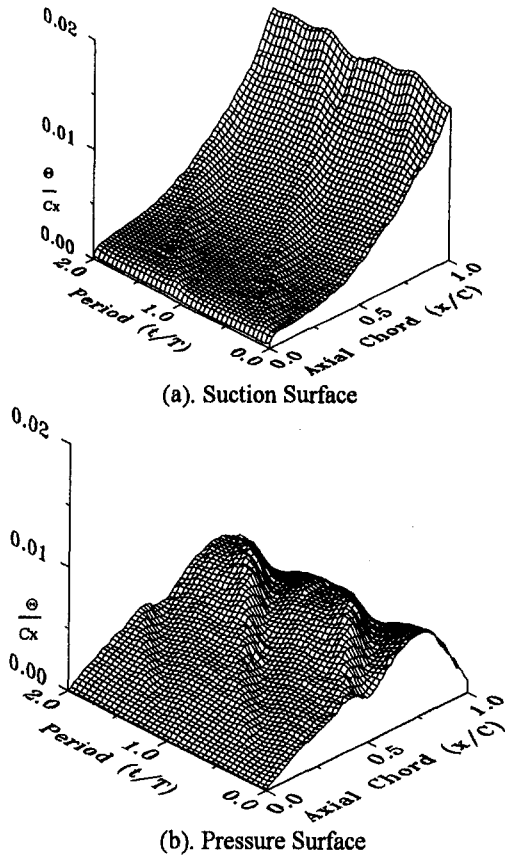

Fig. 14 The histogram of momentum thickness on the stator blade surface

tions is also evaluated. Major conclusions are summarized below:

1 At low reduced frequency (less than 3) disturbance, the grid-dependency problem is not very severe since the grid used for the steady-state viscous flow computations is sufficient to resolve the large wavelength. As the reduced frequency is increased, the wavelength becomes smaller and a dense grid is required to capture the unsteadiness accurately.

2 Although the one-dimensional analysis suggests that 10 grid points are enough to resolve a wavelength, the numerical experiment shows that at least 20 grid points are required to represent a wavelength.

3 The second-order numerical dissipation is very dissipative. It should be set to be zero for all incompressible flow calculation, especially at high reduced frequencies. The effect of the fourth-order dissipation does not affect the solution accuracy significantly. A combination of small numerical dissipation and stability requirement is essential for accurate prediction.

4 The predicted aerodynamic transfer function (C_{Fw}) for a flat plate cascade agrees well with the analytical solution by Whitehead. The blade thickness effect reduces the aerodynamic transfer function appreciably. A cascade with 10 percent thickness reduces the C_{Fw} value by almost 30 percent. For this configuration, the effect of steady loading on the aerodynamic transfer function is not important.

5 For the rotor–stator interaction simulation case, the decay of rotor wake and the time-mean pressures agree very well with the experimental data. The potential effect of downstream stator on the rotor wake is captured very well.

6 The rotor wake decays inside the stator passage due to viscous and turbulence effects. The wake defect becomes insignificant after passing through the stator passage. This indicates that the inviscid assumption made in the linearized analysis and the Euler formulation is not valid.

7 The interaction between the wake and the free-stream induces two vortices on either side of rotor wake inside the stator passage. This causes the wake to smear out as it is transported downstream inside the stator passage.

Acknowledgments

This work is supported by the Office of Naval Research through Contract No. N00014-90-J1182 with J. Fein as the contract monitor. P. J. Morris provided the one-dimensional analysis for the wave decay. D. E. Thompson and P. J. Morris provided valuable suggestions during the course of this work. The authors would like to acknowledge R. C. Stauter of UTRC for providing the experimental data for the UTRC compressor flow computation. The authors also wish to acknowledge NASA for providing the supercomputing resources at the National Aerodynamic Simulation Facility at NASA Ames Research Center.

References

Abhari, R. S., Guenette, G. R., Epstein, A. H., and Giles, M. B., 1992, "Comparison of Time-Resolved Turbine Rotor Blade Heat Transfer Measurements and Numerical Calculations," ASME JOURNAL OF TURBOMACHINERY, Vol. 114, pp. 818–827.

Adachi, T., and Murakami, Y., 1979 "Three-Dimensional Velocity Distribution Between Stator Blade and Unsteady Force on a Blade Due to Passing Wakes," *Bulletin of the Japan Society of Mechanical Engineering,* Vol. 22, No. 170, p. 1074.

Addison, J. S., and Hodson, H. P., 1990, "Unsteady Transition in an Axial Flow Turbine. Part 1." ASME JOURNAL OF TURBOMACHINERY, Vol. 112, pp. 206–221.

Basson, A. H., and Lakshminarayana, B., 1994, "An Artificial Dissipation Formulation for a Semi-implicit Pressure Based Solution Scheme for Viscous and Inviscid Flows," *Int. J. Comp. Fluid Dynamics,* Vol. 2, pp. 253–282.

Chien, K.-Y., 1982, "Prediction of Channel and Boundary-Layer Flows With a Low-Reynolds-Number Turbulence Model," *AIAA Journal,* Vol. 20, No. 1, pp. 33–38.

Cousteix, J., and Houdeville, R., 1983, "Effects of Unsteadiness on Turbulent Boundary Layers," *Von Karman Institute for Fluid Dynamics, Lecture Series* 1983-03.

Dorney, D. J., et al., 1992, "Unsteady Analysis of Hot Streak Migration in a Turbine Stage," *AIAA J. of Propulsion and Power,* Vol. 8, pp. 520.

Dring, R. P., and Joslyn, H. D., 1985, "An Assessment of Single- and Multistage Compressor Flow Modeling," Final Report for Naval Air Systems Command Contract No. N00014-84-C-0354, AD-B102 101.

Fan, S., Lakshminarayana, B., and Barnett, M., 1993, "A Low-Reynolds Number $K-\epsilon$ Model for Unsteady Turbulent Boundary Layer Flows," *AIAA Journal,* Vol. 31, No. 10, pp. 1777–1784.

Fang, J., and Atassi, H. M., 1993, "Numerical Solutions for Unsteady Subsonic Vortical Flows Around Loaded Cascades," ASME JOURNAL OF TURBOMACHINERY, Vol. 115, pp. 810–816.

Fleeter, S., 1973, "Fluctuating Lift and Moment Coefficients for Cascaded Airfoils in a Nonuniform Compressible Flow," *J. of Aircraft,* Vol. 10, pp. 93–98.

Gostelow, J. P., 1984, *Cascade Aerodynamics,* Pergamon Press, New York.

Gundy-Burlet, K. L., Rai, M. M., Stauter, R. C., and Dring, R. P., 1991, "Temporally and Spatially Resolved Flow in a Two-Stage Axial Compressor: Part 2—Computational Assessment," ASME JOURNAL OF TURBOMACHINERY, Vol. 113, pp. 227–232.

Hah, C., 1992, "Navier–Stokes Analysis of Three-Dimensional Unsteady Flows Inside Turbine Stages," AIAA Paper No. 92-3211.

Hall, K. C., and Verdon, J. M., 1991, "Gust Response for Cascade Operating in Nonuniform Mean Flows," *AIAA Journal,* Vol. 29, pp. 1463–1471.

Ho, Y.-H., and Lakshminarayana, B., 1993, "Computation of Unsteady Viscous Flow Using an Efficient Algorithm," *AIAA Journal,* Vol. 31, No. 12, p. 2232.

Ho, Y.-H., 1995, "Numerical Simulation of Steady and Unsteady Viscous Flows in Turbomachinery Blade Rows," Ph.D. Thesis, The Pennsylvania State University.

Hobson, G. V., and Lakshminarayana, B., 1991, "Prediction of Cascade Performance Using an Incompressible Navier–Stokes Technique," ASME JOURNAL OF TURBOMACHINERY, Vol. 113, pp. 561–572.

Hodson, H. P., 1985a, "An Inviscid Blade-to-Blade Prediction of a Wake-Generated Unsteady Flow," ASME *Journal of Engineering for Gas Turbines and Power,* Vol. 107, pp. 337–344.

Hodson, H. P., 1985b, "Measurements of Wake-Generated Unsteadiness in the Rotor Passages of Axial Flow Turbines," ASME *Journal of Engineering for Gas Turbines and Power,* Vol. 107, pp. 467–476.

Issa, R. I., 1985, "Solution of the Implicitly Discretized Fluid Flow Equations by Operator-Splitting," *J. of Computational Physics,* Vol. 62, pp. 40–65.

Kim, S.-W., and Benson, T. J., 1992, "Comparison of the SMAC, PISO and Iterative Time-Advancing Schemes for Unsteady Flows," *Computers Fluids,* Vol. 21, pp. 435–454.

Kunz, R. F., and Lakshminarayana, B., 1992, "Three-Dimensional Navier–Stokes Computation of Turbomachinery Flows Using an Explicit Numerical Procedure and a Coupled $k-\epsilon$ Turbulence Model," ASME JOURNAL OF TURBOMACHINERY, Vol. 114, pp. 627–642.

Leonard, B. P., 1979, "A Stable and Accurate Convective Modelling Procedure Based on Quadratic Upstream Interpolation," *Computer Methods in Applied Mechanics and Engineering,* Vol. 19, pp. 59–98.

Manwaring, S. R., and Fleeter, S., 1993, "Rotor Blade Unsteady Aerodynamic Gust Response to Inlet Guide Vane Wakes," ASME JOURNAL OF TURBOMACHINERY, Vol. 115, pp. 197–206.

Patankar, S. V., 1980, *Numerical Heat Transfer and Fluid Flow,* Hemisphere Publishing Corp., New York.

Pulliam, T. H., 1986, "Artificial Dissipation Models for the Euler Equations," *AIAA Journal,* Vol. 24, No. 12, pp. 1931–1940.

Rai, M. M., 1987, "Navier–Stokes Simulations of Rotor/Stator Interactions Using Patched and Overlaid Grids," *J. of Propulsion Power,* Vol. 3, pp. 387–396.

Rao, K. V., Delaney, R. A., and Dunn, M. G., 1992, "Vane-Blade Interaction in a Transonic Turbine, Part I—Aerodynamics," AIAA Paper No. 92-3323.

Rhie, C. M., and Chow, W. L., 1983, "Numerical Study of the Turbulent Flow Past an Airfoil With Trailing Edge Separation," *AIAA Journal,* Vol. 21, No. 11, pp. 1525–1532.

Stauter, R. C., Dring, R. P., and Carta, F. O., 1991, "Temporally and Spatially Resolved Flow in a Two-Stage Axial Compressor: Part 1—Experiment," ASME JOURNAL OF TURBOMACHINERY, Vol. 113, pp. 219–226.

Stauter, R. C., 1992, private communication.

Van Doormaal, J. P., and Raithby, G. D., 1984, "Enhancements of the SIMPLE Method for Predicting Incompressible Fluid Flows," *Numerical Heat Transfer,* Vol. 7, pp. 147–163.

Whitehead, D. S., 1960, "Force and Moment Coefficients for Vibrating Airfoil in Cascade," British Aeronautical Council Reports and Memoranda No. 3254.

APPENDIX

Numerical Scheme

A detailed description of the numerical scheme is presented in Ho and Lakshminarayana (1993). The code has been modified to improve the discretization accuracy and the coupling between the momentum equation and $k-\epsilon$ turbulence equations. The modifications are described below.

In order to represent the convection term with second-order accuracy, the convection term is discretized with a central differencing scheme. However, the central difference scheme is unstable when solely used for the convection term. The main reason is that the central differencing is not dissipative and the physical viscous terms cannot damp the error at high wave numbers, even in viscous flow computations with small grid spacing (Kunz and Lakshminarayana, 1992). The central difference scheme also introduces the so-called "checkerboard effect" (Patankar, 1980) or uncoupled odd-even grid points. All high-order upwinding schemes used in the time-marching methods are more accurate than the basic upwind scheme, but inherently include certain amount of artificial dissipation (Pulliam, 1986). Basson and Lakshminarayana (1994) also showed that the more accurate QUICK scheme (Leonard, 1979) is equivalent to central differencing plus third-order and fourth-order dissipation. Thus, the disadvantage of these higher order upwind schemes is the lack of control on the amount of numerical dissipation. In view of this, the scheme developed by Basson and Lakshminarayana (1994), with a second-order and a fourth-order artificial dissipation added explicitly, is used to control the numerical dissipation. The expression for the second and the fourth-order dissipation can be represented by

$$+\frac{1}{2}\epsilon_2\left[\Delta\xi\frac{\partial}{\partial\xi}\left(\left|\rho JG_1\right|\frac{\partial\phi}{\partial\xi}\right)+\Delta\eta\frac{\partial}{\partial\eta}\left(\left|\rho JG_2\right|\frac{\partial\phi}{\partial\eta}\right)\right]$$

$$-\frac{1}{8}\epsilon_4\left[\Delta\xi^3\frac{\partial}{\partial\xi}\left(\left|\rho JG_1\right|\frac{\partial^3\phi}{\partial\xi^3}\right)\right.$$

$$\left.+\Delta\eta^3\frac{\partial}{\partial\eta}\left(\left|\rho JG_2\right|\frac{\partial^3\phi}{\partial\eta^3}\right)\right] \quad \text{(A.1)}$$

where ϵ_2 and ϵ_4 are the coefficients of the second and fourth-order dissipation terms. $\Delta\xi$ and $\Delta\eta$ are the grid spacing in ξ and η direction.

The central difference scheme is also used for discretization of the dissipation terms. The discretization of the fourth-order dissipation will result in a six-point formulation and a sparse matrix. In order to use the tridiagonal matrix solving technique (ADI), the fourth order dissipation is treated partially implicitly (Basson and Lakshminarayana, 1994).

As mentioned in the previous section, the central difference formulation will introduce decoupled solutions between odd and even grid points. In order to circumvent this problem, Rhie and Chow (1983) proposed a pressure-weighting scheme to link the odd and even grid points. Basson has proved that this scheme is equivalent to adding a fourth-order artificial dissipation to the pressure equation. Rhie and Chow's pressure-weighting method has too much dissipation and thus affects the accuracy of the solution. Therefore, in the present work, a 10 to 20 percent value of pressure-weighting is used. This is sufficient to provide a smooth pressure field.

For temporal discretization, a backward differencing implicit scheme is selected. Thus, the second-order accuracy in the time domain is preserved. The diffusive terms are approximated by the central differencing scheme. All cross derivatives are treated explicitly and considered as source terms.

The numerical scheme used in this work is the PISO scheme by Issa (1985). Detailed implementation of this algorithm can be found in Ho and Lakshminarayana (1993). In the PISO scheme, the momentum equation and the equations for k and ϵ are solved in sequence. In order to take into account the coupling between the governing equations and the turbulence model, an inner iteration loop is introduced to account for the nonlinear interaction between the flow field and the turbulence. This iteration procedure has been proven to be more accurate than the original PISO scheme (Kim and Benson, 1992). The solution procedure used in the present work is the combination of the PISO scheme and E-factor scheme by Van Doormaal and Raithby (1984). The discretized form of the general transport equation can be written as:

$$(\rho J/\Delta t + a_O)\phi_O = a_E\phi_E + a_W\phi_W + a_N\phi_N + a_S\phi_S + S_\phi \quad \text{(A.2)}$$

where a_i is the influence coefficients of the discretized equations except the time variation term. The subscript O represents the control points and E, W, N, S are the surrounding points. The influence coefficients a_i are first evaluated from the previous time step solution. In order to incorporate the nonlinear effects, the discretized Eqs. (A.2) are modified, by using the idea of Van Doormaal and Raithby, as

$$(\rho J/\Delta t + a_O)^*\phi_O = a_E\phi_E + a_W\phi_W + a_N\phi_N + a_S\phi_S + (S_\phi)^* \quad \text{(A.3)}$$

where ϕ_O^* is the current estimate of ϕ_O for advancing in time, and

$$(\rho J/\Delta t + a_O)^* = (\rho J/\Delta t + a_O)\left[1+\frac{1}{E_R}\right]$$

$$(S_\phi)^* = S_\phi + \frac{(\rho J/\Delta t + a_O)}{E_R}\phi_O^*$$

E_R is chosen so that the diagonal dominant solution matrix is maintained. Van Doormaal and Raithby showed that the limit of E_R is 1 for explicit scheme. Since the time step Δt is usually small in time-accurate computations, the value of E_R can be larger than 1. As shown in Eq. (A.2), if time-dependent terms are removed, the original E-factor scheme is recovered.

Therefore, this E-factor scheme is implemented in the inner iteration loop to update the influence coefficients a_i and ϕ_i during each time step. At convergence of Eq. (A.2), the influence coefficients and the variables are coupled in the time-accurate solutions. The inner iteration is continued until the following convergence criteria are satisfied, i.e.,

$$\frac{|R_\phi^{**} - R_\phi^*|}{R_\phi^*} < \text{tolerance}, \quad R_m^{**} < \text{tolerance} \quad \text{(A.4)}$$

where R_ϕ^{**} is the rms residual of variable ϕ at iteration level **. The subscript m represents the mass balance. The typical tolerance levels for all variables are 1×10^{-3} and 1×10^{-7} for mass residual.

A. Yamamoto
Aeroengine Division,
National Aerospace Laboratory,
Tokyo, Japan

R. Murao

Y. Suzuki[1]

Y. Aoi[2]

Department of Mechanical Engineering,
Aoyama Gakuin University,
Tokyo, Japan

A Quasi-Unsteady Study on Wake Interaction of Turbine Stator and Rotor Cascades

Detailed flow measurements were made to study cascade interaction of turbine stator and rotor, using two linear cascades installed in series. The upstream cascade was moved to several places in the cascade pitchwise direction in order to change the relative location between the two cascades, and measurements were made in the downstream cascade. The result shows that the net total pressure loss generated in the downstream cascade becomes maximum when wakes of the upstream cascade pass the suction side of the downstream cascade passage, while the tip leakage loss generated in the downstream cascade does not change with the relative location of the cascades. The upstream cascade wakes interact with the secondary flows and most strongly with the endwall flow in the downstream cascade passage, making the loss distributions in the cascades fairly unsteady.

Introduction

To achieve higher levels of turbomachinery performance in various types of new engine currently being developed in many places, it is necessary to reveal details of internal flows and loss mechanisms of the turbomachines. The internal flows are three dimensional, and unsteady in nature due to the relative motion between the stationary blades (stator) and the moving blades (rotor) of turbomachines. The loss generation mechanism is, therefore, very complex and unsteady due to this stator–rotor interaction. Effects of stator–rotor interaction on turbine flow fields have been studied so far by, for example, Hodson (1985), Binder et al. (1985), and Sharma et al. (1985, 1988, 1992). They reveal various unsteady flow phenomena occurring in their rotors, with presenting data mainly from the midspan blade-to-blade planes of their rotors. Difficulties of detailed traverse measurements in rotors and limited numbers of studies published so far prohibit us from understanding the unsteady flow mechanisms fully. Three-dimensional internal flows in cascade passages cause strong spanwise fluid mixing and, therefore, the mechanisms of unsteady flow and the associated losses should be discussed from a three-dimensional point of view. The present authors' group has been trying to clarify such unsteady three-dimensional flows using a low-speed axial-flow turbine from this point of view, and some animated color movies produced from the detailed hot-wire data have shown clear but very complex behaviors of the three-dimensional unsteady flow (Yamamoto et al., 1993). Unsteady effects on the cascade loss generation also have not been fully understood yet because of the complexity of the flow behavior.

In the present study, interaction phenomena occurring between upstream and downstream cascades were investigated experimentally in a simple way by changing the relative pitchwise location of both cascades. Although this stationary cascade arrangement might not simulate actual turbine flows very well, the authors believe that the results obtained from this simplified cascade arrangement will give some useful information that contributes to further understanding of the cascade interaction and the loss generation mechanism associated with the interaction.

Experimental Method and Analysis Method

A linear cascade test rig was used in the present tests. The test rig was designed and often used for studying loss generation mechanisms and three-dimensional flow behaviors occurring in turbine cascades. In the present study, two linear cascades were installed in series in the test section, as shown in Fig. 1. The upstream cascade corresponds to a stator cascade and the downstream cascades to a rotor cascade. The pitch widths of both cascades are equal. The relative pitchwise location of both cascades was changed nine times by moving the whole upstream cascade in the pitchwise direction by $\frac{1}{8}$ pitch. The cascade arrangement shown in Fig. 1 corresponds to one of the relative locations tested ($t = \frac{1}{4}T$ where T means the cascade pitch width). The major specifications of each cascade are shown in Table 1. Details of the blade coordinates and the test rig may be seen in Yamamoto (1987, 1989).

Figure 2 shows twelve measuring planes located before, inside, and after the downstream cascade, where detailed flow measurements were made with a five-axis, fully computer-controlled measuring device with a small five-hole Pitot tube of 1.5 mm head size. To minimize the blockage of the probe inside the cascade passage and the interference effect on the flow measurements, the probe was made L-shaped, as described by Yamamoto (1989). The present 1.5 mm head size (d = 1.5 mm) corresponds to $L/d = 6$. This L/d ratio may reduce the interference effect of the probe stem fairly well on the flow at the sensing point of the probe. In the following sections, the results are presented only at four selected relative locations corresponding to $\frac{1}{4}T$, $\frac{2}{4}T$, $\frac{3}{4}T$, and $\frac{4}{4}T$.

The effects of the different relative locations on tip leakage flow and the associated leakage loss of the downstream cascade were also studied with and without tip clearance in the downstream cascade. With tip clearance, the tip gap size was about 1.2 percent of the cascade passage height. The test setting velocity was measured by a Prandtl-type total/static pressure probe located far upstream from the stator cascade and was maintained constant at 40 m/s during the

[1] Current address: Japan Air System Co., Ltd., Tokyo, Japan.
[2] Current address: Mitsubishi Motors Co., Ltd., Tokyo, Japan.

Contributed by the International Gas Turbine Institute and presented at the 39th International Gas Turbine and Aeroengine Congress and Exposition, The Hague, The Netherlands, June 13–16, 1994. Manuscript received by the International Gas Turbine Institute February 15, 1994. Paper No. 94-GT-138. Associate Technical Editor: E. M. Greitzer.

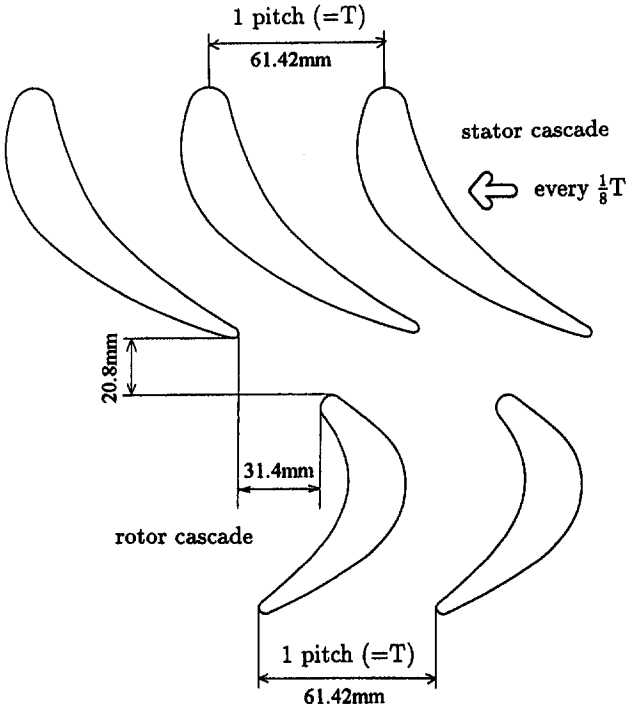

Fig. 1 Arrangement of stator and rotor cascade models (at $t = \frac{1}{4}T$)

present tests. The test Reynolds number based on the outlet velocity and the blade chord of the downstream cascade was 1.8×10^5.

The total pressure loss coefficient and the static pressure coefficient were normalized as follows:

$$CP_t = \frac{P_{ref} - P_t}{0.5\rho V_{ref}^2}, \quad CP_s = \frac{P_s - P_{ref}}{0.5\rho V_{ref}^2}$$

where the atmospheric pressure was used as the reference pressure (P_{ref}) to show both cascade losses on the same basis. Some pressure drop between the atmosphere and the upstream cascade inlet was, therefore, included in the coefficients. The pressure drop is due mainly to the bell mouth and the inlet duct (i.e., the inlet endwalls and the inlet guide plates) up to the upstream cascade inlet, and is considered to be constant during the tests. The setting velocity mentioned before was used as the reference velocity (V_{ref}), which is close to the mass-averaged velocity at the downstream cascade exit.

Secondary flow vectors at each measuring plane were determined as the projection of local flow vectors onto the plane normal to the local camber line direction at the measuring plane. In some of the following figures, gray scale loss contour plots are used that were copied from color pictures of the results, and it may be somewhat difficult for readers to distinguish high and low loss regions because of the same shade of gray. In this case, use the plots to know only the variation of the loss "patterns" rather than the local loss values, which is the main objective of the figures.

Table 1 Major specifications of test cascades

	Stator	Rotor
Blade number	6	6
Pitch	61.42 mm	61.42 mm
Blade inlet angle	0 deg.	49.8 deg.
Blade outlet angle	68 deg.	-63.5 deg.
Stagger angle	39 deg.	-17.2 deg.
Span	96 mm	99.5 mm
Chord length	104.4 mm	73.5 mm
Axial chord	81.5 mm	72.6mm
Aspect ratio	0.912	1.35

Experimental Results and Discussion

Overall View of the Downstream Cascade Flow and Loss Field. Figure 3 shows a typical result obtained at the relative location of $\frac{1}{4}T$, showing three-dimensional flow fields of the downstream cascade without tip clearance. Vectors shown at the cascade inlet and at the outlet indicate the secondary flows at planes 1 and 12, and the vectors drawn on the endwall indicate endwall flows passing near the blade tip endwall. The contours shown in the cascade passage of the left-hand side indicate the total pressure loss coefficient, CP_t, and those of the right-hand side the static pressure coefficient, CP_s.

At both the cascade inlet and the outlet, passage vortices are seen to generate from the upstream and the downstream cascades, and they are rotating opposite to each other. Over the endwall close to the cascade trailing edge, the endwall flow vectors are significantly skewed toward the blade suction side due to the endwall pressure gradient there, forming the passage vortex in the downstream cascade.

Relation Between Overall Loss and Wake Path Through the Downstream Cascade. Mass-averaged overall losses obtained at the inlet and the outlet of the downstream cascade

Nomenclature

C_{ax} = blade axial chord
CP_t = total pressure loss coefficient = $(P_{ref} - P_t)/(0.5\rho V_{ref}^2)$
CP_s = static pressure coefficient = $(P_s - P_{ref})/(0.5\rho V_{ref}^2)$
DLV, DPV = deviation leakage vortex, deviation passage vortex
H = cascade passage height
L = head length of L-shaped Pitot tube
LV = leakage vortex
P_{ref} = reference pressure
P_s = static pressure
P_t = total pressure
PV = passage vortex
SS = suction side
PS = pressure side
t = relative location of two cascades
T = cascade pitch
TCL = tip clearance
V_{ref} = reference velocity
WK_u = wake of upstream cascade
WK_d = wake of downstream cascade
Y = spanwise distance
Z = axial distance
Δ = interval of contour plots

Superscripts

$-$ = pitchwise mass-averaged value
$=$ = overall mass-averaged value

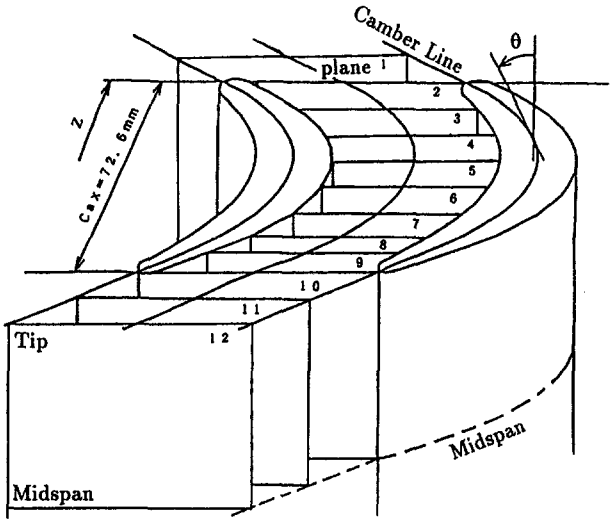

Fig. 2 Measuring planes

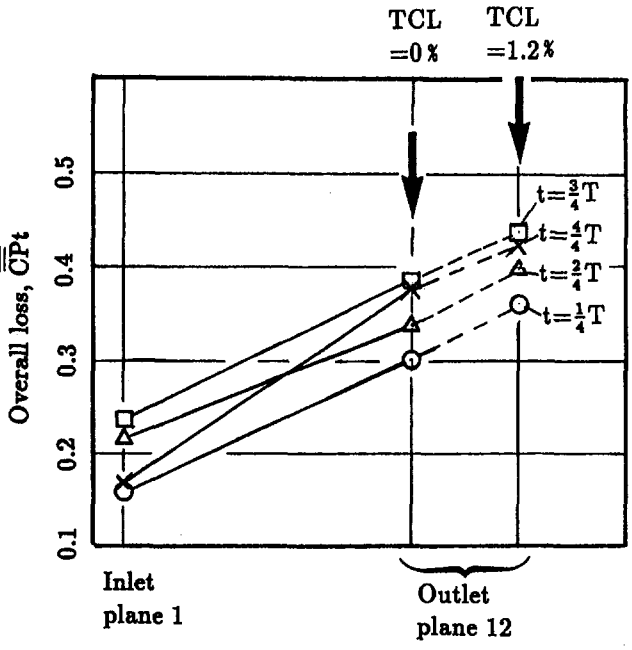

Fig. 4 Overall loss

are shown in Fig. 4 for four relative locations tested. To know the four test conditions, Fig. 5 was prepared to show the paths of the upstream cascade wakes at two blade-to-blade planes located at the midspan ($Y/H = 0.5$) and near the (tip) endwall ($Y/H = 0.98$) in the downstream cascade. Note that the wake paths near the tip endwall are significantly different from those at the midspan since the wakes are skewed and spread widely near the endwall.

As seen in Fig. 4, even the inlet loss (corresponding to the upstream cascade loss) is influenced by the cascade interaction: The inlet loss becomes highest at $\frac{3}{4}T$ when the upstream cascade wake at the midspan passes a little apart from

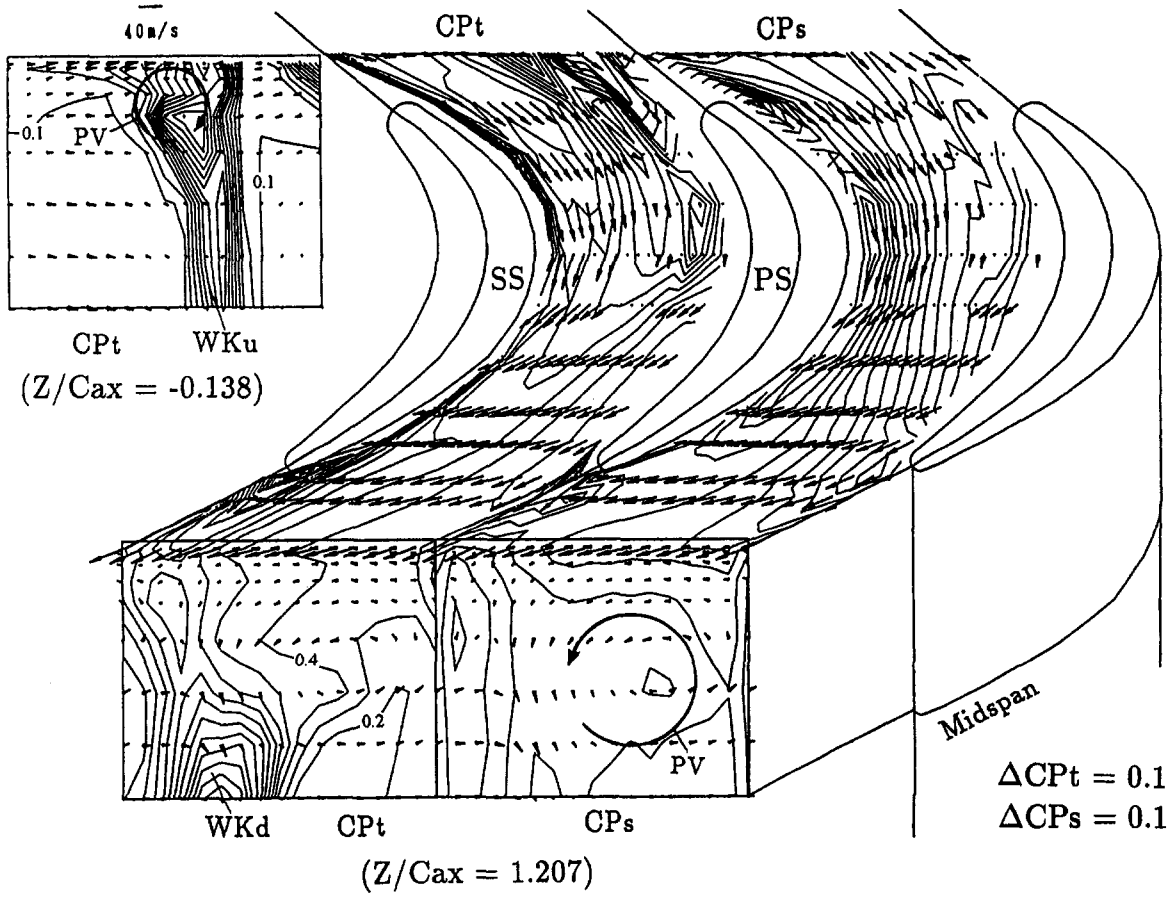

Fig. 3 A typical result of three-dimensional cascade flows obtained at $t = \frac{1}{4}T$ without tip clearance

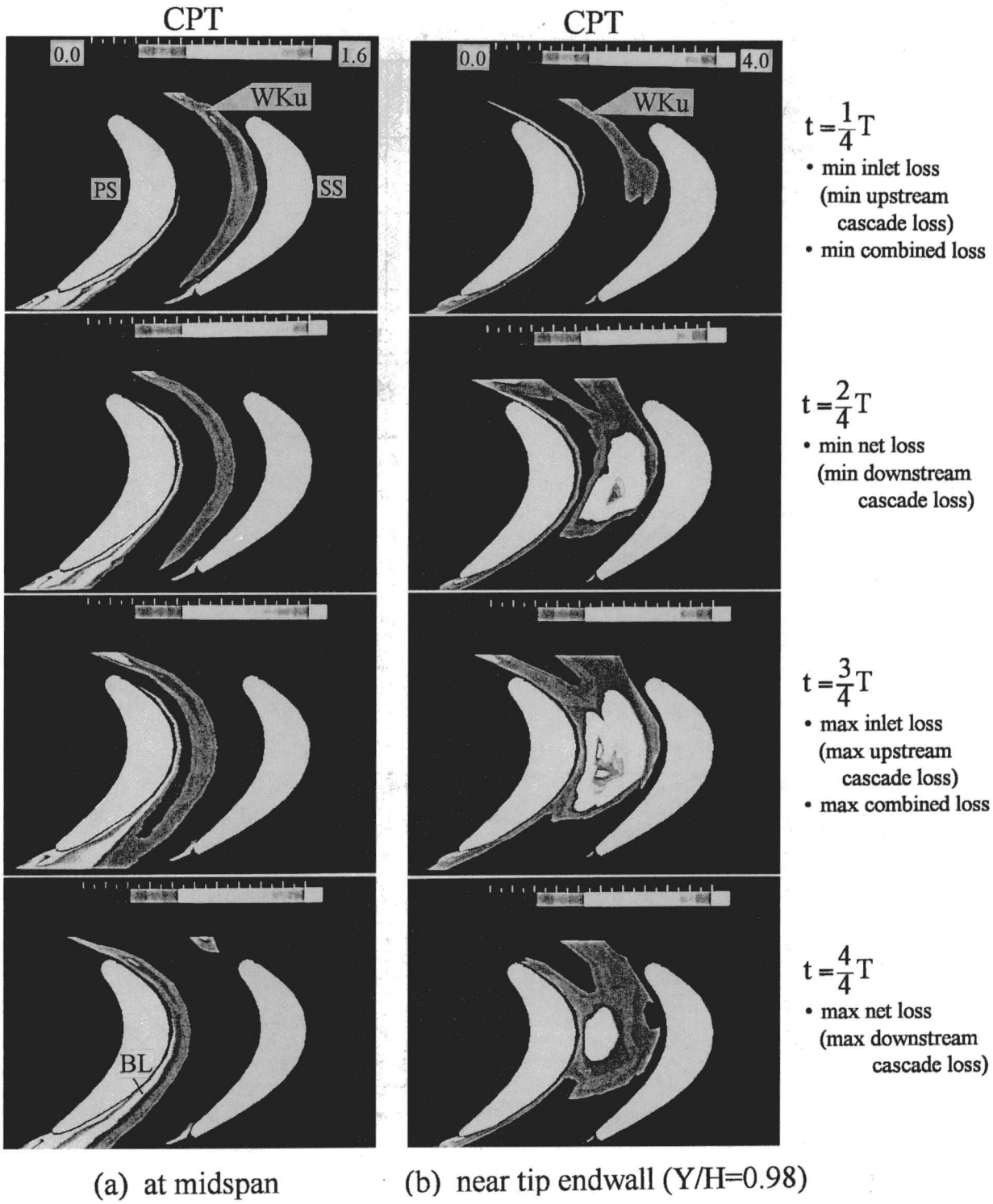

Fig. 5 Location of the upstream cascade wake in the downstream cascade passage without tip clearance

the blade suction surface of the downstream cascade passage, as seen in Fig. 5(*a*), while it becomes lower at $\frac{1}{4}T$ and $\frac{4}{4}T$ when the wake passes near or over the blade surfaces. As seen in Fig. 5(*b*), however, the upstream wakes located near the tip endwall are significantly skewed toward the blade suction side of the downstream cascade passage, and at $\frac{2}{4}T$ to $\frac{4}{4}T$, low-energy fluids from two neighboring wakes tend to enter a passage of the downstream cascade at the same time. At these relative locations, the low energy fluids tend to accumulate over the endwall as shown by closed-form contour plots.

As shown in Fig. 4, the variation of the inlet loss at plane 1 contributes purely to the variation of the outlet loss at plane 12. The outlet loss corresponds to the combined cascade loss generated in both the upstream and the downstream cascades. At $\frac{4}{4}T$, the outlet loss rapidly becomes large, although the corresponding inlet loss was relatively small. Therefore, the net loss generated in the downstream cascade is maximum at this $\frac{4}{4}T$ where the upstream cascade wake (except near the endwall) overlaps the suction surface boundary layer of the downstream cascade, as seen from Fig. 5(*a*). However, as shown in Fig. 4 by the slopes of

loss increase, which are presented by four dashed lines, the net mass-averaged leakage loss generated in the downstream cascade does not depend on the relative locations. These features obtained at these four different relative locations are summarized also in Fig. 5.

Three-Dimensional Movements of the Upstream Cascade Wake in the Downstream Cascade Without Tip Clearance. Figure 6 shows the inlet loss distributions, i.e., the upstream cascade wake profiles for four relative locations. As seen here, the upstream cascade loss is easily affected by the cascade interaction and becomes highest at $\frac{3}{4}T$. At this relative location, the upstream cascade wakes spread widely, particularly near the endwall, due to the interaction between the wakes and the leading edges of the downstream cascade. The spreading low-energy fluids coming from the neighboring two wakes enter the measuring plane 1 at the same time to lead the maximum inlet loss. This condition also makes the inlet endwall boundary layer of the downstream cascade thicker, which causes low-energy fluids to accumulate over the endwall and likely causes the endwall flows to separate within the downstream cascade passage.

Figures 7(a, b) show movements of the upstream cascade wake in two traverse planes, 5 (Z/C_{ax} = 0.414) and 9 (Z/C_{ax} = 0.917), in the downstream cascade. In Fig. 7(a), accumulation of low-energy fluids of the upstream cascade wake is seen over the endwall, particularly at $\frac{2}{4}T$ and $\frac{3}{4}T$, where the upstream wakes spread widely near the endwall. Figure 7(b) shows that the low-energy fluids have almost completely migrated onto the blade suction surface of the downstream cascade and are fluctuating periodically according to the change of the relative location.

Effect of Tip Clearance on the Downstream Cascade Loss. Figures 8(a, b) show loss distributions at the downstream cascade outlet without and with tip clearance. In both cases, the loss distributions are affected by the cascade interaction. The losses shown in Fig. 8(b) show that a strong leakage vortex (LV) appears near the endwall. The size and the intensity of the leakage vortex can be seen to change with the cascade interaction, while the associated net tip leakage loss is not affected by the cascade interaction, as was seen before in Fig. 4.

Vortex Interaction. Figure 9 shows secondary flow vectors and loss contours at the exit of the downstream cascade (plane 12) with tip clearance. Figure 9(o) shows the periodic averaged secondary flows and losses that were obtained by averaging the data of all the eight relative locations tested. In every figure, a passage vortex (PV) and a leakage vortex (LV) can be seen. They interact strongly with each other and are affected by the relative location of both cascades as shown in Figs. 9(a–d).

In order to extract the effects of cascade interaction more clearly, deviations from the periodical average values in the secondary flow vectors and in the loss were obtained by extracting Fig. 9(o) from each of Figs. 9(a–d). The results are shown in Fig. 10. At $\frac{1}{4}T$, a deviation vortex denoted by DPV appears, which rotates clockwise, opposite to the rotational direction of the passage vortex shown in Fig. 9(o). This indicates that the passage vortex is made weaker at $\frac{1}{4}T$ by the cascade interaction than the periodic averaged passage vortex. At $\frac{2}{4}T$, a deviation vortex (DPV) rotating counterclockwise appears near the suction side. At $\frac{3}{4}T$, two deviation vortices (DPV, DLV) rotating opposite to each other are seen near the endwall. The rotational directions of each DPV and DLV are the same as those of the tip-side passage vortex and the tip leakage vortex, respectively. This means that the two vortices become stronger at this cascade arrangement. At $\frac{4}{4}T$, these two deviation vortices (DPV and DLV) become much stronger, and the passage and leakage vortices interact very strongly. The vortex interaction at $\frac{4}{4}T$, thus, may cause the most significant net loss in the downstream cascade. It is also shown at this $\frac{4}{4}T$ seen in Fig. 9(d) that the leakage vortex is pushed into a smaller area at the blade suction corner while the intensity of the vortex increases.

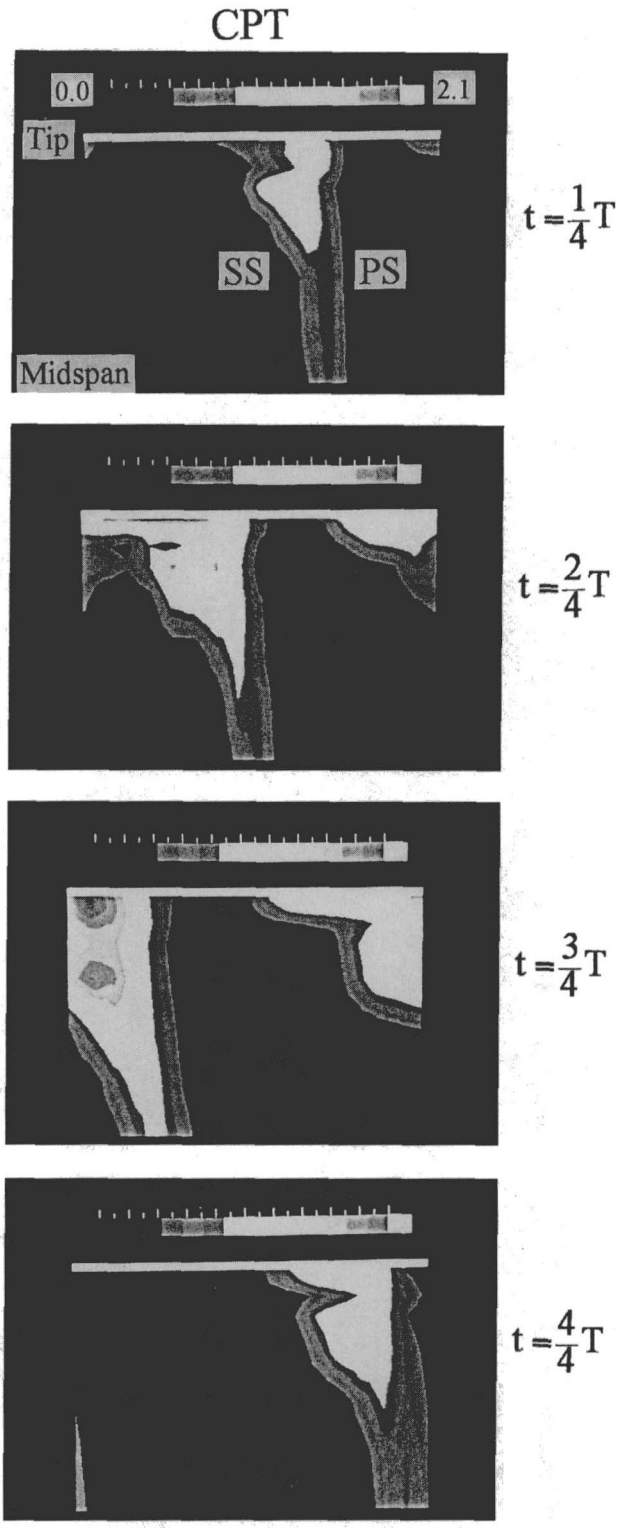

Fig. 6 Upstream cascade loss (plane 1, $Z/C_{ax} = -0.138$)

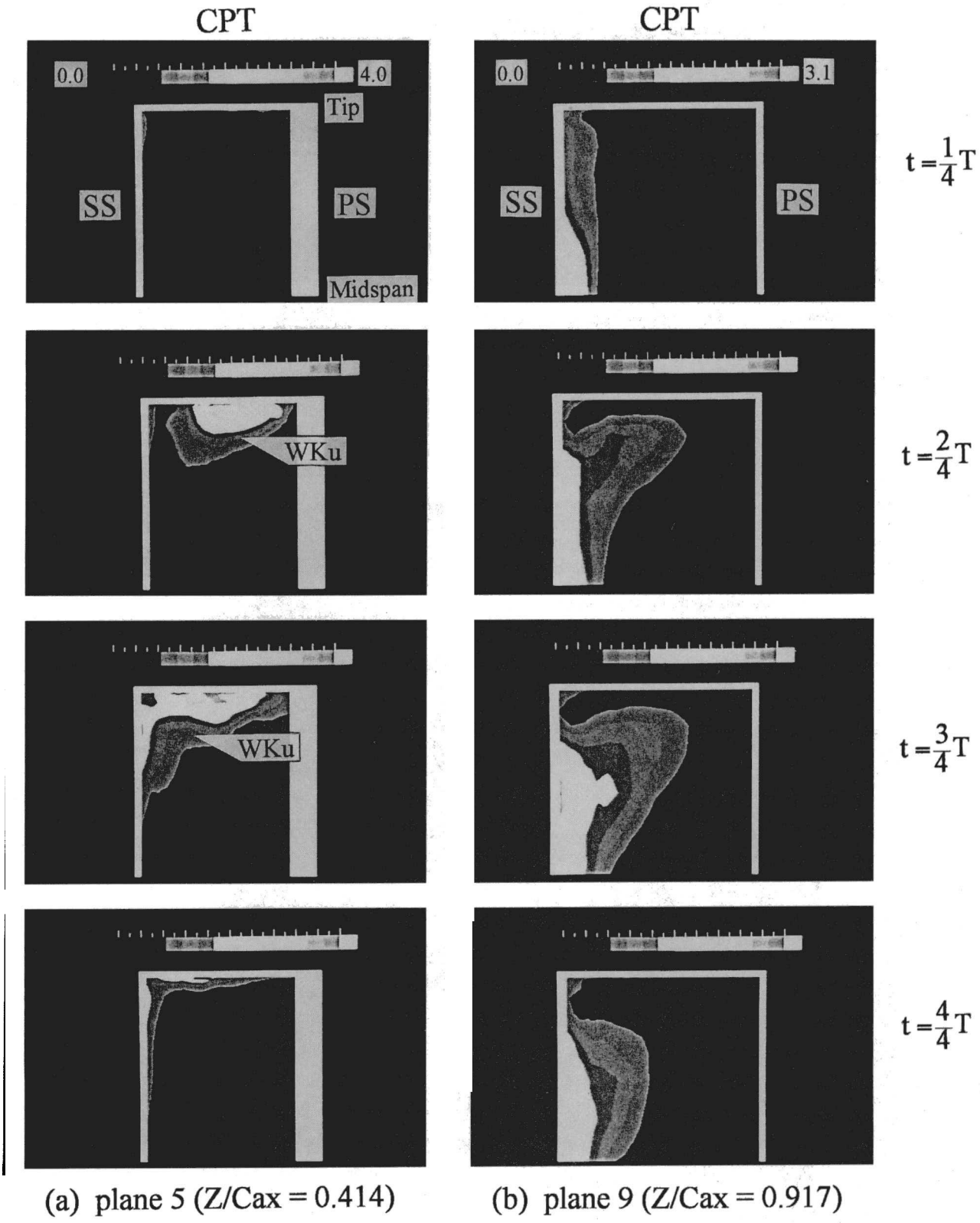

Fig. 7 Loss in downstream cascade passage

Effect of the Cascade Interaction on the Spanwise Loss Distribution. Figure 11 shows spanwise distributions of the pitchwise mass-averaged loss at the inlet and the outlet of the downstream cascade with tip clearance. Figure 11(*a*) shows that the spanwise profile of the inlet loss, i.e., the upstream cascade loss, is influenced by the relative location of the cascades, and the variation of the profiles is largest near the endwall and smallest around the midspan. This is because the secondary flow generated in the upstream cascade is strong near the endwall and interacts with the leading edges of the downstream cascade most strongly there. At the cascade outlet, as shown in Fig. 11(*b*), on the other

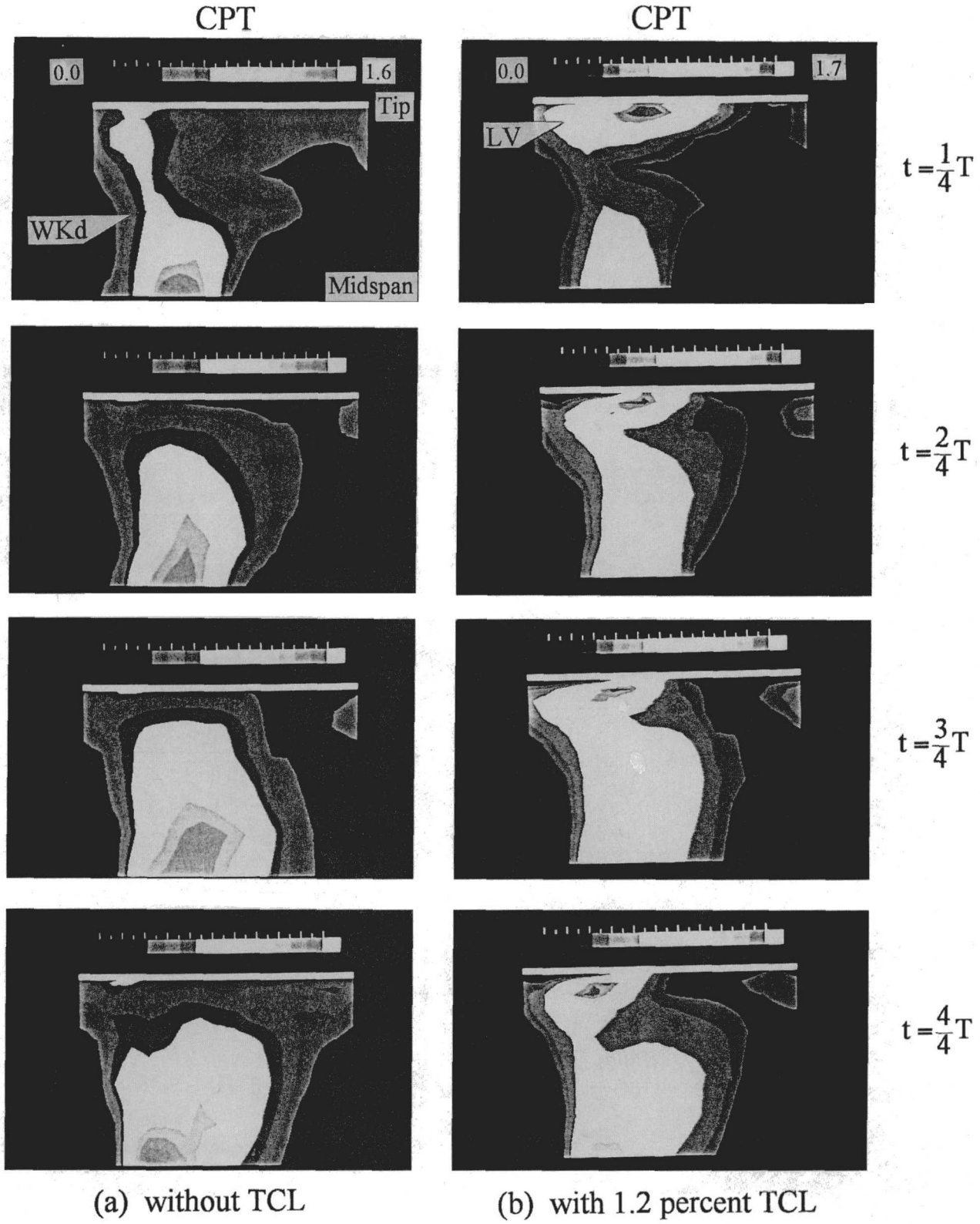

Fig. 8 Downstream cascade loss (plane 12, Z/C_{ax} = 1.207)

hand, the variation spreads over the whole span and becomes more significant around the midspan as well as near the tip. In particular, the loss at $\frac{1}{4}T$ is significantly high near the tip and low between 0.9 and 0.5 span height. The variation occurs due to the spanwise fluid mixing caused mainly by the passage vortices and by their interaction with the leakage vortex in the downstream cascade. Also the spanwise fluid mixing itself is further promoted by the cascade interaction.

Conclusions

1 Even the wakes and the loss of the upstream cascade are influenced by the relative location of both upstream and downstream cascades.

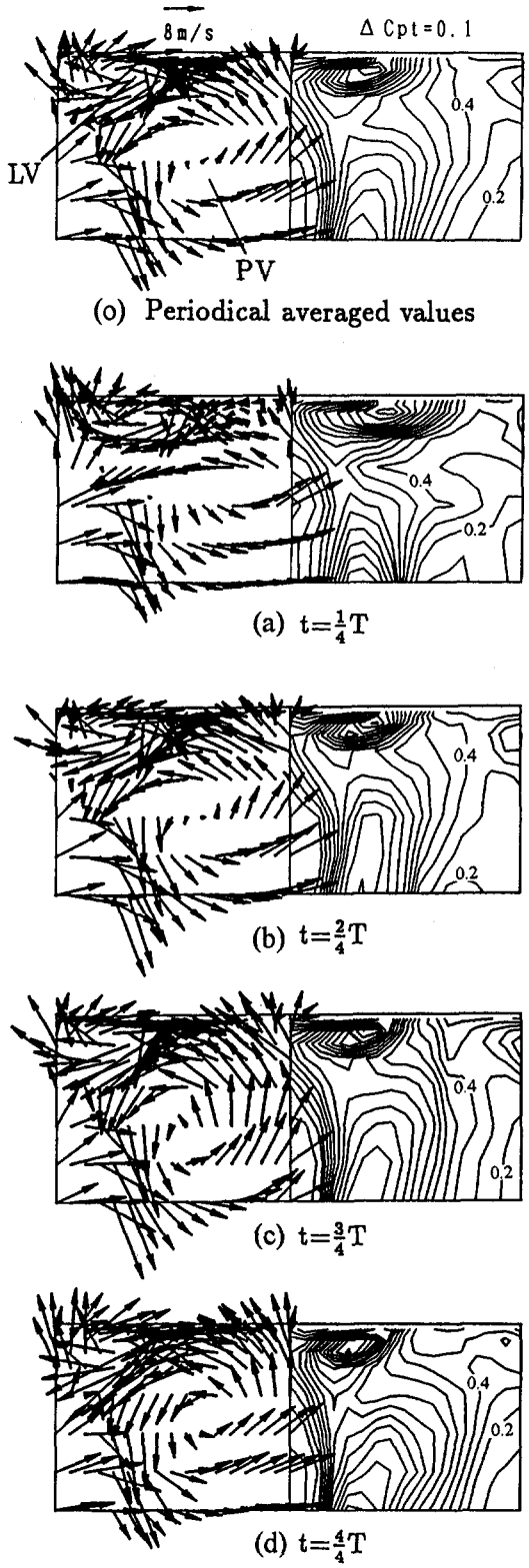

Fig. 9 Secondary flow and loss of downstream cascade with tip clearance (plane 12, Z/C_{ax} = 1.207)

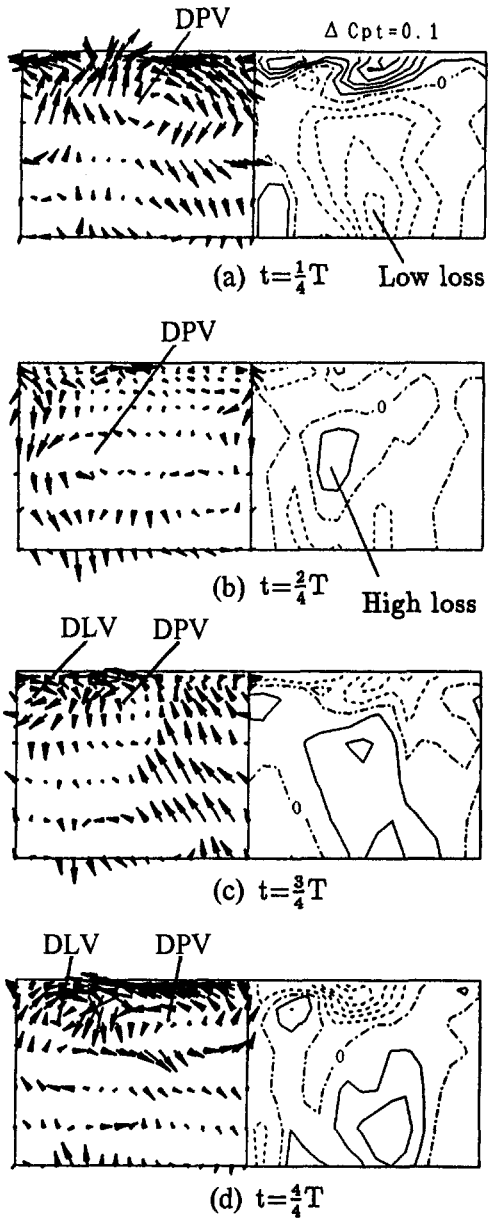

Fig. 10 Deviations of secondary flow and loss from the periodic averaged values obtained at plane 12 with tip clearance (Z/C_{ax} = 1.207)

2 Net loss generated in the downstream cascade becomes maximum when the upstream wake passes over the blade suction surface of the downstream cascade.

3 Net leakage loss generated in the downstream cascade is not influenced by the relative location of both cascades, while the size and the intensity of the leakage vortex change easily with the relative location.

4 The cascade interaction affects the endwall flow most strongly in the downstream cascade where low-energy fluids of the upstream cascade wakes accumulate over the endwall, which likely causes the endwall flow to separate. Spanwise fluid mixing inside the downstream cascade is promoted by the cascade interaction and affects the cascade outlet loss distribution along the whole span significantly.

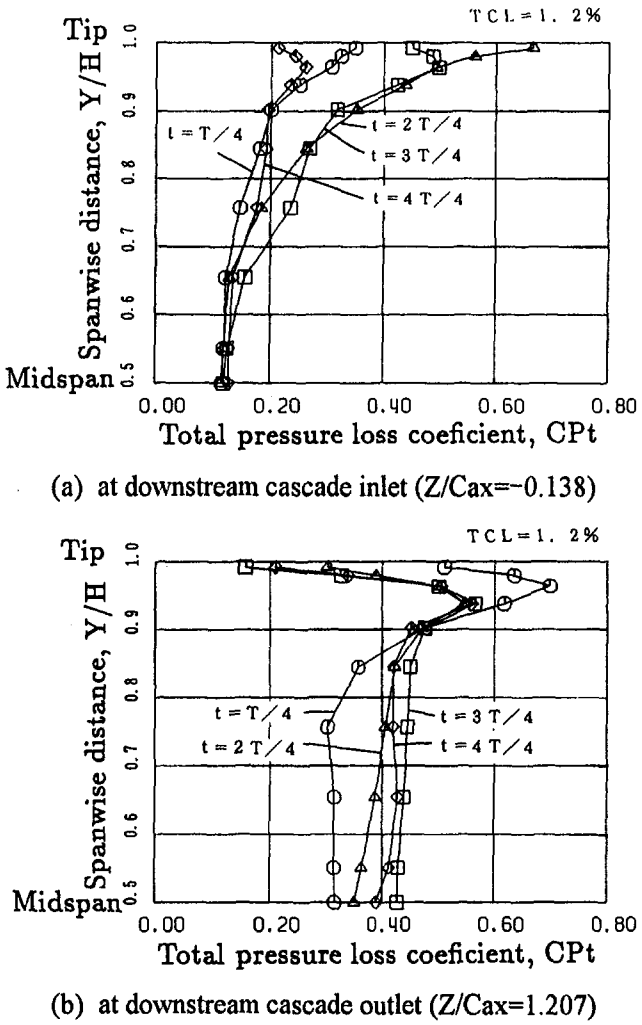

Fig. 11 Interaction effect on spanwise loss distributions with tip clearance

References

Binder, A., Foerster, W., Kruse, H., and Rogge, H., 1985, "An Experimental Investigation Into the Effect of Wakes on the Unsteady Turbine Rotor Flow," ASME *Journal of Engineering for Gas Turbines and Power*, Vol. 107, pp. 458–466.

Hodson, H. P., 1985, "Measurements of Wake-Generated Unsteadiness in the Rotor Passages of Axial Flow Turbines," ASME *Journal of Engineering for Gas Turbines and Power*, Vol. 107, pp. 467–476.

Sharma, O. P., Buttler, T. L., Joslyn, H. D., and Dring, R. P., 1985, "Three-Dimensional Unsteady Flow in an Axial Flow Turbine," *Journal of Propulsion and Power*, Vol. 1, pp. 29–38.

Sharma, O. P., Renaud, E., Buttler, T. L., Milsaps, Jr., Dring, R. P., and Joslyn, H. D., 1988, "Rotor-Stator Interaction in Multi-stage Axial-Flow Turbines," Paper No. AIAA-88-3013.

Sharma, O. P., Pickett, G. F., and Ni, R. H., 1992, "Assessment of Unsteady Flows in Turbines," ASME JOURNAL OF TURBOMACHINERY, Vol. 114, pp. 79–90.

Yamamoto, A., 1987, "Production and Development of Secondary Flows and Losses in Two Types of Straight Turbine Cascades: Part 1—A Stator Case; Part 2—A Rotor Case," ASME JOURNAL OF TURBOMACHINERY, Vol. 109, pp. 186–200.

Yamamoto, A., 1989, "Endwall Flow/Loss Mechanisms in a Linear Turbine Cascade With Blade Tip Clearance," ASME JOURNAL OF TURBOMACHINERY, Vol. 111, pp. 264–275.

Yamamoto, A., Mimura, F., Tominaga, T., Tomihisa, S., Outa, E., and Matsuki, M., 1993, "Unsteady Three-Dimensional Flow Behavior Due to Rotor–Stator Interaction in an Axial-Flow Turbine," ASME Paper No. 93-GT-404.

Endwall and Unsteady Flow Phenomena in an Axial Turbine Stage

H. E. Gallus

J. Zeschky

RWTH Aachen,
Aachen, Federal Republic of Germany

C. Hah

NASA Lewis Research Center,
Cleveland, OH 44135

Detailed experimental and numerical studies have been performed in a subsonic, axial-flow turbine stage to investigate the secondary flow field, the aerodynamic loss generation, and the spanwise mixing under a stage environment. The experimental study includes measurements of the static pressure distribution on the rotor blade surface and the rotor exit flow field using three-dimensional hot-wire and pneumatic probes. The rotor exit flow field was measured with an unsteady hot-wire probe, which has high temporal and spatial resolution. Both steady and unsteady numerical analyses were performed with a three-dimensional Navier–Stokes code for the multiple blade rows. Special attention was focused on how well the steady multiple-blade-row calculation predicts the rotor exit flow field and how much the blade interaction affects the radial distribution of flow properties at the stage exit. Detailed comparisons between the measurement and the steady calculation indicate that the steady multiple-blade-row calculation predicts the overall time-averaged flow field very well. However, the steady calculation does not predict the secondary flow at the stage exit accurately. The current study indicates that the passage vortex near the hub of the rotor is transported toward the midspan due to the blade interaction effects. Also, the structure of the secondary flow field at the exit of the rotor is significantly modified by the unsteady effects. The time-averaged secondary flow field and the radial distribution of the flow properties, which are used for the design of the following stage, can be predicted more accurately with the unsteady flow calculation.

Introduction

Modern design of advanced gas turbines requires increased aerodynamic efficiency with fewer components. To achieve maximum aerodynamic efficiency with highly loaded blade rows, an accurate understanding of the secondary flow field and boundary layer development has become essential for aerodynamic designers. In the past decade, great progress has been made in understanding the flow physics inside a blade row and developing appropriate prediction models. Various numerical methods based on steady, three-dimensional, Reynolds-averaged Navier–Stokes equations have been sufficiently developed so that these tools are routinely used for the optimization of turbomachinery blade rows under design environments (Davis et al., 1988; Dawes, 1986; Denton, 1986; Giles, 1988; Hah, 1987; etc).

Although steady isolated-blade-row analyses are very valuable for turbomachinery design, the flow field in a turbomachine is inherently unsteady as a result of the relative motion of the blade rows. As the axial gap between blade rows is reduced for compact design, the influence of the adjacent blade rows becomes increasingly important for the flow analysis of any specific blade row. A rather simple steady-state multiple-blade-row calculation procedure, which employs a mixing plane concept, has been proposed to account for some of the adjacent blade row effects and to provide more consistent flow conditions for the analysis of specific blade rows in a multistage configuration (Arts, 1985; Dawes, 1986; Denton and Singh, 1979; Ni, 1989; etc.). This simple steady approach for the solution of multiple-blade-rows seems to give surprisingly good steady or time-averaged solutions for many flow fields (for example, Copenhaver et al., 1993) and is used widely for the optimization of multiple blade rows. With a steady multiple-blade-row calculation, mixing planes are introduced between blade rows to establish steady boundary conditions for the adjacent blade rows and any true unsteady interaction effects are not modeled. Theoretically, if the blade interaction has little effect on the time-averaged flow field, the numerical results based on this approach should be accurate enough for aerodynamic design optimization.

The interaction between the stator and the rotor flow fields in a typical turbine stage has been known to affect aerodynamic efficiency, heat transfer, and loss generation. The unsteady interaction between the stator and the rotor flow fields can be divided into the following three forms. The potential flow fields of the two blade rows affect pressure distributions on the blade surfaces and the flow angles at the inlet of the rotor (Hunter, 1982; Joslyn and Dring, 1983). In addition to the potential flow field interaction, the unsteady wake of the stator passing through the rotor has a great influence on the flow and heat transfer of the rotor (Meyer, 1958; Kerrebrock and Mikolajczak, 1970; Hodson, 1985; Dring et al., 1982; etc.). The potential flow interaction and the wake interaction have been studied extensively and a wide range of experimental and analytical studies have been reported (Gallus et al., 1982). The third form of rotor–stator interaction is due to the convection of stator secondary vortices into the rotor flow field (Binder, 1985).

Recent improvements in high-response measurement techniques and numerical techniques provide means for experimental and analytical investigations of blade interactions. The current work is focused on studying the effects of blade row interactions in a single-stage turbine on the time averaged flow field. For the design of multiple turbine stages, accurate assessment of time-averaged flow conditions (static pressure, temperature, exit flow angle, etc.) are necessary at the exit of each blade row. Previous studies indicate that stage exit flow conditions are not predicted well with the steady approach. In particular,

Contributed by the International Gas Turbine Institute and presented at the 39th International Gas Turbine and Aeroengine Congress and Exposition, The Hague, The Netherlands, June 13–16, 1994. Manuscript received by the International Gas Turbine Institute March 2, 1994. Paper No. 94-GT-143. Associate Technical Editor: E. M. Greitzer.

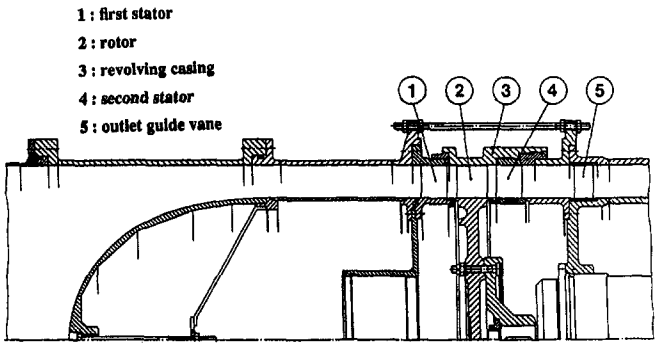

Fig. 1 Turbine test facility

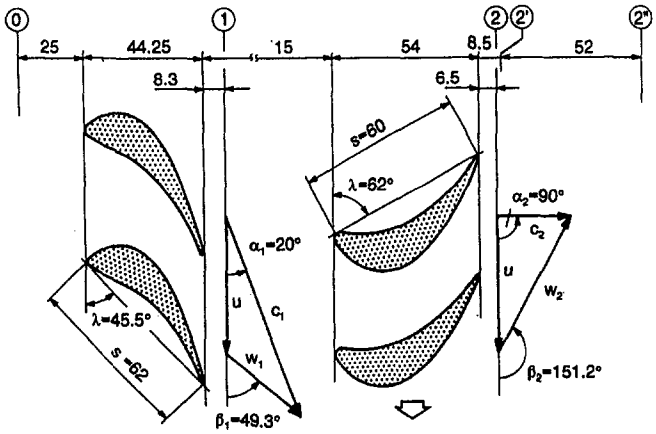

aspect ratio h/s	0.887	0.917
pitch (midspan) t	47.6 mm	41.8 mm
blade number	36	41
Reynolds number, based on chord and exit velocity	6.8×10^5	4.9×10^5
rotational speed	---	3500 rpm
tip diameter	600 mm	600 mm

Fig. 2 Turbine geometry and design data

the flows underturning and overturning near the hub are not modeled properly when the blade loading is increased. The present work is aimed at studying how well a steady-stage calculation procedure predicts the time-averaged flow characteristics of a single-stage turbine. The numerical results are compared with measurements. Furthermore, an unsteady calculation is presented to verify that the major effects of blade row interactions on the steady flow field can be successfully calculated with the current steady calculation method. Further studies are proposed, using some of the results of the unsteady calculation, for the improvement of the current steady-stage calculation method.

Test Facility and Instrumentation

The experiment was carried out in a single-stage axial turbine shown in Fig. 1. For the stator, the Traupel profile is used (Utz, 1972). A modified VKI profile is used for the rotor. Both the stator and the rotor consist of untwisted blades for the convenience of measurement of three-dimensional unsteady flow fields. A cross section of the stage with midspan velocity triangles is shown in Fig. 2. Some of the results from the current turbine stage configuration might be specific to the current stage. However, the detailed unsteady flow data represent typical characteristics of turbine stage flow. The data, along with the numerical results, can improve the understanding of the complex flow physics in modern multistage turbines.

The experiment was conducted in a continuous environment. The total temperature at the turbine inlet was maintained in the range of 308 K + 0.5 by cooling the air. The shaft speed variation was less than 0.2 percent. The Reynolds numbers were constant with an accuracy of 1.0 percent. The flow was surveyed with a pneumatic five-hole probe, three-wire hot-wire probes, and a laser velocimeter. Also, a pneumatic boundary layer probe and a two-wire hot-wire probe was used near the endwall. The static pressure distribution on the rotor blade was measured with a rotating scanivalve. Miniature high response pressure transducers were mounted at 25 axial locations in the casing above the rotor to measure unsteady static pressures on the casing. The averaged absolute Mach number at the inlet of the rotor is approximately 0.45. The details of the calibration of the various probes and the data reduction for the steady and unsteady measurements are given by Zeschky and Gallus (1993).

Numerical Method

The following Reynolds-averaged Navier–Stokes equations are solved for the current problem:

$$\frac{\partial \rho}{\partial t} + \frac{\partial}{\partial x_i}(\rho U_i) = 0 \tag{1}$$

$$\frac{\partial(\rho U_i)}{\partial t} + \frac{\partial}{\partial x_j}(\rho U_i U_j) + 2\rho \epsilon_{ijk}\Omega_j U_k = -\frac{\partial p}{\partial x_i} + \frac{\partial}{\partial x_j}\left[\mu\left\{\frac{\partial U_i}{\partial x_j} + \frac{\partial U_j}{\partial x_i} - \frac{2}{3}\frac{\partial U_k}{\partial x_k}\delta_{ij}\right\} - \rho\overline{u_i u_j}\right] + F_i \tag{2}$$

$$\frac{\partial(\rho e)}{\partial t} + \frac{\partial}{\partial x_j}(\rho U_j e) = \frac{\partial}{\partial x_j}\left[\left.\frac{\mu}{\mathrm{Pr}}\right|_{\mathrm{eff}}\frac{\partial T}{\partial x_j}\right] - \frac{\partial}{\partial x_j}(pU_j) + U_i F_i + \frac{\partial}{\partial x_j}\left[U_i\mu\left\{\frac{\partial U_i}{\partial x_j} + \frac{\partial U_j}{\partial x_i} - \frac{2}{3}\frac{\partial U_k}{\partial x_k}\delta_{ij}\right\}\right] \tag{3}$$

Nomenclature

C_1, C_2, C_3, C_4, c_μ = constant in turbulence closure models
h = span
k = turbulent kinetic energy
M = Mach number
p = pressure
Pt = total pressure
Re = Reynolds number
T = temperature
Tu = turbulence intensity
U, V, W = mean velocity components
u, v, w = fluctuating velocity components
β = relative flow angle
ϵ = turbulence dissipation rate
μ = viscosity
ν = kinematic viscosity
ρ = density

Subscripts

0 = stator inlet condition
1 = rotor inlet condition
2 = rotor exit condition
eff = effective value

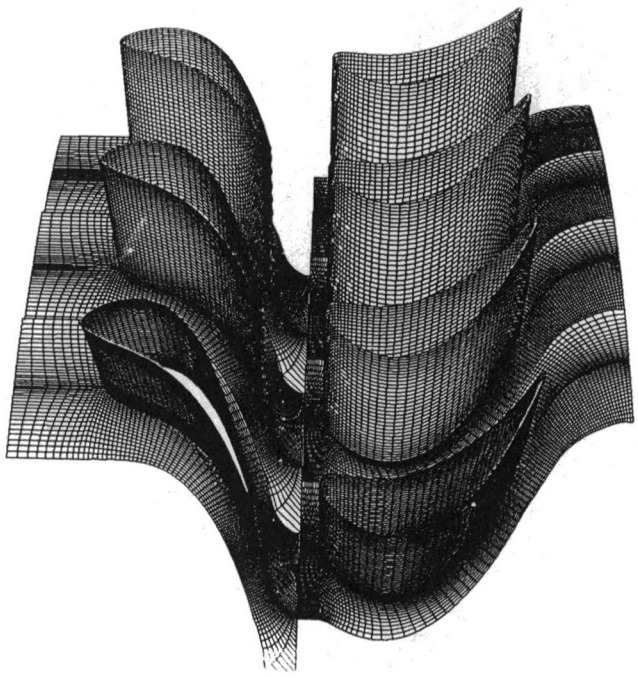

Fig. 3 Computational grid for the turbine stage

$$p = \rho RT \tag{4}$$

where U_i = mean velocity, u_i = fluctuation velocity, e = total energy, Ω_i = angular velocity,

$$\left.\frac{\mu}{\mathrm{Pr}}\right|_{\mathrm{eff}} = \left.\frac{\mu}{\mathrm{Pr}}\right|_{\mathrm{laminar}} + \left.\frac{\mu}{\mathrm{Pr}}\right|_{\mathrm{turbulent}}$$

and

$$e = C_v T + \tfrac{1}{2} U_i U_j$$

Any instantaneous flow variable can be split into three components: the time-averaged component, the periodic fluctuation due to the motion of the rotor relative to the stator frame, and the turbulent fluctuation. The sum of the first two parts is the phase-averaged value, which is a function of time and space. The effects of the turbulent fluctuation are included through the turbulence model. The turbulence is represented through the ensemble-averaged turbulence kinetic energy and the turbulence dissipation rate. These two turbulence variables are obtained by solving unsteady semi-empirical transport equations:

$$\frac{\partial(\rho k)}{\partial t} + \frac{\partial(\rho U_i k)}{\partial x_i} = \frac{\partial}{\partial x_i}\left[\frac{\mu_{\mathrm{eff}}}{\sigma_k}\frac{\partial k}{\partial x_i}\right] - \rho \overline{u_i u_j} U_{ij} - \rho\epsilon - \frac{2\mu k}{\rho^2} \tag{5}$$

$$\frac{\partial(\rho \epsilon)}{\partial t} + \frac{\partial(\rho U_i \epsilon)}{\partial x_i} = \frac{\partial}{\partial x_i}\left[\frac{\mu_{\mathrm{eff}}}{\sigma_\epsilon}\frac{\partial \epsilon}{\partial x_i}\right] - C_1 \frac{\rho\epsilon}{k}(\overline{u_i u_j} U_{ij}) - \frac{\rho\epsilon}{k}\left[C_2 f \epsilon + \frac{2\nu k e^{-C_4 u_* l/\nu}}{l^2}\right] \tag{6}$$

where

$$\mu_{\mathrm{eff}} = \mu + C_\mu(k^2/\epsilon)[1 - \exp(-C_3 u_* l/\nu)]$$

and

$$f = 1 - \frac{0.4}{1.8} e^{-(k^2/6\nu\epsilon)^2}$$

No attempt was made to optimize constants of the turbulence modeling equations for this study. Therefore, standard values of various constants of the turbulence model are used; the values are

$$C_\mu = 0.09, \quad C_1 = 1.35, \quad C_2 = 1.8, \quad \sigma_k = 1.0,$$
$$\sigma_\epsilon = 1.3, \quad C_3 = 0.00115, \quad C_4 = 0.5$$

Two numerical methods were applied to analyze the flow inside the current turbine stage. Although the flow inside any turbine stage is inherently unsteady due to blade row interaction, the present design system is based on the time-averaged flow field. The current study is aimed at examining how well numerical methods simulate the time-averaged flow field. Previous studies (for example, Copenhaver et al., 1993; Saxer and Giles, 1994) have indicated that the steady multiple-blade-row calcu-

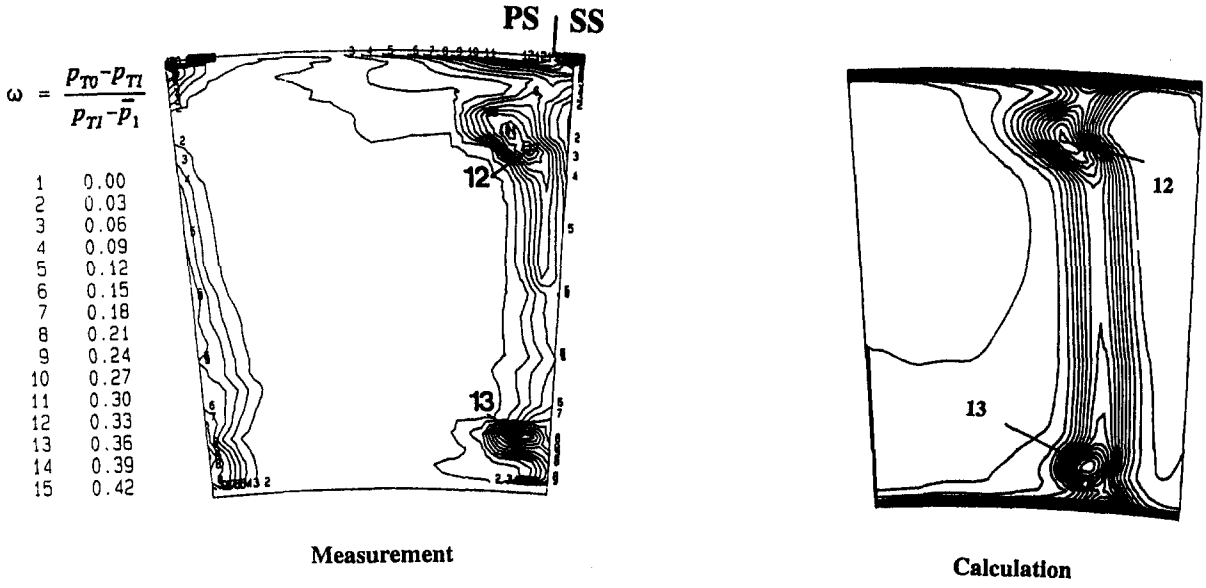

Fig. 4 Comparison of total pressure contours at stator exit

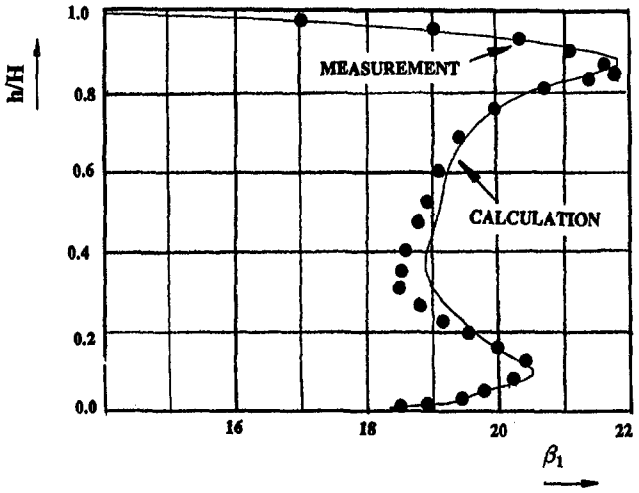

Fig. 5 Comparison of stator exit flow angle

lation approach predicts the time-averaged flow field at the exit of the given stage very well. Therefore, the steady multiple-blade-row calculation was performed first for the present turbine stage and the numerical results were analyzed and compared with the measured data. The comparison between the measurements and the steady-stage calculation indicated that the steady multiple-blade-row calculation procedure predicts the time-averaged flow field very well across the turbine stage. The only significant shortcomings of the steady approach for practical design applications were in the calculated secondary flow field at the exit of the rotor and the spanwise distribution of the stage exit flow angle (Zeschky and Gallus, 1993). To investigate these discrepancies between the time-averaged measurement and the steady-stage calculation, a time accurate calculation was performed for the stage. In the following, the two numerical approaches are briefly described.

In the steady multiple-blade-row calculation, the stator and the rotor flow fields are calculated simultaneously. The inflow condition for the stage is specified at the stator inlet and the outflow condition is specified at the rotor exit. To maintain steady flow conditions, mixing planes are established at the trailing edge of the stator and the leading edge of the rotor. At these mixing planes, circumferential variations of the flow variables are assumed to be mixed out and only radial variations are assumed to exist. The mixing analysis based on the work of Dring and Spear (1991) is used at the mixing planes. Further details of this procedure are given by Copenhaver et al. (1993). In the current steady-stage flow calculation, any unsteady effects on the time-averaged flow field are not represented in the numerical solution.

The unsteady flow calculation was performed to examine the main effects of the blade row interaction on the time-averaged flow field, especially on the secondary flow field at the exit of the stage. The ensemble-averaged flow variables in the current unsteady flow field can be efficiently obtained by coupling the time-dependent stator flow with the time-dependent rotor flow. Therefore, the two flow fields are solved with coupled time-dependent interface boundary conditions. As shown in the computational grid (Fig. 3), an interface is used to transmit flow conditions between two zones. A sliding overlaid grid is used for the present application. A three-dimensional steady Navier–Stokes code, which has been successfully tested for a wide range of turbomachinery flows (Hah, 1983), was extended to execute time accurate calculations. During the development, it was found that high-order discretization schemes are necessary in both space and time to avoid excessive numerical dissipation. For the time-dependent terms, an implicit second-order scheme is used. The details of the numerical procedure of the unsteady flow calculation are explained by Hah et al. (1993).

Results and Discussion

Figure 4 shows a comparison of the total pressure distribution at the exit of the stator. Both measured and calculated results are presented for one stator blade passage. Note that in Fig. 4, the circumferential locations of the domain are not matched between the measurement and the calculation. The calculated aerodynamic loss distribution matches very well with the measurement. The radial distribution of the flow angle at the exit of the stator is compared in Fig. 5. Again, the numerical results from the steady multiple-blade-row calculation represent the overall stator flow field very well. As no other measurements were made for the stator flow field, no further comparisons are presented. The comparisons in Figs. 4 and 5 indicate that the time-averaged stator flow field is adequately calculated with the current steady-stage calculation and the time-averaged inflow to the rotor is also properly modeled.

The calculated time-averaged static pressure distribution on the rotor blade is compared in Fig. 6. Because of the blade row

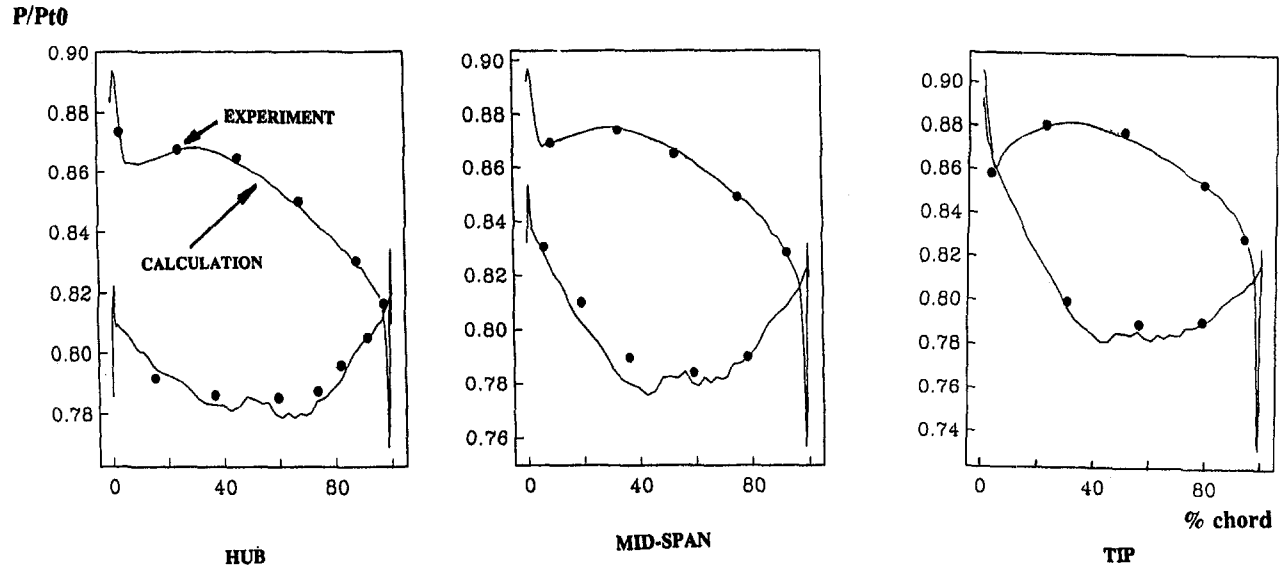

Fig. 6 Comparison of static pressure distribution on the rotor blade

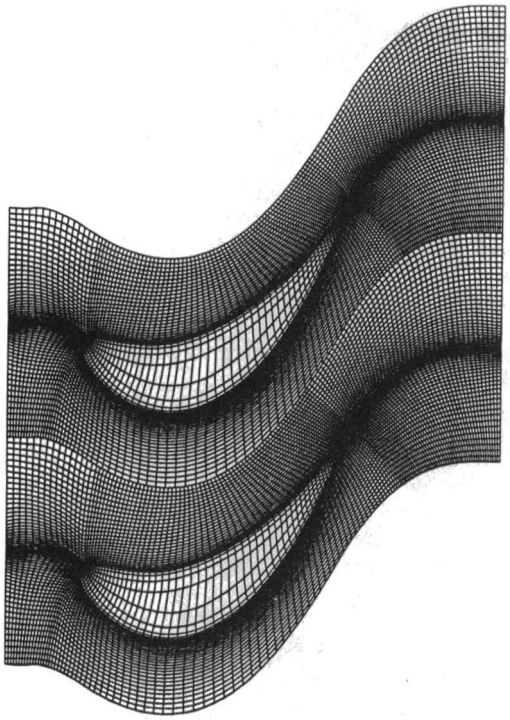

Fig. 7 Computational grid inside the tip clearance

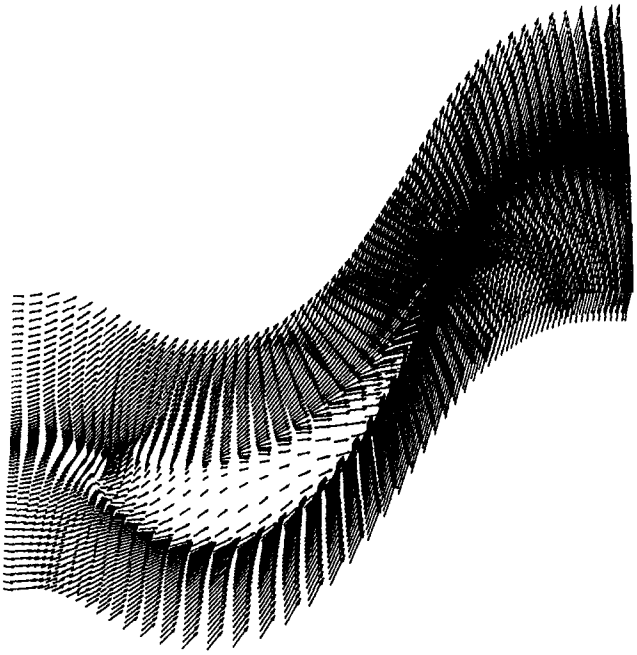

Fig. 9 Calculated velocity vectors inside the tip clearance

interaction, the static pressure distribution on the rotor blade changes periodically. However, the time-averaged blade loadings are adequately calculated with the steady-stage calculation. The good agreement between the steady-stage calculation and the measurements in Fig. 6 is not particularly surprising. Previous studies have also shown that the steady calculation predicts time-averaged loadings very well when proper boundary conditions are used. Unsteady effects on the time-averaged loading are relatively small even in transonic turbine stages.

The detailed static pressure distribution on the endwall was measured with high response pressure transducers mounted on the endwall. The current calculation was performed with a computational grid distributed across the top of the blade tip in order to calculate the details inside the gap. Figure 7 shows the detailed grid inside the tip gap. Ten nodes are distributed from the suction surface of the blade to the pressure side and ten nodes are clustered spanwise inside the clearance. Comparison of the static pressure distribution on the endwall between the measurement and the calculation is given in Fig. 8. Both the measurement and the calculation show the formation of the tip clearance vortex near the suction surface toward to the trailing edge. Again, the steady-stage procedure calculates the time-averaged static pressure distribution very well.

The calculated velocity vectors over the tip inside the tip gap are given in Fig. 9. The velocity vectors near the shroud show the formation of the tip vortex in more detail. Simpler numerical approaches for the tip clearance effects, using wedge-type treat-

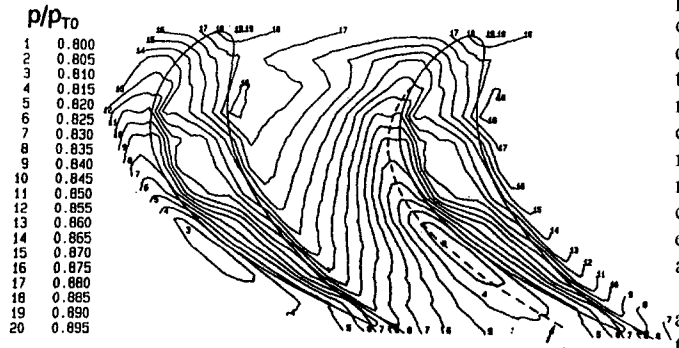

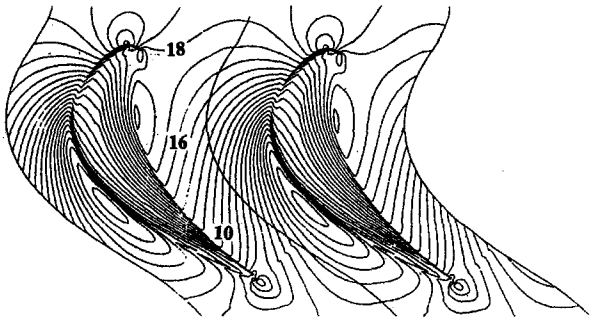

Fig. 8 Comparison of endwall static pressure distribution

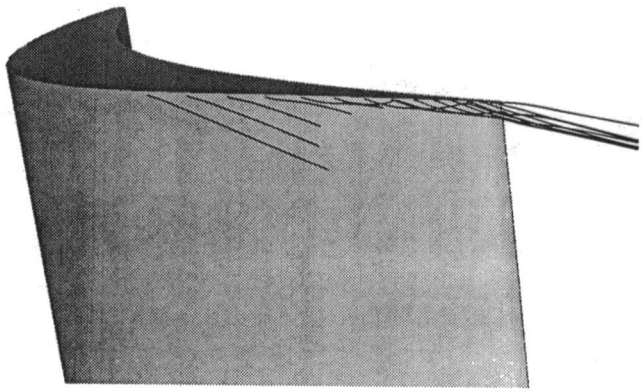

Fig. 10 Particle traces near the suction surface (tip vortex)

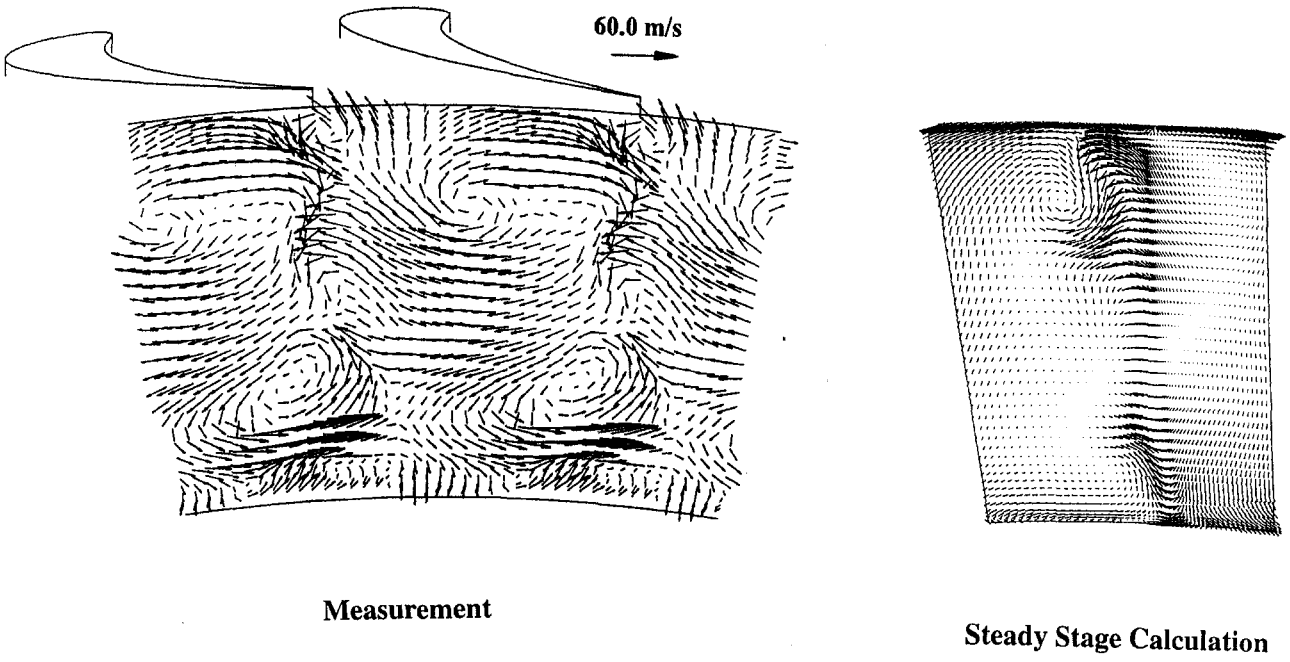

Fig. 11 Comparison of time-averaged secondary velocity at rotor exit (velocity vectors in rotor relative frame)

ments of the tip geometry, probably calculate the gross effects of the tip clearance flow on the main passage flow. However, the strength and the location of the tip vortex cannot be accurately simulated without actually modeling the exact tip blade geometry. Particle traces from the numerical solution are given in Fig. 10 to show a three-dimensional view of the tip clearance vortex. Figure 10 indicates that the tip-clearance vortex is formed very close to the shroud due to the very tight clearance (0.6 percent chord).

The secondary flow fields at the exit of the rotor are compared between the steady-stage calculation and the time-averaged measurement in Fig. 11. The measured results are for two rotor blade passages while the calculated results are across one rotor blade passage. The overall structure of the flow is calculated reasonably well. However, the calculated center of the passage vortex near the hub is located at roughly 15 percent of the span compared to about 30 percent of the span from the measurement. Different sizes of the computational grid were used to analyze the prediction of this hub vortex. The numerical results from a much finer computational grid did not indicate any improvement of the location of the calculated vortex near the hub. Therefore, it was concluded that this disagreement is not due to the inadequate size of the computational grid.

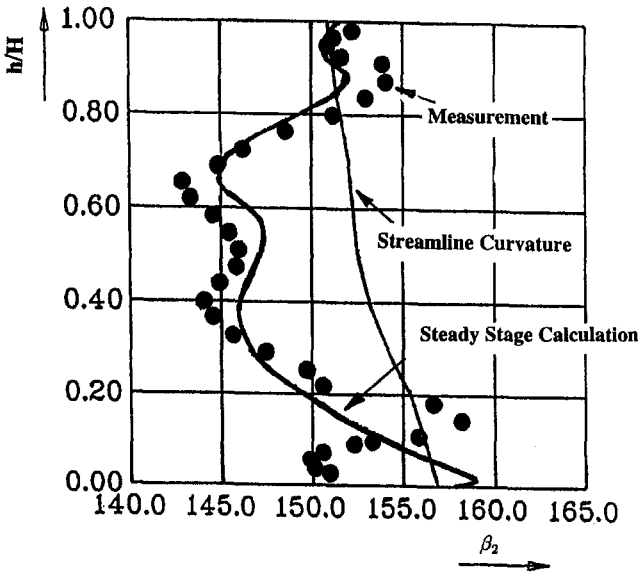

Fig. 12 Comparison of radial distribution of stage exit flow angle

The radial distributions of the stage exit flow angle are compared in Fig. 12. Numerical results based on a simple streamline curvature method are also presented in Fig. 12. The comparison in Fig. 12 is very good considering that the numerical results are based on the steady stage calculation. The only significant shortcoming of the numerical results occurs near the hub. This type of disagreement has also been previously observed in a similar analysis for the flow in a highly loaded turbine stage (for example, Schaub et al., 1993).

An unsteady flow calculation was conducted to investigate whether this discrepancy is due to the unsteady effects on the time-averaged flow field. The time-averaged results for the stator flow fields and the rotor blade loading from the unsteady calculation are virtually the same as those from the steady-stage calculation. Instantaneous secondary velocity vectors at the exit of the rotor at four equally spaced times are shown in Fig. 13 for both the measurements and the calculation. The measured secondary velocity vectors are presented across two rotor blade passages while calculated results are for one rotor passage. Shaded areas in the measured results are regions with high turbulence intensity. The four rotor positions referenced in Fig. 13 are equally spaced by 20 percent of the stator pitch. The results from the unsteady calculation show that the center of the hub vortex has moved significantly away from the hub wall. This movement of the hub vortex is due to the interaction of the secondary flow that is coming out of the stator with the rotor flow field. In Fig. 14, the radial distribution of the stage exit angle is compared between the measurements and various prediction methods. Although the unsteady computation predicts the secondary flow field more accurately at the exit of the turbine stage, it requires about one hundred times more computing resources. Further refinements of the steady-stage analysis methods should be made to improve the accuracy. The unsteady calculation results are being used for this purpose.

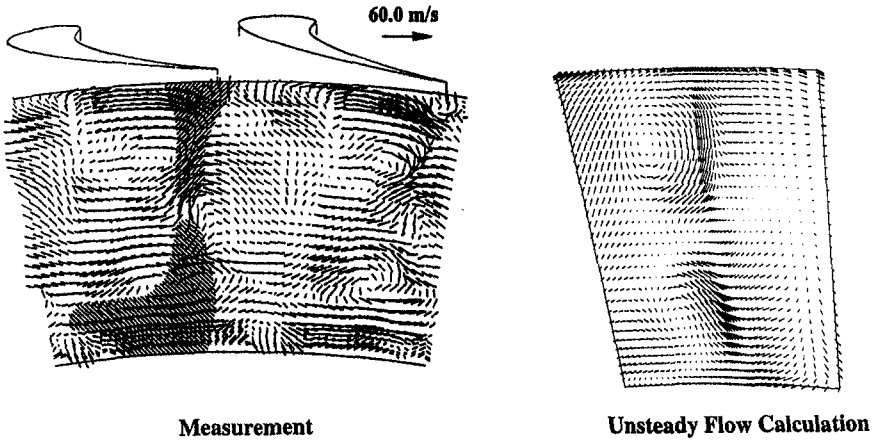

Fig. 13(*a*) Comparison of secondary velocity vectors at rotor exit (position 1)

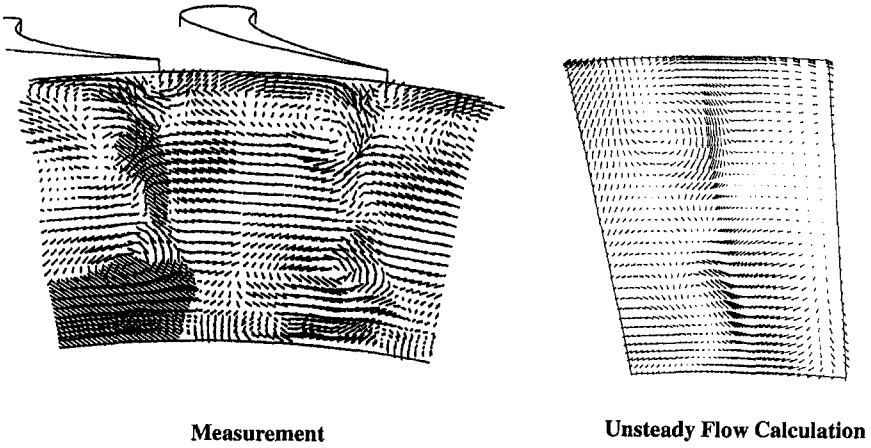

Fig. 13(*b*) Comparison of secondary velocity vectors at rotor exit (position 2)

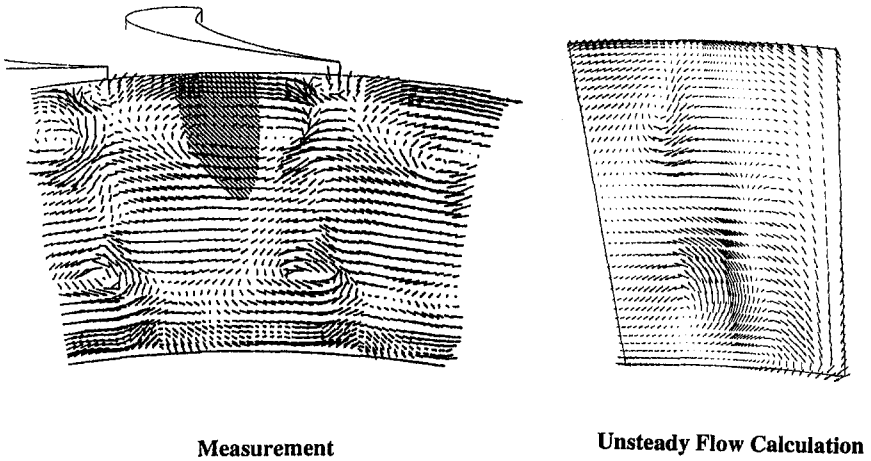

Fig. 13(*c*) Comparison of secondary velocity vectors at rotor exit (position 3)

Concluding Remarks

Detailed experimental and numerical studies have been performed to investigate the development of secondary flows and time-averaged flow characteristics in a single-stage, subsonic, axial turbine. Special attention was focused on examining how well a simple, steady multiple-blade-row calculation predicts time-averaged flow distributions at the exit of each blade row. The current study shows that the numerical method based on a simple steady-state multiple-blade-row procedure calculates most of the time-averaged flow field accurately enough for design applications. However, the radial distribution of the flow angle at the exit of the stage was not properly calculated with the steady approach. The experimental study shows that the passage vortex near the hub of the rotor is transported toward the midspan due to the unsteady interaction between the stator exit secondary flow and the rotor flow field. This interaction transports the hub vortex toward the midspan in the time-averaged flow field. The steady-stage calculation does not model this phenomenon. The unsteady flow calculation gives much better results for the time-averaged secondary flow field at the exit of the rotor and, consequently, the distribution of the stage

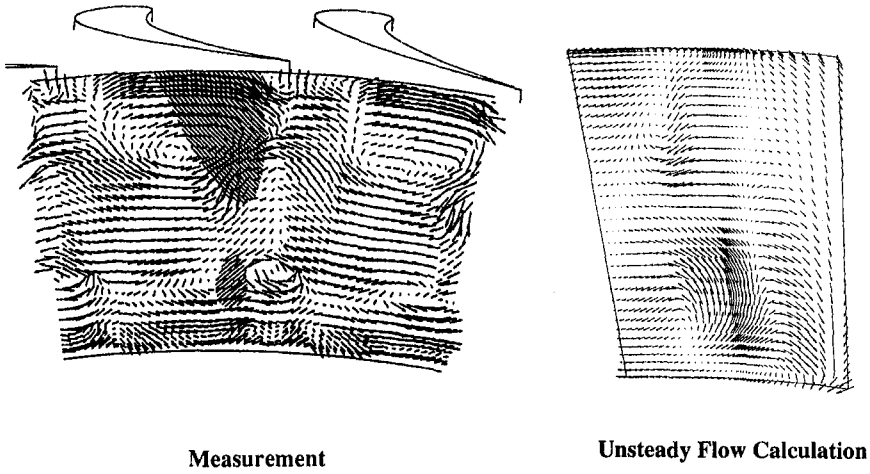

Fig. 13(*d*) Comparison of secondary velocity vectors at rotor exit (position 4)

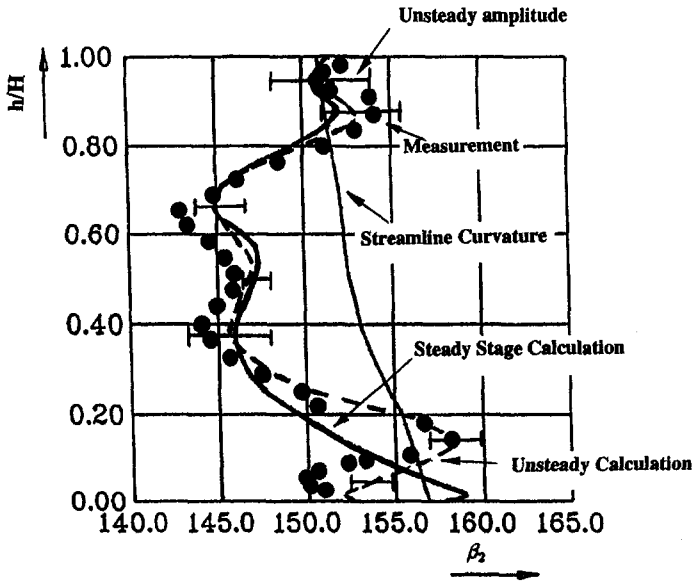

Fig. 14 Comparison of stage exit flow angle

exit flow angle. The current study indicates that accurate prediction of the secondary flows at the exit of the turbine stage requires numerical approaches, which account for three-dimensional as well as unsteady effects. However, it seems that the three-dimensional effects, which can be modeled accurately with a steady multiple-blade-row calculation, are a primary mechanism in determining the time-averaged secondary flow field. The unsteady effects shift the passage vortex core away from the end wall. The cost of the unsteady flow analysis is about two orders of magnitude more than the steady flow analysis. Further research is necessary to improve the steady multiple-blade-row calculation method for practical design applications. The numerical results from the unsteady flow analysis can be used to improve the modeling of the steady-stage calculation procedure.

References

Arts, T., 1985, "Calculation of the Three-Dimensional, Steady, Inviscid Flow in Transonic Axial Turbine Stage," ASME *Journal of Engineering for Gas Turbines and Power,* Vol. 107, pp. 286–292.

Binder, A., 1985, "Turbulence Production Due to Secondary Vortex Cutting in a Turbine Rotor," ASME *Journal of Engineering for Gas Turbines and Power,* Vol. 107, pp. 1039–1046.

Chien, K. Y., 1982, "Prediction of Channel and Boundary-Layer Flows With a Low Reynolds Number Turbulence Model," *AIAA Journal,* Vol. 20, No. 1, pp. 33–38.

Copenhaver, W. W., Hah, C., and Puterbauch, S. L., 1993, "Three-Dimensional Flow Phenomena in a Transonic, High-Through-Flow Compressor Stage," ASME JOURNAL OF TURBOMACHINERY, Vol. 115, pp. 240–248.

Davis, R. L., Hobbs, D. E., and Weingold, H. D., 1988, "Prediction of Compressor Cascade Performance Using a Navier–Stokes Technique," ASME JOURNAL OF TURBOMACHINERY, Vol. 110, pp. 520–531.

Dawes, W. N., 1986, "Development of a 3D Navier–Stokes Solver for Application to All Types of Turbomachinery," ASME Paper No. 86-GT-70.

Denton, J. D., and Singh, U. K., 1979, "Time Marching Methods for Turbomachinery Flow Calculation," VKI Lecture Series, 1979-7.

Denton, J. D., 1986, "The Use of a Distributed Body Force to Simulate Viscous Flow in 3D flow Calculations," ASME Paper No. 86-GT-144.

Dring, R. P., Joslyn, H. D., Hardin, L. W., and Wagner, J. H., 1982, "Turbine Rotor-Stator Interaction," ASME *Journal of Engineering for Power,* Vol. 104, pp. 729–742.

Dring, R. P., and Spear, D. A., 1991, "The Effects of Wake Mixing on Compressor Aerodynamics," ASME JOURNAL OF TURBOMACHINERY, Vol. 113, pp. 600–607.

Gallus, H. E., Groillus, H., and Lambertz, J., 1982, "The Influence of Blade Number Ratio and Blade Row Spacing on Axial-Flow Compressor Stator Blade Dynamic Load and Stage Sound Pressure Level," ASME *Journal of Engineering for Power,* Vol. 104, pp. 633–644.

Giles, M. B., 1988, "Stator/Rotor Interaction in a Transonic Turbine," AIAA Paper No. 88-3093.

Hah, C., 1984, "A Navier–Stokes Analysis of Three-Dimensional Turbine Flows Inside Turbine Blade Rows at Design and Off-Design Conditions," ASME *Journal of Engineering for Gas Turbines and Power,* Vol. 106, pp. 421–429.

Hah, C., 1986, "A Numerical Modeling of Endwall and Tip-Clearance Flow of an Isolated Compressor," ASME *Journal of Engineering for Gas Turbines and Power,* Vol. 108, pp. 15–21.

Hah, C., 1987, "Calculation of Three-Dimensional Viscous Flows in Turbomachinery With an Implicit Relaxation Method," *AIAA Journal of Propulsion and Power,* Vol. 3, No. 5, pp. 415–422.

Hah, C., and Wennerstrom, A. J., 1991, "Three-Dimensional Flowfields Inside a Transonic Compressor With Swept Blades," ASME JOURNAL OF TURBOMACHINERY, Vol. 113, pp. 241–251.

Hah, C., Copenhaver, W. W., and Puterbauch, S. L., 1993, "Unsteady Aerodynamic Flow Phenomena in a Transonic Compressor Stage," AIAA Paper No. AIAA-93-1868.

Hodson, H. P., 1985, "Measurements of Wake-Generated Unsteadiness in the Rotor Passage of Axial Flow Turbines," ASME *Journal of Engineering for Power,* Vol. 107, pp. 466–477.

Hunter, I. H., 1982, "Endwall Boundary Layer Flows and Losses in an Axial Turbine Stage," ASME *Journal of Engineering for Power,* Vol. 104, pp. 184–193.

Joslyn, H. D., and Dring, R. P., 1983, "Negative Incidence Flow Over a Turbine Rotor Blade," ASME Paper No. 83-GT-23.

Kerrebrock, J. L., and Mikolajczak, A. A., 1970, "Intra-stator Transport of Rotor Wakes and Its Effect on Compressor Performance," ASME *Journal of Engineering for Power,* Vol. 92, pp. 359–368.

Meyer, R. X., 1958, "The Effect of Wakes on the Transient Pressure and Velocity Distributions in Turbomachines," ASME *Journal of Basic Engineering,* Vol. 80, pp. 1544–1552.

Ni, R. H., 1989, "Prediction of 3D Multi-stage Turbine Flow Field Using a Multiple Grid Euler Solver," AIAA Paper No. 89-0203.

Saxer, A. P., and Giles, M. B., 1994, "Predictions of Three-Dimensional Steady and Unsteady Inviscid Transonic Stator/Rotor Interaction With Inlet Radial Temperature Nonuniformity." ASME JOURNAL OF TURBOMACHINERY, Vol. 116, pp. 347–357.

Schaub, U. W., Vlasic, E., and Moustapha, S. H., 1993, "Effect of Tip Clearance on the Performance of a Highly Loaded Turbine Stage," *Proceedings of AGARD PEP 82nd Symposium.*

Utz, C., 1972, "Experimentelle Untersuchung der Stromungsverluste in einer Mehrstufigen Axial-Turbine," Thesis ETH, Zurich.

Zeschky, J., and Gallus, H. E., 1993, "Effects of Stator Wakes and Spanwise Nonuniform Inlet Conditions on the Rotor Flow of an Axial Turbine Stage," ASME JOURNAL OF TURBOMACHINERY, Vol. 115, pp. 128–136.

The Flow in a Second-Stage Nozzle of a Low-Speed Axial Turbine and Its Effect on Tip Clearance Loss Development

G. Morphis

J. P. Bindon

University of Natal,
Durban, South Africa

The flow field in a one-and-a-half-stage low-speed axial turbine with varying levels of rotor tip clearance was measured in order to compare the behavior of the second nozzle with the first and to identify the manner in which the second nozzle responds to the complex tip clearance dependent flow presented to it and completes the formation of tip clearance loss. The tangentially averaged flow relative to the rotor blade in the tip clearance region was found to differ radically from that found in cascade and is not underturned with a high axial velocity. There is evidence rather of overturning caused by secondary flow. The axial velocity follows an almost normal endwall boundary layer pattern with almost no leakage jet effect. The cascade tip clearance model is therefore not accurate. The reduction in second-stage nozzle loss was shown to occur near the hub and tip, which confirms that it is probably a reduction in secondary flow loss. The nozzle exit loss contours showed that leakage suppressed the formation of the classical secondary flow pattern and that a new tip clearance related loss phenomenon exists on the suction surface. The second-stage nozzle reduced the hub endwall boundary layer below that of both the first nozzle and that behind the rotor. It also rectified secondary and tip clearance flows to such a degree that a second-stage rotor would experience no greater flow distortion than the first-stage rotor. Radial flow angles behind the second-stage nozzle were much smaller than found in a previous study with low-aspect-ratio untwisted blades.

1 Introduction

The flows in second and subsequent stage nozzles have not received much attention from researchers. The second nozzle flow field of a low-aspect-ratio untwisted design was investigated by Boletis and Sieverding (1991) and the unsteadiness of the flow was measured by Joslyn et al. (1983). Apart from a fundamental interest in the type of flow occurring, the second stage plays an important part in the complete definition and formation of tip clearance and secondary loss because these stator blades provide the only way of correctly quantifying the effect of rotor exit energy and vorticity.

In a linear cascade (Bindon, 1987), it has been found that the tip clearance loss has two main components. The first is the internal gap entropy that is generated within the leakage flow as it passes through the gap. The second is the mixing loss as the leakage flow merges with the mainstream within and downstream of the rotor. Since the leakage vortex radically affects the suction surface pressure distribution, there could also be tip clearance related losses generated in the boundary layer and by boundary layer separation. Using cascade data construed to represent a rotor with work transfer (Morphis and Bindon, 1992), an approximate estimate was obtained regarding rotor performance. However, before any final conclusions can be made regarding the mixing loss and internal gap loss, not only is a real rotor needed, but a downstream nozzle as well to correctly redirect and expand the rotor exit flow.

This paper therefore examines the flow structure in a full annular nozzle downstream of a low-speed unshrouded axial turbine. Because of the importance of tip clearance, the gap size is varied. In a companion paper, Morphis and Bindon (1994) examine the performance (efficiency) of all three blade rows with particular reference to different rotor blade tip shapes. It was found that the second-stage nozzle has a distinctly better efficiency than the first stage and that a streamlined rotor tip shape, with a low internal gap loss, benefits the performance when compared with the flat sharp-edged reference rotor tip. Most of the results in this paper are for the standard flat rotor tip and only minimal reference is made to the small flow structure variations caused by the different rotor tip shapes.

The flow into a first-stage nozzle is relatively "clean" and therefore more closely resembles the ideal cascade model with inlet vorticity evenly distributed on the two casing walls. The other nozzles are always downstream of an axial gap and the flow reflects radial and periodic variations in total enthalpy, incidence, and vorticity.

Distinct aspects of these differing flows have been examined. The skewing of the inlet boundary layer has been studied by Bindon (1979) and Walsh and Gregory-Smith (1987). Boletis and Sieverding (1991), by comparing the real second-stage nozzle flow with their previous skewed study (Boletis et al., 1983), showed that the skewed model has almost no validity and some similarity exists only near the inlet and close to the endwall. Periodic effects on rotor blade flow (for example Blair et al., 1989), is an ongoing and active area of research in heat transfer.

In the full comparison of the flows in a first and second-stage nozzle, Boletis and Sieverding (1991) explored the flow field in front of, within, and downstream of the blades. The general conclusions were that flow angles were significantly different, particularly in the tip region that is affected by tip clearance. Although the radial and tangential loss distributions were different due to the changes in the pattern of migration and generation

Contributed by the International Gas Turbine Institute and presented at the 39th International Gas Turbine and Aeroengine Congress and Exposition, The Hague, The Netherlands, June 13–16, 1994. Manuscript received by the International Gas Turbine Institute March 2, 1994. Paper No. 94-GT-145. Associate Technical Editor: E. M. Greitzer.

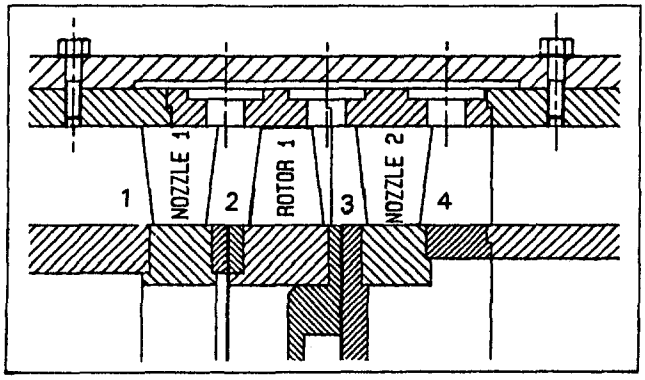

Fig. 1 Turbine cross section and measurement planes

Table 1 Summary of turbine data

	Hub	Mid	Tip
α_1	00.0	00.0	00.0
α_2	66.1	61.7	57.6
α_3	00.0	00.0	00.0
β_2	42.8	13.6	-17.9
β_3	53.1	58.2	62.3
Radius [mm]	142.0	172.5	203.0
Reaction	0.15	0.42	0.58
V_x/U	0.752	0.617	0.526
Nozzle chord [mm]	36.8	41.8	46.5
Rotor chord [mm]	46.3	46.0	46.0
Noz. blade thick. [%chord]	18.5	15.8	14.3
Rot. blade thick. [%chord]	17.3	15.3	15.3

Exit Reynold's number	170 000
Inlet axial velocity [m/s]	29.6
Rotor tip speed [m/s]	56.3
R.P.M	2645
Nozzle Pitch/Chord ratio	0.55
Rotor Pitch/Chord ratio	0.63
Nozzle number of blades	41
Rotor number of blades	43

of low-momentum fluid, no change in loss was found. This is in sharp contrast with the present findings presented in the companion paper (Morphis and Bindon, 1994), where the losses are found to be much lower. More detailed comparisons with the present measurements will be made below.

2 Turbine, Instrumentation, and Definitions

The complete suction-driven low-speed single-stage axial turbine followed by a second-stage stator identical to the first is fully described by Morphis and Bindon (1994). It is shown in Fig. 1 together with the various traverse stations while Table 1 summarizes the design data.

The standard rotor tip clearance was 1 percent of tip chord (0.45 mm, 0.75 percent span, 0.11 percent diameter). The two additional clearances of 2 and 3 percent chord were introduced with two slightly larger rotor casings carefully blended back to the standard dimension in front of the second nozzle.

Since the turbine performance definitions involve isentropic quantities that are defined by pressure, the complex fluctuating flow field behind a rotor cannot be determined with a hot wire or a laser. A quick response probe and transducer system was considered but a conventional five-hole probe that records a mean of the high-frequency pressure field was finally adopted because the results from it are widely accepted and used.

The two-dimensional flow field in front of and behind the two stators is measured with a five-hole United Sensor 3.2-mm-dia probe used in the yaw null mode, where the yaw angle is set by the automated traverse system responding to the differential yaw. Pressures and pitch are found from the probe calibration and the pitch hole pressures.

The repeatability of the turbine rig and instrumentation was examined by performing full two-dimensional traverses for the same rotor on various days. For a series of five runs the efficiencies were found to be repeatable to within 0.05 percent. Although encouraging, this result did not, however, give any indication on the ability of the rig to detect small changes in tip clearance configuration. The second nozzle had a tip clearance of 0.1 mm or 0.22 percent chord necessary for assembly and traversing. An increase in second nozzle efficiency of approximately 0.3 percent was measured for all three rotors when this small clearance was eliminated by inserting a 0.1 mm shim between the blades and the outer casing. The shim was then removed and the efficiency was once again measured to within 0.05 percent of previous runs. The yaw angle was found to be repeatable to within 0.3 deg.

The total-to-static efficiency was defined as follows:

$$\eta_{ts} = \frac{\omega}{h_{o1} - h_{3is}} = \frac{\overline{C_\omega}}{\overline{C_{P_{o1}} - C_{P_{S3}}}}$$

where the work coefficient at a particular grid point was

$$C_{\omega_{ij}} = \frac{\dot{m}_{ij}\rho_{ij}U_{ij}\Delta V_{\theta_{ij}}}{\dot{m}_{\text{ref}_{ij}}q_{\text{ref}_{ij}}} = \frac{\dot{m}_{ij}}{\dot{m}_{\text{ref}_{ij}}}\frac{2\pi\rho_{ij}N_{ij}R_{ij}}{60}\frac{(V_{2_{ij}}\sin\theta_{2_{ij}} - V_{3_{ij}}\sin\theta_{3_{ij}})}{(P_o - P_s)_{\text{ref}_{ij}}}$$

Nomenclature

$C_V = 0.5\rho V^2/q_{\text{ref}}$
$C_{P_{o_{1-2}}} = (P_{o1} - P_{o2})/q_{\text{ref}}$
$C_{P_{o_{3-4}}} = (P_{o3} - P_{o4})/q_{\text{ref}}$
C = dimensionless coefficient
h = specific enthalpy, kJ/kg k
i = incidence, deg
$\dot{m}$ = mass flow rate, kg/S
N = rpm
q = dynamic pressure, Pa
R = radius, mm
U = blade velocity, m/s
V = absolute velocity, m/s
W = relative velocity, m/s
α = absolute angle, deg
β = relative angle, deg
η = efficiency
θ = swirl range
ρ = density, kg/m^3
ω = specific work, kJ/kg

Subscripts

1 = first nozzle inlet
2 = rotor inlet (first nozzle outlet)
3 = rotor outlet (second nozzle inlet)
4 = second nozzle outlet
i, j, m = summation grid variables
is = isentropic
o = total
P = pressure
ref = free-stream inlet reference
s = static
ts = total to static (single stage)
V = velocity
x = axial
θ = swirl component

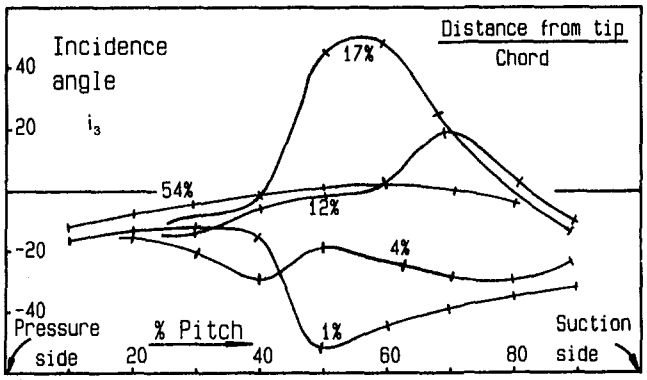

Fig. 2 Second-stage nozzle incidence angle at various distances from the blade tip simulated from linear cascade data including tip clearance (Morphis, 1989)

The coefficients and angles were tangentially averaged for a full nozzle pitch as follows:

$$\bar{Y}_j = \frac{\sum_{i=0}^{m} Y_{ij} \frac{\dot{m}_{ij}}{\dot{m}_{\text{ref}_{ij}}}}{\sum_{i=0}^{m} \frac{\dot{m}_{ij}}{\dot{m}_{\text{ref}_{ij}}}}$$

(where Y_{ij} is a particular coefficient or angle at the (i, j)th grid point). This has the effect of averaging out the tangential variation that is caused by any stationary upstream blade wakes.

3 Rotor Determined Second Stage Nozzle Inlet Conditions

The second-stage nozzle differs from the first in that it is downstream of the rotor. The ability of the rotor to deflect the flow will therefore largely determine the inlet to the second nozzle.

The flow leaving a rotor is periodic and will fluctuate with each blade passing with respect to flow angle and, in the incompressible case, total pressure because of varying degrees of loss and work extraction. Since the present measurements are time averaged behind the rotor, it will be helpful to review the cascade results of Morphis (1989), which show the periodic flow variations that a typical second-stage stator must deal with.

Figures 2 and 3 present the measured cascade exit flow field results transformed to simulate that leaving a rotor by including the hypothetical blade speed. The incidence onto the second stage nozzle (Fig. 2) is shown at varying distances from the tip endwall. Remote from the endwall (a distance of 54 percent

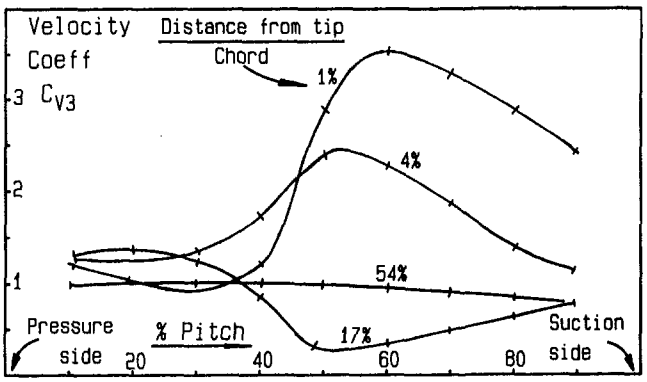

Fig. 3 Second-stage nozzle inlet velocity at varying distances from blade tip simulated from linear cascade data including tip clearance (Morphis, 1989)

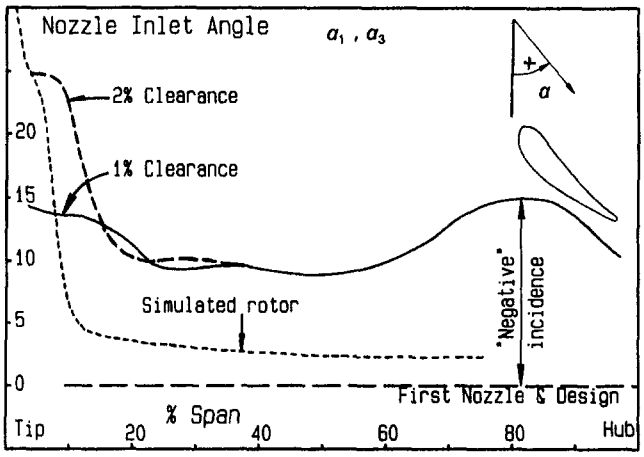

Fig. 4 Tangentially averaged nozzle inlet angle (absolute rotor exit angle) for first stator (α_1 = 0 = design), second nozzle (β_3) at varying clearance and for a nozzle behind the simulated rotor of Bindon and Morphis (1992)

chord), the incidence changes from mildly negative to slightly positive as would be expected at "midspan." Near the tip (a distance of 1 percent chord) where the leakage jet exists as a strong poorly deflected jet over half the blade pitch, the incidence has almost a midspan value near the pressure side and then drops sharply to around −40 deg, also for half of the blade pitch. The leakage jet appears as an extremely high velocity zone as reflected in Fig. 3 where the velocity coefficient peaks at 3.5 (i.e., an inlet velocity 1.9 times the midspan value).

At increasing distances from the tip, the incidence changes through zero before becoming positive by as much as 40 deg on the other side of the leakage vortex. The velocity coefficient at this point shows that the nozzle will receive a velocity half the free-stream value.

When the above-mentioned blade-to-blade simulated rotor flow is tangentially averaged, it can be compared with the present measurements taken at the inlet to the nozzle where the probe responds with a close approximation to the mean of the periodic flow presented to it by the rotor. This is done in Fig. 4 as nozzle inlet angle rather than incidence. Both curves are seen to have similar high positive flow angles (negative incidence) near the wall. At a distance of 17 percent of chord from the tip where Fig. 2 shows the positive incidence associated with the leakage vortex, the velocity here is so low that the mass-based average does not even show a dip and the angle curve does not even fluctuate at that point.

By design, the first-stage inlet angle was zero. The second nozzle is seen to have an inlet angle of near 10 deg at midspan that increases sharply to 25 deg near the tip at a clearance gap of 2 percent chord. At a 1 percent gap, the increase near the tip is much lower due to the smaller poorly deflected leakage flow. There is also an increase of flow angle near the hub due to the rotor hub secondary flow.

Since the inlet angle is caused by the rotor, it is helpful to examine the same flow in the relative frame. Figure 5 shows the rather surprising fact that near the hub, secondary flow creates a large amount of overturning. Even more surprising is the overturning at the tip for 1 percent clearance where leakage flow is expected to be poorly deflected. Even at the larger 2 percent clearance there is almost no underturning. Linear cascade results showed the exact opposite and the mean exit flow angle decreases sharply near the wall due to the contribution of the undeflected leakage jet.

The interpretation of this unexpected result is also shown in Fig. 5. The tangentially averaged flow near the tip is not a poorly deflected high-velocity jet but a low-velocity rather well deflected flow. A possible reason for this is that true relative

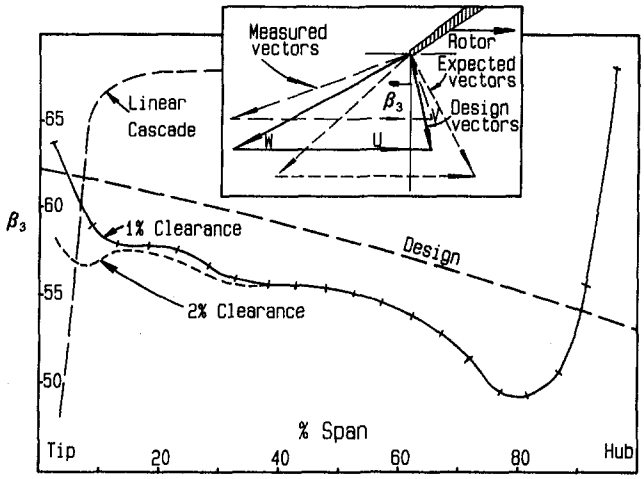

Fig. 5 Radial variation of tangentially averaged relative rotor outlet angle at various clearances

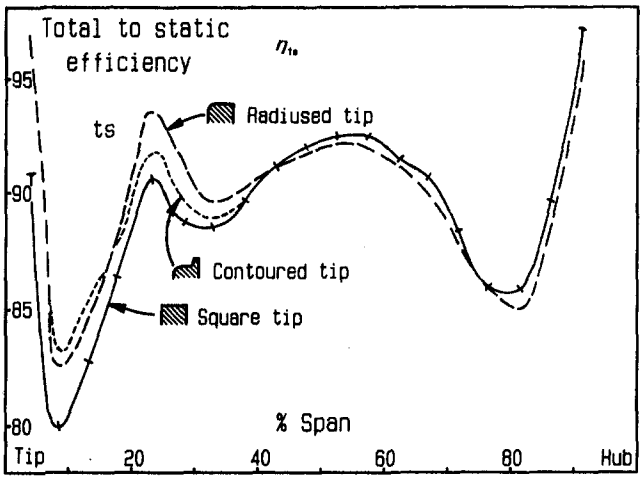

Fig. 7 Radial variation of single-stage efficiency (*ts*) for three different tip shapes at 1 percent clearance

motion in the small gap reduces the leakage effect to such a degree that normal secondary flow can still flourish. This, however, is probably too simplistic an explanation of this complex periodic tip boundary layer flow in which fluid in the laminar sublayer may even be exposed to more than one blade passing.

The radial variation of efficiency of the single stage will be helpful in understanding the part played by tip clearance as well as in understanding why one streamlined rotor tip was found to improve the performance. Figure 6 shows, at different tip clearance gaps, the "streamsurface" efficiency variation radially where the inlet flow at one radius is related to the outlet flow at the same radius. At the tip the sharp drop off in performance is seen at the larger clearances. In Fig. 7, the different efficiency reductions near the tip for the different rotor tip shapes are shown. The gain in performance of the tip with a radiused pressure edge over the reference square tip is seen up to 40 percent span from the tip.

4 Comparisons Between First and Second-Stage Nozzles

The response of the second-stage nozzle to the flow presented to it may now be discussed and also compared to the behavior of the first-stage nozzle.

In Fig. 8 the exit flow angle is shown for the two nozzles and for design. The first nozzle is within one degree of design except for differing secondary flow effects at hub and tip. At the tip some underturning on the inner side of the vortex is evident but there is no overturning against the endwall. At the hub there is very little underturning while right on the wall there is a distinct angle increase.

The angle behind the second nozzle is shown for 1 and 2 percent rotor tip clearance. As can be expected, increasing clearance increases the overturning near the tip. Near the hub, the rotor induces a large zone of underturning, probably due to its own hub secondary flow.

When the nozzle exit angles are viewed as the relative angles presented to a downstream rotor, the effect on rotor inlet can be seen by assuming that if a second-stage rotor were present, it would be identical to the first. The results appear in Fig. 9 and the two curves are very similar with a slightly better angle near the tip of rotor 2 due to tip clearance. Rotors in multistage machines will therefore experience slightly less flow angle distortion when compared to the first rotor.

In the companion paper, Morphis and Bindon (1994), the losses in the second nozzle were shown to be in the region of 30 percent below those of the first nozzle. When the radial variation of loss is examined in Fig. 10 (on a stream tube basis as with efficiency in Figs. 8 and 9), the improvements are seen to be concentrated in the hub and tip regions. This tends to confirm the reasons advanced that the improvements are due to reductions in secondary flow loss. The factors that generate

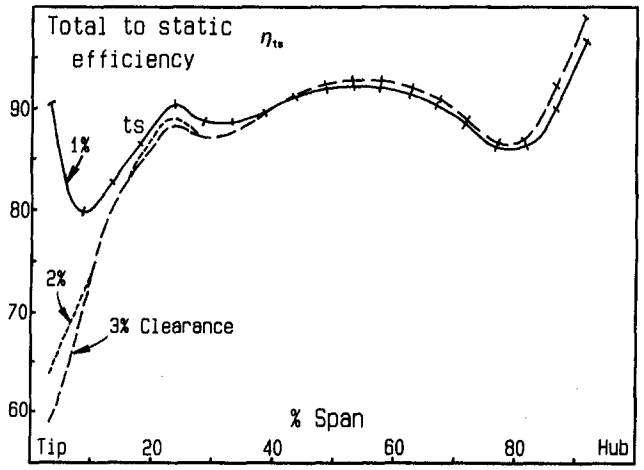

Fig. 6 Radial variation of single-stage efficiency (*ts*) for varying tip clearance (square tip rotor)

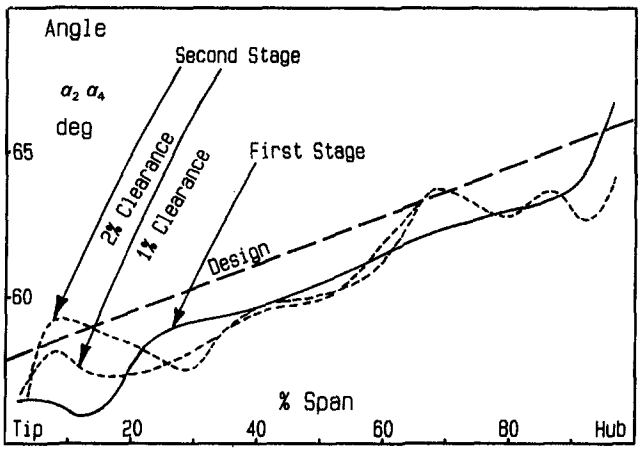

Fig. 8 Tangentially averaged radial variation of first and second-stage nozzle outlet angle at varying clearance and compared with design

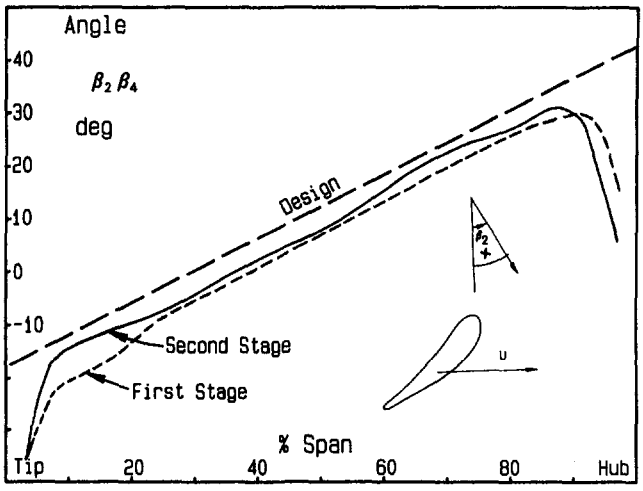

Fig. 9 Tangentially averaged radial variation of first and second-stage nozzle deflection viewed as relative inlet angle to rotor

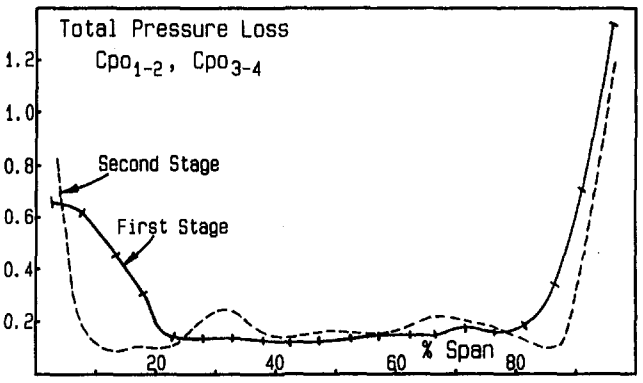

Fig. 10 Radial variation in nozzle total pressure loss for first and second stage

secondary flow are all radically different. The blade loading is lower because at inlet the endwall boundary layers, the leakage flow, and rotor secondary flows are skewed and therefore are already partially deflected. The inlet vorticity is not evenly spread across the inner and outer casings but the majority is some distance from the endwalls.

The unexpected relative rotor flow angles discussed in the previous section were deduced from the absolute frame measurements of angle and velocity. The radial variation of axial velocity coefficient is given in Fig. 11 at the outlet to each of the three blade rows for 1 percent tip clearance and also for the linear cascade of Morphis and Bindon (1992). The linear cascade data are radically different from the real rotor and the velocity increases dramatically against the endwall, while the real distribution follows the normal endwall boundary layer pattern. It is this discrepancy that also created the unexpected relative flow angles at rotor exit. Thus the linear cascade provides a very poor model of real turbine tip processes.

At the hub, the second-stage nozzle has a thinner boundary layer than the first nozzle, a reduction that takes place despite being presented with a relatively thick layer by the rotor. At the tip, all three curves are similar up to 10 percent span from the tip. Between 10 and 30 percent the effects of tip clearance are seen by a reduction at rotor exit that is more than restored by the second nozzle. Although not as quite as marked, this was also seen at 2 and 3 percent clearance. Thus the secondary and tip clearance flows fed to the second-stage nozzle appear to benefit the axial velocity distribution considerably. At midspan, the second nozzle shows an increase over the first nozzle

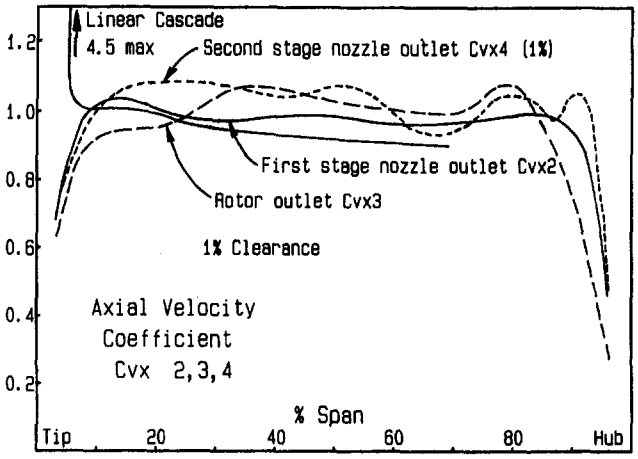

Fig. 11 Radial variation of tangentially averaged axial velocity coefficient behind each blade row for 1 percent rotor tip clearance

that matches well with that expected due to compressibility effects in a constant area annulus.

When a comparison is made between the two nozzles of the radial variation in absolute axial velocity, Fig. 12 also shows the effects of compressibility. At the tip, the second nozzle

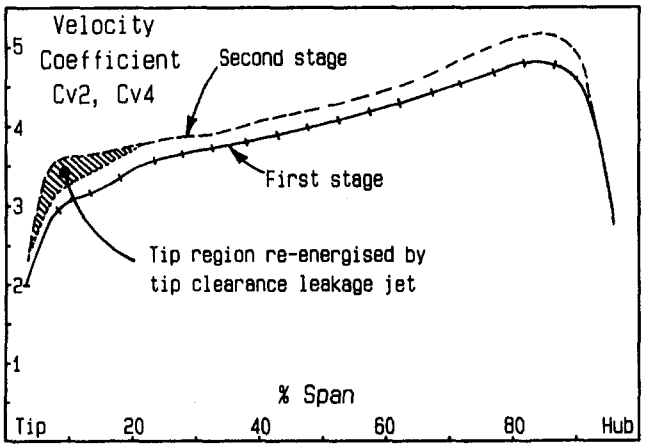

Fig. 12 Radial variation of first and second-stage nozzle outlet velocity coefficient (tangentially averaged, curves similar for all clearances)

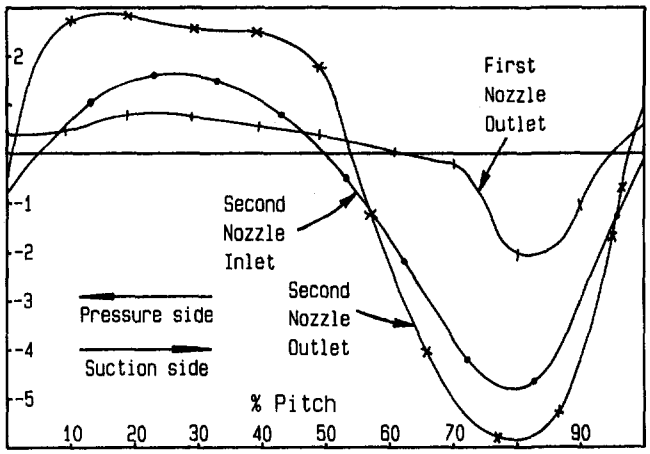

Fig. 13 Tangential variation of second-stage nozzle pitch (radial flow) angle at 27 percent span from tip where angles are the highest

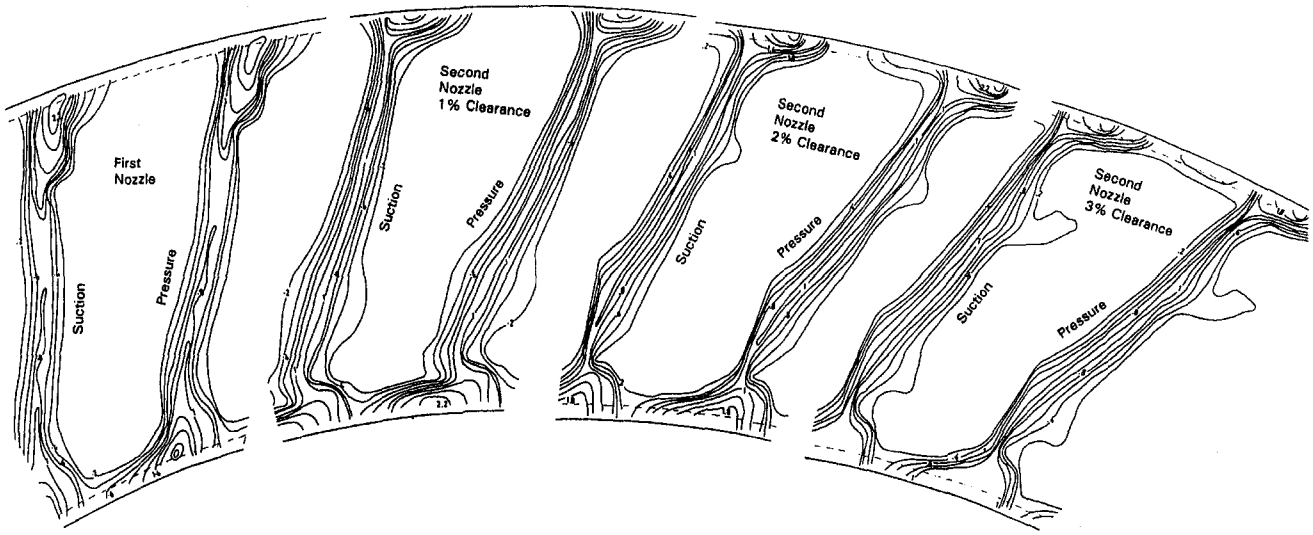

Fig. 14 Total pressure loss contours for first and second-stage nozzle at various rotor clearances

demonstrates a region energized by the tip clearance flow by an amount that shows almost no variation with tip clearance.

5 Radial Flow Angles

Boletis and Sieverding (1991) reported large radially inward (negative) flow angles behind the second stator as high as −32 deg, the magnitude of which was partly attributed to the radial gradient of total pressure arising from constant angle blading. Such blading will also create an inward streamline shift due to radial equilibrium. The blades also have a low aspect ratio, which would form more secondary flow fluid that responds to the radial pressure gradient.

The maximum angles in the present study are only from −5 to −6 deg and all occur at 27 percent span from the tip at rotor exit and second nozzle exit (Fig. 13). There is very little increase in radial flow in either of the nozzles and the largest increase takes place as the first nozzle wake moves through the rotor.

6 Nozzle Exit Plane Loss Contours

Figure 14 compares the total pressure loss contours at the exit planes of the two nozzles, the latter showing the effects of tip clearance. The plots are based on an inlet averaged total pressure.

The significant reduction in overall loss coefficient found in the second-stage nozzle (Morphis and Bindon, 1994) as compared to the first was attributed to differences in secondary flow loss. As already seen in the radial loss variation, the differences lie within 20 percent span zones at hub and tip. The familiar loss areas associated with the corner vortices can be seen in the first nozzle and are almost absent in the second-stage nozzles.

An unusual loss pattern is seen on the suction side of the second nozzle blade wakes at a 30 percent span distance from the tip. It increases in size and prominence with increasing tip clearance. It was also present, slightly more distinctly, with the special rotors with streamlined tip shapes. It is possibly a separation pattern induced by the tip leakage flow. Its nature and importance were not studied and adaptations are required to provide data within these stator blades.

7 Conclusions

The study of the flow field in a one and a half stage low speed axial turbine with varying levels of tip clearance has revealed a number of interesting aspects of tip clearance flow and of flow in a multistage machine.

At the rotor tip the tangentially averaged flow as was found to differ radically from that seen in cascades where a region of underturned flow with a high axial velocity was found. Instead, the real rotor shows a region of overturned flow with a normal endwall boundary layer pattern. The cascade model of tip clearance cannot therefore accurately represent the real flow and a great deal of further investigation is needed.

The most important result of the comparison between the first stage and second stage nozzles was the confirmation that the significant reduction in loss in the second stage is in fact due to reductions of secondary flow. The radial variation of total pressure showed reductions in loss at both hub and tip. The nozzle exit loss contours showed that leakage suppressed the formation of the classical secondary flow pattern. Also seen in the contours at second nozzle exit was a new tip clearance related loss phenomena on the suction surface that needs further investigation.

The second stage nozzle also showed that it was able to thin the hub endwall boundary layer below that of both the first nozzle and that behind the rotor. It also was able to rectify secondary and tip clearance flows to such a degree that a second stage rotor would experience no greater flow distortion than the first stage rotor. The small amounts of leakage related overturning that persists right through the second stage nozzle near the tip thus has very little effect of rotor inlet angle.

Radial flow angles were much smaller (−6 as compared to −32 deg) than previously found by Boletis and Sieverding (1991). The difference is thought to be due to the present use of lower aspect ratio twisted nozzles blades.

References

Bindon, J. P., 1979, "The Effect of Hub Inlet Boundary Layer Skewing on the Endwall Shear Flow in an Annular Turbine Cascade," ASME Paper No. 79-GT-13.

Bindon, J. P., 1987, "The Measurement of Tip Clearance Flow Structure on the Endwall and Within the Clearance Gap of an Axial Turbine Cascade," *Proc. IMechE. Int. Conf.—Turbomachinery Efficiency Prediction and Improvement,* Cambridge, Sept.

Bindon, J. P., 1989, "The Measurement and Formation of Tip Clearance Loss," ASME JOURNAL OF TURBOMACHINERY, Vol. 111, pp. 257–263.

Bindon, J. P., and Morphis, G., 1992, "The Development of Axial Turbine Leakage Loss for Two Profiled Tip Geometries Using Linear Cascade Data," ASME JOURNAL OF TURBOMACHINERY, Vol. 114, pp. 198–203.

Blair, M. F., Dring, R. P., and Joslyn, H. D., 1989, "The Effects of Turbulence and Stator/Rotor Interactions on Turbine Heat Transfer: Part 1—Design Operating Conditions," ASME JOURNAL OF TURBOMACHINERY, Vol. 111, pp. 87–96.

Boletis, E., Sieverding, C. H., and Van Hove, W., 1983, "Effects of a Skewed Inlet Endwall Boundary Layer on the Three Dimensional Flow Field in an Annular Turbine Cascade," AGARD CP 351, Paper No. 16.

Boletis, E., and Sieverding, C. H., 1991, "Experimental Study of the Three-Dimensional Flow Field in Turbine Stator Preceded by a Full Stage," ASME JOURNAL OF TURBOMACHINERY, Vol. 113, pp. 1–9.

Joslyn, H. D., Dring, R. P., and Sharma, O. P., 1983, "Unsteady Three-Dimensional Turbine Aerodynamics," ASME *Journal of Engineering for Power,* Vol. 105, pp. 322–332.

Morphis, G., 1989, "The Measurement of Axial Turbine Tip Clearance Flow Phenomena in a Moving Wall Annular Cascade and in a Linear Cascade," Master's Thesis, University of Natal, Durban, South Africa, Oct.

Morphis, G., and Bindon, J. P., 1994, "The Performance of a Low Speed Single Stage Axial Turbine With Varying Rotor Tip Clearance and Tip Gap Geometry," ASME Paper No. 94-GT-481.

Walsh, J. A., and Gregory-Smith, D. G., 1987, "The Effect of Inlet Skew on the Secondary Flow and Losses in a Turbine Cascade," *Proc. IMechE. Int. Conf.—Turbomachinery Efficiency Prediction and Improvement,* Cambridge, United Kingdom, Sept.

Yaras, M., Sjolander, S. A., 1989, "Losses in the Tip-Leakage Flow of a Planar Cascade of Turbine Blades," Paper #20, AGARD-CP-469, *Secondary Flows in Turbomachines,* Luxembourg, Sept.

Measurements of the Flow in an Idealized Turbine Tip Gap

S. A. Sjolander

D. Cao

Carleton University,
Ottawa, Ontario, Canada

To gain further insights into the details of the tip-gap flow in axial turbines, a test section has been constructed with a single idealized, large-scale tip gap. The single "blade" forms a circular arc with 90 deg of turning and has a constant thickness of 78 mm. For a plain, flat tip four clearances have been examined, varying from 0.292 to 0.667 of the blade thickness (corresponding to physical gap heights of 22.8 to 52.1 mm). The large proportions made it possible to obtain very detailed measurements inside the gap. The paper discusses the structure of the gap flow in some detail. One new feature, involving multiple vortices on the tip, probably helps to explain the "burnout" that sometimes occurs on turbine tips near the pressure side. Quantitative results are presented for the static pressures, total pressures, and velocity vectors through the gap. In addition, contraction coefficients for the flow at the separation bubble, discharge coefficients for the gap, and the gap losses have been extracted for comparison with the assumptions made in recent gap–flow models.

Introduction

The tip-leakage flow is now recognized as an important source of losses in both compressors and turbines, as a source of cooling problems in turbines, and as a source of instability in compressors and fans. For these reasons, a number of studies have been conducted in recent years aimed at obtaining quantitative information about the gap flow as well as an understanding of its structure. For turbines, these studies include those of Bindon (1987, 1989), Sjolander and Amrud (1987), Yaras and Sjolander (1989, 1990, 1992), Yaras et al. (1992), Moore and Tilton (1988), Moore et al. (1989), Heyes et al. (1992), and Heyes and Hodson (1993), and for compressors those of Storer and Cumpsty (1991) and Kang and Hirsch (1993a, b). The present work focuses on the gap flow in turbines.

It is generally agreed that the tip-leakage losses are closely related to the mass flow rate through the gap. Consequently, a number of simplified models have been proposed for predicting the tip-leakage flow rate and its resulting total pressure losses. These models make various assumptions about the nature of the flow in the gap. There appears to be general agreement about the presence of a separation bubble on the blade tip, starting at the pressure surface corner. However, a number of differing assumptions have been made about the subsequent evolution of the flow within the gap. This is illustrated in Fig. 1, which shows two recent simplified models proposed for the gap flow. Moore and Tilton (1988) assumed that the flow was essentially loss-free up to the minimum area section (sometimes called the vena contracta). From there the flow was assumed to undergo a sudden expansion and mix out to uniform conditions at the exit of the gap. The model thus predicts a loss within the gap as a result of the mixing. The model requires a value for the contraction coefficient, σ, and Moore and Tilton estimated this from a potential flow analysis for the flow in a sharp-edged orifice. The static pressure is assumed to be uniform across the gap at the vena contracta. By contrast, Heyes and Hodson (1993) assumed that the mixing will be complete only if the gap length exceeds six gap heights (that is, $t/\tau \geq 6.0$); thus for shorter gap lengths the gap includes a core of loss–free fluid, which they referred to as an isentropic jet. In the model, the fraction of the gap mass flow rate involved in the mixing is assumed to rise linearly from 0 to 100 percent as the gap length increases from 1.5τ to 6.0τ. Heyes and Hodson also make a small correction for the skin friction on the walls of the gap, whereas Moore and Tilton do not include this effect.

The variety of partially contradictory assumptions made about the gap flow is a consequence of the difficulties in obtaining detailed measurements within the typically small dimensions of the tip gaps found in actual machines or created in the laboratory.

To gain further insights into the details of the tip-gap flow in axial turbines, a test section has been constructed with a single, idealized, large-scale tip gap. In the longer term, the test section will be used to investigate modifications to the blade tip that might alter the gap flow. At present, only the baseline case of a flat, square tip has been examined. The large proportions of the tip gap make it possible to obtain detailed measurements within the gap using pressure probes. In addition, the blade tip and the endwall are extensively instrumented with static taps. Surface oil flow visualization is also used to assist in interpreting the flow structures. These data are used here to examine the detailed structure of the gap flow, particularly in relation to the assumptions used in the simple gap-flow models.

Experimental Apparatus and Procedures

The tip-gap test section is shown schematically in Fig. 2. The single "blade" forms a circular arc with 90 deg of turning and has a constant thickness of 78 mm. The blade in effect forms a centerbody in the middle of a curved rectangular channel of constant cross-sectional area. No "tip leakage" occurs at the outside walls of the channel. The blade has interchangeable tips. However, results are presented here only for the baseline case of a plain flat tip with sharp corners. The interior of the blade forms a plenum so that it is possible to eject air through the tip. The tip endwall consists of a plexiglass window, which provides easy visual access for flow visualization.

The test section was intended to simulate approximately the flow conditions at a typical tip–gap location part way along a turbine blade, with the appropriate static pressure difference across the gap and velocities parallel to it at inlet and outlet. It is not intended as a simulation of the complete chordwise gap length. For example, earlier studies (e.g., Sjolander and Amrud, 1987) have suggested a significant amount of endwall boundary layer fluid passes through the gap near the blade leading edge; this effect is not being examined.

The tip clearance is varied by inserting spacers or shims at the "hub" end of the blade. The blocks mounted on the blade

Contributed by the International Gas Turbine Institute and presented at the 39th International Gas Turbine and Aeroengine Congress and Exposition, The Hague, The Netherlands, June 13–16, 1994. Manuscript received by the International Gas Turbine Institute February 11, 1994. Paper No. 94-GT-74. Associate Technical Editor: E. M. Greitzer.

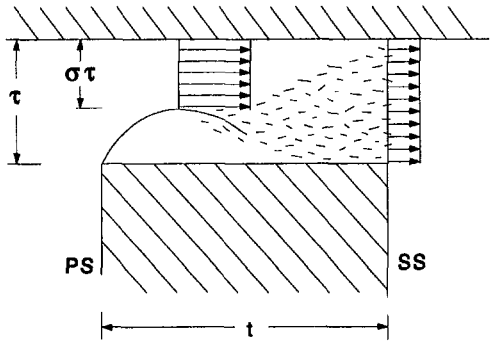

(a) Moore and Tilton (1988).

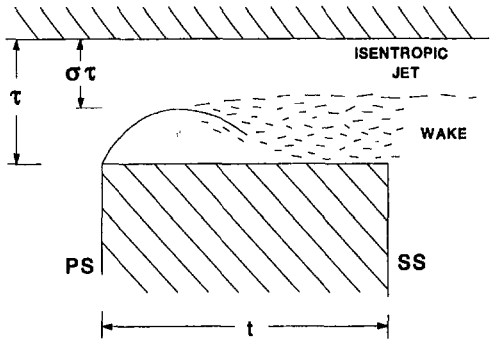

(b) Heyes and Hodson (1993).

Fig. 1 Examples of simple gap-flow models for turbines

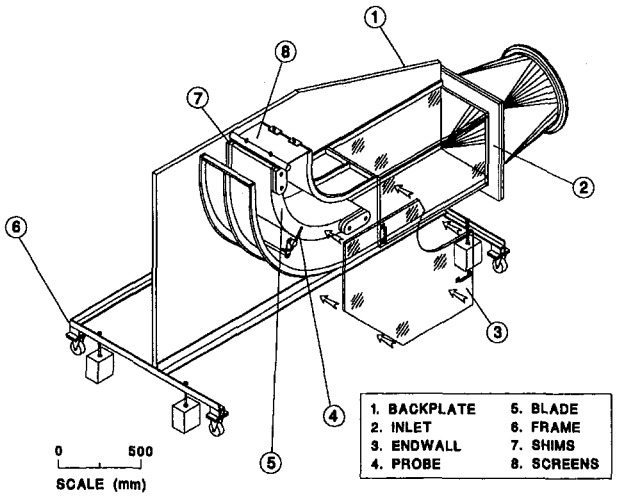

Fig. 2 Test section with large-scale turbine tip gap

tip at the beginning and end of the arc provide accurate control of the gap height. Four tip clearances have been examined in detail, varying from 0.292 to 0.667 of the blade thickness (corresponding to physical gap heights of 22.8 to 52.1 mm and values of t/τ of 3.4 to 1.5). A small amount of data is also presented for a gap height of 0.11 of the thickness (physical height 8.6 mm); however, this small clearance did not lend itself to detailed gap-flow measurements.

The pressure difference across the blade tip is varied by blocking the outlet of the pressure-side channel with screens of different porosities. Cases with two different pressure differences have been examined. The case with high pressure difference gave a ΔC_P of about 6.0, which corresponds roughly to the conditions found across turbine blade tips. To determine the influence of the pressure difference, measurements were also made for another case with about one quarter the driving pressure difference across the tip. A few results are presented for this case. However, unless indicated otherwise, the results presented here are for the high pressure difference.

Most of the measurements were made for a constant value of the Reynolds number of 78,000 ± 3 percent, where the Reynolds number is based on the test section inlet velocity and the blade thickness. Since the blade thickness would typically be about 10 percent of chord, the equivalent blade chord Reynolds number is on the order of 800,000. This is a little high but within the range encountered in actual turbines. The Reynolds number was in fact varied ±50 percent relative to the nominal value and negligible differences were found in the static pressure distributions and the flow patterns revealed by surface flow visualization. The nominal Reynolds number was chosen mainly to provide dynamic pressures that were compatible with the available pressure transducers. The corresponding inlet velocity was about 15 m/s so that conditions are essentially incompressible. The turbulence intensity at the test section inlet was 1.0 ± 0.2 percent, as measured with a hot-wire anemometer and a single normal-wire probe.

Most measurements of the gap flow were made at the 45 deg position of the circular arc. At this position, the endwall is instrumented with a radial row of 18 static taps. The taps are concentrated above the gap but also extend beyond the gap in the upstream and downstream direction. There are also 15 evenly spaced static taps on the blade tip at this position. To identify the chordwise variation in flow conditions, two additional rows of 15 static taps on each of the blade tip and the endwall are located at the 30 and 60 deg positions of the arc. A visual indication of the distribution of all of the taps can be obtained from the plots of the static pressures, Figs. 5 to 7.

Flow-field measurements within the gap were made using a seven-hole pressure probe. The probe was inserted into the gap

Nomenclature

C_D = discharge coefficient for the tip gap

$C_P = (P - P_{in})/\frac{1}{2}\rho V_{in}^2$ = static pressure coefficient

$C_{P_o} = (P_o - P_{o,in})/\frac{1}{2}\rho V_{\text{gap}}^2$ = total pressure loss coefficient

C''_{P_o} = mass-averaged total pressure loss coefficient

P = static pressure

P_{in} = static pressure upstream of blade

P_o = total pressure

$P_{o,in}$ = total pressure upstream of blade

$\text{Re} = \rho V_{in} t/\mu$ = reference Reynolds number

t = blade thickness

V_{gap} = nominal gap velocity, based on $P_{o,in}$ and gap exit P

V_{in} = velocity upstream of blade

x = coordinate normal to blade mean line

z = coordinate in spanwise direction, from endwall

θ = angular position on blade arc

μ = dynamic viscosity

ρ = density

σ = contraction coefficient for the gap flow

τ = tip gap height

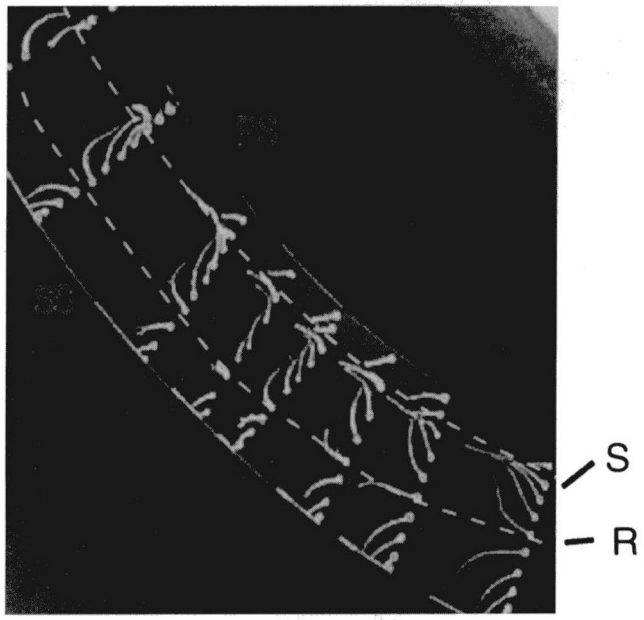

Fig. 3 Flow visualization on blade tip, $\tau/t = 0.292$

from the suction side of the blade, as indicated in Fig. 2, and could be located at any position across the gap width. This probe has been used extensively in earlier studies of tip-leakage flows (e.g., Yaras et al., 1992). It has a tip diameter of 2.4 mm and thus provides very little blockage to the gap flow for the clearances examined. The probe is used in the nonnulling mode and has been calibrated over a range of ±50 deg in both pitch and yaw. The flow angle measurements made with the probe are estimated to be accurate to within ±2 deg and the measured static and total pressures are estimated to be accurate to within ±5 percent of the local dynamic pressure.

All pressures were measured using capacitive–type pressure transducers and converted to digital form, with 12 bit accuracy, using a data acquisition system controlled by a microcomputer.

Experimental Results

Structure of the Gap Flow. The structure of the gap flow was inferred from a combination of surface flow visualization and quantitative measurements. Some of these measurements are presented later. However, for discussion purposes it is convenient to present first the interpretation of the structure of the gap flow.

Figure 3 shows the surface flow visualization obtained on the blade tip for $\tau/t = 0.292$. Very similar results were found for other clearances, at both high and low pressure differences. As mentioned earlier, there is general agreement that a separation bubble is formed on the blade tip starting at the pressure corner. Figure 3 shows clear evidence of a three-dimensional reattachment line (marked R) about three quarters of the way through the gap. However, in the separated region from the pressure corner to the reattachment line, the flow shows an unexpected degree of organization. There is clearly a well-defined three-dimensional separation line, marked S, at about one quarter of the way across the tip. From the pressure corner to this separation line there is evidently attached flow, directed away from the corner, with a reasonably high level of surface shear stress.

The interpretation of the flow pattern on the tip is shown schematically in Fig. 4. The separated flow from the pressure corner is believed to form a well-organized chordwise vortex above the blade tip. Gap velocity data to be presented later support this interpretation. The separation vortex will induce a flow back toward the pressure corner. However, this flow is eventually blocked by the shear flow separating from the corner. The net effect appears to be the formation of a secondary, counterrotating vortex, which separates from the surface at the line marked S. This appears to be the only plausible way to account for the separation line S and the attached flow near the pressure corner. A similar flow pattern is in fact commonly found near the leading edge of a highly swept wing with a sharp leading edge (e.g., Peake and Tobak, 1980). For their compressor flow, Kang and Hirsch (1993a, b) also identified two vortices in the tip region; however, their second vortex originated at the outlet corner of the gap and that was a very different pattern from the one observed here.

The unexpected region of attached flow near the pressure corner will have a reasonably high convective heat transfer coefficient, in addition to the high wall shear stress. This may help to account for the "burnout" that sometimes occurs near the pressure corner of turbine blades.

Static Pressures on the Tip and Endwall

Chordwise Variation. Although the blade is geometrically constant along the arc, the loss of mass flow from the pressure-side channel causes the static pressure difference across tip, and thus the leakage, to vary in the chordwise direction. This is illustrated in Fig. 5 for two extreme cases: in 5(*a*) for a high clearance and large pressure difference; and in 5(*b*) for a small clearance and low pressure difference. For the high pressure difference it is seen that there is a substantial rise in pressure in the gap in the chordwise direction. Thus, the gap flow should vary somewhat in this direction, and this accounts for the shift in the positions of the separation and reattachment lines seen on Fig. 3. From Fig. 5(*b*), the flow would be expected to vary much less in the chordwise direction for the lower pressure difference. Despite these effects, the flow patterns were found to be qualitatively very similar along the gap for all cases and the flow interpretation shown in Fig. 4 is believed to apply to all of them.

Corresponding Tip and Endwall Pressures. The relationship between the tip and endwall pressures at the same chordwise position is examined next. All results were obtained at the 45 deg position.

Figure 6 shows the relationship between the static pressures and the location of the separation and reattachment lines as obtained from the flow visualization for $\tau/t = 0.292$. A similar pattern was found for all clearances. It is noticeable that the separation on the tip is occurring in a region where the pressure gradient is favorable in the direction normal to the mean line. As will be shown later, this is close to the direction of the bulk of the flow through the gap. The fact that separation occurs under these conditions is an indication of the highly three-dimensional nature of the separation.

The vena contracta of the gap flow lies near the plane of minimum static pressure on the endwall. From Fig. 6 it is noticeable that there is a significant pressure difference from the tip

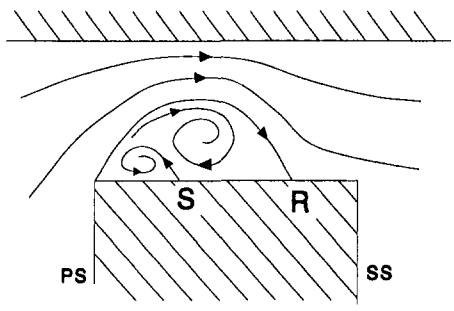

Fig. 4 Interpretation of the structure of the gap flow

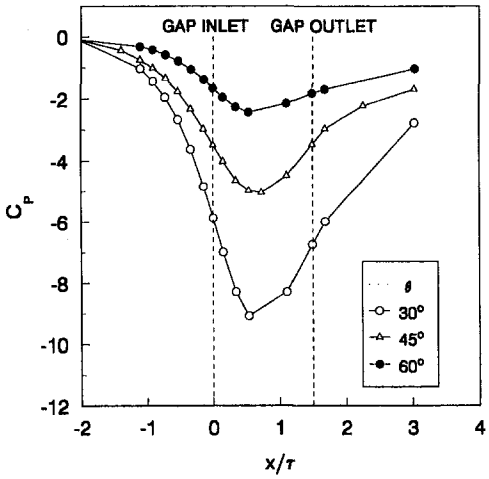

(a) High Pressure Difference, $\tau/t = 0.667$.

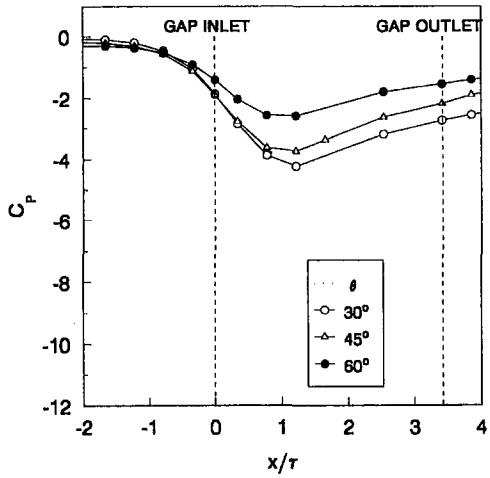

(b) Low Pressure Difference, $\tau/t = 0.292$.

Fig. 5 Chordwise variation of endwall static pressures

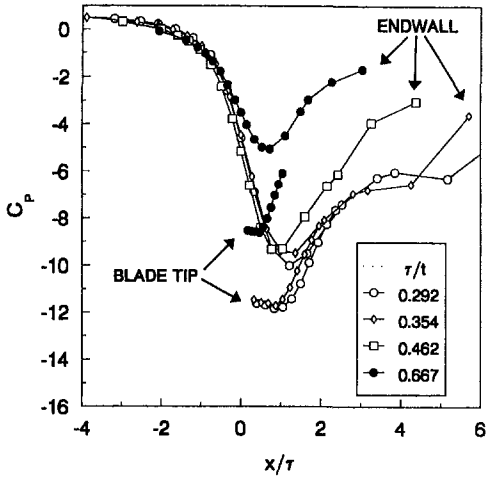

(a) High Pressure Difference.

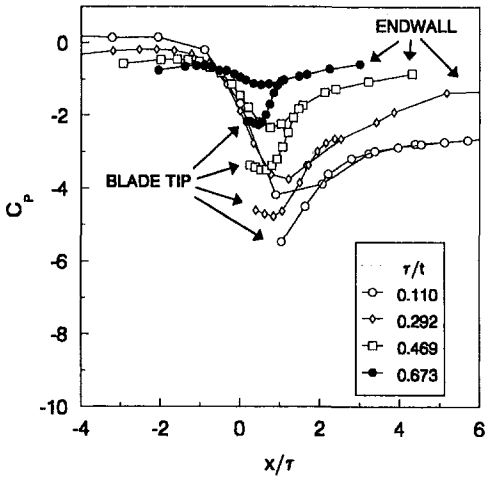

(b) Low Pressure Difference.

Fig. 7 Variation of tip and endwall pressures with clearance

to the endwall at the plane of the vena contracta. It is not known whether any of this pressure difference occurs through the separation bubble, although it is certainly conceivable in view of the organized, vortical nature of the flow in the bubble. In any event, it is clear that the location of the vena contracta is not a plane of constant pressure, as is assumed in some of the gap-flow models.

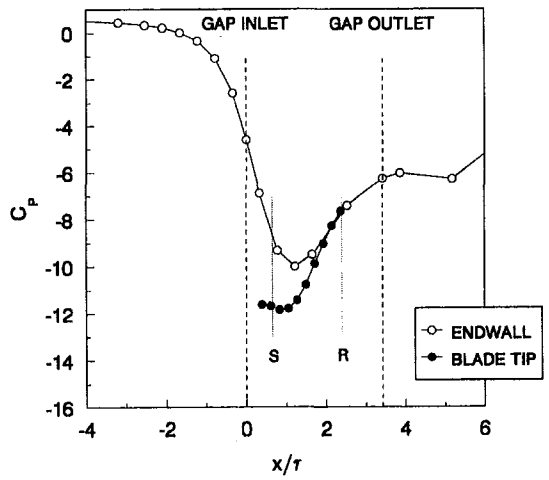

Fig. 6 Tip and endwall pressure distributions for $\tau/t = 0.292$ (with tip separation and reattachment locations from flow visualization)

Figure 7 shows the variation of the wall static pressures as a function of the clearance. Interestingly, for the high pressure difference the static pressure coefficients collapse onto essentially the same curves for the three smallest clearances. This suggests that for these three conditions the leakage flow sees essentially the same driving pressure difference across the gap and that very similar flow patterns occur inside the gap. This is consistent with an observation made earlier by Yaras et al. (1989) that for moderate values of clearance, the gap flow sees a driving pressure difference essentially equal to the undisturbed blade loading near the tip; that is, that there was no attenuation of the blade-to-blade pressure difference all the way to the endwall. From the data in Fig. 7(a), this appears to hold up to a clearance of about $\tau/t = 0.5$. At $\tau/t = 0.667$ a significant attenuation of the endwall pressure has occurred.

The collapse of the curves shown in Fig. 7(a) would be a useful observation for modeling purposes if it were a general result. Unfortunately, as shown in Fig. 7(b), it does not continue to hold for the low pressure difference. For these cases, the gap flow is at a much more oblique angle relative to the mean line and the angle varies with the clearance. As a result, the driving pressure difference applied to the gap flow varies

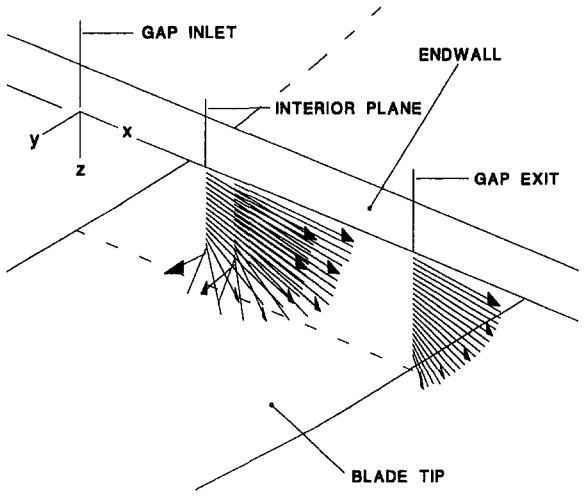

Fig. 8 Velocity vectors in tip gap for $\tau/t = 0.292$

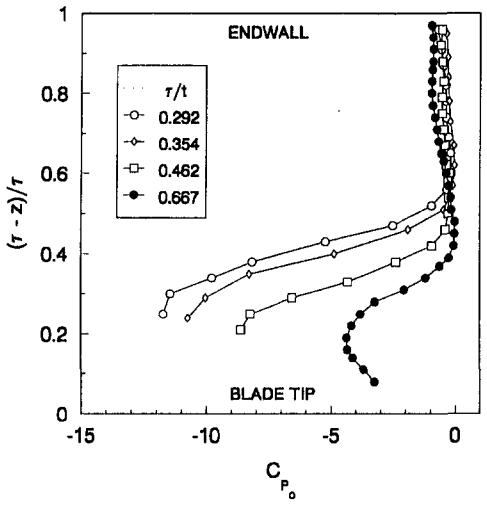

Fig. 10 Total-pressure distributions in the gap—interior plane

with the clearance as the streamtube emerges from the gap at different chordwise positions. On the other hand, the results shown in Fig. 7(*a*) should be more representative of the tip flows seen in actual turbines.

Velocity and Total Pressure Field in the Gap. As mentioned earlier, the flow inside the gap was traversed using a seven-hole pressure probe. The traverses were typically made at the gap outlet and at the plane of the vena contracta. The latter was assumed to be at the location of minimum pressure on the endwall and this was confirmed by traversing at a few closely spaced interior planes for a couple of the cases. A few traverses were also made at the gap inlet. All the measurements were made along the same line normal to the blade mean line, at the 45 deg position of the arc.

Velocity Vectors. Plots of the velocity vectors for the smallest and largest clearances are shown in Figs. 8 and 9, respectively. The bulk of the gap flow is seen to be at almost right angles to the blade mean line. The same behavior was found for the turbine cascade measurements of Yaras et al. (1989). This explains why it is possible to predict the local gap mass flow rate with reasonable accuracy based on the blade loading at the chordwise location of interest. The same would not be the case at lower pressure differences where the leakage streamtube would be at a more oblique angle relative to the blade mean line and would emerge at a significantly different chordwise position from the one where it entered the gap.

The velocity vectors at the interior planes show the presence of a highly organized flow all the way to the blade tip; that is, right through the separated region. This, along with the dramatic variation in the flow direction, supports the interpretation of the separation bubble as a well-defined vortical flow, as suggested by Fig. 4.

Total Pressure Distributions. The corresponding total pressure coefficients across the gap height are shown in Fig. 10, for the interior plane, and Fig. 11, for the gap outlet plane.

Figure 10 confirms that the main flow at the plane of the vena contracta has experienced virtually no loss, as assumed in most gap-flow models. On the other hand, high losses are being generated in the shear layer at the edge of the separated region, as would be expected. It is also noticeable that the shear layer on the endwall is extremely thin. Again, the same conclusion was drawn from earlier measurements in a turbine cascade, both with and without simulated rotation (Yaras and Sjolander, 1992; Yaras et al., 1989).

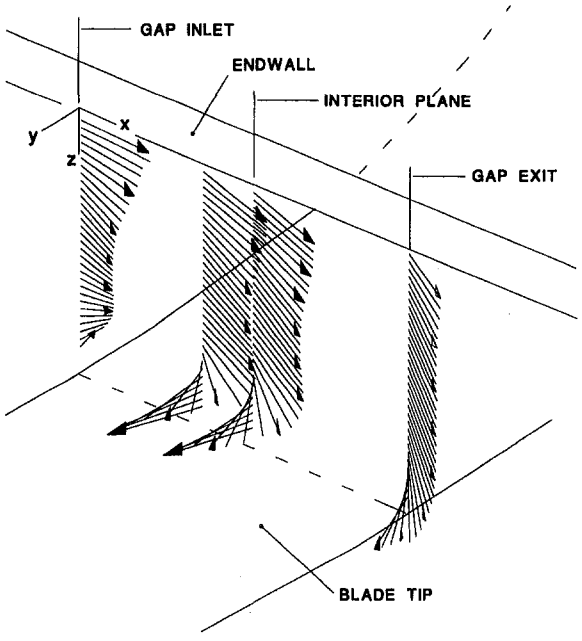

Fig. 9 Velocity vectors in tip gap for $\tau/t = 0.667$

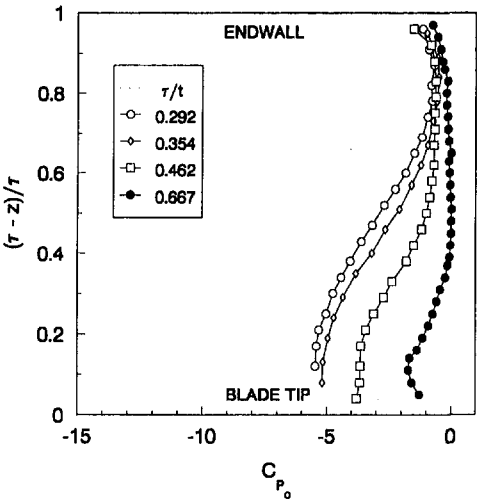

Fig. 11 Total-pressure distributions in the gap—exit plane

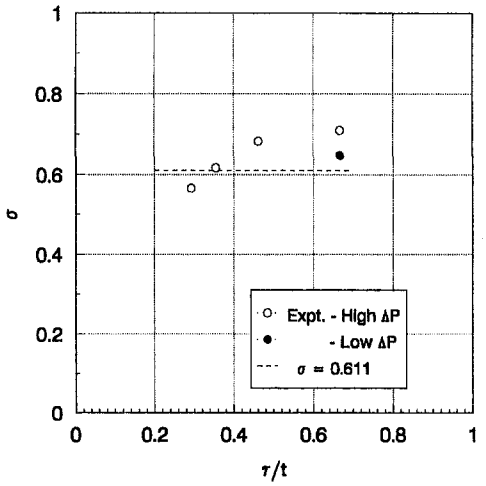

Fig. 12 Gap-flow contraction coefficients—measurements and prediction (Moore and Tilton, 1988)

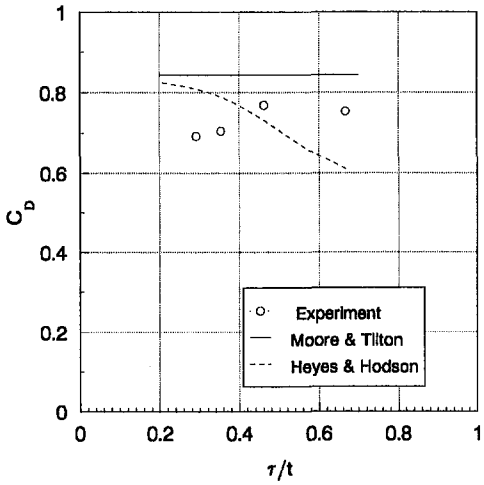

Fig. 13 Gap-flow discharge coefficients—measured and predicted

The gap outlet flows are shown in Fig. 11. It should be noted that the traverses do not apply for precisely the same streamtubes as those shown in Fig. 10, since the flow is not quite normal to the mean line. Thus, some caution must be used in comparing the losses in the two figures for the same clearances.

The total pressure distributions in Fig. 11 show that considerable mixing has occurred in the gap flow by the time it reaches the outlet plane. As would be expected, the mixing extends to a greater fraction of the gap height for the smaller clearances since the length of channel after the reattachment is longer for these cases. Nevertheless, a core of essentially loss-free flow remains present near the endwall for all of the cases, as assumed in the gap-flow models of Yaras et al. (1989) and Heyes and Hodson (1993). For the smallest gap ($\tau/t = 0.292$, $t/\tau = 3.4$), the Heyes and Hodson model would assume that less than half the gap mass flow has experienced mixing. The data from Fig. 11 suggest that this may slightly underestimate the degree of mixing. The assumption that the gap flow is fully mixed out and uniform at the gap outlet for all cases, as used in the Moore and Tilton (1988) model, is clearly less satisfactory.

Overall Gap-Flow Quantities

Contraction Coefficient. Figure 12 shows the measured contraction coefficients as a function of the clearance. The edge of the separation bubble was identified by locating the streamline at which the mass flow rate in the vena contracta was the same as that measured at the gap outlet. The contraction coefficient, σ, was then defined as shown in Fig. 1. Figure 12 also shows the value of σ (0.611) used by Moore and Tilton and Heyes and Hodson, as obtained from the potential analysis for an orifice flow.

As shown in Fig. 12, the observed σ increased with clearance. This was to some degree expected since σ should tend to 1.0 as the clearance becomes large, neglecting any changes in the pressure difference across the gap. The value used in the models is seen to be reasonable but at the low end of the observed range. A single point is shown for the low pressure difference. This case gives a similar, although slightly smaller, value of σ to that for the same clearance at high pressure difference. However, the values for low pressure difference must be regarded as less accurate since the measurements made at the interior and exit planes correspond to somewhat different streamtubes.

Discharge Coefficient. The discharge coefficient, C_D, compares the actual mass flow rate in the gap with the value calculated by assuming a loss-free uniform gap flow. Figure 13 shows the measured values and the values predicted by the Moore and Tilton and Heyes and Hodson models. The Moore and Tilton model predicts a constant value of C_D since it assumes a constant contraction coefficient and that the flow will be fully mixed out at the gap exit, regardless of the clearance. Some variation in C_D with clearance was observed in the measurements. The rise with clearance, at the lower clearances, is consistent with the increase in the contraction coefficient shown in Fig. 12. The decrease in C_D at $\tau/t = 0.667$ reflects the fact that the driving pressure difference seen by the flow near the endwall was beginning to decrease, as observed from Fig. 7(*a*). The C_D predicted by the Heyes and Hodson model is seen to pass through the observed values. The differences are presumably the result of the varying contraction coefficient in the measurements and the mild underestimation by the model of the rate of mixing in the gap. On balance, both models would provide fairly reasonable estimates of the gap mass flow rate.

Losses in the Gap. Finally, Fig. 14 shows the mass-averaged total-pressure losses in the gap. As expected, the Moore and Tilton model overpredicts the gap loss since it assumes complete mixing for all clearances. The Heyes and Hodson model closely follows the trend of the measured losses, correctly taking into account the increase in mixing with increasing gap length. However, it underestimates the gap loss since, as noted from Fig. 11, the model appears to underestimate the degree of mixing that will have occurred in a given gap. Clearly, only a

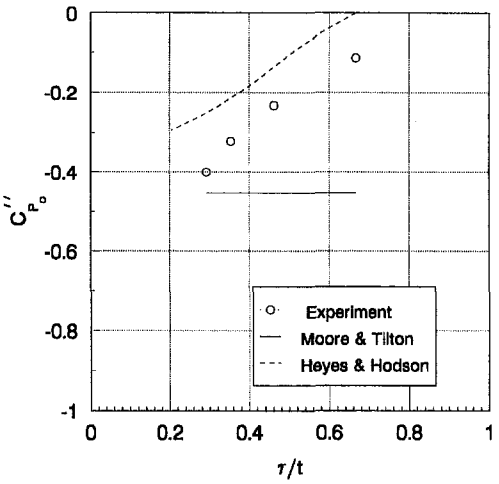

Fig. 14 Mass-averaged losses in gap—measured and predicted

minor adjustment to the mixing relationship would be needed to bring the Heyes and Hodson model into close agreement with the measurements.

It should be noted that earlier studies (e.g., Yaras and Sjolander, 1989) have suggested that the losses within the gap contribute a relatively small fraction of the overall tip-leakage losses; the bulk of the losses appear to occur through the mixing out of the tip-leakage vortex and as a result of wall shear stress beneath the vortex. Thus, while the Heyes and Hodson model is preferred, both models give reasonable predictions of the mass flow rate through the gap and therefore could both be used as a basis for reasonable estimates of the overall tip-leakage losses.

Conclusions

The flow visualization and measurements in the large-scale tip gap have provided new insights into the structure of the clearance flow in turbines. In particular, the separated flow on the blade tip was found to consist of a primary vortex, which in turn induced a secondary, counterrotating vortex. The latter vortex is located beneath the primary vortex and close to the pressure corner. This secondary vortex accounted for a region of attached flow, with relatively high wall shear stress, observed very close to the pressure corner. This region would also be expected to have a fairly high convective heat transfer coefficient and this may help to explain the burnout that sometimes occurs near the pressure corner of turbine blades.

The detailed nature of the quantitative measurements also allows a number of other observations to be made about the gap flow. The vena contracta region of the flow was found to consist largely of loss-free fluid, as is often assumed in gap flow models. On the other hand, the static pressure was not constant across the plane of the vena contracta, as is also often assumed. Downstream of the vena contracta, the flow experiences significant mixing. However, for the clearances examined this mixing was not complete by the gap outlet. Instead, in all cases there remained a core of loss-free fluid near the endwall as the flow emerged from the gap.

The results were briefly compared with the assumptions used in the simple gap-flow models of Moore and Tilton (1988) and Heyes and Hodson (1993). The model of Heyes and Hodson was found to be most consistent with the observed physics. Nevertheless, both models provided reasonable predictions for both the gap mass flow rate and the losses inside the gap.

Acknowledgments

Financial support for this study provided by the Natural Sciences and Engineering Research Council of Canada under Grant No. A1671 and by Pratt & Whitney Canada Inc. is gratefully acknowledged. We are also pleased to acknowledge helpful discussions with W. J. Rainbird about the structure of the gap flow.

References

Bindon, J. P., 1987, "Visualization of Axial Turbine Tip Clearance Flow Using a Linear Cascade," *Proceedings, 8th ISABE,* pp. 436–444.

Bindon, J. P., 1989, "The Measurement and Formation of Tip Clearance Loss," ASME JOURNAL OF TURBOMACHINERY, Vol. 111, pp. 257–263.

Heyes, F. J. G., Hodson, H. P., and Dailey, G. M., 1992, "The Effect of Blade Tip Geometry on the Tip Leakage Flow in Axial Turbine Cascades," ASME JOURNAL OF TURBOMACHINERY, Vol. 114, pp. 643–651.

Heyes, F. J. G., and Hodson, H. P., 1993, "Measurement and Prediction of Tip Clearance Flow in Linear Turbine Cascades," ASME JOURNAL OF TURBOMACHINERY, Vol. 115, pp. 376–382.

Kang, S., and Hirsch, C., 1993a, "Experimental Study on the Three-Dimensional Flow Within a Compressor Cascade With Tip Clearance: Part I—Velocity and Pressure Fields," ASME JOURNAL OF TURBOMACHINERY, Vol. 115, pp. 435–443.

Kang, S., and Hirsch, C., 1993b, "Experimental Study on the Three-Dimensional Flow Within a Compressor Cascade With Tip Clearance: Part II—The Tip Leakage Vortex," ASME JOURNAL OF TURBOMACHINERY, Vol. 115, pp. 444–452.

Moore, J., and Tilton, J. S., 1988, "Tip Leakage Flow in a Linear Turbine Cascade," ASME JOURNAL OF TURBOMACHINERY, Vol. 110, pp. 18–26.

Moore, J., Moore, J. G., Henry, G. S., and Chaudry, U., 1989, "Flow and Heat Transfer in Turbine Tip Gaps," ASME JOURNAL OF TURBOMACHINERY, Vol. 111, pp. 301–309.

Peake, D. J., and Tobak, M., 1980, "Three-Dimensional Interactions and Vortical Flows With Emphasis on High Speeds," AGARD-AG-252.

Sjolander, S. A., and Amrud, K. K., 1987, "Effects of Tip Clearance on Blade Loading in a Planar Cascade of Turbine Blades," ASME JOURNAL OF TURBOMACHINERY, Vol. 109, pp. 237–245.

Storer, J. A., and Cumpsty, N. A., 1991, "Tip Leakage Flow in Axial Compressors," ASME JOURNAL OF TURBOMACHINERY, Vol. 113, pp. 252–259.

Yaras, M. I., and Sjolander, S. A., 1989, "Losses in the Tip Leakage Flow of a Planar Cascade of Turbine Blades," AGARD-CP-469, *Secondary Flows in Turbomachines,* Paper 20.

Yaras, M. I., Zhu, Y., and Sjolander, S. A., 1989, "Flow Field in the Tip Gap of a Planar Cascade of Turbine Blades," ASME JOURNAL OF TURBOMACHINERY, Vol. 111, pp. 276–283.

Yaras, M. I., and Sjolander, S. A., 1990, "Development of the Tip Leakage Flow Downstream of a Planar Cascade of Turbine Blades: Vorticity Field," ASME JOURNAL OF TURBOMACHINERY, Vol. 112, pp. 609–617.

Yaras, M. I., and Sjolander, S. A., 1992, "Effects of Simulated Rotation on Tip Leakage in a Planar Cascade of Turbine Blades: Part I—Tip-Gap Flow," ASME JOURNAL OF TURBOMACHINERY, Vol. 114, pp. 652–659.

Yaras, M. I., Sjolander, S. A., and Kind, R. J., 1992, "Effects of Simulated Rotation on Tip Leakage in a Planar Cascade of Turbine Blades: Part II—Downstream Flow Field and Blade Loading," ASME JOURNAL OF TURBOMACHINERY, Vol. 114, pp. 660–667.

Experimental Investigation and Performance Analysis of Six Low Flow Coefficient Centrifugal Compressor Stages

J. Paroubek

V. Cyrus

SVÚSS,
National Research Institute
for Machine Design,
Praha, Czech Republic

J. Kynčl
ČKD Kompresory a.s.,
Praha, Czech Republic

Some results of a research and development program for centrifugal compressors are presented. Six-stage configurations with low flow coefficient were tested. The stages had channel width parameter $b_2/D_2 = 0.01$ and 0.03. For each value of the width parameter, three different impellers with inlet hub to outlet diameter ratio $d_0/D_2 = 0.3$, 0.4, and 0.5 were designed. Test rig, instrumentation, and data analysis are described. Special attention was devoted to probe calibrations and to evaluation of the leakage, bearing, and disk friction losses. Aerodynamic performance of all tested stages is presented. Slip factors of impellers obtained experimentally and theoretically are compared. Losses in both vaneless diffuser and return channel with deswirl vanes are discussed. Rotating stall was also investigated. Criteria for stall limit were tested.

Introduction

Stages of centrifugal turbocompressors for low flow volume and high discharge pressure applications in petrochemical, ammonia synthesis, or urea synthesis plants possess a variety of specific properties. These have to be considered during the compressor design, experimental investigation, and operation.

The extremely low flow coefficient requirement leads to very narrow flow channels of both rotor and stator part of the stage. Compared to the stage of medium or high flow coefficient and of the same impeller outlet diameter and operation conditions, several observations are pertinent. First, due to a lower hydraulic diameter of the flow channel, higher friction losses appear in the stages with low flow coefficient. Second, the leakage and disk friction losses remain practically the same. This means that they consume a relatively larger amount of power input in the low flow coefficient stage. In addition, due to the narrow flow passages, special instrumentation had to be used for experimental investigation of these stages.

Some results from previous research of low flow coefficient stages were given in papers by Benvenuti (1972), Koizumi (1983), and Casey et al. (1990). The paper by Benvenuti (1972) shows miniature pressure probes designed for measurements in narrow flow channels and presents some results of performance investigation on a low flow coefficient stage. The basic experimental data explaining the influence of the impeller channel width and blade outlet angle on the performance of stages with the same flow coefficient are shown and discussed in papers by Koizumi (1983) and Casey et al. (1990). Koizumi (1983) explains main flow phenomena both in rotor and stator parts of flow channel and dominant effect of viscosity in those stage types. Moreover, Casey et al. (1990) show the influence of impeller blade cutback on stage efficiency.

Our paper presents some results of the systematic research and development program concerning a group of six low flow coefficient stages that were designed and manufactured in the ČKD Kompresory and tested in the SVÚSS.

Contributed by the International Gas Turbine Institute and presented at the 39th International Gas Turbine and Aeroengine Congress and Exposition, The Hague, The Netherlands, June 13–16, 1994. Manuscript received by the International Gas Turbine Institute February 4, 1995. Paper No. 94-GT-43. Associate Technical Editor: E. M. Greitzer.

Rotor dynamic problems form probably the most significant constraint during the design procedure of the low flow volume and high pressure turbocompressors. The results of the rotor dynamic analysis mostly call for higher shaft stiffness, which leads to larger impeller inlet hub to outlet diameter ratio requirement. Therefore, it was the aim of our work to investigate the effect of the d_0/D_2 ratio and the relative outlet width b_2/D_2 on the performance of the stage with low flow coefficient. Data of this sort are missing in the literature and we believe that the designer equipped with such knowledge will be able to meet much better the rotor dynamic demands. Performance analysis of an impeller, a vaneless diffuser, and a return channel and comparison with the data indicated in the literature was made.

Special attention was devoted to the investigation of the nonsteady flow. The reason for this was given by the expected operating area of those stages. High density of the compressed gas substantially magnifies the rotor excitation forces caused by the pressure fluctuations. Therefore, the onset of rotating stall was monitored in the vaneless diffuser.

Aerodynamic Design

The aerodynamic design was made with respect to the request that the stages, immediately after the experimental investigation of their performance, had to be incorporated into the producer's manufacturing program. During the aerodynamic design and experimental investigation, it was necessary to take into account manufacturing tolerances and surface roughness of the flow passages and labyrinth seal clearances, which the factory was able to accomplish. From the point of view of rotor dynamics, the main demand was laid on a short axial length of the stage and a larger diameter of the shaft. With regard to the production costs, effort was directed toward the unification of some parts belonging to the stage. In its structure, the design procedure used was similar to that described by Platt (1981).

The aerodynamic design resulted in three stage configurations with design flow coefficient $\Phi_D = 0.007$ and three stage configurations with $\Phi_D = 0.021$. The design values of isentropic head coefficient χ were expected in range from 0.33 to 0.41 for narrower and from 0.39 to 0.44 for wider stages, respectively. The design values of theoretical head coefficient σ were expected in the range from 0.50 to 0.55 for all six stages. The main impeller dimensions with blade outlet angle $\beta_{b2} = 30$ deg

Table 1 Impeller main dimensions

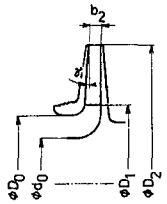

ϕD	STAGE CONFIG.	d_0/D_2	D_0/D_2	D_1/D_2	γ°	Z	b_2/D_2
0,007	A	0,5	0,550	0,605	3,5°	13	0,01
	B	0,4	0,477	0,539	3,8°	11	
	C	0,3	0,391	0,459	4,0°	9	
0,021	D	0,5	0,609	0,707	3,5°	13	0,03
	E	0,4	0,525	0,627	4,0°	11	
	F	0,3	0,455	0,557	4,5°	9	

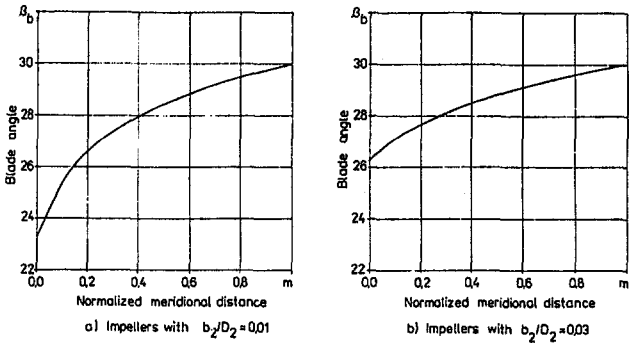

Fig. 1 Typical blade angle distribution

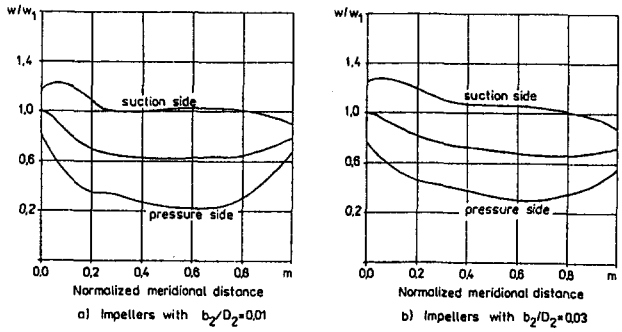

Fig. 2 Typical blade loading distribution at shroud

are given in Table 1. The meridional shape, blade geometry, and the blade number of the impellers in stages A, B, C were designed so that these impellers might have nearly similar blade loading with selected values $d_0/D_2 = 0.3$, 0.4, and 0.5. The impellers of stages D, E, F were derived from those of A, B, C, respectively, by increasing the blade width and by shortening the blade in the inlet portion as a consequence of a larger leading edge diameter D_1. The inlet diameter D_0 and the slope of the shroud disk γ were designed so as to make the diffusion factor (Rodgers, 1978) in the derived impellers roughly the same as in the original ones. We believed that maintaining these criteria justified the use of the same vaneless diffuser and return channel in all three stages with the same relative width b_2/D_2. Typical blade angle and blade loading distributions are given in Figs. 1 and 2 for both A, B, C and D, E, F stages. All these stages had a vaneless diffuser of constant width and diameter ratio $D_4/D_2 = 1.5$.

Test Rig, Instrumentation, and Performance Measurement

Based on the previous design, model stages were manufactured with the impeller outlet diameter $D_2 = 440$ mm and subjected to a systematic experimental investigation of their aerodynamic performance. Special attention was devoted to the surface roughness of impeller channels. The blade channels were milled together with the hub on an NC milling machine with strictly the same technology in order to achieve most possibly the same surface roughness (Ra = 3.2 μm) in all investigated impellers, and then riveted to shroud disks.

The experiments were made on a test rig consisting of an open loop facility, whose sketch is shown in Fig. 3. The air was brought in through a large inlet filter followed by the flow nozzle 1 and the inlet pipe line 2 to the test compressor 3. Having passed through the compressor, the air was delivered by discharge pipe line into the open atmosphere. The flow rate was adjusted by the throttle device 5 in the exit of the discharge piping. The compressor was driven by a variable speed DC dynamometer, which, together with the speed increasing gear 6, allowed us to perform the tests within the required range of 7500–16,500 rpm.

The subsequent Fig. 4 shows the sketch of the tested stages with marked data acquisition stations. Upstream of the stage inlet, station 0, there was a false return channel to simulate outlet flow conditions from the preceding stage in the group of stages. Each of the measuring stations was equipped with pressure, temperature and/or nonsteady probes, whose kind and number are indicated in Table 2.

Nomenclature

b = channel width
c = absolute velocity
d = impeller hub diameter
f = frequency
m = normalized meridional distance
p = pressure
t = time
u = circumferential velocity
w = relative velocity
B_k = amplitude of static pressure = $0.5*(p_{max} - p_{min})/p_{av}$
D = shroud diameter
H_{is} = isentropic head between stations 0 and 7, Fig. 4
H_{th} = theoretical head
M_{u2} = stage Mach number = u_2/a_0
N = power input
N_b = bearing losses
N_h = power actually impressed on the gas = mass flow$*H_{th}$
N_s = leakage losses
N_v = disk friction losses
Q = inlet volume flow
Z = number of blades
α = absolute flow angle relative to tangential direction
β_{b2} = impeller outlet blade angle relative to tangential direction
γ = slope of the shroud disk, Table 1
ξ_{2i} = total pressure loss coefficient between stations 2 and i, i = 4, 5, 7, Fig. 4, $\xi_{2i} = (p_{t2} - p_{t1})/(p_{t2} - p_2)$
η = stage isentropic efficiency (total to total)
η_i = impeller isentropic efficiency (static to total)
μ = slip factor = $c_{u2}/c_{u2\infty}$
σ = theoretical head coefficient = $c_{u2}/u_2 = H_{th}/u_2^2$
φ_2 = outlet capacity coefficient = c_{m2}/u_2
χ = isentropic head coefficient = H_{is}/u_2^2
Φ = flow coefficient = $4*Q/(\pi*D_2^2*u_2)$

Subscripts

c = critical
m = meridional direction
r = related to reference value
rev = revolutions
t = total
th = theoretical
u = circumferential direction
D = design
Wies = Wiesner formula
0 . . . 7 = stage element boundaries or measuring stations, Fig. 4
∞ = infinite number of blades

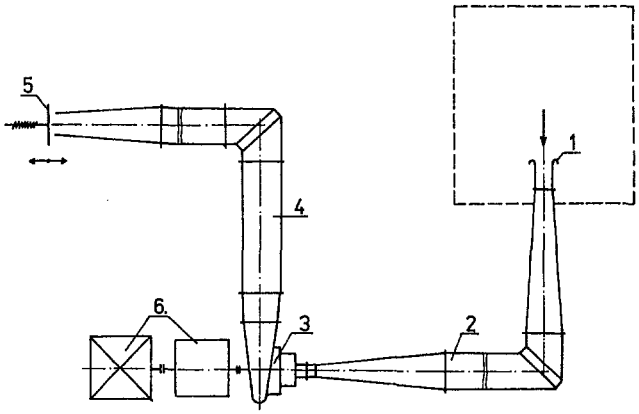

Fig. 3 Test rig

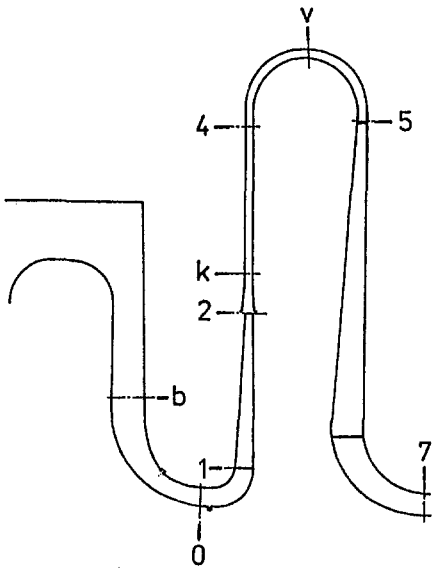

Fig. 4 Meridional flow section

Miniature probes manufactured from stainless tubes of diameter 1 mm to measure the total pressure were employed in most cases due to the extremely narrow channels. The sensor of this probe is shown in Fig. 5. Obviously, when the total pressure is measured by this probe, the error remains less than 1 percent within the range of the incidence angles ±15 deg (Paroubek et al., 1989).

Table 2 Instrumentation list

station	total pressure probes	static pressure taps	shielded thermo-couples	nonsteady flow probes
b			4	
0	4	4		1 x3
k		16		2
4	7 x1	6	4	
v				2
5	7 x2	10		
7	8	8	4	

x1 incl. 3hole "cobra" probe
x2 incl. 4hole cylindrical probe
x3 hot wire probe

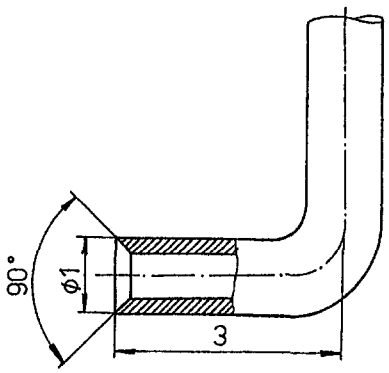

Fig. 5 Total pressure probe hole

To determine the total pressure and the flow angle, a miniature three-hole probe, automatically adjusting to the flow direction, was placed at station 4 amidst the flow channel. At station 5 a special four-hole cylindrical probe calibrated by the indirect method was used.

The static pressure was measured through wall taps of diameter 0.8 mm.

The temperature was measured by shielded thermocouples of diameter 1 mm, calibrated both statically and dynamically.

To explore the nonsteady flow in the stage, pressure sensors manufactured in Tesla Rožnov were applied in the flow channel walls at stations 0, k, v (Fig. 4). At these stations two pressure probes were used whose circumferential positions were mutually shifted to allow us the investigation of the rotating stall.

The pressure signals were transferred in the usual way through the Scanivalve system to the pressure transducers and then, along with temperature and other signals, were read directly by a computerized data acquisition center, where the data were checked and stored for further processing.

The method of evaluation of measured values was very similar to that described by Japikse (1987).

In view of the expected power input distribution, especially in the stages with $b_2/D_2 = 0.01$, the aerodynamic measurements were considerably time consuming. For each test point, the average period required for reaching steady flow conditions was about 50 minutes; in wider stages D, E, F, it dropped roughly to one half. Before testing, the casing of the compressor was thermally isolated to prevent heat transfer.

Results of Aerodynamic Measurements

The ascertained power input distribution versus the flow coefficient of stages B and E at $M_{u2} = 0.9$ is indicated in Figs. 6(a) and 6(b). It can be observed that bearing and disk friction losses consume together more than 60 percent of input power and leakage losses about 5 percent in vicinity of $\varphi_{2r} = 1$ at this M_{2u}. Only about 25–30 percent of input power is actually impressed on the gas in the narrower stages. The N_h/N ratio drops with dropping M_{u2} and reaches only about 15 percent at the lowest M_{u2} measured. It confirms the unavoidable high claims on measuring accuracy and evaluation precision of different sorts of losses and great demand on testing time. Bearing losses and friction losses of rotating wheel were estimated from direct measurements on the stage equipped only with rotating wheel without impeller. The disk friction losses were calculated according to the relations derived from those in the papers by Daily and Nece (1960) and Nece and Daily (1960).

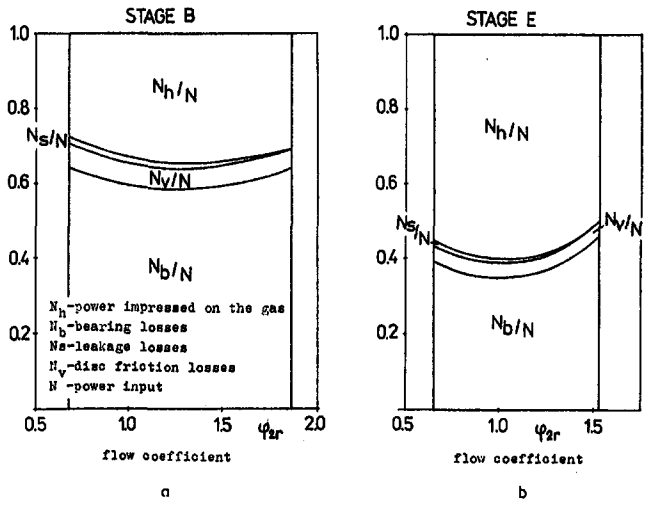

Fig. 6 Power input distribution

Characteristics of Investigated Stages. The fundamental performance characteristics of stages A to C and/or D to F at $M_{u2} = 0.9$ are shown—related to reference values—in Figs. 7(*a*) and/or 7(*b*). Values found in stage B at the Mach number 0.9 have been used as references both in this case and all other cases. The subsequent Figs. 8(*a*, *b*) indicate the effect of Mach number on the performance of stages B and E.

The ascertained curves of theoretical head rise coefficient are almost identical for stages A to C as well as for stages D to F. This indicates that, in terms of the design criteria, each group of stages possesses roughly the same aerodynamic performance.

The Mach number influence (Fig. 8) is also very small in the vicinity of the assumed operating point. The value of σ at the design point is 5 percent higher in the stage with relative width 0.01 than in the group of wider stages D to F. The σ shown in Fig. 8 are compared with σ_∞ and σ_{Wies}. This figure shows the differences between theoretical values based on the assumption of infinite number of blades, the theoretical value calculated using the Wiesner correlation, and the results of aerodynamic measurements. The relations we found have a similar nature to that measured by Koizumi (1983) in stages with $\Phi_D = 0.0072$ having a larger outlet blade angle. However, the ascertained deviation from theoretical values are much lower.

The χ curves shown in Fig. 7(*a*) indicate a significant effect of the hub diameter on the performance of stages A to C over the whole measured interval of the characteristics. The χ value at the design point of stage C with the smallest hub diameter is 7 percent higher than in stage B, and this is again 9 percent higher than that in stage A. In the group of wider stages, χ attains relative values about 1.1 at the assumed operating point and the effect of the hub diameter is significantly lower. From this point of view there is hardly a difference in stages E and F in the vicinity of the design point.

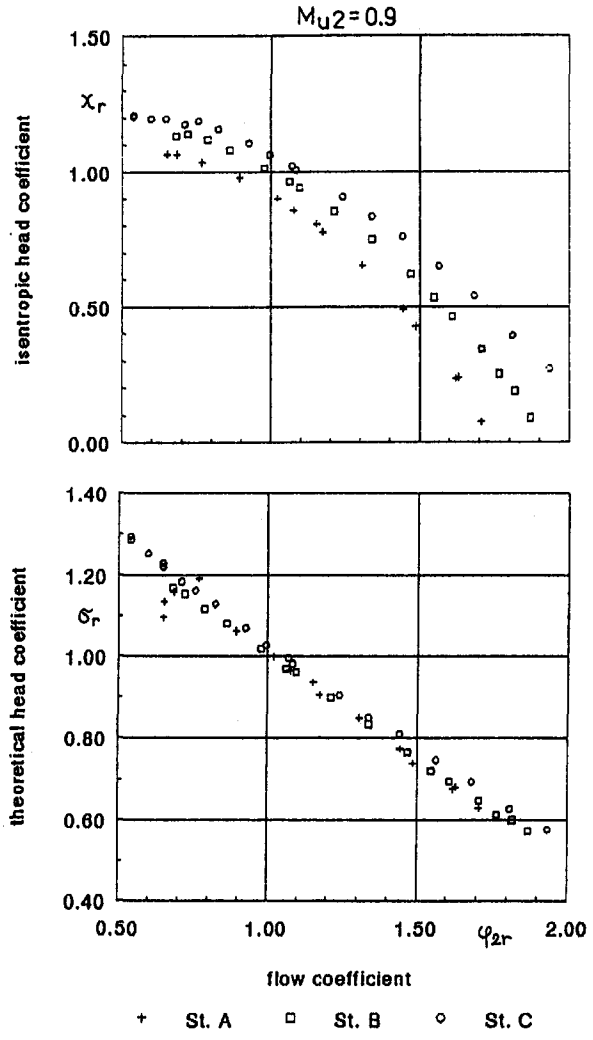

Fig. 7(*a*) Performance characteristics of stages A, B, C

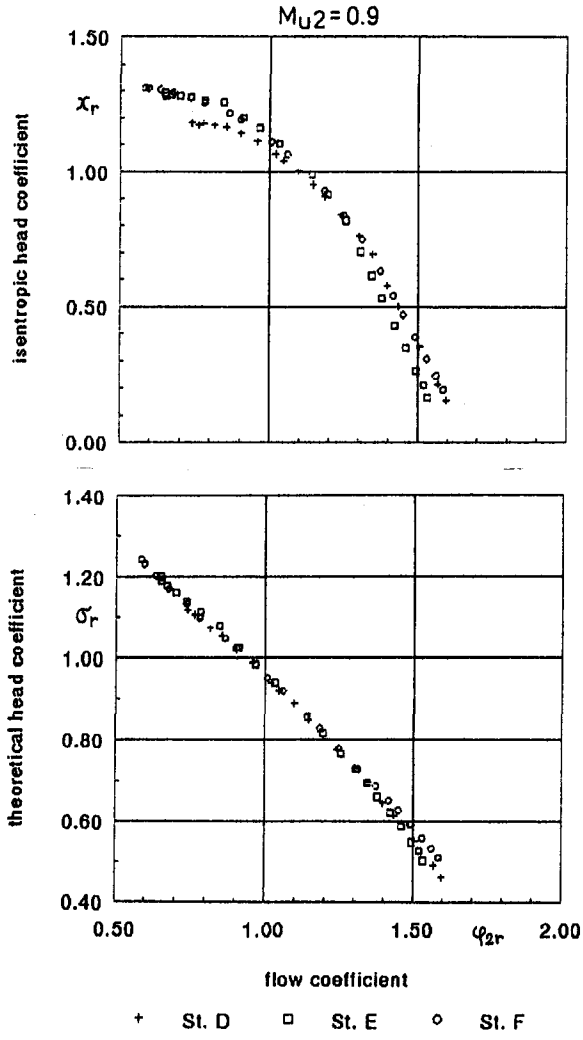

Fig. 7(*b*) Performance characteristics of stages D, E, F

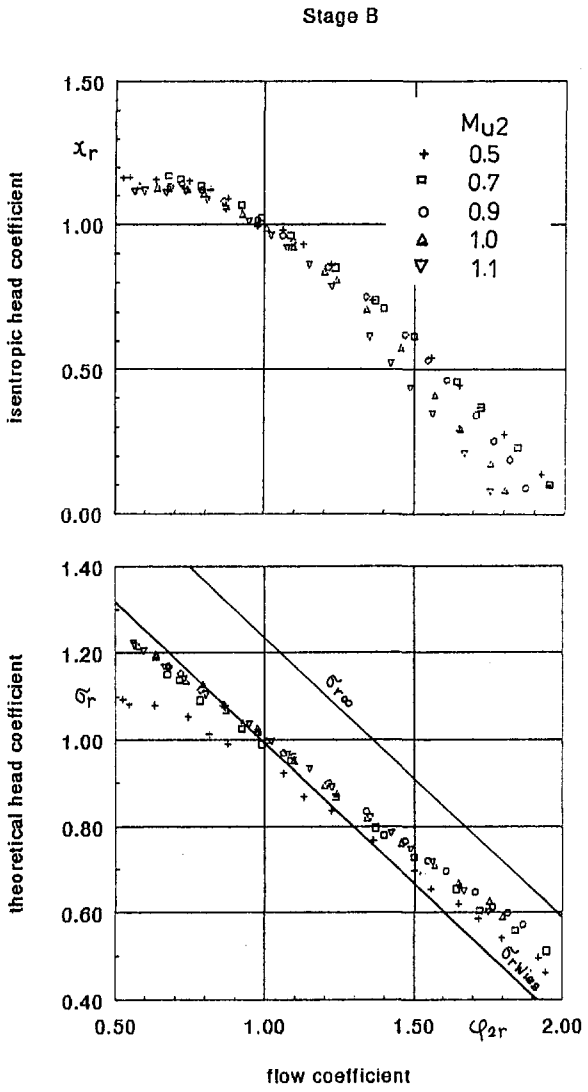

Fig. 8(*a*) Performance characteristics of stage B

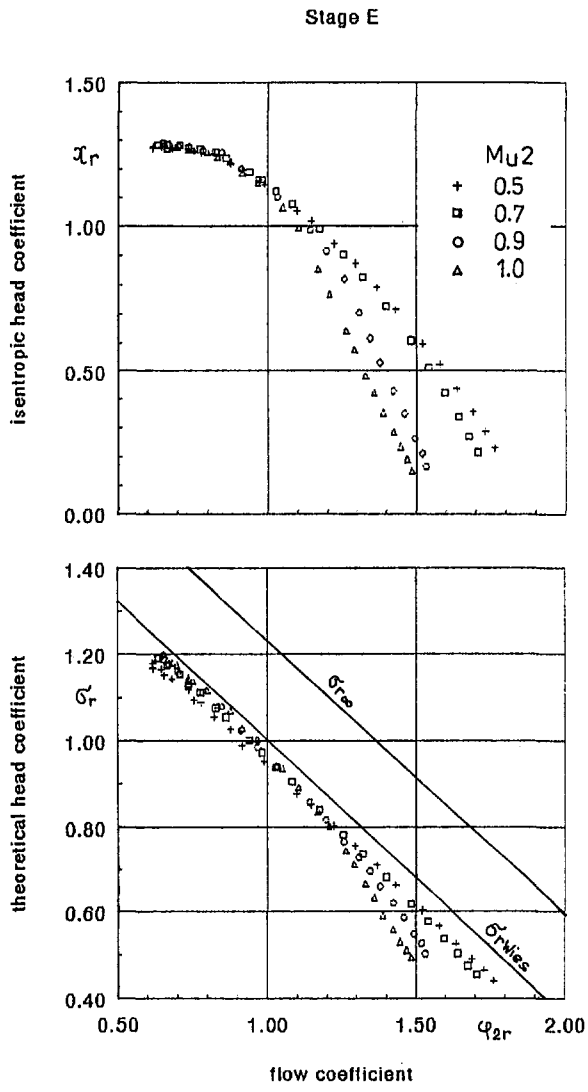

Fig. 8(*b*) Performance characteristics of stage E

Impellers. Figure 9 shows the relative efficiencies of all measured impellers at $M_{u2} = 0.9$. The effect of hub diameter is again more significant in the case of narrower impellers. The A, B, C impeller efficiencies at the design point are 0.88, 1.00, and 1.07, respectively, of the reference value. The efficiency of wider impellers D, E, F is about 30 percent higher at the design point; the efficiency drop is—just as in the narrower impellers—more significant between the impellers with $d_0/D_2 = 0.5$ and 0.4 than between impellers with 0.4 and 0.3. The effect of Mach number at the assumed operating point is shown in Fig. 10. The impeller efficiency drops with rising M_{u2} in all impeller types due to rising hydraulic losses in impeller channels. In the D, E, F impellers a more rapid drop in efficiency was found at the highest measured rotational speed. The reason for this is probably a higher level of relative velocity connected with the existence of local zones of supersonic relative velocity within the impeller channel. Figures 11(*a*) and/or 11(*b*) show the dependence of the impeller outlet to inlet relative velocity ratio on φ_{2r} for stages A, B, C and/or D, E, F at $M_{u2} = 0.9$. The larger drop of relative velocity was indicated in the impeller with larger hub diameter. It is due to lower inlet relative velocity in the stages with lower d_0/D_2 value. For the same φ_{2r} value, the w_2/w_1 ratio is lower for impellers with greater hub diameter. In vicinity of $\varphi_{2r} = 1$ the ascertained ratio w_2/w_1 never reaches limiting values (e.g., $0.65 < w_2/w_1 < 0.75$, Casey et al., 1990), below which a significant performance deterioration is to be expected.

The slip factor of all six impellers versus the flow coefficient is shown in Fig. 12. The ascertained deviations found are in the

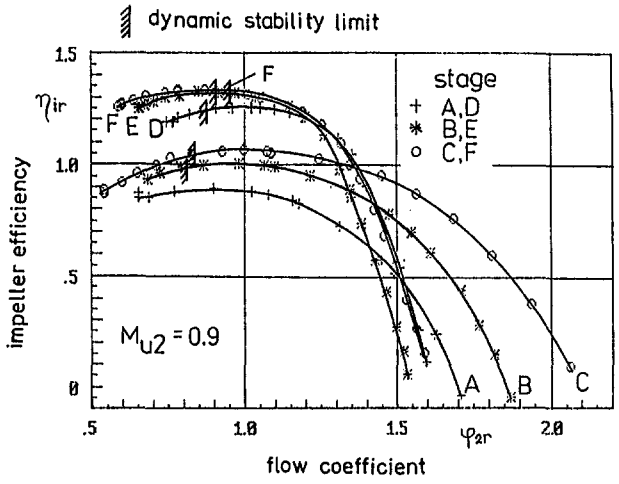

Fig. 9 Impeller efficiency

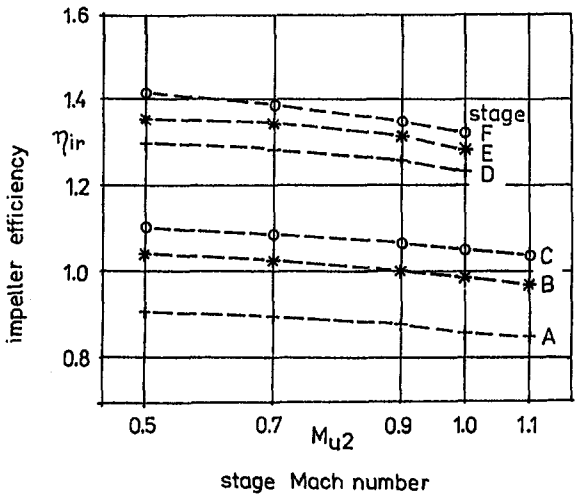

Fig. 10 Impeller efficiency at $\varphi_{2r} = 1$

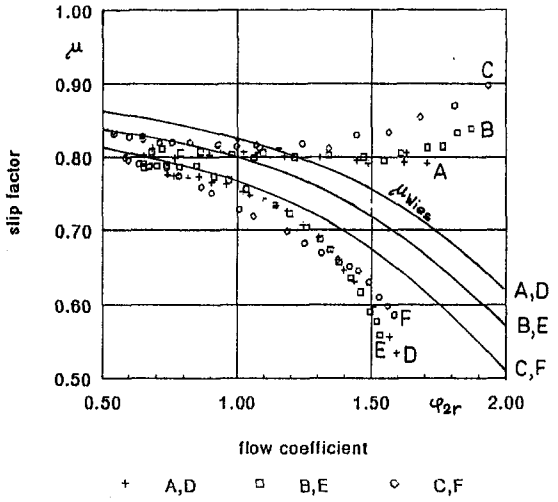

Fig. 12 Slip factor

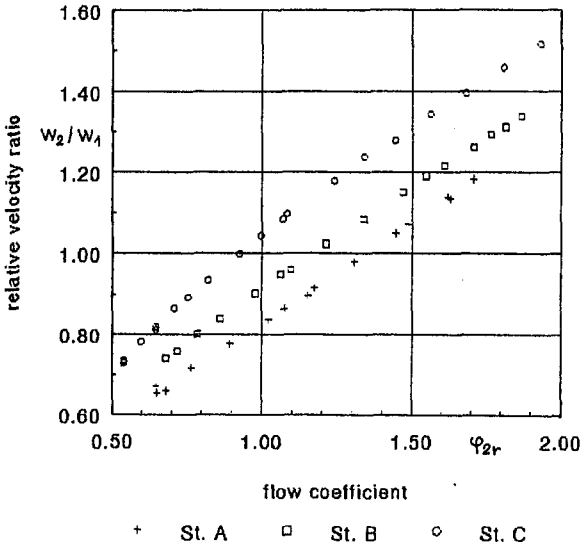

Fig. 11(a) Relative velocity ratio of stages A, B, C

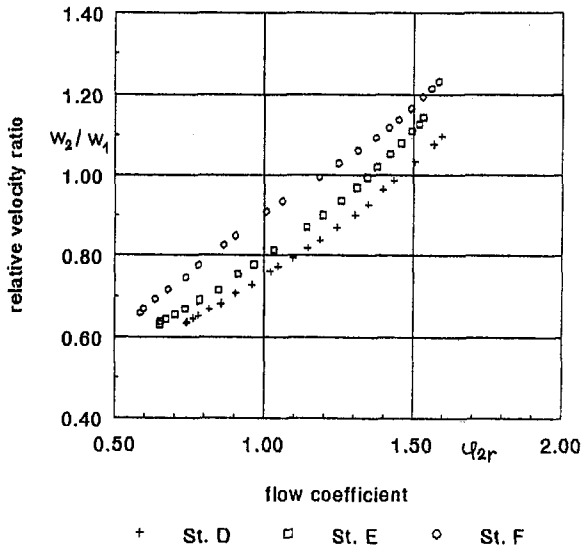

Fig. 11(b) Relative velocity ratio of stages D, E, F

group of narrower impellers much lower than those indicated by Koizumi (1983). In the vicinity of $\varphi_{2r} = 1$, a relatively good agreement between the slip factor measured and calculated according to Wiesner formula was reached in the group of narrower stages. As a main reason for the deviations Koizumi assumes, on the basis of his own analysis, that it comes to an accumulation of a considerable low-energy flow zone along the suction side of impeller blades. In our opinion, low deviations from the Wiesner correlation found on the stages A, B, C in comparison to those by Koizumi are due to the fact that the effect of viscosity is more significant in Koizumi's impellers with substantially greater value of β_{b2}. These impellers are more sensible to flow separations and to the occurrence of jet-wake flow pattern (Adler, 1980). Greater deviations from the Wiesner formula (to 8 percent) were measured at the group of wider stages D, E, F where the effect of viscosity is not as significant as in narrower ones. In our opinion, the reason for this is to be found in the fact that the D, E, F stages have a higher D_1/D_2 ratio at the same blade number in comparison to stages A, B, C. This means that the solidity of blade cascade is lower, which leads to the increasing effect of secondary flows between the suction and pressure sides of the blade and causes flow separation on the suction side.

A substantial qualitative difference was found in these relationships for both investigated impeller groups. The slip factor of the impellers having relative width 0.01 has an almost constant value over a considerable part of the characteristic ($\varphi_{2r} = 0.5 \ldots 1.5$) and rises slightly for higher values of φ_{2r}. On the other hand, the impellers D, E, F show a monotonously decreasing slip factor value with rising φ_{2r}. It corresponds to the results of Benvenuti in the stage with the design flow coefficient 0.012, as can be seen from the subsequent Fig. 13, which compares all three types of impellers. Unfortunately Benvenuti (1972) does not indicate all the necessary data of his stage geometry. Drawing on all available data and comparison in Fig. 13 one can assume that this is a stage with a smaller outlet blade angle and a larger relative outlet width than stages A, B, C. A certain relative width seems to exist for each blade geometry when a qualitative change in flow nature occurs accompanied with the corresponding change of the slip factor curve character.

At the same flow rate, the impellers with greater d_0/D_2 ratio have higher circumferential velocity and therefore relative inlet velocity, too. Provided that the outlet relative velocity remained the same, we find greater relative velocity deceleration and greater losses in these impellers followed with dropping values of χ, η, η_i.

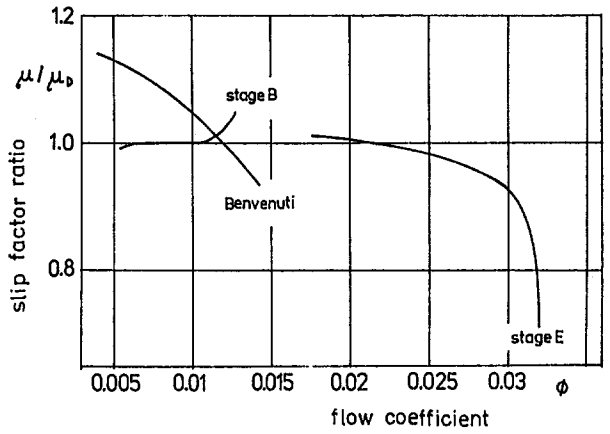

Fig. 13 Comparison of slip factors

Vaneless Diffusers and Outlet Sections. A fundamental view on aerodynamic losses in the outlet stator section is conveyed by Fig. 14(*a*) showing the total pressure loss coefficient distribution between the stations 24, 25, and 27 (Fig. 4) for stages A, B, C and by Fig. 14(*b*) for stages D, E, F, respectively. As we can see from Fig. 14, the loss coefficient distribution is practically the same for all stages with the same outlet width in the predominant part of the characteristic. The differences measured are, in our opinion, the cause of the individual dissimilarity of the individual discharge flow channel components in view of the fact that no systematic dependence along the discharge flow channel was found. The loss coefficient of vaneless diffuser ξ_{24} drops monotonically with increasing flow coefficient and shows a relation typical for friction losses in the whole range of flow coefficients. The value of ξ_{24} in the narrower stages is about four times as high as that of the wider ones. Similar relation was found at the ξ_{25} curve, where the friction losses from station 4 to 5 and the losses due to flow direction change in the return bend are added. The friction losses are the dominant influence on the total loss, too. But in the region of higher flow coefficients, the ξ_{25} value is nearly constant or rises slightly with increasing φ_{2r} value. This indicates flow separation on the inner bend surface. The loss coefficient of the whole output channel ξ_{27} reached its minimum value at $\varphi_{2r} = 1.2$. The dominant part of total losses in the area of lower φ_{2r} is already due to friction losses. At the higher φ_{2r} values it comes apparently to the flow separation on the pressure side of vane profiles, which causes the total loss coefficient rise. The loss coefficient of the whole output channel ξ_{27} is in the vicinity of the value $\varphi_{2r} = 1$ for the stages A, B, C twice as high as for the wider stages D, E, F. A vast difference between both groups of stages was found in the proportion of the individual stage element losses ξ_{24}, ξ_{25} to the total loss coefficient value ξ_{27}. The vaneless diffuser causes about 50 percent of the total losses in the A, B, C stages while only about 20 percent in the case of the D, E, F stages. This is obviously caused by the higher friction losses in the narrow vaneless diffuser flow passage of the A, B, C stages.

Rotating Stall. It follows from Fig. 9 that the rotating stall in vaneless diffuser occurs in a considerable part of stage characteristics. In the narrower and/or wider stages one and/or two zones of rotating stall between the dynamic and static stability limits were found on characteristic (Cyrus and Šprinc, 1993). Relative frequency of static pressure fluctuations in diffuser due to rotating stall was in the range of $f/f_{rev} = 0.07 - 0.12$ for all six investigated stages. Relative amplitude of static pressure B_k at the diffuser inlet was higher approximately by 20–40 percent than that at the station v in the return bend. Figure 15 shows the dependence of relative amplitude B_k on the volume flow rate Q between the static and dynamic stability limits of stage characteristics for stages C and F with different channel width. It is apparent that the relative amplitude B_k has not changed significantly in the considered range of volume flow rate Q for the compressor stage with the narrow channel. On contrary, in the case of compressor stage with wider channel, one can observe strong dependency. This effect can be explained by the damping effect of channel flow in narrower diffuser. The maximum value of static pressure relative amplitude B_k near the surge point (static stability limit) in stage C and/or F was found $B_k = 11$ percent and/or 14 percent. Similar results were obtained at other investigated stages.

Diffuser rotating stall occurs when there is a local return flow in the diffuser. Using the boundary layer method, Senoo and Kinoshita (1977) calculated the inlet flow conditions for which there will be rotating stall, because of local return flow in the boundary layer. Results are summarized in Fig. 16 and show a dependence of critical inlet flow angle on relative diffuser width (Braembussche, 1982). Our experimental data are marked in Fig. 16, too. As diffuser inlet we considered station k (Fig. 4). The differences between our experimental data and the theoretical curve are caused by the fact that Senoo's theoretical assumption on uniform radial velocity distribution at diffuser inlet is not fulfilled. The flow field at impeller outlet is apparently distorted.

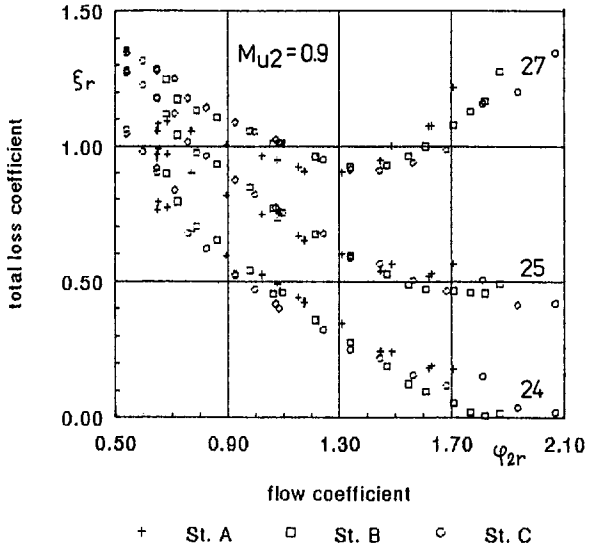

Fig. 14(*a*) Output section loss coefficient of stages A, B, C

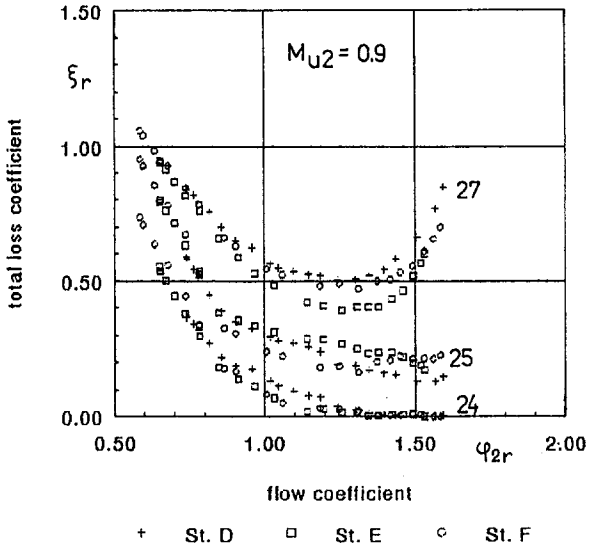

Fig. 14(*b*) Output section loss coefficient of stages D, E, F

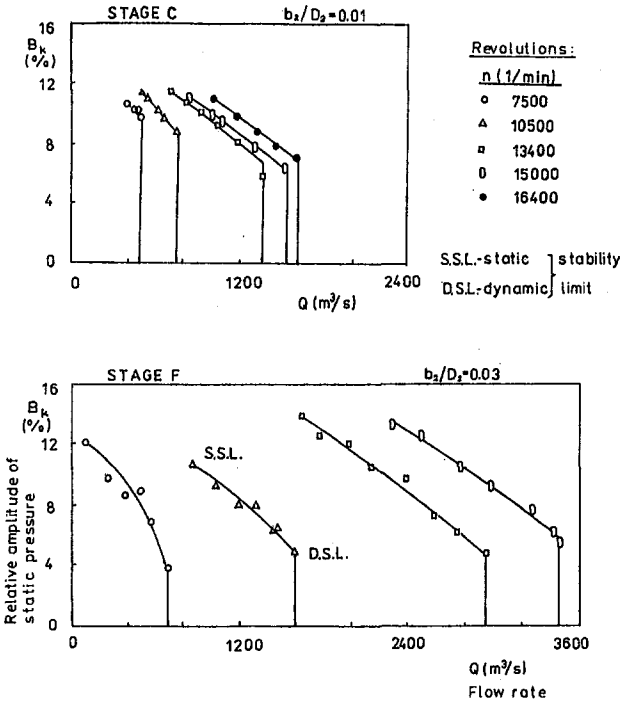

Fig. 15 Relative amplitude of static pressure versus flow rate

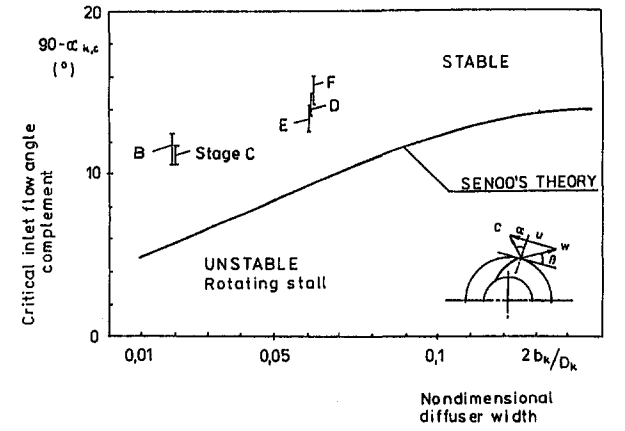

Fig. 16 Critical inlet flow angle complement versus nondimensional diffuser width

Conclusions

We can summarize the main results reached into the following statements:

1 The phenomena governed by the viscosity of the compressed gas have a dominant influence on the aerodynamic performance of all stage elements in view of the fact of extremely narrow flow passages, especially in stages with relative width 0.01.

2 The estimated impeller efficiency of the stages with $b_2/D_2 = 0.01$ was about 30 percent lower than for the stages with $b_2/D_2 = 0.03$ due to large amount of friction losses in the narrow flow channels. As we expected, the impeller efficiency decreases with increasing inlet hub to outlet diameter ratio because of the greater deceleration in the impellers with greater d_0/D_2 ratio. This efficiency drop was larger in the group of narrower impellers.

3 The values of the slip factor in the wider stages have generally been found lower than those from the Wiesner's formula. For the narrower impellers, the slip factor value is nearly independent of the flow coefficient in the dominant part of the characteristic while it decreases monotonously for the wider ones. It seems to be connected with different character of flow pattern in the impellers.

4 Total pressure loss coefficient value of the whole output passage of the stages with $b_2/D_2 = 0.01$ is nearly twice as high as that of the larger stages. The portion of the losses in vaneless diffuser from the whole stator loss in narrower stages is approximately 2.5 times higher as in the wider ones.

5 The rotating stall in vaneless diffuser with relative frequency of pressure fluctuations $f/f_{rev} = 0.07-0.12$ was indicated in a considerable part of the characteristics. The pressure fluctuations in wider stages are more intensive than those in narrower stages. The theoretical prediction method of the rotating stall onset by Senoo and Kinoshita (1977) does not give good results for our stages.

The results presented contributed to our knowledge of performance of low flow coefficient stages. The experimental results obtained also made it possible to assess and to calibrate the performance prediction method used for the aerodynamic design of the subjected stages. The method was verified by a direct comparison of the predicted and test results for stages A, B, C. It has been shown to be necessary to correct the slip factor and to increase the friction coefficient artificially in comparison with the value corresponding to the hydraulic smooth flow channel. After the correction, the results of the prediction were in acceptable agreement with test results. It is to be expected that a future design of new stages or optimization of the already existing ones will not require such detailed experimental investigations. However, the design assessment or the dominant flow effects identification are impossible without further experimental research.

Acknowledgments

The authors would like to thank the ČKD Kompresory, a.s. for permission to publish this paper and many colleagues from the both participating institutions, especially Mr. L. Laštovka and Mr. V. Daněk, who initiated this program.

References

Adler, D., 1980, "Status of Centrifugal Impeller Internal Aerodynamics. Part II: Experiments and Influence of Viscosity," ASME *Journal of Engineering for Power,* Vol. 102, July.

Benvenuti, E., 1972, "Research on Centrifugal Compressor Stages for Low Flow Coefficients," *Quaderni Pignone,* Vol. 15, pp. 11–19.

Braembussche, R. V. D., 1982, "Rotating Stall in Vaneless Diffusers of Centrifugal Compressors," VKI Technical Note 145.

Casey, M. V., Dalbert, P., and Shurter, E., 1990, "Radial Compressor Stages for Low Flow Coefficients," *IMechE 1990,* C403/004, pp. 117–126.

Cyrus, V., and Šprinc, M., 1993, "Nonsteady Flow Investigation in Radial Compressor Stages With Very Low Flow Rate," SVÚSS Int. Report [in Czech].

Daily, J. W., and Nece, R. E., 1960, "Chamber Dimension Effects on Induced Flow and Frictional Resistance of Enclosed Rotating Disks," ASME *Journal of Basic Engineering,* Vol. 82, pp. 217–232.

Japikse, D., 1987, "A Critical Evaluation of Three Centrifugal Compressors With Pedigree Data Sets," ASME JOURNAL OF TURBOMACHINERY, Vol. 109, pp. 1–9.

Koizumi, T., 1983, "Experimental Studies on Performance of Centrifugal Compressors With Very Small Flow Coefficient," *Mitsui Zosen Technical Review,* Vol. 117, pp. 28–39 [in Japanese].

Nece, R. E., and Daily, J. W., 1960, "Roughness Effects on Frictional Resistance of Enclosed Rotating Disks," ASME *Journal of Basic Engineering,* Vol. 82, pp. 553–562.

Paroubek, J., Šťastný, M., and Král, K., 1989, "Aerodynamic Performance of Radial Compressor Stage With Very Low Flow Rate," SVÚSS Int. Report [in Czech].

Platt, M., 1981, "Computerized Compressor Design," *Turbomachinery International,* May–June.

Rodgers, C., 1978, "A Diffusion Factor Correlation for Centrifugal Impeller Stalling," ASME *Journal of Engineering for Power,* Vol. 100.

Senoo, Y., and Kinoshita, Y., 1977, "Influence of Inlet Flow Conditions and Geometries of Centrifugal Vaneless Diffusers on Critical Flow Angles for Reverse Flow," ASME *Journal of Fluids Engineering,* Vol. 99, pp. 98–103.

Velocity Measurements Downstream of the Impellers in a Multistage Centrifugal Blower

G. L. Arnulfi
Istituto di Fisica Tecnica
e di Tecnologie Industriali,
Università di Udine,
Udine, Italy

D. Micheli
Dipartimento di Energetica,
Università di Trieste,
Trieste, Italy

P. Pinamonti
Istituto di Fisica Tecnica e di
Tecnologie Industriali,
Università di Udine,
Udine, Italy

The paper presents the results of an experimental investigation on a four-stage centrifugal blower, having the aim of obtaining an accurate description of the flow field behind the impellers in several operative conditions and for different geometric configurations. Actually, the test plant allows one to change the turbomachinery characteristics assembling one, two, three, or four stages and three different types of diffuser. In this first research step, the blower has been tested in the four-stage vaneless diffuser configuration. The unsteady flow field behind the impellers and in the diffusers has been measured by means of a hot-wire anemometer. A phase-locked ensemble-averaging technique has been utilized to obtain the relative flow field from the instantaneous signals of the stationary hot-wire probes. Several detailed measurement sets have been performed using both single and crossed hot-wire probes, to obtain the velocity vectors and turbulence trends, just behind the blower impellers and in several radial positions of the vaneless diffusers. These measurements have been done at different flow rate conditions, covering unsteady flow rate phenomena (rotating stall) also. The results obtained allowed us to get a detailed flow field analysis in the multistage centrifugal blower, in relation to the geometric configuration and to the differing operating conditions.

Introduction

The detailed study of the flow field in centrifugal turbomachines is essential to an exact understanding of the links existing among the geometric characteristics of the machine, the flow within the same, and its performances in order to be able to enhance the machine's project.

Along with the application of improved computational fluid dynamics codes for the solution of flow in turbomachines, great importance is still attached to the development of experimental measurement techniques, both with the aim of testing the results of CFD codes and to describe the functioning of these machines in detail.

The dramatic developments in the field of computers in recent years have brought significant improvements in the experimental measurement techniques used to this aim, both in terms of measurement instrumentation and of data acquisition and data processing systems; at present large quantities of data can be collected and processed to an extent that was previously unimaginable.

Apart from direct internal flow measurement techniques within the rotating blade channels, other conventional techniques are based on stationary probes positioned just at the impellers' inlet or outlet and in the turbomachine diffusers.

The equipment extensively used to measure the instantaneous velocity field includes laser anemometer (Fradin and Janssens, 1990; Rohne and Banzhaf, 1991; Flack et al., 1987; Eckardt, 1976; Krain, 1981) and hot-wire anemometry (HWA), in particular to study the flow in pumps (Flack et al., 1987), often tested with air (Ubaldi et al., 1993; Jaberg and Hergt, 1989), fans (Cau et al., 1987; Raj and Swim, 1981), blowers (Höfler et al., 1988; Jansen, 1964; Kinoshita and Senoo, 1985; Jiang et al., 1989) and compressors with measurements limited to the flow at the impeller outlet (Olivari and Salaspini, 1975; Ishida et al., 1990; Ligrani et al., 1983; Dickmann, 1972) or in vaned diffusers (Fradin and Janssens, 1990; Inoue and Cumpsty, 1984) or in vaneless diffusers also (Eckardt, 1975; Maksoud and Johnson, 1989; Frigne and Van Den Braembussche, 1984; Kämmer and Rautenberg, 1986).

Different techniques have been applied using HWA with stationary probes in centrifugal turbomachines:

- single-wire probes with fixed positioning in order to obtain the velocity's intensity (Jansen, 1964; Dickmann, 1972; Frigne and Van Den Braembussche, 1984; Kinoshita and Senoo, 1985; Jiang et al., 1989; Ubaldi and Zunino, 1990);
- single-wire probes with several subsequent positioning in order to assess two velocity components (Olivari and Salaspini, 1975; Eckardt, 1975; Höfler et al., 1988; Jaberg and Hergt, 1989; Ishida et al., 1990; Raj and Swim, 1981; Inoue and Cumpsty, 1984) or three velocity components (Ubaldi et al., 1993) and associated turbulence components;
- two-wire *X* probes with fixed positioning for the assessment of a bidimensional velocity field (Ligrani et al., 1983);
- two-wire *X* probes with several subsequent positioning in order to assess a tridimensional velocity field (Cau et al., 1987);
- three-wire probes in order to assess the three velocity components and the six turbulence components simultaneously (Maksoud and Johnson, 1989).

Clearly, each of above-mentioned techniques presents some advantages and some disadvantages (Lakshminarayana, 1981), that have to be evaluated to find the most suitable solution.

This paper deals with the experimental measurements performed on a very interesting centrifugal turbomachine model as it offers the possibility of varying its geometric configuration (number of stages, varying from one to four, and three different configurations of the diffusers).

Contributed by the International Gas Turbine Institute and presented at the 39th International Gas Turbine and Aeroengine Congress and Exposition, The Hague, The Netherlands, June 13–16, 1994. Manuscript received by the International Gas Turbine Institute February 1994. Paper No. 94-GT-41. Associate Technical Editor: E. M. Greitzer.

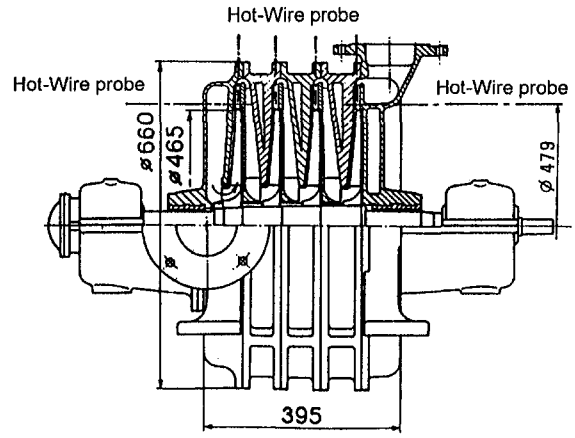

Fig. 1 Test blower and measuring sections

Table 1 Geometric data

IMPELLER		
inlet diameter	160	mm
outlet diameter	465	mm
inlet axial span	23	mm
outlet axial span	8	mm
inlet blade angle	35	°
outlet blade angle	67	°
number of blades	16	
DIFFUSER		
inlet diameter	467	mm
outlet diameter	570	mm
axial span	10	mm

Since this is a multistage machine it offers the possibility of getting a detailed insight of the flow field in the different stages and of comparing these data in different operating conditions.

The aim of this research is to describe the flow within the machine in great detail and possibly to link its characteristic to the particular geometric configuration and performance.

Experimental Procedure

Test Rig and Operating Conditions. Experiments were carried out at the Laboratory of the Dipartimento di Energetica, University of Trieste on the modular centrifugal blower. In this investigation the four-stage set was used; all the stages are identical geometrically, with 16-bladed shrouded impellers and vaneless diffusers with parallel straight walls (Fig. 1). More geometric features are shown in Table 1.

The impeller was driven by a DC motor coupled to a speed increasing gear. The blower operated in open circuit: the air flow entered through a radial inlet pipe. The blower characteristics for the design rotational speed of 3000 rpm are shown in Fig. 2 and the test conditions are pointed out. The design condition is: flow coefficient $\varphi = 0.0065$, pressure coefficient $\psi = 0.44$, power coefficient $\lambda = 0.0085$, efficiency $\eta = 0.33$ (gear mechanical losses and lubricating power included). The flow is stalled for flow coefficient less than 0.0040. The measurements were performed at four stable and four unstable conditions (Table 2).

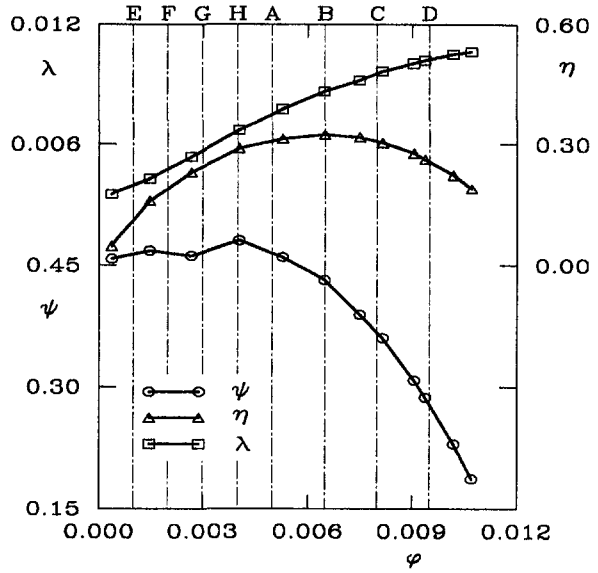

Fig. 2 Performance map of the test blower

Table 2 Investigated operating conditions

	E	F	G	H	A	B	C	D
φ	0.0010	0.0020	0.0030	0.0040	0.0050	0.0065	0.0080	0.0095

Instrumentation and Measuring Technique. Mass flow rate was measured by an orifice flow meter and controlled by a throttling valve in the discharge pipe. Pressures were measured

Nomenclature

b = diffuser axial span
C = absolute velocity
c = fluctuation of the absolute velocity
D = diameter
$\dot{m}$ = mass flow rate
N = number of signals acquired in each point
P = shaft power
PS = pressure side
R = radius
SS = suction side
T = nondimensional velocity fluctuation intensity = $[\sum_N c^2/(N-1)]^{0.5}/C$
Tu = nondimensional tangential Reynolds stress component = $[\sum_N u^2/(N-1)]^{0.5}/C$
Tv = nondimensional normal Reynolds stress component = $[\sum_N v^2/(N-1)]^{0.5}/C$
Tuv = nondimensional shear Reynolds stress component = $[\sum_N uv/(N-1)]/C^2$
t = circumferential blade pitch at the impeller exit
U = impeller peripheral velocity
u = velocity fluctuation component tangential to average velocity
v = velocity fluctuation component normal to average velocity
W = relative velocity
W_s = specific work
x = axial coordinate
y = circumferential coordinate
α = absolute flow angle related to tangential direction
β = relative flow angle related to tangential direction
η = efficiency = $\dot{m}W_sP^{-1}$
λ = power coefficient = $P\rho^{-1}\omega^{-3}D_2^{-5}$
ρ = air density (inlet conditions)
φ = flow coefficient = $\dot{m}\rho^{-1}\omega^{-1}D_2^{-3}$
ψ = pressure coefficient = $W_s\omega^{-2}D_2^{-2}$
ω = impeller angular velocity, rad/s

Subscripts

2 = impeller exit
r = radial

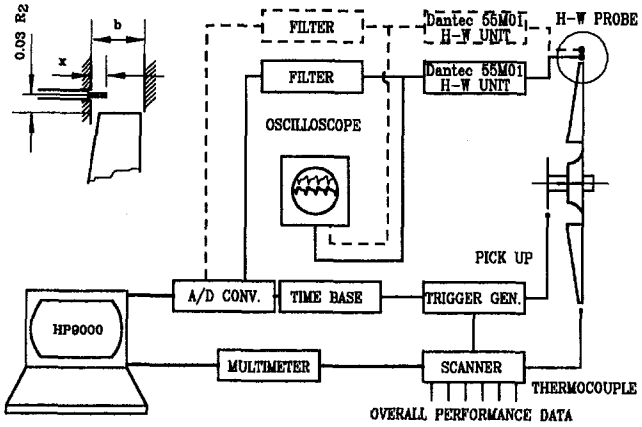

Fig. 3 Schematic of experimental rig

by variable inductance transducers, temperature by type K thermocouples, torque by a load cell, and rotational speed by a magnetic pick-up indicator.

Flow measurement was performed by a constant-temperature hot-wire Dantec anemometer, both with single (55P11) and X-wire (55P62) straight miniature probes. The sensors were tungsten wires, of 5 μm diameter and 1.25 mm length. Two hot-wire units (55M01) with standard bridge (55M10) were used and a low-pass filter at 10 kHz was applied to cut high-frequency noise, the base frequency being 800 Hz (blade passage). The hot-wire instantaneous voltage signals were sent to an analog/digital converter board. The phase reference was taken off by the pick-up device through a time base that provided the trigger signal. The data acquisition system (HP6900) was controlled by a HP9000 computer (Fig. 3).

Every probe was calibrated in a Disa 55D45 unit using a technique that was described in detail by the authors in a previous paper (1993). By composing the King law with a parabolic directional sensitivity law, a calibration surface (voltage in function of velocity intensity and flow angle) was obtained for each wire.

The coefficients of the calibration surface were corrected, in order to take into account the temperature effect, according to the Collis and Williams model (1959), with the fluid properties evaluated according to Morrison (1974).

After calibrating probes a check was done by sample stationary flows (velocity from 60 to 80 m/s, flow angle within the 40 deg allowable calibration zone): mean errors equal to 0.75 percent on velocity and 1 deg on angle approximately were found, with maxima (1.9 percent and 2 deg, respectively) located at the borders of the angular range.

A stationary hot-wire technique for rotor exit flow measurement was used. The phase-locked ensemble-averaging technique (Lakshminarayana and Poncet, 1974; Lakshminarayana, 1981) was adopted for stable operating conditions and 120 records (40 circumferential locations for each of three blade-to-blade channel) were taken on $N = 300$ consecutive revolutions.

Probes were located within the diffusers both radially, at several different distances from the machine axis, and axially, at a distance of 3 percent of the outlet radius from the impeller exit.

When the probe was radially placed, a fixed orientation was adopted and the single wire was set parallel to the machine axis in order to be normal to absolute velocity (in fact negligible axial component was supposed, because of the aspect ratio of the channel). This radial set was used to measure the intensity of the velocity vector and the flow decay downstream of the impeller in the diffusers of all the stages.

On the contrary with probes axially placed, at the outlet of the first and fourth impeller, bidimensional flow measurements

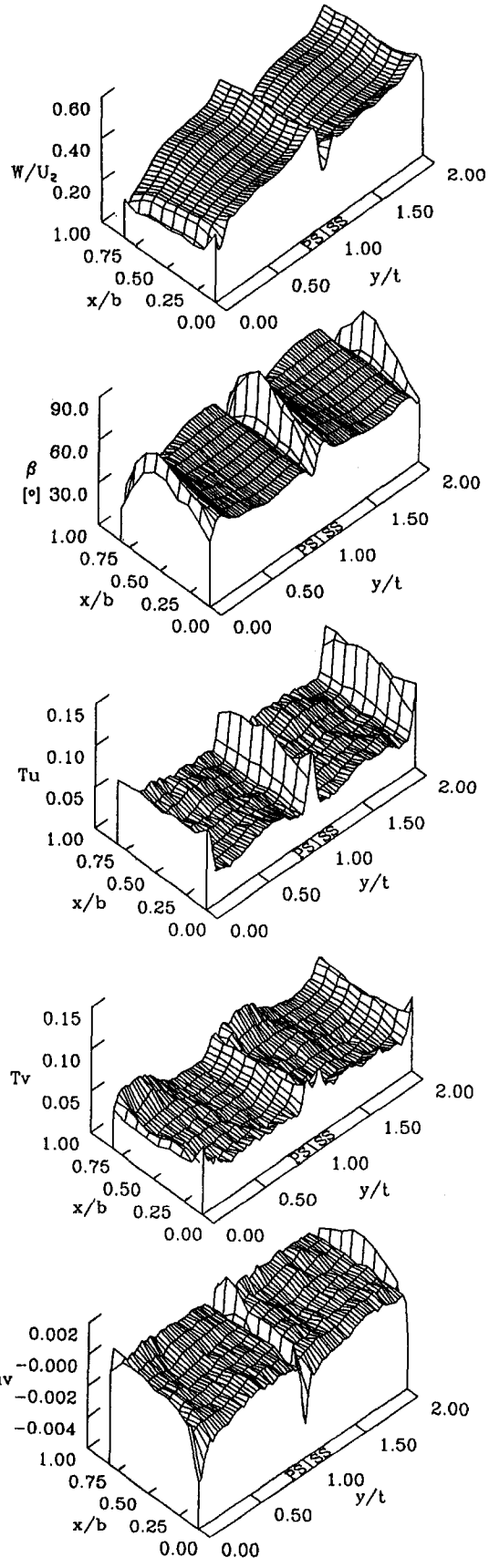

Fig. 4 Flow pattern in the first stage at nominal conditions (φ = 0.0065)

were done, adopting two different techniques to obtain the velocity vector and the Reynolds stress tensor on the blade-to-blade plane; a triple orientation technique with single-wire

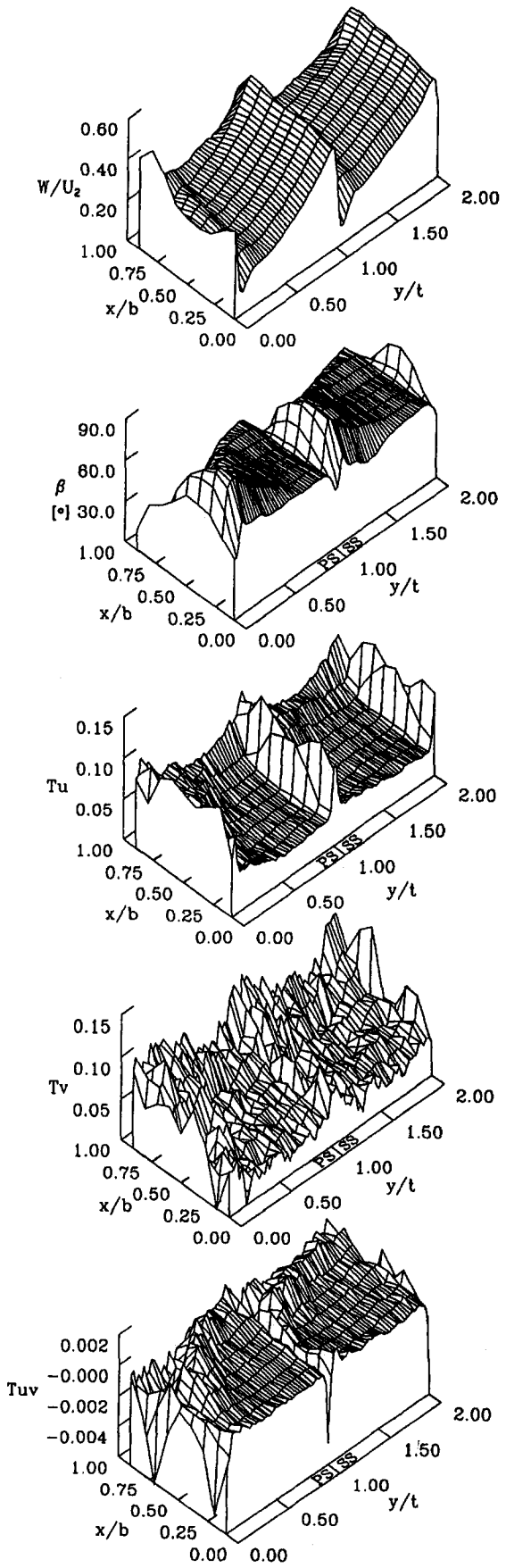

Fig. 5 Flow pattern in the fourth stage at nominal conditions (φ = 0.0065)

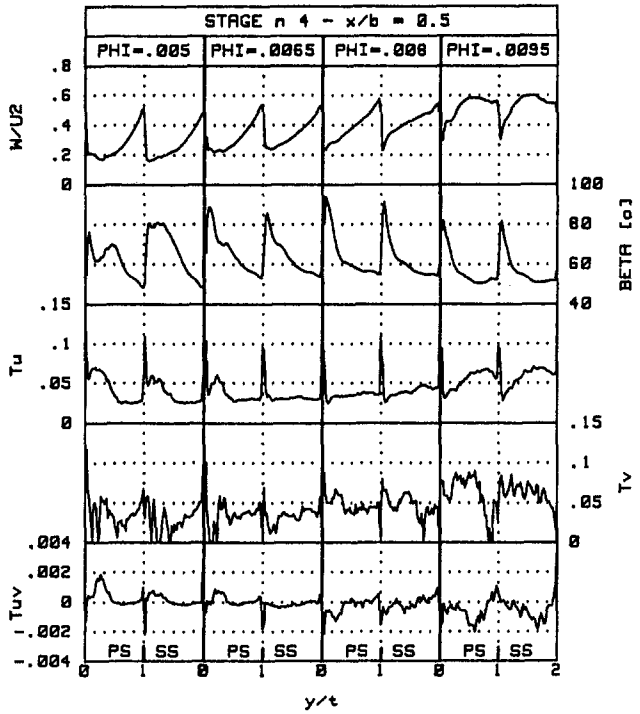

Fig. 6 Blade-to-blade profiles of flow parameters: comparison among different flow rates (stage No. 4: x/b = 0.5)

probe (Olivari and Salaspini, 1975), and a fixed orientation technique with X-wire probe.

To have a significant description of the flow field, in the first stage the X-wire probe were used, in order to obtain a more accurate measurement of Reynolds stress.

Since in the fourth stage the flow field was found not to be bidimensional, but to show zones with considerable axial gradients (above all near the hub), the triple orientation single-wire probe technique was considered more correct in order to obtain the complete velocity vector field.

In fact, the two wires of the X-wire probes should not be too close in order to avoid reciprocal disturbance (Nagano and Tsuji, 1993), but on the other hand they have to perform essentially a point measurement that is possible only in bidimensional flows.

During X-wire probe measurements, the probe orientation was accurately set to minimize the aerodynamic disturbances caused by the tips of wire supports.

Experimental Results

Stable Flow Conditions. Following is a description of the results of measurements carried out with blower in stable op-

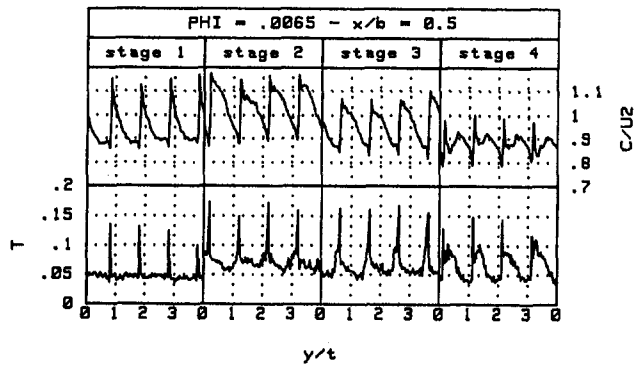

Fig. 7 Blade to blade profiles of flow parameters at x/b = 0.5: comparison among the four stages at nominal conditions (φ = 0.0065)

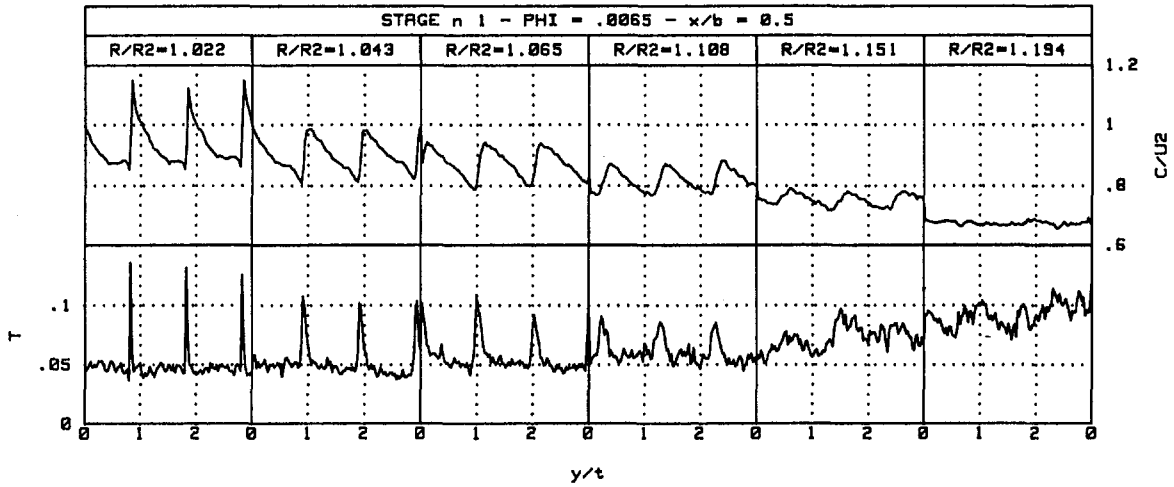

Fig. 8 Flow parameter traces in the first stage diffuser at $x/b = 0.5$: comparison among differing radial position, at nominal conditions ($\varphi = 0.0065$)

erating conditions (A, B, C, D), at the design rotational speed of 3000 rpm, by ensemble-averaged velocity measurements.

Figures 4 and 5 show the conditions of the flow at the outlet of the first and fourth stage, respectively, at the radial position $R/R_2 = 1.03$, at nominal flow rate B ($\varphi = 0.0065$).

Relative velocity W/U_2, relative flow angle β, and turbulent Reynolds stress tensor components Tu, Tv, Tuv are represented as a function of the axial position x/b (0 = shroud, 1 = hub) and of the circumference coordinate y/t for two consecutive blade-to-blade channels (first channel 0 = *SS*, 1 = *PS*).

From a detailed analysis of the outlet flow at the first stage (Fig. 4) very uniform hub-to-shroud trends can be noted both in terms of velocity and turbulence in accordance with Gyarmathy et al. (1991), whereas no gradual variation between hub and shroud as reported by Olivari and Salaspini (1975) and Ishida et al. (1989), nor a wake area near the shroud as reported by Rohne and Banzhaf (1991) could be noted.

Instead relative velocity increases rather regularly in circumference direction from *SS* to *PS*, with a clear discontinuity in correspondence with blade passages; similar trends were reported by Inoue and Cumpsty (1984) and Flack et al. (1987).

The relative flow angle decreases sharply after the *SS*, remaining almost constant in the blade channel and decreasing again at the *PS*.

The turbulence components remain approximately constant and show rather low values for most of the blade channel, with high peaks or remarkable discontinuities in correspondence to blade passages. Therefore, a clear area of higher turbulence could not be noted in proximity of the *PS* as reported by Maksoud and Johnson (1989).

Flow conditions are markedly different at the outlet of the fourth stage (Fig. 5). In the hub-to-shroud direction there are marked differences in the area near the hub showing a higher relative velocity, a lower relative angle, and generally quite higher turbulence components, in accordance with data reported by Maksoud and Johnson (1989). However, relative velocity gradually increases in the blade-to-blade plane from *SS* to *PS* as in the first stage, although a lower relative velocity area may be pointed out near *SS* shroud as reported by Ubaldi et al. (1993) and Eckardt (1975).

The relative angle in the fourth stage presents lesser variations in the entire channel, while the turbulence components highlight an area with higher turbulence near the *SS* hub end. As far as turbulence is concerned, it should be kept in mind that, according to the experience of authors, the different measurement technique (the single-wire probe instead of the two-wire one), can lead to greater errors and represents an obstacle to a really homogeneous comparison with the first-stage results.

A comparison among the different flow rates (A, B, C, D) is summarized in Fig. 6 showing the conditions of the outflow from the fourth stage at a mean axial position ($x/b = 0.5$) and at the radial position $R/R_2 = 1.03$ again.

The trends of the relative velocity show a regular increase from *SS* to *PS* for low and medium flow rates, while a peak area is to be pointed out at the channel center at $\varphi = 0.0095$. A similar situation was reported for a centrifugal compressor by Inoue and Cumpsty (1984).

As regards the relative angle, high values can be noted at $\varphi = 0.0050$ right after the *SS*, while with high flow rates β rapidly decreases after the *SS* and remains around low values in the central part of the blade channel.

The flow turbulence is characterized by higher values of the Tu component near the *PS* for high flow rates, as measured by Olivari and Salaspini (1975), while at low flow rates an area of higher turbulence can be noted near the *SS*. In these conditions the occurrence of a wake area near the *SS* can be hypothesized, which is characterized by low velocity and high turbulence (Ubaldi et al., 1993; Eckardt, 1975).

The different flow conditions at the outlet of the four impellers are compared in Fig. 7 with reference to the nominal flow rate (B).

These results refer to measurements carried out with the single-wire probe radially located and report the absolute velocity C/U_2 and its fluctuation intensity T, in the mean $x/b = 0.5$ section at a 5 mm radial distance from the trailing edge ($R/R_2 = 1.022$). Remarkably different trends can be reported:

- In the first stage velocity rapidly decreases at the *SS* and the values of velocity fluctuation are low in the entire blade-to-blade channel;
- In the second and third stages velocity decreases gradually from *SS* to *PS*, with more discontinuous and in average higher fluctuation values;
- In the fourth stage the absolute velocity decreases sharply after the *SS* showing its relative maximum at the center of the channel, with high fluctuation values near the *SS*, as already shown in Fig. 6 with the turbulence components.

In order to have a picture of the flow trend in the diffusers, Fig. 8 represents the trends of C/U_2 and T measured in correspondence with different radial positions in the first-stage diffuser.

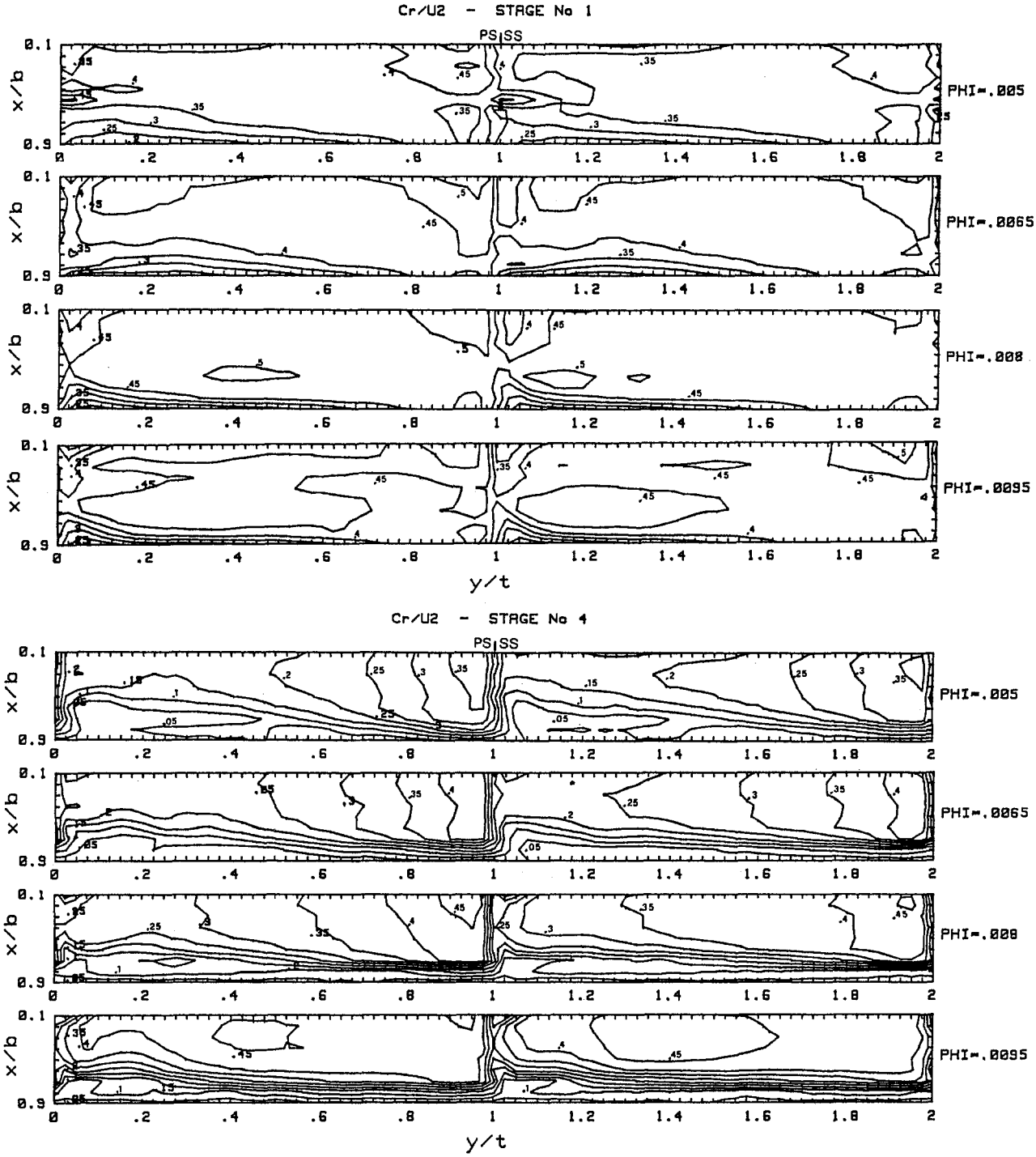

Fig. 9 Isolines of the radial velocity at the first and fourth impellers exit: comparison among different flow rates

These measurements, referring to nominal conditions, were carried out with the single-wire probe radially located to the mean hub-to-shroud position ($x/b = 0.5$), at a distance from the impeller exit varying from a minimum of 5 mm ($R/R_2 = 1.022$) to a maximum of 45 mm ($R/R_2 = 1.194$). The diagram points out the following progressive changes with the increasing radius: decrease of the velocity mean value, decrease in the velocity variation due to the blade passage, circumferential shift of these velocity variations, increase of the fluctuation mean value, decrease of the fluctuation peaks in correspondence with the blade passage.

Similar trends referring to the fluctuation with varying radius are reported by Maksoud and Johnson (1989). In conclusion it can be noted that at a maximum 45 mm distance ($R/R_2 = 1.194$) from the impeller exit, the trend of velocity is only slightly influenced by the blade passage (velocity differences less than 6 percent), with an almost constant fluctuation value around 10 percent.

The flow field can be alternately shown by a representation of the radial isovelocity lines in the section considered; Fig. 9 takes into consideration the conditions at the first and fourth impeller exit.

An analysis of the situation at the first stage still indicates a regular outflow both with varying y/t and x/b coordinates. Only a restricted low radial velocity area can be pointed out near the hub *SS*, which can be clearly noted at high flow rates; thus

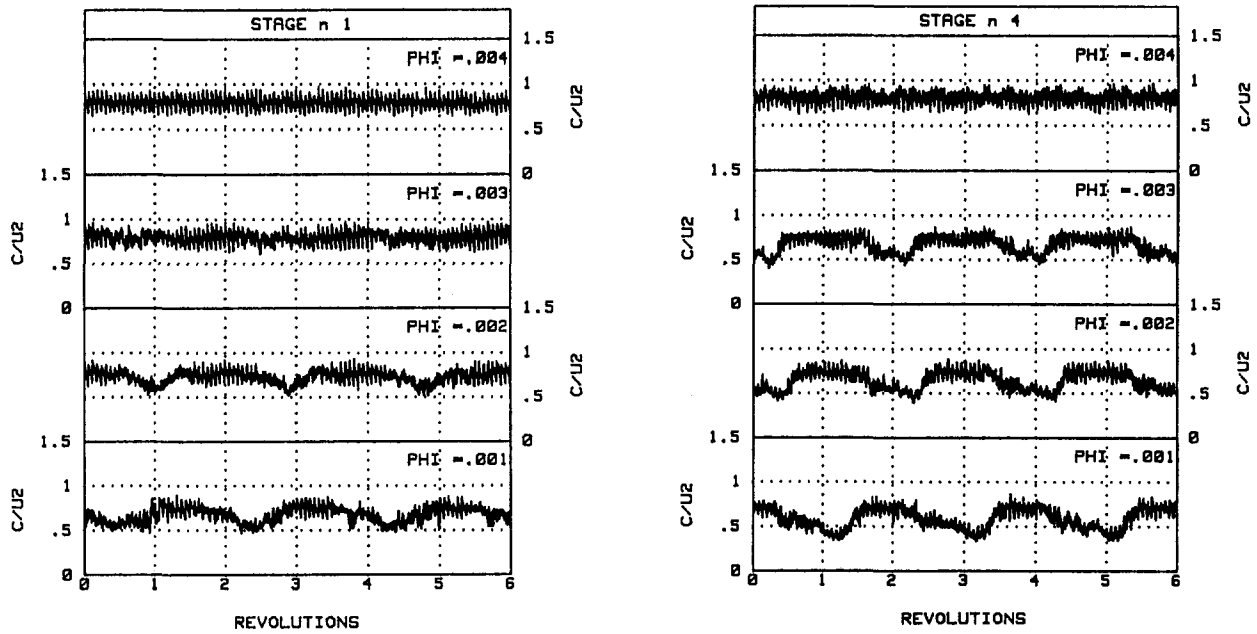

Fig. 10 Velocity traces at the impellers exit in unsteady flow conditions (x/b = 0.5)

there is not a clear wake area in proximity of *SS* at low flow rates as normally happens with compressors (Inoue and Cumpsty, 1984; Gyarmathy et al., 1991; Johnson and Moore, 1983), but greater velocity gradients at high flow are to be noted, as reported by Maksoud and Johnson (1989), and in any case in the area near the hub (Jaberg and Hergt, 1989).

On the contrary, the situation is substantially different in the fourth stage where there are considerable velocity gradients passing from the hub to the shroud; an extended low-velocity area clearly appears near the hub at high flow rates (Jaberg and Hergt, 1989), which is present however also at low flow rates near *SS*. Higher turbulence values correspond to these low radial velocity areas (Figs. 5 and 6).

Unstable Flow Conditions. The subsequent phase has been a study of the trends of instantaneous velocity at the impellers' outlet in unstable conditions in order to observe the modifications of the flow with a diminishing flow rate. All the tests were carried out at nominal rotational speed (3000 rpm). The *X* hot-wire probe was placed axially at the outlets of the first and fourth impellers at an intermediate position (x/b = 0.5), obtaining directly the value of the instantaneous velocity vector in the blade-to-blade plane along all blade channels (40 measurement points for each channel) for N = 32 consecutive revolutions.

Spectral analysis of the velocity signals was performed to gain quantitative information on the frequency characteristics of the observed flow instabilities, using the FFT technique.

Figure 10 shows the trend of instantaneous velocity at the outlet of both the stages for the four flow coefficient values considered (E, F, G, H) starting at φ = 0.0040, that had been already selected as transition value in unstable conditions (Fig. 2).

An analysis of Fig. 10 points out the occurrence of a low-frequency oscillation starting at φ = 0.0030 in the first stage, but just perceptible from φ = 0.0040 in the fourth stage, in which the wave amplitude is greater than in the first one for all the flow rates considered. In both cases this oscillation persists and becomes higher with decreasing flow rate, showing a periodic pattern—corresponding to two impeller rotations approximately—characterizing the presence of the rotating stall (Kinoshita and Senoo, 1985; Ubaldi and Zunino, 1990; Kämmer and Rautenberg, 1986).

Figure 11 shows the corresponding results obtained by means of FFT analysis and reports the power spectra as a function of the frequency made dimensionless in respect to the base rotation frequency of the impeller. Data reported for φ = 0.0040 present a very low uniform background noise. The complete spectra, not reported in the figure, show only the harmonics of the 16 frequency ratio corresponding to the number of blades. From φ = 0.0030 a peak can be observed that is to be attributed to the stall at a frequency equal to one half of the base frequency approximately. With decreasing flow rate this frequency does not change, while the amplitude of the local disturbance is slightly increasing. In the fourth stage amplitudes are always greater than in the first stage, and a harmonic of a higher order can be observed.

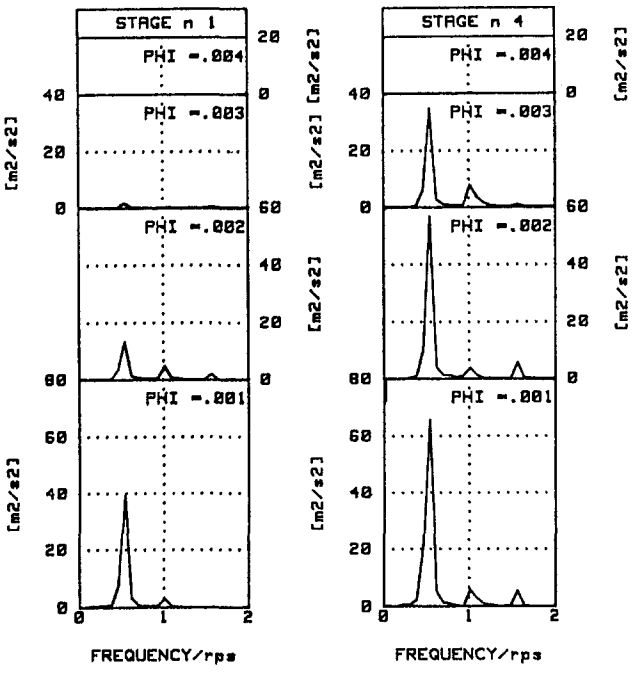

Fig. 11 Power spectra of the velocity at the impeller exit (x/b = 0.5)

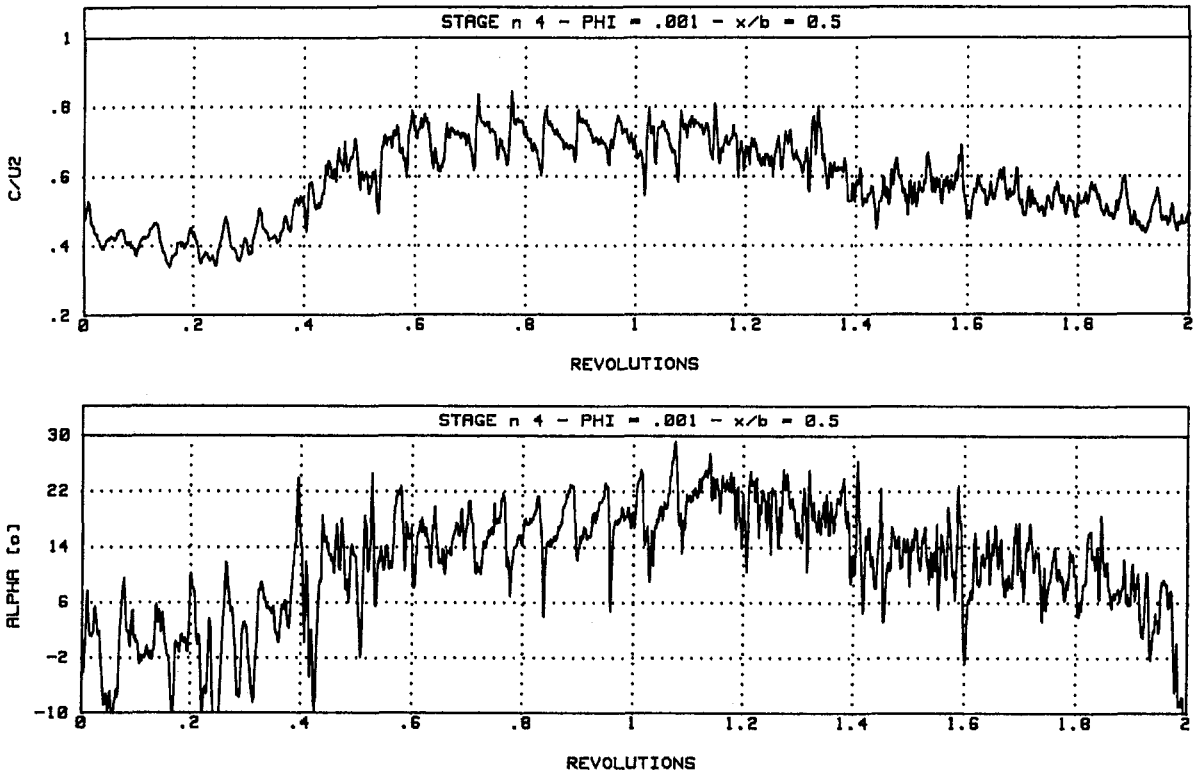

Fig. 12 Absolute velocity and flow angle traces at the fourth impeller exit at x/b = 0.5 at unsteady flow condition (φ = 0.0010)

In order to analyze the flow characteristics in greater detail in these unstable conditions, Fig. 12 shows the absolute velocity intensity trends and its angle for two revolutions only referring to the lower flow rate (φ = 0.0010). Substantial differences can be noted according to the position on the instability wave:

- In the area of the minimum mean velocity (abscissa = 0–0.3) instantaneous velocity tends to increase, passing from *SS* to *PS* with a corresponding marked decrease of the angle, which reaches negative values (reverse flow);
- In the area of increasing mean velocity (abscissa = 0.3–0.65) irregular trends can be noted both for the module and for the angle, with marked oscillations within the blade channels;
- In the area of mean maximum velocity (abscissa = 0.65–1.15) trends similar to those observed in stable conditions can be noted, with a decrease of C from *SS* to *PS* and a corresponding increase of α;
- In the area of decreasing mean velocity (abscissa = 1.15–2) irregular trends with strong oscillations occur again.

Conclusions

The instantaneous flow at the outlet of the impellers of a multistage centrifugal blower has been measured and analyzed in detail at different operating conditions, using a hot-wire anemometer with stationary probes.

With varying flow rates, remarkable differences in the trends of velocity and of turbulence in the blade-to-blade plane could be observed.

Significant differences have been observed for the different stages, particularly the first, intermediate, and fourth one, the latter presenting a flow separation zone in the channel near *SS*.

Moving away from the impeller, the blade passage influence decreases rapidly, reaching almost uniform velocity at the diffuser outlet, but with strong turbulence.

The flow at the outlet of the first impeller is sensibly bidimensional and presents gradual variations from *SS* to *PS* with perceptible gradients only in correspondence with the blade passages.

The flow at the outlet of the fourth impeller is less uniform and presents high values from the hub to the center of the channel in progressively extended areas with the decreasing of the flow rate.

The flow does not present the configuration of the potential theory in the blade-to-blade plane. It also does not show the jet and wake flow typical of centrifugal compressors. It has to be noted that the test blower falls right in the transition zone indicated by Adler (1980).

Finally, data were collected also with the flow in unstable conditions, measuring remarkable velocity oscillations due to the presence of the rotating stall.

In these conditions the detailed analysis of the velocity trends in the blade-to-blade plane pointed out opposite trends in the different oscillation zones, with a flow inversion in the area of minimum velocity.

Acknowledgments

The authors would like to thank the MURST (Italian research ministry—60 percent fund) and CNR (Italian research council) for the financial support granted to this research.

References

Adler, D., 1980, "Status of Centrifugal Impeller Internal Aerodynamics—Part II: Experiments and Influence of Viscosity," ASME *Journal of Engineering for Power*, Vol. 102, pp. 738–745.

Arnulfi, G. L., Micheli, D., and Pinamonti, P., 1993, "Velocity and Turbulence Measurements in a Centrifugal Turbomachine by Hot-Wire Anemometer" [in Italian], *Proc. II MisMac Congr.*, Firenze (I).

Cau, G., Mandas, N., Manfrida, G., and Nurzia, F., 1987, "Measurements of Primary and Secondary Flows in an Industrial Forward-Curved Centrifugal Fan," ASME *Journal of Fluids Engineering*, Vol. 109, pp. 353–358.

Collis, D. C., and Williams, M. J., 1959, "Two Dimensional Convection From Heated Wires at Low Reynolds Numbers," *Journal of Fluid Mech.*, Vol. 16, pp. 357–384.

Dickmann, T., 1972, "Hot-Wire Measurements in Flow Behind Rotating Impeller Vanes," *DISA Information*, No. 13, pp. 23–25.

Eckardt, D., 1975, "Instantaneous Measurements in the Jet-Wake Discharge Flow of a Centrifugal Compressor Impeller," ASME *Journal of Engineering for Power,* Vol. 97, pp. 337–346.

Eckardt, D., 1976, "Detailed Flow Investigations Within a High-Speed Centrifugal Compressor Impeller," ASME *Journal of Fluids Engineering,* Vol. 98, pp. 390–402.

Flack, R. D., Hamkins, C. P., and Brady, D. R., 1987, "Laser Velocimeter Turbulence Measurements in Shrouded and Unshrouded Radial Flow Pump Impellers," *Heat and Fluid Flow,* Vol. 8, No. 1, pp. 16–25.

Fradin, C., and Janssens, G., 1990, "Detailed Measurements of the Flow Field at the Outlet of a Backswept Transonic Centrifugal Impeller Equipped With a Vaned Diffuser," *4th Intern. Symposium ASME Cogen-Turbo,* New Orleans, LA, pp. 249–254.

Frigne, P., and Van Der Braembussche, R., 1984, "Distinction Between Different Types of Impeller and Diffuser Rotating Stall in a Centrifugal Compressor With Vaneless Diffuser," ASME *Journal of Engineering for Gas Turbines and Power,* Vol. 106, pp. 468–474.

Gyarmathy, G., Hunzinker, R., and Spirig, M., 1991, "On the Change of Impeller Flow Non-uniformities With Flow Rate in a Centrifugal Compressor," *IMechE,* C423/054, pp. 143–154.

Höfler, E., Sirok, B., and Kompare, M., 1988, "Aerodynamic Development of High Specific Speed Low-Pressure Turboblower," *Int. Conf. on Hydraulic Machinery,* Turboinštitut, Ljublijana (SLO), pp. 55–63.

Inoue, M., and Cumpsty, N. A., 1984, "Experimental Study of Centrifugal Impeller Discharge Flow in Vaneless and Vaned Diffusers," ASME *Journal of Engineering for Gas Turbines and Power,* Vol. 106, pp. 455–467.

Ishida, M., Senoo, Y., Ueki, H., 1990, "Secondary Flow Due to the Tip Clearance at Exit of Centrifugal Impellers," ASME JOURNAL OF TURBOMACHINERY, Vol. 112, pp. 19–24.

Jaberg, H., and Hergt, P., 1989, "Flow Patterns at Exit of Radial Impellers at Part Load and Their Relation to Head Curve Stability," *3rd Joint ASCE/ASME Conf.,* San Diego, CA, pp. 213–225.

Jansen, W., 1964, "Rotating Stall in a Radial Vaneless Diffuser," ASME *Journal of Basic Engineering,* Vol. 86, pp. 750–758.

Jiang Toung, Yuan Zhe, and Li Zhan Liang, 1989, "Flow Fields Behind Centrifugal Impellers," *Dantec Information,* No. 7, pp. 8–9.

Johnson, M. W., and Moore, J., 1983, "The Influence of Flow Rate on the Wake in a Centrifugal Impeller," ASME *Journal of Engineering for Power,* Vol. 105, pp. 33–39.

Kämmer, N., and Rautenberg, M., 1986, "A Distinction Between Different Types of Stall in a Centrifugal Compressor Stage," ASME *Journal of Engineering for Gas Turbines and Power,* Vol. 108, pp. 83–92.

Kinoshita, Y., and Senoo, Y., 1985, "Rotating Stall Induced in Vaneless Diffusers of Very Low Specific Speed Centrifugal Blowers," ASME *Journal of Engineering for Gas Turbines and Power,* Vol. 107, pp. 515–521.

Krain, H., 1981, "A Study on Centrifugal Impeller and Diffuser Flow," ASME *Journal of Engineering for Power,* Vol. 103, pp. 688–697.

Lakshminarayana, B., and Poncet, A., 1974, "A Method of Measuring Three Dimensional Rotating Wakes Behind Turbomachinery Rotors," ASME *Journal of Fluids Engineering,* Vol. 96, pp. 87–91.

Lakshminarayana, B., 1981, "Techniques for Aerodynamic and Turbulence Measurements in Turbomachinery Rotors," ASME *Journal of Engineering for Power,* Vol. 103, pp. 374–392.

Ligrani, P. M., Van Den Braembussche, R., and Roustan, M., 1983, "Measurements in the Vaneless Diffuser of a Radial Flow Compressor," *Heat and Fluid Flow,* Vol. 4, No. 2, pp. 103–106.

Maksoud, T. M. A., and Johnson, M. W., 1989, "Stress Tensor Measurements Within the Vaneless Diffuser of a Centrifugal Compressor," *Proc. Instn. Mech. Engrs.,* Vol. 203, pp. 51–59.

Morrison, G. L., 1974, "Effects of Fluid Property Variations on the Response of Hot-Wire Anemometers," *J. Phys. E: Sci. Instrum.,* Vol. 7, pp. 434–436.

Nagano, Y., and Tsuji, T., 1993, "Recent Developments in Hot- and Cold-Wire Techniques for Measurements in Turbulent Shear Flows Near Walls," in: *Engineering Turbulence Modelling and Experiments 2,* W. Rodi and F. Martelli, eds., Elsevier Science Publishers B. V., pp. 347–361.

Olivari, D., and Salaspini, A., 1975, "Measurement of Velocity Distribution at the Impeller Exit of a Radial Compressor," VKI Technical Note 106.

Raj, D., and Swim, W. B., 1981, "Measurements of the Mean Flow Velocity and Velocity Fluctuations at the Exit of an FC Centrifugal Fan Rotor," ASME *Journal of Engineering for Power,* Vol. 103, pp. 393–399.

Rohne, K. H., and Banzhaf, M., 1991, "Investigation of the Flow at the Exit of an Unshrouded Centrifugal Impeller and Comparison With the 'Classical' Jet-Wake Theory," ASME JOURNAL OF TURBOMACHINERY, Vol. 113, pp. 654–659.

Ubaldi, M., and Zunino, P., 1990, "Experimental Investigation of the Stalled Flow in a Centrifugal Pump-Turbine With Vaned Diffuser," ASME Paper No. 90-GT-216.

Ubaldi, M., Zunino, P., and Cattanei, A., 1993, "Relative Flow and Turbulence Measurements Downstream of a Backward Centrifugal Impeller," ASME JOURNAL OF TURBOMACHINERY, Vol. 115, pp. 543–551.

Off-Design Flow Measurements in a Centrifugal Compressor Vaneless Diffuser

A. Pinarbasi
Department of Mechanical Engineering,
University of Cumhuriyet,
Sivas, Turkey

M. W. Johnson
Department of Mechanical Engineering,
University of Liverpool,
Liverpool, United Kingdom

Detailed measurements have been taken of the three-dimensional velocity field within the vaneless diffuser of a backswept low speed centrifugal compressor using hot-wire anemometry. A 16 percent below and an 11 percent above design flow rate were used in the present study. Results at both flow rates show how the blade wake mixes out more rapidly than the passage wake. Strong secondary flows inherited from the impeller at the higher flow rate delay the mixing out of the circumferential velocity variations, but at both flow rates these circumferential variations are negligible at the last measurement station. The measured tangential/radial flow angle is used to recommend optimum values for the vaneless space and vane angle for design of a vaned diffuser.

Introduction

The performance of centrifugal compressor diffusers is highly dependent on the flow delivered from the impeller. Measurements from, for example, Krain (1988) and Farge and Johnson (1992) demonstrate that this flow is highly nonuniform and exhibits strong secondary flows. Distinct jet and wake flow regions are observed with the wake on the shroud and the jet near the hub. A strong passage vortex exists that originates in the impeller due to secondary flows. In the diffuser the impeller blade wakes are added to this already complex three-dimensional flow.

The development of these complex flows in vaneless diffusers has been studied by, for example, Inoue and Cumpsty (1984), Mizuki et al. (1985), and Senoo and Ishida (1975). Theoretically the inclusion of vanes within the diffuser should vastly improve pressure recovery, but in practice a significant improvement is only achieved over a limited flow range. This is largely because of the difficulty in achieving sensible vane incidence angles over even a small flow range. The objective of the current study on a vaneless diffuser is to obtain detailed measurements of the flow from which optimum vaneless space and vane geometry can be established for the design of a vaned diffuser. Pinarbasi and Johnson (1994) presented results for the design flow rate for the current impeller and diffuser geometry, whereas the present paper is concerned with off-design conditions.

Experimental Procedure

A schematic of the low-speed centrifugal compressor rig used in the study is shown in Fig. 1. The impeller was a De Havilland Ghost impeller, the geometry of which is given by Johnson and Moore (1980). In order to bring the geometry of this old impeller closer to that of a modern backswept impeller for the current study, the original radial outlet section was replaced to provide a 30 deg backswept outlet angle as shown in Fig. 2. The vaneless diffuser has straight walls and a constant cross-sectional area. The geometry operating conditions and measurement stations are summarized in Table 1.

Three operating points were used in the study. The "design" flow rate of $\dot{m} = 0.1311$ kg/s reported by Pinarbasi and Johnson (1994) corresponded to approximately zero incidence at the impeller blade leading edge. The "below" and "above" design flow rates of 0.1103 kg/s and 0.1450 kg/s were 16 percent below and 11 percent above the design flow rate. Detailed flow measurements within the impeller for similar flow rates are reported by Farge and Johnson (1990, 1992).

Instrumentation and Measurement Technique. A triple hot-wire probe was used to measure the velocities within the diffuser. A single wire (Dantec 55P11) was aligned circumferentially with a double wire (Dantec 55P61) arranged with each wire in the axial radial plane and at 45 deg to both the radial and axial directions. This mutually perpendicular arrangement of wires was therefore capable of resolving the axial, circumferential, and radial velocity components and the directional sign of the axial component. It was assumed that the radial and circumferential components remained positive throughout the flow. There was no evidence in the results of either of these components reducing to zero and hence this assumption was justified.

The hot wires were connected to three constant-temperature anemometer bridges. The wires were then calibrated in two stages in a wind tunnel following the procedure of Jongensen (1971). In the first stage, the velocity/voltage relationship was established with the wire perpendicular to the flow direction. King's law

$$E^2 = A + B \cdot U_e^c \tag{1}$$

was then fitted to the data for each wire using a least rms error technique to establish the calibration coefficients A, B, and C. The second stage of calibration was achieved by varying the wire orientation at fixed wind tunnel velocity to establish the directional coefficients K and H, where

$$U_e^2 = U_n^2 + K \cdot U_t^2 + H \cdot U_b^2 \tag{2}$$

U_n, U_t, and U_b are the normal, tangential, and binormal velocity components relative to the wire. K and H are also obtained by a least rms error curve fitting procedure.

An optical shaft encoder provided a pulse for every $\frac{1}{3}$ deg of impeller rotation. This was used to trigger the simultaneous sampling of the three anemometer voltages through a Microlink data acquisition unit. Readings from 57 measurement points spanning one of the 19 impeller passages were logged on each of 230 consecutive impeller revolutions. The triple wire sensor was traversed in the axial direction in order to provide a mesh of data points for each measurement plane.

Contributed by the International Gas Turbine Institute and presented at the 39th International Gas Turbine and Aeroengine Congress and Exposition, The Hague, The Netherlands, June 13–16, 1994. Manuscript received by the International Gas Turbine Institute February 4, 1994. Paper No. 94-GT-42. Associate Technical Editor: E. M. Greitzer.

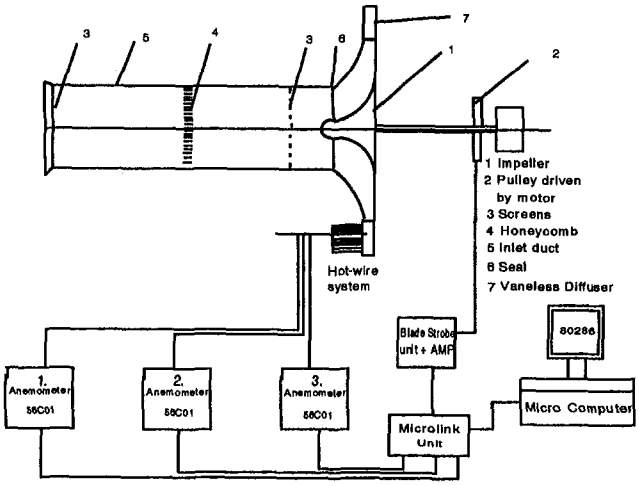

Fig. 1 Schematic of centrifugal compressor test rig

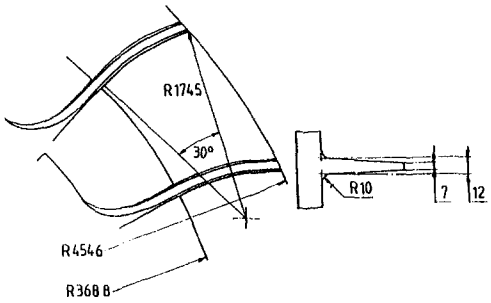

Fig. 2 Backswept impeller blade geometry

Analysis of Results. The 230 readings obtained at each measurement point for each of the three anemometers were used to compute the mean tangential, radial, and axial velocity components using the calibration coefficients. The flow rate was also computed by numerical integration of the radial velocity component over each of the measurement planes. The maximum deviation of this flow rate from the mean for all stations was 6.5 percent, which gives an indication of the overall experimental accuracy.

Mean Velocity Results

The mean velocities on the eight measurement planes in the diffuser are presented in Figs. 3–14. The radial velocity component is presented as a contour and the remaining velocity component in the measurement plane is shown as an arrow.

Station 1. The velocity distributions measured at the above and below design flow rates are shown in Figs. 3 and 4. These flow patterns are very similar to those discussed by Farge and Johnson (1992) at the impeller exit. At the above design flow rate, a very distinct passage wake is observed on the shroud at $y/y_o = 0.3$. A very strong velocity shear gradient separates this

Table 1 Geometry, operating condition, and measurement locations

Impeller Geometry and Operating Condition:

Inlet blade radius at the hub	R_h = 88.75 mm
Inlet blade radius at the shroud	R_s = 283.75 mm
Outlet radius	R_o = 454.6 mm
Backswept blade angle	$\beta = 30°$
Number of the blades	N = 19
Outlet blade span	b = 72.3 mm
Rotating speed	n = 500 rpm

Measurement Locations:

Sta.	1	2	3	4	5	6	7	8
L/R_o	0.02	0.08	0.15	0.21	0.27	0.33	0.39	0.45

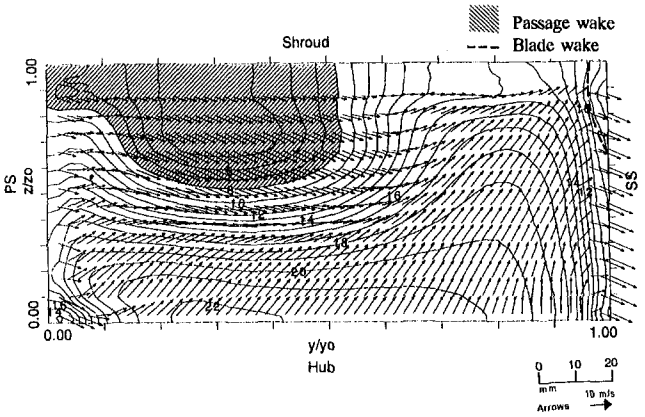

Fig. 3 Above design flow, velocities at station 1 (L/R_o = 0.02)

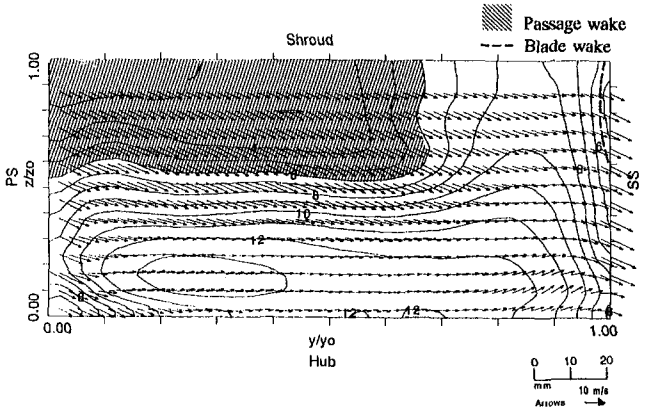

Fig. 4 Below design flow, velocities at station 1 (L/R_o = 0.02)

Nomenclature

A, B, C = King's law calibration coefficients
E = hot-wire anemometer voltage
H, K = directional coefficients for hot wire
L = radial distance from impeller outlet
R_o = impeller outlet radius
U_e = effective cooling velocity
U_r, U_θ, U_z = radial, tangential, and axial velocity components
y = tangential coordinate in measurement plane
y_o = tangential distance between consecutive blade wakes
z = axial coordinate in measurement plane
z_o = axial diffuser width in measurement plane

region from the rest of the flow. The blade wake is observed on the suction side between $y/y_o = 0.95$ and 1. Strong secondary velocities sweep high-velocity fluid from the hub to the shroud near the suction side and low-energy fluid from the blade and passage wakes in the shroud-to-hub direction. The large difference in flow angle between the blade wake and adjacent passage flow led to rapid mixing out of the blade wake at the design flow rate (Pinarbasi and Johnson, 1994).

For the below design flow rate (Fig. 4), the passage wake, jet, and blade wake are less distinct. The location of the passage wake is similar, but the wake is larger and is spread over a much larger proportion of the shroud. The secondary flows are also weaker, particularly the flow up the suction side; however, there is still evidence of opposed secondary flows on either side of the blade wake.

Station 2. Figure 5 shows that the secondary flows are still strong for the above design flow rate at station 2. The rapid variation in flow angle across the blade wake has indeed largely resulted in the mixing out of the blade wake observed at $y/y_o = 0.1$. This is in fact the blade wake from the neighboring passage, which has been convected to its current location by the tangential velocity component. The passage wake has moved more rapidly in this direction, because of its lower radial velocity and hence larger flow angle. The wake has altered shape and has spread over the shroud. It has altered little in size and hence the mixing mechanisms within this region are clearly much weaker than those in the blade wake region.

At the below design flow rate (Fig. 6), the blade wake has been convected further than for the higher flow rate to $y/y_o \approx 0.15$, but again has substantially mixed out. The passage wake has been convected to $y/y_o \approx 0.4$, but has altered little in size. There are now only small variations of secondary velocity in the circumferential direction at this flow rate.

Station 3. The passage wake has continued to move and spread across the shroud between stations 2 and 3 for the above design flow rate (Fig. 7). It has, however, continued to traverse faster than the blade wake, which is still just discernable near the hub. Relatively strong secondary flows are still observed in Fig. 7 with marked variations in the circumferential direction. However, the variations in radial velocity in this direction have now decreased significantly from station 1 with the velocity contours aligned parallel with the diffuser walls.

Mixing out in the circumferential direction is almost complete for the below design flow (Fig. 8) and there is also some evidence of thickening of the hub boundary layer as the peak velocity in the jet region has been displaced toward the center of the passage. The passage wake has now spread almost evenly along the shroud wall. The main variation in radial velocity in the circumferential direction is associated with the blade wake, which is skewed across the passage. This skewing is due to the more rapid translation in the circumferential direction of the low-energy fluid near the hub and shroud walls as compared with the high-energy fluid in the jet.

Station 4. At station 4 for the above design flow rate (see Fig. 9) the passage wake occupies most of the shroud surface. The blade wake is still detected near the hub. There is now some evidence of thickening of the hub boundary layer from the displacement of the jet peak velocity region from the hub wall to $z/z_o \approx 0.1$. The strong axial velocity component near the hub walls is also an indication of diffusion as the jet slows from 22 m/s at station 1 to 17 m/s at the current station.

The below design flow (Fig. 10) now closely resembles a Couette flow between the diffuser walls, although the hub boundary layer is still much thinner than that on the shroud, which is reflected in the off-center position of the peak velocity at $z/z_o = 0.3$.

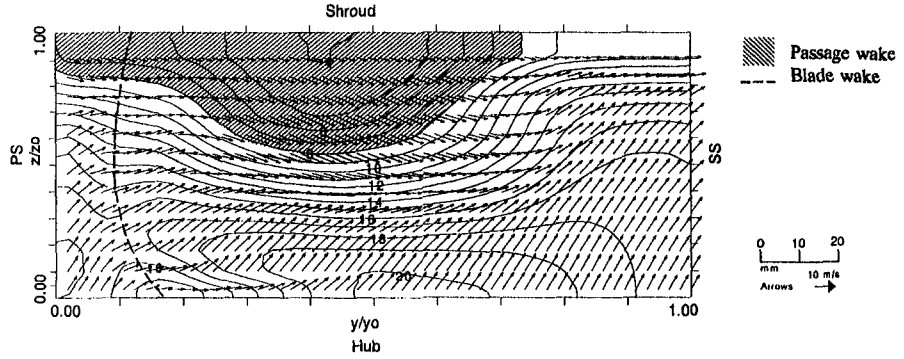

Fig. 5 Above design flow, velocities at station 2 ($L/R_o = 0.08$)

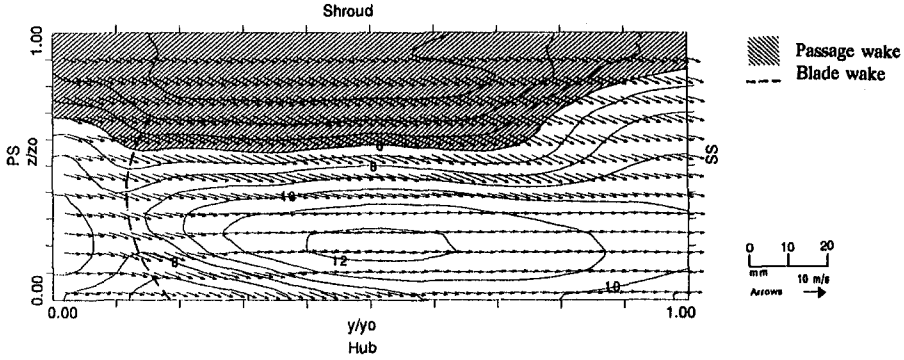

Fig. 6 Below design flow, velocities at station 2 ($L/R_o = 0.08$)

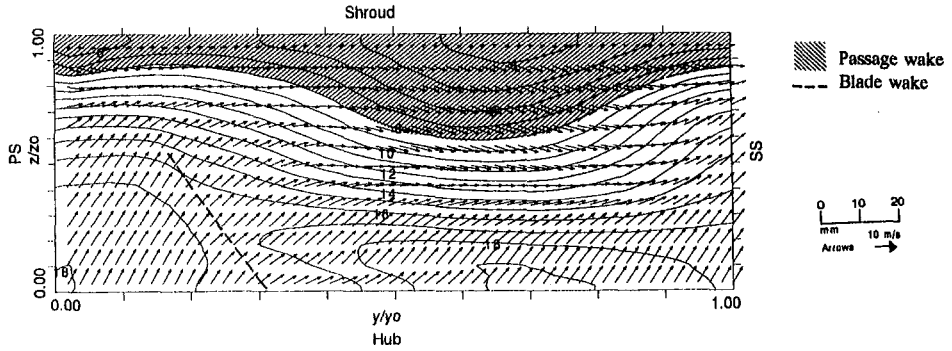

Fig. 7 Above design flow, velocities at station 3 (L/R_o = 0.15)

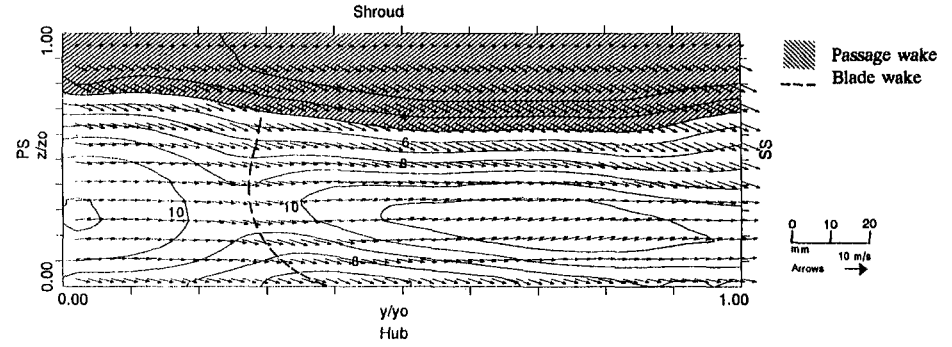

Fig. 8 Below design flow, velocities at station 3 (L/R_o = 0.15)

Stations 5 to 8. As the flow progresses through the diffuser, it continues to tend toward a Couette flow. This process is more advanced in the case of the below design flow as shown by Figs. 12 (Station 6) and 14 (Station 8) than for the above design flow case at the same stations (see Figs. 11 and 13). Figure 14 shows that at the last station for the below design flow, the peak velocity region is at z/z_o = 0.35, and the hub boundary layer is still two to three times thinner than its shroud counterpart. In contrast, for the above design flow rate (Fig. 13), the peak velocity region is still very close to the hub wall

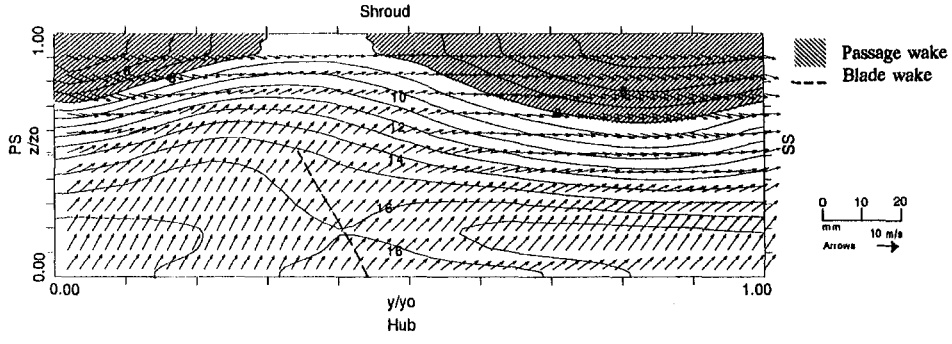

Fig. 9 Above design flow, velocities at station 4 (L/R_o = 0.21)

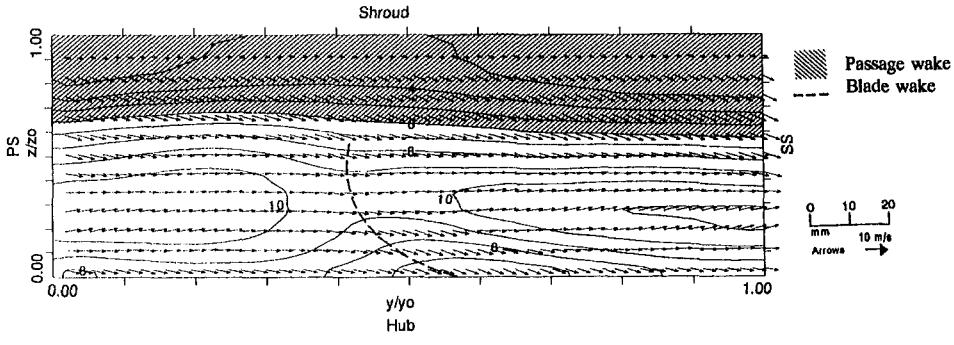

Fig. 10 Below design flow, velocities at station 4 (L/R_o = 0.21)

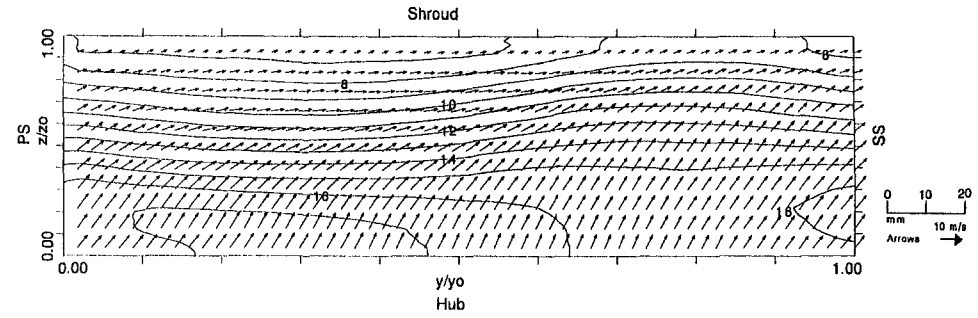

Fig. 11 Above design flow, velocities at station 6 (L/R_o = 0.33)

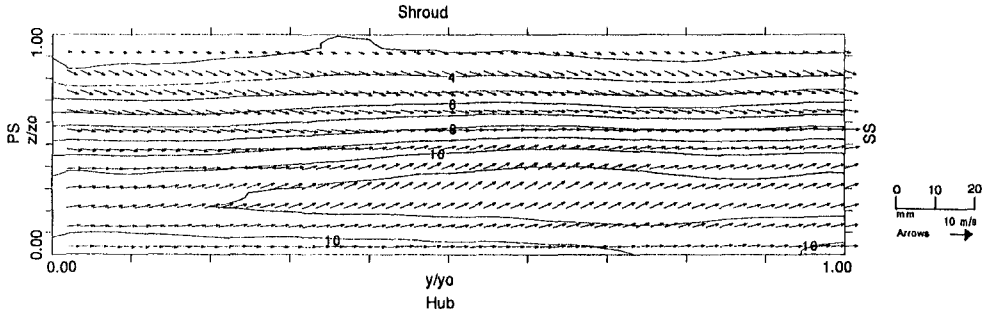

Fig. 12 Below design flow, velocities at station 6 (L/R_o = 0.33)

(z/z_o = 0.1) and the hub boundary layer thickness is perhaps only 10 percent of that on the shroud. The reason for this difference is believed to be the stronger secondary flows observed at the higher flow rate up to station 3, which continue to extract low-energy fluid from the hub boundary layer and hence re-energize it.

Flow Angle Results

Station 1. Figures 15 and 16 show the differences between the flow angle ($\tan^{-1}(U_\theta/U_r)$) for the two flow rates at the diffuser inlet.

At the above design flow rate (Fig. 15) the flow angle variation is extreme with angles as high as 75 deg in the slow moving wake and as low as 10 deg in the rapidly moving jet. For the designer of a vaned diffuser, the axial variation in flow angle can be accommodated by the use of a twisted blade. Large variations in the circumferential direction, however, will inevitably lead to significant incidence angles. It seems likely that in the current unsteady flow higher transient incidence angles may be tolerated without separation than would be the case in a steady flow. However, the magnitude of the incidence angles will still be a good guide to the likelihood of incuring significant separation losses. Figure 15 shows that the circumferential vari-

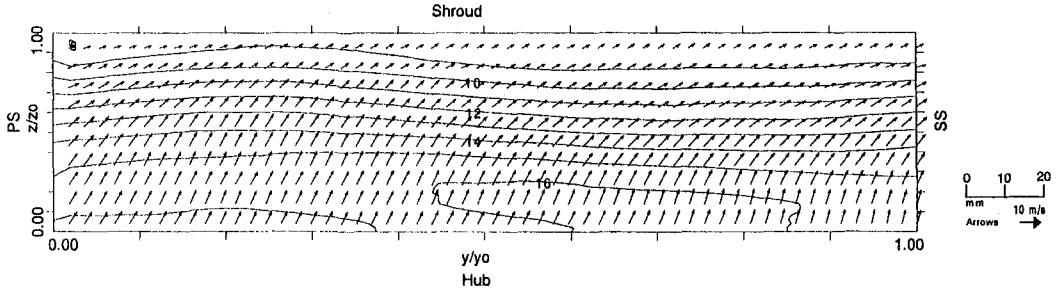

Fig. 13 Above design flow, velocities at station 8 (L/R_o = 0.45)

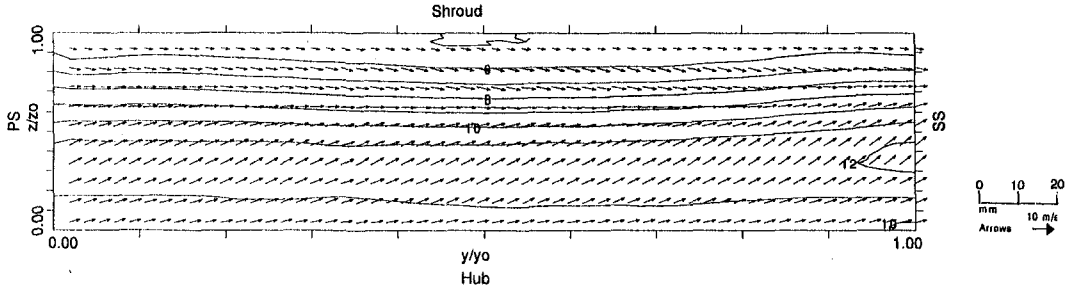

Fig. 14 Below design flow, velocities at station 8 (L/R_o = 0.45)

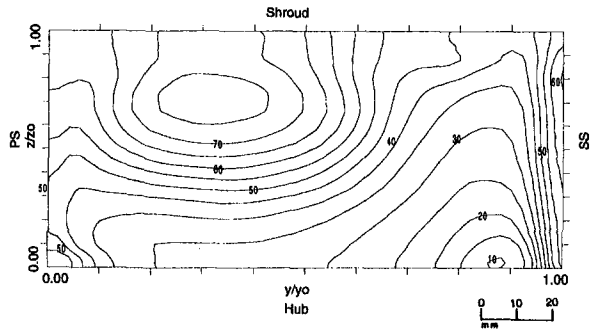

Fig. 15 Above design flow, U_θ/U_r flow angle station 1

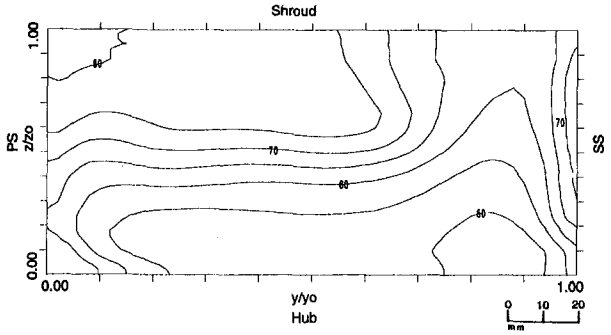

Fig. 16 Below design flow, U_θ/U_r flow angle station 1

ation in flow angle is 30 to 35 deg, which implies, for a correctly set blade, incidence angles of at least ±15 deg will result.

For the below design flow rate (Fig. 16), the flow angle variations are more modest from 50 to 80 deg with only a 15 deg circumferential variation in flow angle. A diffuser vane twisted from around 70 deg at the shroud to around 55 deg at the hub would accept this flow with a maximum incidence variation of ±8 deg where it would be expected that significant separation losses would be avoided.

Station 2. The variation in flow angle for the above design flow rate has moderated considerably at station 2 (Fig. 17) with a circumferential variation of around 20 deg. This would still lead to vane incidence angles of around ±10 deg which could induce significant separation losses.

At the below design flowrate (Fig. 18), the circumferential variation near the shroud is still about 15 deg, but is less than 10 deg closer to the hub.

Station 3. At station 3 for the above design flow rate (Fig. 19), the circumferential variation in flow angle of less than 15 deg is sufficiently low to prevent significant separation losses from a diffuser vane. The circumferential flow angle variation for the below design flow rate (Fig. 20) is now only 5 to 10 deg.

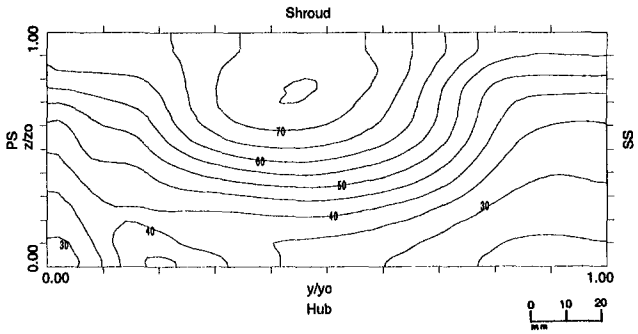

Fig. 17 Above design flow, U_θ/U_r flow angle station 2

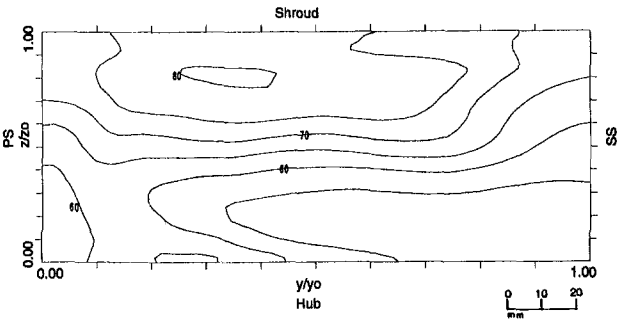

Fig. 18 Below design flow, U_θ/U_r flow angle station 2

Vaned Diffuser Design

The results of this study suggest that when designing a vaned diffuser, a vaneless space extending to $L/R_o = 0.02$ would give good performance at below design flow rates with a blade twisted from about 70 deg at the shroud to 55 deg at the hub. However, a much longer vaneless space is required at above design flow rates where $L/R_o = 0.15$ is more appropriate and the blade should be twisted from around 60 deg near the shroud to 30 deg near the hub.

If a wide range of operation is required between the flow rates considered in the current study and fixed vanes are used in the diffuser, separation losses are inevitable because of the dependence of flow angle, particularly in the jet region, on flow rate as shown by Figs. 19 and 20. However, if a vaneless space extending to station 3 ($L/R_o = 0.15$) is used, a blade twisted from around 65 deg at the shroud to about 45 deg at the hub should limit the incidence angles to ±15 deg and minimize the separation losses.

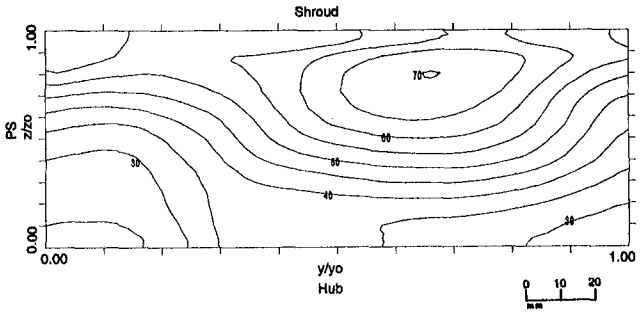

Fig. 19 Above design flow, U_θ/U_r flow angle station 3

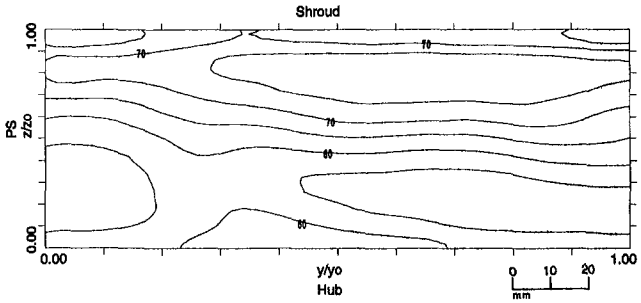

Fig. 20 Below design flow, U_θ/U_r flow angle station 3

Conclusions

1 The blade wake mixes out very much more rapidly than the passage wake within the vaneless diffuser.
2 At the above design flow rate the shear gradients associated with the blade and passage wakes and the secondary flows are much stronger.
3 Circumferential variations in velocity are prevented from mixing out rapidly at the higher flow rate due to the presence of the strong secondary flows.
4 The hub boundary layer is thinner than that on the shroud at the last measurement station. The ratio of the boundary layer thicknesses is around 2:1 for the below and 10:1 for the above design flow rate.
5 The optimum vaneless space for a vaned diffuser increases with flow rate, because of the slower mixing out of circumferential variations. Twisted vanes will also minimize incidence losses.
6 It is impossible to avoid significant incidence losses with fixed vane diffusers if a wide flow range is required, because of the inherent dependence of flow angle on flow rate.

References

Farge, T. Z., and Johnson, M. W., 1990, "The Effect of Backswept Blading on the Flow in a Centrifugal Compressor Impeller," ASME Paper No. 90-GT-231.

Farge, T. Z., and Johnson, M. W., 1992, "Effect of Flow Rate on Loss Mechanisms in a Backswept Centrifugal Impeller," *Int. J. Heat Fluid Flow,* Vol. 13, No. 2, pp. 189–196.

Inoue, M., and Cumpsty, N. A., 1984, "Experimental Study of Centrifugal Impeller Discharge Flow in Vaneless and Vaned Diffuser," ASME *Journal of Engineering for Gas Turbines and Power,* Vol. 106, pp. 455–467.

Johnson, M. W., and Moore, J., 1980, "The Development of Wake Flow in a Centrifugal Compressor," ASME *Journal of Engineering for Power,* Vol. 102, pp. 383–390.

Jongensen, F. E., 1971, "Directional Sensitivity of Wire and Fiber Film Probes," DISA information No. 11, pp. 31–37.

Krain, H., 1988, "Swirling Impeller Flow," ASME JOURNAL OF TURBOMACHINERY, Vol. 110, pp. 122–128.

Mizuki, S., Park, C. W., and Deckker, B., 1985, "Unstable Flows in Vaneless Diffuser of a Centrifugal Compressor at Low Flow Rates," ASME Paper No. 85-IGT-7.

Pinarbasi, A., and Johnson, M. W., 1994, "Detailed Flow Measurements in a Centrifugal Compressor Vaneless Diffuser," ASME JOURNAL OF TURBOMACHINERY, Vol. 116, pp. 453–461.

Senoo, Y., and Ishida, M., 1975, "Behavior of Severely Axymmetric Flow in a Vaneless Diffuser," ASME *Journal of Engineering for Power,* Vol. 97, pp. 375–387.

DISCUSSION

N. A. Cumpsty[1]

I am concerned that some of the measurements in this paper are inaccurate enough to be misleading. My concern centers on the velocity vectors, shown as arrows, in some of the measuring planes. When the arrows spring from a position near a solid surface, but are inclined at a large angle to the surface, there is reason to feel that something may be wrong. This is the case near the hub wall in Figs. 3, 5, 7, 9, 11, and 13, each at a progressively greater distance from the impeller outlet. The odd-numbered figures are for flow rate greater than the design value. (The corresponding even-numbered figures, at a flow rate below that for design, do not show the arrows inclined at large angles to the wall.) I am inclined to think that the measurements at the higher flow rate were compromised in some way. Would the authors care to clarify this for us?

If the measurements represented by the arrows are inaccurate, what about the velocities represented by the contours?

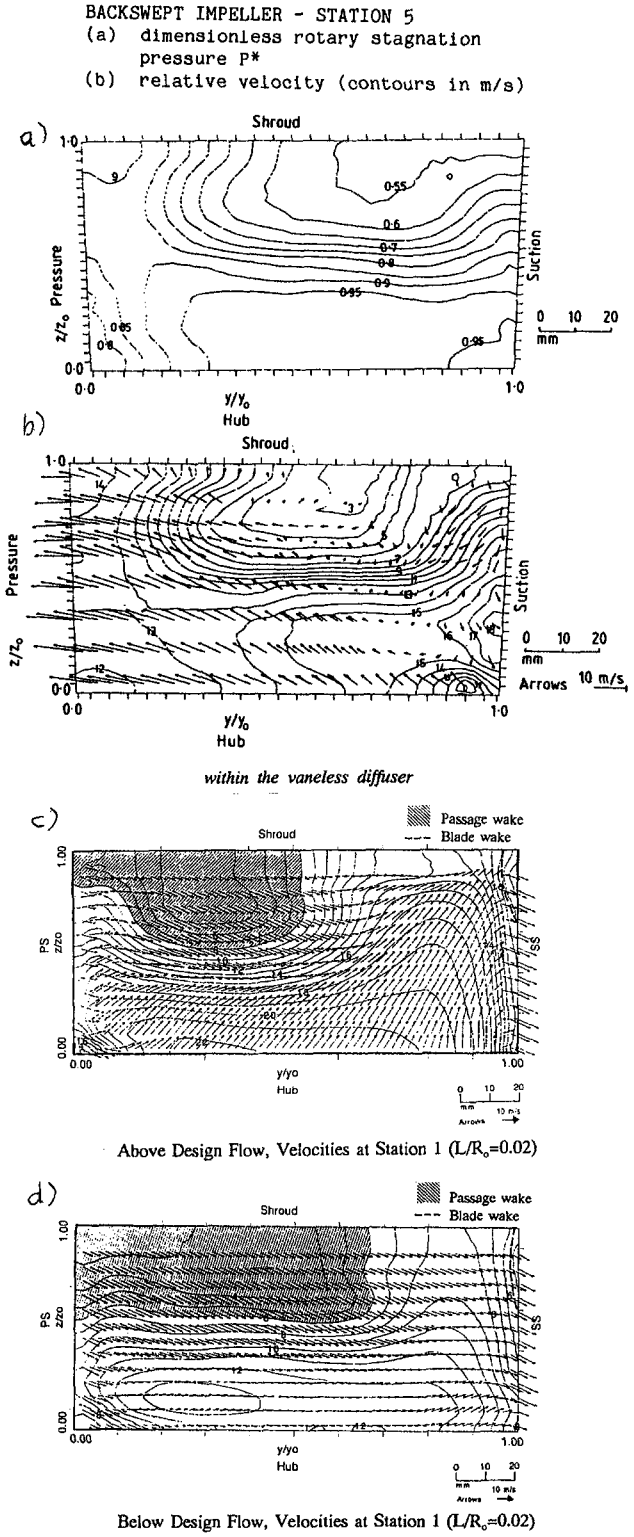

Fig. 21 Comparison of the secondary flow fields between the impeller outlet (in (*b*) at normal operating point with the corresponding dimensionless rotary stagnation pressure *p* in (*a*)), and the diffuser inlet (in (*c*) for high off-design flow at 111 percent and in (*d*) for low off-design flow at 84 percent

[1] Whittle Laboratory, Cambridge University Engineering Department, Madingley Rd., Cambridge CB3 0DY United Kingdom.

Conclusions

1 The blade wake mixes out very much more rapidly than the passage wake within the vaneless diffuser.
2 At the above design flow rate the shear gradients associated with the blade and passage wakes and the secondary flows are much stronger.
3 Circumferential variations in velocity are prevented from mixing out rapidly at the higher flow rate due to the presence of the strong secondary flows.
4 The hub boundary layer is thinner than that on the shroud at the last measurement station. The ratio of the boundary layer thicknesses is around 2:1 for the below and 10:1 for the above design flow rate.
5 The optimum vaneless space for a vaned diffuser increases with flow rate, because of the slower mixing out of circumferential variations. Twisted vanes will also minimize incidence losses.
6 It is impossible to avoid significant incidence losses with fixed vane diffusers if a wide flow range is required, because of the inherent dependence of flow angle on flow rate.

References

Farge, T. Z., and Johnson, M. W., 1990, "The Effect of Backswept Blading on the Flow in a Centrifugal Compressor Impeller," ASME Paper No. 90-GT-231.

Farge, T. Z., and Johnson, M. W., 1992, "Effect of Flow Rate on Loss Mechanisms in a Backswept Centrifugal Impeller," *Int. J. Heat Fluid Flow,* Vol. 13, No. 2, pp. 189–196.

Inoue, M., and Cumpsty, N. A., 1984, "Experimental Study of Centrifugal Impeller Discharge Flow in Vaneless and Vaned Diffuser," ASME *Journal of Engineering for Gas Turbines and Power,* Vol. 106, pp. 455–467.

Johnson, M. W., and Moore, J., 1980, "The Development of Wake Flow in a Centrifugal Compressor," ASME *Journal of Engineering for Power,* Vol. 102, pp. 383–390.

Jongensen, F. E., 1971, "Directional Sensitivity of Wire and Fiber Film Probes," DISA information No. 11, pp. 31–37.

Krain, H., 1988, "Swirling Impeller Flow," ASME JOURNAL OF TURBOMACHINERY, Vol. 110, pp. 122–128.

Mizuki, S., Park, C. W., and Deckker, B., 1985, "Unstable Flows in Vaneless Diffuser of a Centrifugal Compressor at Low Flow Rates," ASME Paper No. 85-IGT-7.

Pinarbasi, A., and Johnson, M. W., 1994, "Detailed Flow Measurements in a Centrifugal Compressor Vaneless Diffuser," ASME JOURNAL OF TURBOMACHINERY, Vol. 116, pp. 453–461.

Senoo, Y., and Ishida, M., 1975, "Behavior of Severely Axymmetric Flow in a Vaneless Diffuser," ASME *Journal of Engineering for Power,* Vol. 97, pp. 375–387.

DISCUSSION

N. A. Cumpsty[1]

I am concerned that some of the measurements in this paper are inaccurate enough to be misleading. My concern centers on the velocity vectors, shown as arrows, in some of the measuring planes. When the arrows spring from a position near a solid surface, but are inclined at a large angle to the surface, there is reason to feel that something may be wrong. This is the case near the hub wall in Figs. 3, 5, 7, 9, 11, and 13, each at a progressively greater distance from the impeller outlet. The odd-numbered figures are for flow rate greater than the design value. (The corresponding even-numbered figures, at a flow rate below that for design, do not show the arrows inclined at large angles to the wall.) I am inclined to think that the measurements at the higher flow rate were compromised in some way. Would the authors care to clarify this for us?

If the measurements represented by the arrows are inaccurate, what about the velocities represented by the contours?

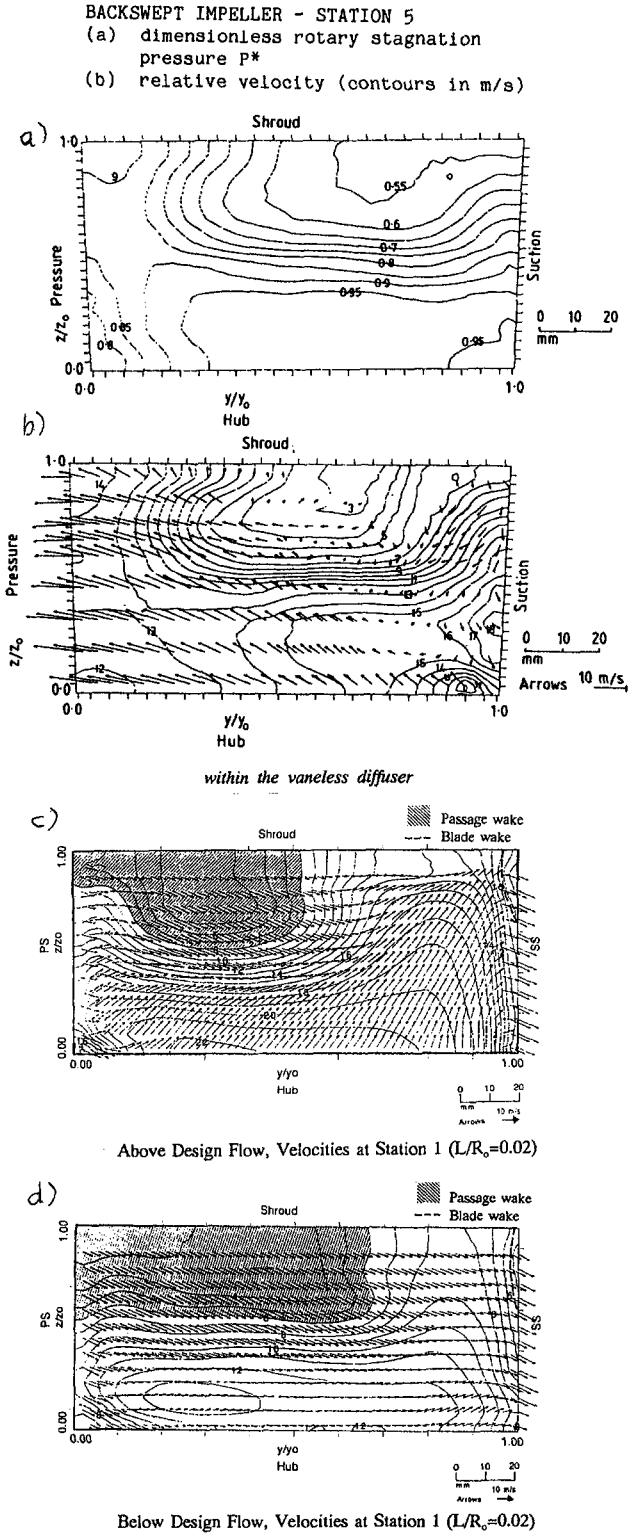

Fig. 21 Comparison of the secondary flow fields between the impeller outlet (in (*b*) at normal operating point with the corresponding dimensionless rotary stagnation pressure *p* in (*a*)), and the diffuser inlet (in (*c*) for high off-design flow at 111 percent and in (*d*) for low off-design flow at 84 percent

[1] Whittle Laboratory, Cambridge University Engineering Department, Madingley Rd., Cambridge CB3 0DY United Kingdom.

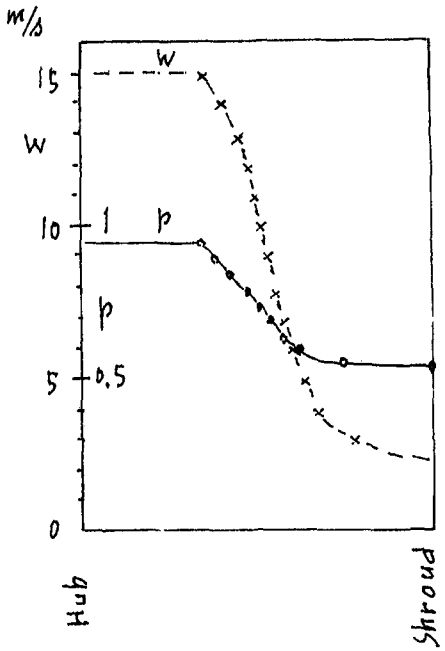

Fig. 22 Profiles of the throughflow w and the dimensionless rotary stagnation pressure p across the longitudinal vortex low for the direction from hub to shroud in the outlet section of the impeller

Y. N. Chen[2]

The authors have continued their very interesting series about secondary flows in centrifugal compressors.

If a comparison is made between the secondary velocity field at the inlet of the vaneless diffuser displayed in Fig. 21(c, d) (taken over from Figs. 3 and 4 of the paper) for the load of slightly above and below the design point on one hand, and the relative secondary velocity field at the outlet of the impeller for the normal operating point given in Fig. 21(b) (taken over from a previous paper of the series carried out by Farge and Johnson, 1990) on the other hand, a quite striking difference can be discovered, despite the very small gap of $0.02R_a$ between the impeller outlet and the diffuser inlet quoted. The relative secondary velocity field over the passage wake in the outlet of the impeller (Fig. 21(b)) shows a clockwise rotational direction, accompanied by a component pointing from hub toward shroud. But the secondary velocity field for the inlet of the diffuser (Fig. 21(c, d)) shows an anticlockwise rotational direction, accompanied by a component pointing from shroud toward hub. The two sets of the flow fields are completely reversed in the direction against each other. The secondary velocity field in Fig. 21(b) cannot be directly transferred into that in Fig. 21(c) or 21(d) by a linear transformation from the rotating frame of the impeller to the absolute frame of the diffuser. The reason for this intransferability must lie in the nonpotential behavior of a certain component of the flow system considered. This component is the passage wake in the blade channel of the impeller.

As shown in the paper of Chen et al. (1991), the passage wake in the blade channel of the impeller is enveloped by a longitudinal vortex, which rotates in the same sense as the projection on this vortex axis of the rotation vector of the impeller axis. This longitudinal vortex is therefore termed "vortex low L" according to the meteorological terminology. It is this vortex that isolates the passage wake of the low velocity against the surroundings of the high velocity.

The velocity field around the center of the passage wake in Fig. 21(b) clearly reveals the rotation pattern of its core, which lies in the deep pressure center depicted in Fig. 21(a). The profiles of the pressure p and the throughflow w across the core of this vortex low for the direction from hub to shroud are evaluated from Fig. 21(a, b) and plotted in Fig. 22. The two

[2] Sulzer Brothers Ltd., Winterthur, Switzerland.

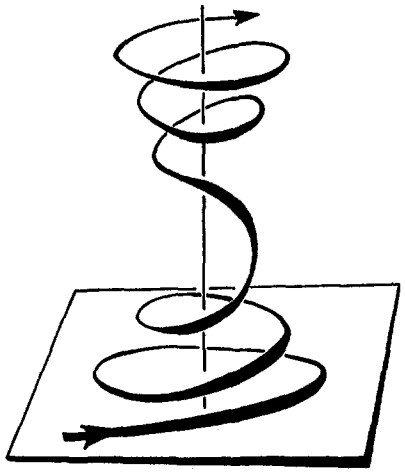

Fig. 23 Conversion of the cyclonic flow of the eyewall of the hurricane into anticyclonic flow when rising out of the eye into the upper free atmosphere (Lugt, 1983)

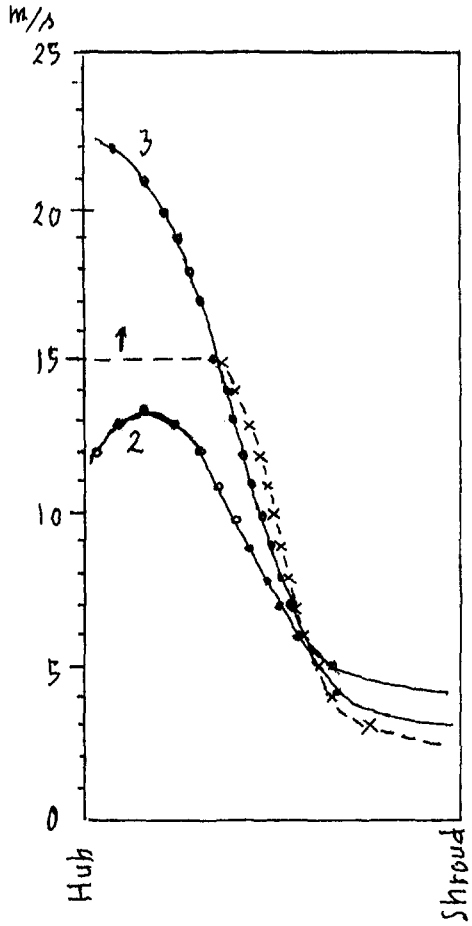

Fig. 24 Comparison of the profiles of the throughflow velocities w between the impeller outlet (curve 1 for normal operating point) and the diffuser inlet (curve 2 for low off-design flow at 84 percent and curve 3 for high off-design flow at 111 percent)

profiles coincide well with each other with respect to the vortex property of the secondary flow.

The deficit in the velocity along the core of the vortex originates from the secondary axial flow through the core within the mean flow field of the surroundings. Therefore, the gradient of the throughflow velocity field around the vortex core is very steep; see $w = 12$ to 5 m/s in Fig. 22. A concentrated secondary flow travels through the core of the vortex backward into the impeller.

The longitudinal vortex low of the blade channel of the impeller is formed along the shroud surface. Since, at the same time, this surface is perpendicular to the rotating axis of the impeller, it also behaves as the surface of a rotating disk. Then, the longitudinal vortex low L is embedded in the Ekman layer of this disk. Therefore, additional Ekman layer vorticity reinforces its intensity.

When this longitudinal vortex has left the impeller as a rotating system, and travels into the diffuser as an absolute frame, the feeding of the vorticity to the vortex ceases to take place. The vortex will expand, similar to the process of vortex compression occurring in the upper region over the eye of a hurricane (Whipple, 1983).

The high-speed rotation of the eyewall is caused by the spirally inward movement of the wind along the Ekman layer of the ground. Due to conservation of the angular momentum, the cyclonic motion of the wind is accelerated to a very high value when reaching the eyewall. During the acceleration, the vorticity of the spirally moving wind increases up to the region of the eyewall, in which the vorticity becomes maximum.

The wind then bends upward into the eyewall and rotates rapidly with it. When the wind has come out of the eyewall into the upper free atmosphere, the feeding of the vorticity no longer exists. The vortex formed by the wind then suffers from the compression with the result of expanding outward. The vorticity of the wind decreases rapidly to its negative value. Then, the rotational movement of the wind reverses its sense and becomes anticyclonic. This is shown in Fig. 23 (Lugt, 1983).

The development of the longitudinal vortex low L coming out of the rotating impeller to the absolute frame of the diffuser will undergo the same process as described above for the wind coming out of the eye of the hurricane. The vortex will expand (Fig. 24) and reverse its rotational sense to the opposite direction. It then becomes a vortex high H with the fluid coming out of the vortex.

The experimental series under the present discussion reveals a valuable phenomenon that the secondary longitudinal vortex low L of the rotating impeller is transferred to the secondary vortex high H, when it travels into the vaneless diffuser as an absolute frame. The vortex compression forms the fundamental mechanism in this transformation process. This process, which is familiar for the hurricane, in thus found in the turbomachinery.

References

Chen, Y. N., Seidel, U., Haupt, U., and Rautenberg, M., 1991, "The Rossby Waves of Rotating Stall in Impellers, Part II: Application of the Rossby-Wave Theory to Rotating Stall," *1991 Yokohama International Gas Turbine Congress, Proceedings,* pp. I/77–88.

Lugt, H. J., 1983, *Vortex Flow in Nature and Technology,* Wiley, New York, pp. 152–153.

Whipple, A. B. C., 1983, *Der Planet Erde, Stürme,* Time-Life Bücher, Amsterdam, pp. 84–90.

Authors' Closure

Response to Prof. N. A. Cumpsty's Discussion. The strong axial component of velocity near the hub wall observed at the above design flow rate in Figs. 3, 5, 7, 9, 11, and 13 is quite distinct from the much weaker component observed for the below design flow rate. This difference also led the authors to question the accuracy of the design flow rate results. For this reason the measurements at station 1 were repeated using different hot-wire probes and a fresh calibration. The velocity results obtained were to within ± 1 m/s in magnitude and ± 5 deg in direction to those shown in Fig. 3, which suggested that the results were repeatable and that the instrumentation had been correctly calibrated. A further check was made by examining the raw data (anemometer voltages and effective cooling velocities) from the double wire (Dantec 55P61). This was arranged with the two wires in the axial–radial plane, with each wire at 45 deg to both the radial and axial directions. Thus, in the case where the axial velocity component is very small, the effective cooling velocity will be the same for both wires. Conversely, if a large axial component exists, the two effective cooling velocities will be significantly different. In the below design case near the hub the two effective cooling velocities were very similar, whereas in the above design case very different values were obtained, which is consistent with the results in Figs. 3 and 4. The authors therefore believe the high axial velocities depicted near the hub at the above design flow rate to be correct.

The most likely explanation for these axial velocities would seem to be diffusion of the flow near the hub wall as the boundary layer thickens. If the maximum radial velocity contour values are considered for stations 1, 2, 3, 4, 6, and 8, these are 12, 12, 11, 11, 12, and 12 m/s at the below design flow rate and 22, 20, 19, 16, 17, 16 m/s at the above design flow rate. This suggests negligible diffusion for the below design flow rate, but strong diffusion from stations 1–4 at the higher flow rate. Furthermore, the peak radial velocity is very close to the hub at the above design flow rate, whereas the hub boundary layer has already thickened at station 1 and the peak is observed at $z/z_0 \simeq 0.2$ for the lower flow rate.

Response to Dr. Y. N. Chen's Discussion. The authors thank Dr. Chen for a very interesting explanation for the change in direction of vorticity within the passage wake as it travels from the last impeller station to the first diffuser station. An alternative explanation relates to the shroud wall boundary condition. The impeller is a shrouded impeller and hence in the wake close to the hub the relative tangential velocity is zero and hence absolute velocity is wr in PS to SS direction (left to right in Fig. 21*b*) as the flow leaves the impeller. When the flow enters the diffuser, this absolute tangential velocity is reduced to zero on the diffuser wall, which leads to very high levels of anticlockwise vorticity close to the shroud. This vorticity will diffuse away from the wall with distance downstream. The rate of diffusion will be high (with distance downstream) in the passage wake as the radial velocities in the wake are very low (less than 5 m/s) and hence the anticlockwise vorticity will quickly overcome the weak clockwise rotation observed in the passage wake in the impeller in Fig. 21(*b*).

profiles coincide well with each other with respect to the vortex property of the secondary flow.

The deficit in the velocity along the core of the vortex originates from the secondary axial flow through the core within the mean flow field of the surroundings. Therefore, the gradient of the throughflow velocity field around the vortex core is very steep; see $w = 12$ to 5 m/s in Fig. 22. A concentrated secondary flow travels through the core of the vortex backward into the impeller.

The longitudinal vortex low of the blade channel of the impeller is formed along the shroud surface. Since, at the same time, this surface is perpendicular to the rotating axis of the impeller, it also behaves as the surface of a rotating disk. Then, the longitudinal vortex low L is embedded in the Ekman layer of this disk. Therefore, additional Ekman layer vorticity reinforces its intensity.

When this longitudinal vortex has left the impeller as a rotating system, and travels into the diffuser as an absolute frame, the feeding of the vorticity to the vortex ceases to take place. The vortex will expand, similar to the process of vortex compression occurring in the upper region over the eye of a hurricane (Whipple, 1983).

The high-speed rotation of the eyewall is caused by the spirally inward movement of the wind along the Ekman layer of the ground. Due to conservation of the angular momentum, the cyclonic motion of the wind is accelerated to a very high value when reaching the eyewall. During the acceleration, the vorticity of the spirally moving wind increases up to the region of the eyewall, in which the vorticity becomes maximum.

The wind then bends upward into the eyewall and rotates rapidly with it. When the wind has come out of the eyewall into the upper free atmosphere, the feeding of the vorticity no longer exists. The vortex formed by the wind then suffers from the compression with the result of expanding outward. The vorticity of the wind decreases rapidly to its negative value. Then, the rotational movement of the wind reverses its sense and becomes anticyclonic. This is shown in Fig. 23 (Lugt, 1983).

The development of the longitudinal vortex low L coming out of the rotating impeller to the absolute frame of the diffuser will undergo the same process as described above for the wind coming out of the eye of the hurricane. The vortex will expand (Fig. 24) and reverse its rotational sense to the opposite direction. It then becomes a vortex high H with the fluid coming out of the vortex.

The experimental series under the present discussion reveals a valuable phenomenon that the secondary longitudinal vortex low L of the rotating impeller is transferred to the secondary vortex high H, when it travels into the vaneless diffuser as an absolute frame. The vortex compression forms the fundamental mechanism in this transformation process. This process, which is familiar for the hurricane, in thus found in the turbomachinery.

References

Chen, Y. N., Seidel, U., Haupt, U., and Rautenberg, M., 1991, "The Rossby Waves of Rotating Stall in Impellers, Part II: Application of the Rossby-Wave Theory to Rotating Stall," *1991 Yokohama International Gas Turbine Congress, Proceedings,* pp. I/77–88.

Lugt, H. J., 1983, *Vortex Flow in Nature and Technology,* Wiley, New York, pp. 152–153.

Whipple, A. B. C., 1983, *Der Planet Erde, Stürme,* Time-Life Bücher, Amsterdam, pp. 84–90.

Authors' Closure

Response to Prof. N. A. Cumpsty's Discussion. The strong axial component of velocity near the hub wall observed at the above design flow rate in Figs. 3, 5, 7, 9, 11, and 13 is quite distinct from the much weaker component observed for the below design flow rate. This difference also led the authors to question the accuracy of the design flow rate results. For this reason the measurements at station 1 were repeated using different hot-wire probes and a fresh calibration. The velocity results obtained were to within ± 1 m/s in magnitude and ± 5 deg in direction to those shown in Fig. 3, which suggested that the results were repeatable and that the instrumentation had been correctly calibrated. A further check was made by examining the raw data (anemometer voltages and effective cooling velocities) from the double wire (Dantec 55P61). This was arranged with the two wires in the axial–radial plane, with each wire at 45 deg to both the radial and axial directions. Thus, in the case where the axial velocity component is very small, the effective cooling velocity will be the same for both wires. Conversely, if a large axial component exists, the two effective cooling velocities will be significantly different. In the below design case near the hub the two effective cooling velocities were very similar, whereas in the above design case very different values were obtained, which is consistent with the results in Figs. 3 and 4. The authors therefore believe the high axial velocities depicted near the hub at the above design flow rate to be correct.

The most likely explanation for these axial velocities would seem to be diffusion of the flow near the hub wall as the boundary layer thickens. If the maximum radial velocity contour values are considered for stations 1, 2, 3, 4, 6, and 8, these are 12, 12, 11, 11, 12, and 12 m/s at the below design flow rate and 22, 20, 19, 16, 17, 16 m/s at the above design flow rate. This suggests negligible diffusion for the below design flow rate, but strong diffusion from stations 1–4 at the higher flow rate. Furthermore, the peak radial velocity is very close to the hub at the above design flow rate, whereas the hub boundary layer has already thickened at station 1 and the peak is observed at $z/z_0 \simeq 0.2$ for the lower flow rate.

Response to Dr. Y. N. Chen's Discussion. The authors thank Dr. Chen for a very interesting explanation for the change in direction of vorticity within the passage wake as it travels from the last impeller station to the first diffuser station. An alternative explanation relates to the shroud wall boundary condition. The impeller is a shrouded impeller and hence in the wake close to the hub the relative tangential velocity is zero and hence absolute velocity is wr in PS to SS direction (left to right in Fig. 21*b*) as the flow leaves the impeller. When the flow enters the diffuser, this absolute tangential velocity is reduced to zero on the diffuser wall, which leads to very high levels of anticlockwise vorticity close to the shroud. This vorticity will diffuse away from the wall with distance downstream. The rate of diffusion will be high (with distance downstream) in the passage wake as the radial velocities in the wake are very low (less than 5 m/s) and hence the anticlockwise vorticity will quickly overcome the weak clockwise rotation observed in the passage wake in the impeller in Fig. 21(*b*).

On Fast-Response Probes: Part 1—Technology, Calibration, and Application to Turbomachinery

C. R. Gossweiler

P. Kupferschmied

G. Gyarmathy

Turbomachinery Laboratory,
ETH Swiss Federal Institute of Technology,
Zurich, Switzerland

A system for fast-response probe measurements in turbomachine flows has been developed and tested. The system has been designed for 40 kHz bandwidth and used with various in-house built probes accommodating up to four piezoresistive pressure transducers. The present generation of probes works accurately up to several bar pressure and 120°C temperature. The probes were found to be quite robust. The use of a miniature pressure transducer placed in the head of a probe showed that a precise packaging technique and a careful compensation of errors can considerably improve the accuracy of the pressure measurement. Methods for aerodynamic probe calibration and off-line data evaluation are briefly presented. These aimed, e.g., in the case of a four-hole probe, at measuring the velocity fluctuations as characterized by yaw, pitch, total pressure, and static pressure and at deriving mean values and spectral or turbulence parameters. Applications of the measuring system to turbomachinery flow in a radial compressor and to a turbulent pipe flow demonstrate the performance of the measuring system.

1 Introduction

Turbomachines with their complex systems of rotating and nonrotating components represent an important class of devices in which fluctuating flows are predominant. The knowledge of the unsteady flow pattern inside turbomachines is necessary to improve performance predictions, dissipation rate, stall, surge, blade flutter, etc. Additionally, with the increased performance of numerical flow computational methods, the need for their "calibration" and validation has grown.

With the availability of miniature silicon pressure transducers, aerodynamic probes have become an important tool for determining periodic and random components of the flow inside turbomachines. These probes are equipped with pressure transducers located directly in the probe head (Castorph, 1975; Kerrebrock et al., 1980; Heneka, 1983; Epstein, 1985; Larguier, 1985).

The advantages of fast-response probes are that they combine the high bandwidth desired with a high signal-to-noise ratio and a high reliability. Additionally, they are far more robust than hot wires.

However, the quality of results obtained by such measurement techniques depends on the thorough knowledge of all system elements shown in Fig. 1 and on an analysis of all arising measurement errors.

This paper describes problems encountered in developing the probes, presents the technological or software-based solutions found, and reports first results in a turbulent flow. A sister paper (Part 2) reports about investigations of aerodynamic effects on fast-response probe measurements. The work is being continued toward further probe miniaturization, comparative measurements, and turbomachinery system applications.

2 Measurement System

In probe design the conflicting requirements of aerodynamics, sensor chip packaging, and microtechnical fabrication must be balanced. After manufacturing, the probe undergoes an electrical calibration of the mounted pressure transducers and an aerodynamic calibration in a reference flow (Kupferschmied and Gossweiler, 1992). These procedures provide the data base required for the evaluation of the data collected in the experiments. For the data analysis and signal processing an open and interactive software environment running on DEC/VAX under VMS has been developed (Herter et al., 1992).

Goals for Fast-Response Probe Measurements. During measurements in turbomachines, aerodynamic probes are subjected to a systematic fluctuation of the flow vector due to blade passing and to turbulent (random) events. Blade passing frequencies in turbomachines are typically of the order of 2–10 kHz and the bandwidth of these systematic fluctuations includes higher harmonics.

Accurate fast-response pressure measurements require a high accuracy both of the DC ("static") and AC ("dynamic") signal components. The DC errors, if large in comparison to the velocity head, reduce the accuracy of the velocity measurement. This sets a lower Mach number limit for the practical use of the probes (in our case M = 0.15–0.20).

The main disadvantage of aerodynamic probes lies in the fact that they are intruded into the flow. It is thus of utmost importance to manufacture probes as small as possible. Apart from the size of the probes and from technical aspects, i.e., to equip them with miniature sensors, the aerodynamic shape plays an important role when choosing the final probe design (see Part 2 of the paper).

Measurement Errors. Analyzing the errors leads to the following:

- Pressure measurement errors are associated with the use of miniature silicon transducers.
- Velocity measurement errors occur due to aerodynamic effects of the flow around probes (Part 2 of the paper).

The total error of a measuring system can be divided into static and dynamic errors, each further subdivided into systematic and random errors (Fig. 2).

To a certain degree all systematic errors can be corrected using the information gained in the calibration. The remaining

Contributed by the International Gas Turbine Institute and presented at the 39th International Gas Turbine and Aeroengine Congress and Exposition, The Hague, The Netherlands, June 13–16, 1994. Manuscript received by the International Gas Turbine Institute February 4, 1994. Paper No. 94-GT-26. Associate Technical Editor: E. M. Greitzer.

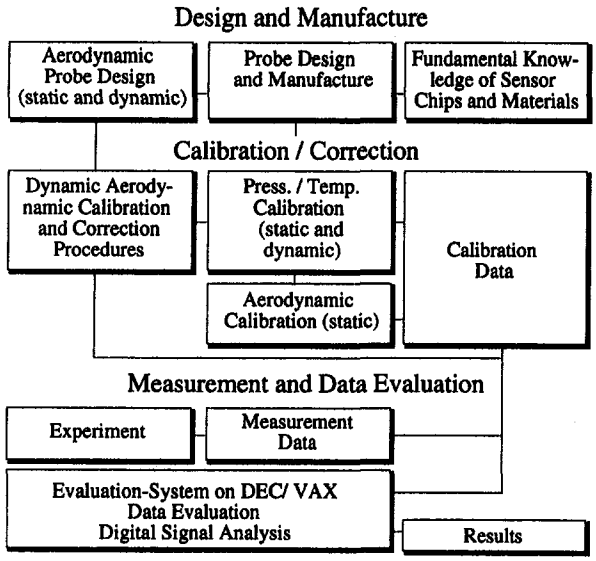

Fig. 1 Fast-response measurement system

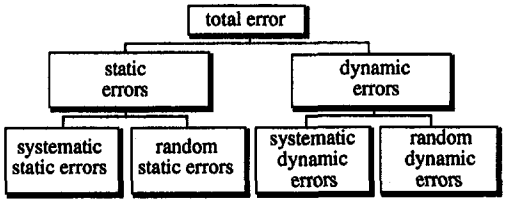

Fig. 2 Classification of measurement errors

systematic and also the random errors must be quantified in order to reduce them by an appropriate measurement strategy.

3 Probe Technology and Sensor Calibration

The use of miniature pressure transducers in aerodynamic probes showed that three main steps are important for an accurate pressure measurement (Gossweiler, 1993):

- testing and selection of the silicon sensor chips
- optimization of the packaging technique
- systematic investigation of all "electrical" pressure measurement errors and establishment of correction procedures.

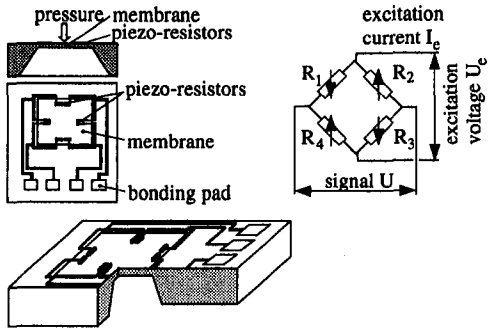

Fig. 3 Schematic of a miniature sensor chip

Table 1 Properties of sensor chips

Typical dimensions (L, W, H)	1.5-2.0, 0.6 -1.2, 0.15-0.5 mm
Typical sensitivity	S = 10 .. 25 mV/V bar
Typical sensitivity with excitation power P_D = 5 mW	S = 30 .. 140 mV/bar
Max. temperature (limitation by resistor noise)	120 °C
Burst pressure of the membrane	3 .. 20 bar
Gauge resistance	R = 1.7 .. 5 kΩ

Sensor Chips. The miniature piezoresistive Wheatstone bridge type pressure sensor chips used for the probes were originally created for the biomedical industry. The chips (Fig. 3) are manufactured by a standard planar process and by silicon micromachining to form the membrane (Kloeck, 1989).

The arrows in the circuit diagram of Fig. 3 indicate the direction of the resistance change when pressure is applied.

Self-heating of the resistors due to the electrical power P_D introduced by the excitation is negligible. A sufficiently high sensitivity is obtained by as little as P_D = 5 mW, which is very low compared to other miniature transducers. Typical chip dimensions and sensor data are listed in Table 1.

Packaging and Probe Manufacture. A fast-response probe design is a compromise between:

- the reduction of the probe dimensions, which is of utmost importance in fluctuating flows
- the shape of the probe dictated by aerodynamic aspects
- the mechanical mounting and environmental protection of the sensor chips (packaging technique).

Nomenclature

c = velocity in the absolute system
fs = full scale
I = current
K = aerodynamic probe calibration coefficient
M = Mach number
MBR = model-based reconstruction
p = pressure
P = power
r = radius
R = resistance
Re = Reynolds number
S = sensitivity
T = temperature
U = voltage
$\bar{U}_{max}$ = time-averaged velocity on pipe centerline
$U(t)$ = axial velocity component in pipe $= \bar{U} + u'(t)$
$V(t)$ = radial velocity component $= \bar{V} + v'(t)$
$W(t)$ = tangential velocity component $= \bar{W} + w'(t)$
ϵ = relative error
γ = flow angle (pitch) relative to the probe
ρ = specific density
φ = flow angle (yaw) relative to the probe

Sub- and Superscripts

D = dissipation
e = excitation
i, j = index
m, n = polynomial exponents
PS = pressure side
s = static
SS = suction side
t = total
$\hat{}$ = indicated value
$\tilde{}$ = phase-locked average
$'$ = time-dependent
$-$ = time-average

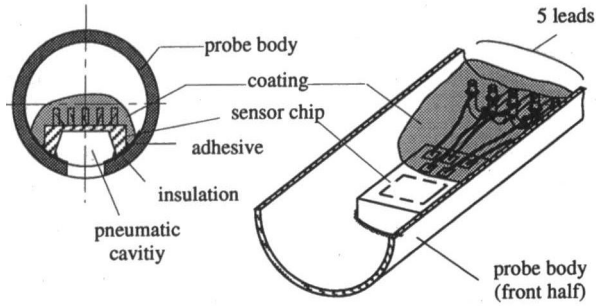

Fig. 4 Sensor packaging into cylinder probe

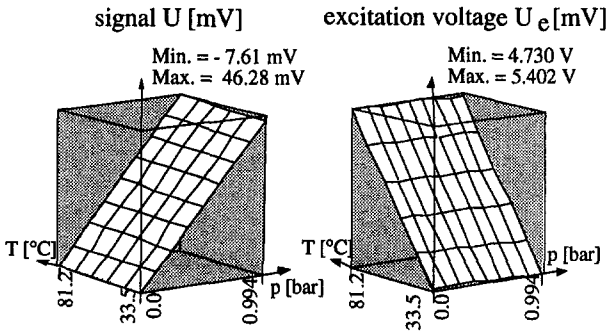

Fig. 6 Electrical calibration data of a sensor

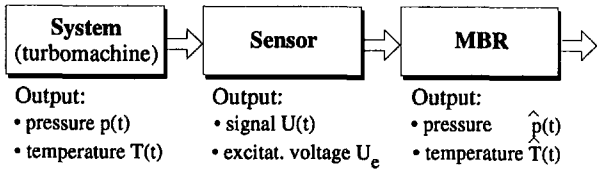

Fig. 7 Model-based reconstruction

The properties, especially the behaviour due to thermal effects, are strongly affected by the packaging technique. Figure 4 shows a typical assembly of a cylindrical single-sensor probe with an outer diameter of 1.8 mm.

The probe body is made of a nickel alloy, which matches well the low thermal expansion of the silicon sensor. The sensor is bonded to the probe body with a soft rubber-like adhesive, which reduces thermal strain imposed on the chip. The pneumatic cavity between the membrane and the probe surface limits the usable frequency range to approximately 35–45 kHz due to cavity resonance. Several single and multisensor probes with different geometries were built using this packaging technique. Figure 5 shows two cylindrical four-sensor probes ($\varnothing$ = 2.5 mm). The probe interior is kept on an accurately known constant reference pressure.

Sensor Properties and Errors. The static and dynamic electrical response of the sensors to pressure and temperature has been investigated systematically. With such knowledge the systematic static errors can be corrected and the remaining static and dynamic errors can be quantified.

Systematic Static Errors and Their Correction. The static sensor properties can be determined by calibrating the pressure transducers in the desired pressure and temperature range (in our case typically $0 \le p \le 1$ bar, $15 \le T \le 80$°C). The transducers are excited with constant current I_e. The variations of the signal $U(p, T)$ and of the excitation voltage $U_e(p, T)$ are recorded. As seen from Fig. 6 (note the different scales), the signal voltage U from the Wheatstone bridge is primarily dependent on the pressure p but also to a certain degree sensitive to temperature T. On the other hand the change of excitation U_e is only a function of the chip temperature.

Typically for piezoresistive transducers thermal zero and sensitivity shift as well as nonlinearity amount to a signal output of about 10 percent fs/50°C (Kloeck, 1989).

Conventionally in pressure transducer technology, thermal shift of zero and sensitivity are compensated to a level of about 1–2 percent fs/50°C by adding external resistors to the Wheatstone bridge. With this technique nonlinearity of the pressure signal remains uncorrected.

In the present work, a Model-Based Reconstruction technique (MBR) has been developed to reduce the systematic static errors and thus to enhance the accuracy of the pressure measurement. This technique uses a mathematical model to describe the relation between the sensor output (signal U, excitation U_e) and the so called "indicated" pressure $\hat{p}$ and temperature $\hat{T}$ (Fig. 7).

Polynomials provide an accurate mathematical model:

$$\hat{p} = \sum_{i}^{m} \sum_{j}^{n} c_{pij} U^i U_E^j \quad \hat{T} = \sum_{i}^{m} \sum_{j}^{n} c_{Tij} U^i U_E^j \qquad (1)$$

With a set of calibration data $U(p, T)$ and $U_e(p, T)$ the parameters c_p and c_T of the model are estimated using a least-squares approximation.

Using this method, both pressure and chip membrane temperature can be measured with the same sensor. Thus the remaining systematic errors can be reduced by an order of magnitude compared to conventional compensation. They are typically within ±0.1 percent fs for pressure and temperature measurement (range of $0 \le p \le 1$ bar; $30 \le T \le 80$°C).

Random Errors of Pressure Measurement. Summarizing the results of Gossweiler et al. (1990a, 1992), and Gossweiler (1993), random errors are due to thermal hysteresis, creep, long-term stability, and electrical resistor noise (Table 2).

Long-term stability errors can almost be eliminated without recalibration of the transducers by adjusting zero and span before the measurements. The factor limiting the resolution of the pressure measurement toward the low pressure levels is the electrical noise.

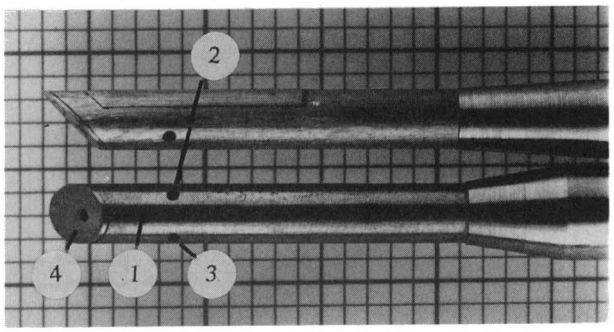

Fig. 5 Cylindrical four-sensor probes (ϕ = 2.5 mm)

Table 2 Typical random pressure errors in the range ($0 \le p \le 1$ bar; $30 \le T \le 80$°C)

thermal hysteresis	< 1 mbar (0.1 % fs)
creep	< 0.06 % fs
long term stability	< 50 mbar / year
electrical resistor noise [RMS]	< 0.1 mbar (0.01 % fs)

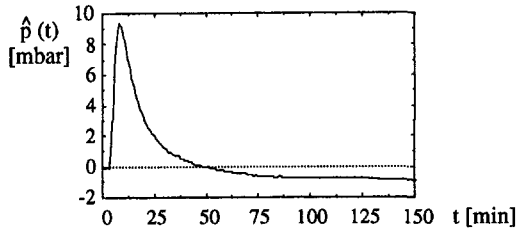

Fig. 8 Dynamic error in indicated pressure

Dynamic Errors of Pressure Measurement. The dynamic errors caused by pressure and temperature fluctuations can exceed the static errors considerably.

Dynamic calibrations of transducers were performed in a shock tube. It revealed that the natural frequency of the diaphragm was approximately 600 kHz. However, the natural frequency of the pneumatic cavity is much lower, namely 70–90 kHz, thus limiting the usable frequency range to 35–45 kHz (Gossweiler et al., 1990b).

Sensors exposed to thermal transients (e.g., during the startup of a turbomachine) show large deviations from the static behavior. Figure 8 shows the dynamic (transient) errors due to thermal transients represented by the indicated pressure $\hat{p}(t)$ of the unloaded transducer. For these results the sensor was exposed to a temperature ramp of $\Delta T = 30°C$ with a gradient of 6°C/min.

The maximum error, caused by transient mechanical strain, can be seen to reach approximately 10 mbar (1 percent fs). After passing the maximum, the strain decays due to the creep of the rubberlike adhesive between chip and probe and hence the indicated pressure returns to the static value ($= -1$ mbar) within approximately 80 minutes.

Systematic studies of this effect led to the quantification of dynamic errors in gain and offset (ϵ_{dS} and ϵ_{dO}, respectively) in Fig. 9.

Thermal transient effects were identified to be responsible for the largest pressure measurement errors occurring in practice. Therefore fast-step temperature changes should be avoided, or, at least, a sufficient time period of the order of an hour should be allowed to let the transient errors decay.

4 Aerodynamic Probe Calibration

Following the electrical calibration of the sensors, the probe undergoes an aerodynamic calibration under steady flow conditions at several Mach numbers. For this purpose, both a subsonic and a transonic facility have been built. Special attention has been paid to obtain steady air flow conditions in terms of temperature (±0.05°C) and total pressure. Uniform velocity profiles and a turbulence level below 0.3 percent could be achieved in the subsonic jet nozzle ($\varnothing = 100$ mm).

To enhance the calibration quality (accuracy and point density) and to limit human exposure to the jet noise, the calibration process is fully automatic. Remotely controlled by a Macintosh computer, the probe is yawed and pitched according to an input task file. Calibration data are collected by a multichannel pressure scanner and a precision multichannel voltmeter. Due to the lower long-term stability of packaged miniature sensors, the aerodynamic calibration duration of fast-response probes should be as short as possible. An easier way to proceed is to use calibration data of a conventional pneumatic probe of nearly identical geometry and to correct small discrepancies by using a few discrete calibration points of the fast-response probe version. Typically, Mach number is varied in steps of 0.2 and the yaw and pitch angles are varied in steps of 2 deg within the ranges of ±30 and ±24 deg, respectively. Flow Reynolds numbers closely corresponded to the actual flow conditions.

5 Probe Data Evaluation

In the following, calibration data of the above-described four-sensor probe is used to illustrate the steps of the ensuing off-line evaluation of flow quantities. The presented calibration coefficients are fitted with mathematical functions to allow an efficient evaluation of large data sets. Low Mach number air flow conditions are considered.

Aerodynamic Calibration Coefficients. The independent flow quantities measurable with this probe type are both yaw and pitch and both total and static pressure. In addition, the temperature information is gained from the sensor's Wheatstone bridge signals. The pressures $p = f(\text{yaw, pitch})$ obtained for each tap from calibration are transformed into a set of nondimensional coefficients for further data evaluation (Kupferschmied and Gossweiler, 1992). For the probe geometry of interest, the following coefficient set shows satisfactory results within a restricted angular field (taps numbered according to Fig. 5):

- Angular sensitivity:

$$K_\varphi(\varphi, \gamma) = \frac{p_2 - p_3}{p_1 - \frac{p_2 + p_3}{2}}, \quad K_\gamma(\varphi, \gamma) = \frac{p_1 - p_4}{p_1 - \frac{p_2 + p_3}{2}}$$

- Pressure sensitivity:

$$K_t(\varphi, \gamma) = \frac{p_t - p_1}{p_1 - \frac{p_2 + p_3}{2}}, \quad K_s(\varphi, \gamma) = \frac{p_t - p_s}{p_1 - \frac{p_2 + p_3}{2}}$$

Aerodynamic Calibration Data Modeling. Discretely collected calibration information must be analytically modeled in order to allow an efficient numerical data evaluation. The probe characteristics are described mathematically either with nonparametric models such as look-up tables (data are in raw form as coordinates x, y, and z; accuracy of interpolations strongly depends on mesh density) or with parametric models where calibration data are fitted with model functions. Polynomials in two variables are adequate for these surface shapes and are described in the literature (e.g., Bohn and Simon 1975).

Flow Data Evaluation. The steps are illustrated in Fig. 10. Indicated values feature a caret. Once the sensor signals have been converted into pressure and temperature by MBR, yaw and pitch angles are determined using either an indirect or a direct method (suitable for both model types).

Total pressure and then static pressure are calculated by taking K_t and K_s at the proper yaw and pitch angles. Angle errors may cause severe errors in pressure. Other quantities such as flow temperature and velocity are computed later on. In a last step, the results are transformed into the mainflow stream coordinate system ($\bar{V} = 0$, $\bar{W} = 0$).

Two different approaches are possible for computing the angles, depending on the way the calibration data were orga-

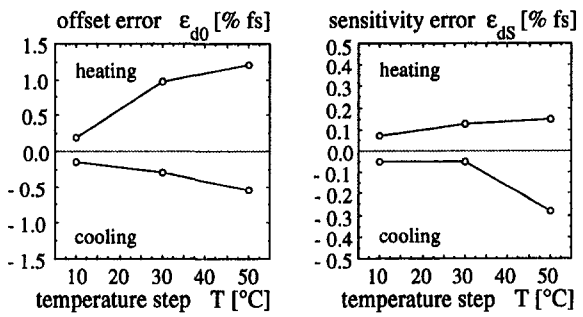

Fig. 9 Dynamic error in gain ϵ_{dS} and offset ϵ_{dO}

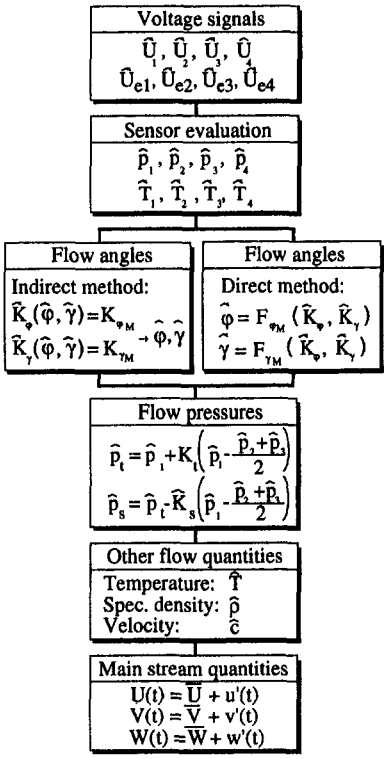

Fig. 10 Measurement data evaluation steps

nized. In the "indirect method," $K_{\gamma M}$ and $K_{\varphi M}$ are plotted as functions of yaw and pitch with a grid corresponding to the calibration mesh. The angles are found by iterations.

If the dependent variables $K_\varphi = f(\varphi, \gamma)$ and $K_\gamma = f(\varphi, \gamma)$ and the independent variables φ and γ are exchanged, each yaw or pitch angle appears to be dependent only on the coefficients K_φ and K_γ ("direct method"; $\varphi = f(K_\varphi, K_\gamma)$, $\gamma = f(K_\varphi, K_\gamma)$). The flow angles can then be calculated directly from these equations and do not require any iteration. An important fact to note is that the dependent variables are no longer equidistant, because fitting parametric models in areas having a low density of points leads to systematic errors in these regions or may even cause oscillations between data points. In comparative tests, the evaluation of 262,000 data points on a VAX 9000-420 mainframe required 15 minutes of CPU time for the indirect method and only about 2 minutes for the direct method (using both parametric or nonparametric models).

This method, using calibration coefficients obtained in steady flow, becomes insufficient if the flow fluctuations are too fast. Such dynamic effects are considered in Part 2 of the paper.

6 Applications

Two different applications are discussed in the following to give a practical illustration of the techniques described in the sections above.

Measurements in the Vaneless Diffuser of a Radial Compressor. The flow at the exit of the impeller was axially traversed at several radial positions in the vaneless diffuser to measure periodic fluctuations (Hunziker et al., 1990; Gossweiler et al., 1990a, b). Turbulence effects had to be eliminated by ensemble averaging (Eckhardt, 1976; Shreeve and Neuhoff, 1984), because only a single-sensor probe was available at the time of the measurements. The technical data of the compressor are listed in Table 3.

Firstly, the time-averaged flow velocity and its yaw direction have been measured with a conventional (i.e., pneumatic) cylindrical two-hole pressure probe ($\varnothing$ = 1.8 mm). Measurements of the systematic fluctuations caused by blade passing were then performed with a fast-response probe ($\varnothing$ = 1.8 mm, equipped with a single pressure sensor) and with a flush-mounted wall static pressure transducer. Phase-locked sampling and ensemble averaging were used for the data reduction (Gyarmathy et al., 1991). The total pressure fluctuations were determined by yawing the probe sensor toward the time-averaged mean flow direction. The time-dependent total pressure signal was calculated by superposing the time-averaged total pressure and the ensemble-averaged fluctuation (Fig. 11). The static wall pressure measured at the same radial position was used to determine the ensemble-averaged dynamic head.

Table 3 Technical data of the radial compressor

Diameter of impeller	280 mm
Diffuser width	17 mm
Number of blades	18
Maximum tip Mach number	$M_u = 0.75$
Typical pressure ratio	1.5
Typical blade passing frequency	6.5 kHz

A determination of the yaw angle fluctuation (Fig. 12) was made possible by yawing the probe plus or minus by 45 deg and then applying the static calibration data to the ensemble-averaged pressures.

The yaw angle φ fluctuates between 16 and 33 deg. Both tangential and radial velocity components are determined from the measurements. Figure 13 shows the radial velocity c_r at two different radial positions r/r_{wheel} = 1.06 and 1.16 in the diffuser. It can be seen that the systematic fluctuations caused by the impeller decay very rapidly in the downstream direction. This fast decay is typical for impeller exit flows (Senoo and Ishida, 1974; Eckhardt, 1976).

The measurements in the radial compressor demonstrated the robustness of the probe. More than 100 operating hours have been accomplished in highly turbulent flow at Mach numbers up to 0.75 and temperatures up to 80°C without any damage or

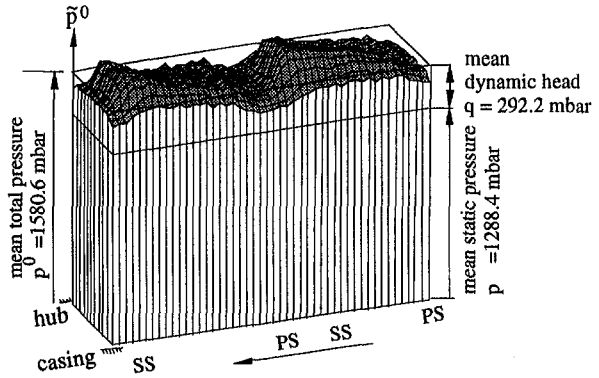

Fig. 11 Time-dependent total pressure distribution (*PS*: pressure side, *SS*: suction side of impeller blade)

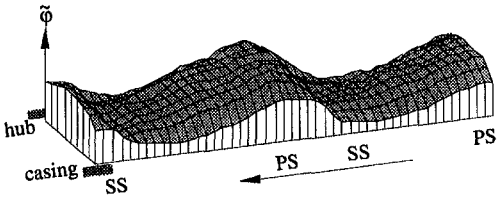

Fig. 12 Time-dependent flow angle (min. 16 deg, max. 33 deg)

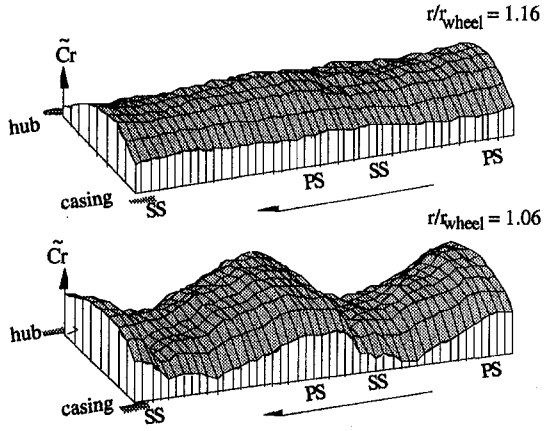

Fig. 13 Decay of systematic fluctuations of the radial velocity in the diffuser

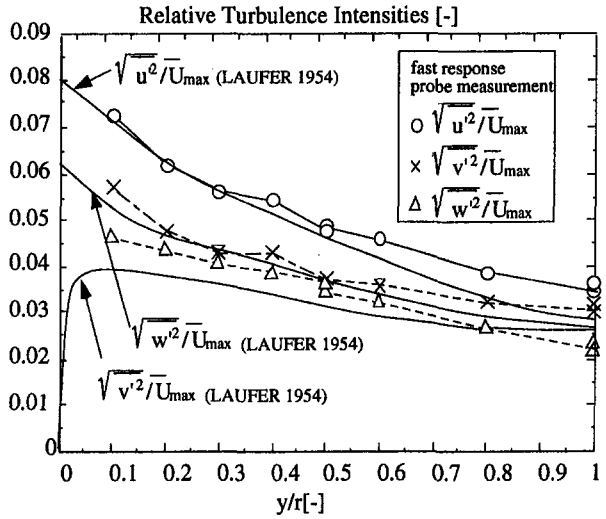

Fig. 15 Normalized turbulence intensities versus normalized pipe wall distance

deterioration, i.e., a change of sensitivity. Further work is aimed at simultaneous velocity and yaw measurement using a three-hole probe.

Measurements in Turbulent Pipe Flow. Measurements with a cylindrical four-sensor probe were performed in a fully developed pipe flow of M = 0.2. The purpose of this experiment was to compare the results to hot-wire data of the well-known experiments from Laufer (1954) and to test the ability of the system to yield turbulence quantities (Gossweiler et al., 1992).

The time-averaged velocity, obtained with simple corrections for shaft influence and blockage, shows good compliance with the power law of turbulent pipe flow (within 2 percent of $\bar{U}_{max}$, data not shown).

An advantage of this technique is the ability to measure pressure. Figure 14 shows the rms values of the total and static pressure fluctuation over normalized wall distance y/r (r: pipe radius, $y/r = 1$: pipe center).

Very often the static pressure is considered to be constant, but it can be seen from Fig. 14 that the fluctuations amount to about 4 percent of the dynamic head.

The normalized turbulence intensities of the three velocity components $U(t)$, $V(t)$, $W(t)$ are compared to Laufer's hot-wire data in Fig. 15 (see also Hinze, 1975).

The turbulence intensity of the U component turns out to be too high at the pipe center. The value for the W fluctuation was determined by yaw angle measurement. It can be seen to be slightly too low. The value for the V fluctuation, obtained by pitch angle measurement, is systematically too high (max. 45 percent). The investigation of dynamic effects of the flow around probes (see Part 2 of the paper and Humm and Verdegaal, 1992) leads to the assumption that this discrepancy is due to dynamic aerodynamic errors in the pitch angle not corrected in the present evaluation.

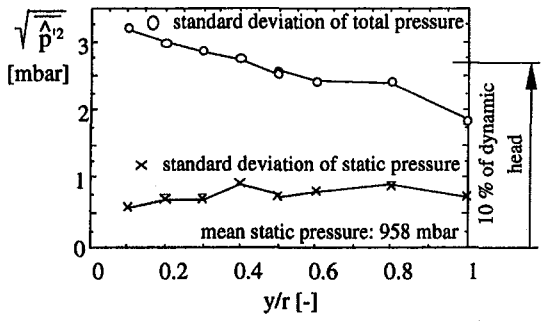

Fig. 14 Standard deviation of total and static pressure fluctuation versus normalized pipe wall distance

The same effects lead to an unsatisfactory correlation for the measurement of the local turbulent shear stress components in the flow (Gossweiler et al., 1992).

Conclusions

The use of miniature pressure transducers in aerodynamic probe heads poses difficult problems for the achievement of a high measurement accuracy. Special attention has to be paid to the packaging technique in order to protect the chips from environmental influences. For the correction of the inherently strong temperature effects shown by piezoresistive silicon sensors, a model-based reconstruction was developed, which, in comparison to other techniques, reduces the errors by an order of magnitude. Thermal transient effects caused by rapid changes in flow temperature were identified to cause the largest pressure measurement errors and therefore must be avoided.

To allow a fast and accurate off-line data evaluation with computers, the aerodynamic calibration data are converted to pressure coefficients and reduced mathematically to efficient model functions.

Application of a single-sensor cylinder probe to the impeller outflow of a radial compressor confirmed the fast decay of periodic (blade-passing) nonuniformities. Application to pipe flow allowed the comparison of turbulence intensities to Laufer's classical hot-wire data with encouraging results.

Acknowledgments

The authors would like to thank the Swiss National Science Fund for the continued financial support of this program. Furthermore we thank our colleagues Dr. Doris Herter and Kevin Kaupert for their cooperation and discussion. For the technical support we thank Peter Althaus, Cornel Reshef, Thomas Künzle, Peter Lehner, Hans Richner, and Hans Suter.

References

Bohn, D., and Simon, H., 1975, "Mehrparametrige Approximation der Eichräume und Eichflächen von Unterschall-bzw. Überschall-5-Loch-Sonden," *ATM Messtechnische Praxis,* Mar.

Castorph, D., 1975, "Messung des instationären Strömungsfeldes einer Kaplanturbine mit elektronischen Miniatursonden," *Forsch. im Ing.-Wesen,* Vol. 41, No. 6.

Eckhardt, D., 1976, "Untersuchung der Strahl/Totwasserströmung hinter einem hochbelasteten Radialverdichterlaufrad," PhD-Thesis, RWTH Aachen.

Epstein, A., 1985, "High Frequency Response Measurements in Turbomachinery," *VKI Lecture Series 1985–03,* Brussels, Belgium.

Gossweiler, C., Humm, H. J., and Kupferschmied, P., 1990a, "The Use of Piezoresistive Semiconductor Pressure Transducers for Fast Response Probe Mea-

surements in Turbomachines," *Proceedings of the 10th Symposium on Measuring Techniques for Transonic and Supersonic Flows in Cascades and Turbomachines,* VKI, Brussels, Sept.

Gossweiler, C., Humm, H. J., and Kupferschmied, P., 1990b, "Dynamic Calibration of Piezoresistive Pressure Transducers in the Frequency Range of Over 500 kHz," *Proc. Micromechanics Europe 1990,* Berlin.

Gossweiler, C., Herter, D., and Kupferschmied, P., 1992, "Fast Response Measurements in a Turbulent Pipe Flow," *Proc. 11th Symp. on Meas. Tech. for Transonic and Supersonic Flows in Cascades and Turbomachines,* Munich, Germany.

Gossweiler, C., 1993, "On Probes and Measuring Techniques for Fast-Response Flow Measurement Using Piezo-Resistive Pressure Transducers," PhD-Thesis [in German] No. 10253, ETH Zürich.

Gyarmathy, G., Hunziker, R., Ribi, B., and Spirig, M., 1991, "On the Change of Impeller Flow Non-uniformities With Flow Rate in a Centrifugal Compressor," *IMechE J.*

Heneka, A., 1983, "Entwicklung und Erprobung einer Keilsonde für instationäre dreidimensionale Strömungsmessungen in Turbomaschinen," Mitteilung Nr. 14. des Institutes für thermische Strömungsmaschinen der Universität Stuttgart.

Herter, D., Chrisander, N. O., and Gossweiler, C., 1992, "AW-System—An Interactive Environment for the Evaluation of Large Time Series," *Proc. 11th Symp. on Meas. Tech. for Transonic and Supersonic Flows in Cascades and Turbomachines,* Munich, Germany.

Hinze, J. O., 1975, *Turbulence,* McGraw-Hill, New York.

Humm, H. J., and Verdegaal, J. I., 1992, "Aerodynamic Design Criteria for Fast Response Probes," *Proc. 11th Symp. on Meas. Tech. for Transonic and Supersonic Flows in Cascades and Turbomachines,* Munich, Germany.

Hunziker, R., Ribi, B., Spirig, M., and Gyarmathy, G., 1990, "On the Influence of Different Impellers on a Radial Compressor Stage With Vaneless Diffuser," *Interfluid Essen FRG.*

Kerrebrock, J. L., Epstein, A. H., and Thompkins, W. T., 1980, "A Miniature High Frequency Sphere Probe," *Measurement Methods in Rotating Components of Turbomachinery,* B. Lakshminarayana, ed., ASME, New York.

Kloeck, B., 1989, "Design, Fabrication and Characterization of Piezoresistive Pressure Sensors, Including the Study of Electrochemical Etch-Stop," PhD Thesis, University of Neuchâtel.

Kupferschmied, P., and Gossweiler, C., 1992, "Calibration, Modelling and Data Evaluation Procedures for Aerodynamic Multihole Pressure Probes on the Example of a Four Hole Probe," *Proc. 11th Symp. on Meas. Tech. for Transonic and Supersonic Flows in Cascades and Turbomachines,* Munich, Germany.

Larguier, R., 1985, "Experimental Analysis Methods for Unsteady Flows in Turbomachines," *ONERA, ISABE 85-7030.*

Laufer, J., 1954, "The Structure of Turbulence in Fully Developed Pipe Flow," NACA Tech. Rep. No. 1174, Update 1975.

Senoo, Y., and Ishida, M., 1974, "Behavior of Several Asymmetric Flow in a Vaneless Diffusor," ASME Paper No. 74-GT-64.

Shreeve, R. P., and Neuhoff, F., 1984, "Measurements of the Flow From a High Speed Compressor Rotor Using a Dual Probe Digital Sampling (DPDS) Technique," ASME *Journal of Engineering for Gas Turbines and Power,* Vol. 106.

On Fast-Response Probes: Part 2—Aerodynamic Probe Design Studies

H. J. Humm

C. R. Gossweiler

G. Gyarmathy

Turbomachinery Laboratory,
ETH Swiss Federal Institute of Technology,
Zurich, Switzerland

The influence of the probe size and geometry on the quality of fast-response measurements in turbomachines has been experimentally investigated. For investigations in the static domain (time-independent flows) probes were calibrated in two continuously operating wind tunnels in the range $0.2 < M < 1.2$. For dynamic calibrations in time-variant flows model experiments in water ($0.025 < k < 0.4$, reduced frequency) were performed. Aerodynamic characteristics were determined for a great number of probe geometries, such as circular cylinders and wedge-type probes with varied apex angles, locations of the sensing holes, and leading edge shapes. The experiments comprised investigations in tolerance ranges for prismatic total pressure probes, yaw angle sensitivity, yaw angle, and Mach number effects on calibration and influence of dynamic yaw angle fluctuation on probe characteristics. As a result of the experiments errors due to static and dynamic aerodynamic effects could be quantified. The majority of the errors arising during measurements in turbomachines can be directly related to the probe size. An important number of these errors are systematic and can be analytically modeled and hence their influence corrected. In fluctuating flows the most severe measurement errors, which often may exceed the quantity of interest, are due to dynamic stall effects. This phenomenon, which is of transient nature and cannot be corrected, is typical for sharp wedge probes, but is not present with circular cylinders, and the effects are much smaller with very blunt wedges.

Introduction

During measurements in turbomachines, aerodynamic fast-response probes are subjected to strongly fluctuating flows with pronounced velocity gradients and a high turbulence level. It is essential for accurate measurements that probes be calibrated under conditions representative of these flows maintaining the dynamic similarities such as Reynolds number Re, Mach number M, and reduced frequency k of the fluctuation. Also, blockage, three-dimensional, and wall proximity effects must not be neglected.

Whereas the literature provides much information on static aerodynamic effects affecting the quality of probe measurements, until now little attention has been paid to the quantification of dynamic effects of the flow around probes. Only Kovasznay et al. (1981) investigated the influence of fluctuating flows in magnitude on pressures registered on probes.

The aim of this paper is to give a survey of the work in the aerodynamic domain with regard to turbomachinery measurements including dynamic effects. The critical comparison of different probe shapes led to a quantification of errors due to aerodynamic effects (static and dynamic) and finally guidelines for the optimum aerodynamic shape of fast-response probes could be discussed.

The probe designs chosen were in accordance with the feasibility to manufacture and assemble the probes using miniature pressure transducers (see Part 1). Therefore, certain shapes (e.g., very sharp wedges) were not included in the investigations since they do not comply with these demands.

Concerning dynamic effects associated with yaw angle fluctuations, the simulation of an exactly defined reference flow in air representing the conditions in turbomachines lies far beyond the current technology. For this reason, the investigations, although confined to the pure incompressible domain, were performed in model experiments in water.

Static Probe Calibration

The purpose of the static aerodynamic probe design studies is to ensure that the set of probe pressure readings obtained under static (steady) flow conditions is an unambiguous and sensitive measure of the flow vector. The demands for aerodynamic probes from static aspects, which go in tandem with dynamic criteria, can be formulated as follows:

- true indication of the total and free-stream static pressure of the flow
- high angular sensitivity expressed by the difference between the two pressure holes per degree yaw
- low Mach number dependence on calibration data
- low yaw angle dependence on calibration data
- unambiguous calibration range as a function of yaw greater than the maximum incidence angle encountered during the measurement
- precise modeling of the calibration data feasible
- measurement as little as possible affected by velocity gradients.

For a number of prismatic probes (circular cylinder and wedge-type probes) the calibration data were recorded in a closed-wall wind tunnel in the range $0.2 < M < 1.2$ and a free jet within $0.3 < M < 0.7$. In addition to a circular cylinder and a three-hole wedge probe for measurements in turbomachines (Fig. 1, probes 13 and 14) various large-scaled wedge probes shown in Fig. 2 were calibrated.

The parameter variations of the wedge geometries (probes 1 to 12) were according to Fig. 1:

- total apex angles $\Theta = 45$, 60, and 90 deg

Contributed by the International Gas Turbine Institute and presented at the 39th International Gas Turbine and Aeroengine Congress and Exposition, The Hague, The Netherlands, June 13–16, 1994. Manuscript received by the International Gas Turbine Institute February 4, 1994. Paper No. 94-GT-27. Associate Technical Editor: E. M. Greitzer.

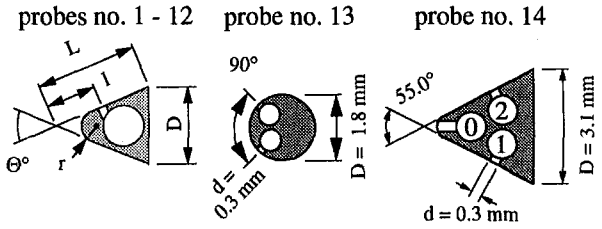

Fig. 1 Parameter variations of probes and miniature probes

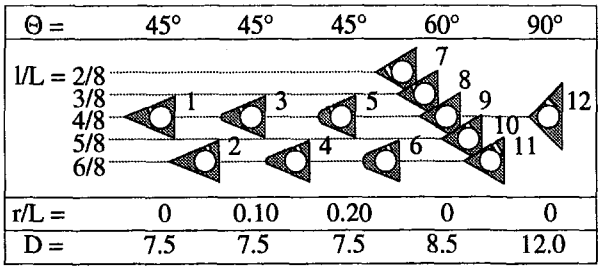

Fig. 2 Wedge probes for static pressure and yaw angle measurement

- nose radius r/L = 10 and 20 percent (wedge probe Θ = 45 deg)
- location of the sensing holes varied from $l/L = \frac{2}{8}$ to $\frac{6}{8}$

In order to avoid undesired three-dimensional effects of the flow around free ending probes the majority of the investigations were confined to fully two-dimensional conditions.

To keep the costs for the experiments low, the probes in Fig. 2 were equipped with only one sensing hole and manufactured in a scaled-up size ($7.5 < D < 12$ mm, diameters of the sensing holes d = 1 mm). However, the scale was chosen such that Reynolds number effects remained negligible.

In order to obtain more detailed information on the flow around probes (quantitatively and qualitatively) interferometric holograms were taken for a selected number of probes at different Mach number ranges.

Total Pressure Measurement. The characteristics of five prismatic probes (Nos. 16 to 20) for total pressure measurement were compared to the Pitot probe (No. 15). The angular tolerance range is defined as the yaw angle range where the deviations between the value registered by the probe p_0 and true total pressure p^0 are less than 1 percent of the dynamic head q. As seen from Fig. 3 the tolerance ranges are widely different, by far the best being the shaftless Pitot probe.

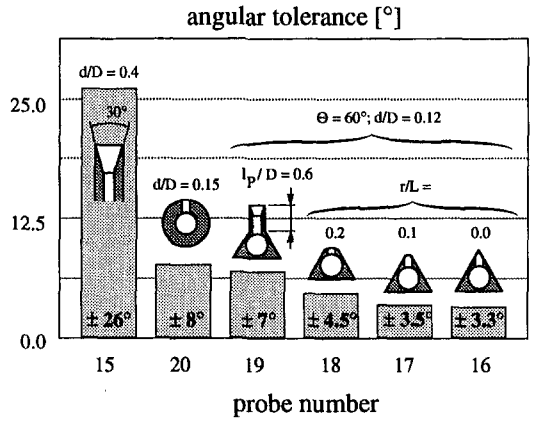

Fig. 3 Tolerance range for total pressure measurement

Wedge-type probes are seen to be not ideal for determining the total pressure of the flow unless they are equipped with a Pitot-type extension (probe No. 19, l_p/D = 0.6). Rounding of the leading edge of the wedges (probes No. 17 and 18) can be seen to improve the angular tolerance range, but the yaw characteristics remain insufficient in comparison to, e.g., the circular cylinder.

Yaw Angle and Static Pressure Measurement. A typical result for a yaw angle characteristic is shown in Fig. 4. The definition for the yaw angle coefficient K_{12} is given by

$$K_{12}(\alpha) = \frac{p_1(\alpha) - p_2(\alpha)}{p^0 - \dfrac{p_1(\alpha) + p_2(\alpha)}{2}} \tag{1}$$

with p^0 being the total pressure in the test section and p_1 and p_2 denoting the values recorded on the pressure side and suction side of the probe, respectively. In this case use of the definition of the calibration coefficient p^0 instead of the pressure indicated by the forward-facing pressure tapping p_0 is more advantageous since a clear distinction between the influence of the total pressure characteristic and effects on the side face of probes becomes possible.

Nomenclature

c = velocity, m/s
c_L = lift coefficient
cp = pressure coefficient normalized to the dynamic head q
d = diameter of sensing hole, mm
D = diameter/width of probes, mm
f = frequency of oscillation (e.g., blade passing), Hz
k = reduced frequency = fD/c_∞
K = pressure coefficient normalized to the probe-dynamic head = $p^0 - (p_1 + p_2)/2$
l = distance of sensing hole from leading edge, mm
L = side length of probes, mm
M = Mach number
n = shaft speed, 1/min
p = pressure, bar, mbar
q = dynamic head = $p^0 - p_\infty$, mbar; for incompressible flows $q = \rho c_\infty^2/2$
r = radius, mm
Re = Reynolds number
Str = Strouhal number
t = time, s
u = tangential velocity, m/s
w = velocity in the relative system, m/s
z = number of blades in an impeller
α = flow angle (yaw) relative to the probe, deg
Θ = total apex angle of wedge probes, deg
ν = kinematic viscosity, m/s^2
τ = period time, s
ω = angular speed, s^{-1}

Sub- and Superscripts

$(\ldots)_i$ = sensing hole i, i = 0, 1, 2
$(\ldots)_D$ = drag
$(\ldots)_L$ = lift
$(\ldots)_{PS}$ = pressure side
$(\ldots)_s$ = static, stall
$(\ldots)_{SS}$ = suction side
$(\ldots)_W$ = wake
$(\ldots)_y$ = resultant value
$(\ldots)_{12}$ = differential $(\ldots)_1 - (\ldots)_2$
$(\ldots)^0$ = e.g., total pressure p^0
$(\ldots)_\infty$ = free-stream conditions
$(\tilde{\ })$ = phase-locked average (periodic mean value)
$(\bar{\ })$ = time-averaged

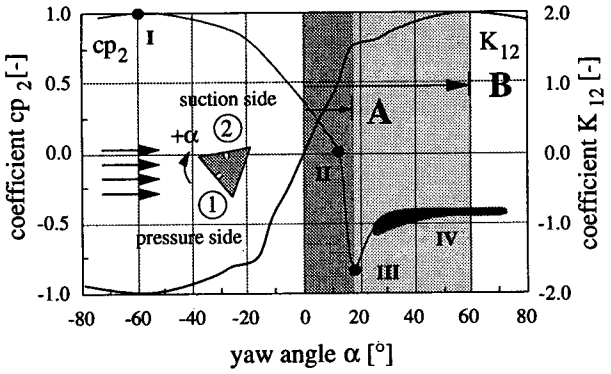

Fig. 4 Definition of calibration ranges

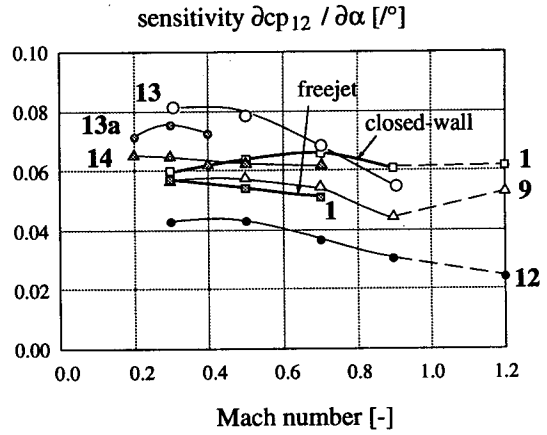

Fig. 6 Sensitivity versus Mach number, 13a: results of the free ending four-hole cylinder probe (see Part 1 of this paper)

The probes were equipped with a single sensing hole. Under the presumption that the flow conditions were fully symmetric the value $p_2(\alpha)$ was determined by $p_2(\alpha) = p_1(-\alpha)$.

Pressure measurements at several positions on the side faces of the probes and holographic interferometry provided the information to identify the main features of the flow around wedges. They can be summarized for the example $cp_2(\alpha)$ of probe 9. Stagnating conditions in point I ($\alpha \approx -60$ deg $\approx 90 - \Theta/2$, when $l/L = 0.5$), change of slope $cp_2(\alpha)$ due to the influence of a laminar separation bubble (II, $\alpha \approx 12$ deg), minimum pressure peak (III, $\alpha \approx 18$ deg) and fully separated flow (IV, $\alpha > 25$ deg). Between III and IV the pressure gradient $\partial p_2/\partial\alpha$ reaches its maximum.

The dark shaded area (A) represents the quasi-linear calibration range where an accurate modeling of the calibration data can be accomplished. To a certain degree also, sensitivity and indication of quasi-static pressure are almost independent on the angle of attack α. Within range B an unambiguous relation between calibration coefficient and yaw angle is possible.

Sensitivity. A high sensitivity improves the angular resolution of the measurement. In Fig. 5 the values

$$\frac{\partial cp_{12}}{\partial\alpha} = \frac{\partial}{\partial\alpha}\left(\frac{p_1 - p_2}{q}\right) \qquad (2)$$

for the different probes at $\alpha = 0$ deg and M = 0.5 are plotted.

It was found that by forming a 45 deg wedge probe with a nose radius of $r/L = 20$ percent (probe No. 5) the sensitivity can be increased by almost a factor of 2. In comparison to the majority of the wedges, the circular cylinder (13) shows better results. Generally, wedge probes with smaller apex angles exhibit higher values $\partial cp_{12}/\partial\alpha$ (e.g., probes Nos. 1, 9, and 12 with $l/L = 0.5$) but the relative location l/L of the sensing hole on the side face plays an even more dominant role, which is in good agreement with the findings from Ainsworth and Strickland (1992) and Cook (1989).

Mach Number Dependence. The effects of Mach number on the calibration characteristics can best be illustrated by plotting the sensitivity versus Mach number (Fig. 6).

Ideally a probe should show a constant value over the whole Mach number range, which is best fulfilled for the 45 deg wedge (probe No. 1). Remarkable are the differences of the characteristics obtained in two different calibration tunnels (closed-wall and free jet) for probe No. 1, which is most likely due to three-dimensional effects occurring on the free ending probe in the free jet. These findings illustrate how important calibration procedures under representative conditions are.

Another indication of Mach number dependence on the calibration can be seen when the probe-static pressure coefficient $K_s = (p_1 + p_2)/(2p_\infty)$ is plotted as a function of M (Fig. 7, for $\alpha = 0$ deg). A value close to the free-stream pressure, when K_s becomes unity, can be measured by using circular cylinders (No. 13) in the range $0 < M < 0.6$, wedge probes with very small apex angles ($\Theta \ll 45$ deg) or locating the sensor to the rear of the probes (e.g., No. 2).

For the wedges K_s (M) is very close to the idealized line const$*p^0/p_\infty$ whereas above M = 0.6 the circular cylinders show a pronounced Mach number dependence.

Yaw Angle Dependence. The influence of the angle of attack α on the sensitivity and unambiguous calibration range is shown in Figs. 8 and 9.

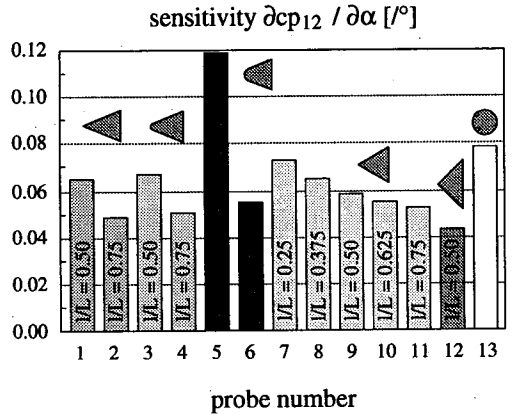

Fig. 5 Sensitivity $\partial cp_{12}/\partial\alpha$ of probes (M = 0.5)

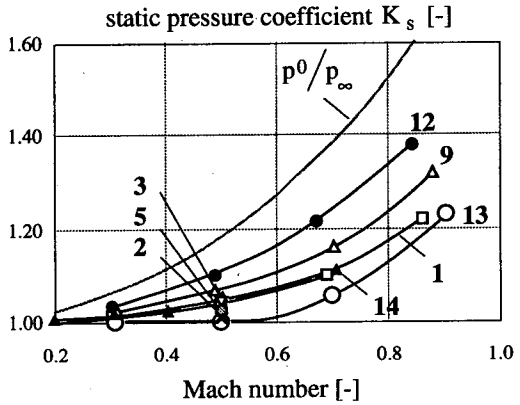

Fig. 7 Static pressure coefficient K_s versus Mach number

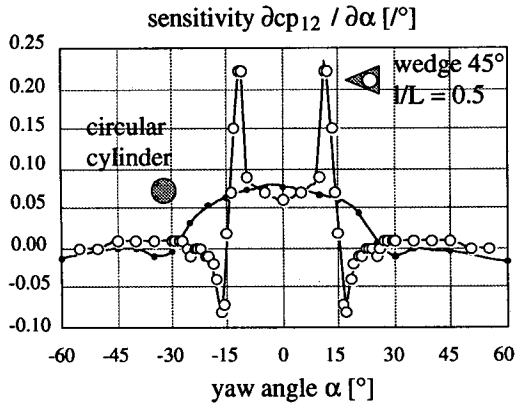

Fig. 8 Sensitivity versus angle of attack α (M = 0.5)

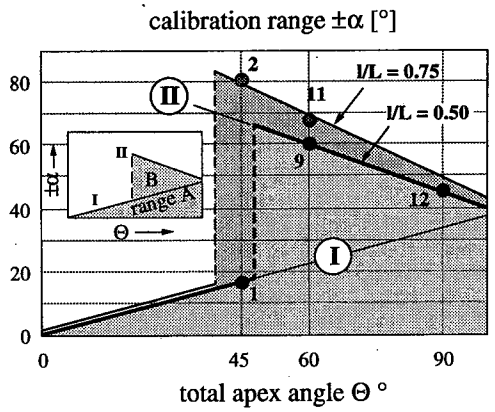

Fig. 10 Calibration ranges versus apex angle Θ

Especially in the range $\alpha = \pm 15$ deg the characteristic for the 45 deg wedge shows an extraordinary strong yaw-angle dependence due to a laminar separation bubble, and it can be seen that an accurate mathematical modeling of such data is not feasible. The same behavior can be observed for the probe-static pressure coefficient (not shown).

The limitation for the unambiguous calibration (range B, Fig. 4) can be obtained from the derivative of Eq. (1):

$$\frac{\partial K_{12}(\alpha)}{\partial \alpha} = (p^0 - p_2)\frac{\partial p_1}{\partial \alpha} - (p^0 - p_1)\frac{\partial p_2}{\partial \alpha} = 0 \qquad (3)$$

The experimentally determined extension of the calibration ranges A and B for the different probe geometries can be seen in Fig. 9. It is noteworthy that for the sharp 45 deg, wedge placing the relative location l/L of the sensing hole from 0.5 to 0.75, range B may be improved by a factor of 4. On the other hand, for the 45 deg wedges with rounded leading edges this effect does not take place.

Wedge probes with increased apex angles do not necessarily exhibit greater calibration ranges B, which can be seen in Fig. 10, where the calibration ranges are plotted versus the apex angle of the probes.

The explanation is given by a closer examination of Eq. (3) for the example of wedges with $l/L = 0.5$. For small apex angles, i.e., $\Theta \leq 45$ deg, the relation $\partial p_1/\partial \alpha \ll \partial p_2/\partial \alpha$ plays the dominant role for the limitation of the calibration range (line I in Fig. 10). By increasing the wedge angle, mainly the factor $p^0 - p_1$, which becomes much smaller, gains in importance and thus

$$(p^0 - p_2)\frac{\partial p_1}{\partial \alpha} > (p^0 - p_1)\frac{\partial p_2}{\partial \alpha} \qquad (4)$$

is fulfilled. In this case the calibration range is exceeded only when the total pressure is registered on the pressure side and $p^0 - p_1$ and hence $\partial p_1/\partial \alpha$ become zero (line II).

Therefore, for wedges with $l/L = 0.5$, the range for the unambiguous calibration data as a function of the apex angle is represented qualitatively by the lighter shaded area.

The effect of the relative location of the sensing holes on the side face of the probes plays a very important role, especially in the case of the 45 deg wedge. By placing the sensing hole toward the rear of the wedge probe ($l/L = 0.75$) Eq. (4) is fulfilled for smaller apex angles (darker shaded area). It can be hypothesized that placing the sensing holes upstream ($l/L < 0.5$) will have the opposite effect.

It is noteworthy that line I in Fig. 10 is identical to the extension of calibration range A, which cannot be influenced by the relative position of the sensing hole. This range has to be considered as the practical limitation for the use of fast-response probes.

Modeling of Calibration Data. The findings from above are substantiated when considering the feasibility to model the calibration data. As shown in Kupferschmied and Gossweiler (1992) the proper modeling of the calibration data is the basis for a precise evaluation and also helps save computing time.

From the calibration data mathematical models by means of 1, 3, and 5 degree polynomials were formed and the overall standard deviation between model and experimental calibration data determined. In Fig. 11 the quantity representing a random error between model and experimental calibration data is plotted versus the angular range of interest for the example of the 45 deg wedge (probe No. 1) and the circular cylinder (No. 13).

For very narrow angular ranges of interest, only a low degree polynomial is required for a good fit of the calibration data. Beyond a range $\pm\alpha = 20$ to 25 deg only very blunt wedges ($\Theta = 90$ deg) or circular cylinders fulfil the requirements for a precise modelling of the calibration data.

Velocity Gradient Effects. Velocity gradients are predominant in turbomachinery flows. It is essential that the yaw angle measurement be as little as possible affected by gradients. How-

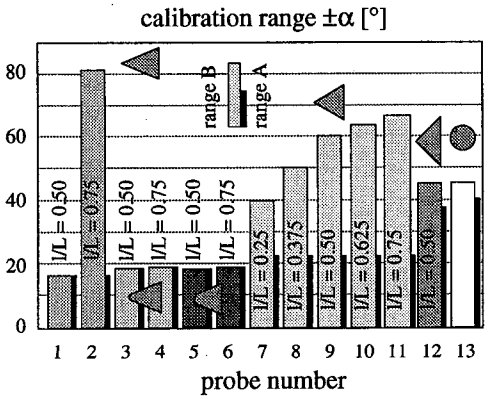

Fig. 9 Calibration ranges (A and B)

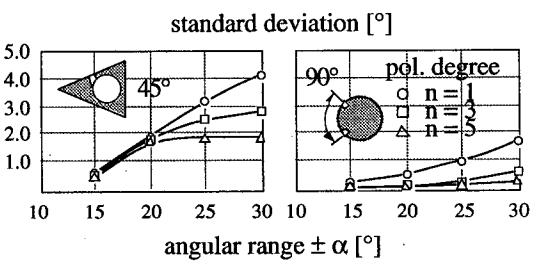

Fig. 11 The rms value between mathematical model and experiment

ever, at least the knowledge of the erroneous yaw angle measurement as a function of the velocity gradient, for enabling correction procedures, is of greatest importance. In experiments described in Humm and Verdegaal (1993) and Humm (1994) the indicated yaw angle of the 55 deg wedge (probe No. 14, Fig. 1) within a shear layer was measured. The measurement error was determined by taking the difference between the yaw angle measured with the wedge and the result of a specially designed probe, which is not, or at least an order of magnitude less, influenced by gradients.

In comparison to the results of a circular cylinder (Kupferschmied and Ribi, 1987) the wedge probe is only a factor of 1.5 less affected by velocity gradients. These findings are in contrast to some of the literature (e.g., Bryer and Pankhurst, 1977) where wedges are considered to be far superior in this domain.

Dynamic Probe Calibration

In Humm and Verdegaal (1992) and Humm (1994) dynamic effects regarding yaw angle fluctuations on probe calibration have been systematically studied.

The strategy adopted for the dynamic calibration of probes was based on model experiments in water. Oscillating scaled-up probe bodies were towed in a channel with stationary water and the dynamic pressures of the sensors in the probe head recorded. By using large probes of about 30 mm diameter in connection with the kinematic viscosity ν of the water, the dynamic similarities representing turbomachinery applications such as reduced frequency

$$k = \frac{f \cdot D}{c_\infty} \approx 0.05 \ldots 0.6 \qquad (5)$$

and Reynolds number

$$\mathrm{Re} = \frac{c_\infty D}{\nu} \approx 10{,}000 \ldots 120{,}000 \qquad (6)$$

agreed well for very low frequencies of oscillation ($1 < f < 10$ Hz) and low free-stream velocities $1 < c_\infty < 5$ m/s, though the Mach number dependence had to be neglected.

The comparison of the dynamic and static calibration data showed that in some cases the errors due to dynamic effects, when applying static calibration data, may rise to the quantity of interest. To some extent the errors can be seen to be dependent on both amplitude and frequency of oscillation while the geometry drastically affects the dynamic errors. Qualitatively, for the wedge-type configurations, the errors show an almost linear increase with the amplitude of oscillation to approximately half the static stall angle α_s and a value for the reduced frequency $k < 0.2$. From the probe geometries tested the circular cylinder was an order of magnitude less affected by dynamic flow phenomena.

The analysis of the experimental data, in context with flow visualization, led to the identification of some dynamic effects, which can be summarized according to the literature:

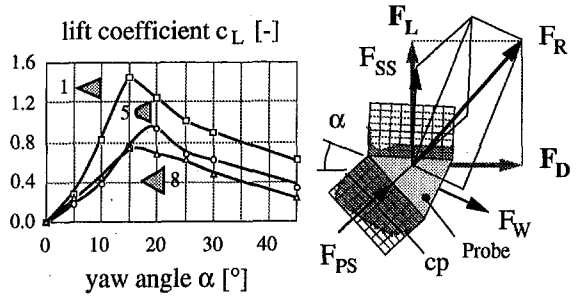

Fig. 12 Lift coefficient c_L versus angle of attack

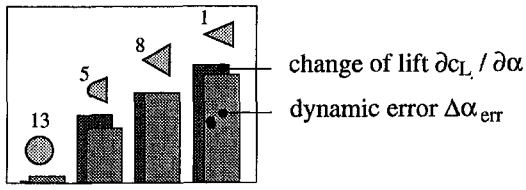

Fig. 13 Change of static lift and dynamic errors

(a) Circulation-induced forces as a consequence of the changing lift $\partial c_L/\partial\alpha$ produced by probes, when subjected to time variant angles of attack.

From interferometric holograms taken under static conditions in air, the lift force F_L was determined by numerical integration of the forces acting on the probes and c_L plotted as a function of the relative angle α of attack (Fig. 12).

From Fig. 12 the change of lift per degree yaw $\partial c_L/\partial\alpha$ at $\alpha = 0$ deg was determined and qualitatively compared to the dynamic errors $\Delta\alpha_{err}$ of the dynamic experiments (Fig. 13).

In spite of the completely different experiments, the correlation between change of static lift $\partial c_L/\partial\alpha$ and dynamic errors $\Delta\alpha_{err}$ is excellent and at least the likely correctness of the dynamic experiments proven.

(b) Inertia effects acting on the probe due to rotational displacement of fluid analogous to translatory oscillations as reported by Kovasznay et al. (1981).

(c) Dynamic boundary layers: As stated by e.g., Telionis (1981), for static flow conditions boundary layers separate when the wall shear stress becomes zero, whereas in dynamic flows thin layers of reversed flows may exist without disturbing the "outer flow," thus causing generally a delay of flow separation (McCroskey, 1977).

(d) Dynamic stall occurs due to a separated vortex propagating rearward from the leading edge, causing transient pressure distributions along the surface of airfoils (Carr et al., 1976). The initiation for this effect is due to the bursting of a laminar separation bubble (Beddoes, 1980).

In the experiments it was found that dynamic stall effects occur in cases when the static stall angle α_s of the wedge probes is already exceeded for very low frequencies of oscillation ($k < 0.05$). For wedge probes with rounded leading edges the effects are much reduced and for circular cylinders the effects do not take place at all.

(e) Coupling of shed vortices (vortex interaction) occurs in cases where the frequency of the flow fluctuation is close to the natural shedding frequency of the vortices ($k = \mathrm{Str} \approx 0.2$). In this case ("lock-on") the dynamic conditions differ from others below or above the critical case.

From the data evaluation it was found that within limits dynamic effects can be mathematically modelled. As long as the reduced frequency is lower than $k \approx 0.175$ and the amplitudes of fluctuation $\hat{\alpha}$ are well below the static stall angle, circulation will act proportionally to the angular velocity of the probes during the experiments and inertia will occur due to angular accelerations of the forced motion. Such, a correction of circulation and inertia errors becomes feasible.

Quantification of Aerodynamic Measurement Errors

In a further step one might want to quantify all the measurement errors occurring during measurements in turbomachines using aerodynamic fast-response probes.

For this example the flow at the exit of the impeller of a radial compressor with a shaft speed $n = 16{,}000\ \mathrm{min}^{-1}$, a wheel diameter of 0.28 m, and a resulting circumferential Mach number $M_u \approx 0.7$ is simulated.

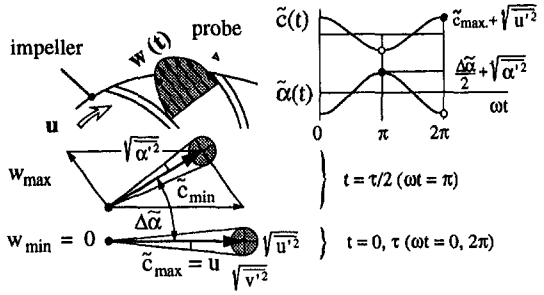

Fig. 14 Simulated exit flow of an impeller

According to Fig. 14 the periodic mean flow vector $\tilde{c}(t)$ in the absolute system is obtained by adding the vectors $w(t)$ of the relative system and the constant value u. Superposed to the mean flow is a cone angle $\pm\alpha' \approx 6$ deg after Browne et al. (1989) (see, e.g., Gossweiler et al., 1992) for a turbulence level of 10 percent.

With $z = 22$ (number of blades) the blade passing frequency of the flow becomes $f = 5.9$ kHz ($\omega = 2\pi f$) and the probe faces a flow vector fluctuating in magnitude and direction approximately by the expression

$$c(t) = \bar{c} + \left(\frac{\tilde{c}_{max} - \tilde{c}_{min}}{2} + \sqrt{\overline{u'^2}}\right) \cos(\omega t)$$

$$\approx 240(1 + 0.2 \cos(\omega t)) \text{ m/s}$$

$$\alpha(t) = -\left(\frac{\Delta\tilde{\alpha}}{2} + \sqrt{\overline{\alpha'^2}}\right) \cos(\omega t) \approx -23 \text{ deg} \cos(\omega t) \quad (7)$$

For these parameters of oscillation the resulting errors for three different probe geometries (circular cylinder, wedges with 45 and 60 deg apex angle) applied to velocity and yaw angle measurement can be quantitatively determined. Since the size of the probes plays an important role, the quantification is performed for probes with $D = 4$ and 8 mm diameter, small and big symbols, respectively (Figs. 15 and 16) and the reduced frequency becomes $k \approx 0.1$ ($D = 4$ mm) and $k \approx 0.2$ ($D = 8$ mm).

The errors due to blockage were determined after the relations given in Wyler (1975) for $M_\infty = 0.7$ and the errors caused by inertia in velocity measurements by the relations given in Humm and Verdegaal (1992) based on the experimental findings in Kovasznay et al. (1981).

Measurement errors arising from Mach number and three-dimensional effects are not included since they can be avoided by carefully calibrating the probes.

As it can be seen from Figs. 15 and 16, errors in both velocity and yaw angle measurement are enormous. From static effects all errors arising like blockage and velocity gradients may be corrected, while exceeding the unambiguous calibration range and inaccurately modeling the calibration data lead to inevitable measurement errors. Dynamic effects denoted as group 1 can

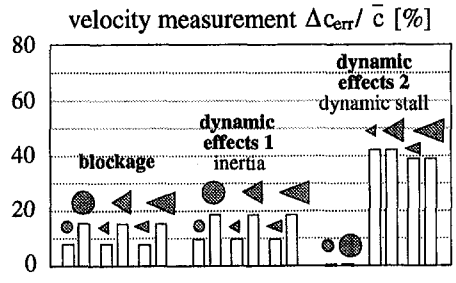

Fig. 15 Errors in velocity measurement

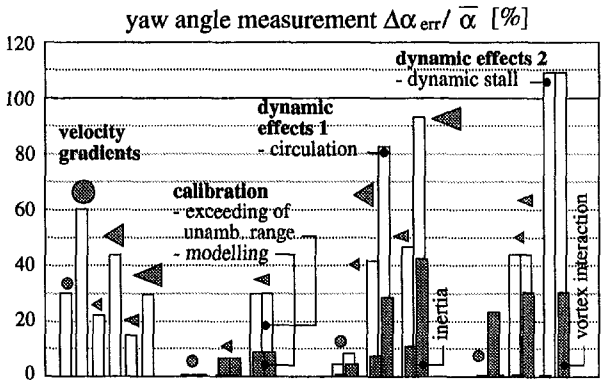

Fig. 16 Errors in yaw angle measurement

be seen to occur proportional to the probe size and, as shown in Humm and Verdegaal (1992), can be analytically modeled and hence the errors corrected. On the other hand dynamic stall leads to transient phenomena and cannot be, as well as vortex interaction, theoretically treated.

Conclusions

Probes should be manufactured as small as possible because errors due to blockage, velocity gradients, dynamic effects like circulation, inertia, and vortex interaction can be directly related to the probe size.

Additionally, the probe shape plays a very important role. Exceeding the unambiguous calibration range, inaccurate modeling of the calibration data and, above all, dynamic stall effects may cause errors that cannot be corrected.

Although sharp wedges offer advantages such as a high sensitivity, a true indication of the free-stream static pressure, and lower susceptibility to velocity gradients, they are, considering the quantified errors, not suitable for measurements in turbomachines. From the geometries tested only very blunt wedges and especially circular cylinders, which are far less affected by dynamic effects, fulfill the requirements for accurate measurements in fluctuating flows.

The experiments described herein were confined to two-dimensional flows, whereas for measurements in turbomachines, usually free ending probes are employed. In some cases the aerodynamic characteristics (e.g., unambiguous calibration range and sensitivity) of the two types of probe will not correspond but the majority of the observings may be applied to both conditions.

The findings in the dynamic domain were obtained in model experiments and it has to be assumed that they do not represent the conditions in turbomachines in every detail. It is evident that much more work is needed to substantiate the results gained so far, and especially Mach number effects in dynamic flow environments have to be included into the investigations.

Acknowledgments

The authors would like to thank the Swiss National Science Fund (SNF) for the financial support of this program.

Furthermore we thank our colleagues Dr. Doris Herter and Kevin Kaupert for their cooperation and discussion. For their technical support we thank Peter Althaus, Thomas Künzle, Peter Lehner, Cornel Reshef, Hans Richner, and Hans Suter.

References

Ainsworth, R. W., and Strickland, A. D., 1992, "Experimenting With Fast-Response Aerodynamic Probe Geometries," *Proceedings of the 11th Symposium on Measuring Techniques for Transonic and Supersonic Flows in Cascades and Turbomachines,* Munich, Germany.

Beddoes, T. S., 1980, "A Qualitative Discussion of Dynamic Stall," AGARD-R-679 Special Course on Unsteady Aerodynamics.

Browne, L. W. B., Antonia, R. A., and Chua, L. P., 1989, "Velocity Vector Cone Angle in Turbulent Flows," *Experiments in Fluids,* Vol. 5.

Bryer, D. W., and Pankhurst, R. C., 1977, "Pressure Probes for Determining Wind Speed and Flow Direction," National Physical Laboratory, Her Majesty's Stationery Office, United Kingdom.

Carr, L. W., McAllister, K. W., and McCroskey, W. J., 1976, "Dynamic Stall Experiments on Oscillating Airfoils," *AIAA Journal,* Vol. 14, No. 1.

Cook, S. C., 1989, "The Development of a High Response Aerodynamic Wedge Probe and Use on a High-Speed Research Compressor," ISABE 89-7118.

Gossweiler, C., Herter, D., and Kupferschmied, P., 1992, "Fast-Response Probe Measurements in a Turbulent Pipe Flow," *Proceedings of the 11th Symposium on Measuring Techniques for Transonic and Supersonic Flows in Cascades and Turbomachines,* Munich, Germany.

Humm, H. J., and Verdegaal, J. I., 1992, "Aerodynamic Design Criteria for Fast-Response Probes," *Proceedings of the 11th Symposium on Measuring Techniques for Transonic and Supersonic Flows in Cascades and Turbomachines,* Munich, Germany.

Humm, H. J., and Verdegaal, J. I., 1993, "Investigation of the Influence of Velocity Gradients on Measurements With a Wedge Probe," Technical Note 92-06, Swiss Federal Institute of Technology, Turbomachinery Laboratory [in German].

Humm, H. J., 1994, "On Aerodynamic Design Criteria for Fast-Response Probes," PhD Thesis, Swiss Federal Institute of Technology, Turbomachinery Laboratory [in German].

Kovasznay, L. S. G., Tani, I., Kawamura, M., and Fujita, H., 1981, "Instantaneous Pressure Distribution Around a Sphere in Unsteady Flow," ASME *Journal of Fluids Engineering,* Vol. 103.

Kupferschmied, P., and Gossweiler, C., 1992, "Calibration, Modelling and Data Evaluation Procedures for Aerodynamic Multihole Pressure Probes on the Example of a Four Hole Probe," *Proceedings of the 11th Symposium on Measuring Techniques for Transonic and Supersonic Flows in Cascades and Turbomachines,* Munich, Germany.

Kupferschmied, P., and Ribi, B., 1987, "Calibration of Pneumatic 4-Hole Probes for Pressure and Velocity Measurements in Inhomogenuous Flow Fields," Diploma work, Swiss Federal Institute of Technology, Turbomachinery Laboratory [in German].

McCroskey, W. J., 1977, "Some Current Research in Unsteady Fluid Dynamics—The Freeman Scholar Lecture," ASME *Journal of Fluids Engineering,* Vol. 99.

Telionis, D. P., 1981, *Unsteady Viscous Flow,* Springer.

Wyler, J. S., 1975, "Probe Blockage Effects in Free Jets and Closed Tunnels," ASME *Journal of Engineering for Power,* Vol. 97, Oct.

The Development of Fast Response Aerodynamic Probes for Flow Measurements in Turbomachinery

R. W. Ainsworth

J. L. Allen

J. J. M. Batt

Department of Engineering Science,
University of Oxford,
Oxford, United Kingdom

The advent of a new generation of transient rotating turbine simulation facilities, where engine values of Reynolds and Mach number are matched simultaneously together with the relevant rotational parameters for dimensional similitude (Dunn et al., 1988; Epstein and Guenette, 1984; Ainsworth et al., 1988), has provided the stimulus for developing improved instrumentation for investigating the aerodynamic flows in these stages. Much useful work has been conducted in the past using hot-wire and laser anemometers. However, hot-wire anemometers are prone to breakage in the high-pressure flows required for correct Reynolds numbers. Furthermore, some laser techniques require a longer run-time than these transient facilities permit, and generally yield velocity information only, giving no data on loss production. Advances in semiconductor aerodynamic probes are beginning to fulfill this perceived need. This paper describes advances made in the design, construction, and testing of two and three-dimensional fast response aerodynamic probes, where semiconductor pressure sensors are mounted directly on the surface of the probes, using techniques that have previously been successfully used on the surface of rotor blades (Ainsworth et al., 1991). These are to be used to measure Mach number and flow direction in compressible unsteady flow regimes. In the first section, a brief review is made of the sensor and associated technology that has been developed to permit a flexible design of fast response aerodynamic probe. Following this, an extensive program of testing large-scale aerodynamic models of candidate geometries for suitable semiconductor scale probes is described, and the results of these discussed. The conclusions of these experiments, conducted for turbine representative mean and unsteady flows, yielded new information for optimizing the design of the small-scale semiconductor probes, in terms of probe geometry, sensor placement, and aerodynamic performance. Details are given of a range of wedge and pyramid semiconductor probes constructed, and the procedures used in calibrating and making measurements with them. Differences in performance are discussed, allowing the experimenter to choose an appropriate probe for the particular measurement required. Finally, the application of prototype semiconductor probes in a transient rotor experiment at HP turbine representative conditions is described, and the data so obtained are compared with CFD solutions of the unsteady viscous flow-field.

Transonic Unsteady Aerodynamic Measurements

One context for the development of two and three-dimensional fast-response aerodynamic probes has been the requirement to be able to investigate the time resolved aerodynamic flow field in an HP turbine stage, operating at engine conditions of Reynolds and Mach number, and to compare these measurements with predictions made with CFD, Fig. 1. There are many other potential applications for such probes. Advances in the design of these probes have been made possible by the new development of mounting the semiconductor sensing element alone (devoid of all associated compensation and connection hardware) on metalwork of suitable geometry for probe measurements. The need for temperature compensation hardware close to the silicon sensor has been eliminated, permitting a considerable degree of flexibility in geometric design. This is achieved by the use of simplified external electronics, and software correction for semiconductor sensitivity to temperature (Ainsworth et al., 1989). A high degree of thermal stability has been achieved in sensor performance, by designing a silicon sensor and its mounting for the application, and repeatabilities of better than 0.05 percent full scale are routinely achieved (Ainsworth et al., 1991). Sensor frequency response has been optimized, enabling the full potential of the probe geometry to be achieved (Ainsworth et al., 1990). All of these developments form the background to the current paper, in developing a new generation of fast-response aerodynamic probes. This paper describes some of the detailed geometric considerations of both two and three-dimensional fast-response aerodynamic probe design, and their resulting impact on performance. Some of the prototype semiconductor probes are shown in Fig. 2.

Two-Dimensional Probe Geometries

In the context of aerodynamic measurements in the near-wake region of HP turbines, a review of the early literature concerned with two-dimensional pneumatic probes revealed the superiority of wedge-type probes over claw or cobra types, Fig. 3. An improved ability to resolve pressure gradients in the circumferential direction arises from the close proximity of the

Contributed by the International Gas Turbine Institute and presented at the 39th International Gas Turbine and Aeroengine Congress and Exposition, The Hague, The Netherlands, June 13–16, 1994. Manuscript received by the International Gas Turbine Institute February 4, 1994. Paper No. 94-GT-23. Associate Technical Editor: E. M. Greitzer.

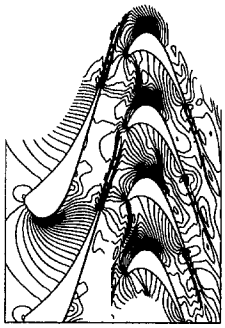

Fig. 1 Predicted instantaneous Mach number in the stage

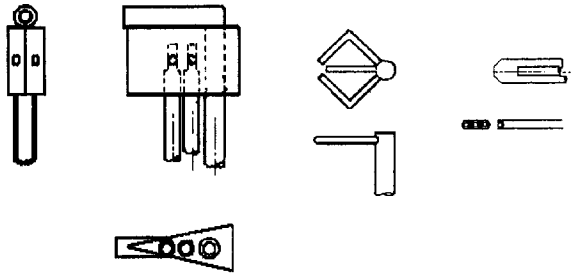

Fig. 3 Wedge, claw, and cobra pneumatic two-dimensional aerodynamic probes

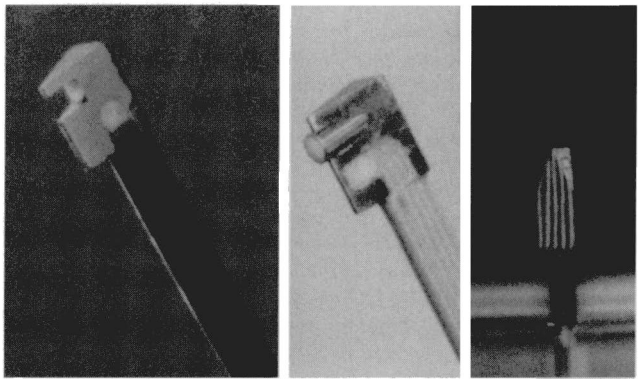

Fig. 2 Prototype semiconductor probes

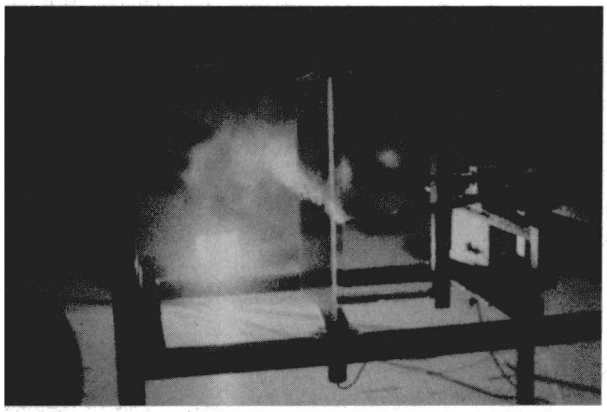

Fig. 4 Large-scale model wedge under test

two yaw pressure ports. A compromise is made over total pressure measurement by allowing this port to be placed at a different radial location. The cobra probe places all three ports in the same radial plane, resulting in poorer resolution in the circumferential direction, especially where rapid pressure gradients in this direction are concerned.

In the present work, the wedge-type geometry was chosen for use as a fast-response two-dimensional probe. In addition to the advantage outlined above, it also allowed the advantages of direct pressure sensor placement to be maximized, since the whole of the two side flanks were available for sensor positioning.

In the present program of work, an experimental study was initiated to determine the effects of wedge included angle, and sensor positioning on probe aerodynamic performance, because of the paucity of information available in the literature. Large-scale model aerodynamic tests were conducted in a wind tunnel with a working section of 2 m by 4 m. A model scale of 50:1 was chosen enabling a probe of engine size to be modeled with a wedge of some 300 mm in flank length, giving dynamic similitude in terms of Reynolds numbers. Naturally, it was not possible to simulate Mach number effects in this atmospheric wind tunnel. In all, two-dimensional tests were conducted on five included wedge angles (20, 30, 40, 50, and 60 deg) at five different tunnel speeds up to 12.5 m/s. For each included wedge angle and tunnel speed combination, the wedge was held at differing angles of yaw to the flow, ranging in value by ±10 deg. Static pressure tappings were placed at five locations on each wedge face, so that the effect of semiconductor transducer location regarding the engine scale probe could be examined.

The differential pressure between the two sides of the wedge was the quantity of greatest interest. The wedge, Fig. 4, was made some 500 mm deep to avoid the readings at the pressure tappings (situated midway between the top and the bottom of the wedge) being affected by end effects. Five tappings were equispaced along this centreline, the two end tappings being placed as close as possible to the leading and trailing edges. This closeness was limited by the steel capillary tubes that connected the tappings to flexible tubing. The pressures were read using a Furness Controls transducer (type FC040) of range 0–100 Pa.

One geometric aspect of engine scale probes that was not investigated experimentally in this study was the effect of wedge leading edge geometry on measured yaw coefficient. The experimental two-dimensional geometries tested here had sharp leading edges, although the geometry used in the numerical study presented later had a radiused leading edge, representative of the semiconductor scale probe.

Two-Dimensional Aerodynamic Model Results. In the discussion of the experimental results, the following definitions are used. Yaw coefficient is defined as the difference in pressure between two tappings on opposite flanks of the wedge divided by the approach dynamic head. Reynolds number is based on tunnel velocity and wedge side face length (300 mm on the model). Yaw sensitivity coefficient is defined as the change in yaw coefficient when yaw angle is varied, divided by the change in yaw angle. A larger value is beneficial, since, for a given data acquisition system voltage resolution, it will permit a finer degree of yaw angle resolution.

Nomenclature

C_{Mach} = Mach coefficient

C_{Pitch} = pitch coefficient

C_{Yaw} = yaw coefficient

γ = ratio of specific heats

x/s = fractional surface distance

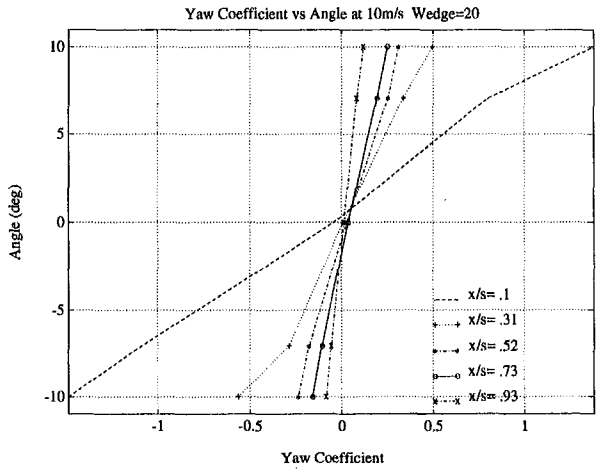

Fig. 5 Variation of yaw coefficient with tapping position

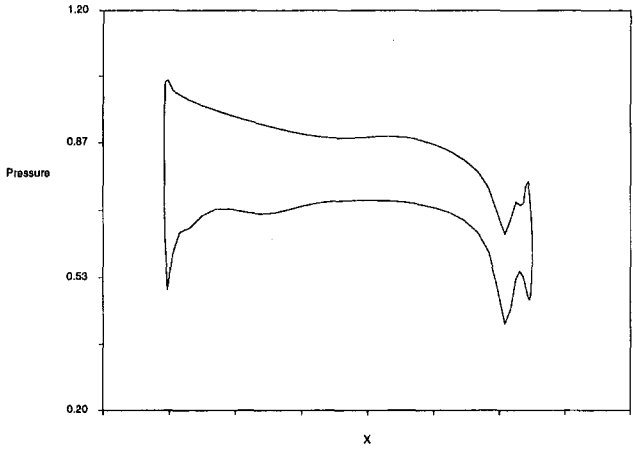

Fig. 7 Predicted static pressure distribution at one instant, 10 deg incidence

Five different included wedge angles were tested (20–60 deg in 10 deg steps) at five different tunnel speeds (Reynolds numbers), and a variety of incident yaw angles to the flow. Detailed results for the 20 and 60 deg wedge angles are presented by Ainsworth and Stickland (1992), where it was shown that varying the Reynolds number had little effect on the measured yaw coefficient. The summary plots at engine values of Reynolds numbers for all wedge geometries are given here. Having concluded from these results that flow Reynolds number does not greatly affect the yaw sensitivity coefficient, a summary plot of the results for a 20 deg included wedge angle at the highest Reynolds number only are plotted in Fig. 5. This clearly shows that sensor location is the important parameter in maximizing yaw sensitivity.

The data from all the wedge angles tested are shown in one plot, Fig. 6, where for the highest Reynolds number, the yaw coefficient is plotted against pressure tapping position for all five included wedge angles. The left-hand set of curves corresponds to the measured yaw coefficient at −10 deg of yaw, the central curves to zero yaw, and the right hand set to +10 deg of yaw. These clearly demonstrate the strong functional relationship between tapping position and yaw coefficient, and a relatively weak dependence on included wedge angle. For positions close to the leading edge of the wedge, the lowest wedge angle produces the highest yaw coefficient, and vice versa in a convincing trend. This trend is reversed at tapping three and beyond ($x/s = 0.5$) where now the higher the included angle the higher the yaw coefficient, as one might expect.

There is one significant difference in the fluid flow between the two sides of the wedge, and that relates to the separation on the leeward side of the wedge at maximum yaw. Flow visualization work conducted on the 20 deg wedge revealed a separation of significant size (35 percent of the total wedge side length). The higher the included wedge angle, the smaller this separation will be, and it will certainly affect the leading tappings most on the smaller wedge angles.

Two-Dimensional Computational Model Results. The code Unsflo (2D, viscous, time resolved) was also used to investigate the aerodynamic behavior of candidate probe geometries. Unsflo was developed by Mike Giles (1988) to analyze both the wake/rotor and the stator/rotor interaction, solving the viscous and inviscid equations of motion. It has extremely novel and flexible features in the way it handles arbitrary stator/rotor pitch ratios, and incorporates highly accurate nonreflecting boundary conditions, which minimize nonphysical reflections at inflow and outflow boundaries.

In the case of computations carried out here for comparison with the experimental data, each of the stator and rotor passages were represented by a grid resolution of 120 × 30 points, and the unsteady calculation was undertaken at representative Reynolds and Mach numbers. For the wedge flow, a grid resolution of 120 × 60 was used. Space permits only a small fraction of this work to be reported here. The static pressure distribution over both surfaces of a 23 deg wedge at 10 deg of incidence, and one instant in time, is presented in Fig. 7. This confirms the large-scale model testing, namely that moving the sensors forward increased probe yaw sensitivity. It also revealed a large fluctuation in static pressure close to the rear of the probe associated with the shedding of the Von Karman vortex street from the rear of the probe, Fig. 8, again indicating the desirability of keeping pressure sensors close to the leading edge of the wedge.

Conclusions for Semiconductor Scale. The major conclusion from both the computational and experimental work carried out is that the sensors measuring yaw pressure should be placed as close to the probe leading edge as possible. This maximizes probe yaw coefficient sensitivity, while minimizing both interference from the shed vortex static pressure field and dynamic error effects. Based on this finding, a final two-dimensional probe was produced for testing in the rotor. These trials are described at the end of this paper.

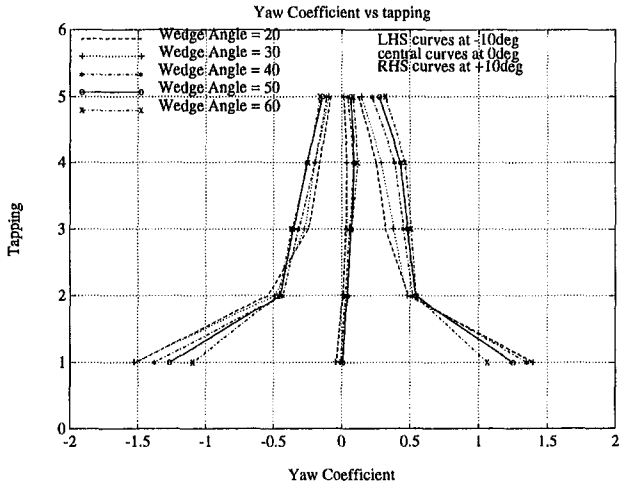

Fig. 6 Composite plot for all wedge angles

Three-Dimensional Probe Geometries

There are a variety of geometries possible for a three-dimensional velocity probe including the conventional pneumatic five-

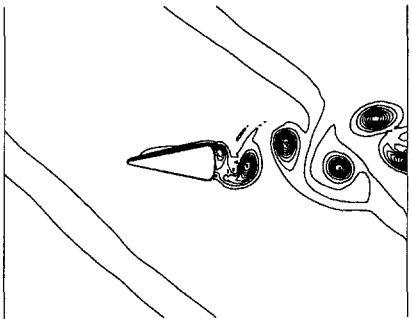

Fig. 8 Entropy contours showing predicted vortex street from the rear of the probe, 10 deg incidence

holed probes such as Koschel and Pretzsch (1988), the four-holed wedge probe developed by Heneka (1983), and the four-holed pneumatic pyramid probe of Shepherd (1981). Having considered the available literature on past developments of pneumatic three-dimensional aerodynamic probes, several features became clear. First, it was clear that while five-hole probes had predominated in past investigations, in fact a perfectly satisfactory device could be made with only four measurement points, a feature that was particularly appropriate in optimizing space for surface-mounted sensors and reducing the processing required for fast response data. Second, in studying the performance of conical-type probes, Dominy and Hodson (1993) had shown that the prismatic style of design of Shepherd was far less sensitive to Reynolds number variations, because any separations would be held fixed at the sharp edges of the pyramid. For the present work, this insensitivity would relieve the necessity of calibrating the device at all Reynolds numbers, in addition to the Mach, yaw, and pitch conditions that would have to be reproduced. The four-holed wedge probe suffers the disadvantage that in pitch there will only be one transducer sensitive to any changes in incidence and therefore would be expected to be less sensitive than the pyramid probe. In calibrating their version of the Heneka four-holed wedge probe Cherrett et al. (1992) reported in addition to a lower sensitivity, a strong interdependency of the coefficients, which would be unsatisfactory for inversion. Bearing these points in mind, work was concentrated on the Shepherd pyramid probe configuration.

As with the two-dimensional probes, large-scale low-speed aerodynamic modeling of potential three-dimensional geometries was initiated with a family of 25:1 scale prismatic probes specified with semi-angles of 15, 22.5, 30, and 45 deg, Fig. 9.

Three-Dimensional Pyramid Probe—Aerodynamic Model Results. The calibration data can be presented and used in a variety of differing ways. Shepherd developed a zoning system

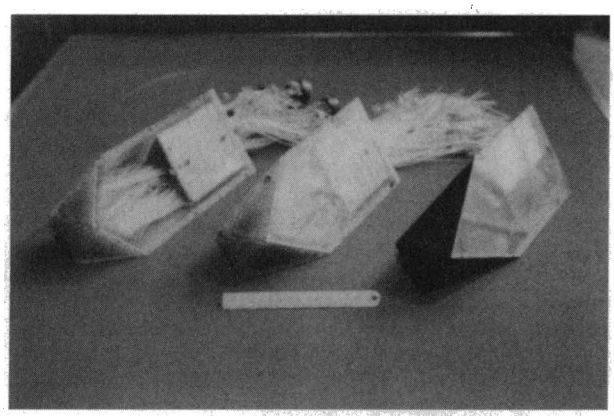

Fig. 9 Large-scale models of pyramid probes

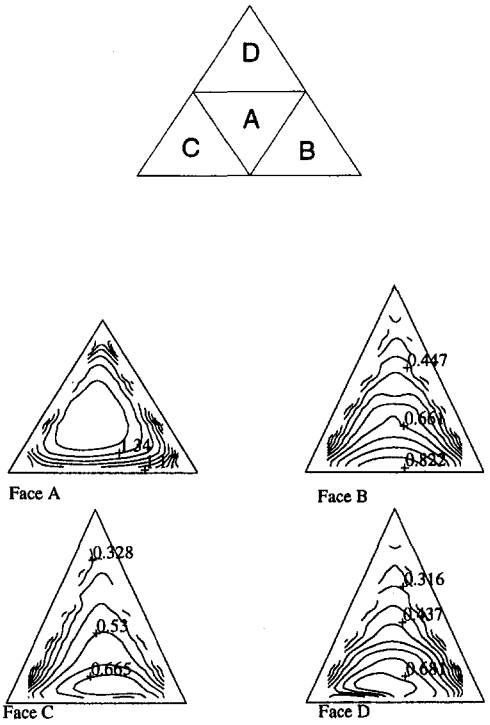

Fig. 10 Experimental surface pressure map over 45 deg large-scale pyramid probe

to avoid problems with asymptotic coefficients, which has allowed calibration over a wide range of incidence but does introduce problems with boundary mismatch errors between the zones. The more conventional approach used in the present work is to generate the calibration coefficients similar to those used in five-hole probe work as first proposed for a four hole probe by Sitaram and Treatser (1985). Each calibration coefficient consists of a differential pressure measurement, a function of flow incidence, and this has been normalized by the dynamic head to ensure independence from velocity variations. At high Mach numbers, compressibility affects the calibration, and so a third coefficient becomes necessary for the small semiconductor scale probes. Naturally, in the large-scale low-speed tests this was not investigated.

In the adopted terminology the yaw and pitch coefficients become:

$$C_{\text{yaw}} = \frac{P_b - P_c}{P_a - \dfrac{(P_{b+}P_{c+}P_d)}{3}}; \quad C_{\text{pitch}} = \frac{P_d - \left(\dfrac{P_{b+}P_c}{2}\right)}{P_a - \dfrac{(P_{b+}P_{c+}P_d)}{3}}$$

A surface pressure map for one incidence of pitch and yaw is given in Fig. 10 where contour lines of pressure coefficient (face static divided by tunnel dynamic pressure) are plotted over the surface of the 45 deg probe head. In practice, for the prototype semiconductor probe at small scale, the prismatic face pressures are measured with a sensor of finite, albeit small, size. To generate aerodynamic coefficient values that would simulate the performance of the prototype semiconductor probe, average values of face static pressures over the equivalent sensor area on these surface pressure maps were taken to produce a complete calibration characteristic.

A convenient method of presenting the calibration data for the three-dimensional velocity probe is in the form of a calibration map of these pitch and yaw coefficients derived from the probe plotted on lines of constant yaw and pitch. An ideal probe

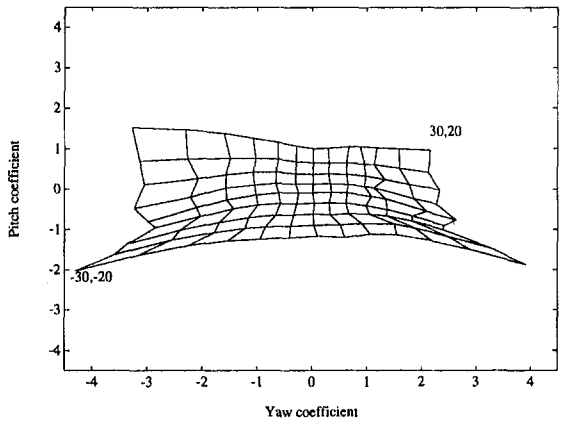

Fig. 11 Pitch and yaw coefficients, plotted at constant values of pitch and yaw

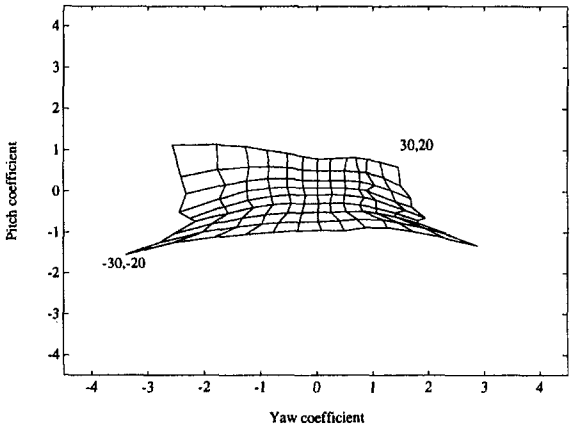

Fig. 13 Influence on calibration surface of moving sensors away from prismatic edges

would have a uniform orthogonal grid, the size of which would indicate the sensitivity of the probe. The real calibration surface is far from this ideal, and in practice the calibration coefficients are found not to be completely independent. In Fig. 11, these calibration data are shown with the yaw coefficient plotted on the horizontal axis and pitch coefficient on the vertical, for values of constant pitch and yaw, each at increments of 5 deg. In this plot the yaw has been varied over ±30 deg while pitch has been varied over ±20 deg.

Using surface-mounted pressure transducers gives great flexibility for construction of the probe and allows transducers to be placed in positions that have not been possible with previous techniques. Since the surface pressures over the whole large-scale model probe had been measured (at appropriate aerodynamic conditions) it was possible by averaging the static pressure data sets over different areas to simulate the influence of the position of the pressure sensor on the probe aerodynamic sensitivity. Unlike pneumatic probes where the hole in the sensing surface has a large influence on the localized flow, surface-mounted transducers maintain the surface integrity and therefore the results from this study can be applied with confidence. The influence of sensor positioning was quite dramatic. In Figs. 11, 12, 13, and 14, the effect of moving the sensors closer to the face edges is shown. It can be seen that the aerodynamic coefficients increase markedly as the sensor site is moved closer to a prismatic edge, and this agrees well with parallel work on wedge probe geometries. As the chip is moved back, it can be seen that the calibration map collapses onto itself at the higher angles of attack. An investigation with smoke streamers revealed that flow separation over the prismatic edges has a considerable influence over the probe performance. In the current design, the separation is fixed at the prismatic edges, but the flow reattaches farther up the sensing face. This position of the reattachment was found to be constant over the range of relevant Reynolds numbers. For the rearward positioned sensor, as the width of the face decreases, the flow gains a lateral component. This combines with the unsteadiness associated with reattachment of separated flow to cause the loss of sensitivity when the sensor is positioned to the rear of the side prismatic face.

Prototype Semiconductor Probes

Probe Descriptions. With the information gained from the large-scale model testing and computational modeling, a range of semiconductor probes were constructed. Wedge probes were manufactured with wedge angles from 23 to 60 deg, some of which are shown in Fig. 2. They were calibrated over a Mach number range of 0.5 to 1.0, at engine Reynolds numbers, and at up to ±62.5 deg of yaw. A portion of these results is given below.

From the range of semiconductor pyramid probes constructed (Fig. 2), the results from a probe, based on an included semi-angle of 45 deg and with sensors centrally mounted on the probe flanks are given below. This probe was calibrated at Mach numbers from 0.3 to 1.0 and over ±30 deg of yaw and ±20 deg of pitch.

Two-Dimensional Aerodynamic Calibration Results. The results obtained using a 30 deg wedge probe are given in Figs. 15–17. First, for one Mach number, the pressures from each of the three sensors (two side faces and the "total" sensor)

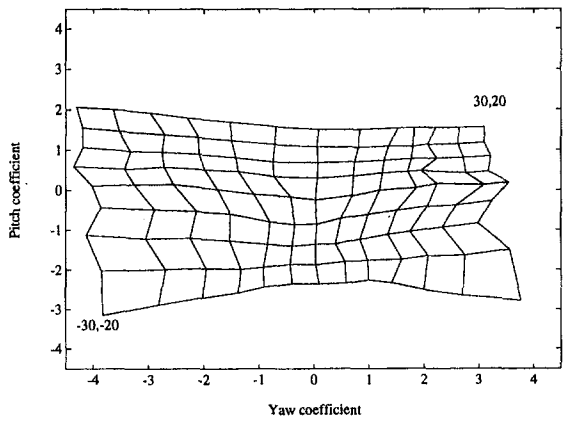

Fig. 12 Influence on calibration surface of moving sensors closer to prismatic edges

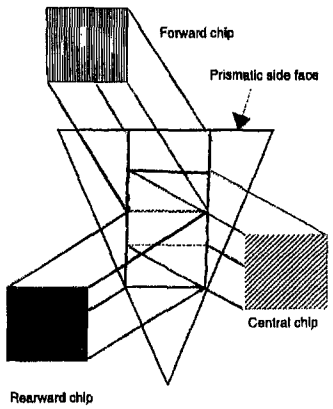

Fig. 14 Relative positions of sensors in Figs. 11–13

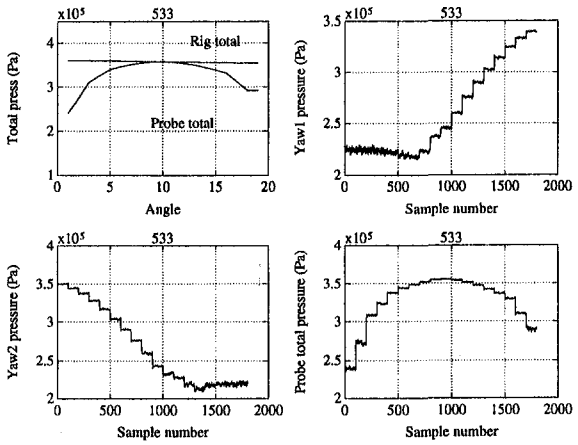

Fig. 15 Raw pressures obtained from the three sensors

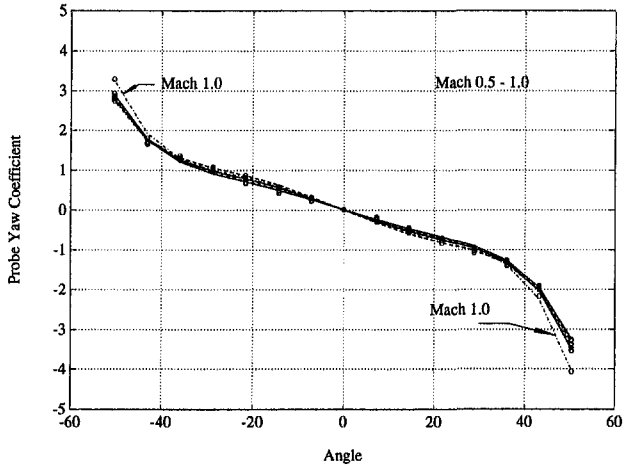

Fig. 16 Plot of probe yaw coefficient, M = 0.5–1.0

are plotted in Fig. 15, as the probe was yawed. Clearly each of the 19 positions of yaw angle may be discerned. The composite plot of yaw coefficient (nondimensionalized by probe dynamic head) at all Mach numbers is given in Fig. 16.

The crucial feature of this plot, demonstrating the excellent DC stability of this construction method, lies in the fact that the two yaw sensing devices gave the same measurement at zero yaw angle throughout the long calibration. In addition, the

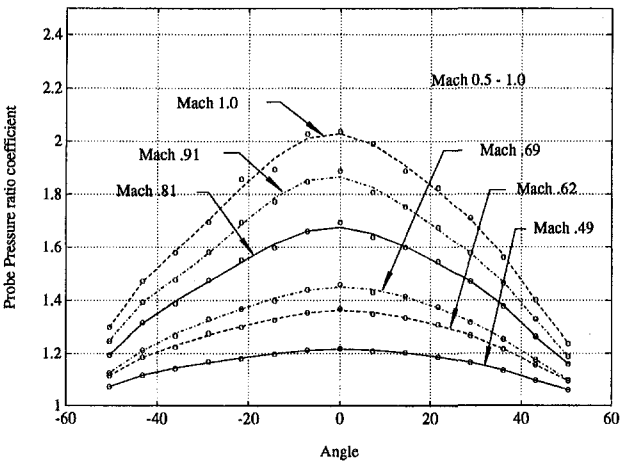

Fig. 17 Probe pressure ratio variation with yaw and Mach number

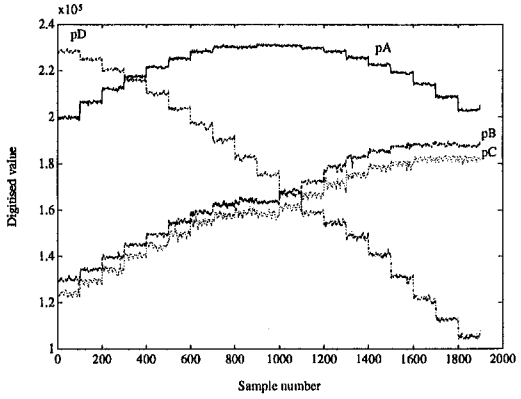

Fig. 18 Raw data obtained from semiconductor pyramid probe during calibration, Mach 0.8, zero yaw, pitch traverse

yaw coefficient is very insensitive to Mach number, indicating that a high degree of confidence in angle measurement could be obtained even if the Mach number were not well known, providing the dynamic head were correct.

The probe, however, may also be used to measure Mach number as illustrated by Fig. 17, where the response of the probe measured pressure ratio (probe total/probe static) to Mach number and yaw angle may again clearly be seen.

The conclusion from these tests was that a very viable two-dimensional semiconductor aerodynamic probe had been created, with a yaw coefficient insensitive to Mach number and an excellent DC stability over a long period of testing. Further testing will compare the performance of the family of geometries constructed, and examine the dynamic behavior in a rotor facility.

Three-Dimensional Aerodynamic Calibration Results. The raw data from each of the four semiconductor sensors, with the probe held at zero pitch angle, while rotated through 19 angles of yaw, all at constant Mach and Reynolds numbers, are shown in Fig. 18. Each step in yaw can clearly be distinguished and verifies the stability of the readings at each increment. By applying the temperature and pressure calibrations, these data can be converted into calibration coefficients and are plotted in a similar fashion and over the same range as the large-scale model data in Fig. 19. Since compressibility affects the calibration, this plot is of the yaw and pitch coefficients at a constant Mach number of 0.8. It is interesting (and encouraging) to see similar features occurring in both the large-scale data and those obtained from the semiconductor probe; compare Fig. 11 with Fig. 19.

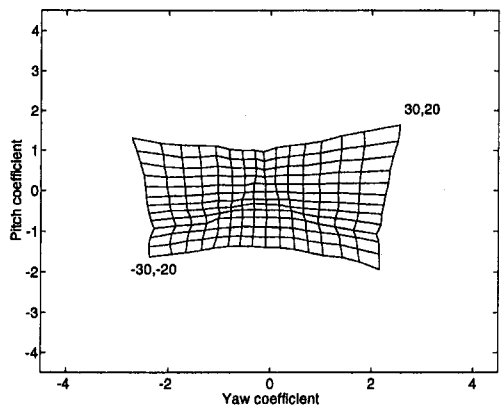

Fig. 19 Pitch and yaw coefficients, plotted at constant values of pitch and yaw for semiconductor pyramid probe at Mach 0.8

Discussion of Calibration Surfaces. One of the benefits of presenting the calibration in the form shown in Fig. 19 is that the spacing of the grid lines indicates the sensitivity of the probe to flow direction and thus highlights flow directions where the probe performance will be poor. In general the calibration maps show good uniformity and orthogonality over the calibration range, but closer examination of the plot will reveal several distinct features. First, the sensitivity to positive pitch is less than to negative pitch. Furthermore there is a distinct 120 deg division of the map surface, the border of which corresponds to a region of poor sensitivity. The reasons for this behavior can be found by examining the geometry of the probe combined with the definition of the coefficients used.

Each calibration coefficient chosen must be designed to be a strong function of its primary measuring parameter and as independent as possible from all others. In the current work the important parameters are the Mach number, flow direction, and Reynolds number. The importance of the Reynolds number has been removed by careful design of the probe head to make the probe Reynolds number independent. The coefficients used to measure yaw and pitch angle consist of a pressure differential normalized by a dynamic head estimated from the probe. The true dynamic head is obviously a direct function of the Mach number and the total pressure. The sensitivity of the probe to flow incidence is therefore determined by two factors: first, the pressure differential found across the probe as a result of flow incidence, and second, its ability to measure the dynamic head.

To find a dynamic head, the probe has to measure both a total and a static pressure. In measuring the total pressure an intrusive probe will only ever record the stagnation pressure due to inevitable losses. When flow is at an incidence to the probe the apparent total pressure will be even lower since the effective sensing area is no longer normal to the flow. Static pressure measurement is even more problematic since it is impossible to record static pressure without some recovery of the dynamic head. Incidence of the flow relative to the probe increases the problem. The consequence of these effects is that the probe dynamic head will always be underestimated and although it might be possible to minimize the errors, the methods are likely to be incompatible with direction measurement. The Pitot-static tube is a well-established method of measuring dynamic heads but by nature of its design is insensitive to flow directions. Since the yaw and pitch coefficients are normalized against the dynamic head, at high incidences where the probe dynamic head is grossly underestimated, the coefficients become very large, even asymptotic. At the higher incidences the driving force on the probe characteristic for these coefficients is therefore not a differential pressure measurement but the measurement of the dynamic head. The outer boundary of the calibration map is very much a function of how the probe dynamic head is estimated.

The second influence on the calibration characteristic is more related to the actual differential pressures measured across the probe geometry. The 120 deg boundaries found on the calibration map are not surprising when the 120 deg symmetry of the probe is borne in mind. These boundaries can be related to the actual flow over the probe and the complex pattern of flow separation that occurs. To record a differential pressure, the variation of surface pressure with incidence for two different sides must be considered. A differential pressure has to be used to remove the unknown static pressure from the absolute value of pressure. In minimizing the number of transducers, and thereby the size of the probe, the surfaces on which the differential pressure measurements are made are not orthogonal. This results in the differing sensitivities to pitch and yaw. Face D has a surface normal in the pitch direction. If the surface pressures on the three side faces are considered during a traverse in the pitch direction but at zero yaw, the variation of face D surface pressure with incidence differs considerably from that of the other two faces B and C whose surface normals are not in the pitch direction, Fig. 18. There is an almost linear variation in surface pressure with incidence on face D, except for a discontinuity that occurs at small negative incidence to the face and a leveling off as the face approaches the total pressure. In the case of faces B and C, the discontinuity is again present, but this time results in almost complete insensitivity to change in angle in this region. The highest pressures achieved on these faces are well below the total pressure and are attained at lower angles than the peak pressures on face D. The lower peak pressures of faces B and C are expected because they will always be inclined to any flow purely in the pitch direction. If in addition to a pitch traverse, the probe is positioned at some incidence in yaw, the general features of the face pressures remain the same, although the position of the discontinuity changes and the absolute highest values change. The discontinuity is a result of the separation bubble that occurs behind the prismatic faces at positive incidence. The size of the separation bubble varies with incidence and it affects any pressure sensor under it. During the transition from being in attached flow to separated flow, the linear variation of surface pressure with incidence is lost and the discontinuity of the characteristic occurs. During this process the sensitivity of the pressure measuring surface is lost with implications for the overall aerodynamic performance of the probe. For faces B and C, which are no longer normal to the pitch direction, this transition from attached to separated flow occurs over a wider range of angles and therefore results in an insensitivity over a wider range of angles. If a prismatic probe had not been selected then this separation would not be in a fixed position and the zones of probe poor sensitivity would become a function of Reynolds number, with obvious consequences for confidence in readings.

If a traverse in the yaw direction is considered, some of the symmetry is restored. Faces B and C, which are used for the yaw coefficient, are completely symmetric in yaw and any differences are therefore as a result in minor fabrication anomalies. However, once again the separation of the flow over the probe results in a loss of sensitivity of each face for flow at small angles of positive incidence relative to the individual face. The combined result from these features is a calibration map, which is symmetric in yaw but not in the pitch direction.

Clearly with these features in mind it would be worth considering if some other geometry would be preferable. It quickly becomes apparent that the pyramid geometry is the most suitable. The three-dimensional wedge probe has only one pressure transducer in the pitch plane and is therefore highly limited. To use this probe the static pressure in the pitch direction is estimated based on the average of the two side faces. This results in a pitch coefficient highly dependent on the yaw angle. Furthermore, separation over the pitch surface will make the three-dimensional wedge probe insensitive to positive pitch at certain angles because it is the only surface from which pitch information becomes available. If a conical probe were selected the benefits of Reynolds number insensitivity would be lost and by increasing the number of side faces, for instance to make a five or seven-sided prismatic probe, would produce too large a probe.

Compressibility Effects. The discussion so far has concentrated on the directional performance of the probe at a constant Mach number. In practice the face pressures are dependent on Mach number, and in order to determine the flow completely, the calibration surfaces must be measured over the operating range of Mach numbers. In the same way that both the pitch and yaw coefficients are related to the true pitch and yaw angle, so a Mach coefficient (based on probe apparent total to static pressure ratio) may be related to the true Mach number. This Mach number coefficient, recorded in calibration, can then be used in conjunction with the yaw and pitch coefficient to resolve the flow completely:

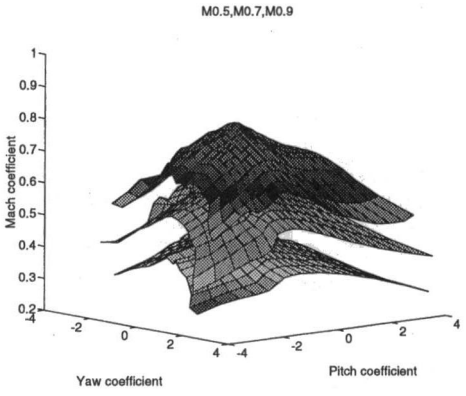

Fig. 20 Calibration space for semiconductor pyramid probe

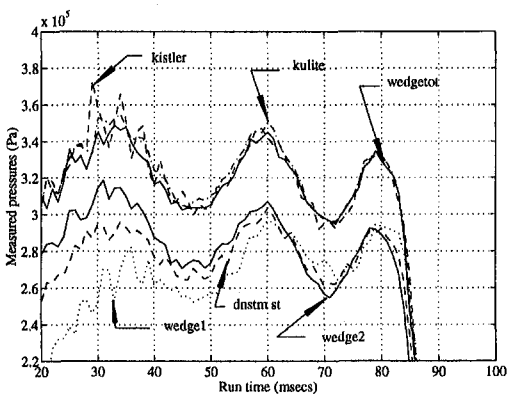

Fig. 21 Rotor measurements made using two-dimensional semiconductor probe, and tunnel instrumentation, at slow sampling rate, 400 Hz

Mach coefficient

$$= \left[\frac{2}{\gamma - 1} \left[\left(\frac{P_b + P_c + P_d}{3} \right)^{-(\gamma-1)/\gamma} - 1 \right] \right]^{0.5}$$

The calibration space is determined by a plot of yaw, pitch, and Mach number coefficients versus yaw, pitch, and Mach number as shown in Fig. 20, although to avoid confusion only three of the Mach surfaces calibrated are plotted here. In this calibration space every flow condition is a represented by a unique vector, and using an interpolative inversion technique, experimental readings from the probe may be converted into flow velocity.

By reprocessing the original data set, it is possible to estimate the potential errors resulting from the use of this probe and the importance of the regions of poorer sensitivity for the probe, discussed in the previous section, become quite clear since they determine the regions of highest errors in angle measurement.

Measurements With Two-Dimensional Wedge Probe in the Oxford Rotor Facility

A fast response wedge probe of 30 deg included angle, with yaw sensors mounted as close to the leading edge of the wedge as possible, was mounted downstream of the HP turbine in the rotor facility. Referring to Fig. 1, the probe was inclined at an angle of 19 deg to the axial direction, since this was the indicated mean flow direction at turbine exit in the absolute frame of reference from throughflow analyses. Because the rotating assembly in this experiment is unbraked, the turbine rotor accelerates during the runtime, and consequently flow incidence changes during the run. Data are sampled at 400 Hz throughout the 200 ms run, and when the rotor is at the correct speed, the fast data acquisition system, operating at 500 kHz, is triggered. In this manner, fast data are acquired at what is calculated to be the correct incidence. Full details of the tunnel operation and data acquisition are given in Ainsworth et al. (1988). The insertion of the wedge probe downstream of the rotor served the dual function of measuring the run conditions at the instant the fast data acquisition system was triggered, as well as testing the fast response wedge probe in an environment where wide bandwidth dynamic measurements were required.

First, data obtained at the slow sampling rate of 400 Hz from the fast response probe, two total pressure probes, and a sidewall static pressure tapping are presented in Fig. 21. The trace labeled "Kistler" corresponds to the total pressure measured using a remotely mounted transducer attached to a pitot probe via a pneumatic tube. The trace labeled "Kulite" relates to that measured using a standard production transducer (XCQ-062) mounted within a pitot probe. The total pressure measured by the total sensor on the wedge probe is labeled "wedgetot." It will be seen that all three are in close agreement because of the low bandwidth of the measurement at this sampling rate. The Kistler trace exhibits fluctuations due to the wave motion down the pneumatic tube, which attenuate gradually. Also on this plot are the pressures measured by a downstream static tapping (labeled "dnstm st") and those obtained from the yaw sensors on the wedge probe, "wedge1" and "wedge2." The pressure difference between the wedge side faces, the yaw pressure, was measured by the latter probe throughout the run and is plotted in Fig. 22, together with an indication of the instant at which the fast data acquisition was triggered (the cross-hair). As mentioned earlier, because of the acceleration of the rotor, flow angles change throughout the run, and the measured yaw pressure confirms this.

Of more interest in the present context are the results obtained from the fast response wedge probe at the fast sampling rate of 500 kHz. First, the measured yaw pressure, total and "static" (mean of the two yaw pressures) are presented in Figs. 23 and 24. It will be observed that during each rotor passing period the total and static pressure traces intersect. This is not as strange as it may first seem. In practice, the probe total pressure is somewhat below the true total pressure (the probe is calibrated aerodynamically to determine this factor), while the probe "static" pressure lies above the true static—at low Mach numbers and incidence such as may occur in the turbine wake region, they overlap. These results are used to provide an experimentally determined probe pressure ratio (probe total/probe static) and probe yaw coefficient. Applying the probe aerodynamic calibrations to these measurements yields the derived Mach number and flow yaw angle, as functions of time (Figs. 27 and 25). The small gaps in the derived measurements correspond to areas where the primary measurements (yaw coefficient and probe pressure ratio) lie outside the calibration matrix for the probe. These derived measurements are compared with predic-

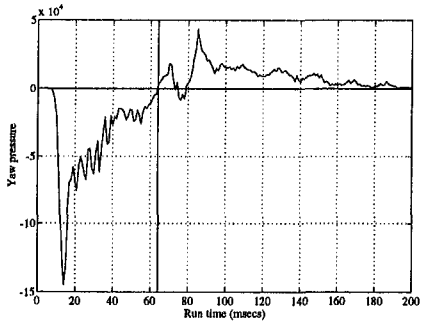

Fig. 22 Yaw pressure measured by semiconductor wedge probe

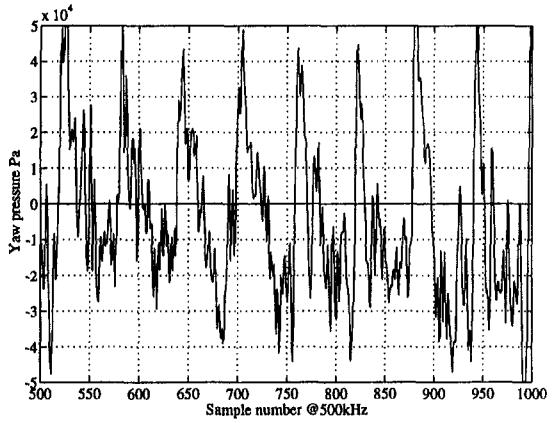

Fig. 23 Yaw pressure measured by two-dimensional semiconductor wedge probe, sampled at 500 kHz

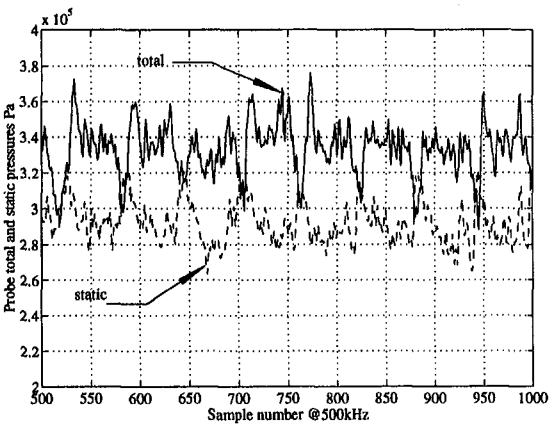

Fig. 24 Fast response total and static pressure, measured by two-dimensional semiconductor wedge probe, sampled at 500 kHz

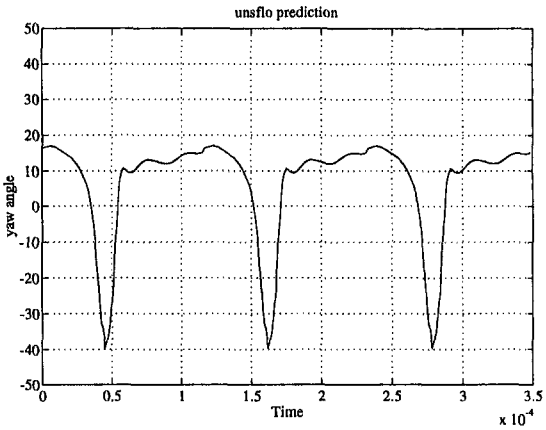

Fig. 26 Predicted time variation of yaw angle

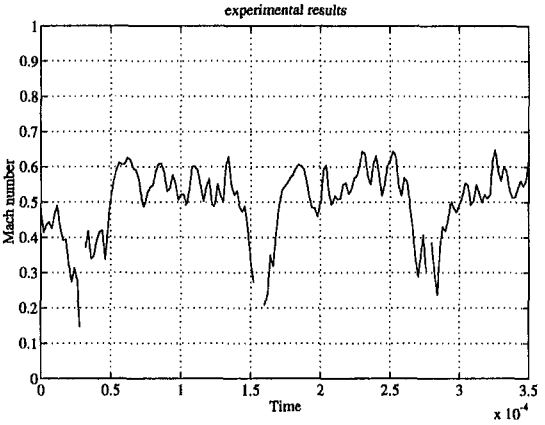

Fig. 27 Derived (measured) Mach number

tions, made using Unsflo, of the time-varying yaw angle and Mach number downstream of the rotor. The agreement between the two is seen as extremely encouraging at this stage. First, in terms of yaw angle, the waveforms of the two appear to be very similar, as does the range of the perturbation. In Mach number terms, again the two are very similar, in absolute terms as well as waveform. It should be emphasized that while these initial results seem most encouraging, future work will examine the challenges introduced by the intrusive and dynamic nature of these measurements. It is evident that the bandwidth of the experimental data is considerably higher than that of the CFD solution.

Conclusions

The use of surface-mounted semiconductor sensors in the context of fast response aerodynamic probes has been shown to be a versatile method for producing the necessary electrical stability and frequency response. This method of construction has allowed the positioning of the sensing elements to be optimized in terms of the measurement required. Large-scale aerodynamic models of two-dimensional and three-dimensional

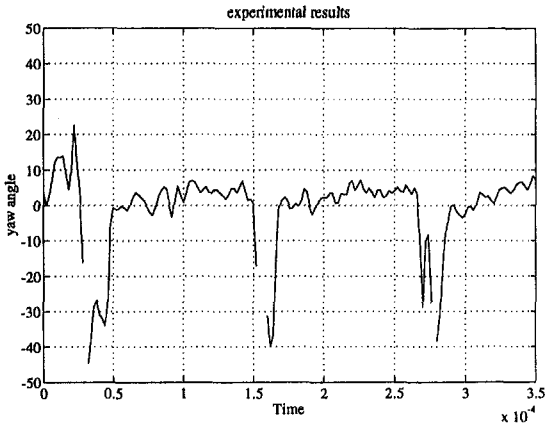

Fig. 25 Derived (measured) fast response yaw angle

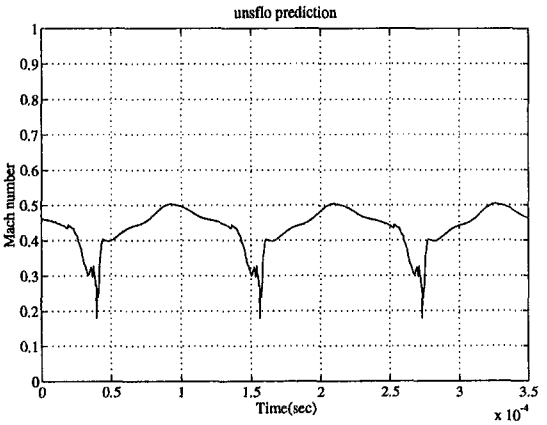

Fig. 28 Predicted time variation of Mach number

probe geometries have been constructed, and used to determine these optimum positions. CFD has further confirmed the experimental findings in the case of the two-dimensional geometries.

Prototype semiconductor probes have been constructed, and their aerodynamic calibration under engine conditions of Mach and Reynolds numbers are presented and discussed. By the long time-scale nature of this calibration, their excellent DC stability has been demonstrated.

Time-resolved measurements downstream of a HP turbine rotor operating at engine conditions of Mach and Reynolds numbers taken using a two-dimensional fast response probe at 500 kHz sampling rate are presented and compared with CFD predictions. The agreement between the two is seen as most encouraging, although issues of probe intrusive effects and dynamic response will be studied as part of the future work plan.

Future work with the three-dimensional probe will involve its use in the rotor facility, and further studies of geometric and dynamic effects.

Acknowledgments

The wholehearted and enthusiastic support for our semiconductor sensor work from Dr. A. D. Kurtz, President of Kulite Semiconductor Inc., is most gratefully acknowledged. Gratitude is also expressed to the SERC and Rolls-Royce in supporting the Oxford Rotor experiment for trials of these probes. Dr. Mike Giles' patience in supporting the Unsflo work was much appreciated. Finally, thanks are due to Dr. Martin Oldfield and Alistair Main for their enthusiastic discussions, particularly on data reduction techniques.

References

Ainsworth, R. W., Schultz, M. R., Davies, C. J., Forth, M. A., Oldfield, M. L. G., and Sheard, A. G., 1988, "A Transient Flow Facility for the Study of the Thermofluid-Dynamics of a Full Scale Stage Turbine Under Engine Representative Conditions," ASME Paper No. 88-GT-144.

Ainsworth, R. W., Allen, J. L., and Dietz, A. J., 1989, "Methods for Making Unsteady Aerodynamic Pressure Measurements in a Rotating Turbine Stage," AGARD PEP CPP-468.

Ainsworth, R. W., and Allen, J. L., 1990, "Investigating the Performance of Miniature Semi-conductor Pressure Transducers for Use in Fast Response Aerodynamic Probes," *Proceedings of 10th Symposium on Measuring Techniques in Transonic and Supersonic Flows,* Brussels, Belgium.

Ainsworth, R. W., Dietz, A. J., and Nunn, T. A., 1991, "The Use of Semiconductor Sensors for Blade Surface Pressure Measurement," ASME *Journal of Engineering for Gas Turbines and Power,* Vol. 113, p. 159.

Ainsworth, R. W., and Stickland, A. D., 1992, "Experimenting With Fast Response Aerodynamic Probe Geometries," *Proc. of the 11th Symposium on Measuring Techniques for Transonic and Supersonic Flow in Cascades and Turbomachines,* Munich, Germany.

Cherrett, M. A., Bryce, J. D., and Hodson, H. P., 1992, "3D Pneumatic and 2D Dynamic Probes: Their Development and Subsequent Use in a Transonic Fan," *Proc. of 11th Symposium on Measuring Techniques for Transonic and Supersonic Flow in Cascades and Turbomachines,* Munich, Germany.

Dominy, R. G., and Hodson, H. P., 1993, "An Investigation of Factors Influencing the Calibration of Five-Hole Probes for Three-Dimensional Flow Measurements," ASME JOURNAL OF TURBOMACHINERY, Vol. 115, pp. 513–519.

Dunn, M. G., Seymoor, P. J., Woodward, S. H., George, W. K., and Chupp, R. E., 1988, "Phase-Resolved Heat-Flux Measurements on the Blade of a Full-Scale Rotating Turbine," ASME Paper No. 88-GT-173; ASME JOURNAL OF TURBOMACHINERY, Vol. 111, 1989, pp. 8–19.

Epstein, A. H., and Guenette, G. R., 1984, "The MIT Blowdown Facility," ASME Paper No. 84-GT-116.

Giles, M. B., 1988, "Calculation of Unsteady Wake Rotor Interaction," *AIAA Journal of Propulsion and Power,* Vol. 4, pp. 356–362.

Heneka, A., 1983, "Instantaneous Three Dimensional Flow Measurements With a Four Hole Wedge Probe," *Proc. 7th Symposium on Measuring Techniques for Transonic and Supersonic Flow in Cascades and Turbomachines,* Aachen, Germany.

Koschel, W., and Pretzsch, P., 1988, "Development and Investigation of Cone Type Five Hole Probes for Small Gas Turbines," presented at the 9th Symposium on Measuring Techniques for Transonic and Supersonic Flows in Cascades and Turbomachines, Oxford, United Kingdom.

Sitaram, N., and Treatser, A. L., 1985, "A Simplified Method of Using Four Hole Probes to Measure Three-Dimensional Flow Fields," ASME *Journal of Fluids Engineering,* Vol. 107, pp. 31–35.

Shepherd, I. C., 1981, "A Four Hole Pressure Probe for Fluid Flow Measurements in Three Dimensions," ASME *Journal of Fluids Engineering,* Vol. 103, No. 4, pp. 590–594.

S. R. Kidd

J. S. Barton

P. Meredith

J. D. C. Jones

Department of Physics,
Heriot-Watt University,
Edinburgh, United Kingdom

M. A. Cherrett

K. S. Chana

Defense Research Agency,
Pyestock, Farnborough,
United Kingdom

A Fiber Optic Probe for Gas Total Temperature Measurement in Turbomachinery

This paper describes the design, operation, construction, and demonstration of a new type of high-bandwidth unsteady temperature sensor based on fiber optics, and capable of operating in a high-speed multistage research compressor with flow representative of jet engine conditions. The sensing element is an optical coating of zinc selenide deposited on the end of an optical fiber. During evaluation in aerodynamic testing, a 1 K gas temperature resolution was demonstrated at 9.6 kHz and an upper bandwidth limit of 36 kHz achieved.

Introduction

Aeroengine development continues to demand exacting improvements in compressor performance. Military aeroengines require increased thrust-to-weight ratio and decreased cost of ownership while maintaining adequate levels of stable operating range and efficiency. Improving efficiency is the primary aim of civil engine development. These requirements are responsible for generic trends in modern compressor design. Fewer rotor stages tend to be used, which increases the aerodynamic stage loading. Blade chords tend to be longer, which, coupled with the increased aerodynamic loading, increases the influence that each row exerts on neighboring rows. The reduced aspect ratio of the blades also increases the complexity of the boundary layer flows on the blades, and on the end walls. The consequence of these trends is that the unsteady flow field within the compressor becomes more significant and needs to be taken into account during the design and development of future compressors.

In response to these trends, there is a growth in the attention being paid to unsteady blade row interaction in turbomachinery. However, because of the problems associated with taking unsteady aerodynamic measurements in high-speed turbomachinery, there are few measurements in engine-relevant compressors and there is consequently a poor empirical understanding of the fundamental flow processes involved. Nevertheless, concerted effort since the mid-1980s has overcome many of the problems associated with taking wide-bandwidth pressure measurements in high-speed compressors and such sensors have been employed in engine-relevant machines (Cherrett and Bryce, 1992). Unfortunately, the situation is less satisfactory when unsteady temperature measurements are considered. Both unsteady pressure and temperature measurements are required if the compressor efficiency and entropy flux are to be measured accurately. Further, it is recognized that the measurement systems used to derive steady-state blade row performance do not respond properly to the highly pulsatile filed behind rotor rows. Therefore, there is a need for pressure, and particularly temperature, measurement systems capable of resolving the fluctuating flow field so that more accurate steady-state measurements can be derived.

This paper introduces a new type of sensor for high-bandwidth gas temperature measurement, based on interferometry using optical fibers. The paper describes the development of a probe based on the fiber optic sensor, and the results of a demonstration of the probe in a continuous flow compressor test rig. The sensor represents the development of an earlier interferometric sensor for the measurement of heat flux in turbomachinery applications (Kidd et al., 1993). Similar techniques may also be applied to the measurement of pressure at high bandwidth.

Objectives. The aim of the work reported in this paper was to demonstrate the feasibility of an optical fiber-based sensor to measure unsteady temperature fluctuations in high-speed compressors. Unsteady pressure measurements in such a compressor reveal periodic and random flow effects (Cherrett and Bryce, 1992). A corresponding measurement of unsteady temperature was sought in the same compressor, operating under the same conditions. For this purpose it was required that the optical fiber sensor have (*i*) a wide-frequency bandwidth of up to 60 kHz to resolve the main flow features associated with blade passing frequencies of up to 12 kHz; (*ii*) small physical size (diameter $\leq$6 mm) to allow insertion of the probe between closely spaced compressor blade rows; (*iii*) robustness to withstand the harsh physical environment (i.e., high-transonic Mach number flows containing oil droplets). A gas temperature resolution of less than 1 K was desirable, with a sensor operating range up to 600 K.

Existing Measurement Techniques. There exist a variety of temperature sensors for unsteady measurements in turbomachinery, though none have a bandwidth as high as 60 kHz. Thermocouple response is limited to about 1 kHz (Forney et al., 1993); constant current hot-wire sensors are cross-sensitive to gas velocity fluctuations; thin-wire resistance thermometers are less sensitive to velocity but require compensation as a function of flow speed and show aging effects in use (LaRue et al., 1975), while the most promising technique is the aspirat-

Contributed by the International Gas Turbine Institute and presented at the 39th International Gas Turbine and Aeroengine Congress and Exposition, The Hague, The Netherlands, June 13–16, 1994. Manuscript received by the International Gas Turbine Institute February 4, 1994. Paper No. 94-GT-34. Associate Technical Editor: E. M. Greitzer.

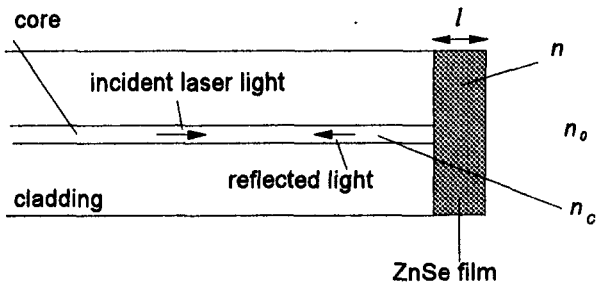

Fig. 1 Thin film sensing element deposited on the end face of an optical fiber (not to scale): film thickness = l, film refractive index = n; n_c and n_0 are the refractive indices of the fiber core and the medium in which the fiber is immersed

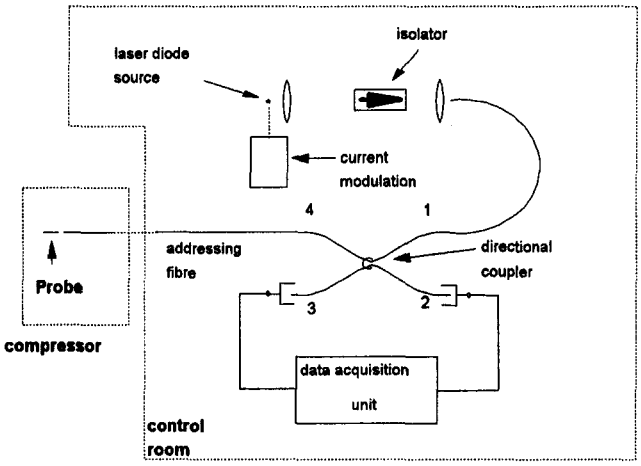

Fig. 2 Basic optical arrangement for optical fiber gas temperature probe

ing probe with a reported bandwidth of about 20 kHz, described by Ng and Epstein (1983). This probe consists of a pair of hot wires operating at different overheat ratios upstream of a choked orifice. While this configuration is more robust than an isolated hot wire (and is capable of providing pressure measurements as well), the wires are still prone to aging and the calibration procedure required is complex.

Summary of Fiber Optic System. The sensing element is a thin optical film deposited on the end face of a single mode optical fiber (Fig. 1). Laser light launched into the input end of the fiber is partially reflected by both sides of the film. The two reflected beams differ in phase by an amount proportional to the film's optical thickness. Interference between the two beams results in a total reflected light intensity that is a periodic function of the optical phase difference between the beams. This phase difference is a linear function of the mean temperature of the film, since the film thickness and refractive index depend linearly on temperature. The reflected signal can therefore be used as a measure of the film temperature.

The basic optical arrangement is shown in Fig. 2. Laser diode light is launched into one arm of a fiber directional coupler. This evenly splits the incoming light between the fibers leading to the probe and an intensity reference detector. The signal reflected from the sensor returns to the coupler, where it is split evenly between fibers leading to the signal detector and back to the isolation optics (which prevent this light from reaching the laser diode).

Unlike conventional sensors, the fiber optic probe has no electrical connections to the measurement area, thus eliminating electrical interference. Connecting fiber lengths of 200 m are feasible, allowing the launch and detection optics and signal processing to be situated remote from the extreme noise and vibration of an operating compressor rig.

The fiber sensor possesses several features implying its potential for high-bandwidth temperature measurement. The optical power required to interrogate the sensor is too small to produce a significant heating effect; thus, cross-sensitivity to velocity is negligible. The film thickness is only a few μm, such that the thermal mass is low, leading to small thermal time constants. Interferometry is capable of resolving very small changes in optical path length, thus ensuring high temperature sensitivity. The dielectric nature of the sensor avoids several noise sources, thus allowing the intrinsically high temperature resolution of the technique to be exploited.

Fiber Sensor Theory

Sensing Mechanism. The sensor is a thin film interferometer used in reflection, deposited on the face of a single mode optical fiber. The optical phase difference ϕ between the front and back surface reflections is

$$\phi = 4\pi nl/\lambda \tag{1}$$

where n is the refractive index of the film, l the film thickness, and λ is the illumination wavelength. A mean temperature change ΔT_m of the film therefore results in a phase change:

$$\Delta\phi = \frac{4\pi l}{\lambda}\left[\frac{dn}{dt} + \frac{n}{l}\frac{dl}{dt}\right]\Delta T_m \tag{2}$$

where dn/dT represents the thermo-optic coefficient of the film, and dl/dT is its thermal expansivity. If the film's absorption is negligible, the optical intensity reflected at normal incidence takes the form (Heavens, 1965)

$$I(\phi) = I_0\left[\frac{a - b + c\cos\phi}{a + b + c\cos\phi}\right] \tag{3}$$

where a, b, c are defined in terms of the refractive indices:

Nomenclature

C = stagnation point velocity gradient
D = diameter
I = optical intensity
N = number of rotor revolutions
a, b, c = constants in optical transfer function
h = heat transfer coefficient
k = thermal spatial frequency
l = sensor length or thickness
n = sensing film refractive index
t = time
u = mean flow velocity
x = position
α = thermal diffusivity
κ = thermal conductivity
λ = optical wavelength
ν = kinematic viscosity
ϕ = optical phase
ω = optical angular frequency
A_0 = wave amplitude
Pr = Prandtl number
$\bar{P}_{(t)}$ = ensemble-averaged signal
$P'_{(t)}$ = random unsteadiness
n_c = fiber core refractive index
n_0 = gas refractive index
T_m = mean temperature of sensing element
T_g = gas total temperature
κ_f = fluid thermal conductivity
ϕ_0 = phase constant

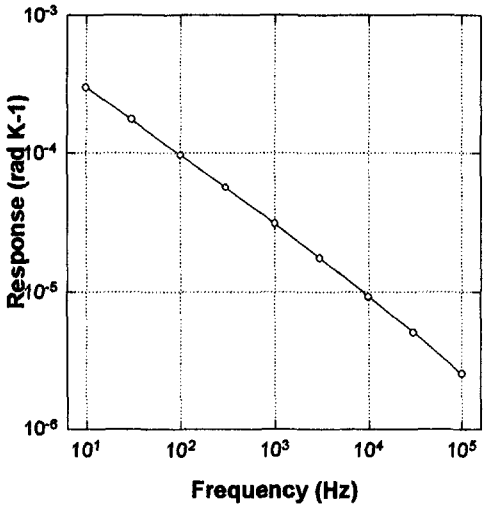

Fig. 3 Calculated frequency response of a 2.4 μm zinc selenide film fiber sensor to a unit amplitude oscillation in air temperature

$$a = (n_c^2 + n^2)(n^2 + n_0^2)$$
$$b = 4n_c n^2 n_0$$
$$c = (n_c^2 - n^2)(n^2 - n_0^2) \quad (4)$$

in which n_c and n_0 are the refractive indices of the optical fiber core and of the medium in contact with the film. Thus the temperature dependence of phase ϕ results in a temperature-dependent optical intensity at the signal photodetector, which follows the periodic function of Eq. (3). The response to a temperature change ΔT_m small enough to give rise to a phase change $\Delta\phi \ll 1$ rad will be approximately linear, with a sensitivity depending on the slope of the cosine function at the operating point. For a given laser wavelength and ambient temperature, the operating point is determined by the film thickness l, which can be chosen to avoid operation near the turning points of the cosine where the sensitivity approaches zero.

The optical coating employed was zinc selenide. This material has a relatively large thermo-optic coefficient dn/dT and is suitable for deposition in a thin film by vacuum evaporation (section 5.1). The laser wavelength was ~830 nm, at which $n \sim 2.6$ and $dn/dT \sim 1.0 \times 10^{-4}$, with low optical absorption (Buller et al., 1989). For fused silica and air respectively, $n_c = 1.46$ and $n_0 = 1.00$. Using Eq. (2) and noting that the thermal expansion term is small compared with the thermo-optic coefficient, we find that a mean sensor temperature change of ~1700 K corresponds to an optical phase change of 2π. Therefore in the application considered the sensor is always operating in the small signal regime.

Thermal Modeling of the Sensor Response. The thermal response of the fiber end face exposed to a gas flow (Fig. 1) can be considered in the simplest case as a one-dimensional problem with axial heat conduction into the sensor fiber. If the gas total temperature is time-varying, $T_g(t)$, a thermal disturbance will propagate through the film, giving rise to a time-varying mean temperature $T_m(t)$ averaged along the sensor length, which can be measured according to Eq. (2). The frequency response to thermal oscillations can be calculated from the analytic solution for heat conduction into a semi-infinite rod exposed at its end to a harmonically oscillating ambient temperature. If the gas total temperature varies with unit amplitude as $T_g(t) = \cos \omega t$, the temperature at a distance x into the film is given by (Luikov, 1968)

$$T(x, t) = A_0 e^{-kx} \cos(\omega t - kx - \phi_0) \quad (5)$$

where

$$A_0 = \left[1 + \frac{2k}{H} + \frac{2k^2}{H^2}\right]^{-1/2};$$
$$k = (\omega/2\alpha)^{1/2} \quad \text{and} \quad H = h/\kappa \quad (6)$$

in which α and κ are the thermal diffusivity and thermal conductivity of the thin film, h is the heat transfer coefficient at the sensor surface, and ϕ_0 is a frequency-dependent phase constant. Integration of $T(x, t)$ through the film thickness l gives a mean temperature oscillation at frequency ω, amplitude A_m given by

$$A_m(\omega) = (A_0/2kl)[2(1 + e^{-2kl}) - 4e^{-kl} \cos kl]^{1/2} \quad (7)$$

The expected sensor response to an oscillating gas temperature can be calculated, provided the heat transfer coefficient h from the gas to the sensor is known. This can be estimated by assuming that the sensor is located at the stagnation point of the oncoming flow, which is a good approximation as the fiber core is small compared to its diameter. The heat transfer coefficient at the stagnation point of a body with axisymmetric geometry can be written as (White, 1991)

$$h = \kappa_f 0.762 \, \mathrm{Pr}^{0.4}(C/\nu)^{1/2} \quad (8)$$

where κ_f is the thermal conductivity, Pr the Prandtl number, ν the kinematic viscosity of the fluid, and C is a stagnation point velocity gradient. For a flat-nosed body of diameter D in a mean flow velocity u for a Mach number below 1, White estimates that

$$C = 1.35u/D \quad (9)$$

Equations (8) and (9) can be used to calculate a heat transfer coefficient to the end face of a cylindrical fiber in specified mean flow conditions, and the response of the sensor is then found from Eq. (7). In the high frequency limit, this model predicts a weak dependence of the calibration on mean flow u.

The calculated frequency response to a unit amplitude thermal oscillation is shown in Fig. 3 for a 2.4 μm length sensor. This response can be compared with a shot noise of 1 $\mu\mathrm{rad}/\sqrt{\mathrm{Hz}}$ (this noise source being the fundamental limit associated with the random Poisson statistics of the photon flux from which an intensity measurement is made). We have demonstrated that a 1 $\mu\mathrm{rad}/\sqrt{\mathrm{Hz}}$ noise level is an achievable noise level in our signal detection system.

Signal Processing

The transfer function in Eq. (3) is periodic, and its slope, the small-signal sensitivity to phase fluctuations, is similarly periodic. The output signal in single wavelength operation would be dependent on the operating point. The output is made independent of operating point by illuminating the interferome-

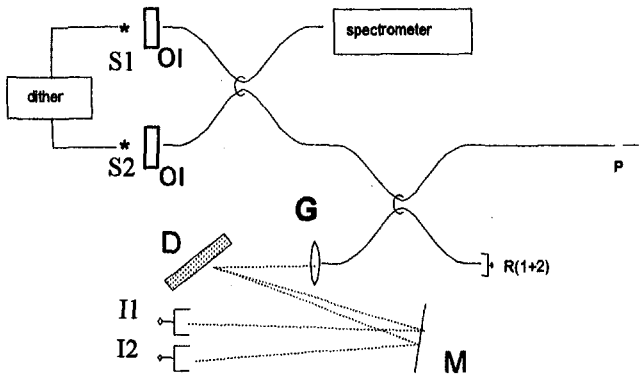

Fig. 4 Two wavelength operation of thin film sensor: S1, S2 = laser diode sources; OI = optical isolators; M = mirror; P = probe; G = graded index lens; D = diffraction grating; R(1 + 2) = reference detector; I1, I2 = signal detectors

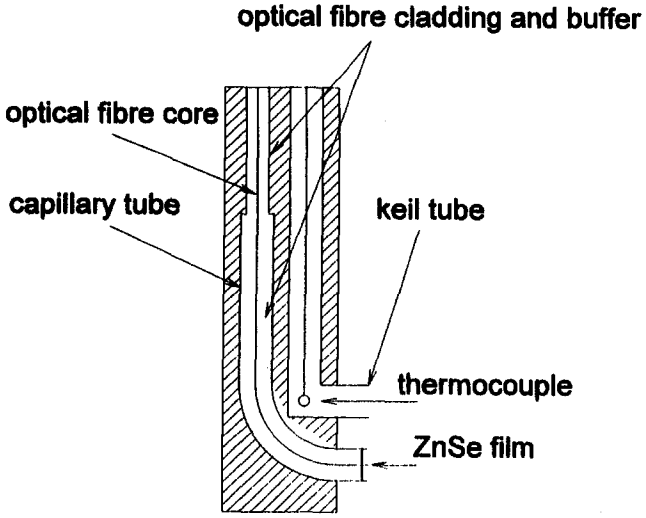

Fig. 5 Schematic arrangement of optical fiber right-angle probe for use in test compressor

ter with two wavelengths, λ_1 and λ_2, chosen to give a phase shift of $\pi/2$ between the resulting transfer functions, so that two signals in quadrature are recorded. Light from two separate laser diodes is combined by a directional coupler before launch into the addressing fiber, and the λ_1 and λ_2 outputs I_1 and I_2 are separated spatially by a diffraction grating to two photodetectors (Fig. 4). The sensor temperature change ΔT is given by the amplitude $(\Delta I_1^2 + \Delta I_2^2)^{1/2}$, which can be computed from data acquired from the sensor.

Probe Design and Construction

Thin Film Deposition. ZnSe films were deposited on the cleaved ends of optical fibers by a vacuum vapor deposition technique. This was carried out in a fully automated Balzers 550 box coater, in which a molybdenum boat containing high purity (99.99 percent) ZnSe powder was resistively heated to ~900°C. Base pressures of $\sim 2 \times 10^{-6}$ Torr were maintained during evaporation, which was controlled at a deposition rate of 0.5 nm s^{-1}. Prior to coating, the cleaved fiber ends were heat soaked by a radiant heater inside the coating unit, to improve coating adhesion and the optical quality of the deposited film.

During evaporation, film thickness was monitored by a quartz crystal monitor. Film thicknesses of up to 2.4 μm were successfully deposited. Fused silica substrates (~25 mm in diameter) were coated simultaneously as a coating witness, to enable measurement of the refractive index and thickness of the coating by spectrophotometric analysis.

Probe Design. The probe for use in the compressor measurements is shown in Figs. 5 and 6. The primary requirement was to provide a rugged mounting for the optical sensor and protection for the fiber optic feedout. The probe body was adapted from a conventional pneumatic wedge probe fitted with an adjacent shielded thermocouple sensor. As such, the configuration is typical of that used routinely in high-speed compressor testing, although it is recognized that future work may be required to formulate designs more suited to wide-bandwidth temperature sensors.

The principal problem of the probe design was how to support the optical fiber through a 90 deg turn of bend radius 3 mm in such a way as to secure the end of the sensing optical fiber. Two solutions were engineered: The fiber was supported in a preformed bend in either glass or metal capillary tube. A schematic of the metal capillary tube-based probe is shown in Fig. 5 and a photograph of a probe operated in the test compressor in Fig. 6.

The metal capillary tube-based probe was constructed as follows: (*i*) A 5 m length of single mode optical fiber was cleaved at one end; (*ii*) this end was vacuum coated with a 2.4-μm-thick ZnSe film; (*iii*) a length of metal capillary tube was tempered and a bend of radius 3 mm and length 90 deg formed; (*iv*) the capillary tube was trimmed to length to provide a supporting stem of 40 mm and 3 mm length projecting forward; (*v*) the fiber was drawn through the capillary tube and positioned with the ZnSe film retracted from the flush end of the tube by 20 μm; (*vi*) the tube was lightly crimped to clamp the fiber in position; and (*vii*) the capillary tube was secured inside the stainless steel wedge probe with epoxy adhesive.

Aerodynamic Testing

Heated Vortex Shedding. A method of generating thermal oscillations at kHz frequencies is required in a test experiment. Some previously reported techniques are measurement of the spectrum of thermal fluctuations in a heated turbulent jet (LaRue et al., 1975), and both DC and AC electrical heating of a wire in an airstream (Schacher and Fairall, 1978). We have used vortex shedding from a heated bluff body. In this case a metal wire carrying direct current is exposed transversely to an air flow. Vortices are shed from the wire at a frequency determined by the flow velocity, generating thermal fluctuation in the wake where warm air and ambient air are mixing at the vortex shedding frequency. This arrangement will also reveal any cross-sensitivity to air velocity, as a velocity fluctuation will still be present at the vortex shedding frequency when the heating current is removed (Ng and Epstein, 1983).

The vortex shedding wire was situated 20 mm downstream of the exit of a small open jet wind tunnel. The working section at the outlet was 80 mm square, with a flow velocity range from 5 to 12 ms^{-1} and a measured turbulence intensity of 0.4 percent. The sensor was positioned ~1 mm behind the shedding wire facing upstream with the fiber axis horizontal, so that the mean flow was incident normally on the fiber end face. To measure

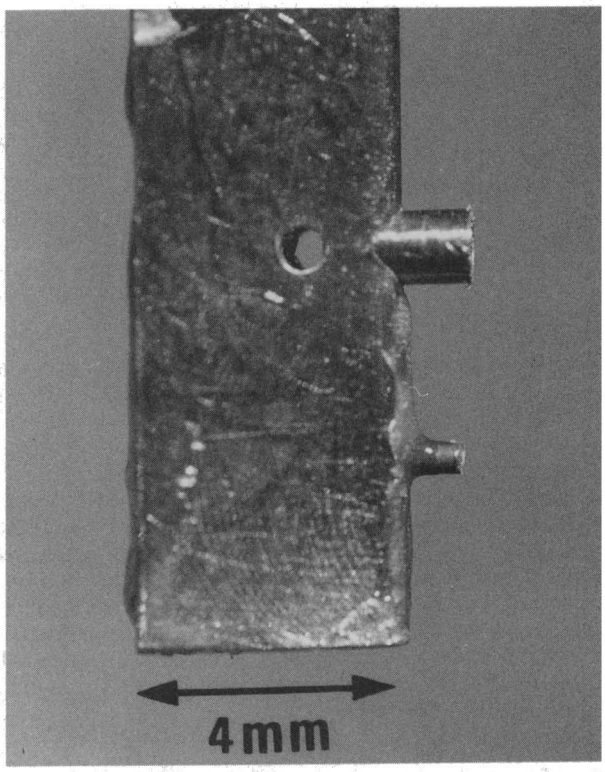

Fig. 6 Detail of probe constructed for compressor trials

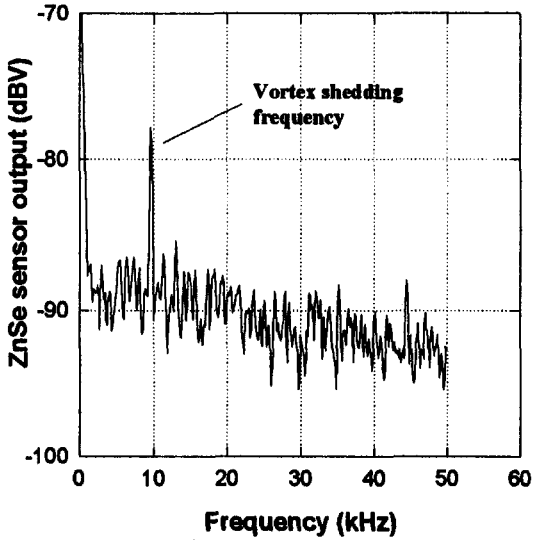

Fig. 7 Spectrum of the fiber sensor signal with heating current applied to the vortex shedding wire; vortex shedding frequency = 9.6 kHz

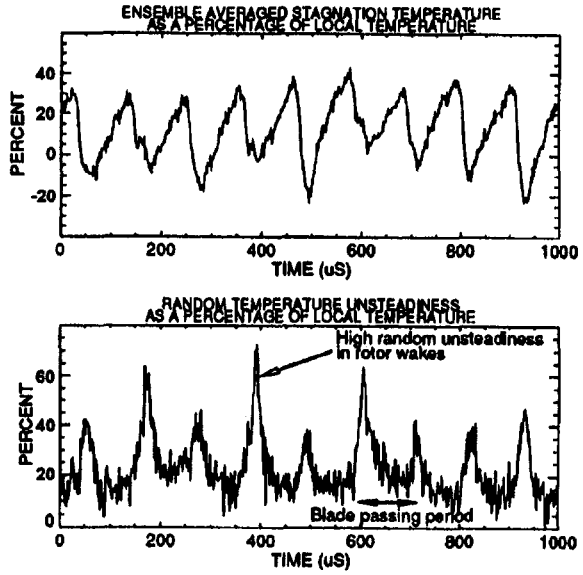

Fig. 8 (A) Phase-locked average output signal from fiber temperature sensor close to the hub behind the first stage rotor in compressor trials; (B) random unsteadiness of the temperature signal

the vortex shedding frequency, a conventional hot-wire anemometer probe was mounted with its sensing wire coplanar with and at the same height as the sensor end face, ~5 mm to one side. Both the fiber and the hot-wire probe could be translated together vertically relative to the shedding wire.

The shedding wire was 0.15-mm-dia nichrome alloy, and for the flow speeds available, the frequencies range from 4 to 13 kHz without applied heating. If the shedding wire is heated above ambient temperature, the Reynolds number of the air close to the wire is decreased, and the vortex shedding frequency is reduced, an effect reported by Lecordier et al. (1991) for a flow regime similar to that used here.

At an air velocity of 10.5 ms^{-1} (Re = 104) the vortex shedding frequency was 11.3 kHz with no heating current applied. With 9 W DC heating power, the vortex frequency decreased to 9.6 kHz, which is typical of the reduction observed by Lecordier et al. (1991). The output signal was monitored by a spectrum analyzer with a linewidth setting of 125 Hz and the results are shown in Fig. 7. A clear spectral peak 10 dB above the noise floor appears at the shedding frequency with heating applied. There was no signal at 11.3 kHz when the heating was removed, returning the shedding wire to ambient temperature, which implies that the thin film sensor has no significant cross-sensitivity to air velocity fluctuations, and is only responding to air temperature fluctuations under these conditions. The estimated temperature amplitude at the measurement point was 3 K (see Discussion).

Demonstration in Compressor Test Facility. Trials were carried out to expose the temperature sensor to the flow field behind the first stage rotor of a highly loaded five-stage core compressor. The measurements were taken at several spanwise stations while the machine was operating close to peak efficiency on the design speed characteristic. Typical aerodynamic parameters for the first stage at this condition are given in Table 1. Unsteady pressure measurements were also taken, and similar measurements taken in an earlier build of this machine have been reported in detail by Cherrett and Bryce (1992). This was the first time unsteady temperature measurements had been attempted in this machine.

During both pressure and temperature measurements, the data were recorded in two modes: as continuously sampled data, and as multiple data recorded phase-locked to a once-per-revolution trigger pulse. The latter were subsequently processed to reveal the ensemble-averaged temperature variations and the random unsteadiness found in the data (see appendix). In both modes, the signals were sampled at 500 kHz.

Ensemble-averaged stagnation temperature measurements taken close to the hub (at 10 percent span with the probe aligned to the mean flow angle) are shown in Fig. 8. These can be compared with corresponding stagnation pressure measurements, Fig. 9, taken with a Kulite gage at the same spanwise

Table 1 Typical flow parameters behind first compressor stage

Parameter	Value
flow speed (ms^{-1})	225
mean total temperature (K)	339.5
stage temperature rise (K)	50
mean total pressure (kPa)	112
stage pressure ratio	1.58

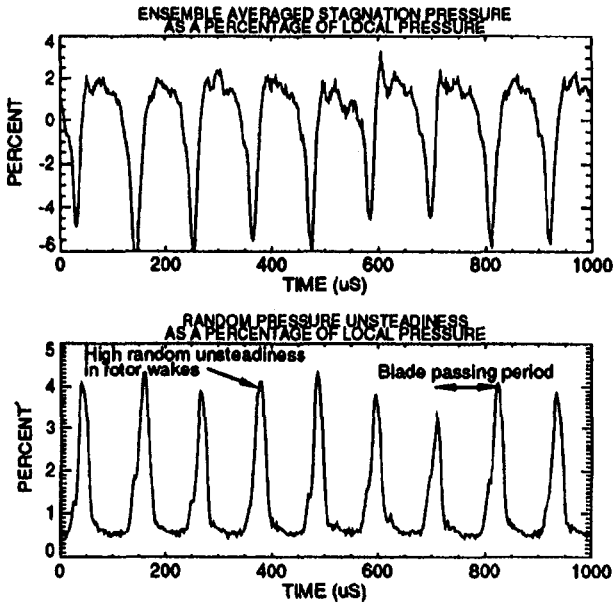

Fig. 9 (A) Phase-locked average pressure transducer signal taken under similar run conditions to those in Figure 8; (B) random unsteadiness of the pressure signal

position, although during a different run. Also shown are the corresponding random temperature and pressure unsteadiness. There is encouraging qualitative agreement between both temperature and pressure data, particularly regarding the increased random unsteadiness associated with the blade wakes.

The power spectrum of a section of continuously sampled data was computed via its Fourier transform and shown in Fig. 10. The dominant component to the spectrum is at the blade passing frequency of 9.2 kHz. However, components at two, three, and four times the blade passing frequency are clearly observed above the noise floor, indicating a lower limit on the sensor bandwidth of ~36 kHz. In these preliminary experiments, no effort was made to compensate for optical power fluctuations, thus increasing the noise floor.

Data were recorded for about one hour's total exposure to the flow, until the signal was lost. The probe was later examined, showing that part of the ZnSe coating had been damaged, presumably by particulates or oil droplets in the flow.

Discussion

The compressor trials in the previous section were undertaken to demonstrate the feasibility of using an optical fiber sensor in a realistic aerodynamic test facility, rather than as a detailed investigation of the unsteady temperature field in the compressor. Calibration of the data obtained in these trials was not a critical issue, and was performed by comparing the unsteady temperature compressor data with the heated vortex shedding data. The 9.6 kHz vortex shedding signal was close to the blade passing frequency of 9.2 kHz in the radial traverse; therefore the frequency dependence of the sensor's response does not affect the comparison. The sensing film was 2.4 μm of ZnSe in both cases. The heating power of 9 W applied to the vortex shedding wire, if dissipated by convection, would result in a mean air temperature rise in the wake of ~6 K, or an amplitude of 3 K in mixing ambient and heated air. The ZnSe film optical response to this amplitude of gas temperature oscillation was determined in the vortex shedding experiment. Thus the sensor response observed in the compressor can be scaled to gas temperature amplitude, allowing for the estimated change in gas-to-sensor heat transfer coefficient between the two experiments. Typical signals at blade passing frequency corresponded to 15 K total temperature amplitude. This is an initial estimate subject to assumptions in the heat transfer modeling, and further work on temperature calibration is in progress.

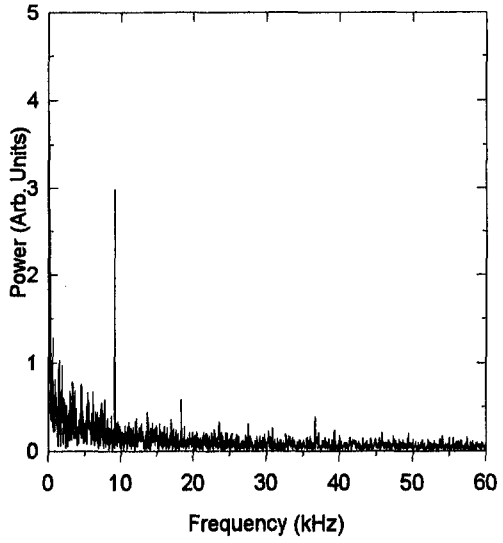

Fig. 10 Power spectrum of fiber sensor signal while located at 10 percent

The sensor coating was damaged after about one hour's exposure to the flow in the compressor. However, the ZnSe coating in this trial sensor was unprotected, and technology exists to apply suitable protective coatings that are sufficiently thin to prevent an adverse effect on the high-frequency thermal response. This new optical technique therefore has potential for application in high-bandwidth unsteady temperature measurement in continuous flow.

Fiber optic sensors based on interferometry have potential for other applications in aerodynamics test facilities. For example, we have shown previously that fiber Fabry Perot interferometers are suitable for the measurement of heat flux in transient flow wind tunnels (Kidd et al., 1992, 1993). Furthermore, other transduction principles, such as the strain optic effect in special optical coatings, or miniature air-spaced interferometers, may be applicable for high bandwidth pressure measurement.

Conclusions

We have described an all-optical temperature sensor that has demonstrated a response to air temperature fluctuations, estimated to be 3 K amplitude, at approximately 10 kHz in a low-speed vortex shedding experiment. The sensor is not sensitive to small velocity fluctuations. The optical sensor has been incorporated into a probe and run in a test compressor in mean flows of Mach 0.7. No electrical connection was required between the sensor and the control room. Signals well above noise were obtained in ensemble-averaged data, showing a strong component at the 9.2 kHz blade passing frequency, and response to at least 36 kHz. Typical temperature amplitudes were estimated to be 15 K in a radial traverse from hub to tip, in comparison with the temperature rise of 50 K in the compressor stage. Further work is in progress to define the probe characteristics more fully, with attention to calibration and frequency response in conditions experienced in turbomachinery.

Acknowledgments

This work was partially supported by the Defence Research Agency, Pyestock, and the Department of Trade and Industry, UK, contract number 2195/27 RAE-P. The authors wish to thank C. G. Burton, J. D. Bryce, I. R. I. McKenzie, and P. A. Lyes, all of DRA Pyestock, for their contributions to the planning and execution of the work reported in this paper.

References

Buller, G. S., Paton, C. R., Smith, S. D., and Walker, A. C., 1989, "Optically Bistable Nonlinear Interference Filters for Use With Near-Infrared Laser Diodes," *Optics Comm.*, Vol. 70, pp. 522–528.

Cherrett, M. A., and Bryce, J. D., 1992, "Unsteady Viscous Flow in a High-Speed Core Compressor," ASME JOURNAL OF TURBOMACHINERY, Vol. 114, pp. 287–294.

Forney, L. J., Meeks, E. L., Ma, J., and Fralick, G. C., 1993, "Measurement of Frequency Response in Short Thermocouple Wires," *Rev. Sci. Instrum.*, Vol. 64, pp. 1280–1286.

Heavens, O. S., 1965, *Optical Properties of Thin Solid Films*, Dover, New York.

Kidd, S. R., Sinha, P. G., Barton, J. S., and Jones, J. D. C., 1992, "Interferometric Fibre Sensors for Measurement of Surface Heat Transfer Rates on Turbine Blades," *Optics & Lasers in Engineering*, Vol. 16, pp. 207–221.

Kidd, S. R., Barton, J. S., Jones, J. D. C., Chana, K. S., and Matthews, I. W., 1993, "Fibre Optic Interferometric Heat Transfer Sensors for Transient Flow Wind Tunnels," ASME Paper No. 93-GT-218.

LaRue, J. C., Deaton, T., and Gibson, C. H., 1975, "Measurement of High Frequency Turbulent Temperature," *Rev. Sci. Instrum.*, Vol. 46, pp. 757–764.

Lecordier, J. C., Hamma, L., and Paranthoen, P., 1991, "The Control of Vortex Shedding Behind Heated Circular Cylinders at Low Reynolds Numbers," *Expts. in Fluids*, Vol. 10, pp. 224–229.

Luikov, A. V., 1968, *Analytical Heat Diffusion Theory*, Academic Press, London.

Ng, W. F., and Epstein, A. H., 1983, "High-Frequency Temperature and Pressure Probe for Unsteady Compressible Flows," *Rev. Sci. Instrum.*, Vol. 54, pp. 1678–1683.

Schacher, G. E., and Fairall, C. W., 1978, "Producing Small Scale Temperature Fluctuations in an Airstream," *Rev. Sci. Instrum.*, Vol. 49, pp. 1432–1434.

White, F. M., 1991, *Viscous Fluid Flow*, McGraw-Hill, New York.

APPENDIX

Phase-Locked Data Processing

The discontinuous phase-locked data were processed on-line to determine the following parameters:

(a) *Ensemble-averaged signal,* i.e., $\tilde{P}_{(t)} = (1/N) \sum_{n=1}^{N} P_{(n,t)}$

(b) *Random unsteadiness,* i.e., $P'_{(t)} = [(1/N) \sum_{n=1}^{N} (P_{(n,t)} - \tilde{P}_{(t)})^2]^{1/2}$

where $P_{(n,t)}$ is an instantaneous AC-coupled signal; N is the number of consecutive rotor revolutions during which phase-locked data capture was carried out in response to a once-per-revolution pulse; and t is the duration of each of the segmented data records (typically 512 or 2048 samples, depending on the recorder module capacity).

Such processing is an established technique, which accentuates the periodic unsteadiness correlated with the rotor. As the data are captured in response to a once-per-revolution signal, the rotor is in the same position each time the recording cycle is initiated and differences in the flow field associated with individual rotor passages are retained.

D. E. Van Zante[1]
Department of Mechanical Engineering,
Iowa State University,
Ames, IA 50011

K. L. Suder

A. J. Strazisar

Internal Fluid Mechanics Division,
NASA Lewis Research Center,
Cleveland, OH 44135

T. H. Okiishi
Department of Mechanical Engineering,
Iowa State University,
Ames, IA 50011

An Improved Aspirating Probe for Total-Temperature and Total-Pressure Measurements in Compressor Flows

The aspirating probe originally designed by Epstein and Ng at MIT was modified by replacing the two platinum-coated tungsten hot wires normally used with platinum–iridium alloy wires. The resulting improved unsteady total pressure and total temperature resolution of the modified probe is demonstrated. Flowfield measurements were made downstream of NASA Rotor 37 for a part-speed operating condition to test the performance of the probe. Time-resolved blade-to-blade total temperature and total pressure as calculated from the two platinum–iridium hot-wire voltages are shown. The flowfield measurements are compared with independent measurements of total pressure with high response transducers and total temperature calculated from laser anemometer measurements. Limitations of a more often used unsteady temperature data reduction method, which involves only one aspirating probe hot-wire voltage and a high-response pressure measurement, are discussed.

Introduction

The accurate measurement of the aerodynamic performance parameters for flow through an axial-flow, transonic compressor stage is still an important engineering problem. The three-dimensionality, compressibility, and unsteadiness of transonic compressor stage flow can contribute to fluid temperature, pressure, and velocity measurement errors that result in a significant misrepresentation of rotor and stage efficiency.

The aspirating probe invented by researchers at MIT (Ng and Epstein, 1983) is intended to be a tool for accurately measuring time-resolved total temperature and total pressure in compressor flows. However, personal experience with this probe revealed serious limitations. Some of these limitations have been overcome with a simple improvement involving a change in hot-wire material.

The main objective of this paper is to share details about the improved aspirating probe with readers who may be interested in using the aspirating probe as it was originally intended.

Aspirating Probe

The voltage, V, required to maintain a conventional hot wire at a constant temperature, T_w, is a function of the wire-to-fluid temperature difference, $(T_w - rT_T)$, and fluid mass flux, (ρU), at the wire plane. The functional relationship is:

$$V^2 = f(\rho U)(T_w - rT_T) \tag{1}$$

In an unsteady compressible flow, ρ, U, T, and P all fluctuate with time, making the hot-wire data extremely difficult to interpret. To overcome this difficulty, Ng and Epstein (1983) placed a pair of co-planar hot wires operating at different overheat ratios in a channel whose exit is choked. Figure 1 is a schematic of this channel.

The continuity equation for one-dimensional channel flow at the sonic orifice is

$$(\rho U)^* = \left(\frac{P_T}{\sqrt{T_T}}\right)\sqrt{\frac{\gamma}{R}}\left(\frac{2}{\gamma+1}\right)^{(\gamma+1)/[2(\gamma-1)]} \tag{2}$$

By applying mass conservation in the channel, Eq. (2) can be written as

$$\rho U = \left(\frac{P_T}{\sqrt{T_T}}\right)\frac{A^*}{A_c}\sqrt{\frac{\gamma}{R}}\left(\frac{2}{\gamma+1}\right)^{(\gamma+1)/[2(\gamma-1)]} \tag{3}$$

which states that (ρU) is a function of free-stream total pressure and total temperature. Equation (1) may thus be expressed as

$$V^2 = f\left(\frac{P_T}{\sqrt{T_T}}\right)(T_w - rT_T) \tag{4}$$

For a constant-temperature hot wire we also have

$$V^2 = \frac{(R_s + R_w)^2}{R_w}\pi l \kappa \mathrm{Nu}\,(T_w - rT_T) \tag{5}$$

By equating Eqs. (4) and (5) and grouping parameters that are fixed for a set probe geometry and gas composition into constants, the working equation for the wires becomes

$$V_i^2 = \left[C_i\left(\frac{P_T}{\sqrt{T_T}}\right)^{n_i} + D_i\right](T_{w_i} - rT_T) \tag{6}$$

where

$$C_i, n_i, D_i = f(T_T, l_{hw}, d_{hw}, \mathrm{Nu}) \tag{7}$$

The subscript i refers to the hot-wire number, either 1 or 2, and the constants C_i, n_i and D_i are determined from a calibration procedure. This was the version of Eq. (6) originally derived by Ng and Epstein (1983). From his experiences in using the probe for P_T and T_T measurements, Dr. Ng determined that D_i was negligible and he dropped it from the working equation. This reduced formulation of Eq. 6, with $D_i = 0$, was used by Alday and Ng (1991), Alday et al. (1993), and Van Zante (1992).

To calculate T_T and P_T using the two hot wire voltages, V_1 and V_2, the two simultaneous equations

[1] Present address: NASA Lewis Research Center, Cleveland, OH 44135.

Contributed by the International Gas Turbine Institute and presented at the 39th International Gas Turbine and Aeroengine Congress and Exposition, The Hague, The Netherlands, June 13–16, 1994. Manuscript received by the International Gas Turbine Institute February 18, 1994. Paper No. 94-GT-222. Associate Technical Editor: E. M. Greitzer.

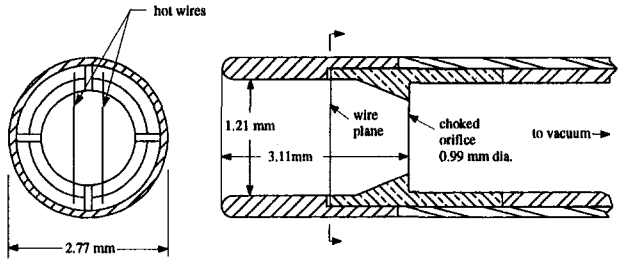

Fig. 1 Schematic of aspirating probe

$$V_1^2 = \left[C_1 \left(\frac{P_T}{\sqrt{T_T}} \right)^{n_1} + D_1 \right] (T_{w_1} - rT_T)$$

$$V_2^2 = \left[C_2 \left(\frac{P_T}{\sqrt{T_T}} \right)^{n_2} + D_2 \right] (T_{w_2} - rT_T) \qquad (8)$$

must be solved. The two hot wires in the choked channel provide two measurements from which T_T and P_T can be deduced using Eq. (8) and thus form the basis for the aspirating probe design and operation. A more in-depth discussion of the aspirating probe design is available in Ng and Epstein (1983) and Ng (1983).

The independence of the two relations in Eq. (8) will determine the probe sensitivity to T_T and P_T and thus the shape of the calibration space. The difference between the hot-wire temperatures, $|T_{w_2} - T_{w_1}|$, influences the independence of the two simultaneous equations; thus, if T_{w_1} is nearly equal to T_{w_2}, the equations will be almost identical and therefore have limited independence. Solving these equations with limited independence is like attempting a solution represented by the intersection of two nearly parallel lines. The calibration constants are also functions of total temperature, hot-wire length and diameter, etc., but these factors have a lesser effect on the independence of the equations than the wire temperatures. The greater the separation in wire temperatures, the more independent the two hot-wire equations will be with improved sensitivity to temperature and pressure.

Performance of Original Probe

The original version of the aspirating probe used a 5 μm (0.0002 in.) diameter tungsten hot wire for channel 1 and an 8.9 μm (0.00035 in.) diameter tungsten hot wire for channel 2. The overheat ratios for the wires were 1.8 and 2.0, giving wire temperatures of 216°C (420°F) and 263°C (505°F) respectively.

For an independent measure of total pressure, a Kulite model XCQ-062 semiconductor pressure transducer was mounted beside the aspirating probe. To reduce thermal drift, the transducer was thermally compensated by the manufacturer as well as with an external sense resistor as described by Cherrett and Bryce (1991). Figure 2 shows a front view of the combination probe. The aspirating probe is on the left and the Kulite is on the right.

Calibrations of the aspirating probe were accomplished in a static air tank at different constant temperatures and variable pressure to determine the constants C_i, n_i, and D_i. Calibrations were obtained at ambient temperatures, 60.0, 71.1, 82.2, 93.3, 104.4, 116.6, and 127.7°C (140, 160, 180, 200, 220, 240, and 260°F) at pressures from 101.4 kPa to 241.3 kPa (14.7 to 35 psia). The initial calibration procedure used is identical to that used in previous applications of the aspirating probe (Alday and Ng, 1991; Van Zante, 1992). Equation (6), with $D_i = 0$, was written in logarithmic form and a linear least-squares routine was used to determine the calibration constants for each wire at each calibration temperature.

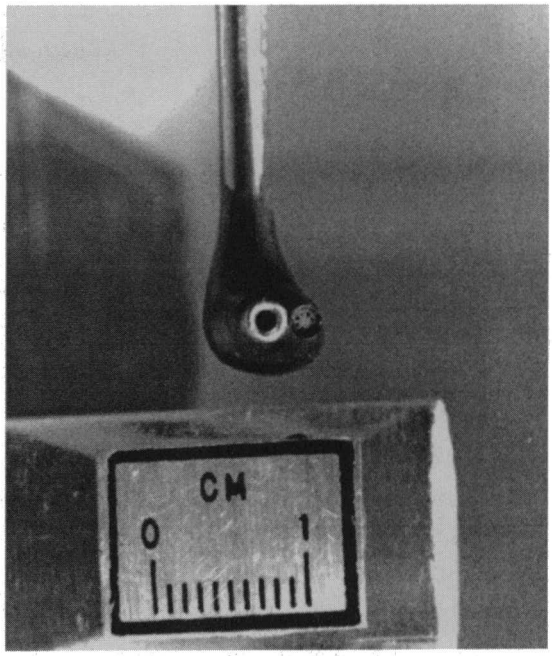

Fig. 2 NASA1 high-response probe

A set of calibration constants, C_i and n_i, was determined for each wire for each constant temperature calibration. Figure 3 shows the calibration space for the tungsten hot wires as hot wire 1 voltage versus hot wire 2 voltage for the range of calibration temperatures and pressures. For clarity only five constant-temperature lines are shown. Each line of + symbols is a constant-temperature line and each + symbol represents a pressure value from 68.9 kPa (10 psia) in the lower left to 275.8 kPa (40 psia) in the upper right in increments of 6.9 kPa (1 psi).

Each constant-temperature calibration line was generated from the constants derived from a calibration at that temperature. Ng and Epstein (1983) stated that calibration constants from the ambient temperature calibration could be used to predict the probe performance at higher temperatures. For the current range of calibration temperatures and pressures, this was not the case. Therefore, with this initial calibration procedure, a more extensive calibration was needed and calibration constants were calculated for every calibration temperature.

In his application of the aspirating probe to determine P_T, T_T, and species concentration, Kotidis (1989) also followed an

Nomenclature

A^* = throat area at sonic orifice
A_c = channel area at wire plane
R_s = series resistance of anemometer
R_w = resistance of a hot wire at operating temperature
V = anemometer bridge voltage
γ = ratio of specific heats
R = gas constant for air
U = fluid velocity in choked channel
ρ = density of air
P_T = total pressure of fluid being measured
T_T = total temperature of fluid being measured
T_w = wire operating temperature
l = hot-wire length
d = hot-wire diameter
r = ratio of static to total temperature of fluid being measured
κ = fluid thermal conductivity
Nu = Nusselt number
C, n = hot-wire calibration constants

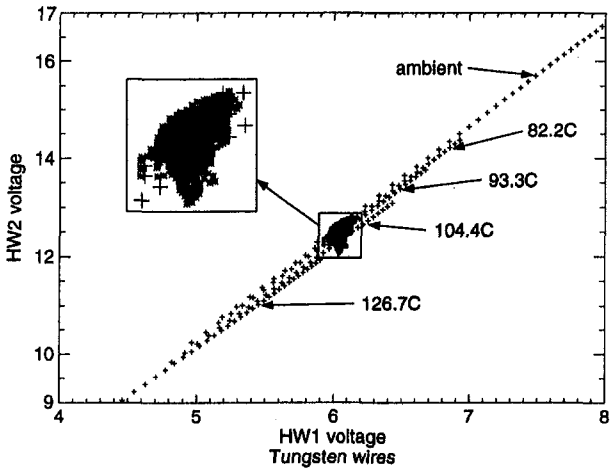

Fig. 3 Original calibration space of aspirating probe with representative data shown

accurate but less time-intensive calibration procedure. He used the original working equation with three constants, C_i, n_i, and D_i, and determined the temperature dependence of the constants. Kotidis's formulation of the probe equations was simplified to remove the species concentration dependence. Because the Kotidis formulation of the probe governing equations accounts for the temperature dependence of C_i, n_i, and D_i, a subset of the initial calibration data can be used to characterize the probe behavior over the same region as the initial calibration procedure. An extensive "reference" calibration is done at room temperature. The remainder of the anticipated operating region for the probe is characterized by acquiring a series of "random" pressure/temperature points throughout the region. Since it requires one third to one half as many calibration points, this refined calibration procedure is much less tedious and time consuming than the initial procedure. The Kotidis calibration procedure was used to generate the calibration space that was used for data reduction in this report.

The extremely narrow wedge shape of the initial calibration space in Fig. 3 indicates that the sensitivity of the aspirating probe to pressure and temperature variations is poor. Very small changes in hot-wire voltage correspond to large changes in temperature and pressure. The asterisks overlaid on the calibration space in Fig. 3 are measurements acquired downstream of Rotor 37 at midspan at a part-speed operating condition. Several thousand measurements are shown. Since the measurements were acquired across all the blade passages, the envelope of the measurements indicates the excursions in pressure and temperature across the blade pitch as well as passage-to-passage flow nonuniformities in the rotor. The measurement envelope is large relative to the calibration space; a significant portion of the data actually lies outside of the calibration space. Because of poor probe sensitivity, the excursion of "data" outside of the calibration space was probably due to the inability of the probe to respond correctly to the dynamic fluctuations of P_T and T_T in the compressor. It is not reasonable to reduce these data to total pressures and total temperatures using the two hot-wire voltages because of the poor instrument sensitivity and data scatter.

To overcome this severe sensitivity limitation, total temperature was alternately calculated using the total pressure from the Kulite transducer and only one hot-wire voltage from the aspirating probe as suggested by Ng and his students (Morris et al., 1992). The limitations of this data reduction method will be discussed later. Instead of combining the outputs of two different high-response instruments to measure a time-resolved temperature, a better solution is to modify the aspirating probe to improve its sensitivity so it can be used alone for this measurement.

As mentioned previously, the ability of the probe to follow changes in total pressure and total temperature is related to the performance of the hot-wire anemometry in the flow environment and to the independence of the simultaneous equations, Eq. (8) for wires 1 and 2, which must be solved for P_T and T_T.

The performance of a hot wire and anemometer is related to the wire-to-fluid temperature difference, $(T_w - rT_T)$. The total temperature downstream of Rotor 37 is significantly above ambient thus reducing the wire-to-fluid temperature difference possible with tungsten which has a limited maximum temperature. This reduces the frequency response of the wire and leads to nonlinearity in the anemometer response. In a flow with temperature fluctuations, Smits et al. (1983) recommends high overheat ratios to avoid contamination of the mass flow signal from the fluctuating temperature. As ambient temperature rises, very high overheat ratios or wire temperatures are required. This is the case in an environment like the flow downstream of Rotor 37.

Modified Aspirating Probe

Because of the relatively low maximum operating temperature of tungsten hot wires, the optimum conditions of high wire temperature and significant spread between wire temperatures are out of reach for this material. Thus platinum–iridium alloy wires were chosen to replace the tungsten wires. Table 1 summarizes both tungsten and platinum–iridium wire properties. The platinum iridium (Pt/Ir) alloy wires allow high wire temperatures and also have a high enough maximum temperature to permit a significant spread between wire temperatures.

The tungsten wires of the original aspirating probe were replaced with 6.3 μm (0.00025 in.) diameter platinum iridium alloy wires on channels 1 and 2 of the anemometer. The operating temperatures of the wires were set to 260°C (500°F) and 371°C (700°F) for wire 1 and 2, respectively. Because of the different temperature coefficient of resistance for platinum iridium relative to tungsten, the overheat ratios were 1.21 and 1.31, respectively.

The modified probe was calibrated and the resulting calibration space is shown in Fig. 4 to the same scale as the tungsten wire calibration space shown in Fig. 3. All eight constant-temperature lines are shown and each line represents a pressure range of 68.9 to 275.8 kPa (10 to 40 psia). A data set taken with the modified aspirating probe at conditions equivalent to the data set shown in Fig. 3 is superimposed on the calibration space. The calibration space is more "open," which allows much better resolution of total temperature and pressure. In addition, the data scatter is reduced considerably and the region of data scatter corresponds to reasonable changes in temperature and pressure.

Because of the improved performance of the modified probe, it is now possible to determine time-resolved total temperature and total pressure from the two hot-wire voltages. Also a comparison of unsteady temperature and pressure measured with the two wires and unsteady pressure and temperature measured with one wire and the Kulite can be done.

Data Reduction

Earlier data reduction methods used a single set of calibration constants and, using either both V_1 and V_2 or the Kulite pressure value and one hot wire voltage, solved Eq. (8) ($D_i = 0$) by an iterative method. These data reduction methods assume that C_i and n_i are not functions of T_T. For the present study this was not a reasonable assumption and a more rigorous data reduction procedure was followed.

The calibration space was parameterized in terms of two independent variables, u and v, using a spline geometry subroutine package called DT_NURBS (Boeing and U.S. Navy, 1992). Two surfaces result:

Table 1 Summary of hot-wire material properties

Type	Max $T_{ambient}$ °F (°C)	Max T_{sensor} °F (°C)	Temp coef of resistance (/°C)
Tungsten	300 (150)	570 (300)	0.0042
Platinum iridium	1400 (750)	1470 (800)	0.0009

$$S_1: \quad P_T(u, v), \quad V_1(u, v), \quad V_2(u, v)$$
$$S_2: \quad T_T(u, v), \quad V_1(u, v), \quad V_2(u, v) \qquad (9)$$

A second-degree B-spline surface was interpolated through the calibration data to form each surface. Reducing the experimental data to T_T and P_T was done using a Newton–Raphson style root finding method on the parameterized surfaces. This is a convenient way of manipulating the calibration space because any data pair can be used. For example, (V_1, V_2) or (V_1, P_T) can drive the iteration procedure to find the u, v values for the third unknown, either (P_T, T_T) or T_T, respectively. The method is also fast, which is essential because of the large volume of data requiring reduction.

The Experiment

Flowfield measurements were acquired using the modified aspirating probe downstream of NASA Rotor 37 in the single-stage compressor research facility at the NASA Lewis Research Center. Detailed design and aerodynamic performance data for the rotor are presented in Reid and Moore (1978) and Moore and Reid (1980). Figure 5 shows the compressor flowpath and measurement locations.

The rotor was designed for a total pressure ratio of 2.1, a weight flow of 20.2 kg/s (44.5 lb/s), and a rotor tip speed of 454 m/s (1490 ft/s) at a design speed of 17,200 rpm. For this study the rotor was operated at 60 percent speed; see Table 2 for an operating condition summary. Aspirating probe and high-response pressure probe measurements were acquired at the station 3 axial plane of the compressor for this part speed condition. Laser fringe anemometer measurements were acquired just upstream of station 3 at 9.4 cm (3.7 in.) axial distance.

The aspirating and pressure probe signals were digitized with a 12 bit resolution A/D system. The A/D system samples were phase-locked to the rotor by using the output pulse train of a shaft angle encoder to trigger the digitizer. The shaft angle encoder used the elapsed time between once-per-revolution (OPR) pulses, which originated from the rotor disk to calculate the output pulse frequency required to generate a given number of pulses per revolution. The required frequency was fed to a frequency-agile clock within the encoder, which then generated the desired number of clock counts independent of rotor speed drifts. The shaft angle encoder was configured to give 1656 counts per revolution or 46 counts per blade passage. The resulting nominal sampling frequency is shown in Table 2. Each hot wire of the aspirating probe was operated by a separate Dantec model 55M01 constant temperature anemometer.

A careful calibration of the aspirating probe and Kulite was done to minimize calibration uncertainties, which would predominantly result in bias errors. When only the noise levels of each hot wire signal are taken in account, the corresponding total pressure and total temperature variations calculated are approximately ±1.24 kPa and ±0.80 K. For the Kulite, the noise level translates to ±0.20 kPa. For the one-wire/Kulite data, noise results in a ±0.72 K temperature band. Hot-wire aging, Kulite sensor aging, and Kulite amplifier drift all can cause significant shifts of the instrument calibrations. Since we are presently concerned mainly with the response of the probe to changes in total pressure and temperature, the shifts in the calibrations are not yet a serious problem.

Since the Kulite total pressure sensor was mounted next to the aspirating probe, there was some concern about the impact of angular sensitivity effects on the accuracy of its total pressure measurement. Additionally, laser anemometer measurements indicated large flow angle variations from core flow to wake. Total pressure was therefore measured independently using a Kiel type probe fitted with a Kulite XCQ-062-50A high response pressure transducer. Because of electronic noise this transducer has a resolution of ±0.45 kPa. This probe is insensitive to flow angles up to ±40° as determined in a calibration jet. Pressure measurements were acquired with this Kiel probe at the same axial measurement location as the aspirating probe and adjacent Kulite.

Velocity and flow angle data were acquired using a two-channel laser fringe anemometer (LFA) system. The LFA data have a resolution of 184 points per blade passage and were acquired slightly upstream of the station 3 measurement location. The LFA data from farther upstream suggests that negligible wake decay occurred from the LFA measurement location to the aspirating probe measurement location.

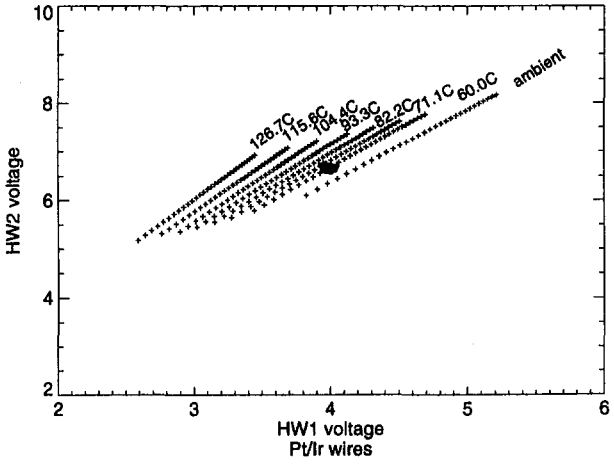

Fig. 4 Calibration space with platinum–iridium wires with representative data set shown

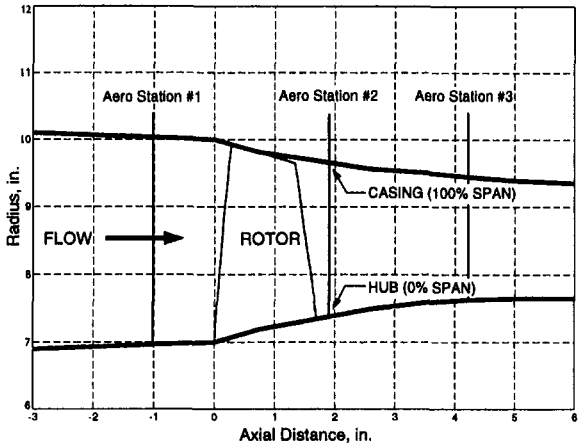

Fig. 5 Rotor 37 flowpath and measurement locations

Table 2 60 percent speed operating conditions

RPM	10,300
Weight flow (kg/s)	13.7
Pressure Ratio	1.25
Blade Passing Frequency (Hz)	6,200
Sampling Frequency (Hz)	284,280

The data were averaged using an OPR ensemble-averaging method to show flow structure. OPR averaging indexes the averaging by the number of counts per revolution to give information for an average revolution. The data could be further averaged by indexing by the number of counts per blade to give information for an average passage. The pressure probe and aspirating probe data are presented below as three characteristic passages of an average revolution. The LFA data are for an average passage that is repeated three times.

Results

Measurements were made at the 60 percent speed operating condition using the aspirating probe and adjacent Kulite transducer, the high-response Kiel-headed pressure probe, and the LFA system, all at or near station 3. The improved sensitivity of the aspirating probe allowed measurement of pressure and temperature fields using the two hot-wire voltages only. The two-wire measured pressure field is compared to that measured using the Kulites mounted on both the aspirating probe and the Kiel-headed probe. In addition, the two-wire measured temperature field is compared to that field calculated with the Euler turbine equation from LFA velocity data and with that field measured with one wire and the adjacent Kulite.

Two-Wire Results

Figures 6 and 7 show the blade-to-blade views of the total pressure and total temperature fields measured using the two wire voltages. Three representative blade passages are shown and the annulus boundary is represented as a black border with the upper line being the casing (100 percent span) and the lower line being the hub (0 percent span). Contour level increments are consistent throughout all of the figures; however, for better clarity and contrast the contour level shading does not always represent the same contour value between the figures. Each blade wake shows clearly as a region of higher total temperature. The total temperature increases approximately 5.0°C (9°F) above the core flow temperature. This temperature increase corresponds to an increase in total pressure as shown in Fig. 6. The total pressure increases approximately 6.9 kPa (1.0 psi) above the core flow pressure. All temperatures and pressures are measured in the absolute reference frame.

As an independent check of the temperature response of the aspirating probe, total temperature was calculated with the Euler turbine equation from the tangential velocities measured with the LFA system. Figure 8 shows the blade-to-blade total temperature contours for an average passage repeated three times. Because of the different circumferential measurement locations of the LFA system and aspirating probe, the blade wakes do not appear in exactly the same circumferential position in Figs. 8 and 7. However, the character of the temperature signatures is very similar. The wakes appear narrower in Fig. 8 due to the superior spatial resolution of the LFA system. The total temperature difference is approximately 3.3°C (6°F) from core flow to blade wake as compared to 5.0°C (9°F) for the two-wire results. Because the LFA data represent an average passage, the temperature increase in the wake could be attenuated in the averaging process by passage-to-passage flow nonuniformities in the rotor. The absolute levels of total temperature obtained with the aspirating probe and the Euler equation calculations do not match exactly. Absolute value differences like this are caused by aging of the hot wires, which causes a "DC" type shift in the temperatures and pressures calculated from the hot-wire voltages. The magnitude of the fluctuations, however, is not influenced by wire drift. Because pre- and post-calibrations were not done immediately preceding and following this aspirating probe data set, a standard combination probe P_T/T_T measurement at 30 percent span was used to help determine wire drift. All aspirating probe hot-wire voltages were corrected in post-processing so that the average of the two-wire P_T and T_T measurements at 30 percent span match the standard probe measurement at 30 percent span. The issue of calibration drift will be addressed in more detail in a following section.

The total pressure data measured with the improved aspirating probe can be compared with the pressure signature measured with the high-response Kiel probe as shown in Fig. 9. The blade wakes are shifted circumferentially because of different instrument measurement locations in Figs. 6 and 9. The character of the pressure signatures is similar but the pressure transducer shows a variation of only 6.9 kPa (1 psi) from core flow to wake while a 10.2 kPa (1.5 psi) variation is suggested by the aspirating probe. The pressure probe measures the pressure over a larger face area than the aspirating probe and this may account for some of the attenuation of the wake. The absolute level of pressure can also vary because of hot-wire aging.

The comparisons with independent instrumentation measurements confirm that the improved aspirating probe is responding adequately to pressure and temperature fluctuations with the two wire voltages only used for data reduction as originally intended. It is now informative to compare the results of earlier

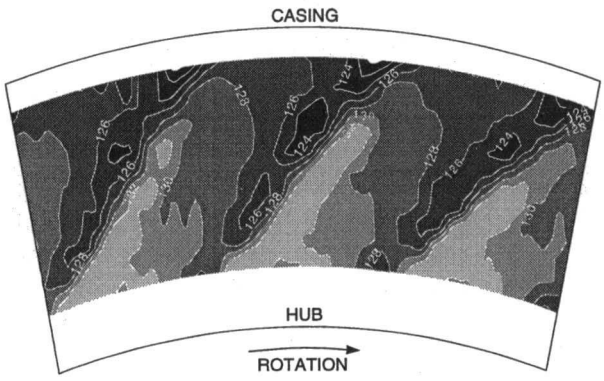

Fig. 6 Blade-to-blade view of total pressure (kPa) in three passages at station 3 calculated from the aspirating probe hw1 and hw2 voltages

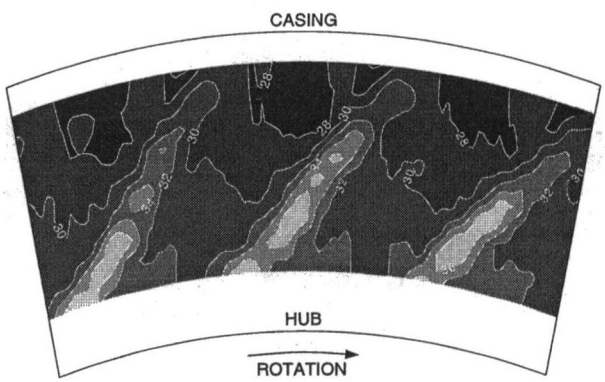

Fig. 7 Blade-to-blade view of total temperature (°C) in three passages at station 3 calculated from the aspirating probe hw1 and hw2 voltages

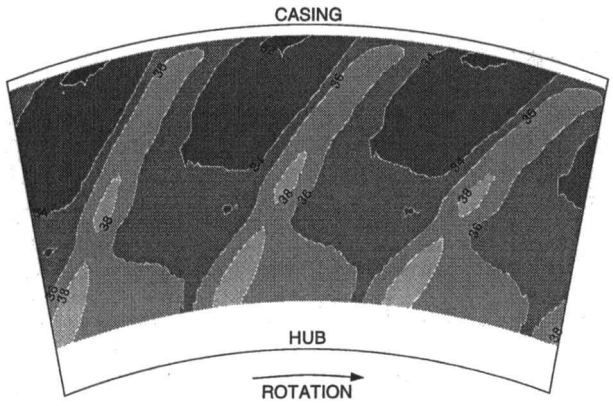

Fig. 8 Total temperature (°C) contours calculated from LFA velocities near station 3

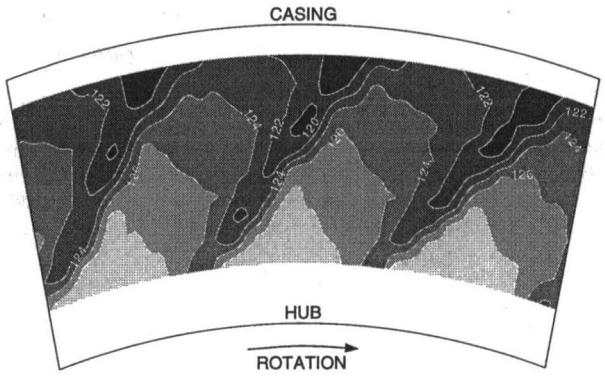

Fig. 10 Total pressure (kPa) contours at station 3 from the Kulite transducer mounted beside the aspirating probe

data reduction techniques with the results of the two-wire method.

One-Wire/Kulite-Based Results

Because of aspirating probe sensitivity problems, earlier data reduction methods used a total pressure measurement from a Kulite XCQ-062-25G pressure transducer mounted beside the aspirating probe and only one of the hot-wire voltages to calculate total temperature. Figures 10 and 11 show the total pressure measured with the Kulite transducer and total temperature field calculated from the Kulite pressure and hot wire 1 voltage.

The character of the pressure contours of Figs. 9 and 10 is similar; however, the absolute values of the pressures are different due to amplifier drift and aging of the semiconductor transducers. More frequent calibration of the transducers would have helped reduce these differences. The similarities indicate that the transducer mounted beside the aspirating probe is capturing the total pressure fluctuations and that blockage effects from the proximity of the aspirating probe are not significant for this flow case. While the total pressure measurement is reasonable as expected, the total temperature measurement using only one wire and a pressure transducer is less acceptable.

The total temperature contours of Fig. 11 do not have the well defined structure of those obtained with two wires shown in Fig. 7. The blade wake appears "washed out" in Fig. 11; the T_T rise in the wake is not as well defined. Figure 12 demonstrates this by showing a comparison of the blade wakes at 30 percent span as measured with two wires and with one-wire/Kulite. Both temperature signatures had their respective minimum values subtracted. For the one-wire/Kulite results the parameters of wake width and depth are not accurately represented. The two-wire results consistently show a prominent blade wake as anticipated from the LFA measurements. The width and depth of the wake are readily visible. The two-wire measurements are apparently more sensitive to the unsteady total temperature fluctuations and are thus better able to resolve the wake flow.

The total temperature field of Fig. 11 is strongly influenced by the total pressure value used to solve Eq. (8), by the time shift applied to bring the hot-wire response and Kulite response into phase with each other, and by the differing frequency response characteristics of the Kulite and the hot wire.

Past experience with data reduction using Kulite pressure and a single hot-wire voltage has shown that the resultant total temperature mimics trends in the total pressure signal. The pressure and temperature waveforms follow each other even when the pressure waveform is purposely shifted significantly out of phase with the hot wire signal before data reduction. Data reduction using the Kulite pressure assumes that the pressure signal measured by the Kulite and the pressure signal as calculated from the two wires are identical. Figures 6 and 10 show that the pressure signals are similar but not identical and thus the total temperature calculated by the two-wire and the one-wire/Kulite methods are not the same.

Because the Kulite transducer and aspirating probe are mounted side by side, the spatial separation of these instruments is likely to cause a time shift or lag between the signals. In previous applications the time lag had a negligible effect on the results (Alday et al., 1993). For the improved aspirating probe, the time lag between the Kulite signal and the hot-wire signal has a significant effect on the shape of the temperature waveform and on the magnitude of the temperature variations calculated. A cross correlation of the pressure waveform calculated using the two hot-wire voltages and the pressure waveform

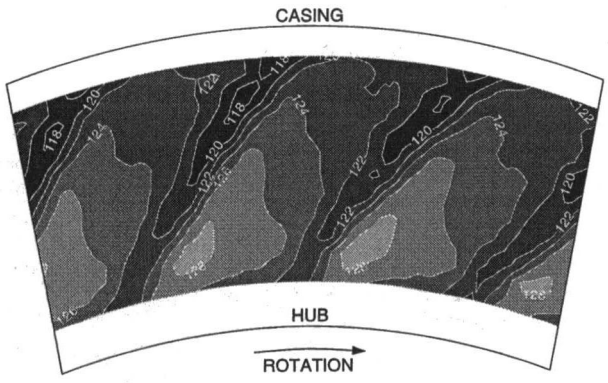

Fig. 9 Total pressure (kPa) contours at station 3 from the high-response Kiel probe

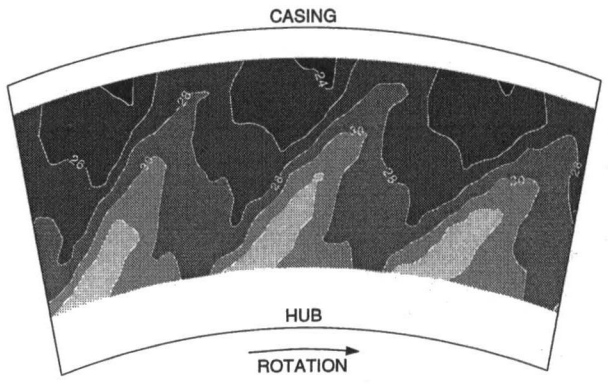

Fig. 11 Total temperature (°C) contours at station 3 calculated from the Kulite pressure and hot wire 1 voltage

measured with the adjacent Kulite transducer indicated a shift of +2 encoder counts for the Kulite signal relative to the hot wire signals. Thus the first data point of the Kulite signal was reduced with the third point of the hot-wire 2 signal to determine a total temperature. This shift is opposite of what is expected due to spatial separation indicating that there is a residence time in the aspirating probe associated with when a change occurs at the face of the probe to when it is sensed at the hot wire plane. Kotidis (1989) found a similar time lag in the signals due to convection time in the aspirating channel.

Well-tuned hot-wire anemometers have a frequency response of at least 60 kHz according to the manufacturer's specifications. The response of the aspirating probe is limited by the geometry of the aspirating channel. The frequency response of a slightly larger aspirating probe was found to be approximately 20 kHz (Kotidis, 1989). The frequency response of the current size probe has not been experimentally verified but should be at least 20 kHz also (Alday and Ng, 1991). The frequency response of the Kulite transducer is influenced by its mounting beside the aspirating probe in a sharp edged recess and the B-screen used to shield the transducer. The manufacturer claims no effect on dynamic response from the B-screen out to 20 kHz. For aerodynamic reasons several researchers expect the response to be less. If the Kulite transducer is not able to resolve the pressure fluctuation adequately though the wake, the total temperature calculated using the Kulite and one hot wire will be compromised. This total temperature signature does not adequately show the structure of the flowfield indicated by the two-wire results and the LFA based temperature calculations.

Total temperature data obtained with the Kulite pressure as an input value are inferior to the two-wire data. The lack of similarity of Fig. 11 compared with Figs. 7 and 8 supports this conclusion.

Remaining Limitations

Even with the improved sensitivity of the modified aspirating probe, some problems still exist with angle sensitivity, frequency response, and absolute value resolution.

The aspirating probe has a round lip entrance region to improve the acceptance angle range for off axis flows. The probe is insensitive to flow angles up to ±12.5° (Alday et al., 1993). The data presented in this paper were acquired far downstream of the rotor where flow angle changes between the core flow and wake flow are 5 to 6° according to LFA data. Just downstream of Rotor 37 the flow angle changes across the blade wakes are 30 to 40°. Because of the limited acceptance angle range of the aspirating probe, measurements in the more hostile flow region close to Rotor 37 must be interpreted carefully.

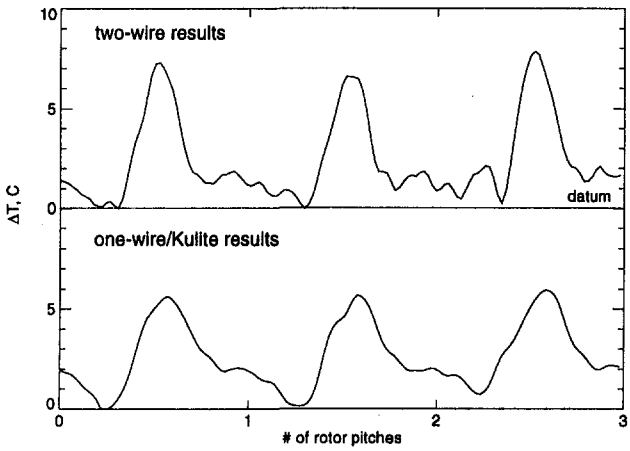

Fig. 12 Comparison of blade temperature wakes at 30 percent span

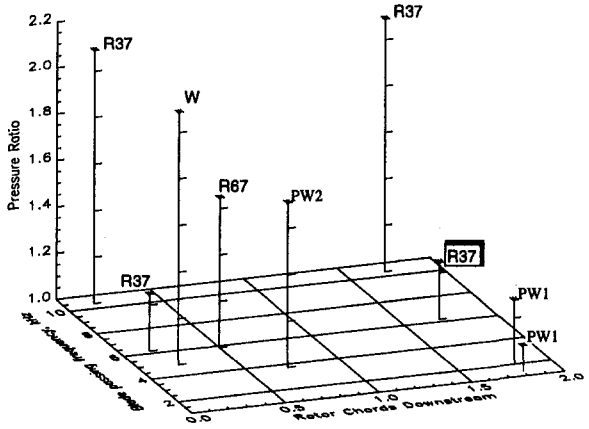

Fig. 13 Comparison of compressor operating conditions for past and present aspirating probe applications

For high-speed applications the frequency response of the aspirating probe may not be adequate to resolve unsteady flow phenomena. At 60 percent speed the blade passing frequency is 6.2 kHz, thus the aspirating probe can capture at least four harmonics. The design speed blade passing frequency is 10.3 kHz, of which the aspirating probe can capture only two harmonics. The LFA system data indicate narrow, well-defined triangular-shaped wakes downstream of Rotor 37. The spectral representation of such a waveform requires multiple harmonics and in some applications the aspirating probe may not have the frequency response to capture the necessary harmonics.

Figure 13 shows the flow regimes for past and present applications of the aspirating probe. PW1 and PW2 are Pratt and Whitney fans. W is a Wennerstrom high throughflow rotor tested in the MIT blowdown facility. R37 and R67 are NASA Rotors 37 and 67. The only total pressure and total temperature measurements obtained with only two wires were acquired downstream of Rotor 37 at part-speed operation, the compressor operating condition highlighted in the figure. The other measurements were made with an adjacent pressure probe and only one wire of the aspirating probe. Severe challenges remain in making reliable aspirating probe measurements in the aggressive flow regions close to the exit of high-pressure-ratio, high-speed rotors.

Because of calibration shifts due to aging of the hot wires, determining absolute values of pressure and temperature is still difficult. The smaller temperature coefficient of resistance of platinum–iridium wires makes them more susceptible to this problem than tungsten wires. Small changes in wire resistance will cause large changes in wire temperature. The only way to judge the drift of the wires is to do pre- and posttest calibrations of the probe to bracket the drift of pressure and temperature values after data acquisition. Hot-wire aging should not affect the magnitude of the pressure and temperature variations measured by the probe as much as the absolute level of the results.

Summary

The use of platinum–iridium wires in the aspirating probe has enabled the current researchers to achieve a large difference in the operating temperature of the two wires while simultaneously maintaining a large temperature difference between the wires and the flowfield temperature. These temperature characteristics were vital to the successful application of the two-wire technique to aspirating probe data reduction.

Since the aspirating probe calibration constants are functions of total temperature, a calibration must be done that characterizes the range of temperatures and pressures of interest for the experiment. This complete set of calibration information must

be incorporated into the data reduction procedure to achieve good results.

Use of the one-wire/Kulite data reduction technique has been required in previous investigations due to temperature limitations that arise when using tungsten hot wires. In the present investigation, unsteady pressure and temperature results were generated with the two-wire technique and compared to those calculated from the same set of measurements with the one-wire/Kulite technique. Comparisons between the two aspirating probe techniques, independent Kulite pressure measurements, and temperatures calculated from laser anemometer measurements indicate that the two-wire technique generates improved results relative to the one-wire/Kulite technique.

An additional benefit resulting from the success of the two-wire technique is that the Kulite pressure transducer, which has been piggy-backed onto the aspirating probe in both the present and previous investigations, is no longer required. Removal of the Kulite will result in a 50 percent reduction in the physical size of the aspirating probe head and the resulting flow blockage. Also, the problems associated with taking measurements in different meridional planes are eliminated.

The remaining limitations of the aspirating probe include angle sensitivity, frequency response, and absolute value resolution.

Acknowledgments

This work was done at the NASA Lewis Research Center under grant number NAG3-1302. We are grateful to Dr. Wing Ng for his useful suggestions and to Dr. David Davis for his help with hot-wire concerns.

References

Alday, J., and Ng, W., 1991, "The Correlation of Randomness With High Tip Losses in an Axial Flow Fan Stage," Master's thesis, Virginia Polytechnic Institute and State University, Blacksburg, VA.

Alday, J., Osborne, D. J., Morris, M. B., and Ng, W., 1993, "Flow Randomness and Tip Losses in Transonic Rotors," ASME Paper No. 93-GT-189.

Boeing Computer Services and United States Navy, 1992, Naval Surface Warfare Center, David Taylor Model Basin. *DT_NURBS Spline Geometry Subprogram Library User's Manual,* Oct.

Cherrett, M., and Bryce, J., 1991, "Unsteady Viscous Flow in a High Speed Core Compressor," ASME JOURNAL OF TURBOMACHINERY, Vol. 113, pp. 287–294.

Kotidis, P. A., 1989, "Unsteady Radial Transport in a Transonic Compressor Stage," Tech. Rep. GTL #199, Gas Turbine Laboratory, Massachusetts Institute of Technology, Sept.

Moore, R. D., and Reid, L., 1980, "Performance of Single-Stage Axial-Flow Transonic Compressor With Rotor and Stator Aspect Ratios of 1.19 and 1.26, Respectively, and With Design Pressure Ratio of 2.05," Tech. rep., NASA TP-1659.

Morris, M. B., Osborn, D. J., and Ng, W. F., 1992, "Flow Randomness and Tip Losses in Transonic Rotors," Tech. rep., Virginia Polytechnic Institute and State University, Mech. Engr. Dept., May.

Ng, W., 1983, "Time-Resolved Stagnation Temperature Measurement in a Transonic Compressor," PhD thesis, Massachusetts Institute of Technology, Cambridge, Oct.

Ng, W. F., and Epstein, A. H., 1983, "High-Frequency Temperature and Pressure Probe for Unsteady Compressible Flows," *Review of Scientific Instruments,* Dec., pp. 1678–1683.

Reid, L., and Moore, R. D., 1978, "Design and Overall Performance of Four Highly Loaded, High Speed Inlet Stages for an Advanced High-Pressure Ratio Core Compressor," Tech. rep., NASA TP-1337.

Smits, A., Hayakawa, K., and Muck, K., 1983, "Constant Temperature Hot-Wire Anemometer Practice in Supersonic Flows," *Experiments in Fluids,* pp. 83–92.

Van Zante, D. E., 1992, "Slow and Fast-Response Instrument Flowfield Measurements Downstream of a Transonic Axial-Flow Compressor Rotor," Master's thesis, Iowa State University.

Darryl E. Metzger Memorial Session Paper

Surface Heat Transfer From a Three-Pass Blade Cooling Passage Simulator

M. K. Chyu

V. Natarajan

Department of Mechanical Engineering,
Carnegie Mellon University,
Pittsburgh, PA 15213

Using an analogous mass transfer system based on naphthalene sublimation, the present research focuses on investigating the local heat transfer characteristics from three-pass smooth and turbulated blade cooling passages. To simulate the actual passage geometry, the test model is incorporated with trapezoidal cross sections including variable passage sizes. Measured local mass transfer results reveal strong evidence of velocity redistribution over the trapezoidal flow area. Elevated mass transfer always exists in the vicinity of a sharp turn. However, in the present study, one of the most notable mass transfer increases is perceived in the third pass, downstream to the second turn, where the flow area is reduced severely. Overall, the combined effects of the three-pass and two sharp turns virtually double the mass transfer as compared to its straight counterpart with fully developed, turbulent flow. With a pitch-to-height ratio equal to 10 and 90 deg orientation, the rib turbulators produce approximately an additional 30 percent of overall mass transfer enhancement in comparison to the smooth case. Locally, rib-induced enhancement varies with different surfaces and passes. The greatest enhancement lies on the first pass, about 40 percent; the other two passes are comparable, less than 20 percent.

Introduction

Cooling of turbine blades is often accomplished by bleeding a portion of compressor air into the blades internal passages before it is discharged into the mainstream. As shown in Fig. 1, the internal passage is generally in serpentine form and comprises multiple passes with sharp turns. Transport phenomena inherited in such a complex configuration represent one of the most challenging issues in design of gas turbines. Since the mid-1980s, many laboratory studies on blade cooling have employed either two-pass or, to a much lesser extent, three-pass channels with a uniform cross sections.

For the two-pass (one turn) configuration, Metzger and coworkers (1986, 1987, 1988), Boyle (1984), Han and Chandra (1987), and Chyu (1991) have performed a series of studies on flow visualizations, pressure measurements, and regional heat transfer for both smooth and rib-roughened channels. While these heat transfer studies are primarily experimental, numerical simulations using CFD techniques have revealed detailed transport features (Wang and Chyu, 1992). For the three-pass (two turns) configuration, Chyu (1991) and Han and Zhang (1991), employing the naphthalene sublimation technique with a heat-mass analogy, have investigated the heat transfer distribution in a square cross-sectioned channel. Further, using the liquid-crystal thermographic technique, Abuaf and Kercher (1994) examined the thermal performance of a three-pass turbine blade with one wall heated.

In reality, the blade geometry and shape are far from being straight and rectangular. To boost aerodynamic efficiency, blade airfoil is characterized by strong curvature. The shape of an internal passage usually has a nearly trapezoidal or triangular cross section with strong variation in aspect ratio. Such a geometric variation may induce substantial difference in both flow and heat transfer compared to those models with straight rectangular channels. It is thus the prime objective of the present study to discern the heat transfer in a channel geometry similar to that of actual blade cooling passages. Results obtained from this study will be compared with those of generic, rectangular-shaped models.

The passage geometry studied here, as sketched in Fig. 2, is a three-pass channel of trapezoidal cross section. The two sidewalls (also referred as the channel "top" and "bottom" walls; i.e., surfaces 2, 4, 9, and 10) for all cross sections are of a 10 deg inclination. Except for the first pass, the flow area exhibits a continuous linear variation along the flow direction. This is facilitated by a nominal, 3 deg inclination for the partitioned wall between the second and the third passes. Even with such an area variation, all three passes are designed to have an identical width (25.6 mm, approximately 1 in.) at the passage midspan; i.e., along the o-o' plane. In fact, the entire first pass and the second pass in streamwise average have the same hydraulic diameter of 25.6 mm, equal to the characteristic width aforementioned. For a given mean flow velocity, the amount of mass flow rate under these conditions, in essence, is equivalent to that of a 25.4 mm (1 in.) square duct used in a generic three-pass model by Chyu (1991). The hydraulic diameter for the third pass is considerably smaller, about 16.2 mm or 63 percent of that of the first two passes. The passage lengths for all passes are maintained the same at 152 mm, which is approximately six times the characteristic width. Connecting the three passes are two identical 180-deg sharp turns. Corners of both turns are rounded with the same radius of curvature at one-half the channel width measured at the midsection of the model.

To discern the transport features inherited in the complex system as described above, information is required concerning detailed local heat transfer distribution over the entire channel. Instead of using a wide range of Reynolds numbers typically for obtaining average Nu–Re correlation, the present local study is performed under a single Reynolds number at Re = 5.0 ×

Contributed by the International Gas Turbine Institute and presented at the 39th International Gas Turbine and Aeroengine Congress and Exposition, The Hague, The Netherlands, June 13–16, 1994. Manuscript received by the International Gas Turbine Institute February 15, 1994. Paper No. 94-GT-164. Associate Technical Editor: E. M. Greitzer.

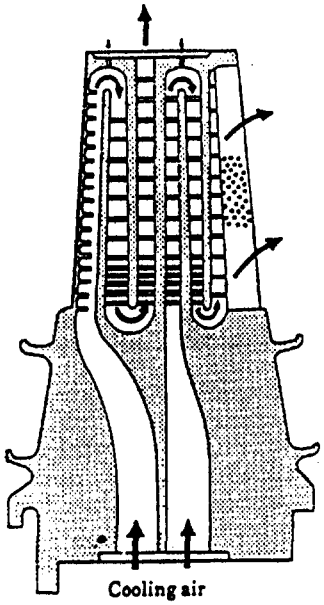

Fig. 1 Gas turbine blade

10^4. With this given Reynolds number, heat transfer enhancement by the surface-mounted rib turbulators is also investigated, and comparison is made with the smooth case without turbulators. As sketched in Fig. 2(*b*), a number of square ribs, made of 2-mm-sized balsa rod, are mounted on the two principal, i.e., the top (surfaces 2 and 9) and the bottom (surfaces 4 and 10) walls. All ribs are positioned at 90 deg relative to the mainstream of the straight section, and spaced uniformly with a pitch-to-height ratio (p/e) of 10. While modern blade designs often employ ribs oriented differently than in the present tests, the current 90 deg case serves as a baseline case for further studies.

Besides similarity in passage shape, another important feature addressed in this study is the accurate simulation of the thermal condition on the passage walls. In reality, because the blade material is highly conductive, all wetted surfaces including both principal walls and partitioning walls are virtually isothermal. Nevertheless, these are not the boundary conditions used by most of the previous studies, wherein typically only one, certainly not all, of the surfaces is heated. With these objectives in mind, it appears that conventional thermal methods are unsuitable, since maintaining perfect isothermal condition as well as local insulation can be very difficult, if not impossible. The present study chooses an analogous mass transfer system based on the naphthalene sublimation (Eckert, 1976). To obtain highly accurate, point-resolved, local mass transfer data, the experiment uses an automated, computer-controlled measurement system to obtain the naphthalene sublimation depth during a data run (Goldstein et al., 1985; Chyu and Wu, 1989).

Data Reduction and Heat-Mass Transfer Analogy

The heat transfer coefficient in the present study is defined as

$$h = q/(T_w - T_{in}) \tag{1}$$

Correspondingly, the mass transfer coefficient is given by

$$h_m = m/(\rho_{v,w} - \rho_{in}) \tag{2}$$

Note that the reference temperature, T_{in}, in Eq. (1) is different from that for the conventional duct flow, where the bulk temperature is often used. The choice is made based on the fact that bulk temperature is difficult to evaluate in a flow system dominated by turning and recirculation, such as the present one.

Analogy between Eqs. (1) and (2) implies that $(T_w - T_{in})$ and q in heat transfer are equivalent to $(\rho_{v,w} - \rho_{in})$ and m in mass transfer. Due to the nonexistent naphthalene concentration at the passage inlet, the naphthalene vapor concentration at the inlet, ρ_{in}, is zero, and Eq. (2) reduces to

$$h_m = m/\rho_{v,w} \tag{3}$$

Moreover, as the mass transfer system is essentially isothermal, the naphthalene vapor pressure and vapor concentration at the wall are constant. This is equivalent to a constant wall boundary condition in a heat transfer study. As a result, the magnitude of the local heat or mass transfer coefficient, as presently defined in Eqs. (1) and (2), is directly proportional to that of the local heat or mass flux.

Local mass transfer from a naphthalene plate can be evaluated from the change of surface elevation, which is equivalent to the change in naphthalene thickness. The change of elevation or thickness due to sublimation is given by

$$dy = m\, dt/\rho_s \tag{4}$$

where ρ_s is the density of solid naphthalene. Note that dy and m are functions of local coordinates of the mass transfer active surface. Combining Eqs. (3) and (4) and integrating over the test duration yields

$$h_m = (\rho_s \Delta y)/(\rho_{v,w} \Delta t) \tag{5}$$

The mass transfer Stanton number is defined by

$$\mathrm{St} = h_m/U \tag{6}$$

If, as is often the case, the wall temperature varies slightly during the test run, $\rho_{v,w}$ can be represented by the time-averaged naphthalene concentrations at the surface. This is obtained from numerical integration of the concentrations determined at the measured surface

Nomenclature

D_h = mean hydraulic diameter for passes 1 and 2
h = heat transfer coefficient, Eq. (1)
h_m = naphthalene mass transfer coefficient, Eq. (2)
L = length of pass
m = mass transfer flux of naphthalene from surface
Pr = Prandtl number
q = heat flux from wall
Re = Reynolds number, based on hydraulic diameter and mean velocity at inlet
Sc = naphthalene–air Schmidt number = 1.9
St = naphthalene mass transfer Stanton number = h_m/U
St_o = naphthalene mass transfer Stanton number in turbulent fully developed duct flow, Eq. (7)
T_w = wall temperature
T_{in} = channel inlet temperature
t = time
U = mean velocity of the first pass
x, y, z = coordinate system, see Fig. 2
$x1$ = local coordinate system for second pass, with origin at upstream corner of second turn, see Fig. 4
Δ = finite difference operator
$\rho_{v,w}$ = vapor mass concentration or density of naphthalene at wall
ρ_{in} = vapor mass concentration or density of naphthalene at duct inlet, zero in the present study
ρ_s = density of solid naphthalene

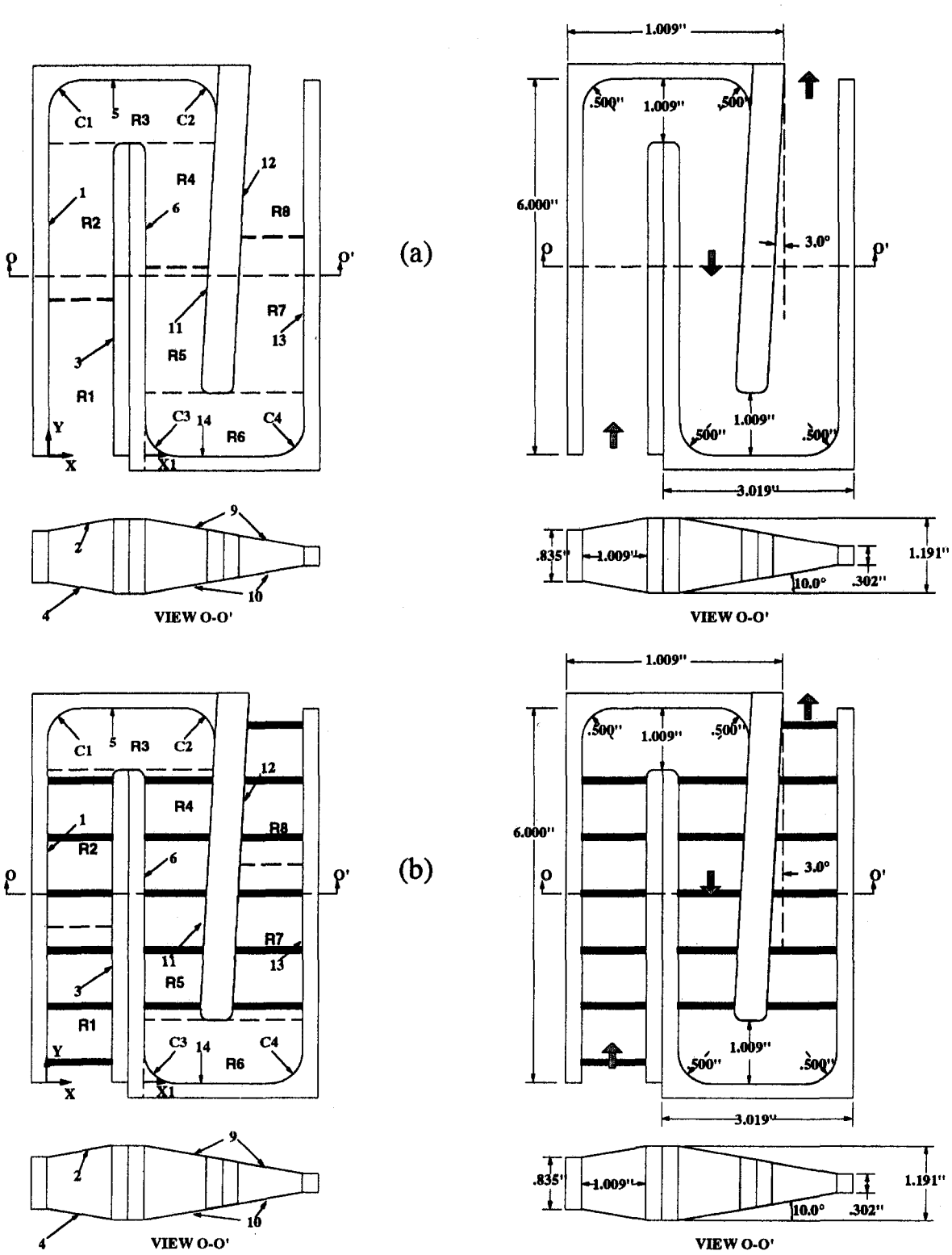

(i) Coordinate System and Partition into regions

(ii) Dimensions of passages

Fig. 2 Test geometry: (*a*) smooth channel; (*b*) ribbed channel

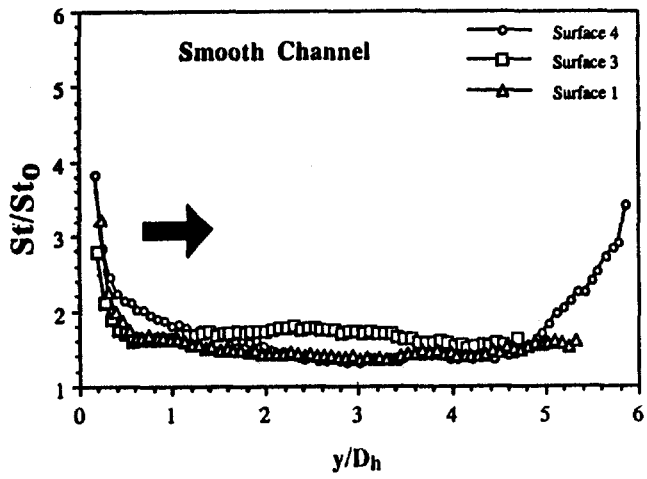

(a) Smooth case

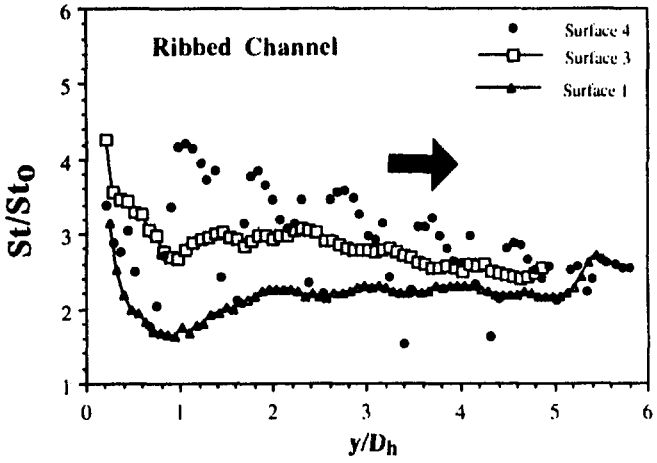

(b) Ribbed case

Fig. 3 Local mass transfer distributions in pass 1

temperature. A correlation, in the form of a third-degree Chebyshev polynomial interpolation, proposed by Ambrose et al. (1975), is used to determine naphthalene vapor pressure. From this, $\rho_{v,w}$ is evaluated using the ideal gas law and the wall temperature.

Experimental Procedure

Schematics of the test geometries are given in Figs. 2(*a, b*), for the smooth and ribbed channel, respectively. As illustrated, the test channel is comprised of 14 separate segments, including 12 flat plates and 2 corner plates, all made of aluminum. Each of the surfaces is individually cast and coated with naphthalene. They are then left in plastic wrappings overnight to enable the naphthalene surface to attain thermal equilibrium with the surrounding atmosphere. The experimental laboratory is well air-conditioned to prevent any distortion in the room temperature during a test run.

The experiment starts with a reference measurement of surface profile for each of the naphthalene coated plates. Such a measurement is performed using a computer-controlled, data acquisition system exclusively designed for acquiring local subliming rate from a planar surface (Goldstein et al., 1985; Chyu and Wu, 1989). Typical spacings between adjacent measurement locations are 1.5 mm (0.06 in.) and 2.3 mm (0.09 in.) along the spanwise and streamwise directions, respectively. This implies that approximately 1100 data points are collected for each of the surfaces in the straight section of the channel. The total number of local data points is more than 14,000. After the measurement, the plates are assembled to form the three-pass channel, which is connected to an in-house compressor line. The naphthalene-coated surfaces are exposed to the free-stream air for a period of about 30 minutes, after which the setup is disassembled and the surface profiles are measured again and the local sublimation rate is determined.

To further ensure the quality of the local data, all the individual plate constituents are weighed on a high-precision electronic balance with an accuracy of a microgram (10^{-6} g) both prior to and just after the air exposure. Average mass transfer between the integrated local data and weighed results agrees within 4 percent. Besides validating the local measurement system, the weighing technique also provides a means to determine the mass transfer from the rounded-corner regions, where surface curvature prohibits a sensible pointwise measurement. This is done by subtracting the mass transfer rate from the flat section (surfaces 5 and 14), based on the integrated local data, from that of the overall weighed results of the corner specimen.

Results and Discussion

As a rational measure of heat transfer enhancement relative to a straight channel, the mass transfer results are presented as St/St_o, where St represents the spanwise-averaged, streamwise-resolved mass transfer Stanton number, and St_o represents the Stanton number in a fully developed turbulent duct flow based on the Dittus–Boelter correlation (Kays, 1986):

$$St_o = 0.023\ Sc^{-0.6}\ Re^{-0.2} \tag{7}$$

Another intent to normalize the Stanton number is to diminish the dependency on the Schmidt number, hence the value of St/St_o from the present mass transfer study is virtually equal to that of heat transfer. Note that the terms "streamwise" and "spanwise" are chosen in accordance with the primary flow direction over a specific surface or region of interest. Along the straight section of all passes (in Fig. 2), the streamwise direction is the y axis, and the spanwise direction is either the x or the z axis, depending on the surface orientation. In the turning region, the streamwise direction becomes the x axis, and the spanwise direction is the y axis for the top and bottom surfaces (2, 4, 9, and 10), and z axis for the side surfaces (5 and 14).

Figures 3–6 present streamwise St/St_o distributions along the dimensionless coordinate (x/D_h or y/D_h). Due to symmetry, only the results of surfaces 4 and 10 are presented. In the actual measurement, however, the entire set of surfaces are measured

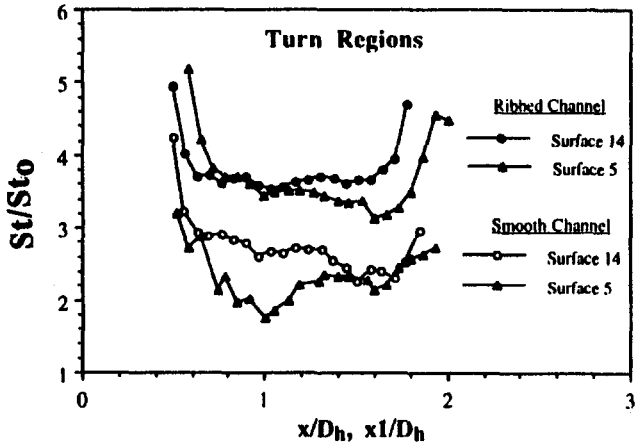

Fig. 4 Local mass transfer distributions in turn regions

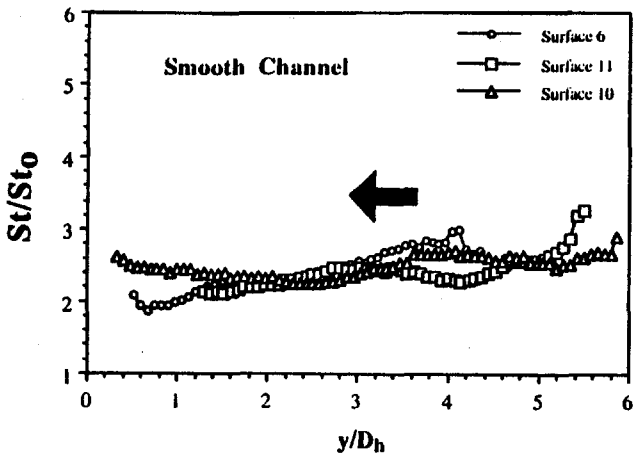

(a) Smooth case

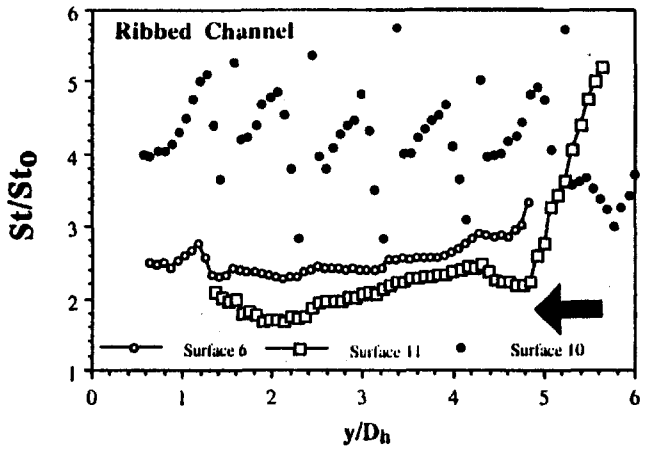

(b) Ribbed case

Fig. 5 Local mass transfer distributions in pass 2

and nearly identical results are obtained between symmetric surfaces (2, 4) and (9, 10). Each of these figures consists of two sub-figures, (*a*) and (*b*), for the smooth case and the corresponding ribbed case, respectively. Figure 7 shows the average mass transfer from the different regions of the channel. The entire channel is divided into eight regions labeled *R*1 to *R*8, as shown in Fig. 2.

For the smooth channel, the mass transfer coefficient in the first pass, shown in Fig. 3(*a*), displays a developing characteristic with very high values of St/St_o near the duct entrance, and levels off further downstream. The mass transfer on surface 4, however, rises again when $y/D_h > 5$, due to the turn effect. Because of the velocity-profile redistribution with its center (or maximum) shifted toward the wider side of the trapezoidal channel, surface 3 reveals a relatively higher (about 20 percent), mass transfer than other participating walls. A similar trend has been reported by Metzger et al. (1987) in a triangular channel, which represents the limiting case of the current trapezoidal geometry.

A comparison of Figs. 3(*b*) and 3(*a*) reveals the significance of rib-induced mass (heat) transfer augmentation. One striking observation is that the ribs promote stronger transport nonuniformity, as the levels of difference in the local St/St_o among all the participating surfaces widen substantially. However, the magnitudes of St/St_o on the average are comparable between surfaces 3 and 4 (~2.8) and are higher than that of surface 1 (~2.1). Although surface 4, on which the ribs are mounted, has the greatest enhancement effect overall (~80 percent for $x/D_h \leq 5$), other participating surfaces also display significant increase in mass transfer as compared to the smooth case. The increases are approximately 40 percent for surface 1 and 65 percent for surface 3. Such a broad effect suggests that the presence of ribs significantly alters the nature of the core flow in the channel with more effective mixing. Locally, the ribs produce a wavy, periodic pattern in St/St_o on surface 4. This is typical for boundary layers separated over a transverse rib and reattached near the midpitch between two adjacent ribs. To a much lesser extent, this wavy pattern also exists in the local mass transfer distribution on other smooth surfaces (1 and 3) near the corner junction with the ribbed surface 4.

Figure 4 shows the streamwise distribution of St/St_o over the surfaces of the first turning region (*R*3, see Fig. 2). According to several recent studies (Cheng et al., 1992; Wang and Chyu, 1992), flow features around a sharp, 180-deg turn are dominated by the form-induced flow separation and reattachment in conjunction with the Dean-type secondary flowfield. The collective results shown in Fig. 3 (surface 1, $y/D_h \geq 5$), Fig. 4 (surface 5), and Fig. 5 (surface 11, $y/D_h \geq 5$) suggest that local mass transfer enhancement within the turn is largely attributable to

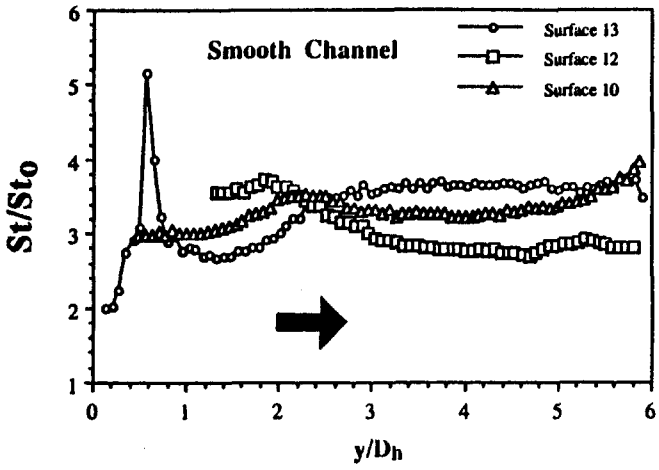

(a) Smooth case

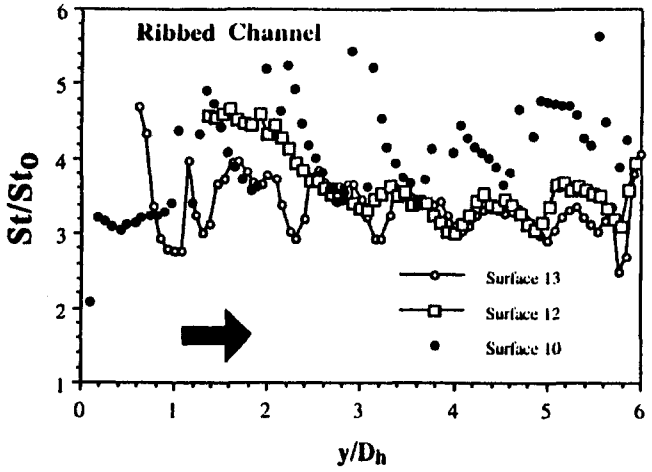

(b) Ribbed case

Fig. 6 Local mass transfer distributions in pass 3

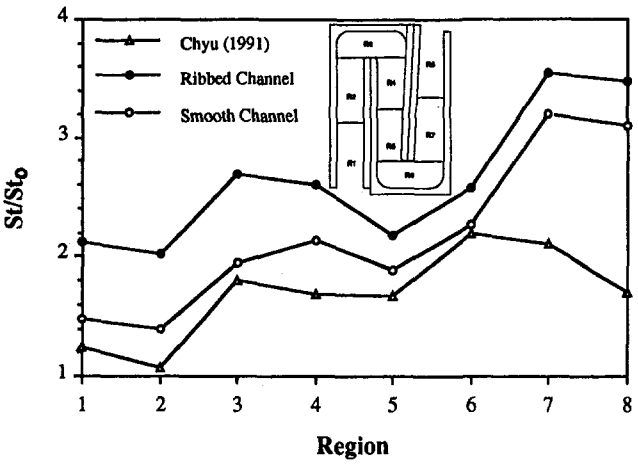

Fig. 7 Regional averaged mass transfer

flow impingement as the flow bulk fails to negotiate with the sharp turn. While there are no ribs installed at the turn, the presence of ribs in the preturn regions induces a nearly 60 percent mass transfer enhancement at the turn over its smooth counterpart. Despite such a difference in magnitude, St/St_o over surface 5 displays a similar trend for both smooth and ribbed cases.

Downstream of the first turn, the flow characteristics in the second pass are further complicated by the streamwise tapering of the passage cross section. For the smooth channel, mass transfer on all the participating surfaces (6, 10, and 11) shows a similar distribution and magnitude, as presented in Fig. 5(a). The average value of St/St_o over each surface area is about the same at 2.4. The postturn flow feature apparently exhibits a strong mixing, which surpasses other factors responsible for local nonuniformity. However, this is not the case for the ribbed channel. As shown in Fig. 5(b), the mass transfer on the rib-mounted wall (surface 10) not only shows obvious periodicity but also has much elevated values in St/St_o, about 60 percent higher than the smooth case. For surface 6, which is the first partitioned wall and widest side of the passage cross section, the rib enhancement on the mass transfer is rather marginal, about 6 percent on average. For surface 11, the second partitioned wall with inclination, the presence of ribs inhibits the mass transfer, particularly in the vicinity of the first turn. Using a square duct of uniform cross section, Han and Zhang (1991) have reported that the mass transfer in the second pass is strongly influenced by the secondary flow with its nature varying with the rib angle. The secondary flow associated with the present 90 deg rib orientation may be unfavorable from the standpoint of convective enhancement in the region. Another factor hindering the mass transfer from surface 11 may be rib-blockage related. Since the ribs block nearly 20 percent of the flow passage near the corner junction between surfaces 10 and 11, the excessive flow resistance may deplete flow out of the region and lower the transfer coefficient.

The St/St_o distribution over the second turn is collectively shown in Fig. 4 (surface 14) and Fig. 5 (surfaces 6 and 10, $y/D_h < 1$). It displays considerable similarity with that of its first-turn counterpart. This is evidenced by a comparison between surfaces 5 and 14 shown in Fig. 4. The sharp rises in mass transfer on these surfaces are largely caused by flow impingement as flow exits from the straight section of the passage and turns around 180 deg. Despite the similarity, some differences between the two turns are noted. Compared to the smooth channel case, the rib-induced mass transfer enhancement is approximately 40 percent for surface 14, and about 60 percent for surface 5 in the first turn. In addition, for the smooth case, the mass transfer on the outer wall of the pre-turn region is much lower for the second turn (Fig. 5(a), surface 6, $y/D_h < 1$) than for the first turn (Fig. 3(a), surface 1, $y/D_h > 5$). Although the actual causes need to be explored further, the combined effects of redistributed momentum in a trapezoidal-shaped passage and the channel tapering are partially responsible for such a phenomenon. Note that surface 1 is the narrowest side of the trapezoidal cross section in pass 1, while surface 6, on the contrary, is the widest side of a converging channel in pass 2. Hence the transport features in the vicinity of these surfaces are expected to be distinctly different. Possibly due to the overwhelming presence of the ribs, the aforementioned phenomenon is absent for the case of ribbed channel. The corresponding values of St/St_o between two turns are quite comparable.

Convective transport in the third pass is significantly affected by the reduced flow area—only 40 percent of that in the first two passes. The flow area is further reduced in the case of ribbed channel. Note that the two ribs, mounted in-line on the top and the bottom walls, combined block over 60 percent of the flow area near surface 13, resulting in the narrowest section of the entire passage model. As illustrated in Fig. 6(b), such an effect is evident as the profiles of St/St_o for all the participating surfaces show a periodic pattern with the ribs' pitch. Despite the scattered local data, the area-averaged values of St/St_o for all the constituent surfaces are quite comparable, about 3.7 for surfaces 10 and 12, and 3.4 for surface 13. For the smooth case, shown in Fig. 6(a), the straight section ($y/D_h > 1$) of all the participating surfaces reveals more or less constant, but consistently high, values in St/St_o. As a combined effect of the postturn recirculation in its vicinity and potential relaminarization associated with the duct convergence, surface 12 exhibits relatively lower mass transfer than the other two surfaces (10 and 13), by about 10 percent. The area-averaged St/St_o is 3.3, 3.0, and 3.3 for surfaces 10, 12, and 13, respectively. Hence the rib enhancement in the third pass is relatively mild as compared to the first pass and comparable to the second pass.

Region-Averaged Mass Transfer. Figure 7 gives the area-averaged mass transfer enhancement for the different regions of the three-pass model. The entire model is divided into eight regions as labeled in Fig. 2. The general trend is that mass transfer increases near the turning region, with the most significant increase located either at the turn or in the postturn region. For the smooth case, such a turn-induced enhancement over the entire three-pass model results in an average St/St_o about 2.1. In addition, consistent rib enhancement over the corresponding smooth case prevails over the entire passage. The overall average enhancement is about 28 percent. Among the three passes, the greatest rib enhancement lies on the first pass, about 40 percent, and is comparable for the second pass and the third pass, less than 20 percent.

For comparison, also plotted in Fig. 7 are the data extrapolated from a generic study for a smooth, three-pass model with a constant cross section and $L/D_h = 8$ (Chyu, 1991). Despite the differences in test geometries, the overall trends in the regional average St/St_o for the two smooth cases show excellent agreement for the first six regions. Further, corresponding values of the local St/St_o are agreeable within 20 percent. This highlights an important realization that although the effect of trapezoidal tapering in the geometry has a profound effect on the local mass transfer, the corresponding effect on surface-averaged mass transfer is rather moderate. Such an observation is, however, valid only for the first six regions without severe reduction in flow area. For regions seven and eight in the third pass, the mass transfer Stanton numbers are very high in the present tests; with as much as 100 percent increase compared to the square channel (Chyu, 1991).

Concluding Remarks

The local heat transfer characteristic in a three-pass, blade cooling passage has been investigated using an analogous mass

transfer system based on the naphthalene sublimation. One unique feature is that the design of the present test model is to simulate actual passage geometry with trapezoidal cross sections and area variation in the streamwise direction. A surface profile measurement system, automated by microcomputer control, is proven to be very effective in resolving phenomena requiring a large number of local data points.

The presence of two sharp turns produces more than a twofold overall heat transfer as compared to its straight counterpart. Locally, heat transfer is high at both the turn and postturn regions. For the present channel configuration, very high heat transfer prevails in the third pass where the flow area is reduced to nearly 40 percent of its upstream passages. A comparison with existing data from a generic study based on a square duct implies that a trapezoidal cross section has little effect on the overall heat transfer. However, due to velocity redistribution over the asymmetric flow area, the local effects are quite substantial.

Mounting transverse ribs on two of the principal walls generally changes the nature of the core flow. As a result, heat transfer enhanced by the rib turbulators prevails for virtually all the wetted surfaces. However, such an enhancement is often hindered by much reduced flow area blocked by the ribs. In the present configuration, the overall rib-induced enhancement is about 28 percent.

Acknowledgment

With a funding provided by Textron-Lycoming Corp., this work was initiated by the first author (MKC) during his tenure at Arizona State University (ASU). He would like to express his deepest appreciation of the late Professor Darryl E. Metzger at ASU for his encouragement and assistance during this study.

References

Abuaf, N., and Kercher, D. M., 1994, "Heat Transfer and Turbulence in a Turbulated Blade Cooling Circuit," ASME JOURNAL OF TURBOMACHINERY, Vol. 116, pp. 168–177.

Ambrose, D., Lawrence, I. J., and Sprake, C. H. S., 1975, "The Vapor Pressure of Naphthalene," *J. Chem. Thermo.*, pp. 1173–1176.

Boyle, R. J., 1984, "Heat Transfer in Serpentine Passages With Turbulence Promoters," ASME Paper No. 84-HT-24.

Cheng, K. C., Shi, L., Kurokawa, M., and Chyu, M. K., 1992, "Visualization of Flow Patterns in a 180-Degree Sharp Turn of a Square Duct," presented at the Fourth Intl. Symp. on Transport Phenomena and Dynamics of Rotating Machinery, Honolulu, HI.

Chyu, M. K., and Wu, L. X., 1989, "Combined Effects of Rib Angle-of-Attack and Pitch-to-Height Ratio on Mass Transfer From a Ribbed Surface," *J. Exp. Heat Transfer,* Vol. 2, No. 4, pp. 291–308.

Chyu, M. K., 1991, "Regional Heat Transfer and Pressure Drop in Two-Pass and Three-Pass Flow Passages With 180-Degree Sharp Turns," ASME *Journal of Heat Transfer,* Vol. 113, pp. 63–70.

Eckert, E. R. G., 1976, "Analogies to Heat Transfer Processes," in: *Measurements in Heat Transfer,* E. R. G. Eckert and R. J. Goldstein, eds., Hemisphere Publishers, New York.

Fan, C. S., and Metzger, D. E., 1987, "Effects of Channel Aspect Ratio on Heat Transfer in Rectangular Passage Sharp 180-deg Turns," ASME Paper No. 87-GT-113.

Goldstein, R. J., Chyu, M. K., and Hain, R. C., 1985, "Measurement of Local Mass Transfer in the Region of the Base of a Protruding Cylinder With a Computer-Controlled Data Acquisition System," *Int. J. Heat Mass Transfer,* Vol. 28, pp. 977–985.

Han, J. C., and Chandra, P. R., 1987, "Local Heat/Mass Transfer and Pressure Drop in a Two-Pass Rib-Roughened Channel for Turbine Airfoil Cooling," NASA CR-17963; AVSCOM-TR-87-C-14.

Han, J. C., and Zhang, P., 1991, "Effect of Rib-Angle Orientation on Local Mass Transfer Distribution in Three-Pass Rib-Roughened Channel," ASME JOURNAL OF TURBOMACHINERY, Vol. 113, pp. 123–130.

Kays, W. M., 1986, *Convective Heat and Mass Transfer,* McGraw-Hill, New York.

Metzger, D. E., and Sahm, M. K., 1986, "Heat Transfer Around Sharp 180-Degree Turns in Smooth Rectangular Channels," ASME *Journal of Heat Transfer,* Vol. 108, pp. 500–506.

Metzger, D. E., Veduls, R. P., and Breen, D. D., 1987, "Effect of Rib Angle and Length on Convection Heat Transfer in Rib-Roughened Triangular Ducts," *Exp. Heat Transfer,* Vol. 1, pp. 31–44.

Metzger, D. E., Fan, C. S., and Plevich, C. W., 1988, "Effects of Transverse Rib-Roughness on Heat Transfer and Pressure Losses in Rectangular Ducts With Sharp 180 degree Turns," presented at the AIAA 26th Aerospace Sciences Meeting.

Wang, T. S., and Chyu, M. K., 1992, "Effects of Turning Configuration on Flow and Heat Transfer in Blade Internal Cooling Passage," presented at the Int. Symp. on Heat Transfer in Turbomachinery, Athens, Aug. 24–28.

Darryl E. Metzger Memorial Session Paper

The Influence of Secondary Flows Near the Endwall and Boundary Layer Disturbance on Convective Transport From a Turbine Blade

R. J. Goldstein

H. P. Wang

M. Y. Jabbari

Department of Mechanical Engineering,
University of Minnesota,
Minneapolis, MN 55455

A naphthalene sublimation technique is used to investigate convective transport from a simulated turbine blade in a stationary linear cascade. In some of the tests undertaken, a trip wire is stretched along the span of the blade near the leading edge. The disturbance produced by tripping the boundary layers on the blade near the leading edge causes early boundary layer transition, creates high mass transfer rate on the pressure side and in the laminar flow region on the suction side, but lowers the transfer rate in the turbulent flow region on the suction side. Comparison is made with other heat and mass transfer studies in the two-dimensional region far from the endwall and good agreement is found. Near the endwall, flow visualization indicates a strong secondary flow pattern. The impact of vortices initiated near the endwall on the laminar–turbulent transition extends three-dimensional effects to about 0.8 chord lengths on the suction side and to about 0.2 chord lengths on the pressure side away from the endwall. The effect of the passage vortex and the new vortex induced by the passage vortex on mass transfer is clearly seen and can be traced along the suction surface of the blade. Close to the endwall the highest mass transfer rate on the suction surface is not found near the leading edge. It occurs at about 27 percent of the curvilinear distance from the stagnation line to the trailing edge where a strong main flow and the secondary passage flow from the pressure side of the adjacent blade interact. The influences of some small but very intense corner vortices and the passage vortex on mass transfer are also observed on both surfaces of the blade.

1 Introduction

High performance and greater endurance of an aircraft gas turbine engine generally require the conflicting goals of higher turbine inlet gas temperature and moderate blade temperature and temperature gradients. To optimize these contrasting requirements, the heat transfer coefficient along the blade must be moderated and controlled. The heat transfer to turbine blades is influenced by a variety of parameters, including Reynolds numbers, incoming flow disturbance, secondary flows, boundary layer transition, curvature, unsteady wakes, and the interactions among these parameters. A substantial discussion of basic transport mechanisms and the prediction of thermal loads in aircraft gas turbines has been given by Graham (1990). A detailed understanding of the heat transfer from a hot gas to blade surfaces is required in the durability analysis of turbine blades.

A comprehensive review of the structure of secondary flows in turbine cascades has been given by Sieverding (1985). Some experimental information about secondary flow from visualization studies is provided by Marchal and Sieverding (1976), Sonoda (1985), Hazarika et al. (1986), Goldstein and Spores (1988), Langston (1990), Joslyn and Dring (1992), Schulz et al. (1990), and Jabbari et al. (1992). The influence of high free-stream turbulence on turbine blade heat transfer and on the laminar–turbulent transition have been reported experimentally for the two-dimensional region away from the endwall by Bayley and Priddy (1981), Krishnamoorthy (1982), Arts and Graham (1985), and Wittig et al. (1985). Recently Gregory-Smith and Cleak (1992) investigated the effects of inlet turbulence on heat transfer close to the endwall.

In the present study a naphthalene sublimation technique, which eliminates the effect of conduction inside a solid material and permits detailed local measurements, is employed to investigate the mass transfer from a simulated turbine blade including the influence of disturbances, boundary layer transition, secondary flows and the interactions among these parameters. Early local mass transfer investigations have been reported by Goldstein and Spores (1988) on the endwall in a cascade and Chen and Goldstein (1992) on the suction surface of a blade and part of the pressure surface. The present work provides a more complete picture of mass transfer from the blade in the same cascade both in two-dimensional and three-dimensional flow regions. Comparison is made with earlier heat and mass transfer experiments and good agreement has been achieved. The convective transport flows can be inferred from the local mass transfer results combined with the flow visualization results.

2 Naphthalene Mass Transfer

The parameter in naphthalene sublimation mass transfer corresponding to a local heat transfer coefficient is the local mass transfer coefficient,

Contributed by the International Gas Turbine Institute and presented at the 39th International Gas Turbine and Aeroengine Congress and Exposition, The Hague, The Netherlands, June 13–16, 1994. Manuscript received by the International Gas Turbine Institute February 15, 1994. Paper No. 94-GT-165. Associate Technical Editor: E. M. Greitzer.

$$h_m = \frac{\dot{m}}{\rho_{v,w} - \rho_{v,\infty}} \tag{1}$$

where $\dot{m}$ is the mass transfer rate per unit area. In a steady-state naphthalene sublimation experiment a thin layer (~0.06 mm) of solid naphthalene will sublime during a moderate time period ($\Delta\tau$), when the naphthalene-coated blade is exposed to an air flow in a wind tunnel. Thus,

$$\dot{m} = \frac{\rho_s \Delta t}{\Delta\tau} \tag{2}$$

where Δt is the thickness change due to naphthalene sublimation. The density of naphthalene vapor in the free-stream $\rho_{v,\infty}$ is usually equal to zero because the wind tunnel is open to vapor-free air. The vapor density at the wall $\rho_{v,w}$ can be evaluated from the vapor pressure $P_{v,w}$ of naphthalene (a function of temperature) using the ideal gas law. So the local mass transfer coefficient can be expressed in the form,

$$h_m = \frac{\rho_s \Delta t}{(P_{v,w}/RT_w)\Delta\tau} \tag{3}$$

Since $P_{v,w}$ (and therefore $\rho_{v,w}$) is very sensitive to temperature, it is important to limit the variation of the mainstream temperature, which would directly affect the surface temperature of naphthalene. An empirical equation, recommended by Ambrose et al. (1975) is employed to obtain the vapor pressure.

Sherwood (Sh) and mass transfer Stanton (St_m) numbers are two commonly used dimensionless mass transfer coefficients,

$$\mathrm{Sh} = \frac{h_m C}{D} \tag{4}$$

$$\mathrm{St}_m = \frac{h_m}{U_{in}} = \frac{\mathrm{Sh}}{\mathrm{Re}_{in}\mathrm{Sc}} \tag{5}$$

where D is the diffusion coefficient of naphthalene in air; its value is a function of temperature and total static pressure. A detailed discussion on this coefficient can be found in a study by Chen (1988).

An analogy between heat and mass transfer is employed in this study to compare the naphthalene sublimation measurements with the results from direct heat transfer experiments. A discussion on this analogy was given by Eckert (1976). A local heat transfer coefficient in a low-speed flow is usually defined as

$$h = \frac{q}{T_w - T_\infty} \tag{6}$$

In naphthalene sublimation mass transfer, the vapor pressure at the wall $P_{v,w}$ is usually constant because the naphthalene surface is maintained at a constant temperature. According to the analogy, the results from naphthalene sublimation measurements can be compared to heat transfer from a surface with a constant wall temperature if Schmidt number and Prandtl number are equal. When they are not, empirical equations are commonly used to correlate the analogy, which can be expressed, for heat transfer, as

$$\mathrm{Nu} = C\,\mathrm{Re}^p\,\mathrm{Pr}^n \tag{7}$$

A corresponding equation can be obtained for mass transfer,

$$\mathrm{Sh} = C\,\mathrm{Re}^p\,\mathrm{Sc}^n \tag{8}$$

If Reynolds numbers are identical for both cases, these two equations can be combined in a form of ratio

$$\frac{\mathrm{Nu}}{\mathrm{Sh}} = \left(\frac{\mathrm{Pr}}{\mathrm{Sc}}\right)^n \tag{9}$$

If the heat and mass transfer Stanton numbers are used, the ratio will be

$$\frac{\mathrm{St}}{\mathrm{St}_m} = \left(\frac{\mathrm{Pr}}{\mathrm{Sc}}\right)^{n-1} \tag{10}$$

where n is usually taken to be $\frac{1}{3}$ to 0.4, depending on the different flow regimes. In the present study, $\frac{1}{3}$ is adopted for comparison.

Nomenclature

C = chord length of blade = 0.1691 m in present study; constant, defined in Eqs. (7) and (8)
C_p = specific heat of air
D = diffusion coefficient of naphthalene in air
F = local similarity function = $F(x, \eta)$
h = heat transfer coefficient
h_m = mass transfer coefficient
k = conductivity of air
$\dot{m}$ = mass transfer rate per unit area
Nu = Nusselt number = hC/k
n = power index defined in Eqs. (7) and (8)
Pr = Prandtl number = $\mu C_p/k$
$P_{v,w}$ = vapor pressure of naphthalene at wall
p = power index defined in Eqs. (7) and (8)
q = heat flux
R = gas constant for naphthalene vapor = 64.87 J/kg-K
Re_{in} = inlet Reynolds number = $U_{in}C/\nu$ ≈ 123,000 or 88,900
Re_{ex} = exit Reynolds number = $U_{ex}C/\nu$ ≈ 176,000 or 126,000 in present study
Sc = Schmidt number = ν/D, taken to be ~2.28 for naphthalene
Sh = Sherwood number = h_mC/D
S_p = curvilinear (streamwise) coordinate along pressure side; $S_p = 0$ at stagnation line and $S_p = -1.063C$ at trailing edge
S_s = curvilinear (streamwise) coordinate along suction side; $S_s = 0$ at stagnation line and $S_s = 1.352C$ at trailing edge
St = heat transfer Stanton number = $h/\rho C_p U_{in}$
St_m = mass transfer Stanton number = h_m/U_{in}
Δt = thickness change of naphthalene due to sublimation
T_w = surface temperature of blade
T_∞ = main stream temperature
U_{in} = incoming velocity ≈ 11.8 or 8.4 m/s in present study
U_{ex} = exit velocity ≈ 17.0 or 11.9 m/s in present study
U_∞ = local free-stream velocity
u = velocity along blade
XYZ = coordinates of the data acquisition system (see Fig. 3)
x = curvilinear (streamwise) coordinate along blade
Z = spanwise coordinate of blade starting from endwall
α = thermal diffusivity of air
β_1 = blade inlet angle = 44.3 deg
β_2 = blade outlet angle = −62.7 deg
η = local similarity variable = $y(U_\infty/\nu x)^{1/2}$
μ = viscosity of air
ν = kinematic viscosity of air
Θ = coordinate of the data acquisition system (see Fig. 3)
ρ = density of air
ρ_s = solid density of naphthalene ~ 1145 kg/m^3
$\rho_{v,w}$ = vapor density of naphthalene at wall
$\rho_{v,\infty}$ = vapor density of naphthalene in free stream; $\rho_{v,\infty} = 0$ in this study
$\Delta\tau$ = time interval in forced convection experiment
Ψ = local similarity stream function = $(U_\infty \nu x)^{1/2} F(x, \eta)$

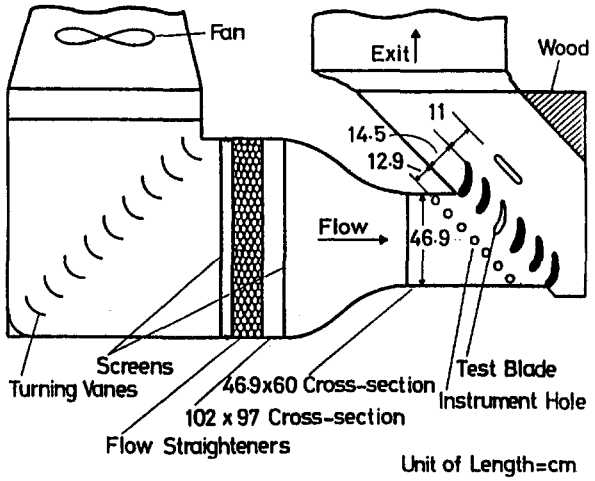

Fig. 1 A schematic view of the wind tunnel and cascade

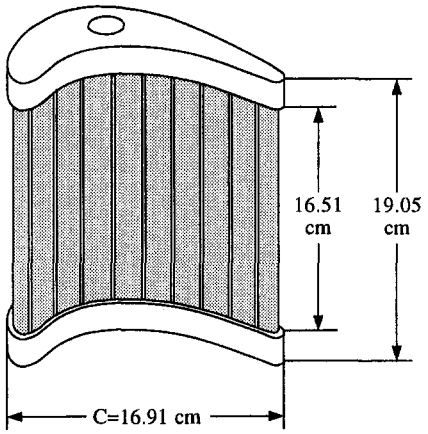

Fig. 2 Test blade used for naphthalene mass transfer measurement

The magnitude of Prandtl number for air is about 0.7 and the value of the Schmidt number for naphthalene diffusion into air is approximately 2.28 depending slightly on the temperature. A detailed discussion about this Schmidt number is given by Cho (1992).

3 Apparatus and Instrumentation

3.1 Wind Tunnel and Linear Cascade. The open wind tunnel used is shown schematically in Fig. 1. The test section was originally designed to conduct experiments on film cooling from a turbine blade cascade and later was extended to perform naphthalene mass transfer from a blade and film cooling from an endwall of the cascade as well. The instrument holes ahead of the cascade and the slot behind it are used to measure the flow velocities, pressures, and temperatures. The nozzle contracts the flow at an area ratio of 3.5 and a tripping wire is placed at the exit of the contraction to make the endwall boundary layer turbulent and uniform.

The linear cascade consists of six scaled-up CF6-50 blades. The two blades in the middle can be lowered through the tunnel floor or raised through the tunnel top wall. One of these, the test blade, is coated with naphthalene over a section of its length. The test blade can be lifted up to penetrate the top endwall to study the endwall effect on mass transfer from the blade or moved down to the middle of the test section to investigate phenomena in the two-dimensional flow region. Its position of orientation is determined such that the test surface of the blade will face the central passage. The test blade, therefore, is located at the place shown in Fig. 1 for the mass transfer experiments on the suction side. It is switched to the adjacent position when the pressure side is studied. Some experiments are conducted in one run on both sides when the pressure surface faces the main passage. We observed little difference of the results on the suction side, which faces the two different passages. The other four blades are the fixed solid ones. The height of the test section is 60 cm and the width is 46.9 cm. The aspect ratio (span/chord) of the blade is 3.5 and the pitch/chord ratio is 0.775. The cascade geometry is shown in Table 1.

3.2 Test Blade. The large-scale test blade used for naphthalene mass transfer measurement is shown in Fig. 2. The active (naphthalene-coated) midspan of the blade has a height of 16.51 cm. A layer of naphthalene is cast on this roughened surface all around the blade using a well-polished mold. The thickness of the naphthalene layer is about 1.63 mm. The top and bottom metal shoulders, which bound the cast naphthalene, have the same profile as the other blades of the cascade. The cast naphthalene is nominally flush with the two shoulders. The test blade, after casting, will have a very smooth surface and act aerodynamically like a real blade of the cascade. There is a very tiny hole on the top metal edge, which is used to align the blade and determine the starting point during the process of data acquisition. Two copper-constantan (type T) thermocouples are imbedded in the cast naphthalene to obtain the naphthalene surface temperature during experiments.

3.3 Data Acquisition Control System. A microcomputer-controlled four-axis data acquisition system is used to measure local values of sublimation depth over the naphthalene surface of the test blade. The system is composed of an IBM-XT microcomputer, a motor-controller, a digital multimeter, a signal conditioner, an LVDT (Linear Variable Differential Transformer) depth gage and a four-axis positioning table. The whole system is made from commercially available subassemblies. It has a very high accuracy and a good repeatable performance in experiments. It has been shown that, due to random false signals such as noise and vibration, the root mean squared (rms) random error of the system tested on a corresponding metal (nonsubliming) blade is about 0.18 μm, while the average sublimation depth on the surface of the naphthalene-coated blade is usually controlled to be ~60 μm. This contribution to the measurement error is ~0.3 percent. The system employs a fast data acquisition to avoid extra free-convection loss during measurements. Generally a rate of about 2400 readings per hour can be taken. A detailed description and qualification of this system is given by Hain et al. (1991).

The four-axis ($XYZ\Theta$) positioning table shown in Fig. 3 is a major component of the system. It is used to position the test piece and the LVDT probe. The coordinates (XYZ) of the probe are the input values and will be given to the computer, which moves the probe to the requested place. The test blade itself can be rotated by the Θ-axis motor controller. One restriction to naphthalene elevation measurements is that the probe has to be normal to the curved surface. This criterion is satisfactorily met by the performance of this positioning table with four degrees of freedom. Note the changes in surface contour due to

Table 1 Cascade geometry data

Number of blades	6
Chord length of the blade - C	169.1 mm
Axial chord of the blade	145.3 mm
Pitch	131.1 mm
Aspect ratio (Span/Chord)	3.548
Blade inlet angle	44.3°
Blade outlet angle	-62.7°
Reynolds number - Re_{ex} (based on chord and exit velocity)	~176,000 126,000

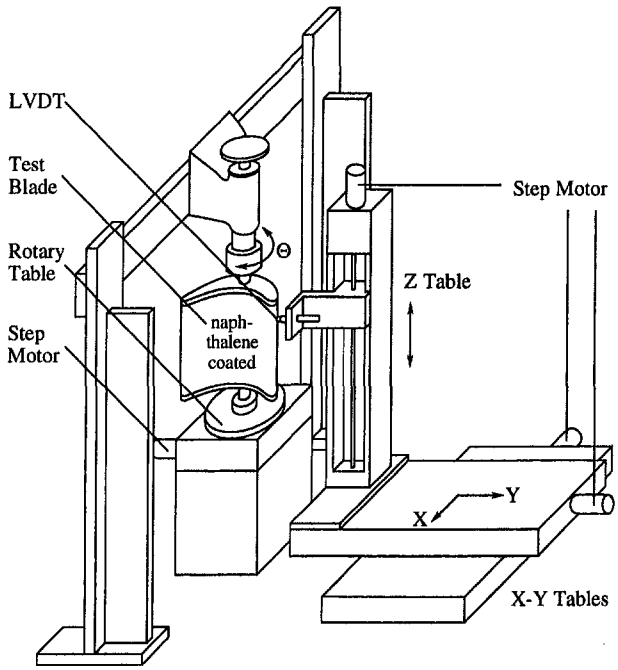

Fig. 3 Four-axis data aquisition positioning system

sublimation do not significantly affect the orientation of the probe relative to the blade. The computer performs the following steps. At the beginning, the X, Y, and Θ motor controllers position the probe at a designated location of $XY\Theta$ and the probe tip gently touches one of the two metal edges. Then it can be moved on the naphthalene surface up or down by the Z-motor-controller to scan vertically at this current $XY\Theta$ coordinate. When it stops at a given Z location, the LVDT probe senses the surface elevation and the signal conditioner sends this message to the multimeter from which the reading is taken by the computer and stored in it. The probe then goes to the next Z location and repeats the same procedure as above. After all the vertical locations are visited, the probe is positioned at the next specified $XY\Theta$ coordinate and another vertical scan is executed. This process continues until all the required $XY\Theta$ positions are visited.

4 Experimental Procedure

4.1 Casting. A smooth solid naphthalene surface can be achieved through a casting process using a well-polished mold. Since the test blade is relatively large, caution must be taken to avoid scars, air bubbles, or early freezing in the mold during the casting process. The attached naphthalene layer should adhere tightly to the roughened metal surface. But this requirement sometimes is not easily satisfied, especially on a concave (e.g., turbine blade pressure) surface. Since the temperatures and thermal expansion coefficients of the metal mold and naphthalene are different, the rates of contraction of the two materials are expected to be different. A poor casting can cause the naphthalene layer to separate from the metal surface. These technical problems can yield unrepeatable and incorrect experimental results. In order to diminish the possibility that the cast naphthalene will be stripped off the metal surface, several grooves are cut into the metal along the midspan of the test blade. When the melted naphthalene solidifies on the grooved surface, the grooves help to hold the naphthalene tightly. The results of repeatability tests have shown the success of this arrangement.

4.2 Test Procedure. When a smooth and solid surface of naphthalene is obtained from casting, the test blade is placed in the four-axis positioning system, illustrated in Fig. 3. The scanning of the surface contour is conducted. The readings of local surface elevation on the blade are obtained and recorded in the computer. Then the blade is brought to the wind tunnel and positioned in the cascade. After it is exposed to the air flow for a period of time (typically 40 to 60 minutes), the blade is brought back to the four-axis acquisition system. It can be aligned and adjusted again to the same position as before with the aid of the alignment hole on the upper metal shoulder. The test blade is then scanned to get the second set of surface elevations with the same $XYZ\Theta$ coordinates used in the first scan. A reference line calculated from end positions on metal shoulders before and after the exposure corrects the end shoulders of both measurements to the same elevation. The difference between the before-and-after readings at each location indicates the amount of sublimed material, from which the local mass transfer coefficient can be determined.

When not in a testing position, the blade with coated naphthalene is usually sealed in a plastic box to prevent excess sublimation loss due to natural convection. The data acquisition is performed in a temperature-controlled room. It takes about 50–80 minutes, depending on how many measurement points are taken, to complete the whole process. The setup time before and after the blade is exposed to the wind tunnel is 3–10 minutes. The total free sublimation loss during the processing is relatively small, about 5–10 percent of the total average loss of naphthalene, and a correction for it is included.

4.3 Two-Dimensional and Three-Dimensional Experiments. When conducting the two-dimensional flow experiments, the test blade is installed in the cascade near the center height of the test section where a more uniform two-dimensional flow is expected. The stagnation line of the blade is determined in this region through surface flow visualization using an oil-lampblack technique. In some tests, a trip wire 1 mm in diameter is used to trigger the disturbance in the boundary layer on the blade. It is glued onto the naphthalene surface close to the leading edge of the blade on either suction or pressure side depending on the test being conducted. Its location is at $S_p/C = -0.0375$ on the pressure side and at $S_s/C = 0.0616$ on the suction side. In addition, with the motivation of comparison of the trip wire case and simulation of roughness in the leading edge region, a run is conducted with a #320 sandpaper glued on the leading edge from the suction surface to up to $S_p/C = -0.0375$ on the pressure surface to trigger the disturbance. Only the pressure side is investigated for this purpose.

To study mass transfer in the three-dimensional flow region near the endwall, the test blade is moved up into the endwall. One metal shoulder and about 1 mm naphthalene layer are totally embedded into the endwall. Thus, a near-90-deg sharp-edged corner is formed at the junction between the endwall and the active blade surface. It should be noted that with actual blades a finite radius would be present that could influence some of the flow and transport phenomena near the corner. The local mass transfer coefficients can be obtained right up to the endwall to study three-dimensional effects, especially the effect caused by tiny corner vortices between the blade and the endwall.

5 Results and Discussion

5.1 Two-Dimensional Flow With No Trip Wire on the Blade. The two-dimensional-flow Sherwood number distributions of mass transfer from both suction and pressure sides of the blade are plotted in Fig. 4 for two exit Reynolds numbers, 176,000 and 126,000. These data are taken from the midspan region of the blade. The pressure and velocity distributions around the blade can be found in Chen and Goldstein (1992).

Laminar boundary layer wedge-flow similarity solutions, based on the velocity profile given by Chen and Goldstein (1992), are used to determine the Sherwood number on both surfaces of the blade for $\mathrm{Re}_{ex} = 176{,}000$; these results are also

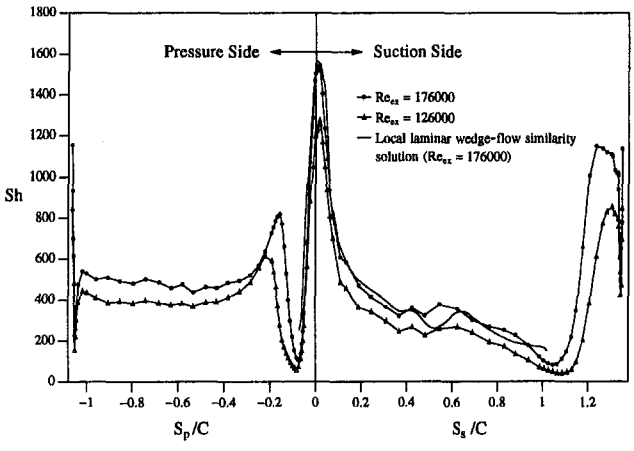

Fig. 4 Sherwood number distribution along the curvilinear direction on both sides of blade in midspan region

shown in Fig. 4. The exact similarity solution of laminar boundary layer flow can be obtained only if a power law variation of the free-stream velocity profile along the x direction is assumed, i.e., $U_\infty \sim x^m$. For an arbitrarily varying free-stream velocity, an approximate answer, a local similarity solution, can be obtained if the parameter m is adopted as $m = (x/U_\infty)(dU_\infty/dx)$. The main feature of the analysis is that the similarity function is not only a function of η (the conventional similarity variable $\eta = y(U_\infty/\nu x)^{1/2}$), but also of the distance x, i.e., $F = F(x, \eta)$. It is assumed that the velocity profile and the stream function in the boundary layer follow the same forms of the similarity convention, $u/U_\infty = F'(x, \eta)$ and $\psi = (U_\infty \nu x)^{1/2} F(x, \eta)$. After the substitution of all the related variables into the two-dimensional boundary layer x-momentum equation, a similar wedge-flow Falkner–Skan equation can be obtained except for some additional x-related terms of $F(x, \eta)$. An assumption is made that the effects of these terms are small and can be ignored for calculation convenience. The same method is used for thermal analysis.

According to heat and mass transfer analogy, some mass transfer relations can be readily obtained based on heat transfer results. Naphthalene mass transfer is a typical example of the analogy in which one replaces Prandtl number by Schmidt number and Nusselt number by Sherwood number. The local feature is implied in the parameter m. A detailed description on this method can be found in the literature by Sparrow et al. (1970) and Eckert (1972). The advantage of this method is simple and accurate at small x. When x is large (far downstream) or m is a strong function of x, some errors could be introduced. The value of m in this analysis is less than or equal to unity; $m = 1$ corresponds to the stagnation flow and $m = 0$ to a flat plate case. When $m = -0.09042$, the laminar boundary layer starts to separate at that x and local similarity solution fails afterward.

It is seen from Fig. 4 that at both Reynolds numbers there are the same general trends and similar variations in the distributions. The mass transfer rate around the leading edge is higher than the rate at the trailing edge. Higher Reynolds number results in higher mass transfer all around the blade as expected.

On the suction side, the maximum mass transfer is not reached on the stagnation line of the blade. This interesting phenomenon was also observed by Arts and Graham (1985), Wittig et al. (1985), and Chen and Goldstein (1992) in their heat (or mass) transfer measurements over turbine blades with an elliptic leading edge. Ota et al. (1983) found that when a stagnation line is not at the tip of a long axis of an ellipse, the peak heat transfer may be off the impingement line. This conclusion is confirmed in this study as well. The maximum mass transfer occurs at $S_s/C = 0.015$ for both Reynolds numbers. After this peak, the rate of mass transfer drops rapidly along this suction (convex) surface and, as inferred from the agreement with the local similarity solution, the flow appears to be laminar. Due to the variation of the blade curvature and the local flow acceleration, some minor peaks in mass transfer are found around $S_s/C \approx 0.5$ and the local similarity solution shows the same trend. As the "laminar" boundary layer grows, far downstream at about $S_s/C = 1.05$ for $\mathrm{Re}_{ex} = 176{,}000$ and $S_s/C = 1.1$ for $\mathrm{Re}_{ex} = 126{,}000$, the minimum mass transfer is obtained. From this one may infer that a laminar separation occurs around these locations. From this minimum, the mass transfer rate climbs quickly to a high value, which is probably due to transition and turbulent reattachment. This turbulent flow is apparently maintained until it reaches the corner of the trailing edge. Because of the abrupt change in curvature near the trailing edge, the boundary layer undergoes separation and the mass transfer rate is quickly reduced to a low value at that corner. Since the vortices shed from the trailing edge can cause a significant increase on heat or mass transfer at the trailing edge, the mass transfer rate increases quickly with position after the turbulent separation to almost the same level as the second high peak of the turbulent reattachment.

On the pressure side of the blade, the rate of mass transfer (Fig. 4) decreases sharply from the leading edge and reaches a minimum at $S_p/C \approx -0.07$ with $\mathrm{Re}_{ex} = 176{,}000$ being slightly earlier than $\mathrm{Re}_x = 126{,}000$. This low minimum indicates laminar flow separation. The local similarity solution accurately predicts this location. It must be noted that this separation bubble is usually not clearly seen from a conventional heat transfer experiment. The major reason for this is probably the conduction (which smooths out the effect of large variations in heat transfer coefficient) inside a blade, different cascade geometry shapes, and different inlet flow angles. An oil-lampblack surface flow visualization clearly confirms this separation line and the reattachment line following the dip. After the separation the flow undergoes transition and reattachment as on the suction side. As indicated by the following peak in Sh, the flow with higher Reynolds number, $\mathrm{Re}_x = 176{,}000$, reattaches to the surface earlier ($S_p/C \approx -0.15$) than the lower Reynolds number flow ($S_p/C \approx -0.21$). Following this maximum, the pressure side experiences an accelerating turbulent boundary layer flow and the mass transfer rate is almost unchanged for about half the concave side length until the flow reaches the corner of the trailing edge where turbulent separation and vortex shedding occur as on the suction side.

Using the analogy between heat and mass transfer (Eqs. (9)–(10) with $n = \frac{1}{3}$), the present mass transfer results can be compared with the earlier heat transfer as well as mass transfer measurements. Figure 5 shows the comparison of heat transfer Stanton number with a heat transfer experiment with a 31.6

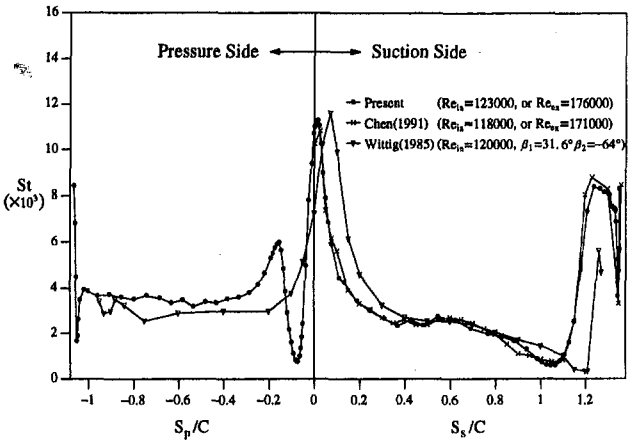

Fig. 5 Comparison of heat transfer Stanton number along the curvilinear direction of blade

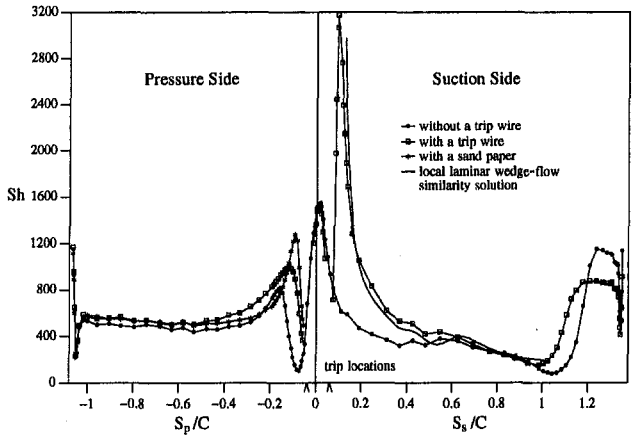

Fig. 6 Comparison of Sherwood number with tripping near the leading edge (Re_{ex} = 176,000)

degree inlet blade angle reported by Wittig et al. (1985) and a mass transfer experiment by Chen and Goldstein (1992), with the same inlet angle and blades as used in the present study. The velocity distributions around the blade are very similar in the two cascades. The original data given by Wittig et al. (1985) were dimensional heat transfer coefficient, and the Stanton numers have been scaled by estimating the properties. The Reynolds numbers are almost the same for these three measurements. The results agree very well. The naphthalene sublimation technique can give more detailed information about separation, transition, and reattachment, because there is no conduction or radiation effects to cloud the convective transport measurements. The distribution of heat (mass) transfer rate is dependent on flow inlet angle β_1, which would affect the peak locations of the highest heat transfer near the leading edge and the boundary layer transition on both sides of a blade.

5.2 Two-Dimensional Flow With Trip. Figure 6 shows the mass transfer in the two-dimensional flow region with the boundary layer tripped near the leading edge of the blade. The resulting distribution is quite different from the distribution discussed above. Though the mass transfer near the leading edge is not influenced by the downstream trip on the suction side, there is a very sharp increase and then decrease in Sherwood number after the trip wire. This is probably because the flow reattaches with a tiny but very intense vortex immediately behind the wire, causing a high mass transfer rate. After that high peak the mass transfer rate varies as though the boundary layer flow were laminar. The local laminar wedge-flow similarity solution is shown on the same figure for comparison, with the virtual origin of laminar flow starting at one-tenth of the chord length (S_s/C = 0.1). Note that the trip does not immediately initiate transition to turbulence at this Re. Since it is disturbed by the trip wire, the laminar boundary layer appears to undergo the transition somewhat earlier (about S_s/C = 1.0), compared to the value for flow without the trip wire (about S_s/C = 1.1). It is interesting to note that after transition ($S_s/C > 1.0$), the mass transfer coefficient of the tripped flow does not reach a value as high as that of the untripped, the former being about 20 percent lower than the latter. A related effect may be the finding by Arts and Graham (1985) of a reduced turbulent heat transfer, after transition on the suction side, when they increased the main stream turbulence.

On the pressure side, the mass transfer does not have as marked a change after the trip wire as on the suction side, probably because transition occurs early even in untripped flow where the curvature changes rapidly. However, the existence of the wire does make a difference. The separation bubble occurs early with the trip wire, which induces earlier reattachment at S_p/C = −0.09 where a higher mass transfer rate is observed, compared to the untripped flow at S_p/C = −0.15. Then the boundary layer becomes turbulent afterward. The mass transfer rate is almost uniform during the stretch from S_p/C = −0.4 to −1.0 similar to that with untripped flow, but the tripped flow has about 15 percent higher mass transfer than the untripped. The sandpaper acts just like another trip wire. The flow separates and reattaches earlier than in the other two cases, but there is almost the same rate of mass transfer as with the wire-tripped flow downstream on the blade.

5.3 Three-Dimensional Flow Region. Near the endwall the flow is no longer even close to two dimensional because of strong secondary flows. A very complicated flow pattern has been observed in the near-wall region from a surface flow visualization (Jabbari et al., 1992) on the same cascade. The present mass transfer results agree well with their observations. The local mass transfer distributions close to the endwall along the spanwise direction Z/C at different S_s/C on the suction side and at different S_p/C on the pressure side are presented in Figs. 7 and 11, respectively. The corresponding contour maps and three-dimensional plots of these local values are shown in Figs. 8–10 for the suction surface and Figs. 12–13 for the pressure surface.

When the flow approaches the cascade near the endwall, a horseshoe vortex is formed near the leading edge and its two legs are carried downstream on both sides of a blade by the flow. It can be seen from Figs. 7 and 8 that the horseshoe vortex does not have a strong influence on mass transfer near the leading edge on the suction side where the flow can still be considered two dimensional ($Z/C > 0.1$), except close to the endwall where the high peak of mass transfer indicates a small but very intense leading edge corner vortex. The low mass transfer rate at the location next to that high peak is believed to be caused by the upwash flow produced by the counterrotating pair of horseshoe and leading edge corner vortices. The highest mass transfer rate (Sh ≈ 2600) is found near the

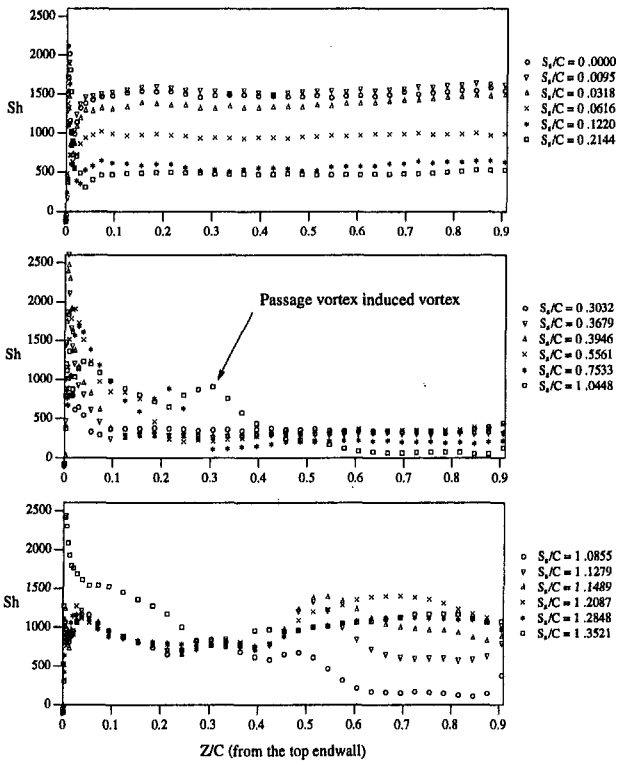

Fig. 7 Local Sherwood number distribution on suction side of cascade near the endwall (Re_{ex} = 173,000); Note: midspan is at Z/C = 1.77

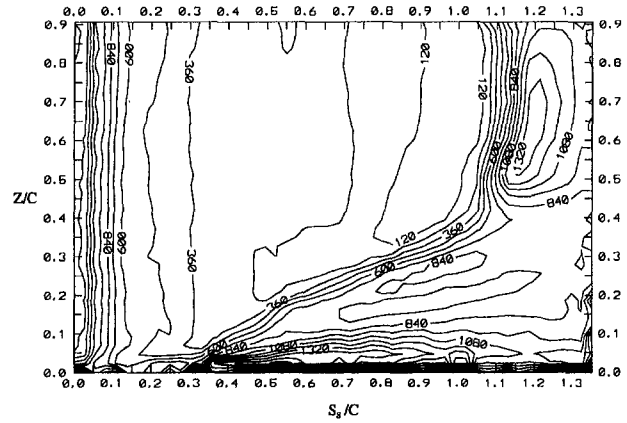

Fig. 8 Contour of Sherwood number distribution on the suction side near the endwall (Re_{ex} = 173,000); note: midspan is at Z/C = 1.77

endwall-blade junction at $S_s/C \approx 0.37$, which indicates that there is a strong combined convergence of flow in that region from the main flow and the pressure-to-suction side cross flow. The surface flow visualization on the endwall reported by Jabbari et al. (1992) appears to support this observation. The passage vortex influence on the suction side probably originates near that location. The counterrotating suction leg vortex is pushed away from the endwall and moves above the passage vortex along the suction surface. This observation agrees with the study of light-sheet flow visualization by Marchal and Sieverding (1976). The impact of the suction leg of the horseshoe vortex on mass transfer from the blade surface is unclear downstream. Its effect probably gradually diminishes as it interacts with the passage vortex and the main flow.

Past one-third of the chord length, the passage vortex becomes dominant. Its core is close to the suction surface and is gradually lifted from the endwall as it moves farther downstream. Still the region of $S_s/C < 1.0$ and $Z/C > 0.4$ is closely two dimensional in mass transfer. When the passage vortex develops, a new vortex is formed above it at about $S_s/C = 0.4$. Its path can be clearly seen from either the local distribution (Fig. 7) or the contour map (Fig. 8) or the three-dimensional plot (Fig. 10), and can be easily traced from about $S_s/C = 0.37$ to $S_s/C = 1.1$. The locus of local peak mass transfer results caused by this new vortex is shown on Fig. 9, which is a partial enlargement of Fig. 8. Jabbari et al. (1992) found, from surface flow visualization, that this vortex is initiated close to the endwall corner at about $\frac{1}{3}$ of the chord length. This vortex climbs up the blade suction surface and is carried downstream by the passage vortex. Sonoda (1985) also observed this new vortex at about the same location in his kerosene vapor flow visualization.

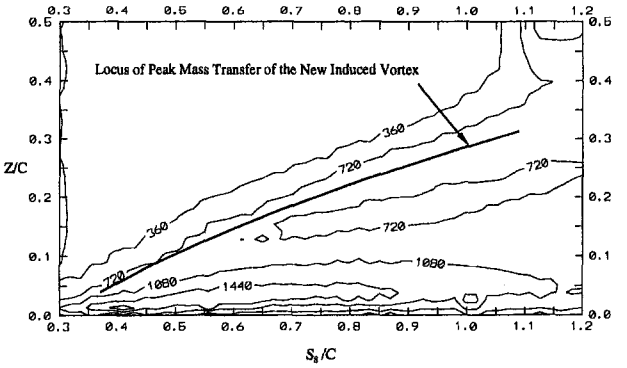

Fig. 9 Trace of the new passage-vortex-induced vortex (partial enlargement of Fig. 8); note: midspan is at Z/C = 1.77

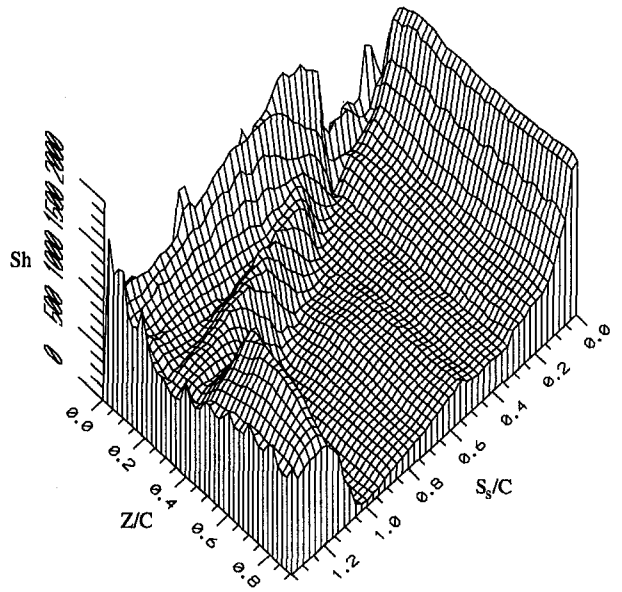

Fig. 10 Three-dimensional plot of Sh distribution on suction side (Re_{ex} = 173,000); note: midspan is at Z/C = 1.77

We know from the previous two-dimensional measurements that the two-dimensional flow transition occurs and the boundary layer quickly reaches the turbulent state after $S_s/C > 1.0$. The interaction among this passage vortex induced vortex, the passage vortex, and the laminar transition as well as the turbulent boundary layer creates a complicated three-dimensional image. As indicated by the mass transfer, it extends the three-dimensional region to about $Z/C = 0.8$ and raises the mass transfer rate to about 20 percent higher than that in the two-dimensional region. Thus this new vortex has a significant in-

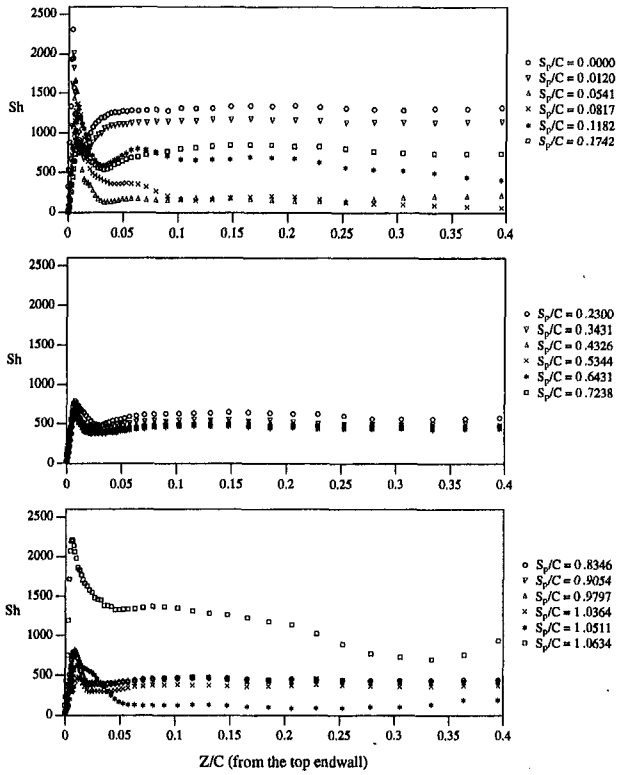

Fig. 11 Local Sherwood number distribution on pressure side of cascade near the endwall (Re_{ex} = 170,000); note: midspan is at Z/C = 1.77

fluence of mass transfer on the suction side. It, as well as the passage vortex, also would carry away film cooling air injected at and near the leading edge from a blade and increases the heat transfer along its path (Goldstein and Chen, 1987).

Close to the endwall, a very high peak in mass transfer is found, which gradually decreases downstream, probably due to the upwash motion by the passage vortex. Because of a large pressure gradient in the cascade passage, the pressure leg of the horseshoe vortex is pushed toward the suction side and becomes a part of the passage vortex. This passage vortex upwashes the suction surface and induces quite high mass transfer near the corner. When it moves downstream it gradually expands in size, but its strength near the corner is decreased at the same time. When the vortex reaches $S_s/C = 1.1$, its effect on the suction surface has been greatly diminished. In the downstream region the influence of another corner vortex is observed from the mass transfer results. This corner vortex probably originates near $S_s/C \approx 0.6$ where a small peak and valley are found in the local spanwise mass transfer distribution. This corner vortex develops as it goes toward the trailing edge. At the trailing edge, due to the vortex shedding between the endwall and the trailing edge, a complex flow pattern is formed. The rate of mass transfer is very high close to the endwall.

On the pressure surface the mass transfer distribution is relatively simple. One can observe from Figs. 12 and 13 that three-dimensional effects on mass transfer are confined to a very narrow region ($Z/C < 0.2$). Near the leading edge the situation is quite similar to that on the suction side. The corner vortex still imposes a very strong influence of mass transfer at the leading edge on the pressure side. Its effect, however, quickly decreases away from the leading edge. The pressure leg of the horseshoe vortex, like the suction leg, has little influence on mass transfer near the leading edge. Downstream, as mentioned in the previous discussion of two-dimensional flow, where the laminar flow begins to separate and undergoes transition and reattachment, the pressure leg of the horseshoe vortex is forced toward the suction side. The interaction between the vortex and the different boundary layer regimes causes the early separation and reattachment near the endwall and creates a higher mass transfer rate in this area than in the two-dimensional zone. The mass transfer rate stays almost constant after the transition on the pressure side and the corner vortex does not play a significant role even near the endwall. Thus, except in the transition zone and near the trailing edge, the three-dimensional effects on mass transfer on the pressure side only stretch from the endwall to about $Z/C = 0.1$.

6 Conclusions

The mass transfer around a simulated turbine blade in a linear cascade is obtained for both two-dimensional and near-endwall flow regions. The disturbance caused by trip wires placed on the blade near the leading edge is investigated. Higher Reynolds numbers impose higher mass transfer on the blade, as expected. The flow disturbance created near the leading edge has a stronger influence on the suction side than on the pressure side, particularly on the onset of laminar–turbulent transition. It can trigger early boundary layer separation, transition, and reattachment on both sides of the blade and increase the mass transfer. On the suction side, after the transition near the trailing edge, a decrease (~20 percent) of turbulent mass transfer is observed with tripping, in agreement with some researchers, while the turbulent mass transfer in the middle of the pressure side is about 15 percent higher than with an untripped boundary layer.

Close to the endwall the mass transfer rate is much higher than in the two-dimensional flow region, especially on the suction side. The pressure side mass transfer is not greatly affected by proximity to the endwall. On the suction side the highest mass transfer rate is not found near the leading edge as in the two-dimensional flow. It occurs from $S_s/C = 0.35$ to $S_s/C = 0.4$, where several of the vortices converge. The large horseshoe vortex has little impact on mass transfer around the leading edge, but has a strong influence downstream. The effects of the passage vortex and the new vortex induced by it on mass transfer are clearly seen from the mass transfer results and can be traced along the suction surface. The leading edge corner vortex is responsible for high mass transfer close to the endwall at the leading edge and the passage vortex affects the mass transfer downstream. The interaction between the vortices and the laminar–turbulent transition extends the three-dimensional zone to about $Z/C = 0.8$ on the suction side and to about $Z/C = 0.2$ on the pressure side. It results in an early boundary layer transition and a significant increase in mass transfer. Due to the strong secondary flow on the suction side the main stream turbulence may not penetrate easily into the boundary layer to raise the mass transfer rate close to the endwall. The pressure side may be affected more significantly by the free-stream turbulence because the effects of the secondary flows on this side are small.

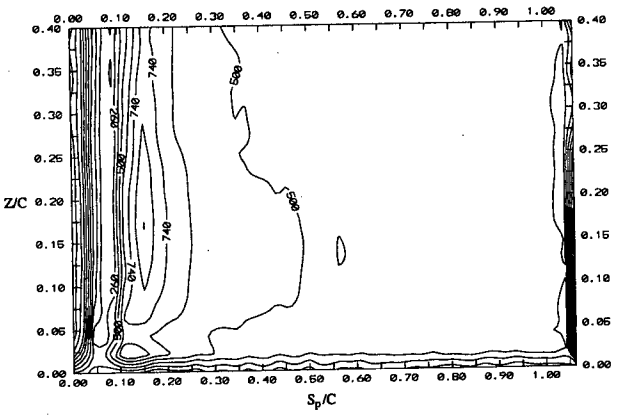

Fig. 12 Contour of Sherwood number distribution on the pressure side near the endwall (Re_{ex} = 170,000); note: midspan is at Z/C = 1.77

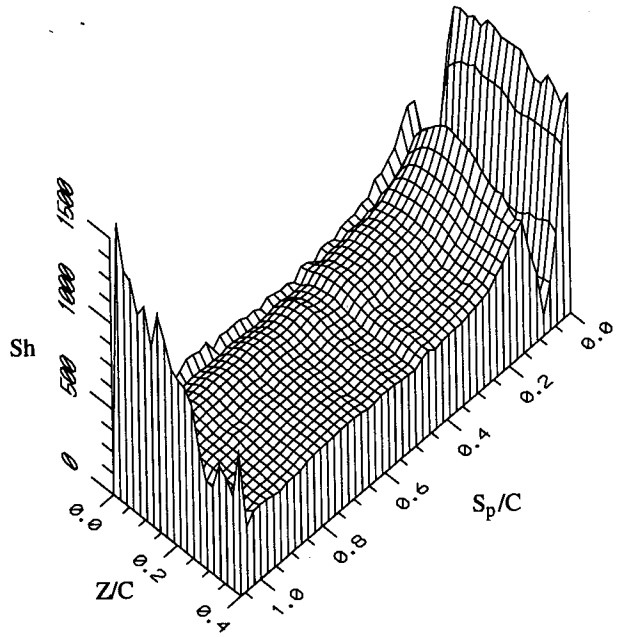

Fig. 13 Three-dimensional plot of Sh distribution on pressure side (Re_{ex} = 170,000); note: midspan is at Z/C = 1.77

References

Ambrose, D., Lawrenson, I. J., and Sprake, C. H. S., 1975, "The Vapour Pressure of Naphthalene," *Journal of Chemical Thermodynamics*, Vol. 22, No. 5, pp. 213–228.

Arts, T., and Graham, C. G., 1985, "External Heat Transfer Study on a HP Turbine Rotor Blade," AGARD-CP-390, *Heat Transfer and Cooling in Gas Turbines,* pp. 5.1–5.6.

Bayley, F. J., and Priddy, W. J., 1981, "Effects of Free Stream Turbulence Intensity and Frequency on Heat Transfer to Turbine Blading," ASME *Journal of Engineering for Power,* Vol. 103, pp. 60–64.

Chen, P. H., 1988, "Measurement of Local Mass Transfer From a Gas Turbine Blade," Ph.D. Thesis, University of Minnesota, Minneapolis, MN.

Chen, P. H., and Goldstein, R. J., 1992, "Convective Transport Phenomena on the Suction Surface of a Turbine Blade Including the Influence of Secondary Flows Near the Endwall," ASME JOURNAL OF TURBOMACHINERY, Vol. 114, pp. 776–787.

Cho, H. H., 1992, "Heat/Mass Transfer Flow Through an Array of Holes and Slits," Ph.D. Thesis, University of Minnesota, Minneapolis, MN.

Eckert, E. R. G., 1976, "Analogies to Heat Transfer Processes," *Measurement in Heat Transfer,* E. R. G. Eckert and R. J. Goldstein, eds., Hemisphere Publishing, New York.

Eckert, E. R. G., and Drake, R. M., 1972, *Analysis of Heat and Mass Transfer,* McGraw-Hill, New York, pp. 293–295, 326–327.

Goldstein, R. J., and Chen, P. H., 1987, "Film Cooling on a Turbine Blade With Injection Through Two Rows of Holes in the Near-End-Wall Region," ASME JOURNAL OF TURBOMACHINERY, Vol. 109, pp. 588–593.

Goldstein, R. J., and Spores, R. A., 1988, "Turbulent Transport on the Endwall in the Region Between Adjacent Turbine Blades," ASME *Journal of Heat Transfer,* Vol. 110, pp. 862–869.

Graham, R. W., 1990, "Recent Progress in Research Pertaining to Estimates of Gas-Side Heat Transfer in an Aircraft Gas Turbine," ASME Paper No. 90-GT-100.

Gregory-Smith, D. G., and Cleak, J. G. E., 1992, "Secondary Flow Measurements in a Turbine Cascade With High Inlet Turbulence," ASME JOURNAL OF TURBOMACHINERY, Vol. 114, pp. 173–183.

Hain, R., Wang, H. P., Chen, P. H., and Goldstein, R. J., 1991, "A Microcomputer-Controlled Data Acquisition System for Naphthalene Sublimation Measurement," *Proceedings, 11th ABCM Mechanical Engineering Conference,* Sao Paulo, Brazil, Dec.

Hazarika, B. K., Raj, R., and Boldman, D. R., 1986, "Three-Dimensional Fluid Flow Phenomena in the Blade End Wall Corner Region," ASME Paper No. 86-GT-179.

Jabbari, M. J., Goldstein, R. J., Marston, K. C., and Eckert, E. R. G., 1992, "Three Dimensional Flow at the Junction Between a Turbine Blade and Endwall," *Warme- und Stoffubertragung,* Vol. 27, pp. 51–59.

Jilek, J., 1986, "An Experimental Investigation of the Three-Dimensional Flow Within Large Scale Turbine Cascade," ASME Paper No. 86-GT-170.

Joslyn, D., and Dring, R., 1992, "Three-Dimensional Flow in an Axial Turbine: Part 1—Aerodynamic Mechanisms," ASME JOURNAL OF TURBOMACHINERY, Vol. 114, pp. 61–70.

Krishnamoorthy, V., 1982, "Effects of Turbulence on the Heat Transfer in a Laminar and Turbulent Boundary Layer Over a Gas Turbine Blade," ASME Paper No. 82-GT-146.

Langston, L. S., 1990, "Research on Cascade Secondary and Tip-Leakage Flows-Periodicity and Surface Flow Visualization," AGARD-CP-469, *Secondary Flows in Turbomachines.*

Marchal, P., and Sieverding, C. H., 1976, "Secondary Flows Within Turbomachinery Bladings," AGARD-CP-214, *Secondary Flows in Turbomachines.*

Ota, T., Aiba, S., Tsuruta, T., and Kaga, M., 1983, "Forced Convection Heat Transfer From an Elliptic Cylinder of Axis Ratio 1:2," *Bulletin of the JSME,* Vol. 26, No. 212, pp. 262–267.

Schulz, H. D., Gallus, H. E., and Ladshminarayana, B., 1990, "Three-Dimensional Separated Flow Field in the Endwall Region of an Annular Compressor Cascade in the Presence of Rotor-Stator Interaction: Part 1—Quasi-Steady Flow and Comparison With Steady-State Data," ASME JOURNAL OF TURBOMACHINERY, Vol. 112, pp. 669–678.

Sieverding, C. H., 1985, "Recent Progress in the Understanding of Basic Aspects of Secondary Flows in Turbine Blade Passages," ASME *Journal of Engineering for Gas Turbine and Power,* Vol. 107, pp. 248–257.

Sonoda, T., 1985, "Experimental Investigation on Spatial Development of Streamwise Vortices in a Turbine Inlet Guide Vane Cascade," ASME Paper No. 85-GT-20.

Sparrow, E. M., Quack, H., and Boerner, C. J., 1970, "Local Nonsimilarity Boundary-Layer Solutions," *AIAA Journal,* Vol. 8, No. 11, pp. 1936–1942.

Wittig, S., Schulz, A., Bauer, H. J., and Sill, K. H., 1985, "Effects of Wakes on the Heat Transfer in Gas Turbine Cascades," AGARD-CP-390, *Heat Transfer and Cooling in Gas Turbines,* pp. 6.1–6.13.

Journal of Turbomachinery

Technical Brief

Advanced Turbofan Blade Refurbishment Technique

W. B. Roberts[1]

Fuel burn and performance retention in high-bypass-ratio turbofan engines is a major concern for the airline industry. The transonic fan is the single component that accounts for the greatest fuel burn in a high-bypass fan engine. In addition, fan blades suffer more rapid erosion and surface roughening due to lower-atmosphere particulates and runway debris than do core compressor blades. Understanding the mechanism by which blade surface deterioration degrades performance may allow manufacturers to develop design and manufacturing strategies aimed at minimizing long-term performance degradation and may also lead to the development of cost-effective repair strategies for in-service fans. The latter point is the subject of this note.

Suder et al. (1995), in the first paper of this issue, have recently completed an investigation of the performance deterioration of a transonic core compressor rotor caused by the addition of both smooth and rough coatings to the blade surface. By applying a rough coating to various portions of the blade surface, they identified the blade leading edge and the portion of the blade suction surface ahead of the rotor passage shock as the regions of the blade that contributed most to performance loss when roughness was added.

The purpose of the work reported here is to investigate whether the lessons learned from the work of Suder et al. can be used to reduce the in-service performance deterioration of a fan on a high bypass ratio turbofan engine. To this end, a back-to-back test was done on the fan of an RB211-22B engine with the cooperation of Delta Airlines. The fan and engine were first overhauled per normal airline practice and cell-tested to establish that the engine performance met flight acceptance standards. This test, which the engine passed, also established a performance baseline for the overhauled engine. At this point the fan blade leading edge had not been filed or scraped and the blade surfaces had not been polished because the leading edge damage and blade surface roughness fell within the acceptable limits specified by the manufacturer for normal overhaul practice.

After the cell test, the fan was removed from the engine and sent to Sermatech International where the following additional operations were performed:

1 The blade surfaces were polished to a finish of 20 rms μin.
2 Leading edge roughness due to particle impact damage was removed and the leading edge was polished to a finish of 20 rms μin.
3 The leading edge shape was rounded and the leading edge thickness was reduced over the first 5–10 percent of chord.

The first two operations were guided by the work of Suder et al. The final operation was performed to reduce the chance of triggering transition at the leading edge and left the blade within the minimum thickness specifications in the manufacturers repair manual and within the tolerance on the blade drawings. A schematic of the leading edge reprofiling is shown in Fig. 1.

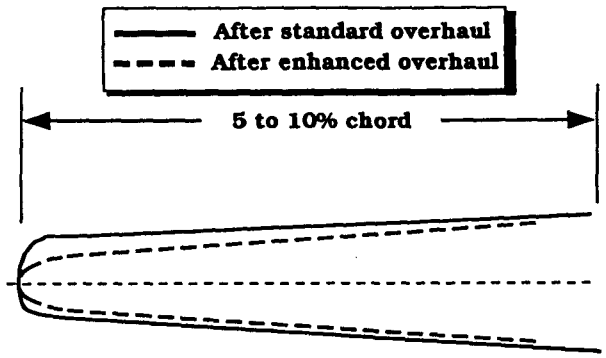

Fig. 1 Blade leading edge shape before and after enhanced refurbishment

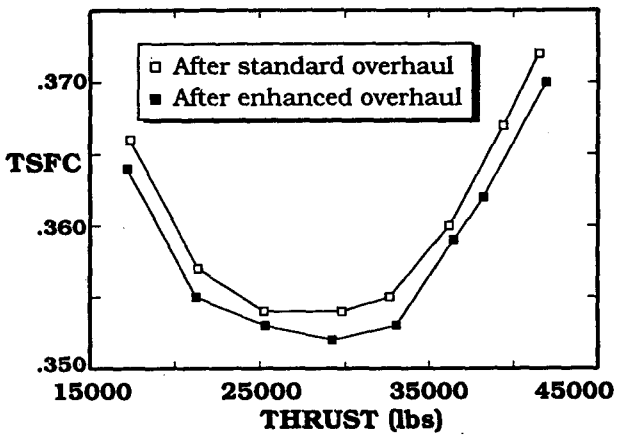

Fig. 2 Comparison of thrust-specific fuel consumption before and after enhanced refurbishment

[1] Flow Application Research and Sermatech International Inc., Fremont, CA 94539.

Contributed by the Turbomachinery Division for publication in the JOURNAL OF TURBOMACHINERY. Manuscript received at ASME Headquarters June 1995. Associate Technical Editor: N. A. Cumpsty.

Upon completion of the additional fan rework, the fan was mated to the waiting baseline engine, and the engine was retested in the same test cell. When corrected to ICAO Standard Day Sea Level conditions, the test results indicated a 0.7 percent drop in thrust specific fuel consumption (lb fuel/lb thrust/hr) relative to the baseline engine after the enhanced fan overhaul, as shown in Fig. 2. In addition a comparison of the engine exhaust gas temperature (EGT) over the range of thrust levels tested for the engine indicated a 5°F drop in EGT on average. Based on the results of Suder et al. (1995) it appears that 70–80 percent of this performance gain is due to the thin smooth leading edge and the remainder to the highly polished finish of the blade. If we assume that the fan blade surfaces will deteriorate at the normal rate in service, these changes translate into fuel savings and additional time-between-overhaul, which more than cover the additional cost of the enhanced fan overhaul procedure. Based on the success of this initial demonstration, further tests on full-scale fans are currently being planned.

Note that as illustrated in Fig. 1, there is almost no loss of blade chord during this refurbishment and therefore future blade refurbishment is not impaired.

Acknowledgments

The author would like to thank Mr. James Justice of Delta Airlines and Dr. Anthony J. Strazisar of NASA-Lewis Research Center for their help during the preparation of this note.

References

Suder, K. L., Chima, R. V., Strazisar, A. J., and Roberts, W. B., 1995, "The Effect of Adding Roughness and Thickness to a Transonic Axial Compressor Rotor," ASME JOURNAL OF TURBOMACHINERY, Vol. 117, this issue, pp. 491–505.